Metabolic and Blood Flow Properties of Functional Brain Networks Using Human Multimodal Neuroimaging

Seyedeh Fatemeh Razavipour

A Thesis
In the Department
of
Physics

Presented in Partial Fulfillment of the Requirements
For the Degree of
Doctor of Philosophy (Physics) at
Concordia University
Montreal, Quebec, Canada

November 2022

CONCORDIA UNIVERSITY

SCHOOL OF GRADUATE STUDIES

This is to certify that the thesis prepared

By: Seyedeh Fatemeh Razavipour

Entitled: Metabolic and Blood Flow Properties of Functional Brain Networks Using Human

and submitted in partial fulfillment of the requirements for the degree of

Doctor Of Philosophy Physics

complies with the regulations of the University and meets the accepted standards with respect to originality and quality.

Signed by the final examining committee:

_____ Chair
Dr. Emily Coffey

_____ Thesis Supervisor
Dr. Christophe Grova

_____ Thesis Supervisor
Dr. Claudine Gauthier

_____ Thesis Supervisor
Dr. Christopher Steele

_____ Examiner
Dr. Habib Benali

_____ Examiner
Dr. Pablo Bianucci

_____ Examiner
Dr.

_____ Examiner
Dr.

_____ External Examiner
Dr. Bratislav Misic

Approved by _____
Dr. Pablo Bianucci , Graduate Program Director

«Date» _____
Dr. Pascale Sicotte , Dean

Abstract

Metabolic and Blood Flow Properties of Functional Brain Networks Using Human Multimodal Neuroimaging

Seyedeh Fatemeh Razavipour, Ph.D.
Concordia University, 2022

The brain has a high energetic cost to support neuronal activity, requiring both oxygen and glucose supply from the cerebral vascular system. Additionally, the brain functions through complex patterns of interconnectivity between neuronal assemblies giving rise to functional network architectures that can be investigated across multiple spatial scales. Different brain regions have different roles and importance within these network architectures, with some regions exhibiting more global importance by being involved in cross-network communication while other being predominantly involved in local connections. There are indications that regions exhibiting a more global role in inter networks connectivity are characterized by a higher and more efficient metabolic profile, leading to differences in metabolic properties when compared to more locally connected regions. Understanding the link between oxygen/glucose metabolism and functional features of brain network architectures, across different spatial scales, is of primary importance.

This thesis consists of three original studies combining human brain resting-state multimodal neuroimaging and transcriptional data to investigate the glucose/oxygen metabolic costs of brain functional connectivity. We quantified glucose metabolism from positron emission tomography, and oxygen metabolism and functional connectivity from magnetic resonance imaging. In the first study, we highlight how the oxygen/glucose metabolism of brain regions can non-linearly relate to their functional hubness, within the resting-state networks of the brain across a nested hierarchy. We found that an increase in oxygen/glucose metabolism is associated with a non-linear increase in functional hubness where increase rates are both network- and scale-dependent. In the second study, we show specific transcriptional signatures that characterize the oxygen/glucose metabolic costs of regions involved in network global versus local centrality. This study highlights the different metabolic profiles of local and global regions, with gene expression related to oxidative metabolism and synaptic pathways being enriched in association with spatial patterns in common with resting blood flow and metabolism (oxygen and glucose) and globally-connected regions. In the third study, we demonstrate that there are oxygen/glucose metabolic costs to the functional integration and segregation of resting-state networks. We highlight that the metabolic costs of functional integration could reflect the hierarchical organization of the brain from unimodal to transmodal regions.

Acknowledgements

My Ph.D. program was financially supported by the following research grants and bursaries: (i) *Fonds de recherche du Québec Nature et technologie — Research Team Support Program*, from Dr. C. Grova; (ii) *Canadian Institutes of Health Research*, from Dr. C. Grova; (iii) *Savoy Foundation* from Dr. C. Grova; (iv) *Heart and Stroke Foundation of Canada*, from Dr. C. Gauthier; (v) *Fonds de recherche du Québec Santé* — Doctoral Training Scholarship; (vi) *International Tuition Award of Excellence*, from Concordia University; (vii) *Graduate Fellowship*, from Physics Department in Faculty of Arts and Science of Concordia University.

I would like to express my gratitude to my supervisors Dr. Christophe Grova and Dr. Claudine Gauthier for their expertise, guidance, and support throughout this program. Special thanks also go to Dr. Habib Benali for his assistance and valuable comments at each stage of this program. I am also thankful to Dr. Bianucci for his encouragement.

I am grateful to the members of the Multimodal Functional Imaging and Quantitative Physiological Imaging Laboratories for their help and friendship.

Finally, I am deeply indebted to my family for their unwavering support and love.

Thank You All

Dedication

This thesis is dedicated to my parents.

Contribution of Authors

This thesis was authored by myself, under the supervision Dr. Christophe Grova and Dr. Claudine Gauthier. Together, we designed the studies, developed the methodologies, conducted the analyses, interpreted the results, and wrote the manuscripts. This present thesis consists of three original studies, in which the contributions of each co-author other than myself and my supervisors are summarized below. All data acquisitions were carried out by me, with the assistance of some co-authors as well as some members of the PERFORM Centre and the McConnell Brain Imaging Centre (special acknowledgments: Antonys Melek, Stephane Frenette, Dalia Sabra, Avner Fitterman, Ümit Aydin, and Michael Ferreira).

Manuscript 1: Multiresolution Metabolic Profile of Functional Hubness in the Resting Human Brain — [*in preparation for submission to Proceedings of the National Academy of Sciences journal*]

Authors: Seyedeh Fatemeh Razavipour, Obaï Bin Ka'b Ali, Kangjoo Lee, Stephan Grimault, Stephan Blinder, Jean-Paul Soucy, Claudine Gauthier, Christophe Grova

- Obaï Bin Ka'b Ali: designed and performed Bayesian analyses, assisted with data acquisitions, and contributed significantly on reviewing and editing the manuscript
- Dr. Kangjoo Lee: introduced SPARK pipeline, assisted with pilot data acquisitions and functional hubness investigations of pilot data, and contributed on reviewing the manuscript
- Dr. Stephan Grimault: assisted with the implementation of ASL sequences
- Dr. Stephan Blinder: assisted with PET data analyses
- Dr. Jean-Paul Soucy: assisted with the design of PET data acquisition and data analysis protocols, as well as overall interpretations of the results and contributed on reviewing the manuscript

Manuscript 2: Investigating the transcriptional profile of the blood flow and metabolic cost of functional global and local network connectivity — [*in preparation for submission to NeuroImage journal*]

Authors: Seyedeh Fatemeh Razavipour; Stephan Blinder; Boris Bernhardt, Christophe Grova, Claudine Gauthier

- Dr. Stephan Blinder: assisted with PET data analyses
- Dr. Boris Bernhardt: assisted with useful discussions on PLS analyses as well as overall interpretations of the results and contributed on reviewing the manuscript

Manuscript 3: Investigating the metabolic and blood flow costs of functional integration and segregation in resting-state networks — [*in preparation*]

Authors: Seyedeh Fatemeh Razavipour, Stephan Blinder, Jean-Paul Soucy, Claudine Gauthier, Christophe Grova

- Dr. Stephan Blinder: assisted with PET data analyses
- Dr. Jean-Paul Soucy: assisted with the design of PET data acquisition and data analysis protocols, as well as overall interpretations of the results and contributed on reviewing the manuscript

Table of Contents

List of Figures

network; DMnet_5: default mode network; BG_THAL_1: basal ganglia and thalamus; FPTCnet_7: frontoparietal task control network.

Figure 3.3 (A) Graphical posterior predictive checks. Red colors are the original observations (in the entire dataset), and blue ones are the predictions. To summarize the distribution of the data for every $\mathcal{H}$, we overlaid for each distribution four vertical lines with different thicknesses, to represent equal-tailed credible intervals at 50%, 80%, 95%, and 99%, from thickest to thinnest respectively. Blue shaded areas correspond to the credible intervals at 50%, 80% and 95%. Horizontal black lines are the median estimates. See also Figure 3.10, Figure 3.11, Figure 3.12, and Figure 3.13 for further detailed results . (B) Brain mappings of the estimated posterior median of scaling exponents within MIST7 and MIST20 for CMRGlc, $CMRO_2$, CBF, and OEF. The same set of two parasagittal slices in the left hemisphere (at -18.5, and -10.8 mm) is shown every time and highlights the cerebellum, amygdala, caudate, hippocampus, nucleus accumbens, pallidum, putamen, and thalamus. The color-bar is global for all figures.

Figure 3.4 Posterior summaries of scaling exponents within the whole brain, all the networks of MIST7 and four networks of MIST20. The colored vertical lines delimit the 89% highest density credible intervals of, and the black horizontal lines are the median of the estimated posteriors. The number on the left side of each vertical line indicates probability that the scaling exponent is between 0 and 1 (i.e., the probability of a concave down increasing power-law) and the corresponding text indicates an interpreted evidence ratio. A star symbol at the end of a text (i.e., when probabilities are less than 0.5) indicates that the interpreted evidence ratio applies to the alternative hypothesis (i.e., non-concave down increasing power-law). Note that the probability values reported here as 0.00 or 1.00 are not true zeros or ones. See also Figure 3.14. MIST labels are detailed in the text as well as in Table 3.2.

Figure 3.5 Posterior summaries of scaling differences between the networks of MIST7 for CMRGlc, $CMRO_2$, CBF, and OEF. The comparisons ROW $\geq$ COLUMN indicate that the difference was calculated between the posterior of ROW and COLUMN . Here we report comparisons only for the lower triangular. The color-bars are median estimates of posterior differences. The numbers on the upper diagonals give the lower (L) and upper (U) bounds of the 89% highest density credible intervals of the posterior differences. The size of each circle represents probability of direction (i.e., maximum between probability of positive difference and probability of negative difference), the horizontal tick marks on the top of each circle delimit probabilities of 0.5, 0.75, and 1, and a star symbol on the top-right of a circle indicate if the probability is greater than or equal to 0.89. The numbers on the diagonals summarize the lowest (L) and highest (U) probability of directions found on each row. Note that the probability values reported here as 1.00 are not true ones. See also Figure 3.15, Figure 3.16, Figure 3.17, and Figure 3.18. MIST labels are detailed in Table 3.2.

Figure 3.6 Posterior summaries of scaling differences between responses within the whole brain, all the networks of MIST7 and four networks of MIST20. The colored vertical lines delimit the 89% highest density credible intervals of, and the black horizontal lines are the median of the estimated posteriors. The number on the left side of each vertical line indicates probability of positive difference and the corresponding text indicates an interpreted evidence ratio. A star symbol at the end of a text (i.e., when probabilities are less than 0.5) indicates that the interpreted evidence ratio applies to the hypothesis of negative difference instead of positive. Note that the probability values reported here as 0.00 or 1.00 are not true zeros or ones. See also Figure 3.19. The labels of MIST20 are detailed in Table 3.2.

equal-tailed credible intervals at 50%, 80%, 95%, and 99%, from thickest to thinnest in that order. Red colors are the original observations, and blue ones are predictions. Blue shaded areas correspond to the credible intervals at 50%, 80% and 95%. Horizontal black lines are the median estimates. The ordering of the tiles from left to right, then top to bottom, is such that the networks of MIST7 are directly followed by their (network) children in MIST20. The labels of MIST7 and MIST20 are detailed in Table 3.2. These figures suggest well behaved fits and illustrate how partial pooling operated.

Figure 3.14 Posterior summaries of scaling exponents within the networks of MIST20 for CMRGlc, $CMRO_2$, CBF, and OEF. The colored vertical lines delimit the 89% highest density credible intervals of, and the black horizontal lines are the median of the estimated posteriors. The number on the left side of each vertical line indicates probability that the scaling exponent is between 0 and 1 (i.e., the probability of a concave down increasing power-law) and the corresponding text indicates an interpreted evidence ratio. A star symbol at the end of a text (i.e., when probabilities are less than 0.5) indicates that the interpreted evidence ratio applies to the alternative hypothesis (i.e., non-concave down increasing power-law model). Note that the probability values reported here as 0.00 or 1.00 are not true zeros or ones. The labels of MIST20 are detailed in Table 3.2.

Figure 3.15 Posterior summaries of scaling differences between the networks of MIST20 for CMRGlc. The comparisons $ROW \geq$ COLUMN indicate that the difference was calculated between the posterior of ROW and $COLUMN$. Here we report comparisons only for the lower triangular. The color-bars are median estimates of posterior differences. The numbers on the upper diagonals give the lower (L) and upper (U) bounds of the 89% highest density credible intervals of the posterior differences. The size of each circle represents probability of direction (i.e., maximum between probability of positive difference and probability of negative difference), the horizontal tick marks on the top of each circle delimit probabilities of 0.5, 0.75, and 1, and a star symbol on the top-right of a circle indicate if the probability is greater than or equal to 0.89. The numbers on the diagonals summarize the lowest (L) and highest (U) probability of directions found on each row. Note that the probability values reported here as 1.00 are not true ones. The labels of MIST20 are detailed in Table 3.2. This figure provides evidence of the existence of scaling differences between networks.

Figure 3.16 Posterior summaries of scaling differences between the networks of MIST20 for $CMRO_2$. The comparisons $ROW \geq$ COLUMN indicate that the difference was calculated between the posterior of ROW and $COLUMN$. Here we report comparisons only for the lower triangular. The color-bars are median estimates of posterior differences. The numbers on the upper diagonals give the lower (L) and upper (U) bounds of the 89% highest density credible intervals of the posterior differences. The size of each circle represents probability of direction (i.e., maximum between probability of positive difference and probability of negative difference), the horizontal tick marks on the top of each circle delimit probabilities of 0.5, 0.75, and 1, and a star symbol on the top-right of a circle indicate if the probability is greater than or equal to 0.89. The numbers on the diagonals summarize the lowest (L) and highest (U) probability of directions found on each row. Note that the probability values reported here as 1.00 are not true ones. The labels of MIST20 are detailed in Table 3.2. This figure provides evidence of the existence of scaling differences between networks.

Figure 3.17 Posterior summaries of scaling differences between the networks of MIST20 for CBF. The comparisons $ROW \geq$ COLUMN indicate that the difference was calculated between the posterior of ROW and $COLUMN$. Here we report comparisons only for the lower triangular. The

color-bars are median estimates of posterior differences. The numbers on the upper diagonals give the lower (L) and upper (U) bounds of the 89% highest density credible intervals of the posterior differences. The size of each circle represents probability of direction (i.e., maximum between probability of positive difference and probability of negative difference), the horizontal tick marks on the top of each circle delimit probabilities of 0.5, 0.75, and 1, and a star symbol on the top-right of a circle indicate if the probability is greater than or equal to 0.89. The numbers on the diagonals summarize the lowest (L) and highest (U) probability of directions found on each row. Note that the probability values reported here as 1.00 are not true ones. The labels of MIST20 are detailed in Table 3.2. This figure provides evidence of the existence of scaling differences between networks.

Figure 3.18 Posterior summaries of scaling differences between the networks of MIST20 for OEF. The comparisons $ROW \geq$ COLUMN indicate that the difference was calculated between the posterior of ROW and $COLUMN$. Here we report comparisons only for the lower triangular. The color-bars are median estimates of posterior differences. The numbers on the upper diagonals indicate the lower (L) and upper (U) bounds of the 89% highest density credible intervals of the posterior differences. The size of each circle represents probability of direction (i.e., maximum between probability of positive difference and probability of negative difference), the horizontal tick marks on the top of each circle delimit probabilities of 0.5, 0.75, and 1, and a star symbol on the top-right of a circle indicate if the probability is greater than or equal to 0.89. The numbers on the diagonals summarize the lowest (L) and highest (U) probability of directions found on each row. Note that the probability values reported here as 1.00 are not true ones. The labels of MIST20 are detailed in Table 3.2. This figure provides evidence of the existence of scaling differences between networks.

Figure 3.19 Posterior summaries of scaling differences between CMRGlc, $CMRO_2$, CBF, and OEF within the networks of MIST20. The colored vertical lines delimit the 89% highest density credible intervals of, and the black horizontal lines are the median of the estimated posteriors. The number on the left side of each vertical line indicates probability of positive difference and the corresponding text indicates an interpreted evidence ratio. A star symbol at the end of a text (i.e., when probabilities are less than 0.5) indicates that the interpreted evidence ratio applies to the hypothesis of negative difference instead of positive. Note that the probability values reported here as 0.00 or 1.00 are not true zeros or ones. The labels of MIST20 are detailed in Table 3.2. This figure provides evidence of the existence of scaling differences between CMRGlc, $CMRO_2$, CBF, and OEF.

Figure 4.1. Resting-state neuroimaging data derivatives. a. Average physio-metabolic (CMRGlc, $CMRO_2$, CBF, and CVR) and network centrality (GE, EC, LE, CC) brain maps estimated from 20 subjects. Data are shown for the left cerebral cortex only and projected on a semi-inflated (25%) mid-surface of the ICBM 2009c asymmetric brain template. Regional values were defined using the Schaefer 2018 7 networks atlas with 100 parcels in the left hemisphere. b. Pearson's linear correlation coefficients between neuroimaging brain maps. The * symbol indicates two-tailed p-values smaller than 0.05. CMRGlc: cerebral metabolic rate of glucose; $CMRO_2$: cerebral metabolic rate of dioxygen; CBF: cerebral blood flow; CVR: cerebrovascular reactivity; GE: global efficiency; EC: eigenvector centrality; LE: local efficiency; CC: clustering coefficient.

Figure 4.2. Relating gene expression to resting-state neuroimaging data. PLS analysis was used to identify spatially covarying patterns of gene expression and neuroimaging biomarkers. a. Latent variables effect sizes (i.e., percentage of covariance explained between gene expression and neuroimaging data). A triangle on the top indicates right-tailed p-values smaller than 0.05 as

obtained from spatial autocorrelation-preserving permutation testing. The box charts are the permuted effect sizes and represent median (line inside a box), 0.25 and 0.75 quantiles (bottom and top edges of a box, the distance between which is called interquartile range), outliers (defined as values away from the bottom or top of the box more than 150% the interquartile range), and nonoutlier minimum and maximum (bottom and top whiskers of a box). Note that significance is assessed on eigenvalue distributions and not effect size distributions. b. Neuroimaging loadings with respect to the pattern of gene scores for a particular latent variable are calculated as the Pearson's linear correlation coefficient between neuroimaging brain maps (indicated on the rows) and the PLS-derived pattern of gene scores for that latent variable. Latent variables are indicated on the columns by a number and ordered according to their accounted percentage of data covariance explained from highest to lowest. A * symbol indicates bootstrap-estimated 95% confidence intervals not including zero (i.e., reliable loadings). c. Latent variables gene and neuroimaging score distributions for the first three latent variables.

Figure 4.3. Enrichment analysis of the genes of latent variable 1 with highest (50%) positive loadings. A subset of significantly (i.e., positive false discovery rate smaller than 0.05) enriched gene ontologies (GOs) is shown. a. GO biological processes. b. GO pathways.

Figure 4.4. Enrichment analysis of the genes of latent variable 2 with highest (50%) negative loadings. A subset of significantly (i.e., positive false discovery rate smaller than 0.05) enriched gene ontologies (GOs) is shown. a. GO biological processes. b. GO pathways.

Figure 4.5. Enrichment analysis of the genes of latent variable 3 with highest (50%) negative loadings. A subset of significantly (i.e., positive false discovery rate smaller than 0.05) enriched gene ontologies (GOs) is shown. a. GO biological processes. b. GO pathways.

Figure 4.6. Cell-types deconvolution. The ratio of genes preferentially expressed in seven cell types is shown for the genes of latent variable 1 (a.), latent variable 2 (b.), and latent variable 3 (c.), using their highest (50%) positive (red) or negative (blue) loadings. A triangle on the top indicates positive false discovery rates smaller than 0.05 (i.e., significant ratios) as obtained from bootstrap resampling. The box charts are the null ratios and represent median (line inside a box), 0.25 and 0.75 quantiles (bottom and top edges of a box, the distance between which is called interquartile range), outliers (defined as values away from the bottom or top of the box more than 150% the interquartile range), and nonoutlier minimum and maximum (bottom and top whiskers of a box). Astro: astrocyte; micro: microglia; oligo-p: oligodendrocyte precursor; oligo: oligodendrocyte; endo: endothelial cells; neuron-e: excitatory neurons; neuron-i: inhibitory neurons.

Figure 4.7. Neuroimaging loadings with respect to neuroimaging scores. Neuroimaging loadings with respect to the neuroimaging scores of a particular latent variable are calculated as the Pearson's linear correlation coefficient between neuroimaging brain maps (indicated on the rows) and the PLS-derived pattern of neuroimaging scores for that latent variable. Latent variables are indicated on the columns by a number and ordered according to their accounted percentage of data covariance explained from highest to lowest. A * symbol indicates bootstrap-estimated 95% confidence intervals not including zero (i.e., reliable loadings). A high loading in absolute magnitude indicates that a particular neuroimaging biomarker highly contributes to the PLS-derived pattern of neuroimaging scores. We can observe how the first latent variable possessed (global) features of almost all neuroimaging biomarkers (except EC) whereas the other latent variables distinguished between different sets of neuroimaging biomarkers (e.g., the second latent variable distinguished between physio-metabolic and global centralities on one side, and local centralities on the other side).

direction of the first component is indicated by the solid line while the direction of the second component is indicated by the dash-dotted line. We understand here that the signed distance mapping with respect to the line of best fit can capture the same qualitative information as the score mapping along the second principal component. Indeed, in the PCA plane, scores along the second principal component are y-coordinates. Similarly, the signed distance mapping with respect to a line perpendicular to the line of best fit that passes though the center of the point cloud can capture the same qualitative information as the score mapping along the first principal component.

Figure 6.1. Aerobic glycolysis using glycolytic index (GI). (A) Voxel wise linear regression of CMRGlc on $CMRO_2$. GI is defined as the residuals of the linear regression scaled by 1000. (B) Distribution of aerobic glycolysis in resting human brain using GI (number of subjects = 33, groupwise t-test, $|Z|>4.4$, $P < 0.0001$). Figure adapted from (Vaishnavi et al., 2010)

List of Tables

Introduction

The brain is a complex organ exhibiting a multi-scale spatiotemporal functional organization shaped by networks of interacting neuronal units. The neuronal synaptic and non-synaptic connections at the molecular and micro-scale levels connect together to form polyfunctional neuronal circuits, cortical layers and columns at the mesoscale and regional levels. At the mesoscopic scale, brain regions composed of locally segregated neuronal populations with similar structural and functional properties tend to cluster together, shaping specialized communities or modules, that are connected at distance by the so-called hub regions. Hub regions have diverse connectional fingerprints and underlie the global integration of functional activity across brain regions. They have a crucial role in building integrative networks and systems at the macroscale to support perception, cognition, and action.

Network neuroscience aims at understanding the organizational features of neuronal networks to understand cortical functions and the role of functional units at different scales. In graph theory, networks are described as nodes, defined for a specific scale of interest (e.g., neurons, regions, networks), and edges characterizing functional (or structural) connections. Measuring the statistical associations between time courses of nodes reveals the Functional connectivity (FC) between distant brain regions or brain networks (Fornito et al., 2016). Functional magnetic resonance imaging (fMRI) monitoring slow hemodynamic processes within the whole using the blood-oxygenation level-dependent (BOLD) contrast, can be considered to investigate this network organization. The BOLD signal is mainly sensitive to local fluctuations of deoxyhemoglobin concentrations and changes in cerebral blood flow and volume, elicited by changes in neuronal bioelectrical activity through neurovascular coupling processes (Gauthier & Fan, 2019; E. M. C. Hillman, 2014) . Therefore, fMRI allows assessing whole brain activity, as an indirect but sensitive non-invasive neuroimaging technique, a key methodology to characterize brain networks (Glover, 2011; Kim et al., 2021).

In their seminal study published 1995, Biswal and colleagues used resting state-fMRI (RS-fMRI), i.e. fMRI acquisition “at rest” without any explicit task or stimulus, to first describe resting-state FC (Biswal et al., 1995), demonstrating for the first time similar spatio-temporal correlation structure of BOLD signals in the motor network, during rest and during a motor task. RS-fMRI signal captures spontaneous slow fluctuations of the baseline hemodynamic state of the brain. About a decade later, several RS-fMRI studies demonstrated the stability of RS networks within a healthy control group (Biswal et al., 1995; De Luca et al., 2006; Salvador et al., 2005; M. P. van den Heuvel et al., 2008). Brain networks measured using RS-fMRI have been characterized by specific alterations in the context of several neurological or psychiatric conditions, such as Alzheimer’s disease, epilepsy, and schizophrenia (Cataldi et al., 2013; Garrity et al., 2007; Greicius & Menon, 2004; Rombouts et al., 2005; Sorg et al., 2007; Whitfield-Gabrieli, 2009).

Neuronal activity is also metabolically expensive. While there are no significant local energy reserves in the brain, its metabolic expenditure accounts for nearly 20% of whole-body oxygen and glucose usage. Hence, neuronal cells require tight interactions with complex network of glial cells and the vascular system to receive metabolic substrates and remove waste and metabolic by-products (Bélanger & Magistretti, 2022; Ioannou et al., 2019; Kugler et al., 2021).

The topological organization of brain network, featuring underlying functional segregation and integration properties, relies on a balance between minimizing the resource cost (ensuring short

path length connections) and meanwhile maximizing the flow of information among the different networks (through few long-range connections) (Bassett & Bullmore, 2017; M. Lin et al., 2013; Meunier et al., 2010; Samu et al., 2014). Tomasi et al (D. Tomasi et al., 2013) were among the first to investigate the relationship between the topological features of brain networks and metabolism, suggesting a non-linear relationship between glucose metabolism and hubness measured using degree centrality graph theoretical metric. Degree centrality reflects the number of connections per region and such non-linear relationship with metabolism was reported to follow a power law function, suggesting high glucose metabolic efficiency in long-range hub regions (D. Tomasi et al., 2013) and indicate a higher metabolic cost for hubs. This finding was also consistent with other MRI-based and PET results showing a significant correlation between functional connectivity strength and CBF both at the whole brain scale and across networks (Hubbard et al., 2021; Leontiev et al., 2013; Tak et al., 2015), as well as with CMRGlc (Palombit et al., 2022). In another study, (Shokri-Kojori et al., 2019) measured synchrony between energy utilization and brain activity, using PET and fMRI data, reporting agreement between energy utilization and brain activity within the medial-visual and default-mode networks, while energy utilization exceeded brain activity within the frontoparietal network.

The molecular and biological processes and metabolic pathways that form the basis brain activity and network dynamics happen at the cellular level. However, the exact mechanisms that underlie the BOLD signal and macroscopic hemodynamic responses captured by fMRI are not also fully understood. A new opportunity to explore the link between microscale and macroscale brain mechanisms is to use human brain transcriptional data to explore the links between neuroimaging and gene expression information at the cellular scale (Colantuoni et al., 2011; Fornito et al., 2019; M. J. Hawrylycz et al., 2012; Kang et al., 2011; Keil et al., 2018; M. Li et al., 2018). Since the emergence of neuroimaging-genetics, several studies have investigated the transcriptional signatures associated with brain functional connectivity properties (Berto et al., 2022; Fulcher & Fornito, 2016; M. Hawrylycz et al., 2015; Shen et al., 2022; Vértes et al., 2016; Z. Yang et al., 2016). Hawrylycz et al (2012) showed that highly connected brain regions are located within the areas that have the highest physiological and genetic signatures for learning, cognition, and memory tasks (M. J. Hawrylycz et al., 2012). When combining genetic neuroimaging and cell types analysis, another study suggested that cell types with genetically similar signatures tend to connect to each other, despite physical distance (Arnatkevičiūtė et al., 2019). In their study, Fulcher & Fornito (2016) reported that hub regions were distinctive in terms of metabolic pathways assessed through transcriptional data analysis(Fulcher & Fornito, 2016), paving the way for the work presented in this PhD thesis.

Given the suspected metabolic uniqueness of brain regions or networks depending on their functional attributes, the main purpose of this thesis is to investigate the glucose/oxygen metabolic costs associated with resting-state brain functional connectivities across different spatial resolutions. To do so, we considered two types of neuroimaging modalities: PET and MRI we acquired at our centre, the PERFORM centre of Concordia University. We also considered an atlas of human brain transcriptional data to characterize the genetic signature or our proposed metabolic and network measures. PET data were used to estimate brain maps of glucose consumption CMRGlc, while calibrated MRI data, acquired with breathing gas manipulations, were used to

estimate brain maps of baseline $CMRO_2$, CBF, OEF and CVR on the one hand, and measures of resting-state brain functional connectivity characteristic at the voxel, regional, and network levels on the other hand.

In our first study, we promoted the use of a new sparse decomposition method to reliably estimate functional hubness at the voxel level (indicating a discrete number of networks a specific voxel is associated with) developed in our laboratory (K. Lee et al., 2016). We characterize the relationship between such discrete measures of functional hubness with glucose/oxygen metabolic costs, within known large-scale resting-state networks. Such detailed analysis was developed using an original hierarchical Bayesian model to carefully take into account all sources of variability in the data. In the second project, we proposed an original investigation of regional-based measures of network local/global properties (reflecting characteristics of functional integration and segregation) and spatial profiles of metabolic/hemodynamic patterns (glucose, oxygen, CBF, CVR) to assess how they covary with their underlying genetic, molecular, and cellular determinants, provided by an atlas of human brain transcriptional data. In our third project, we compared a promising network-level hierarchical measure of functional information integration (assessing the amount of shared informational content within and between brain networks) (Marrelec et al., 2008) with glucose/oxygen costs, assessing the metabolic cost of functional integration within and between large-scale resting-state networks.

This thesis is organized as follows: Chapter 1 to Chapter 2 are state-of-the-art chapters reviewing essential background information

Chapter 1 introduces the basics of the central nervous system, which includes the main cerebral cell types involved in shaping brain functional activity. We then describe what are the main metabolic substrates used by the brain, as well as some complementary energy substrates and their pathways. Finally, we present how neuroimaging techniques can be considered to explore those physio-metabolic properties of the normal brain.

Chapter 2 presents the functional and topological organization of the brain along three spatial scales: the microscale (molecular, cells level), the mesoscale (brain region level) and the macroscale (brain networks level). In the second part of the chapter, we are reviewing what methodologies have been proposed, using graph theory and other complementary methods, to characterize resting-state functional networks and notably their connector hubs.

We are then presenting three manuscripts, Chapters 3, 4 and 5, which are then detailed, forming the main original contributions of this thesis.

Chapter 3 — Multiresolution Metabolic Profile of Functional Hubness in the Resting Human Brain presents our work on the relationship between oxygen and glucose metabolism and functional hubness at rest, within the normal brain. We used RS- fMRI to quantify brain maps of functional hubness using sparsity-based general linear model analysis, offering a unique way to assess in a reliable manner connector hubness at the voxel level (K. Lee et al., 2011, 2016, 2022). To measure brain metabolism, we considered calibrated fMRI to provide an absolute estimation of baseline oxygen metabolism and FDG-PET to estimate the brain maps of glucose metabolism. In this original study, we proposed a multiscale spatial analysis of the oxygen and glucose

metabolism profile of functional hubness in the resting healthy human brain, promoting the use of a hierarchical Bayesian model to take into account variability in the data. Using our proposed Bayesian model, we highlighted the ways functional hubness relates to oxygen and glucose metabolism within the known large-scale resting-state networks of the brain across several levels of spatial resolutions. Our results further demonstrated that an increase in hubness, measured using discrete sparse techniques, was associated with a network-dependent non-linear increase in metabolism, suggesting that connector hubs are efficient in terms of oxygen/glucose metabolism.

Chapter 4 — Investigating the transcriptional profile of the blood flow and metabolic costs of functional global and local network connectivity presents our work on the association between neuroimaging metabolic/hemodynamic data and functional network features with micro-scale human brain gene expression data, extracted from an atlas of human brain transcriptional data. Such multivariate comparison of high dimensionality dataset was done using partial least squares modelling (Krishnan et al., 2011). In this study, we investigated the transcriptional profile underpinning the spatial architectures shared between the spatial profiles of oxygen/glucose metabolism, CBF and CVR, and graph-theoretical-based measures of functional local/global network centralities. Our results are suggesting that centrally-connected brain regions, associated with a high metabolic cost, are associated with greater expression of genes involved in synaptic pathways and oxidative metabolism.

Chapter 5 — Investigating the metabolic and blood flow costs of functional integration and segregation in resting-state networks presents our work investigating the relationship between glucose/metabolism of brain networks and a measure of functional information integration. We employed a hierarchical integration measure to estimate within- and between-functional integration among networks at two spatial resolutions, describing the brain as a combination of 7 17 consistent resting state networks (Eickhoff et al., 2018; Marrelec et al., 2008). Our results suggest that the glucose/oxygen metabolic costs of functional information integration reflect the hierarchical organization of the brain from primary sensorimotor (or unimodal) to polysensory association (or transmodal) areas.

Chapter 6 concludes this thesis with a detailed general discussion of the main results, contributions, limitations, and perspectives of our proposed studies.

Chapter 1: Brain energy metabolism

This chapter will introduce the basics of the metabolic demands associated with brain neuronal activity, starting from the cellular level. We will also introduce the main neuroimaging techniques we considered in this thesis to measure neuronal and metabolic features of brain activity. First, we are describing the main cell types and neuro-physiological processes that shape brain functional activity, from the cellular resolution. Then, we summarize the main metabolic pathways that support brain neuronal activity. Finally, after introducing the bio-physical and methodological background of the main neuroimaging techniques considered in this thesis, we reviewed the spatial variation of the main physio-metabolic features of brain activity at rest in the normal, healthy adult brain.

1.1 Basics of central nervous system

Our nervous system is composed of the central nervous system (CNS) and the peripheral nervous system (PNS). The CNS itself is also composed of the brain, the spinal cord and the cranial nerves that are originated from the brain and are responsible for controlling different activities such as smell, visual activity, eye movements, or facial sensations. The brain nervous system is made up of mainly two types of cells: neurons and glial cells(J. Zhang, 2019).

1.1.1 Neurons

Neurons are the primary functional units of the nervous system. They transmit information by generating electrical signals called action potentials. The neuron cell body is called the soma, where the nucleus of the cell is located and where most protein synthesis is taking place. The body of the neurons is composed of various branched appendages: some are short branches known as dendrites and the others are long extensions called axons (Figure 1.1). Signal reception and integration occur within the dendrites and cell bodies of the neurons. Excitatory signals cause neurons to generate an electrical impulse (through depolarization of membrane potential), and inhibitory signals repress electrical signal firing (through hyperpolarization of membrane potential). The inhibitory and excitatory state of a neuron depends on the summation of thousands of input signals received and integrated throughout its dendrites. When this summation leads to neuronal firing, the neuron produces an action potential which propagates along the axon (Nicholls et al., 2001; Rye et al., 2013). Action potentials are initiated at the axon hillock where the axon connects to the cell body. At the end of the axon, the branches end up into many bulbous ridges known as axon terminals (or nerve terminals) where neurons connect with target cells (Kandel et al., 1995). The detail steps of the action potential process will be discussed below subsections. Neurons can be classified according to their shape: Multipolar, Unipolar, bipolar, and Pseudo-unipolar neurons. However, neurons differ from one another structurally, functionally, and genetically, as well as in how they form connections with other cells. It is therefore difficult to recognize and categorize every single type of neuron since even in small brain areas multiple types of neurons exist (Bentivoglio, 1998). For example, in the cerebellum, we can find Golgi cells, Lugaro cells, and Purkinje cells, which have a highly complex dendritic tree that allows them to receive – and integrate – an enormous number of synaptic inputs, basket cells, Cerebellum candelabrum cells, etc. (Figure 1.2). (Mazzarello, 1999). A single neuron cannot do much in isolation, since the functions of the nervous system rely on collections of neurons working together. To support these functions, singular neurons connect to others allowing neuronal networks to support or inhibit brain activity, to transmit or to process information (A. B. Byrne et al., 2016; Davidoff, 1977; Kandel et al., 1995; Matthews, 1976)

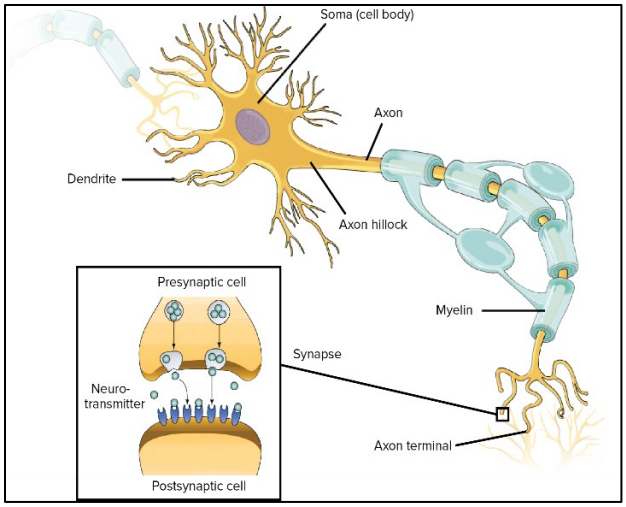

Figure 1.1 Pictorial representation of structure of a neuron and intercellular communication. Figure adapted from (Young et al., 2016).

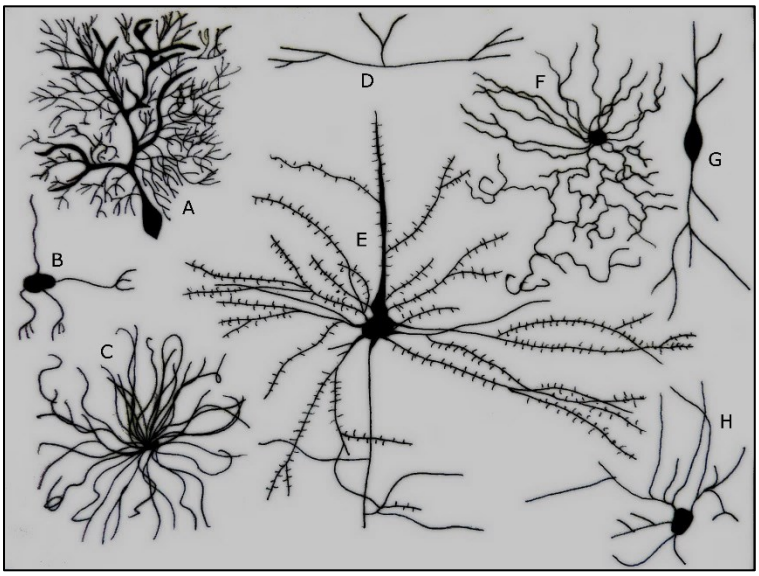

Figure 1.2 Different types of neurons. A: Purkinje cell; B: granule cell; C: motor neuron; D: tripolar neuron; E: pyramidal cell; F: chandelier cell; G: spindle neuron; H: stellate cell. Figure credit: Ferris Jabr; based on reconstructions and drawings by Cajal (y Cajal, 1995).

1.1.2 Glial cells

Glial cells are more numerous than neurons and are mainly responsible for providing protection and support for the neurons' functions by maintaining cell homeostasis, removing debris, forming myelin, providing metabolites etc. There are six main types of glial cells in the nervous system: Microglia, Oligodendrocytes, Schwann, Satellite glial, Ependymal cells, and Astrocytes (D. Purves et al., 2001).

Microglia cells are related to the immune system and Oligodendrocytes and Schwann cells produce myelin, insulating the axons and allowing faster propagation of neuronal activity. Satellite cells cover the surface of nerve cell bodies in some ganglia. Ependymal cells, which cover the ventricles of the brain and the central canal of the spinal cord and have hairlike cilia that help the circulation

of cerebrospinal fluid. Astrocytes are the most numerous types of glial cells in the brain and play an important role in both functionality and maintenance within the nervous system (Bergles et al., 2010; Hanani, 2005; Simon et al., 2016). Astrocytes often have few branches that are highly branched, leading to their being named "star cells". At the end of their processes, they have special structures called end-feet. Astrocytes have several functions, possibly more functions than any other cell type in the nervous system. Astrocytes form a scaffold for the entire CNS and occupy a large proportion of CNS space, constituting most of the structure that builds up the brain and spinal cord. Astrocytes also play a critical role in ensuring energy homeostasis (D. Purves et al., 2001; Verkhratsky & Nedergaard, 2018). Astrocytes contribute to providing one of the key metabolic substrates, called lactate to neurons. In addition, while neurons have no way to store energy, astrocytes are essential to store small amounts of energy in the form of glycogen which can be converted to lactate when neurons lack access to oxygen and glucose. Astrocytes also contribute to the blood-brain barrier (BBB), which is the barrier that prevents large molecules from the bloodstream to enter the CNS, unless these molecules are transported using specific transporters. Components of the blood vessel themselves are the main components of the blood-brain barrier, but astrocytic end-feet are plastered all over cerebral blood vessels and therefore contribute to the BBB. Finally, astrocytes play a role in neuronal communication by clearing out synapses. Astrocytes extend their processes and end-feet all over the synapses so that the end-feet plaster the synapses to clear out neurotransmitter molecules released by the synapse for communication (Eddleston & Mucke, 1993; Heller & Sadava, 2009; Rye et al., 2013).

1.1.3 Vascular cells

The vascular system in the brain has particular interaction with both glial and neuronal cells. Blood vessels not just deliver essential nutrients, but also remove metabolic waste products from the brain parenchyma (Zlokovic, 2011).

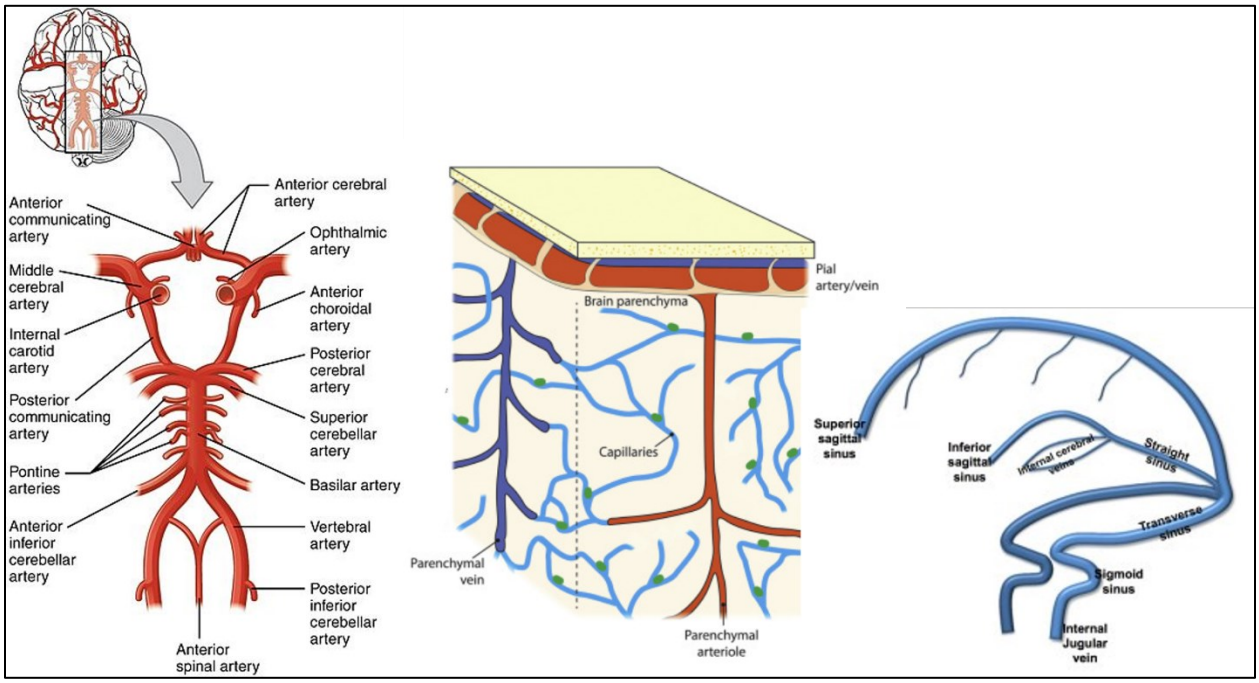

Figure 1.3 Anatomy of the cerebrovascular tree of the brain. Left: circle of Willis; Middle: pial arteries carry blood across the brain surface and penetrate orthogonally into the parenchyma; Right: cerebral venous system components.

Figure adapted from (Anna Chruścik, Kate Kauter, Louisa Windus, 2013; Garcia & Longden, 2020; Thorell et al., 2015)

The cerebral circulation of the brain from the neck starts with two branches: the internal carotid (ICA) and vertebral arteries. The vertebral arteries branch provides blood to the posterior cerebrum, the cerebellum as well as the brain stem, and joins the ICA to form the basilar artery (Cipolla, 2009). ICA enters the skull and supplies the anterior cerebrum and merges with branches of the vertebral arteries forming an arterial ring known as the circle of Willis at the base of the brain. The circle of Willis branches into the posterior, middle, and anterior cerebral arteries, each supplying different regions of the cerebral cortex (D. Purves et al., 2001) (Figure 1.3). A large artery that branches from the circle of Willis called the middle cerebral artery, makes the heavily interconnected network of pial arteries and arterioles on the cortex's surface. The pial arteries are highly branched and form a collateral network that is extrinsically innervated by the peripheral nervous system (Coulson et al., 2004). From the Pial arteries, parenchymal arterioles penetrate orthogonally into the brain. Penetrating arterioles dive toward the white matter, in turn giving rise to the capillary bed, a vast surface area where blood is exchanged between brain cells and the vascular system (Zlokovic, 2011) (Figure 1.3). The capillaries return blood to the venules which further converge to form the brain's surface pial veins. Large cortical veins within the subarachnoid space ultimately connect to venous sinuses contained within the dura mater and large cerebral venous that return the blood to the heart (Cipolla, 2009; Garcia & Longden, 2020). In summary, the venous system includes the cerebral veins, the dural sinuses, the meningeal veins, and the posterior fossa veins (Kiliç & Akakin, 2008). The cerebral veins are divided into internal or external cerebral veins. The external veins consist of the cortical veins and the sagittal sinuses which drain the superficial surfaces of the cerebral hemispheres, and the internal veins include the straight sinus, transverse sinus and sigmoid sinus (SS) as well as draining the deeper cortical veins (Figure 1.3).

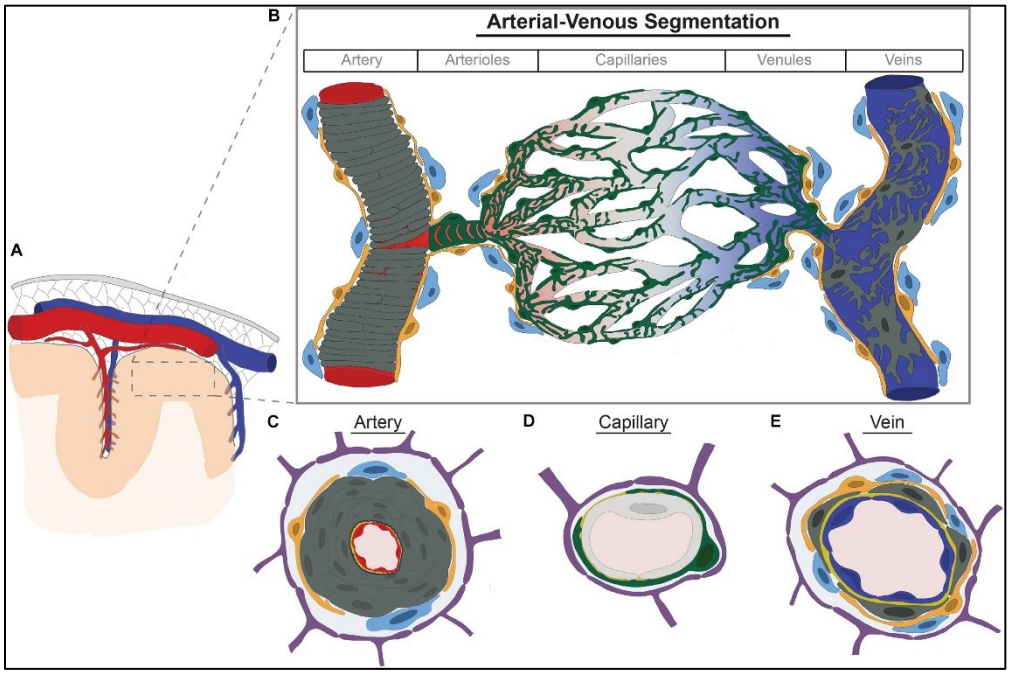

Figure 1.4. Brain vascular cell diversity along the arterial-venous axis. (A) Large arteries (red) and cortical veins 0(blue) pass through the subarachnoid space (gray mesh) inside the dura mater (gray). (B) Each vessel along the

arterial-venous mesh includes of different cell types: endothelial cell (shown in red in artery, gray in capillary, and blue in vein), vascular smooth muscle cells (dark gray), pericytes (green), perivascular fibroblasts (yellow), and perivascular macrophages (light blue). (C, D, E) Different vessel compartments: artery, capillary, and vein. Figure adapted from (Ross et al., 2020)

Blood vessels are composed of three layers: the tunica intima, tunica media and tunica adventitia, and are composed of three types of cells. The first type of cells is Endothelial cells, building the innermost tunica intima layer and lining the luminal and inner wall of the vessels. The second type of cells is smooth muscle cells (SMCs) that circumferentially envelop the surface of the vascular tube to make up the tunica media layer of all vessels except capillaries (Bergers & Song, 2005; Iadecola, 2017). More recently two types of cells called perivascular macrophages (PVMs) and perivascular fibroblast-like cells (PVFBs), are also defined that reside within the tunica adventitia layer (Saunders et al., 2018; Vanlandewijck et al., 2018; Zeisel et al., 2015). Capillaries are not lined with SMCs instead have a discontinuous layer of the third type of vessel cells called pericytes (Schaeffer & Iadecola, 2021). The outermost and supportive layer of blood vessels, tunica adventitia, is primarily composed of fibroblasts, extracellular matrix (ECM) and progenitor cells. The SMCs and pericytes are collectively referred to as mural cells and have a crucial role in the regulation of blood pressure, control of blood distribution and providing structural support and integrity to the vessel wall (A. Lin et al., 2021; Zhuge et al., 2020). In addition to these cell types, Astrocyte end-foot twist around the outer layer of vessels and create the Virchow Robin space a perivascular space that is important for brain interstitial fluid and cerebrospinal fluid exchange and called “glymphatic system” (Wardlaw et al., 2020).

The Endothelial cells are key constituents of the heavily restricting brain vascular barrier, the BBB. BBB tightly regulates brain parenchyma homeostasis, prevents it from the influx of toxins, plasma proteins, and pathogens, protects it from inflammation, injury, and disease, and still meets its dynamic metabolic needs, permits regulated molecular transport (Daneman & Prat, 2015; Sweeney et al., 2019). In general, BBB allows gases, e.g., carbon dioxide and oxygen, lipophilic and other molecules that are smaller than 400 Da and prevents other substrates to cross the vessel layers without regulated transport systems (Banks, 2009; Sweeney et al., 2019). Across most of the brain regions, BBB is continuous without any cessation (Sweeney et al., 2019; Z. Zhao et al., 2015), while in some regions like choroid-plexus and subfornical organ it contains intracellular pores and has high permeability (Ghersi-Egea et al., 2018). Breakdown of Endothelial cells has been implicated in age-related neurodegeneration disorders, cerebral blood flow reduction, toxic factors leakage, and disruption of brain hemostasis and neuronal dysfunction (Bell et al., 2012; Iadecola, 2017; Zlokovic, 2008).

The mural cells, a term referring to SMCs and PCs, face the most variation among vascular cell types across the vasculature compartment and along the arterial-venous axis (Winkler et al., 2011); Figure 1.4B–E). While in larger arteries (diameters> 100 μm), the SMCs are continuous and shape concentric rings, in smaller arteries and arterioles, they become discontinuous cells with rod-like processes ((Iadecola, 2017; Shiraishi et al., 1986); Figure 1.4C–D) and in venules and veins, SMCs remain discontinuous with stellate configuration ((Hill et al., 2015; Smyth et al., 2018; Vanlandewijck et al., 2018); Figure 1.4E). Within pre-capillary arterioles, SMC cells are responsible for regional blood perfusion regulation and coupling with neural activity (Fernández-Klett et al., 2010; Hill et al., 2015; Kisler et al., 2017). They have receptors for numerous vasoactive molecules, such as adenosine, prostaglandins and flow-related stimuli and hence largely

contribute regulation and autoregulation of cerebral blood flow (He et al., 2016; Kisler et al., 2017; Koller & Toth, 2012)

As the vessel gets smaller, the SMCs discretely transit to PCs cells or different compositions, including ensheathing PCs, pre-capillary PCs, vSMC-PCs hybrids, or precapillary SMCs (Uemura et al., 2020). Various morphologic heterogeneity also has been suggested for PCs cells across brain regions and different vessel compartments, including ensheathing or transitional PCs, mesh, thin-strand, or helical and stellate configurations (Arango-Lievano et al., 2018; Hartmann et al., 2015; Smyth et al., 2018); Figure 1.4B). However, throughout capillaries and post-capillary venules, PC cell has a mesh-like or thin-strand morphology. The functionality of PCs is not completely clear, however, their facilitatory role in transport subtracts, modulating capillary diameter in response to neuronal or astrocytic signals and blood perfusion regulation has been suggesting for them (Hartmann et al., 2015; Smyth et al., 2018).

Perivascular fibroblasts and macrophages are found in arteries, arterioles, venules, and veins, but not capillaries. PVFBs are placed within the Virchow-Robin space and are loosely connected to vessel walls. Their functionality has not been fully characterized yet, but it has been suggested that they are progenitors of PC cells and stabilize the vasculature for PCs formation (Rajan et al., 2020).

Like PVFBs, PVMs cells also reside in the Virchow-Robin space around the arterioles and venules (Lapenna et al., 2018; T. Yang et al., 2019). They mainly contribute to the phagocytosis of pathogens as well as protective immune responses (Kierdorf et al., 2019; Lapenna et al., 2018). They also promote BBB properties and tight junction protein expression of Endothelial cells (Zenker et al., 2003).

1.1.4 Action potentials

In neurons and their surrounding fluid, the most abundant ions are Na+, K+ and Cl-. The concentration of K+ and organic anions is higher inside the cells whereas the concentration of Na+ and Cl- is higher outside the cell. At rest, ions are moving in and out of the neuron regularly to maintain the concentration gradient on each side of the membrane between -40 to -90 mV. Because of this baseline potential difference, the membrane is said to be polarized. If this potential becomes more positive than the resting state, the cell is said to be depolarized, and if it becomes more negative the cell is said to be hyperpolarized. When an electrical trigger is applied to the axon of a neuron, which is a signal coming from another cell connected to the neurons, a transient electrical current, called Action Potential (AP), is conducted down the axon. AP is an all-or-nothing response, which means when the membrane potential reaches resting potential (−70 mV), it causes positive ions to flow into the cell body and depolarize the membrane potential. The depolarization phase also called the raising phase is rapid (~ 1 s) and is followed by a rapid falling repolarization stage. That brings membrane potential back to its resting potential by inhibiting the influx of positive ions. The last part of the action potential is the hyperpolarization, which is also called undershoot and after that, the membrane potential will return to the resting membrane potential (Kandel et al., 1995; Nicholls et al., 2001; Rye et al., 2013). Figure 1.5 depicts how cell membrane polarity changes during the action potential.

The first step before the generation of an action potential is a trigger event, which is a signal coming from another cell connected to the neurons, causing positive ions to flow into the cell body and depolarizing the membrane potential when bringing it close to 0 mV. If the cell body becomes sufficiently depolarized, reaching a specific threshold, then it can trigger the opening of a voltage-gated sodium channel at the axon hillock and an action potential will be sent down along the axon.

The next step of the action potential is the depolarization of the axonal membrane. During this step, voltage-gated sodium channels open and Na+ ions flow into the axon and depolarize it. The opening of one channel depolarizes the membrane further, leading to the opening of other sodium channels and as the potential passes the along the axon the positive charges also move down along the axon. The other stage of the action potential is the repolarization. Repolarization brings back the cell to its resting potential by closing the sodium channels and thereby inhibiting the influx of positive ions. At the same time, the potassium channels open and potassium ions move outwards. All this means that the cell loses its positive polarity and returns to its resting potential. The last part of the action potential is the hyperpolarization, which means that the neuron becomes more negative than its normal resting membrane potential. However, after potassium channels become deactivated, the sodium-potassium pump restores the polarity of the cell to its resting potential (Kandel et al., 1995; KhanAcademy, 2017; Nicholls et al., 2001; D. Purves et al., 2001; Simon et al., 2016).

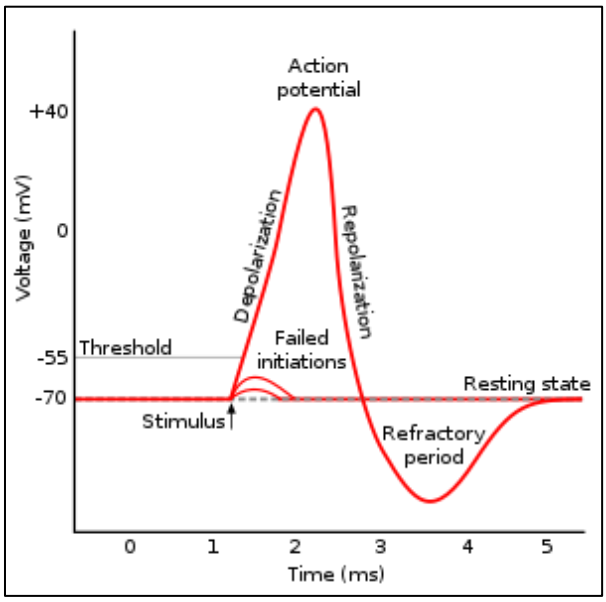

Figure 1.5 Diagram of cell membrane's polarity changes over action potential steps. Figure adapted from Wikipedia (CC BY-SA 3.0; Chris 73, Diberri, tiZom).

1.1.5 Postsynaptic potentials

The firing of an action potential in one neuron (the presynaptic neuron) causes the transmission of a signal to another neuron (the postsynaptic neuron) at the level of the synapse. Synapses are formed between the axon terminals of the sending neuron and the cell body or dendrites of the receiving neuron. In our brain, most of the signal communication in synapses is chemical. Chemical transmission requires the release of neurotransmitters from presynaptic to postsynaptic cells through a small gap between them called the synaptic cleft. Inside the axon terminal of presynaptic neurons, there are membrane-bounded spheres filled with neurotransmitter molecules called synaptic vesicles. When an action potential arrives at the axon terminal, voltage-gated calcium (Ca2+) channels open and calcium ions, which have a much higher concentration outside the cell than inside, rush into the cell. These Ca2+ ions cause the synaptic vesicles to fuse with the membrane and release neurotransmitters into the synaptic cleft (Bergles et al., 2010; J. H. Byrne, 2016; Kennedy, 2016; Simon et al., 2016). Figure 1.6 represents the detailed steps of chemical transmission in the synapse.

The target cell integrates the signals received at different locations (spatial summation), which means receiving hundreds of inputs from the cells that synapse with it, or in the same place but at slightly different times (temporal summation) to decide whether to fire an action potential or not. Such input can cause two types of potential in the neuron's membrane potentials: Excitatory Postsynaptic Potentials (EPSPs) which is indeed a depolarizing event that causes the membrane potential to become more positive and closer to the membrane resting threshold; or, Inhibitory Postsynaptic Potentials (IPSPs) which is a hyperpolarizing event that causes the membrane potential to become more negative and further away from the membrane resting threshold (Heller & Sadava, 2009; Hodgkin & Huxley, 1952; KhanAcademy, 2017; Pereda, 2014).

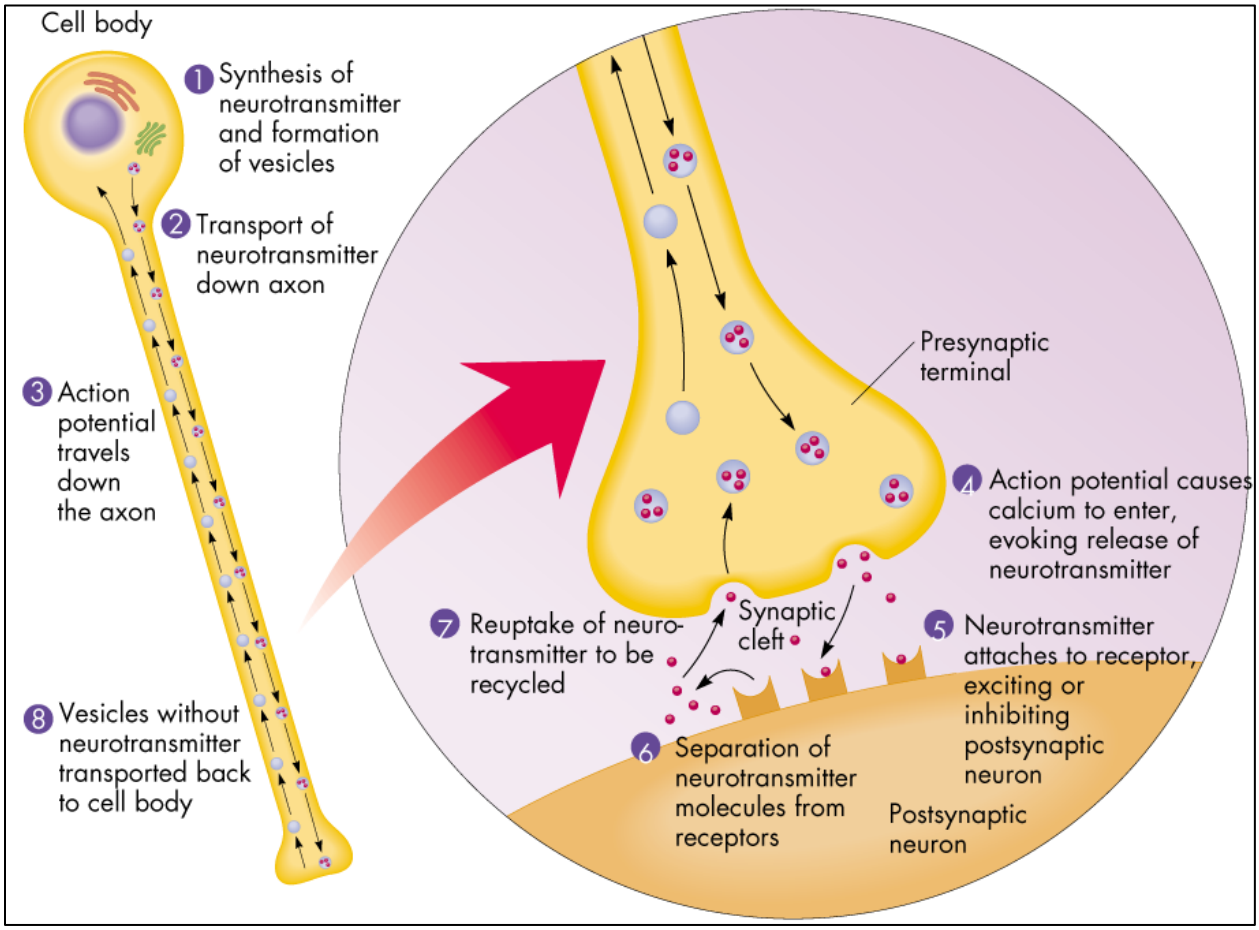

Figure 1.6 Stages of chemical transmission in a synapse. Figure adapted from (Dubey et al., 2018)

After releasing the neurotransmitters in the synaptic cleft and transferring the signal from the presynaptic neurons to the postsynaptic neuron, the remaining neurotransmitters may be broken down by an enzyme, may be taken back up into presynaptic neuron, may be washed out by nearby astrocytes cells or may diffuse away (Pereda, 2014).

1.1.6 Neurotransmitters

The neurotransmitters, chemical messengers, can broadly be categorized into conventional and unconventional groups. Conventional neurotransmitters are stored in synaptic vesicles and get released when Ca2+ enters the axon terminal in response to an action potential and adhere to receptors on the postsynaptic membrane. Some of the most important conventional

neurotransmitters include glutamate, γ-aminobutyric acid (GABA), glycine, ATP and adenosine (Blaustein et al., 2011; Goldman, 2010). In contrast to the conventional neurotransmitters, the unconventional ones are not stored inside the vesicles, and rather than interacting with the receptors on the plasma membrane of their target cells, they pass through them and directly act on the molecules inside the cell. The two main unconventional neurotransmitters are the endocannabinoids, and the gaseous neurotransmitters such as nitric oxide (NO), and carbon monoxide (CO) (Squire et al., 2012). Neurotransmitters are either excitatory or inhibitory. For example, glutamate and glycine are the two main excitatory neurotransmitters in the brain while GABA is the main inhibitory neurotransmitter. However, the inhibitory or excitatory attributes of neurotransmitters also depend on the context and the different types of receptor proteins that are present on the postsynaptic target cell (Blaustein et al., 2011; Deutch et al., 2014; Kandel et al., 1995)

1.2 Basics of brain metabolism

Metabolic pathways can be broadly divided into two categories based on their effects: a) "building up" or anabolic pathway; and b) "breaking down" or catabolic pathway. Anabolic pathways form complex molecules from simpler ones and to do so they require an input of energy. For instance, building proteins from amino acids. Catabolic pathways involve breaking down complex molecules into simpler ones, resulting in an energy release (Berg et al., 2002b). This energy is then stored in some complex molecules such as glycogen and lactate. Some chemical reactions in a pathway do not occur automatically and require an enzyme to make them occur (Berg et al., 2002b; Heller & Sadava, 2009; KhanAcademy, 2017; Reece et al., 2014)

The three main sources of nutrients for cell metabolism are carbohydrates, proteins, and fats. However, as our body cannot directly use their energy, they are required to be broken down into usable energy in the form of adenosine triphosphate (ATP) molecules. The main carbohydrate molecule used in the body is glucose. It is used in the intercellular form of glucose-6-phosphate(G-6P) which subsequently can be broken down into pyruvate and later converted to Acetyl-coenzyme A (CoA) or it can be stored in the form of glycogen (Alberts et al., 2002). Through a metabolic pathway called glycogenesis, astrocytes as well as certain large neurons in the brainstem, store the G-6P as glycogen. Later in the glycogenolysis pathway, this reserved glycogen can be re-converted to G-6P and enter the ATP production pathway. However, when compared to concentration contents in the liver and the muscles, glycogen concentration in the brain is extremely small, about 100 and 10 times lower, respectively, and can therefore be barely considered as a metabolic storage (Albert et al., 2009; Alberts et al., 2002; Simon et al., 2016).

The second main source of nutrients are the proteins, which are composed of several amino acids. They can be broken down into their constituent amino acids and used in various steps of other pathways, for instance, glucose catabolism, subsequently converting G-6P into pyruvate or acetyl-CoA. Amino acids can also be used for the synthesis of enzymes, transporters, cell genetic information, neurotransmitters and some peptide hormones like insulin and glucagon (El Bacha et al., 2010).

Finally, the last main source of nutrients is complex fats, which can be broken down into triglycerides, and then degraded into glycerol and fatty acids. The glycerol then can be converted to pyruvate, and fatty acids and directly be turned into acetyl-CoA through a beta-oxidation pathway. The fatty acids can also be converted to ketone bodies or contribute to the biosynthesis

of cholesterol, steroids, bioactive molecules such as arachidonic acid and eicosanoids, or steroid hormones (Panov et al., 2014; Tracey et al., 2018).

All these conversions except one are bi-directional. The only uni-directional conversion is pyruvate to acetyl-CoA. Furthermore, the predominant way our body generates energy from all these sources of nutrients (glucose, fatty acid and amino acids) is through cellular respiration by using acetyl-CoA in the tricarboxylic cycle (TCA). The TCA cycle is the main metabolic pathway used to produce ATP (Berg et al., 2002c, 2002b; Betts et al., 2013; Mergenthaler et al., 2013)

Adenosine triphosphate (ATP) constitutes the main energy currency or energy store in biological systems (Dunn & Grider, 2022). This complex molecule is composed of adenosine, which includes an adenine connected to ribose, and three phosphoryl groups that have high energy bonds (Figure 1.7). These bonds are providing high energy levels since they have electrons in high energy states. When these bonds are broken, the electrons go back to their baseline state at a lower energy level, by releasing energy. Through the hydrolysis reaction of ATP, one phosphoryl bond breaks in the presence of an ATPase enzyme, which results in the formation of adenosine with two phosphoryl groups, or ADP with positive hydrogen, a phosphate, and roughly 30 kJ/mol of energy (Dunn & Grider, 2022; Knowles, 1980).

$$ATP + H_2O \rightarrow ADP + P_i + H^+ + \text{energy} \quad (1.1)$$

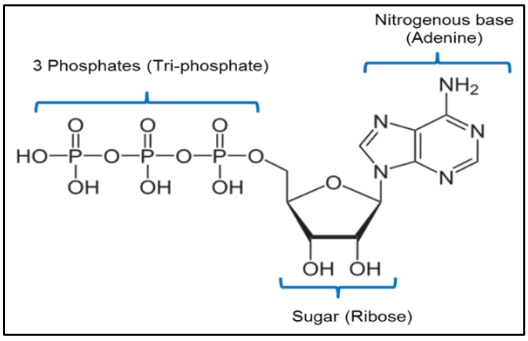

Figure 1.7 Adenosine triphosphate.

1.2.1 Glucose: the major metabolic source for our brain

The mass of the brain accounts for only 2% of the whole body, however, it consumes 20% of glucose and 20% of oxygen body utilization at rest, most of which is used to support synaptic transmission, including the maintenance of ion gradients. Moreover, the brain cannot store the energy it needs by increasing its mass. The brain can only keep small amounts of glucose (1-3 mM), oxygen (50-100 µM), glycogen (2-4 mM), and creatine (8–10 mM) (Thompson et al., 2016). Hence, the brain relies on nutrients supplemented in real-time by the rest of the body in normal conditions. Therefore, the brain is dependent on an efficient blood circulation system to be able to provide the components it requires and remove the waste produced of its chemical reactions (Leithner & Royl, 2014).

Glucose is the main energy substrate for brain cells. In addition, glucose also contributes as a precursor for glycolipids and glycoproteins present in neural cells, and for the synthesis of important neurotransmitters like glutamate, GABA, and acetylcholine (Mergenthaler et al., 2013).

1.2.1.1 Cellular respiration

In the presence of oxygen, glucose (C6H12O6) is mainly metabolized through a process called cellular respiration, in which six molecules of oxygen and one glucose molecule ($C_6H_{12}O_6$) are broken down into molecules of carbon dioxide (CO_2) and water (H_2O). This process produces between 30 and 38 ATPs per glucose, depending on the coupling efficiency of oxidative phosphorylation (Chaudhry & Varacallo, 2022; Mergenthaler et al., 2013).

$$C_6H_{12}O_6 + 6O_2 \rightarrow 6H_2O + 6CO_2 + [\![30,38]\!]ATP \quad (1.2)$$

1.2.1.2 Glycolysis

The first step of cellular respiration is glycolysis, during which the six-carbon glucose molecule is split into two three-carbon molecules called pyruvate. Glycolysis occurs within the cytosol of the cell in the presence of the phosphofructokinase enzyme. Glycolysis consists of an energy-requiring phase and an energy-releasing phase (Chaudhry & Varacallo, 2022). During the energy-requiring phase, a phosphate group is transferred from ATP to glucose, converting two ATPs into two ADPs while generating a glucose 6-phosphate(G-6P) molecule, which is more reactive than glucose. Since glucose with phosphate cannot readily cross the membrane, G-6P remains trapped inside the cell. Afterwards, using the catalyzer phosphofructokinase, G-6P is first converted to fructose 6 phosphate (F-6P) and then into the unstable fructose 1(F-1),6-bisphosphate(6-BP). Then, this new unstable sugar molecule (F-6P) gets split in half to form a glyceraldehyde-3-phosphate (Gl-3P), which can be used for the energy-releasing phase and dihydroxyacetone phosphate (DHAP). DHAP also can be easily re-converted to glyceraldehyde-3-phosphate and used in the energy-releasing phase of glycolysis (Berg et al., 2002a; Betts et al., 2013; Cooper, 2000). During the energy-releasing phase, each three-carbon sugar is converted to pyruvate, also a three-carbon molecule (Figure 1.8). In addition, two ADPs are turned into ATPs and one reduced oxidized nicotinamide adenine dinucleotide (NAD+) is converted to nicotinamide adenine dinucleotide (NADH). Therefore, the net products of this process are two molecules of ATP produced (4 ATPs produced versus 2 ATPs used) and two molecules of NADH. NADH is an electron carrier coenzyme which generates almost three ATPs for every NADH to NAD+ oxidation event, whereas NAD+ functions as a sink for electrons. Phosphofructokinase is the key regulatory enzyme for catalyzing the steps of glycolysis: conversion of F-6-P to F-1,6-BP. It is activated by F-1,6-BP and inhibited by citrate (Ahmad et al., 2022; Chaudhry & Varacallo, 2022; KhanAcademy, 2017).

At the next step of cellular respiration, pyruvate oxidation occurs in the mitochondrial matrix in the presence of the pyruvate dehydrogenase complex. Pyruvate is split into one carbon dioxide and a two-carbon molecule (Berg et al., 2002a; Betts et al., 2013). Then, NAD+ is reduced to NADH with the oxidation of two carbons and finally, two oxidized carbon molecules are attached to CoA, which is an organic molecule derived from vitamin B5, to form acetyl-CoA. Acetyl-CoA works as a fuel for the citric acid cycle in the next stage of cellular respiration (Figure 1.9).

$$\text{Pyruvate} + 2NAD^+ + 2CoA \rightarrow 2\text{Acetyl-CoA} + 2NADH + 2H^+ + 2CO_2 \quad (1.3)$$

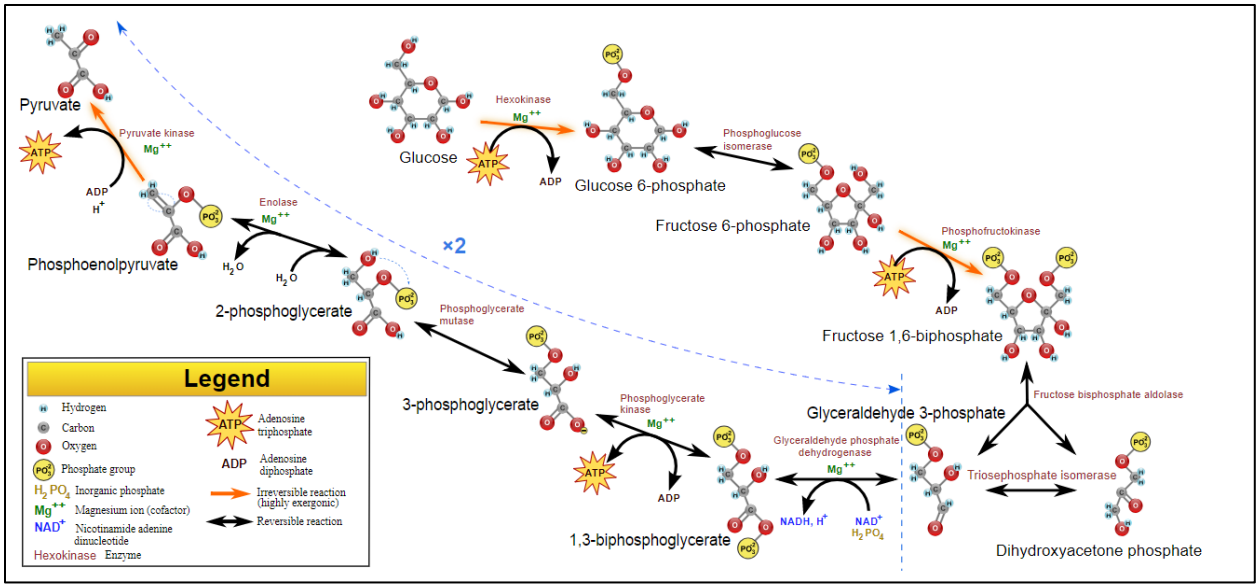

Figure 1.8 Glycolysis diagram. Figure adapted from Wikipedia (CC BY-SA 3.0; YassineMrabet).

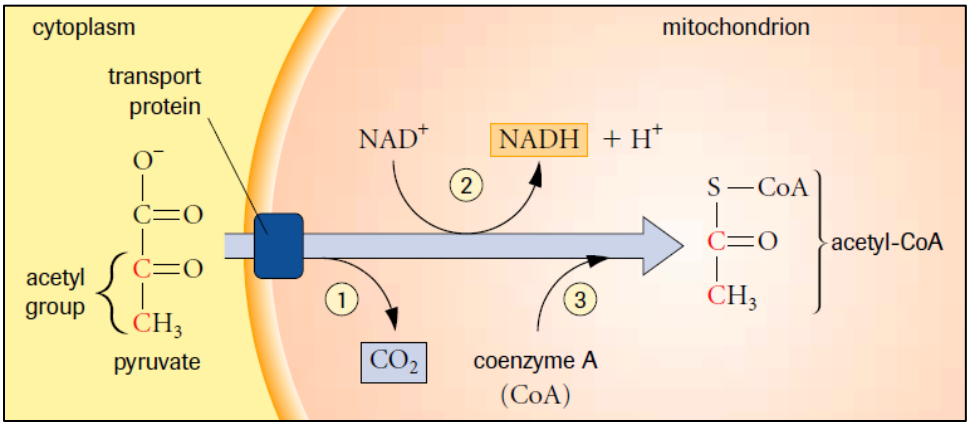

Figure 1.9 Pyruvate oxidation diagram. Figure adapted from (Rye et al., 2013).

Therefore, the net products of glycolysis process are two molecules of ATP produced (4 ATPs produced versus 2 ATPs used) and two molecules of NADH as below:

$$\text{Glucose} + 2\text{NAD}^+ + 2\text{ADP} + 2\text{P}_\text{i} \rightarrow 2\text{Pyruvate} + 2\text{NADH} + 2\text{ATP} + 2\text{H}^+ + 2\text{H}_2\text{O} \quad (1.4)$$

1.2.1.3 Citric acid cycle (TCA)

The next step of cellular respiration is named the citric acid or Krebs cycle (Figure 1.10). It occurs in the mitochondrial matrix and is a closed loop, whose role is to regenerate the molecules that have been used during the previous steps of cellular respiration. During the first step of this cycle, acetyl-CoA combines with oxaloacetate, which is a four-carbon acceptor molecule, to form six-carbon citrate (D. L. Nelson et al., 2008; Reece et al., 2014). After a rearrangement, citrate releases two of its carbons as carbon dioxide molecules to build one molecule of NADH per reaction. The enzyme isocitrate dehydrogenase which catalyzes these reactions is the key regulator of the citric acid cycle, speeding it up or slowing it down based on the energy that is needed by the cell. The remaining four-carbon molecule experiences a series of additional reactions. First, an ATP

molecule is produced, or in some cells, a similar molecule called Guanosine-5-triphosphate (GTP). Then, the electron carrier Flavin adenine dinucleotide (FAD) is reduced to $FADH_2$. Finally, another NADH is produced. These reactions reform the starting molecule, oxaloacetate so that in the end the cycle can start again with the addition of one acetyl-CoA. Overall, one cycle of the citric acid cycle generates two carbon dioxide molecules and produces three NADH, one $FADH_2$ and one ATP or GTP (Szarka et al., 2014). The citric acid cycle runs twice for each molecule of glucose used for cellular respiration since two pyruvates - and thus, two acetyl-CoAs - are generated from each glucose (Berg et al., 2002a).

$$\begin{aligned} &\text{Acetyl-CoA} + 3\text{NAD}^+ + \text{ADP} + \text{FAD} + \text{P}_\text{i} \\ &\rightarrow \text{ATP} + 3\text{NADH} + 3\text{H}^+ + 2\text{CO}_2 + \text{FADH}_2 \end{aligned} \tag{1.5}$$

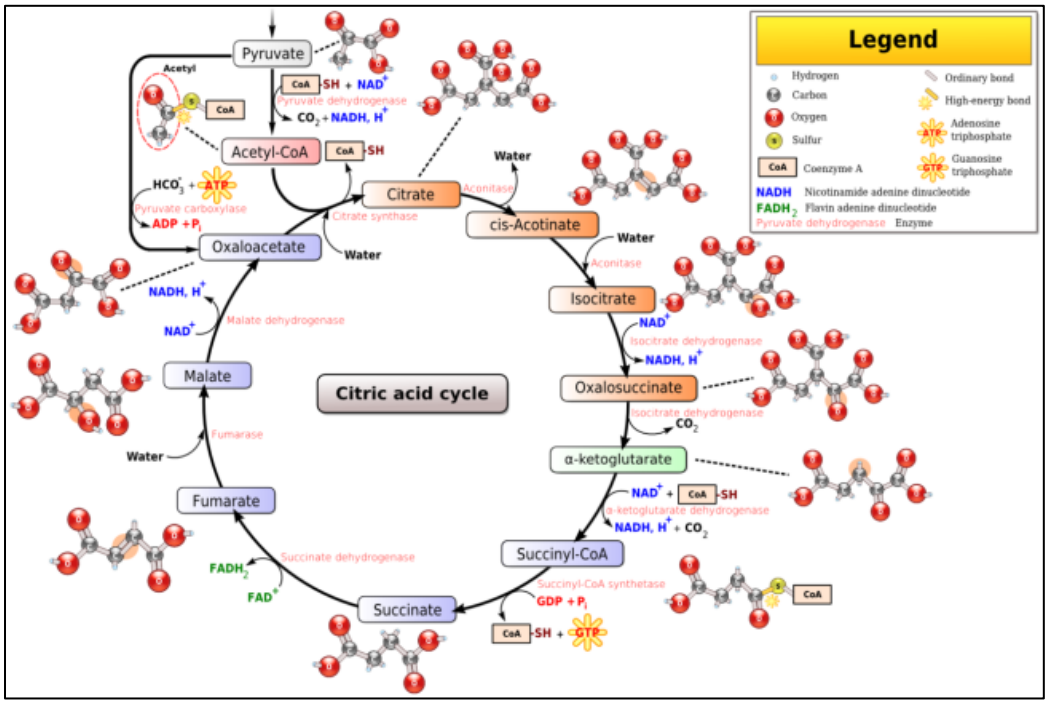

Figure 1.10 Citric acid cycle. Figured adapted from Wikipedia (CC BY-SA 3.0; Narayanese, WikiUserPedia, YassineMrabet, TotoBaggins).

1.2.1.4 Oxidative phosphorylation

Oxygen is required for the last step, oxidative phosphorylation. Oxidative phosphorylation is built up from two main parts: a) the electron transport chain, in which the electrons in the inner membrane of the mitochondria are transferred from one molecule after the other, releasing energy and making an electrochemical gradient (Figure 1.11,(Ahmad et al., 2022; KhanAcademy, 2017)) the chemiosmosis, in which the energy stored in the gradient is used to produce ATP. The oxygen is used at the end of the electron transport chain, where it combines with the electron and proton to form a water molecule (Berg et al., 2002a; Betts et al., 2013). Without enough oxygen, another process called lactic acid fermentation or anaerobic respiration takes place, which produces fewer ATP molecules. Cells which lack a sufficient number of ATP molecules for a long period of time may even die (Reece et al., 2014).

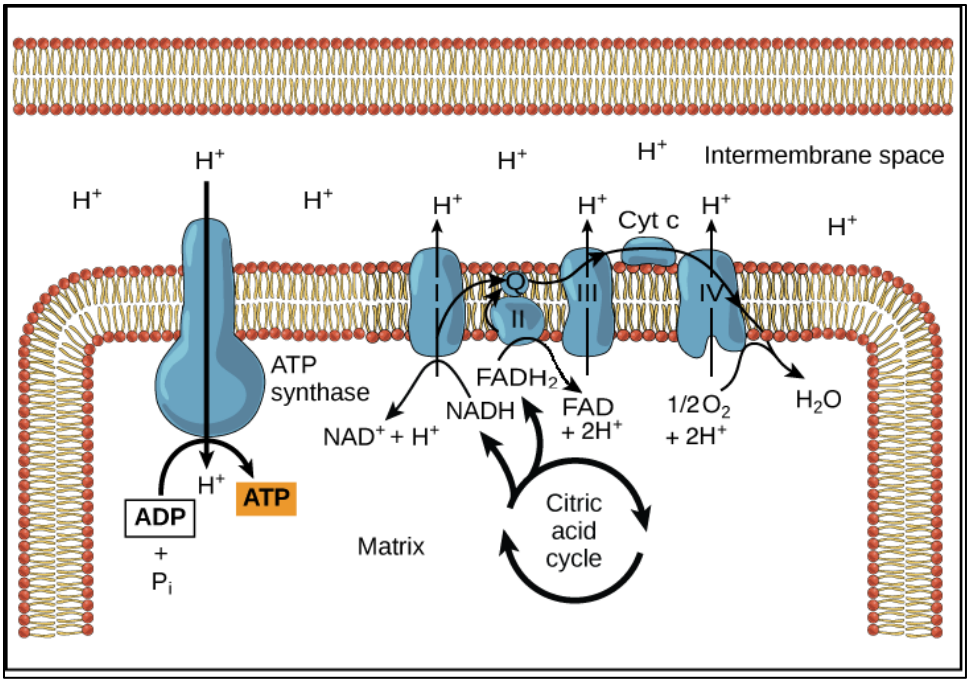

Figure 1.11 Oxidative phosphorylation image modified from "oxidative phosphorylation" by OpenStax's college Biology (CC BY 3.0).

1.2.2 Non-oxidative metabolism

During the first step of cellular respiration, in the glycolysis phase, glucose is broken down into two pyruvates and two ATPs. Then, if there is enough oxygen available, the pyruvate enters the TCA cycle and electric transport chain to produce more (up to 30-36) ATPs (Robert Bear, 2016). However, in the absence of oxygen, the cell enters another chemical reaction called lactic acid fermentation which is one of two major forms of fermentation or anaerobic respiration. The goal of lactic acid fermentation is not to produce more ATPs, but rather to recycle pyruvate and NADH. Indeed, instead of using the pyruvate in the TCA cycle, it uses it to oxidize NADH to NAD^+ in the presence of lactic acid dehydrogenase as a catalyzer. The produced lactate can later be removed through to the bloodstream or reconverted to pyruvate later for use in the TCA cycle and oxidative phosphorylation once oxygen is again available (Betts et al., 2013; Reece et al., 2011; Szarka et al., 2014).

$$2\text{Pyruvate} + 2\text{NADH} \rightarrow 2\text{Lactate} + 2\text{NAD}^+ \quad (1.6)$$

1.3 Other Energy Substrates for the Brain

While some organs like the liver have the capacity to produce energy using different pathways, the brain has limited options. Protein metabolism is barely used in the brain, because of the production of ammonium ($NH4^+$) which is toxic to brain cells (Betts et al., 2013; Thrane et al., 2013). The brain normally uses glucose as its main energy substrate. However, under particular circumstances (like being on ketogenic diet, fasting, intense exercise, early life, diabetes or in neuropathological conditions) creatine (Cr), ketone bodies (KBs), lactate, and fatty acids (FAs) can be used as alternative sources of energy (Panov et al., 2014; Tracey et al., 2018). Among them lactate is considered as an important metabolite source for the brain. The brain uses lactates under many conditions including high intensity exercise, hypoxia, and shock (Riske et al., 2017).

1.3.1 Creatine (Cr)

Creatine (Cr) is used to a small extent through its conversion into its high-energy phosphorylated analogue phosphocreatine (PCr). However, the BBB has a very limited permeability for Cr (Braissant, 2012), and the brain cells must rely mostly on the endogenous synthesis of Cr in astrocytes (Béard & Braissant, 2010; Braissant, 2012; Philip et al., 2020). Cr is synthesized in two steps. First, arginine, that is a basic amino acid, and glycine combine to form guanidino acetic acid (GAA) in a reaction catalyzed by AGAT, subsequently, creatine is formed by methyl group transfer from S-adenosyl-L-methionine to GAA catalyzed by GAMT (Béard & Braissant, 2010; Philip et al., 2020). Then through a process in which the ADP converts to ATP, PCr dephosphorylation can yield energy for brain cells (mainly astrocytes), by transferring its N-phosphoryl group from PCr to ADP (Figure 1.12, (Brody, 1999)).

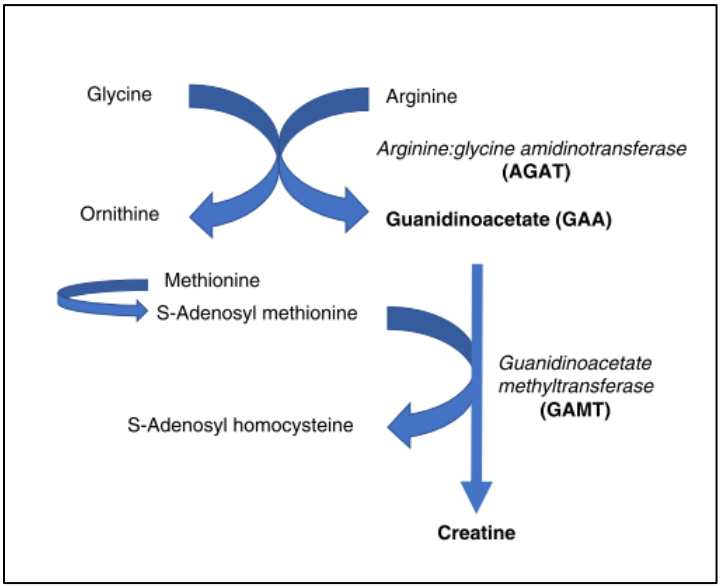

Figure 1.12 Endogenous creatine synthesis. Arginine and glycine combine to form guanidino acetic acid (GAA) and ornithine in a reaction catalyzed by arginine: glycine amidino transferase (AGAT). GAA is then methylated to form creatine. The enzyme guanidinoacetate methyltransferase (GAMT) catalyzes this reaction and s-adenosyl methionine acts as the methyl donor. Figure adapted from (Philip et al., 2020).

1.3.2 Fatty acids (FAs)

FA can cross the BBB using the FA transporter, albeit very slowly, and then pass through the beta-oxidation pathway in mitochondria to be oxidized to acetyl-CoA (Schönfeld & Reiser, 2013). During the beta-oxidation pathway, the FA (C_n-acyl-CoA) is first converted to acyl-CoA (2 carbons shorter version) in the cytosolic compartment by reducing the FAD to FADH. Then its acyl group is transferred from CoA to carnitine using the carnitine-acyl-CoA transferase enzyme across the inner membrane of the mitochondrion. In the next step, the acyl CoA is oxidized to acetyl-CoA, water, 5 ATP, FADH, and NADH.

The overall reaction formula for one cycle of beta-oxidation is:

$$\begin{aligned} &C_n\text{-acyl-CoA} + FAD + NAD^+ + H_2O + CoA \\ &\rightarrow C_{n-2}\text{-acyl-CoA} + FADH_2 + NADH + H^+ + \text{Acetyl-CoA} \end{aligned} \tag{1.7}$$

In general, FAs are not an ideal source of energy for the brain. First, ATP production using beta-oxidation of FA requires more oxygen than glucose oxidation which can pose a risk of hypoxia.

Second, this pathway produces superoxide, which enhances the oxidative stress of neurons. And third, not only is FA crossing of the BBB very slow, but the beta-oxidation pathway itself is slower than using blood glucose as fuel (Eaton, 2002; Schönfeld & Reiser, 2013). Nevertheless, some recent studies confirmed the usage of FA in astrocytes and neurons in addition to other substrates. Furthermore, brain FAs or their metabolites have important contributions to many anti-inflammatory and neuroprotective pathways as well as in the ketone body production pathway (Ebert et al., 2003; Panov et al., 2014).

1.3.3 Ketone bodies

Ketone bodies, aside from glucose, are the main alternative metabolic resource for the brain. Ketone bodies are mainly produced in the liver, and to some extent in the kidney (Jensen et al., 2020). They circulate in the blood stream and can cross the BBB (Jensen et al., 2020; Nehlig, 2004; Pierre & Pellerin, 2005), in addition to a low-level contribution from astrocytic production (Jensen et al., 2020) mainly using beta-oxidation of FAs. In the presence of a high supply of FA, which results in the production of high levels of acetyl-CoA, acetyl-CoAs are used for ketone body formation instead of going through the TCA cycle. To do so, acetoacetyl-CoA is produced from two acetyl-CoA by the enzyme thiolase. At the next step, another acetyl-CoA group is combined with acetoacetyl-CoA via reaction with 3-hydroxy-3-methylglutaryl-CoA (HMG-CoA) synthase (HMGCS2), hence forming 3-hydroxy-3-methylglutaryl-CoA (HMG-CoA). Then the enzyme HMG-CoA lyase removes an acetyl-CoA from HMG-CoA to produce the ketone body acetoacetate (AcAc) which either be later degraded to acetone (with minimal energy contribution) or using beta-hydroxybutyrate dehydrogenase (BHD) enzyme and hydrogen from NADH, form the ketone body beta-hydroxybutyrate (BHB). BHB and AcAc can later reduce to acetyl-CoA and enter the TCA cycle in either neurons or astrocytes (Jensen et al., 2020; Nehlig, 2004; Pierre & Pellerin, 2005).

1.3.4 Lactate and pyruvate

Lactate and pyruvate are two other energy substrates for human brain cells which can be formed from glucose within the brain parenchyma or readily imported from the circulation and enter the cells through specialized transporters (Brooks, 2009; Riske et al., 2017). They can be metabolized in the mitochondria through the TCA cycle and oxidative phosphorylation to produce energy in the form of ATP (Figure 1.13). In the case of lactate, recent magnetic resonance spectroscopy (MRS) experiments showed that under basal plasma lactate condition (1.0 mM), lactate can be taken up by the human brain and when it is fully oxidized, it accounts for up to 8–10 % of its energy requirements. Through the mechanism called astrocyte-neuron lactate shuttle (ANLS), the glutamate released by neurons in synapse space is co-transported with sodium to astrocytes (Kasischke, 2009). The influx of sodium results in the disruption of the sodium gradient inside the astrocytes and triggers the activity of the sodium-potassium ATPase (Na^+/K^+ ATPase) by consuming ATP per extrude of three sodium. The absorbed Glutamates are mainly converted to glutamine at the expense of another ATP, which a large proportion of that later will be recycled to neuronal terminals to refill the glutamate vesicular pool. The energy burden of glutamate uptake by astrocyte promotes glucose uptake, which later through the glycolysis pathway yield lactate. The produced lactate using the monocarboxylate transporters (MCTs) is released, and is taken up by neurons and, after conversion to pyruvate, is processed oxidatively in mitochondria to produce 14–17 ATPs per lactate molecule (Bak et al., 2009; Magistretti & Allaman, 2015; Morgenthaler et al., 2006; Pierre & Pellerin, 2005)

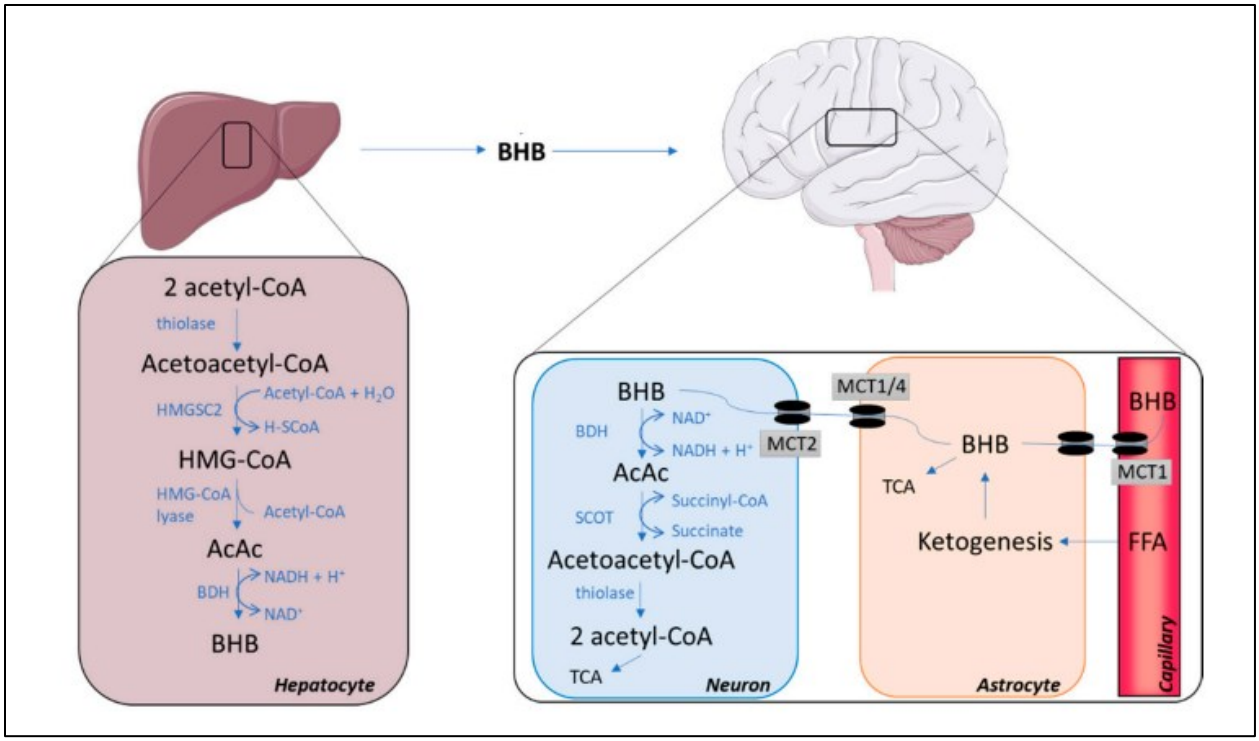

Figure 1.13 Pathways involved in synthesis and catabolism of ketone bodies. AcAc, acetoacetate; Acetyl-CoA, acetyl coenzyme A; BHB, beta-hydroxybutyrate; BHD, beta-hydroxybutyrate dehydrogenase; FFA, free fatty acids; HMG-CoA, 3-hydroxy-3-methylglutaryl-CoA; HMGCS2, 3-Hydroxy-3-Methylglutaryl-CoA Synthase 2; MCFA, medium-chain fatty acids; MCT, monocarboxylate transporter; SCOT, succinyl-CoA:3-ketoacid Coenzyme A transferase; TCA, tricarboxylic acid cycle. Figure adapted from (Jensen et al., 2020)

1.4 Coupling of Neuronal Activity, Blood Flow, and Energy Metabolism

As previously mentioned, the brain is a very energy-demanding organ. However, the brain also has physical space restrictions and lacks any reservoir to store the fuel it needs. This means the brain requires a high degree of temporal and spatial coordination with the blood circulation system. Any interruption in blood supply for more than a few minutes (for example in the case of blood occlusion) will result in ischemic stroke with neurological deficits, tissue damage, and even death. Even if the flow is not completely stopped, but just reduced or does not match the metabolic demands, it can lead to BBB disruption, intracranial pressure, inflammatory cascades, tissue damage, and resulting cognitive impairment (Bélanger et al., 2011; Iadecola, 2017; Venkat et al., 2016). As such, any neural activity requires a timely and spatially accurate hemodynamic response that increases cerebral blood flow (CBF), with tight coupling between neuronal activity, cerebral blood flow (CBF), and metabolism. These hemodynamic responses to neural activity including changes to CBF and metabolic expenditure can be captured and imaged using neuroimaging techniques such as functional magnetic resonance imaging (fMRI) and positron emission tomography (PET), which will be introduced and discussed in detail in the next sections.

The compartments and mechanism that maintain the coupling between the neural activity and CBF encompass the anatomical and metabolic interactions between the neurons, vascular components (i.e., endothelial cells, pericytes, vascular smooth muscle cells) and glial cells (i.e., astrocytes and, microglia, and oligodendrocytes) and are collectively called the neurovascular unit. (Figure 1.14) The neurovascular unit is a key player in ensuring a continuous supply of oxygen, glucose, and

other nutrients to the brain cells, while keeping the brain homeostasis balanced (i.e., keeping both chemical and physical equilibrium within intercellular and extracellular cells). In the aging brain, as well as under neurological diseases such as epilepsy, dementia, hypertension, and diabetes, the neurovascular unit is often compromised (Iadecola, 2017). In general, two mechanisms have been proposed to regulate and control CBF and modulate neurovascular coupling. The first one is called the metabolic model and proposes that by-products of neural activity and energy changes in neurons and astrocytes and molecules or ions that transiently accumulate in the extracellular space regulate vascular vasodilation or vasoconstriction. Some of these by-products include hydrogen (H+), Calcium Ca2+, lactate, adenosine, and changes in extracellular pH, which can all induce some vasoactive effects (Attwell et al., 2010; Mächler et al., 2016; Morgenthaler et al., 2006; Roy & Sherrington, 1890). In the second scenario, which is called the feedforward or signalling model, neural activity activates neurovascular signalling pathways which results in the release of specific neuropeptide molecules and vasoactive by-products of synaptic activity, such as K+, nitric oxide (NO) and prostanoids that mediate vasodilation or vasoconstriction and neurovascular coupling in anticipation or at least in parallel with neural activity (Attwell et al., 2010; Cauli & Hamel, 2010; Filosa & Iddings, 2013). Among these mediators, NO is an important mediator of neurovascular coupling. It can be produced by neurons, glial cells, vascular cells, and endothelial cells lining the cerebral vessels (Attwell & Iadecola, 2002; Hosford & Gourine, 2019). Glutamate (the principal excitatory neurotransmitter) triggers a receptor-mediated NO formation in both neurons and glia. While both mechanisms have experimental support (Attwell et al., 2010; Bouzier-Sore et al., 2003; Cauli & Hamel, 2010; Filosa & Iddings, 2013; Kleinfeld et al., 2011; Petzold & Murthy, 2011), some evidence such as the delay (seconds) between initiation of neuronal activity and the vascular response(Gordon et al., 2016), the disproportionate CBF increase as compared to the tissue oxygen need (Leithner & Royl, 2014), and increases in CBF under conditions of excess oxygen and glucose (Gladden, 2004; Magistretti & Allaman, 2015) support the predominance of the second model (Attwell et al., 2010; Magistretti, 2016). However, considering the time and spatial limits of different mediators, both mechanisms are most likely involved in actively and efficiently maintaining neurovascular coupling processes (Hosford & Gourine, 2019; Iadecola, 2017; Magistretti, 2016).

It is important to mention that for those two mechanisms for coordinating the coupling between neuronal activity, blood flow regulation and metabolism (e.g., oxygen, glucose), astrocytes are playing an important role, mainly because of their position and association with both neuronal synapses on one hand and local vasculature (microvasculature) on the other hand. For example, astrocytes are influencing blood flow regulation by absorbing extracellular K+ released by neural activity into the end feet next to the microvasculature (Attwell et al., 2010; Magistretti, 2016). In another suggested mechanism, the glutamate released by synaptic activity results in Ca2+ increases in astrocytes which can trigger the release of arachidonic acid and a sequence of events leading to vascular vasodilation (Iadecola, 2017).

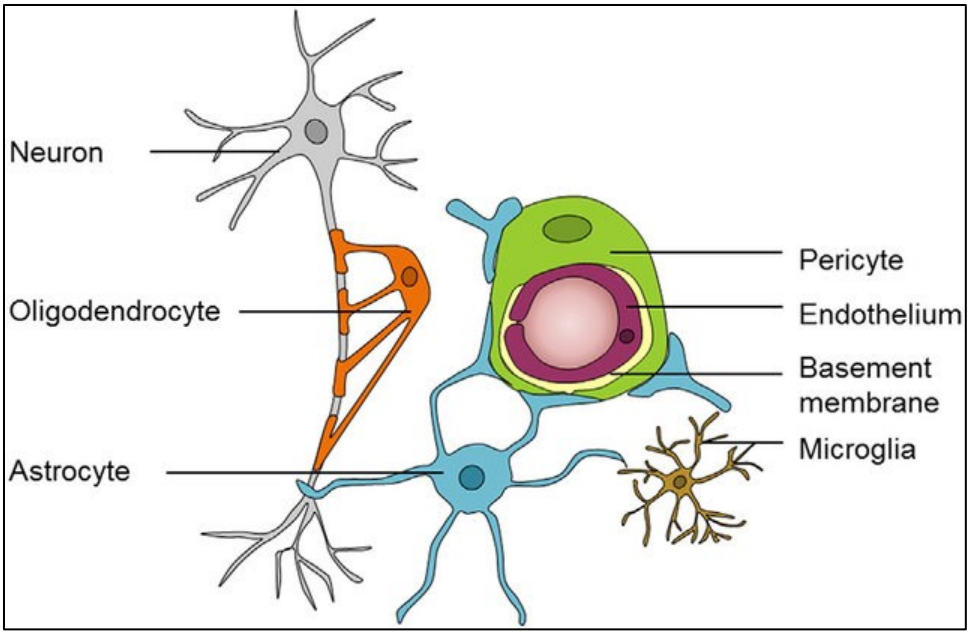

Figure 1.14 The neurovascular unit at the level of brain capillary. In the capillary site, where the neurons have closets interaction with the vascular system, the NVC is comprised of pericytes and endothelial cells, glia including astrocytes, oligodendrocytes, microglia, and neurons. Figure adapted from (A. R. Nelson et al., 2016).

During the above section, I covered the key mechanisms associated with brain cell metabolism and signaling, including the main nutrition and metabolic pathways, as well as the cell types that are involved in brain functioning and metabolism. Here after I introduce the major advanced neuroimaging techniques used to map these processes.

1.5 Imaging methods to monitor brain metabolism

Biomedical imaging techniques provide an important opportunity to study the anatomical and physiological properties of the brain. Among several versatile imaging methods, magnetic resonance imaging (MRI), and positron emission tomography (PET) share the common characteristics of being non-invasive, reproducible, and safe. These methods allow mapping of the structures and functions of the human brain at the mm spatial scale (0.5-3.5 mm). However, while PET is particularly useful for measuring brain metabolism due to its metabolic specificity, the temporal resolution (~minutes) of a PET scanner is such that it reduces its sensitivity to the very early and statistically small changes in brain function. On the other hand, MRI and more specifically functional MRI offers higher temporal resolution (at the second scale) and provides a better ability to identify some dynamic components of functional changes, while characterizing the NVC processes (Bassett & Sporns, 2017). None of those techniques can reach the actual time scale of neuronal bioelectrical activity (at the millisecond scale), for which only electrophysiology techniques such as scalp Electroencephalography (EEG) or Magnetoencephalography (MEG) can provide direct access to neuronal activity, at the price of lower spatial resolution (source localization methods being required to infer cortical activity from scalp recordings). Therefore, PET and fMRI are only offering indirect measures of neuronal activity, through its associated metabolism and hemodynamic components.

In this subsection, I introduce the main Imaging techniques we use in our project to investigate the physiological metabolic feature of the human brain.

1.5.1 Positron emission tomography (PET)

PET is an imaging modality from the field of nuclear medicine and molecular imaging. PET quantitatively measures biochemical and physiological processes in vivo using radionuclide-tagged tracer molecules (tracers). Positrons are emitted by the breakdown of the radionuclide. Gamma rays called annihilation photons are created when positrons collide with electrons near the decay event (Bettinardi et al., 2002). The scanner then detects the annihilation photons, which arrive at the detectors in coincidence at 180 degrees apart from one another. The time-coincident imaging of high energy (511 keV) gamma rays allows accurate attenuation correction using computed tomography (CT). CT scanning is based on the measurement of attenuation of x-rays with uniform and specific energies emitted from the source beam inside the scanner. In a hybrid PET/CT system the x-ray source and the corresponding CT detector field are rotated around the subject inside the machine. Based on the coincidence detection, one can infer that the corresponding annihilation was somewhere along the line. Knowing the attenuation coefficient of tissue in the body, and tomographic reconstruction techniques, a 3-D dimensional anatomical image of the concentration of the radiotracer can be reconstructed (Tong et al., 2010) (Figure 1.15). It thereby provides accurate molecular imaging of the regional function of the body at the biochemical level. For PET imaging, we are considering positron-emitting isotopes with a short half-life, such as C-11, N-13, O-15 or F-18, that can be incorporated into biological substrates such as glucose, H_2O, NH_3, CO_2 or O_2, to name of few, without disturbing or altering the biological activity of cells (Boellaard, 2009; Emre Erdi, 2007).

Inferring biological metabolic processes from PET data consists in analyzing and mathematically modelling the delivery of the labelled tracer as input and tissue responses with a parameter called binding potential. The measured tissue response takes into account the sum of radioactivity from all radiolabeled species which cross the BBB and potentially bind the receptor in the tissue of interest. The contribution of individual species and metabolic rates should be derived using the mathematical models of radiotracer kinetics and estimating the binding potential (Kinahan & Fletcher, 2010; Shoghi & Gropler, 2015). To estimate the binding potential, which is required for PET quantitative analysis, on needs to measure the amount of radiolabeled metabolite in blood plasma, i.e., the arterial input function (AIF). The gold standard for determining the AIF consists in sampling whole-blood activity including biological metabolites and tracer simultaneously with the PET scan for each subject. However, since tracers and metabolites also bind other cells or membranes non-specifically, a radiolabeled metabolite-corrected input function is often necessary. This is estimated by correcting the plasma concentration to the whole-blood ratio of radioactive metabolites though an arterial sampling line. Even though estimating the binding potential using the AIF estimation from arterial blood sampling is more accurate, it imposes additional discomfort on the subjects and, together with the subsequent analysis of blood samples, is a laborious procedure (Shoghi & Gropler, 2015). Another semi-quantitative PET analysis procedure, overcoming the disadvantages of using an arterial sampling line, consists in considering a reference region model, allowing a useful simplification for non-invasive quantification of the AIF(Kinahan & Fletcher, 2010).

The most common metabolite that can be imaged using PET is glucose and oxygen. The glucose and oxygen consumption rate can be estimated using PET with ^{18}F (110 min half-life time) and ^{15}O (2 min half-life time) labelled isotopes respectively. Among ^{18}F-18 labelled radiotracers, fluorodeoxyglucose (FDG) is the most commonly used PET tracer and the only one approved by the Food and Drug Administration (FDA) for routine clinical use (ref). ^{18}F-FDG is a gold standard

to quantify glucose metabolism in the body and the brain. To measure brain oxygenation processes, ^{15}O-PET can be considered for $CMRO_2$ measurement, while it needs more specialized equipment and a complex setup for quantification due to the short half-life of 2-min of ^{15}O, i.e. the local access to a cyclotron able to synthesize such isotope just before injection, making it largely inaccessible (Ishii et al., 2004).

^{18}F-FDG PET allows the determination of glucose consumption based on the qualitative evaluation of regional uptake of ^{18}F-FDG tracer. Both ^{18}F-FDG and glucose share a common carrier called glucose transporters at the blood-brain barrier to transport from plasma into the brain, where after hexokinase enzyme phosphorylates ^{18}F-FDG to ^{18}F-FDG-6-phosphate (^{18}F-FDG-6-P) equivalently as it phosphorylates glucose to glucose-6-phosphate. However, due to the presence of ^{18}F in the formulation, the ^{18}F-FDG-6-P is trapped inside the cell and can't be further metabolized as glucose-6-phosphate (Murakami et al., 2014).

In this context, the standardized uptake value (SUV) method is a semi-quantitative ^{18}F-FDG PET method used in this thesis for measuring brain glucose metabolism. SUV estimates the relative uptake rate of the FDG radiotracer in kBq/(mL), which reflects the relative glucose metabolic rate of glucose in brain tissue. By taking a reference ROI in the brain as a reference region (Byrnes et al., 2014; Kinahan & Fletcher, 2010), SUV measure can be estimated using the formula:

$$\mathrm{SUV} = C_t/(\mathrm{ID}/w_t \times D) \tag{1.8}$$

where C_t is the decay-corrected activity concentration in the tissue (in MBq/cc which can be converted to MBq/(kg) by dividing by tissue density 1 g/cc), ID is the injected dose (in MBq), and w_t is the subject's weight (in kg). $D = 2^{-\Delta_t/T_{1/2}}$ is a decay factor with Δ_t being the time elapsed between injection and scanning (approximately 1 hour), and $T_{1/2}$ is the half lifetime of the ^{18}F-FDG radiotracer (6582 s). Then, SUV ratios (i.e., glucose metabolism rate maps) are determined by employing a normalization procedure, i.e., a rescaling to the tracer activity value within preferential tissue such as the cerebellum and pons. Among them, absolute quantification ^{18}FDG PET studies showed that the pons provides more stable estimates than the cerebellum (Nguyen et al., 2006; Verger et al., 2021). While it's been shown that there is a good agreement between the PET relative and absolute measure and for example the SUV values shown to have a high correlation (r=0.84) with glucose metabolic rate (Boellaard, 2009; Doot et al., 2007; Hyder et al., 2013); yet in non-normal physiological cases with significant global reductions of brain metabolic activity, such as patients with neurodegenerative dementia, the PET absolute measurement is favored and more liable (Berti et al., 2014).

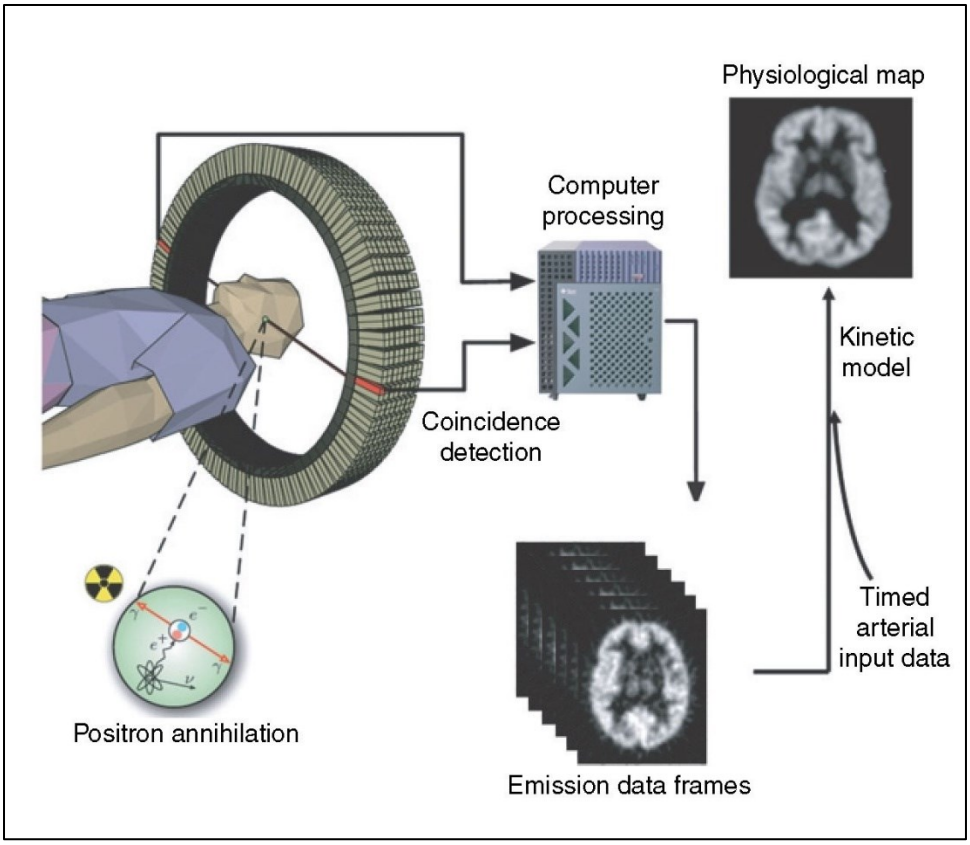

Figure 1.15 Schema showing the processing steps of PET imaging: decay of radionuclide, positron emission, PET/CT scanner gamma ray coincidence detection, 3-dimensional trace concentration reconstruction, physiological map modeling. Figure adapted from (Matta et al., 2011).

1.5.2 Magnetic resonance imaging (MRI)

Magnetic resonance imaging (MRI) is an imaging technique based on the principles of nuclear magnetic resonance (NMR). NMR is a physical phenomenon that results from specific magnetic properties of certain atomic nuclei with an odd number of proton and/or neutrons called NMR-active nuclei. In the presence of a strong static magnetic field (B_0), the spin of such nuclei points toward the direction of B_0 (lower energy sate) and they also precess with the resonance called Larmor frequency. The Larmor frequency is determined by the gyromagnetic ratio (γ) of the particular magnetic moment. Applying a second perpendicular magnetic field (B_1), at the Larmor frequency, cause most of the spins to point against (higher energy) the (transverse direction) of the B_0. After removing B_1, within time T1 and so-called longitudinal relaxation rate R1 (R1=1/T1), the nuclei recover their resting energy state and get aligned with B_0 and during time T2 and transverse relaxation (R2=1/T2)) the transverse magnetization of the nuclei vanishes. Most MRI of methods relies on Hydrogen nuclei of water to map different types of tissue based on different T1 and T2 relaxation times. MRI scans involve the collection of several images based on spatial location as well as on weighting based on T1 or T2. A sample with low T1 appears bright in a T1-weighted image (Figure 1.16) (Filler, 2009).

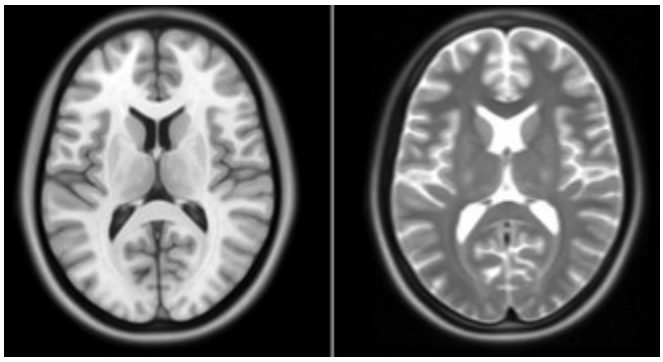

Figure 1.16 MRI T1 and T2 weighted images comparison. In the T1 image (left brain) the white matter (WM) and fat are bright, and cerebrospinal fluid (CSF) and cortex are dark. In T2 (right brain), CSF is bright, fat is light, cortex is light gray, and WM is dark gray. Figure adapted from (Fonov et al., 2011).

Functional MRI (fMRI) is typically performed using the blood-oxygen-level dependent (BOLD) signal, which is a water-1H MRI technique sensitive to regional change in the concentration of paramagnetic deoxygenated hemoglobin (dHb) and diamagnetic oxygenated hemoglobin (Hb) following neural activity. As mentioned in previous sections, any increase in neural activity involves oxygen (and other metabolic substates like glucose) consumption and consequently a local increase in dHb concentration. This phenomenon is also coupled with the release of vasodilators which results in a large CBF increase by arteriole vasodilatation, resulting in a large increase in Hb concentration by dilution (Hoge, 2012). Overall, decreasing the concentration of paramagnetic dHb, while the diamagnetic Hb increases, results in an increase of the blood-oxygen-level-dependent (BOLD) signal following neural activity (Rouquet et al., 2015). This means that any variation in the BOLD signal reflects regional changes in blood flow, blood volume, and energy expenditure of neurons (oxygen consumption. Therefore, oxidative phosphorylation which consumes oxygen, causes changes in blood flow, thereby affecting the dHb and Hb concentration and hence the BOLD signal (Bélanger et al., 2011). The ratio between the increase in blood flow and oxidative metabolism is thought to be about 2:1 in healthy brain tissue (Griffeth & Buxton, 2011). However, depending on the brain region and task, as well as other conditions such as caffeine intake and disease, this ratio may change (Buxton, 2010). During neuronal activity, the release of nitric oxide plays an important role in vasodilation, which lead to cerebral blood volume change (CBV) changes (Kobari et al., 1994; Krieger et al., 2012). Classic hemodynamic models have assumed that the BOLD signal's effective site, among vascular compartments, is within venules and capillaries. Therefore, it's been postulated that the changes in cerebral blood volume (CBV) are dominated by the venules side (Mandeville & Marota, 1999). However, more recent studies attribute the largest fractional CBV changes to arterioles (J. J. Chen & Pike, 2009; Griffeth & Buxton, 2011; C. H. Hillman et al., 2007; Nabavi et al., 2001; F. Zhao et al., 2007). The changes in CBV have a power law relationship with CBF: $CBV \sim CBF^{\alpha}$, where α is the Grubb constant and has been reported to range from 0.38 to 0.50 for total blood volume (Grubb Jr et al., 1974; Wesolowski et al., 2019).

Given the importance of the vascular component of the BOLD signal, combining BOLD with a measure of CBF allows a more complete understanding of the physiological changes that occur during brain activation. In fact, fMRI approaches dedicated to measure CBF can detect the arterial and capillary weighting signal better than BOLD, and are believed to be even closer to the actual locations of cerebral activation than the BOLD signal itself (Chini et al., 2021), which is prone to bias from veins (Kay et al., 2019). Arterial spin labelling (ASL) methods are the most common

fMRI methods to measure either absolute values of CBF or relative changes in CBF. ASL uses blood water as an endogenous tracer, where the blood water-1H is magnetically tagged before it arrives in the tissue, during the time called the arterial arrival time (AAT). The amount of labelled blood delivered to the tissue is measured (Detre et al., 1992) and compared to a control image obtained without tagging. The basic principle of this method is based on subtracting two consecutively acquired images, the first one called the tag image, acquired after tagging the blood water and the second image called the control image, acquired after the magnetized water is washed out over time (i.e., a regular BOLD image). The tagging is usually performed at the level of the carotids, followed by the so-called post-labelling delay to allow the tag to reach the brain and diffuse into brain tissue. This way, the subtraction image provides information about the amount of labelled blood present in the imaged area. ASL in a non-invasive technique that provides images of local CBF with reasonable spatial and temporal resolution. Furthermore, a dual echo implementation of this method can be used to acquire BOLD and ASL signals simultaneously (Ances et al., 2008; Detre et al., 1992; Ogawa et al., 1992). However, ASL suffers from a low signal-to-noise ratio (SNR) as the signal difference between the tag and control image is only about 0.5% to 1.5% of the total MR signal. Sufficient SNR is usually achieved by repeating the experiment several time to allow averaging or by considering advanced biophysical models to quantify absolute perfusion values (Petersen et al., 2006).

1.5.2.1 BOLD signal modelling

Considering the complexity of the BOLD signal and its complicated relationship with blood flow, volume, and more importantly, oxidative metabolism, accurate modelling of the BOLD signal is required. Even though in humans the gold standard for measuring brain oxygen metabolism, CBF and also CBV remains PET imaging, such acquisitions are complex, requiring several injections of radioactive tracers to the subject, expensive and require the local presence of a cyclotron used to produce ^{15}O and $H_2{}^{15}O$. A typical PET acquisition dedicated to map $CMRO_2$, CBF and CBV would require the sequential administration of $C^{15}O$, ^{15}O and $H_2{}^{15}O$, which exposes the patient to a large radiation dose (~8300 MBq). Furthermore, considering the short half-life of ^{15}O, a cyclotron is required on-site, increasing the cost of the acquisition (Maaniitty et al., 2020; Muzik et al., 2013). An equivalent technique to measure these parameters with MRI would therefore be advantageous since it would lower cost and ionizing radiation exposure, and be more accessible (Ito et al., 2005; Smielewski et al., 2002).

BOLD signal calibrated fMRI models are able to quantitatively measure brain activity by estimating metabolic changes as an index of neuronal activity variation by exploiting the $CMRO_2$-CBF and CBV-CBF coupling in the BOLD response. The earliest calibrated fMRI models were used in conjunction with task-evoked fMRI to estimate task-based $CMRO_2$ changes and to study physiological differences among groups across the lifespan or in disease (Davis et al., 1998; Goodwin et al., 2009; Hoge et al., 1999b; Restom et al., 2008). However, recent developments have focused on measuring baseline absolute $CMRO_2$ (Bulte et al., 2012; Gauthier et al., 2011; Gauthier & Hoge, 2012) due to the importance of baseline oxidative metabolism in understanding diseases with altered oxygen extraction fraction (OEF), like stroke, carotid occlusion, ageing, dementia and other cerebrovascular diseases (Gauthier & Fan, 2019; Hoge, 2012).

The first calibrated MRI model (Bulte et al., 2009; Davis et al., 1998; Hoge et al., 1999a), called the hypercapnic model, was proposed to exploit changes induced by altering the arterial partial pressure of carbon dioxide ($PaCO_2$). This was achieved by breathing a moderate concentration of CO_2 (5%) to cause vasodilation and a blood flow increase without changing oxidative metabolism,

thereby evoking a purely vascular BOLD signal change. Both CBF and the BOLD signal are measured using a dual-echo sequence arterial spin labelling sequence to estimate the maximum possible BOLD signal change, called M. This is the signal one would measure if all dHb present at baseline were removed from brain voxels. The hypercapnia model relates these parameters as follows:

$$M = \left(\frac{\Delta BOLD}{BOLD}\right) / \left(\frac{1 - CBF^{-(\beta-\alpha)}}{CBF_0}\right) \tag{1.9}$$

where, α shows the CBF-CBV coupling and its value is assumed to be between 0.18 and 0.20 to reflect the venous contribution (J. J. Chen & Pike, 2009), and β describes the field-dependent impact of dHb on transverse relaxation and is assumed to be between 1.3 and 1.5 at 3T. In the hypercapnic model, it is also assumed that that arterial blood is completely oxygen saturated. Arterial oxygen saturation is typically higher than 97% in healthy adults. Iso-metabolism during the CO_2 inhalation is another assumption in this model (Hoge et al., 1999b).

The hypercapnic model describes the relationship between M and $CMRO_2$ during the task-evoked experiment as follows:

$$\frac{CMRO_2}{CMRO_{20}} = \left(\frac{CBF^{1-\frac{\alpha}{\beta}}}{CBF_0}\right)\left(1 - \frac{\frac{\Delta BOLD}{BOLD_0}}{M}\right)^{\frac{1}{\beta}} \tag{1.10}$$

where, CBF is the CBF during the task, and CBF_0 is the resting sate CBF (Gauthier & Fan, 2019).

The other type of calibrated MRI is the hyperoxia model, based on changes in venous saturation from alterations in the arterial partial pressure of oxygen (PaO_2) (Chiarelli, Bulte, Wise, et al., 2007). This model was suggested due to dyspnea and discomfort during the CO_2 breathing in a hypercapnic challenge (Feihl & Perret, 1994; Gauthier & Fan, 2019; Manning & Schwartzstein, 1995). In this model, to avoid significant vasoconstriction, a relatively low concentration of O_2 is provided to estimate the M value using the BOLD signal and dHb of venous blood, estimated using the respiratory trace and a physiological model based on the Severinghaus equation (Dash et al., 2016; Honda et al., 1979). Since CBF is assumed to be largely unchanged during inhaled partial hyperoxia, the change in CBF is usually assumed to be 0 in this model. The other assumed constant of this model is the baseline OEF, as well as the same α and β as in the hypercapnia model.

$$\frac{\Delta BOLD}{BOLD} = M \times \left(1 - \left(\frac{CBF}{CBF_0}\right)^{\alpha} \times \left(\frac{[dHb]_v}{[dHb]_{v0}} + \frac{CBF}{CBF_0} - 1\right)^{\beta}\right) \tag{1.11}$$

Using this model the flow changes are assumed rather than measured when calculating M, hence it was found to display less variation compared to the hypercapnia model, and is more preferential, particularly in studying distressed subjects or aging-related cognitive change (Chiarelli, Bulte, Piechnik, et al., 2007; Gauthier & Fan, 2019), it is thought that the assumed constant value for CBF is responsible for the lower M variation, but ultimately results in an underestimation of M and $CMRO_2$, especially during task-evoked challenges (Gauthier & Fan, 2019).

In the next phase of development of the calibrated fMRI models, resting values were estimated, including voxel-wise maps of $CMRO_2$, OEF and other BOLD signal modelling

parameters(Englund et al., 2020). OEF is the balance between oxygen extraction and blood flow. It is an important hemodynamic measure which reflects the efficiency of oxygen utilization by the tissue, and even slight changes in OEF indicate a physiological perturbation and local autoregulatory failure. Resting OEF is around 36 percent and has limited variation across brain regions between 20 and 55 percent (Thompson et al., 2016)

In the method proposed by Bulte et al. (Bulte et al., 2012), the hypercapnic challenge was used to estimate M, and responses to hyperoxia were used to obtain baseline voxel-wise maps of OEF, AAT and CBV.

The generalized calibration model (GCM) went a step further and combined both hypercapnic and hyperoxic models to create a single model that could be used for both. The GCM incorporates CBF in the equation linking the arterial content of O_2 (Ca_{O_2}) and venous concentration of O_2 (Cv_{O_2})

$$Cv_{O_2} = Ca_{O_2} - \left(\frac{Ca_{O_2}|_0 \times OEF_0}{\frac{CBF}{CBF_0}} \right) \tag{1.12}$$

$$Ca_{O_2} = \left(\varphi.[Hb].Sa_{O_2}\right) + (Pa_{O_2}.\epsilon) \tag{1.13}$$

where ϕ is the oxygen-carrying capacity of hemoglobin which is species-dependent and ϵ is the solubility coefficient of oxygen in the blood. In humans the following values can be used: ϕ=1.34 mlO_2/g Hb, ϵ=0.0031mlO_2/(dl blood·mmHg). The fractional arterial oxygen saturation Sa_{O_2}(Honda et al., 1979; Severinghaus, 1979) is related to the partial pressure of O_2 (PaO_2), which reflects the amount of oxygen gas dissolved in the blood, via the Severinghaus equation as below:

$$Sa_{O_2} = \frac{1}{{23400}/{(Pa_{O_2} + 150Pa_{O_2})} + 1} \tag{1.14}$$

The Pa_{O_2} can be estimated from average end-tidal O_2 values, which is the concentration of O_2 in the in exhaled breath and represents the functional reserve capacity.

This model, by employing any arbitrary combination of changes in O_2 and CO_2, has been shown to be more stable than both the hypercapnia and hyperoxia models (Bulte et al., 2012; Gauthier et al., 2011; Gauthier & Hoge, 2012; Hoge, 2012). Resting metabolism can be estimated using this model by using two or more breathing manipulations (hypercapnia and hyperoxia), and simultaneously measuring the BOLD signal, ASL and end-tidal O_2 values. In the model proposed by Gauthier and Hoge, the GCM model is defined as a nonlinear equation relating the BOLD, CBF and end-tidal O_2 signals with two unknown parameters M and OEF. Hence using this framework, the resting OEF can be estimated by detecting the intersection point of two M vs OEF curves constructed using breathing challenges with two different O_2 and CO_2 concentrations.

One advantage of the GCM as a framework for studying brain physiology is that in addition to CBF, OEF, and $CMRO_2$, we are also able to estimate Cerebrovascular reactivity (CVR) maps. CVR demonstrates the ability of cerebral vessels to dilate or constrict in response to challenges, in this case, inhalation of CO2. CVR is a measure of the vascular reserve, which is complementary to steady state information captured by CBF and CBV. Aging and diseases such as arterial stenosis, stroke, small vessel disease, brain tumors and injuries can affect CVR (Hou et al., 2020)

CVR is measured using the equation:

$$CVR = \Delta MRI / \Delta End\text{-}tidal\text{-}CO_2 \quad (1.15)$$

Where the MRI can be the BOLD signal or the CBF from ASL, ΔMRI and $\Delta End\text{-}tidal\text{-}CO_2$ are calculated as the difference between baseline and the hypercapnic challenge.

The GCM has some limitations linked to its assumptions. Even though the GCM model is found to be powerful to estimate OEF and M values, the iso-metabolism under hypercapnia and a small and/or non-existence CBF variation during hyperoxia assumptions have been shown to lead to up to 33% variations in $CMRO_2$ across days in a recent 7T MRI studies (Gauthier & Fan, 2019).

In an extended version of these calibrated models, several varying levels of hypercapnia interleaved with hyperoxia challenges, as well as combined challenges are applied, to simultaneously modulate CBF and arterial oxygen levels(Wise et al., 2013). Furthermore, a Bayesian estimation framework was implemented to uncover with greater stability the cerebrovascular dependent parameters in the BOLD signal model. In this model, in addition to $CMRO_2$ and OEF maps, maps of the α parameter which relates the relative increases in CBF to CBV and the β exponent that relates the deoxyhemoglobin concentration to the relaxation rate 2 (Wise et al., 2013) can be obtained. The estimated range for α and β exponent among healthy adults (acquired on a 3T whole-body MRI system) using this model, were 0.33±0.06, and 1.35±0.13 respectively.

1.6 Spatial variability of metabolic features within the healthy adult brain

In this subsection we review the physiological importance and regional variability of physio-metabolic measures, which we discussed in the previous section, including cerebral glucose and oxygen metabolism as well as cerebral blood flow and oxygen extraction fraction.

1.6.1 Cerebral metabolic rate of Glucose (CMRGlc)

In the normal state glucose oxidation is the primary energy source for the adult human brain's neuronal activity. The Glucose level in the brain is around 1–3 mM, of which at least 95% contribute to oxidative metabolism and nearly 5% to aerobic glycolysis to produce energy (Hyder et al., 2013). However, Glucose is not only required to provide ATP to fuel brain energy demands, of which a large proportion is consumed for action and postsynaptic potentials generation, maintaining the ion gradients and neuronal resting potential (Hall et al., 2012; Ivannikov et al., 2010), but also is a precursor for neurotransmitter synthesis (Dienel, 2012). Under the physiological condition the amount of glucose a resting brain utilizes, per unit mass tissue and per unit time, the cerebral metabolic rate of glucose (CMRGlc), is ranging from 4 to 7 nmol/mL (Aanerud et al., 2012; Poulsen et al., 1997).

As mentioned in the imaging subsection, PET is the leading neuroimaging technique that allows the determination of CMRGlc consumption based on the qualitative evaluation of regional uptake of ^{18}F-FDG tracer.

The earliest study of 18F-DG PET demonstrated that there is a positive correlation in gray matter structures between the brain vascular density and glucose metabolism as well as a negative correlation with lactate dehydrogenase (LDH), the enzyme that converts lactate into pyruvate in the cytosol of a cell (Borowsky & Collins, 1989). The recent cell type analysis showed that the capillary density has around 20% variation across brain regions (Ventura-Antunes et al., 2022). In addition to capillary density variation that affects glucose usage, there is also metabolic difference

not only in terms of the amount of energy usage but also in the end-product of the glucose pathway across the brain's cell types. Among the most abundant cell types in the brain, such as excitatory and inhibitory neurons, oligodendrocyte, astroglia, endothelial cells, and microglia, neurons have shown to demand higher energy demands, as well as being enriched with enzymes for oxidative metabolism (Mächler et al., 2016). On the other hand, even though glial cells and astrocytes have mitochondria, they are mainly using glycolysis, through which they can provide pyruvate and lactate for neurons (Yellen, 2018). Despite all the sources of variabilities and heterogeneities, ^{18}FDG-PET studies have shown that the regional variations of resting CMRGlc across the brain were just around ±10% from the mean (Thompson et al., 2016).

The highest CMRGlc level is within putamen, dorsal posterior and anterior cingulate cortex, primary visual cortex, and primary and association auditory cortex, and the lowest within the amygdala, hypothalamus, temporal pole area, part of cingulate cortex and anterior entorhinal cortex (Thompson et al., 2016). The whole brain resting CMRGlc is about 0.26 μmol/g/min, and it has a lower range in the white matter (~0.22 μmol/g/min) and greater values in the gray matter (~0.28 μmol/g/min) (Thompson et al., 2016; Vavilala et al., 2002)(Figure 1.17, Figure 1.18). Glucose metabolism also is shown to have a correlation with brain regional activation, especially within default mode and associated network. These areas are known to have a high number of functional connections to other regions of the brain. Such findings would confirm not only the metabolic cost of brain functional activity but also their non-homogeneous metabolic demands across different brain areas (M. Bernier et al., 2017).

However, it is important to mention that the kinetic model considered for PET glucose metabolism estimation is actually assuming homogeneity of blood flow and transporter rates between plasma and cerebral tissue within brain regions, as well as similar phosphorylation rates for glucose and ^{18}F-FDG (Berti et al., 2014; Sokoloff, 1977). However, the cerebral blood flow (CBF) measurements, even at rest, is contradicting such an assumption, since CBF non-homogeneity across brain regions has been reported (J. J. Chen & Pike, 2009; Pantano et al., 1984). Hence adding perfusion information included in a CBF map would be of great interest to better understand the regional brain metabolic feature of CMRGlc. In addition, the cerebral metabolic rate of oxygen ($CMRO_2$) provides complementary information that would help reveal the regional variation of oxidative versus non-oxidative pathways of glucose. Besides CBF, another important brain metabolic measure is the oxygen extraction fraction (OEF), which assesses the fraction of arterial oxygen extracted by brain tissue from the brain vasculature. Since this happens mainly within the capillary bed, OEF has a tight connection with cerebral capillary density. Characterizing OEF would help reveal the role of brain vasculature properties in brain functioning and metabolic profiles. Therefore, in the next section, we will review the regional features of these above-mentioned physiological biomarkers (CBF, OEF), besides the other brain metabolic demand, $CMRO_2$, that all help obtain a more complete picture of brain metabolic behaviour and functioning.

1.6.2 Cerebral blood flow (CBF)

Cerebral blood flow is defined as the blood volume that flows per unit mass per unit time. It reveals several key physiological biomarkers of the brain like microvascular density and reactivity, as well as indirectly assessing regional brain metabolism (Barber et al., 1970). Glucose in the brain can be stored in the form of glycogen in glial cells (mainly in astrocytes), which amounts up to 3–12 μ mol/g and would last for a few minutes, in absence of glucose supply (Brown, 2004). On the other hand, the oxygen storage molecules in the brain, Neuroglobin, a protein with oxygen-binding capacity, has a very low molecular storage capacity (~ 1 nmol/mL) and can maintain brain oxygen

content around 30 nmol/mL, lasting only for a second in absence of oxygen supply (Leithner & Royl, 2014; Madsen et al., 1995; Pearigen et al., 1996). CBF increment has a direct influence on enhancing the PO_2 level, thus, it has been postulated that the main role of CBF is to keep a moderate safety margin of the brain oxygen content and a partial pressure of O_2 (PO_2) around the 25 mm Hg, therefore allowing a proportion of oxygen extracted from the capillary's networks around 30% to 50% ratio, which is larger than the amount of glucose extraction (~10%). Indeed, approximately six molecules of oxygen are extracted from brain circulation per one molecule of glucose (Aanerud et al., 2012; Choi et al., 2004; Madsen et al., 1995). Under normal physiological conditions, the average brain tissue PO_2, measured using the fibre optic method (Ortiz-Prado et al., 2010), is ranging from 20 to 30 mm Hg. However, PO_2 exhibits significant microregional variability across brain regions, with considerably lower values in regions that are distant from micro-vessels (Aanerud et al., 2012; Devor et al., 2011). Indeed, the PO_2 level across the brain depends on multiple factors, including the geometry of the vascular network, the density of the capillaries, the metabolic rate of oxygen and the capillary oxygen content. The average capillary oxygen level varies between 40 to 50 mm Hg across brain regions (Vovenko, 1999).

Blood perfusion allows the circulating of important brain metabolic substrates like glucose, and oxygen, but also less demanded metabolites such as ketone bodies and lactate (Bélanger et al., 2011). Blood perfusion also plays a critical role in removing the metabolic waste products that have a substantial contribution to neurovascular couplings (Gjedde, 2007; Leithner & Royl, 2014), such as lactate (Ido et al., 2001; Mintun et al., 2004), CO_2, or heat (Katz-Brull et al., 2006; Yablonskiy et al., 2000).

In general, the blood flow, even though it does not strictly fulfill all the requirements, can be defined as the flow in a tube by Ohm's law, with the assumption that such flow is steady, laminar, and uniform through thinned-walled non-distensible tubes (Coulson et al., 2004). In summary Ohm's law states that flow is proportional to the difference in inflow and outflow pressure (ΔP) divided by the resistance to flow (R): flow = $\Delta P/R$. According to this law, brain cerebral blood flow is regulated by the pressure difference across vascular segments over its resistance. Where the pressure is called cerebral perfusion pressure (CPP) and the total resistance is called cerebrovascular resistance (Fantini et al., 2016).

The CPP drives the oxygen delivery to cerebral tissue. Normal CPP values range between 60 and 80 mmHg depending on the individual subject's physiology. CPP is defined as the difference between the mean arterial pressure (MAP), which is the weighted average of the systolic and diastolic pressure, and the intracranial pressure (ICP). ICP is the pressure of the cerebrospinal fluid (CSF) in the subarachnoid space, which its measurement requires the invasive placement of a pressure monitoring sensor in the skull (Munakomi & Das, 2022). The normal range for resting MAP is from 70 to 100 mmHg while resting ICP values are ranging from 5 to 15 mmHg. Therefore, ICP has less impact on CPP when compared to MAP values (Mount & Das, 2021). Indeed, any factor that may change the perfusion pressure and the resistance of the system through vessels diameters (e.g., vasodilation, vasoconstriction) and the blood viscosity, like hematocrit level, will significantly impact the CBF (Henriksen et al., 2018). The index of cerebral vessels' ability to dilate or constrict in response to arterial pressure is denoted by a physiological measure called cerebrovascular reactivity (CVR), which can provide highly complementary information to CBF (W. Li et al., 2020). Since the largest pressure changes actually occur within the arterioles along the vascular tree, the site of CVR response to a vaso-active stimulus is thought to be there(Lennox & Gibbs, 1932) . In addition to the arterioles, other large vessels, such as the internal carotid artery

and middle cerebral artery also contribute to resting CVR response (Coverdale et al., 2014; Verbree et al., 2014). The partial pressure of CO_2 (PCO_2) is another key regulator of both CBF and CVR, since even small fluctuations in PCO2 level, will induce cascade reactions in brain vasculature and results in large changes in CBF (Henriksen et al., 2013; Hoiland et al., 2011). As a result, the CVR can actually be measured by employing a hypercapnic challenge. To do so, subjects will breathe air containing a low concentration of CO_2, to induce vasodilatation of the vessels. CVR is then estimated as the ratio of the change in BOLD (or CBF) signal to the amount of increase in blood PCO_2 (Poublanc et al., 2015).

While several signalling molecules, such as nitric oxide, adenosine, reactive oxygen species, prostaglandins, and other eicosanoids have been suggested to play a potential role in regulating CVR(Hoiland et al., 2019), the most accepted molecular signalling mechanisms is the following: the blood transportation of absorbed CO_2 from lung alveolus to brain and exchange with perivascular space induces a pH decrease within perivascular segments. That causes blockage of calcium channels in arteriolar smooth muscle cells and subsequently produces a reduction in local calcium concentration, relaxation in arteriolar smooth muscle cells and local vasodilation that all induce the CVR contrast measured by bold and CBF signal (Krishnamurthy et al., 2021).

The gold standard to measure the CBF is using PET with spatial resolution on the order of typically ~3-5 mm, with intravenous injection of [^{15}O] H_2O (Ito et al., 2021; Meyer et al., 1987). As already mentioned in more detail in the imaging technique subsection, the other popular MR-based technique to measure CBF is arterial spin labelling (ASL). Both PET using ^{15}O-labeled oxygen and ASL allow quantifying absolute measures of CBF and dynamics of the arterial tracer delivery (magnetized water in MRI and radiotracer in PET) (Fantini et al., 2016).

Indeed, considering the complexity and cost of employing labelled O_2 (which requires a cyclotron on site) as well as the ethical concerns for employing the radioactive tracer in PET acquisition, especially for healthy subjects, the completely non-invasive and still less expensive ASL technique, despite having low resolution (~4.5×4.5×7.5 cm3 for 3T MRI) and moderate signal-to-noise (SNR), is more favourable. Zhang et al (K. Zhang et al., 2014) conducted a study to compare CBF estimations using both techniques in resting healthy human brain and showed a significant correlation ($p<0.05$) between ^{15}O-PET and pCASL, while reporting a higher regional range of CBF values using ASL across cortical areas. The whole brain resting CBF was estimated about 50 ml/ (100 g min), with lower values in the white matter [~20 ml/(100 g min)] and larger values in the gray matter [~80 ml/(100 g min)] (Vavilala et al., 2002). The largest CBF values were reported within the putamen, the thalamus, dorsal posterior and anterior cingulate cortex, primary and association auditory cortex, and primary visual cortex. The lowest CBF values were reported within the temporal pole area, hypothalamus, and primary somatosensory cortex (Thompson et al., 2016) (Figure 1.17, Figure 1.18). The regional variation of CBF has been also shown to have a meaningful correlation with CMRGlc, which suggests using CBF as a potential surrogate for CMRGlc measure. A study investigated the dependency between blood perfusion, measured by ASL and CMRGlc, acquired by FDG-PET, showed that the regional correlation between the two modalities was the highest within the striatum (R=0.8), moderate within the temporal (R=0.59) and frontal lobes (R=0.52) and poor in all other structures (R=0.3), particularly in mesial structures such as the hippocampus (R= 0.0026), amygdala (R= 0.18), and insula (R=0.14) (Cha et al., 2013). Blood perfusion also is tightly coupled with brain functional connectivity features, specifically within regions with higher number of connections, so-called hubs regions, which confirm the physiological basis of functionally important brain regions

(Lahijanian et al., 2016; Liang et al., 2013; Palombit et al., 2022; D. Tomasi & Volkow, 2010) (Figure 1.17, Figure 1.18).

1.6.3 Oxygen extraction fraction (OEF)

The brain circulation carries oxygen to the capillary bed, where the oxygen is then diffused to brain tissue. The proportion of oxygen that is extracted from vasculature is called the oxygen extraction fraction (OEF). OEF is measured as the difference between arterial and venous oxygen content over arterial oxygen content. Under normal physiological conditions, the arterial oxygen content is relatively uniform throughout the brain and therefore the OEF is mainly proportional to venous oxygenation (Jiang & Lu, 2022). OEF measure depends on the interplay between several physiological and anatomical factors, such as the kinetics of O_2 offloading from hemoglobin (Hb) as well as dynamics of Hb and the mean transit time, which is determined by the blood flow, and the capillary density (Skattebo et al., 2020; Wagner, 2008). Indeed, by measuring OEF levels across different brain cortical layers using photon imaging of resting-state microvascular PO_2, Baoqiang Li et al. (B. Li et al., 2020) reported that the oxygenation heterogeneity and intracapillary resistance to oxygen delivery decrease with a depth of the cortical layers. On the other hand, they found that the oxygen demands were increasing with cortical layer depth, where layer IV was exhibiting a homogenous capillary network with the largest OEF values. It is also worth mentioning that the non-neuronal cell types, like glial and endothelial cells, are relatively constant across the cortical layers, and the largest density of neurons was reported between layers IV and VI, suggesting that neurons require a higher metabolic and especially oxygen demand (B. Li et al., 2019).

Whereas the ^{15}O-PET is considered the gold standard to estimate the voxel-wise map of OEF (Fan et al., 2020) the distinctive magnetic property of blood oxyhemoglobin within the arteries and deoxyhemoglobin in venous provided a non-invasive and less expensive opportunity for both global and regional OEF measurements using fMRI techniques (Rodgers et al., n.d.). In general, there are two approaches for OEF estimation using MRI technique: voxel-wise and whole-brain OEF methods. The Jugular venous blood which primarily drains the cerebral hemispheres and accounts for more than 90% of intracranial circulation, is the most favourable sampling resource in whole-brain OEF estimation methods (M. J. Purves, 1972; Qin et al., 2011). Even though the whole-brain OEF estimation techniques do not provide OEF regional information across the brain, they are more stable when compared to OEF estimations at voxel level (Barhoum et al., 2015). The MRI techniques allow estimating of OEF at the voxel level either consist of T2-based methods, such as quantitative susceptibility mapping (QSM) (Kudo et al., 2016) and quantitative BOLD (qBOLD) (Yablonskiy et al., 2000), or calibrated fMRI techniques (Fan et al., 2020; Hoge, 2012; Jiang & Lu, 2022). The T2-based methods are assuming, under a fixed hematocrit level, a one-to-one correspondence between the blood oxygenation and blood T2 relaxation signal. Therefore, those techniques are able to estimate venous oxygenation which is quite close to OEF values (Bolar et al., 2011; H. Lu & Ge, 2008; Thulborn et al., 1982). QSM methods are based on the paramagnetic property of deoxyhemoglobin that produces a susceptibility difference between blood and tissue, which has a linear relationship with blood oxygenation (Haacke et al., 2010; J. Zhang & Liu, 2015). Quantitative BOLD methods are based on the local field inhomogeneities, and transverse signal decay induced by the paramagnetic deoxyhemoglobin in the “extravascular” space (Gordji-Nejad et al., 2014; Zhu & Chen, 2017). On the other hand, in the second family of approaches to map OEF, the calibrated fMRI methods consist of dual acquisitions of BOLD and perfusion signals (using arterial spin labelling technique) and modelling the BOLD and ASL signal

changes in response to assumed iso-metabolic (i.e., does not change $CMRO_2$) hypercapnic and hyperoxic gas challenge as a function of deoxyhemoglobin (Gauthier & Hoge, 2012; Germuska & Wise, 2019). However, all OEF estimation methods suffer from low SNR, and a moderate correlation (R~0.4) has been reported between voxel-wise OEF map estimation methods (Cho et al., 2021; Gauthier & Fan, 2019). Also Cho et al conducted a study to investigate OEF estimations using PET and MRI approaches, considering QSM-qBOLD and separate ^{15}O-PET acquisition and they did not find a significant correlation between the two methods (Cho et al., 2021). Overall, calibrated fMRI, which has been already covered in more detail in the imaging techniques section, provided higher OEF values when compared to the other two techniques. This technique despite controversial findings exists regarding their iso-metabolic assumption as well as the need for employing gas challenges, by providing a non-invasively combination of important physiological maps including CBF, CVR, and cerebral metabolic rate of oxygen ($CMRO_2$) in one acquisition session, is more favourable and less expensive.

Moreover, inter-subject variability level is also very challenging for OEF estimation methods. Some studies have reported higher inter-subject variability among the healthy population using calibrated MRI OEF estimation methods (up to ~16%) (Liu P 2016) compared to 15O-PET (~13%, Ito H 2004). However, others reported contradictory results, suggesting lower inter-subject variability for MRI techniques, when compared to PET approaches (20.5% for PET and 7.6% for QSM-qBOLD technique (Ma et al., 2020). OEF inter-subject variability has also been shown to be positively associated with age, systolic blood pressure, and an individual's end-tidal PCO_2 (R~50%). When taking into account these three factors in the analysis, inter-subject variability of OEF maps was reduced by R~73% (Hou et al., 2020).

Overall, both PET and MRI-based methods provide similar levels of regional variability across brain regions for resting state OEF, around 10%. For the whole brain, reported baseline OEF values were respectively 30.8 ± 4.0% using PET and 32.9 ± 4.4% using MRI-based modalities, whereas 34.4 ± 7.0% and 32.5 ± 2.4% for grey matter, and 32.2 ± 6.8 and 35.7 ± 3.0% for white matter were respectively reported. The largest OEF values were found in the occipital lobe, precuneus, putamen and temporopolar area, and the lowest within entorhinal, insular cortex, and anterior cingulate cortex (Ma et al., 2020; Thompson et al., 2016) (Figure 1.17, Figure 1.18).

1.6.4 Cerebral metabolic rate of oxygen ($CMRO_2$)

The brain consumption of oxygen accounts for 20% of whole-body usage and still brain does not have significant oxygen storage. Instead, it substantially relies on blood circulation and receives almost 15% of cardiac output to fulfill its blood perfusion demands which are around 15-20% of the body's blood supply (Rolfe & Brown, 1997). To answer its high oxygen costs, the brain relies on tight coordination with a dense network of blood circulation, extracting the oxygen from capillaries to the brain tissue and mitochondrion through diffusion and precisely regulating the oxygen gradient (Leithner & Royl, 2014). The cerebral metabolic rate of oxygen consumption ($CMRO_2$) is defined as the amount of oxygen consumed per unit mass tissue and per unit time and is proportional to the product of OEF and CBF ($CMRO_2 \approx OEF \times CBF$) The physiologic level of $CMRO_2$ is around 30 nmol/(mL/second), while the oxygen content of the brain tissue is around 30 nmol/mL. Therefore, if the blood supply stops, it would sustain the physiological $CMRO_2$ level only for one second (Aanerud et al., 2012; Leithner & Royl, 2014). The minimum PO_2 gradient from the capillary to the tissue for maintaining the brain physiologic $CMRO_2$ level is around 10 to 20 mm Hg (Aanerud et al., 2012; Devor et al., 2011; Ito et al., 2005). While CBF level has been suggested as a key factor to balance the physiological $CMRO_2$ level, several studies reported high

correlations between CBF and $CMRO_2$ maps (Henriksen et al., 2018; Liang et al., 2013; Thompson et al., 2016), however, both baseline and task brain metabolism experiments confirmed that the CBF variation is not tightly accompanied by $CMRO_2$ (Gjedde et al., 2005; Griffeth & Buxton, 2011; Leontiev & Buxton, 2007). Even at rest, CBF values are larger than the level that would be required to support physiological $CMRO_2$. Indeed, oxidative metabolism can increase within a limit (~15%) without a concomitant CBF increase (Leithner & Royl, 2014). In some studies, a nonlinear relationship model has been proposed between CBF and $CMRO_2$ dynamics (Hyder et al., 1998; A.-L. Lin et al., 2012). There are also other parameters regulating $CMRO_2$ mechanisms, including changes in ADP availability, mitochondrial PO_2, dynamics of the respiratory cascade for oxygen, inhibitory effects of ATP and NO on cytochrome c oxidase and changes in intracellular Ca2+ concentrations (Leithner & Royl, 2014).

Broadly, the main neuroimaging techniques consider for estimating the $CMRO_2$ can be grouped into PET and MRI-based methodologies. The PET technique that is considered as a gold standard to measure the $CMRO_2$, requires the injection of a ^{15}O-H_2O tracer (Ohta et al., 1992), which can be combined with a separate PET scan with a ^{15}O inhalation tracer to include the CBF and OEF estimation as well (Kudomi et al., 2013). However, the issue of applying ionizing radiation, particularly for healthy control groups, as well as the cost and complexity of PET techniques, make the non-invasive MRI techniques more desirable alternatives. The MRI methods to estimate the $CMRO_2$, are based on quantitative modeling of either MRI magnitude or phase data. The magnitude modeling methods include T2-based, qBOLD, and calibrated fMRI methods, while the phase modeling consist of QSM (Fan et al., 2020; Gauthier & Hoge, 2013; Jiang & Lu, 2022).

The inter-subject variability was reported around 12.8% ± 1.1% for ^{15}O-PET (Coles et al., 2006). Similar inter-subject variability values were found when estimating $CMRO_2$ using calibrated fMRI (12.3 ± 10%, (Merola et al., 2018). The variability of mean cortical $CMRO_2$ using different MRI techniques is actually relatively high (Merola et al., 2018) and ranges from 127±7 μmol/100 g/min (T2-based, (Jain et al., 2010)) to 184 ± 45 μmol/100 g/min (calibrated fMRI, (Betts et al., 2013; Wise et al., 2013). The mean cortical $CMRO_2$ using PET studies is around 3.3 ± 0.5 ml/100 g/min (Fan et al., 2020; Ibaraki et al., 2004).

Using PET methods, the largest $CMRO_2$ values were reported within the posterior cingulate, the occipital lobe, the putamen, and the fusiform gyrus, whereas the smallest $CMRO_2$ values were reported within the hypothalamus and the Entorhinal Cortex (Ibaraki et al., 2019; Thompson et al., 2016). The regional $CMRO_2$ values estimated using MRI techniques provided similar ranges of variability with slightly larger values within the occipital lobe (Henriksen et al., 2021; Ma, 2020) (Figure 1.17, Figure 1.18).

The brain oxygen metabolism measured by the $CMRO_2$ metric has been shown to have a meaningful correlation with other physiological and functional features of the brain. For example, using PET quantitative techniques to measure absolute baseline values of CMRGlc, CBF and $CMRO_2$, Hyder et al. (Thompson et al., 2016) reported overall whole-brain global coupling between these three measures, while the largest spatial correlation was found between $CMRO_2$ and CMRGlc ($R = 0.82$) and slightly lower between $CMRO_2$ and CBF ($R \sim 0.80$). However, another study (Liang et al., 2013) assessing $CMRO_2$ and CBF using the calibrated fMRI technique, and CMRGlc using FDG-PET, reported a higher spatial correlation between CBF with CMRGlc ($R = 0.54$, $P < 0.0001$) and lower correlation between $CMRO_2$ and CBF ($R = 0.31$, $P = 0.005$). The $CMRO_2$ regional variability has also been shown to have meaningful coupling with brain regional

activity, especially within brain hubs regions that are predominantly located in the posterior cingulate cortex/precuneus, medial prefrontal cortex, and lateral temporal and parietal cortices (Liang et al., 2013). These regions are mostly part of default mode networks that is responsible for the higher cognitive activity and brain integration and exhibits a higher level of both oxygen and glucose metabolism and CBF at rest (Raichle et al., 2001). However, as suggested before, the CBF level is larger than the amount that is required to maintain a physiological $CMRO_2$ level at rest but even more during tasks. The fMRI studies have demonstrated degrees of uncoupling between the CBF and $CMRO_2$, showed a larger CBF increase when compared to $CMRO_2$ (P. T. Fox & Raichle, 1986; Frahm et al., 1996). The voxel-wise connectivity analysis of $CMRO_2$ data also found spatial patterns consistent with four resting-state subnetworks: frontoparietal and default mode that are part of association networks and auditory and occipital-visual, which belong to primary networks (Hubbard et al., 2021).

Glucose oxidation is the main pathway bringing energy to the brain. Most glucose molecules will be used to produce ATP to maintain the equilibrium state of ion concentration, especially in support of membrane depolarization through ATPase channel activity (Thompson et al., 2016). The amount of oxygen consumed for complete oxidation of different glucose derivations varies with their number of carbon atoms. Hence full oxidation of one molecule of glucose (a 6-carbon molecule) requires six molecules of oxygen during the tricarboxylic acid (TCA) cycle, which can produce up to 32-38 ATP (as well as 6 molecules of carbon dioxide and water). This is almost 16-17 times higher than the amount of ATP generated through the glycolysis or non-oxidative pathway (Hyder et al., 2013). However, the end products of glycolysis, i.e., lactate and pyruvate, provided mainly by the astrocytes, can also enter the TCA cycle and be fully oxidized. The oxidative and non-oxidative pathways of glucose usually are characterized by the so-called oxygen to glucose index (OGI). OGI is defined as the ratio of arteriovenous deficits in oxygen vs. glucose and is measured by dividing the absolute $CMRO_2$ by CMRGlc (Thompson et al., 2016). Non-oxidative or aerobic glycolysis pathways are characterized by an OGI value lower than 6, reflecting the production of lactate or other metabolites like ketone bodies that remain in the tissue without yielding carbon dioxide and water through metabolism. One can also consider other complementary measures such as the oxygen-carbohydrate index and the oxygen-carbohydrate ketone index, which, as opposed to OGI that only consider glucose, are taking into account the oxidation of lactate and lactate plus ketones. Lactate and lactate plus ketones can be taken up from the blood supply and then oxidized, particularly during physical exercise and starvation (Benveniste et al., 2018). The absolute OGI mean ± SD values (excluding the cerebellum) using PET acquisition were reported as 5.17 ± 0.95 for the whole brain, 5.26 ± 0.99 for the gray matter, and 4.83 ± 0.60 for the white matter. PET absolute measurements already showed that there is a remarkably spatial agreement not only between regional OGI and OEF variation but also within nearly 90% of all brain voxels (with PET spatial resolution of 2.5 mm3) (Thompson et al., 2016). This study also showed that both OGI and OEF values were significantly higher ($P<.001$) within grey matter than in white matter, and that both OEF and OGI have are exhibiting small regional differences (<10%) throughout the gray matter. Therefore, Hyder et al. (Thompson et al., 2016) suggested that no particular brain region was exhibiting a higher level of aerobic glycolysis and subsequently low oxidative phosphorylation rates. These results were in contradiction with the one reported by Vaishnavi et al. (Vaishnavi et al., 2010), another PET study proposing a relative and dimensionless glycolytic measure called glycolytic index (GI), estimated by taking the scaled residuals above and below the voxel-wise linear regressions of normalized CMRGlc on normalized $CMRO_2$. Vaishnavi et al. (Vaishnavi et al., 2010) suggested non-uniform GI distribution across

the brain and proposed a predominant aerobic glycolysis metabolic profile for medial and lateral parietal and prefrontal cortices areas. More recently Blazey et al. (Blazey et al., 2018) from the same lab as Vaishnavi et al. (2010), considered the PET data set allowing absolute quantification provided by Hyder et al. (Thompson et al., 2016). By carefully taking into account inter-subjects' variability, they indeed reported regional differences in aerobic glycolysis within the gray matter, therefore showing consistent results with Vaishnavi et al. results, using the data set provided by Hyder et al.

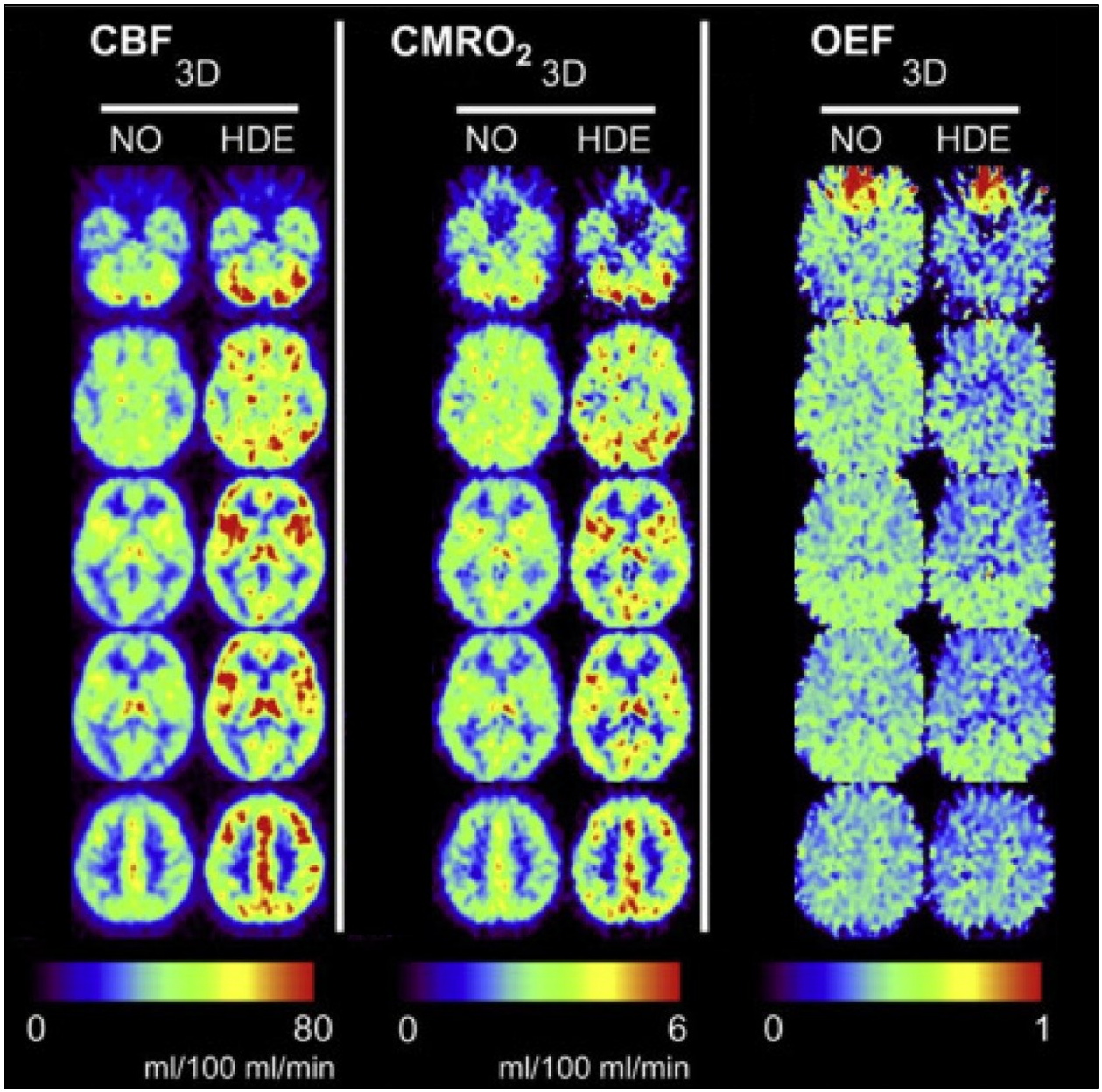

Figure 1.17 Healthy subject dynamic maps of CBF, $CMRO_2$, and OEF from [^{15}O]-oxygen PET in the same healthy subject acquired a 3d scanner without scatter correction (NO) and with hybrid dual-energy (HDE) scatter correction. Figure adapted from (Fan et al., 2020).

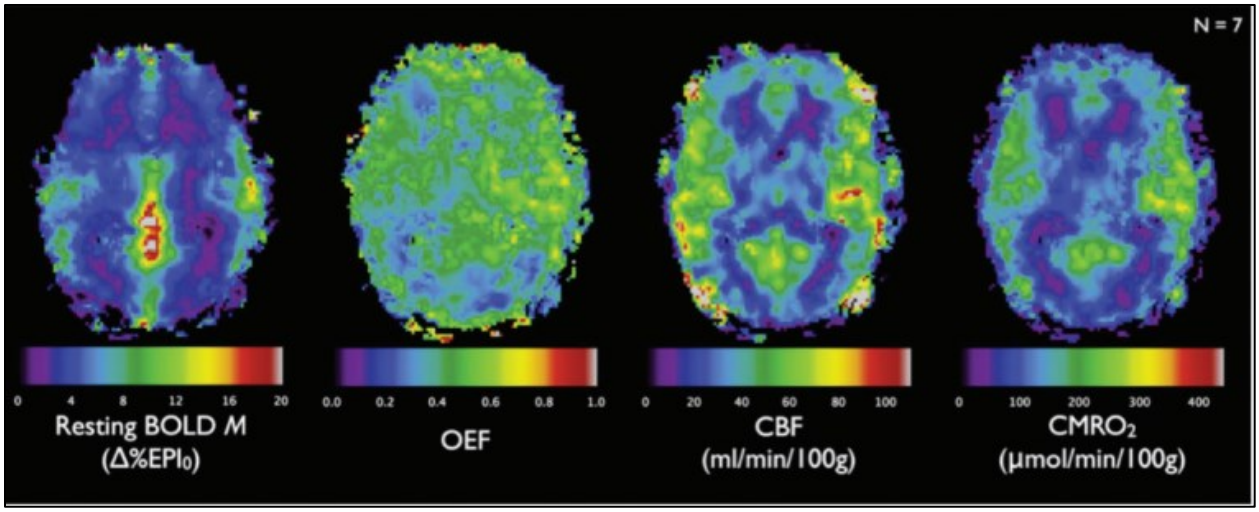

Figure 1.18 Group average maps of resting-state parameters obtained from dual gas (hyperoxia and hypercapnia) calibrated bold. Figure adapted from (Gauthier & Hoge, 2012).

In summary, even if glucose is the main energy substrate, which through an oxidative pathway and metabolizing oxygen, provides major brain ATP demands, it is also important to consider other brain physiological biomarkers, such as CBF, OEF, $CMRO_2$ and CVR, providing complementary information about brain vasculature system and metabolic regional heterogeneity. In terms of acquisition options, even if PET and especially PET absolute measurements are still considered as the gold standard for these metrics, acquisition cost, complexity of implementation and complication of employing short-life radioactive tracer, non-invasive MRI techniques provide more desirable alternatives with comparable precision (Fan et al., 2020; Gauthier & Fan, 2019; Wise et al., 2013). The brain metabolic demands are non-homogeneous and there is regional variability not only in terms of the metabolic level but also metabolic pathway, and both rest-state and task fMRI studies showed such variability has tight coupling with brain functional activity. Over recent decades such coupling has been firmly confirmed by literature and more recent studies now are trying to model the relationship between brain metabolic and functioning profile, in which considering all these measures together, would provide a more complete figure for analysis the brain complicated organization. And finally, in this thesis, such a relationship, using key metabolic physiological markers, including CMRGlc, $CMRO_2$, CBF, OEF and CVR will be carefully investigated.

1.7 Summary

In this chapter, we introduced the main principles of brain neuronal and metabolic background forming and supporting brain functional activity. We started by explaining the physiological details of cell types involved in neuronal signaling. We reviewed the main brain metabolic pathways, including oxidative and non-oxidative pathways of glucose metabolism, as well as the metabolic pathways using other metabolites such as Cr, FAs, and Ketone bodies. We then summarized the brain vascular system, and neurovascular coupling processes. We also reviewed the cell types, and chemicals contributing to the coupling between brain signaling, blood circulation and metabolism at the cellular and molecular level, underpinning what are the mechanisms one can investigate at the meso and macro spatial scales using neuroimaging techniques. Then, we introduced the underlying physics principles considered for detecting neuro-metabolic features using major neuroimaging techniques including PET, resting state fMRI, ASL,

and quantitative fMRI. We further explained the semi-quantitative SUV method considered to estimate CMRGlc, GCM model to estimate $CMRO_2$, CBF, OEF and CVR maps. These measures of metabolic/hemodynamic properties of brain activity using FDG-PET and calibrated fMRI will be considered in our original contributions, in our three studies described in Chapter 3, 4 and 5. Finally, we proposed a literature review of the spatial variation and physiological details of four major brain physio-metabolic features that we considered in this thesis, namely baseline measures of CMRGlc, $CMRO_2$, CBF, and OEF.

Chapter 2: Brain Functional Connectivity

In this chapter, we will discuss the main methods dedicated to analyzing brain functions at different spatial scales. We will first introduce brain functional organization at the cellular, at the voxel/region and at the network/system scales (Figure 2.1). Then we will discuss the concept of brain network organization and resting state networks. Finally, we will review the main methods dedicated to assessing functional connectivity patterns, assessing resting-state brain functional networks and topological organization.

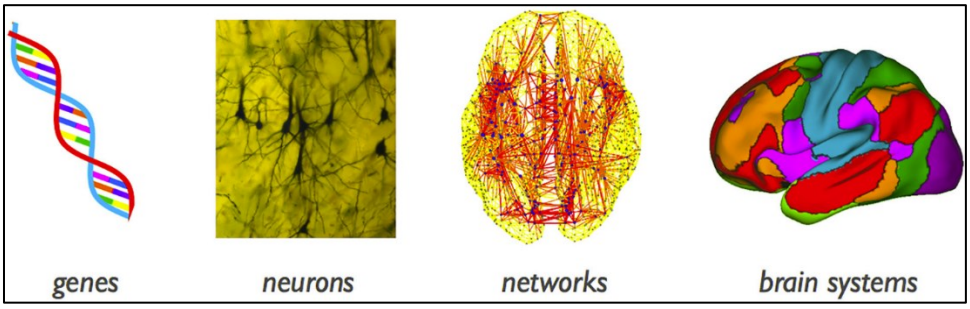

Figure 2.1 Microscale to the Macroscale Level of Human Brain Anatomy and Function. Figure adapted from (Traag et al., 2019).

2.1 Brain functional organization at multi-resolution

Brain structural and functional organization can be characterized at different spatial scales ranging from individual neurons and cell types at molecular microscales, circuits of neuronal cortical layers, columns and cortical regions at intermediate mesoscale and brain networks and systems at the larger macroscale (Figure 2.2) (Dumoulin et al., 2018; Rah et al., 2015). Moreover, brain organization at every level does not work independently, instead, there is a bidirectional interaction between brain scales. For instance, molecular processes involving synaptic and non-synaptic connections at the microscale affect the meso and macro scale connections and activities, while simultaneously, dynamics of brain networks constraint molecular components of the neurons and synaptic formation (Bassett & Sporns, 2017; Haken, 1983).

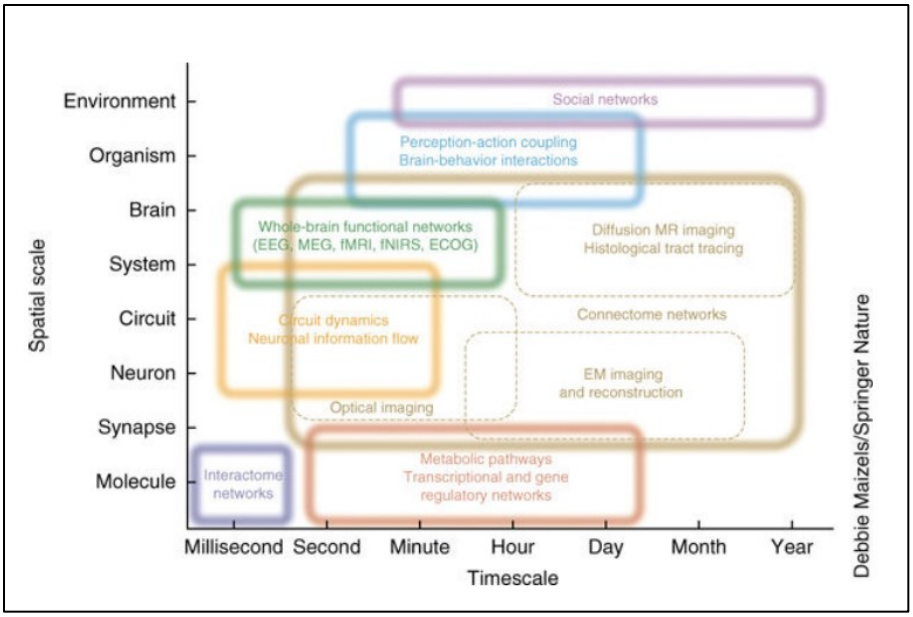

Figure 2.2 Brain organization on multiple spatial and temporal scales. adapted from (Bassett & Sporns, 2017)

2.1.1 Brain function at the molecular resolution

At the molecular resolution, also called microscale resolution, the brain can be described as a mosaic structure composed of neurons and their dendritic and axonal projections, as well as other cell types using specific genetic, cellular, molecular, and developmental processes.

The first attempts to understand this microscopic organization of interconnected neuronal compartments were done by Hubel and Wiesel measurements at the single neuron level using non-human invasive electrophysiology (Hubel & Wiesel, 2005), in parallel with seminal works by Ramon y Cajal, Golgi, and others (1853-1934), proposing very detailed, high-quality drawings of neurons and their microscopic circuit. The early experiments by Nobel-winner neuroscientists like Camillo Golgi proposed a neuronal unit that was including the neurons' soma, axons and dendrites with continuous synaptic connections between cell bodies of the nervous system. The compartment model introduced by Cajal contradicted such a proposal and for the first time claimed that the neurons are discrete cells, that are connected with each other by synaptic junctions (Figure 2.3), the model that is now proven to be true (Wernicke, 1970; y Cajal, 1995).

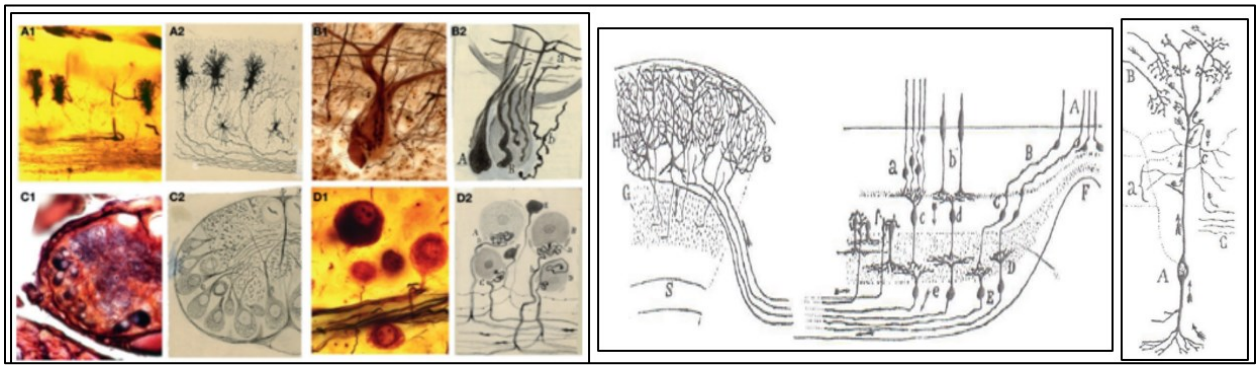

Figure 2.3. The pioneering work of Ramón y Cajal. (a) Santiago Ramón y Cajal first microscopic slide preparations of nervous tissue, a sketch of typical neurons (retinal cone), dendrites, soma and synaptic connection between the cells bodies of the nervous system (Garcia-Lopez et al., 2010; y Cajal, 1995).

From these first microscopic models of the nervous system, it was postulated that brain communication organization and anatomical structure of synaptic connections are driven by two important features: (i) minimization of axonal wiring cost, maintaining cellular material and space and hence metabolic charge, and (ii) minimization of information transmission between neurons, optimizing temporal aspects of neuronal communication (de Robertis et al., 1962; y Cajal, 1995), a concept that is now commonly accepted among scientific communities (Niven & Laughlin, 2008)

Several microanatomy studies around the beginning of 20th century revealed that the common cell types in the human brain are the neurons, the glial cells, monocytes, macrophages and microvascular endothelial cells. Among them, the neurons are the main sources of bioelectrical signalling activity via voltage-gated ion channels and synaptic potentials via neurotransmitter-activated ion channels. Among brain cell types, the most predominant ones are the neurons and glia cells, which communicate with each other mainly through synaptic connections. Synaptic cleft where neurotransmitter exchange is taking place consists, ensuring the connection between white matter fibre tracts, therefore defining the underlying structural framework of brain networks (Rah et al., 2015). Different types of neuronal cells have been mentioned in the previous chapter (1.1.1 Neurons). In this section, we further characterize their contribution to bioelectrical potentials. Pyramidal cells consist of excitatory lengthy cells with distinct dendritic, soma, and axonal zones, which because of their geometrical organization (dendrites being parallel to each other and perpendicular to the cortical surface) are the main contributors to bioelectrical signalling one can record at distance using scalp ElectroEncephaloGraphy (EEG). On the other hand, interneurons are often organized along a spherical shape, with a close field configuration, therefore contributing less to the EEG signal. Figure 2.4 shows the main cell types in the brain and the degree to which each contributes to the field potential and therefore EEG signals (Jessen et al., 2017).

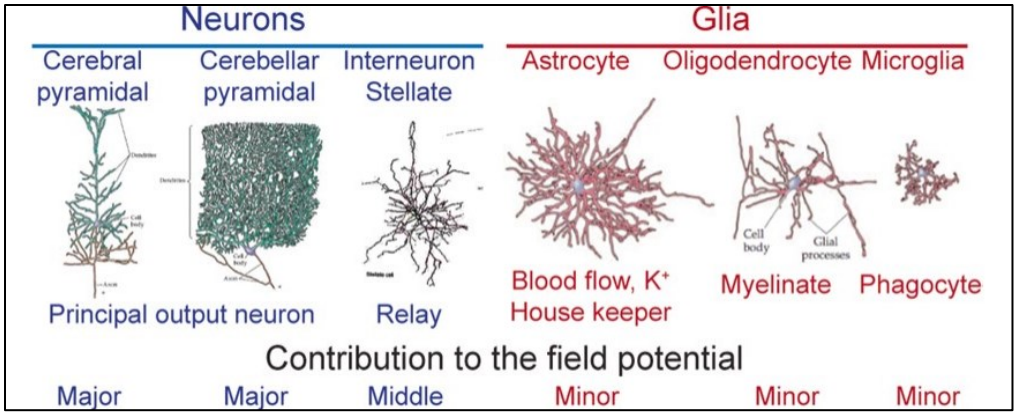

Figure 2.4. Predominant cell types in the brain and their contribution to field potentials. Adapted from (Mathiesen et al., 2014)

In recent years, using advanced technologies such as microarray and/or Ribonucleic acid (RNA)-sequencing techniques from post-mortem brain tissue allowed measuring expression of genes in thousands of brain regions, allowing the introduction of several brain transcriptomic schemes of the brain. The gene ontology (GO) and pathway analysis of genetic expression data from multiple brain regions, provides a great opportunity in exploring the detailed biological basis underpinning of the brain microstructure. The pathway analysis of the genes models the interactions of gene-gene products, while the GO describes three main classes of biological information: (i) the molecular function, which reveals the molecular-level activities performed by an individual or

multiple gene products (i.e. a protein or RNA), (ii) the cellular component, providing information on the anatomy and the locations relative to cellular structures where a gene product performs a function, and (iii) the biological process, that is accomplished by multiple molecular activities (Tzourio-Mazoyer et al., 2002). The most significant human transcriptome datasets currently available are presented in Figure 2.5. Among them, the Allen Human Brain Atlas (AHBA) is the most popular one, providing a high spatial resolution dataset covering all cortical and subcortical regions (Colantuoni et al., 2011; Diez & Sepulcre, 2021; Habib et al., 2017; M. J. Hawrylycz et al., 2012; Kang et al., 2011; Miller et al., 2014). This atlas consists of microarray expression of 20,737 genes, measured by 58,692 probes from 3702 spatially distinct tissue samples obtained from six healthy post-mortem brains.

In addition, more recently, the single-cell RNA sequencing methodology allows for assessing genome-wide expression profiles of brain cells, which represent exquisite information of brain-specific cellular topological data. In studies combining cell type-specific gene markers and genomic atlases, the mixture of seven major neural cell types, including pyramidal neurons, interneurons, astrocytes, microglia, oligodendrocytes, ependymal cells, endothelial cells, and mural cells, have been successfully differentiated (Figure 2.4). Using such unique data, it becomes possible to extract the cell type profile for several human genes from available brain genomic atlases (Darmanis et al., 2015; Diez & Sepulcre, 2021; Habib et al., 2017; Lake et al., 2018; M. Li et al., 2018; Y. Zhang et al., 2016).

Human transcriptome databases

Database	Subjects	Number of Samples	Number of genes	Spatial distribution	Temporal distribution
Allen Human Brain Atlas (AHBA)	6	3,702	20,737	Whole brain	24–57 years
Human Brain Transcriptome	57	1,340	17,565	16 brain regions	5.7wpc–82 years
Brain Cloud	269	269	~14,500	Dorsolateral prefrontal cortex (BA46/9)	14wpc->80 years
Developmental Transcriptome (BrainSpan)	35	492	17,604	16 brain regions	8wpc–40 years
Human Prenatal Brain Development (BrainSpan)	4	1,203	29,180	~25 areas (9 layers per area)	15wpc-21wpc
Genotype-Tissue Expression project (GTEx)	399	3,326	19,670	13 brain regions	20 years -71 years

Single-cell transcriptome databases

Database	Subjects	Number of single nuclei	Samples	Years
Allen Cell Type Database: M1 - 10x genomics	2	76,533	Primary motor cortex	50,60 years
Allen Cell Type Database: Multiple Cortical Areas	50	49,495	Middle temporal gyrus, anterior cingulate cortex, primary visual cortex, primary motor cortex, primary somatosensory cortex, primary auditory cortex	18–83 years
Single-cell analysis of transcriptional and epigenetic states in the human adult brain	6	>60,000	Visual cortex, frontal cortex, and cerebellum	20 years – 49 years
Genotype-Tissue Expression project – Single-Cell data	5	14,963	Hippocampus, frontal cortex	40 years – 65 years
Human brain transcriptome diversity at the single-cell level	8 adults 4 fetal	466	Temporal lobe	21 years – 63 years 16–18w
PsychENCODE - Human Brain Development	3 adults 9 prenatal	17,093	Dorsolateral frontal cortex	18 years -64 years 5pcw-20pcw
RNA-Seq of human astrocytes	14 adult 6 fetal		Temporal lobe	8 years – 63 years 17–20 pcw

Figure 2.5. The details of key publicly available single-cell and transcriptome databases. Figure adapted from (Diez & Sepulcre, 2021).

2.1.2 Voxel and regional resolutions

The intermediate and mesoscale analysis of brain structure refers to functional subdivisions of the nervous system, in so-called "local processing units". The mesoscale is the intermediate scale between the molecular/microscale describing ion channels, individual neurons and cells variations, and the larger macroscale which aims at describing maps of the brain systems and networks, that capturing whole brain dynamics associated with scalp recording of bioelectrical signals, measured using EEG or MagnetoEncephaloGraphy (MEG), as well as cerebral blood flow and metabolism, measured by several neuroimaging techniques, including mainly fMRI and PET.

Typically, analysis of brain anatomical and functional at the mesoscale consists of tracing axonal projections and short-distance multi-synaptic connections using optical imaging and histological tract-tracing approaches (Bota et al., 2015; Oh et al., 2014; Shih et al., 2015; Stephan et al., 2001). Moreover, recent advances in MR diffusion imaging and tractography methodology (Thomas et al., 2014) allow extracting the trajectory and strength of long-distance white matter projections across the circuit architecture of the whole brain, therefore allowing the identification of brain sub-network units (Assaf et al., 2013; Donahue et al., 2016; Khambhati et al., 2017). Such techniques

that derived support from neuroanatomical research in brain atlases with named brain regions (Brodmann & Garey, 2006; Geyer et al., 2011), and are combined with histological methods (tissue processing, dissection) as well as more recently non-invasive imaging of neuroanatomical structure, provide informative representations of both local activity, long-distance connectome of neural circuit and neuroanatomical structure as well as introducing brain-wide high-resolution structural connectome (Figure 2.6).

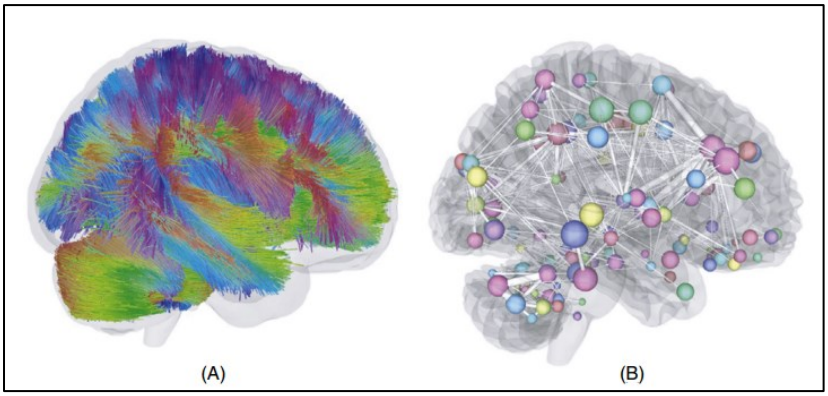

Figure 2.6. An example atlas of the structural connectome. (A) The underlying structural characteristics of axonal fibre bundles in a colour-coded surface (red–blue–green indicates the orientation at the x–y–z axis, respectively) were revealed by diffusion magnetic resonance image. (B) The atlas was then used to build the connectome graph showing the connections between brain regions using an anatomical parcellation. Figure adapted from (Wu et al., 2022).

It is worth mentioning that the notion of mesoscopic scale is quite variable in the literature. In practice, the mesoscale level is a complementary level that describes neuronal circuit architecture typically on the spatial scale of a few millimetres to centimetres (Bohland et al., 2009), therefore as an intermediate resolution between the "microscale" and the "macroscale" levels (Hans Liljenström, 2012). The main focus is therefore on scales that are larger than single or a few neuronal units, and smaller than the entire brain networks, therefore mainly referring to layers or columns within brain cortical areas, characterized by their summed activity of a large number of interconnected neuronal elements exhibiting synchronous oscillatory neuronal activity resulting in spatial homogeneity. Such spatial mesoscale arrangements result in multiple closely interacting regions, sharing local characteristics and/or function or connectivity fingerprints, resulting in a so-called parcellation of the whole brain (Eickhoff et al., 2018). In general, the concept of brain parcellation refers to the definition of a "detailed to simplified" partition of the brain into homogeneous regions. The definition of these parcels, reporting closely interacting areas or networks that help understand the brain organization and function, depends on research objectives (Craddock et al., 2013). In this sense, the very first parcellation of the brain was the one proposed by Brodman, characterizing brain regions based on their cytoarchitecture properties (Brodmann, 1909,(Zilles, 2018)) where later an English translation of his monography was introduced by Laurence Garey in 1994 (Garey, 1999). Several parcellation atlases have then been proposed based on either anatomical and/or functional neuroimaging data (Lawrence et al., 2021). For instance, Aubert-Broche et al. (Aubert-Broche et al., 2009) demonstrated that hierarchical clustering of brain regions based on their T1/T2/PD MR properties was providing a partition of brain regions very similar to the seminal work of Brodmann. Such parcels/networks integrate the information from hundreds of thousands of voxels and compress them into manageable sets of partitions and distinct entities, usually of a few hundred regions (Eickhoff, Yeo, and Genon 2018). The defined brain partitions need to fulfill three main criteria: (i) parcels should be either functionally and/or

anatomically homogeneous, (ii) meanwhile reflecting the functional and/or anatomical heterogeneity across brains, (iii) as well as accounting for spatial relationships between defined parcels (Fornito et al., 2013). In Figure 2.7 we are presenting a few examples of parcellations/atlases of the whole brain or of the cortex, that have been derived from either anatomical or functional neuroimaging data. The illustrated atlases that have been derived from anatomical imaging, include the automated anatomical labelling atlas AAL (Tzourio-Mazoyer et al., 2002), featuring 82 parcels and covering the whole brain, the Eickhoff-Zilles atlas EZ, (Ball et al., 2007), featuring 116 parcels covering the whole brain, the Harvard-Oxford atlas HO (Nunez & Williamson, 1996) featuring 111 parcels covering the cortical surface, and Talaraich and Tournoux (TT,(Talairach, 1988) atlas with whole brain coverage and 97 parcels(Figure 2.7.A). The illustrated atlases that have been derived from functional imaging, mainly resting state fMRI, (first row) include the Yeo atlas (Thomas Yeo et al., 2011) featuring 7 and 17 networks with cortical coverage (Figure 2.7.B), and Multiresolution Intrinsic Segmentation Template atlas MIST (Urchs et al., 2019) atlases. Figure 2.7.B second row shows the 400-area cerebral cortex parcellation using muti resolutional Shaefer atlas (Schaefer et al., 2018) where the color of each parcel was assigned based on its spatial overlap with the original 7-network and 17-network parcellations. Schaefer atlas is functional atlas includes cortical parcels ranging from 100 to 1000 parcels that is derived from resting state fMRI data from 1489 subjects. Figure 2.7.C shows the MIST atlas (Urchs et al., 2019), offering whole brain coverage, within hierarchical/nested structure composed of 7, 12, 20, 36, 64, 122, 197, 325 and 444 parcels respectively.

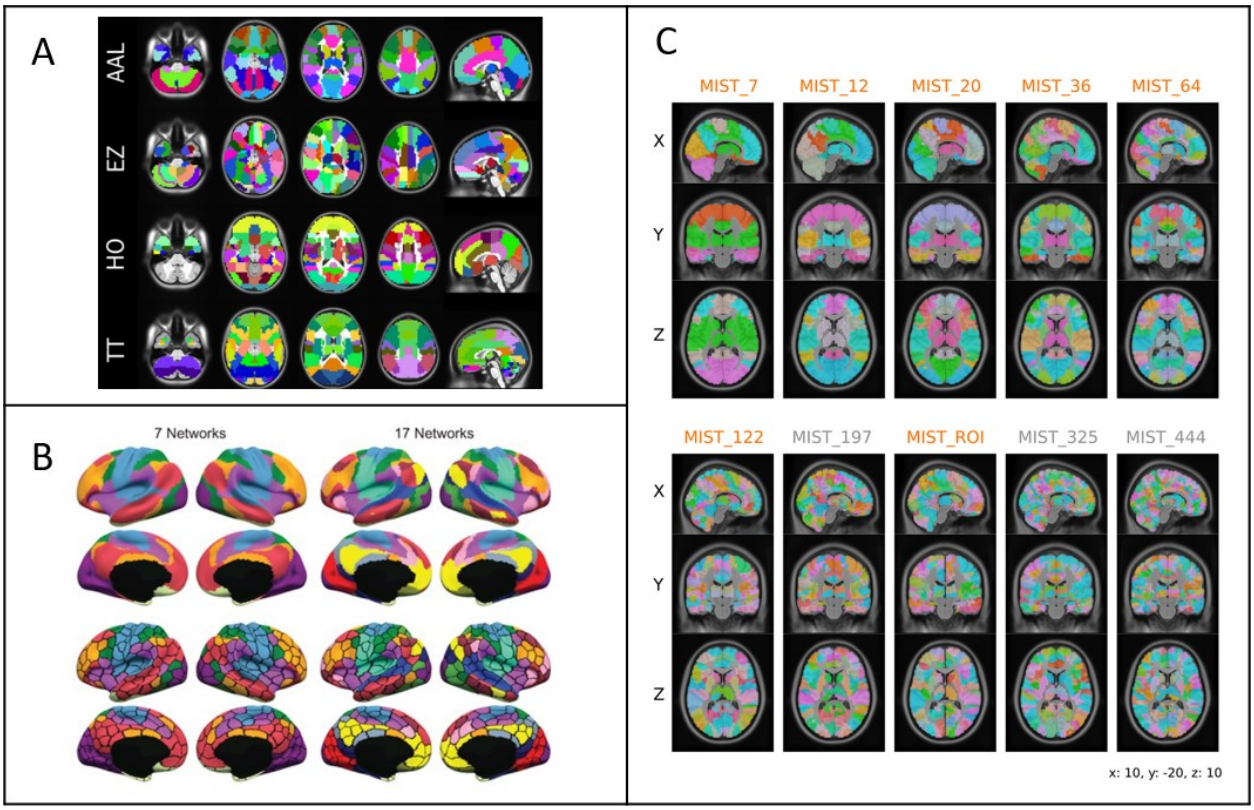

Figure 2.7 Some examples of brain parcellations. There are plenty of schemes to divide the brain into discrete areas based on anatomical and functional criteria. This figure includes six exemplar brain parcellation atlas. A) Anatomical parcellations: AAL (automated anatomical labeling) and Harvard Oxford (HO) are derived from anatomical landmarks (sulci and gyral) while EZ (Eickhoff - Zilles) and TT (Talariach Daemon) atlases are derived from post-

mortem cyto- and myelo-architectonic segmentations; B) Functional parcellations: the first row shows Yeo-7 and Yeo-17 network parcellations, while the second row shows Schaefer 400-area parcellations where each parcel is assigned a network color based on spatial overlap with networks from Yeo-7 or Yeo-17. C) Functional parcellations: Multiresolution Intrinsic Segmentation Template (MIST) atlas providing a hierarchical decomposition of functional brain networks across nine resolutions (7 to 444 functional parcels). Reproduced from (Craddock et al., 2013; Schaefer et al., 2018; Thomas Yeo et al., 2011; Urchs et al., 2019).

2.1.3 Network resolution

At the macroscale level, we are considering brain regions and the large-scale communication organizations between them. A current hypothesis of brain activity, supported by theoretical and empirical studies, is that brain functional connectivity is driven and shaped by structural connectivity between brain regions, although these regions may be functionally specialized (Messé et al., 2014; Suárez et al., 2020). Hence, there is a fundamental coupling between brain structure and function (Messé et al., 2014; Suárez et al., 2020). Here we at first introduce the anatomical structure of brain organization, and then in a specific section below the large-scale brain functional networks.

The brain as a whole entity can be anatomically described/divided in different ways. The human brain is usually described as the association of three major units: (i) the forebrain (or prosencephalon), (ii) the midbrain (mesencephalon), and (iii) the hindbrain (rhombencephalon) (Nieuwenhuys, 1998).

The hindbrain includes two main subregions the upper region called metencephalon and lower one called myelencephalon, in which most of the cranial nerves as well as the fourth cerebral ventricle are placed in this brain region. In general, the hindbrain regions are involved in involuntary and unconscious functions. The lower region consists of the medulla oblongata which assists in the regulation of autonomic functions, such as breathing and heart rate, whereas the upper part, the metencephalon contains the pons and cerebellum regions. The pons region is mainly responsible for controlling autonomic functions like sleep and arousal states. The cerebellum is involved in motor control and relates the information between muscles and regions of the forebrain controlling the body motion.

The next division is the midbrain, which together with the hindbrain composes the brainstem. The midbrain also contains the channels connecting the fourth and third ventricles, and also some cranial nerves like the ones that are responsible for eye movement. In general, the midbrain is involved in an involuntary role such as regulating movement, and processing auditory and visual information (Regina Bailey, n.d.; White, 1989).

The forebrain is the third brain division, and it is also the largest one. It contains almost two-thirds of the brain mass. In contrast to the brainstem, the forebrain is responsible for controlling both voluntary and involuntary functions. The forebrain includes two subdivisions: the telencephalon and the diencephalon.

The diencephalon includes the thalamus, the hypothalamus, and the pineal gland. In general, the diencephalon division contributes to regulate some autonomic functions like respiration, blood pressure, and body temperature. It also secretes some hormones that affect the pituitary gland, through which it can adjust some biological processes such as metabolism, growth, reproductive organs development, as well as emotional responses that affect the autonomic nervous and skeletal muscular systems. The thalamus and the hypothalamus are part of limbic system, the system that governs and adjusts many of our survival behaviour like fear and anger and the

emotions/motivations that control them. The thalamus is also involved in sensory perception and movement, as well as in controlling sleep cycles. The last subregion, the pineal gland, is a pinecone-shaped gland of the endocrine system, that by secreting melatonin is able to regulate sleep-wake cycles and influence sexual development.

The last component of the forebrain is the telencephalon, or cerebrum, which forms the main and largest portion of the brain. By a deep groove called the longitudinal fissure, the telencephalon is divided into two major parts: the right and left cerebral hemispheres. These two parts are connected to each other, at the bottom through the corpus callosum. The surface of the cerebrum has a grayish-brown color and is called gray matter. It contains 14 and 16 billion neurons and glial cells that together form the cerebral cortex. Beneath the cerebral cortex, connecting fibers between neurons form a white-coloured area, called the white matter. The cerebral cortex has folded structure with small groove sulci, large groove fissures and bulges between the grooves called gyri. In each hemisphere, the cerebrum is divided into four main lobes: the frontal, parietal, occipital, and temporal lobes. Each lobe is then further segregated into areas associated with particular functions (White, 1989).

The frontal lobe is the largest lobe among the four lobes. As suggested by its name, it is located in in the front of the brain. The frontal lobe is separated from adjacent lobes parietal and temporal lobes with two boundaries: the central sulcus that separates the frontal and parietal and the lateral sulcus, also called the Sylvian fissure, which separates the frontal and temporal lobes. The frontal lobe function can be broadly divided into two categories: mental or executive action and physical action, in which five specific cortical sub-areas of frontal lobe are responsible for accomplishing them. These five regions starting from central sulcus toward the front of the brain include the primary motor cortex, the motor association cortex, the frontal eye field, the prefrontal cortex and Broca's areas, which are respectively responsible for: voluntarily muscle movement; planning and coordination of movement; planning, control, and execution of eye movements; executive function, behavior, and personality; stimulating the muscle movement and speech production (Salazar, 2017).

The second lobe is parietal lobe, which is mainly involved in sensory functions, rather than motor functions. It features three boundaries separating it from its adjacent lobes: the central sulcus forming the boundary with the frontal lobe, the lateral sulcus forming the boundary with the temporal lobe and the parieto-occipital sulcus forming the boundary with the occipital lobe. The parietal lobe includes three subregions to fulfill the somatosensory functions. Starting from the central sulcus towards the occipital lobe, the first one is called primary somatosensory cortex, which is responsible for awareness of somatic sensation, as well as touch, pain, and sensation. The next subregion is somatosensory association cortex, which is involved in processing and analyzing the somatic sensation, memory and recognition of sensation, and predictive/spatial awareness. The last one, which is called the posterior association area, also contributes to predictive and spatial awareness. It is also responsible for processing the somatosensory information received from parietal lobe, the visual information from the occipital lobe, and the auditory information from the temporal lobe, therefore allowing multimodal integration (Moore et al., 2019; Patestas & Gartner, 2016).

The third lobe is the temporal lobe: it is mainly accountable for processing the auditory-related stimuli. In addition to its main lateral sulcus (Sylvian fissure) boundary, it is also segregated from occipital lobe using an imaginary boundary called the pre-occipital notch. The temporal lobe

contains five major sub-regions, in which starting from lateral sulcus boundary, including primary auditory cortex, auditory association cortex, primary olfactory cortex, and the Wernicke's areas, which are placed adjacent to parietal lobe boundary on the dominant hemisphere. Broadly speaking the functionality of these four sub-regions can be denoted respectively as awareness of auditory stimuli; processing, analyzing, and distinguishing the memory and especially from sounds and visions; awareness and processing the smells stimuli; and understanding of the language (Moore et al., 2019; Patestas & Gartner, 2016).

The fourth lobe is the occipital lobe, which is located in the posterior part of the brain. It is separated from the parietal lobe with the parieto-occipital sulcus, and from the temporal lobe with the pre-occipital notch. The occipital lobe includes two main cortical areas: the primary visual cortex, which is responsible for conscious awareness of visual stimuli coming from the eyes, and second subregions associated visual cortex that process and analyzes the visual information, understanding, recognizing, and memorizing such information (Moore et al., 2019; Patestas & Gartner, 2016).

Primary sensations are being handled specifically in every lobe: touch (parietal lobe), vision (occipital lobe), auditory (temporal lobe), and smell (temporal lobe). There is also an area located in the depth of the lateral sulcus, called the insular cortex, where taste sensation is processed (Adair & Meador, 2003; Larner, 2018). The insular cortex also contributes to process of visceral sensations, autonomic control, and vestibular control/equilibrium.

The other separate regions, which are not attributed to the previous mentioned lobes, are defined as limbic areas, belonging to the limbic system that has been briefly mentioned above. The main components of the limbic system are the cingulate gyrus, which surrounds the corpus callosum, and the para-hippocampal gyrus. In addition to the forenamed thalamus and hypothalamus, it also includes two other sub-regions called the amygdala, and the hippocampal formation. Overall, these limbic areas are playing a key role in learning, memory, emotions, behavior, and smell function of the brain (Catani & Thiebaut de Schotten, 2012).

Even though each of the mentioned lobes and areas is involved in specific roles and functions, it is now accepted that they do not function alone, independently of other structures(Javed et al., 2022). Indeed, when accomplishing a specific task or responding to a stimulus, brain regions are interacting through large-scale networks, communicating through complex relationships and signalling routes (or messaging pathways). Neuronal connections through synapses are ranging from local connections (region of 5 - 8mm in diameter) to more distant connections, from one gyrus to the other, from one lobe to the other, from one hemisphere to the other, from one lobe of deep brain structures, or from deep brain structures to cortical regions. Indeed, the brain is organized as networks of specialized components spanning different spatial resolutions (e.g., cortical area, sub-area, neuronal population or neuron) that are involved in dynamic connections, which mediate continuous processing, transporting, and sharing of relevant information. This means that even though the brain works in functionally segregated regions at multiple levels of organization, its functional specialization and integration characteristics are not exclusive, but rather complementary.

2.2 Brain functional connectivity analysis

Neuroimaging techniques, and among them specifically fMRI data using the whole brain BOLD signal time series, measures the temporal dependency of slow functional hemodynamic activity

elicited by neuronal activity, within different brain regions (M. P. Van Den Heuvel et al., 2010; Lurito et al., 2000). Even if it measures brain activity indirectly through hemodynamic processes, resting state fMRI allows monitoring the continuous flow of the information processing and information transfer within and between different brain regions, which are linked functionally and form complex integrative brain networks. The statistical analysis of such processes of information synchronization within brain networks is denoted by functional connectivity analysis. Whereas the functional connectivity reveals the statistical relationships (e.g., covariance or cross-correlation) between local hemodynamic processes (BOLD signal), actual physical synaptic connections can be estimated non-invasively at the macroscale level with diffusion MRI (or invasively at the microscale/mesoscale levels with neuronal tracers), thus introducing the notion of structural connectivity, derived from anatomical features (Basser & Roth, 2000; Deco et al., 2009; Turner et al., 1990). Functional connectivity assessed using fMRI is dependent but does not directly correspond to structural connectivity and physical synaptic connections. However, it has been shown that there is a significant statistical relationship between the structural and functional connectivity patterns (Adachi et al., 2012; Hutchison et al., 2013).

Specifically, the analysis of functional connectivity of BOLD signals acquires during rest, in which the participants are instructed to stay still and without particular thinking, keeping their eyes closed or open, is called resting state fMRI (RS-fMRI). RS-fMRI can reveal the level of the spontaneous and low-frequency oscillations (∼ 0.01–0.1 Hz) functional co-activation and communication among the brain regions that are anatomically segregated, resulting in the identification of the so-called resting state fMRI (RS-fMRI) brain networks (Biswal et al., 1995; Cordes et al., 2001), that have been found to be highly reliable and reproducible from subject to subject (M. D. Fox & Raichle, 2007).

The underlying neuronal basis of RS-fMRI has been confirmed by multiple studies, showing high functional and anatomical overlap between the resting-state patterns and anatomical connections (Cordes et al., 2000, 2001). However, the link between indirect slow hemodynamic fluctuations measured using fMRI and underlying bioelectrical neuronal signals measured through electrophysiology techniques still remains unclear, despite several studies suggesting different mechanisms linking hemodynamic signals measured using fMRI and underlying neuronal bioelectrical signals (Brookes et al., 2011; Hipp et al., 2012)

It also does not mean that the RS-fMRI recording is not contaminated with non-neural sources, featuring notably cardiac, respiratory oscillations (> 0.3 Hz) and other physiological signals of non-neuronal origins. Indeed, to access the spontaneous low frequency signal of neural sources, recorded BOLD RS-FMRI signal needs to be cleaned. Several strategies have been proposed to remove the influence of those non-neuronal physiological or artifactual fluctuations, for instance monitoring external physiological signals during the scan and/or regressing the non-gray matter signals out of the fMRI signal (Dipasquale et al., 2017; Weissenbacher et al., 2009). Using high sampling rate to avoid aliasing of these physiological fluctuations followed by filtering could also be considered (Cordes et al., 2000, 2001; M. P. van den Heuvel et al., 2008).

2.2.1 Resting-state brain networks

Investigating the patterns of functional connectivity between different brain regions, especially using neuroimaging techniques, is an active field of research, and several methodologies to measure them have been proposed. Overall, several resting-state fMRI data analysis approaches suggested similar patterns of functional connectivity, defining the so-called resting state functional

network (RSN), which also are strongly correlated with underlying structural connectivity (Deco et al., 2014; Meier et al., 2016; Robinson, 2012; Robinson et al., 2014; Suárez et al., 2020). The most consistent resting-state networks reported across these studies include the primary sensorimotor network, the primary visual and extra-striate visual network, a network consisting of bilateral temporal/insular and anterior cingulate cortex regions, left and right-lateralized networks consisting of superior parietal and superior frontal regions and the so-called default mode network consisting of precuneus, medial frontal, inferior parietal cortical regions and medial temporal lobe (Biswal et al., 1995; De Luca et al., 2006; Salvador et al., 2005; M. P. van den Heuvel et al., 2008). It is also worth mentioning that each of these brain networks could be associated with white matter pathway backbone pathways (Greicius et al., 2009; M. P. Van Den Heuvel et al., 2010; Toosy et al., 2004) that support the stability of their spatiotemporal organization and functional roles (Figure 2.8) (Damoiseaux et al. 2006; Smith et al. 2009; van den Heuvel and Hulshoff Pol 2010; Doucet et al. 2011).

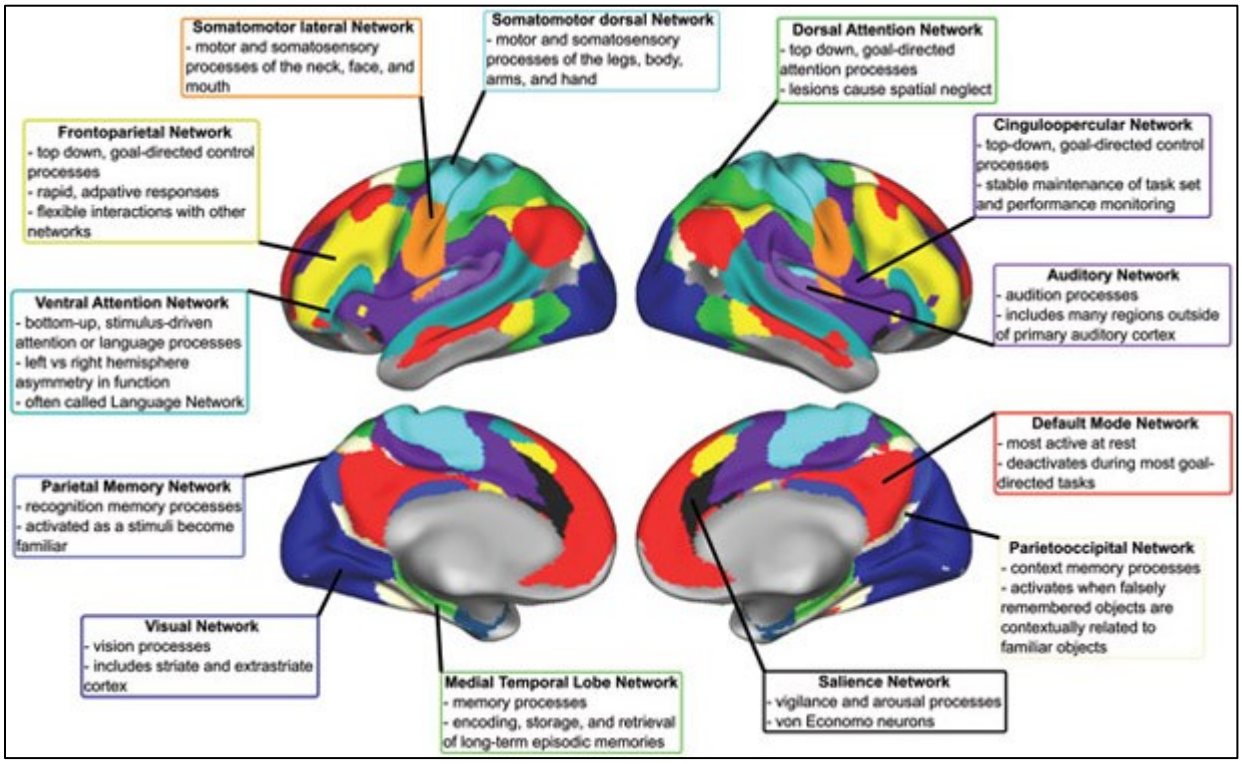

Figure 2.8. Color coded surface-based presentation of the most recent and consistent resting state networks. Figure adapted from (Seitzman et al., 2019)

Interestingly, the RSNs identified using Rs-fMRI were largely consistent using other measurements design (Bellec et al., 2009) such as with task-evoked activations (Kitzbichler et al., 2009; Toro et al., 2008), diffusion imaging (Damoiseaux et al., 2006), maps of anatomical connectivity (Andrews-Hanna et al., 2007; Shehzad et al., 2009) and electrophysiology either on the scalp (Laufs et al., 2003) or on the cortex (Brookes et al., 2011; Hipp et al., 2012; Shmuel & Leopold, 2008). The reorganization of these RSN architectures has been associated with several neurological diseases, for instance, epilepsy (Centeno & Carmichael, 2014)(review from Constable), Alzheimer disease (Badhwar et al., 2017) or schizophrenia (S. Li et al., 2019). These

findings are suggesting that RSN estimated from RS-fMRI could potentially be considered to define biomarkers of several neurological conditions.

2.2.2 Graph theorical strategy

Our brain is inherently a system featuring spatially embedded networks defining graphs of comprehensive connections occurring at multiple scales, including the molecular interactions, the synaptic connections and neuronal wiring, and distant brain areas communicating using structural connections through long-range bundles of fibers, allowing to characterize whole-brain dynamics at rest, during tasks, or during specific behaviors (Bassett & Siebenhühner, 2013; Doucet et al., 2011; Mišić & Sporns, 2016).

Graph theory is a branch of mathematics that can represent the connectomic and topological features of brain as sets of nodes and edges that represent system elements and their interrelations (Fornito et al., 2016). In graph theory, the neuronal elements of the brain defining the nodes depend on the scale of interest and can be defined as neurons, regions or networks. The edges are then characterizing the type of connections between those nodes. Using such definitions, graph theory allows defining a mathematical model of brain that can be summarized as an N×N adjacency matrix (also called a connection matrix), where zero or non-zero entities denote respectively the absence or presence of a connection between two nodes. Such representation can be either directional, in case of having access to reciprocal connections using anatomical networks constructed from tract tracing studies (Liao et al., 2017) or undirected. The links can also be either binary, therefore confirming the existence of a connection between the nodes or weighted, featuring information about connection strengths (Fornito et al., 2013; C. Zhong et al., 2015). When underlying anatomical information is available, the weights of the edges can also represent the size, density, or coherence of the anatomical tracts, whereas, in functional networks, the weight of the edges are representing magnitudes of connection strengths (Rubinov & Sporns, 2010).

Even though statistical analysis of binary graph networks is easier, weighted non-binary graphs provide additional complementary information on the structure of the network, while allowing discarding of eventual spurious connections featuring non-significant weight values (Saramäki et al., 2007).

The very first applications of graph theory when studying brain networks were proposed in the context of fMRI functional connectivity analyses. fMRI connectivity matrices are usually estimated by reporting Pearson correlation between time series of the BOLD signal from different brain regions (nodes), estimated for every possible pair of nodes. These connectivity matrices can then be arbitrarily thresholded to binarize the edges, resulting in estimating a graph of large-scale functional networks (Achard et al., 2006; Ortiz et al., 2005; Salvador et al., 2005; Sporns et al., 2005; Stam, 2004). However, the turning point of these studies was the connection matrix of the human brain introduced by Sporns in 2005 denoted the “human connectome” model (Sporns et al., 2005). The proposed “human connectome” model was including three main steps: (i) estimating the structural connectivity matrix from diffusion-weighted MR imaging data, (ii) performing voxel-wise all-to-all functional connectivity analyses of fMRI and/or magnetoencephalography (MEG) functional data, and (iii) employing a cluster analysis of correspondences between the structural and functional connectivity matrices to identify regions exhibiting consistent structure-function relationships in the human brain (Sporns et al., 2005). Figure 2.9 represents the common scheme for graph theory analysis, starting from acquisition of brain signal (e.g. fMRI), preprocessing including the regression of the non-neuronal signals (like physiological systemic

fluctuations, head motion), brain parcellation for regional data analysis and dimensionality reduction, estimation of a corrected BOLD time course per region (brain parcel), estimation of a connectivity matrix featuring the correlation between the time courses of every parcel, binarization of connectivity matrix by thresholding (optional), estimation of brain networks from the connectivity matrices and finally topological analysis of the whole brain network properties using graph theory metrics.

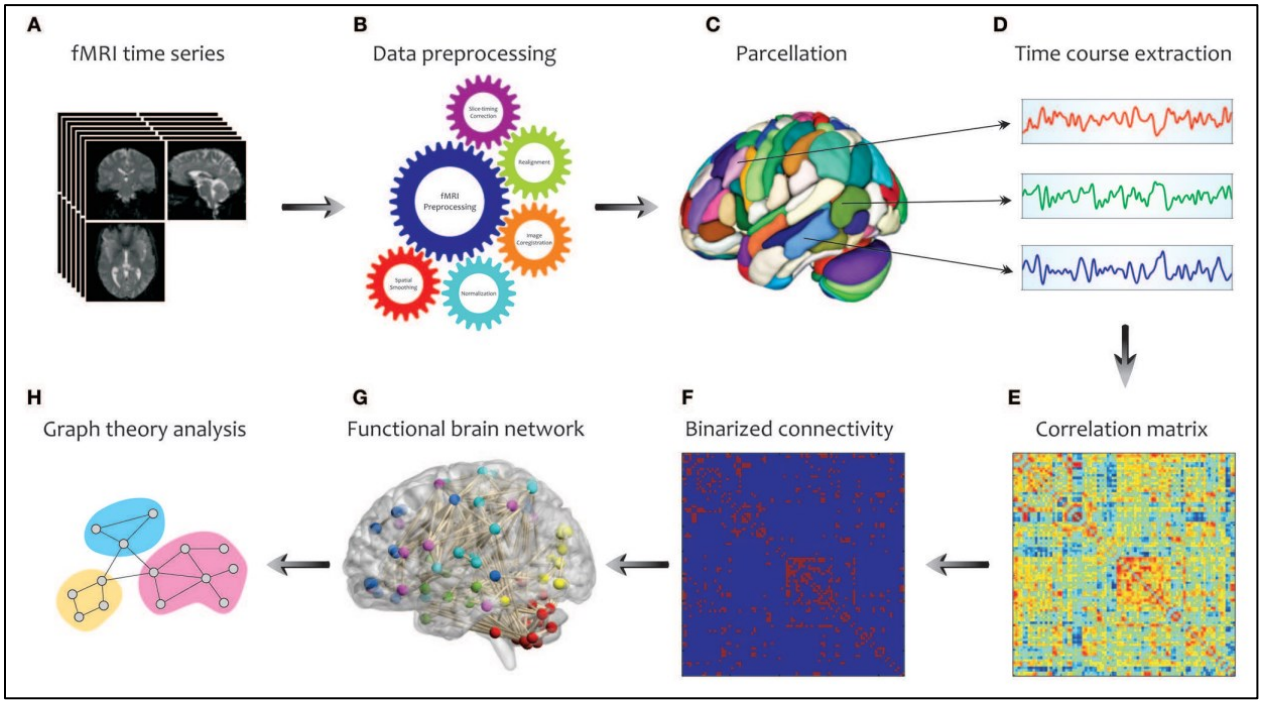

Figure 2.9. Schematic representation of brain network construction and graph theoretical analysis using fMRI data. Figure adapted from (Farahani et al., 2019)

Representing the brain connectivity information using graph theory, revealed three key concepts of brain topological organization: small-worldness, degree distribution, and modularity, that were repeatedly reported across both anatomical and functional data using different analysis techniques (Cole et al., 2016; Downes et al., 2012; Schroeter et al., 2015). The notion of "small-world" architecture, first introduced by (Milgram, 1967) for social network, consists in a network which behaves nearly regularly, favoring local connections, and occasionally random, featuring few long-distance connections, therefore maximizing communication efficiency between regions (Watts & Strogatz, 1998) (Figure 2.10). Such network model includes short characteristic path length, which favours integrated processing of information over the whole networks, as well as a high clustering coefficient, that favours segregated processing within functionally specialized sub-population of nodes (Sporns & Kötter, 2004). The characteristic path length is defined as the average of the minimum number of edges that are required to link two nodes to each other. The clustering coefficient of a node is defined as the fraction of its neighbours that are also connected to each other. These two topological characteristics are important to characterize the functional segregation and integration of the networks, important characteristics of most physiological systems. The small-world architecture allows a balance between minimizing the resource cost and meanwhile maximizing the flow of information among the system's networks (Bassett &

Bullmore, 2006; Bullmore & Sporns, 2012; M. Lin et al., 2013; Meunier et al., 2010; Samu et al., 2014).

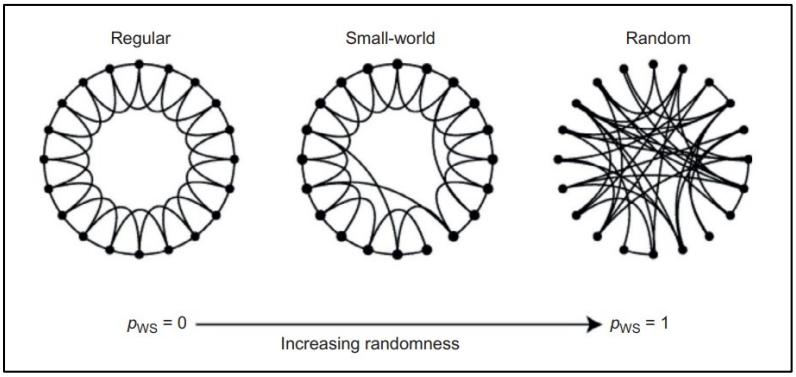

Figure 2.10. Schematics of Small-world networks by Watts and Strogatz (Watts & Strogatz, 1998). p_{WS}*: randomness probability. Small-world networks are not completely regular nor random, instead, they are characterized by both local clustering and short paths. Reproduced from* (Fornito et al., 2016)

In graph theory, the concept of node degree is defined as the mean number of edges attached to each node (also called the mean degree of the graph). When considering undirected graphs models, edges connect nodes symmetrically and there is no distinction between the source and the target of a connection. In a binary graph, the edge weight is either zero or one. Centrality measures quantify the importance of a node relative to other nodes in the network, whereas nodes featuring high centrality are also called hubs (M. P. van den Heuvel & Sporns, 2013). Using resting state fMRI analysis, the brain functional hubs have been mainly reported in the precuneus, posterior cingulate, lateral temporal, superior and inferior parietal, and medial and lateral prefrontal cortices (Achard et al., 2006; Buckner et al., 2009; K. Lee et al., 2016). While the Degree centrality is a most simplistic centrality measure, there are other centrality metrics that consider more advanced communication properties of nodes. For example, eigenvector centrality also accounts for the quantity and quality of the connections associated with a node. Such a metric assigns a high centrality to a low-degree node when it is connected to high-degree nodes, through the summation of the centrality of its neighbours. This measure requires estimating the eigenvectors and eigenvalues of the adjacency matrix. An eigenvector of A is a nonzero vector x that, when multiplied by A, satisfies the condition $Ax = \lambda x$. The scalar λ is the corresponding eigenvalue of A and represents the factor which, when multiplied with x, is equal to Ax . The eigenvector centrality of a node i is defined as the i_{th} entry of the eigenvector belonging to the largest eigenvalue of A. Alternatively, the eigenvector metric for each node can also be defined as to the summed centrality of its neighbors (see Table 2.1 for definition). The Closeness centrality measures the average length of the shortest paths between a particular node and the rest of the network. Betweenness centrality expresses the fraction of all shortest paths in the network that contain that specific node (See Table 2.1 for the full definitions).

In addition to nodes' characteristics, analyzing the graph theorical metrics also reveals interesting information about network organization. As an example, the distribution of degrees values comes from the theorem introduced by Barabási and Albert (Baraba, 1999): within a complex graph structure, he proposed that a new edge will be more likely connected to the nodes featuring higher degree, or hubs regions. Using such a model, there is a high probability that the resulting graph will contain at least a few highly connected hub nodes, resulting in a decreasing power-law

distribution of degree values within the graph. Actually, the work of Barabási (among others) confirmed the existence of a decreasing power-law, i.e. heavy-tailed, distribution of degrees values, not only in brain functional/structural networks, but also in several empirically observed nervous systems, from cultured cellular networks to whole brain electrophysiological and hemodynamic recordings (Baraba, 1999; Beggs & Plenz, 2003; Kitzbichler et al., 2009; Linkenkaer-Hansen et al., 2001).

Another key topological concept of brain organization is its modularity, which means that the brain can be decomposed into clusters (modules) of nodes that are more densely connected with each other, than to the nodes in any other modules (Figure 2.11 Simon, 1962). The modularity of the brain implicates functional specialization and local segregation within the integrated network while allowing communication between modules through connector hubs. Such a structure supports the robustness and adaptability of brain connectivity networks (Bullmore & Sporns, 2009).

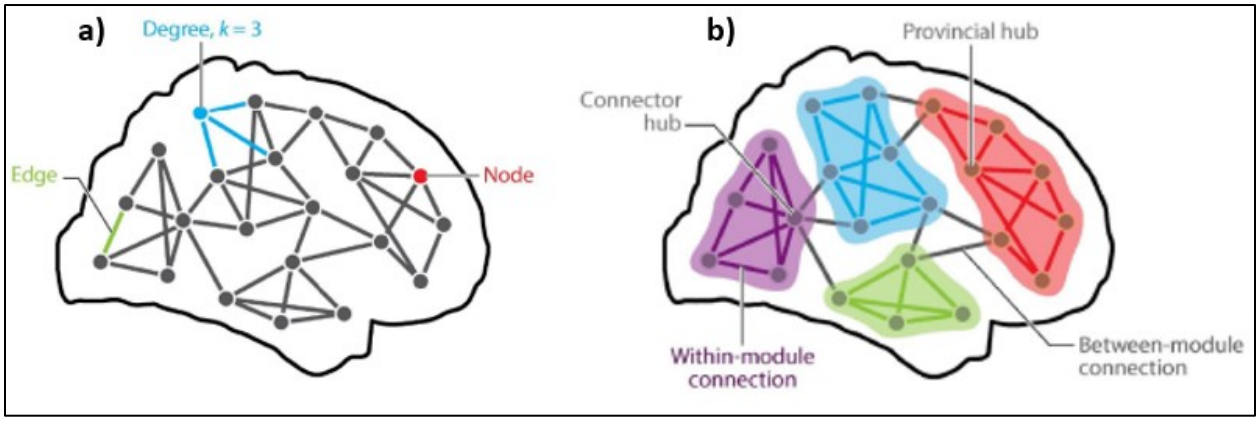

Figure 2.11 Some illustrative measurement that quantifies the topology of brain networks. (a) The graph representation of node, edge and degree (b) The modularity of the brain networks. Reproduced from (Sporns & Betzel, 2016).

Assessing modularity using graph theory measures can be broadly divided into agglomerative and divisive methods. For agglomerative methods, the edges are added to an empty graph that includes just the nodes, until obtaining an optimized cluster. For divisive methods, we start from a complete graph and edges are then removed, until an optimized subset of nodes is obtained. In the context of divisive approaches, the community detection algorithm is the most popular one. These methods search for optimal partition within the brain connectivity matrix by maximizing intra-cluster edge density against a random edge rewiring null model (Blondel et al., 2008). In other versions, (Blondel et al., 2008) a heuristic method is used with an aggregation algorithm iteratively maximizing the difference between the actual and expected number of edges in initial defined modules by moving the nodes, until no extra change in the network is obtained. Walktrap is another approach for modularity detection in graph theory that includes random walks approach. It consists in merging separate detected modules in a bottom-up manner, in which each module is obtained by random walks in the network until getting trapped into densely connected parts corresponding to a module (Pons & Latapy, 2005; Traag et al., 2019).

2.2.2.1 Brain functional hub regions

Within functional brain networks, some nodes are playing important role in neural communication and interactivity of the brain function, they are called hubs. Whereas hubs have been commonly

estimated as regions exhibiting high degree centrality metrics, other hub detection approaches consist of aggregating sets of measures that examine global aspect of hub topology, presenting advantages and more accuracy in hubs detection. The analysis proposed by Sporns and colleagues (Bassett & Sporns, 2017) revealed that indeed hubs in brain networks have specific topological characteristics. They are central and exhibit high number of connections to several other nodes. They also have the ability to communicate with many other nodes through a small number of connections. They also play an important role in brain integration, clustering, or modulation, as well as whole network stability. In 2010, van den Heuvel developed a consensus-based definition of hubs from structural connectivity networks and suggested four main characteristics graph metrics to score a region as a hub: high degree centrality, high betweenness, low clustering coefficient and low shortest path (Figure 2.12 (M. P. Van Den Heuvel et al., 2010)).

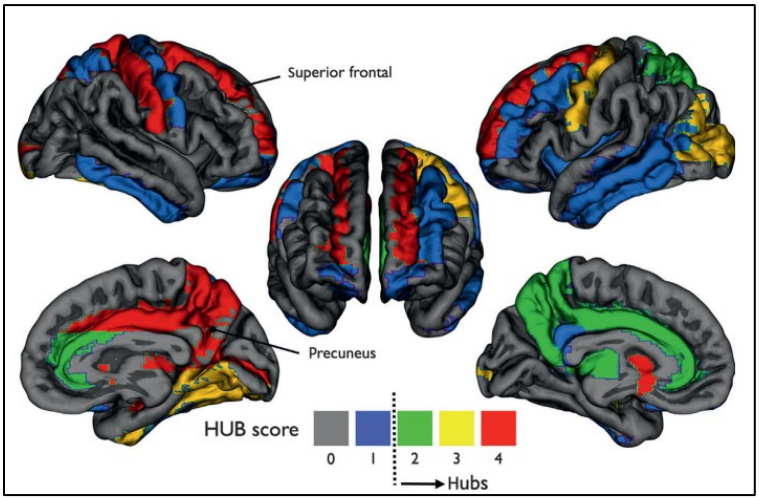

Figure 2.12. Node-specific hub scores. Adapted from (M. P. Van Den Heuvel et al., 2010)

In addition, the hubs' edge distribution, and their topological position in modules of brain network play an important role in between and within module communication (Guimerà et al., 2005). Accordingly, Guimera suggested in 2005, that the hubs regions can be grouped into connector and provincial hubs, where provincial hubs are mostly connected to nodes within their own module, while intermodular communications are mediated by a few connector hubs that are distributed across multiple different modules (Figure 2.11) (Díaz Parra, 2018; Guimerà et al., 2005; M. P. Van Den Heuvel et al., 2010). Connector hubs are often placed in sub-regions of the association cortices: the precuneus, medial and superior frontal, orbitofrontal, superior and inferior parietal, cingulate, middle and superior temporal, temporal pole, supramarginal, angular, and fusiform gyri, as well as sub-regions of subcortical and primary sensory areas (Bullmore & Sporns, 2012; Gratton et al., 2012). These areas are indeed mainly served as interconnected cores, allowing integration across different networks as well as playing important role in maintaining a balance between network segregation and integration. (Bertolero et al., 2017). These regions also are associated with higher metabolic demands than other brain regions (Liang et al., 2013; D. Tomasi et al., 2013; Vaishnavi et al., 2010), which makes them more vulnerable to many neurological disorders (Buckner et al., 2009; Crossley et al., 2014).

Table 2.1. Mathematical definitions of selected graph theorical measures. Table adapted from (Rubinov & Sporns, 2010).

Measure	Binary and undirected definition	Weighted and directed definition
Basic concepts and measures		
Basic concepts and notation	N is the set of all nodes in the network, and n is the number of nodes. L is the set of all links in the network, and l is number of links. (i,j) is a link between nodes i and j, $(i,j \in N)$. a_{ij} is the connection status between i and j: $a_{ij} = 1$ when link (i,j) exists (when i and j are neighbors); $a_{ij} = 0$ otherwise ($a_{ii} = 0$ for all i). We compute the number of links as $l = \sum_{i,j \in N} a_{ij}$ (to avoid ambiguity with directed links we count each undirected link twice, as a_{ij} and as a_{ji}).	Links (i,j) are associated with connection weights w_{ij}. Henceforth, we assume that weights are normalized, such that $0 \leq w_{ij} \leq 1$ for all i and j. l^w is the sum of all weights in the network, computed as $l^w = \sum_{i,j \in N} w_{ij}$. Directed links (i,j) are ordered from i to j. Consequently, in directed networks a_{ij} does not necessarily equal a_{ji}.
Degree: number of links connected to a node	Degree of a node i, $$k_i = \sum_{j \in N} a_{ij}.$$	Weighted degree of i, $k_i^{\mathrm{w}} = \sum_{j \in N} w_{ij}$. (Directed) out-degree of i, $k_i^{\mathrm{out}} = \sum_{j \in N} a_{ij}$. (Directed) in-degree of i, $k_i^{\mathrm{in}} = \sum_{j \in N} a_{ji}$.
Shortest path length: a basis for measuring integration	Shortest path length (distance), between nodes i and j, $$d_{i,j} = \sum_{a_{uv} \in g_{i \leftrightarrow j}} a_{uv},$$ where $g_{i \leftrightarrow j}$ is the shortest path (geodesic) between i and j. Note that $d_{i,j} = \infty$ for all disconnected pairs i,j.	Shortest weighted path length between i and j, $d_{ij}^{\mathrm{w}} = \sum_{a_{uv} \in g_{i \leftrightarrow j}^{\mathrm{w}}} f(w_{uv})$ where f is a map (e.g., an inverse) from weight to length and $g_{i \leftrightarrow j}^{\mathrm{w}}$ is the shortest weighted path between i and j. Shortest directed path length between i to j, $d_{ij}^{\rightarrow} = \sum_{a_{ij} \in g_{i \rightarrow j}} a_{ij}$ where $g_{i \rightarrow j}$ is the directed shortest path from i to j.
Number of triangles: a basis for measuring segregation	Number of triangles around a node i, $$t_i = \frac{1}{2} \sum_{j,h \in N} a_{ij} a_{ih} a_{jh}.$$	(Weighted) geometric mean of triangles around i, $t_i^{\mathrm{w}} = \frac{1}{2} \sum_{j,h \in N} \left(w_{ij} w_{ih} w_{jh}\right)^{1/3}$. Number of directed triangles around i, $t_i^{\rightarrow} = \frac{1}{2} \sum_{j,h \in N} \left(a_{ij} + a_{ji}\right)\left(a_{ih} + a_{hi}\right)\left(a_{jh} + a_{hj}\right)$.

Measure	Binary and undirected definition	Weighted and directed definition
Measures of integration		
Global efficiency	Global efficiency of the network (Latora & Marchiori, 2001), $E = \frac{1}{n}\sum_{i\in N} E_i = \frac{1}{n}\sum_{i\in N}\frac{\sum_{j\in N, j\neq i} d_{ij}^{-1}}{n-1}$, where E_i is the efficiency of node i.	Weighted global efficiency, $E^{\mathrm{w}} = \frac{1}{n}\sum_{i\in N}\frac{\sum_{j\in N, j\neq i}\left(a_{ij}^{\mathrm{w}}\right)^{-1}}{n-1}$. Directed global efficiency, $E^{\rightarrow} = \frac{1}{n}\sum_{i\in N}\frac{\sum_{j\in N, j\neq i}\left(a_{ij}^{\rightarrow}\right)^{-1}}{n-1}$
Eigenvector centrality	Eigenvector centrality (Bonacich, 2007) of a node i is proportional to the sum of the centralities of the vertices to which it is linked, $\lambda C_i = \sum_{j\in N} a_{ij} C_j$, where λ is the largest eigenvalue of the adjacency matrix $\left(a_{ij}\right)_{ij}$ (and $\{C_i\}_i$ the coefficients of the corresponding (leading) eigenvector).	Weighted eigenvector centrality of i, $\lambda C_i = \sum_{j\in N} w_{ij} C_j$. In directed networks (M. Newman, 2010), left and right eigenvectors are defined separately by considering respectively outgoing connections, $\lambda C_i = \sum_{j\in N} a_{ij} C_j$, and incoming connections, $\lambda C_i = \sum_{j\in N} a_{ji} C_j$.
Measures of segregation		
Clustering coefficient	Clustering coefficient of the network (Watts & Strogatz, 1998), $C = \frac{1}{n}\sum_{i\in N} C_i = \frac{1}{n}\sum_{i\in N}\frac{2t_i}{k_i(k_i-1)}$, where C_i is the clustering coefficient of node i ($C_i = 0$ for $k_i < 2$).	Weighted clustering coefficient (Saramäki et al., 2007), $C^{\mathrm{w}} = \frac{1}{n}\sum_{i\in N}\frac{2t_i^{\mathrm{w}}}{k_i(k_i-1)}$. Directed clustering coefficient (Fagiolo, 2007), $C^{\rightarrow} = \frac{1}{n}\sum_{i\in N}\frac{t_i^{\rightarrow}}{\omega_i}$, where $\omega_i = \left(k_i^{\mathrm{out}} + k_i^{\mathrm{in}}\right)\left(k_i^{\mathrm{out}} + k_i^{\mathrm{in}} - 1\right) - 2\sum_{j\in N} a_{ij}a_{ji}$.
Local efficiency	Local efficiency of the network (Latora & Marchiori, 2001), $E_{\mathrm{loc}} = \frac{1}{n}\sum_{i\in N} E_{\mathrm{loc},i} = \frac{1}{n}\sum_{i\in N}\frac{\sum_{j,h\in N, j\neq i} a_{ij}a_{ih}\left[d_{jh}(N_i)\right]^{-1}}{k_i(k_i-1)}$, where $E_{\mathrm{loc},i}$ is the local efficiency of node i, and $d_{jh}(N_i)$ is the length of the shortest path between j and h, that contains only neighbors of i.	Weighted local efficiency, $E_{\mathrm{loc}}^{\mathrm{w}} = \frac{1}{2}\sum_{i\in N}\frac{\sum_{j,h\in N, j\neq i}\left(w_{ij}w_{ih}\left[d_{jh}^{\mathrm{w}}(N_i)\right]^{-1}\right)^{1/3}}{k_i(k_i-1)}$ Directed local efficiency, $E_{\mathrm{loc}}^{\rightarrow} = \frac{1}{2n}\sum_{i\in N}\frac{\sum_{j,h\in N, j\neq i}(a_{ij}+a_{ji})(a_{ih}+a_{hi})D_{ijh}}{\omega_i}$, where $D_{ijh} = \left[d_{jh}^{\rightarrow}(N_i)\right]^{-1} + \left[d_{hj}^{\rightarrow}(N_i)\right]^{-1}$ and $\omega_i = \left(k_i^{\mathrm{out}} + k_i^{\mathrm{in}}\right)\left(k_i^{\mathrm{out}} + k_i^{\mathrm{in}} - 1\right) - 2\sum_{j\in N} a_{ij}a_{ji}$.

Measure	Binary and undirected definition	Weighted and directed definition
Modularity	Modularity of the network (M. E. J. Newman, 2006), $Q = \frac{1}{l}\sum_{i,j\in N}\left(a_{ij} - \frac{k_i k_j}{l}\right)\delta_{m_i,m_j}$, Where m_i is the module containing node i, and $\delta_{m_i,m_j} = 1$ if $m_i = m_j$ and 0 otherwise.	Weighted modularity (M. E. J. Newman, 2004), $Q^{\mathrm{w}} = \frac{1}{l^{\mathrm{w}}}\sum_{i,j\in N}\left[w_{ij} - \frac{k_i^{\mathrm{w}} k_j^{\mathrm{w}}}{l^{\mathrm{w}}}\right]\delta_{m_i,m_j}$. Directed modularity (Leicht & Newman, 2008), $Q^{\rightarrow} = \frac{1}{l}\sum_{i,j\in N}\left[a_{ij} - \frac{k_j^{\mathrm{out}} k_i^{\mathrm{in}}}{l}\right]\delta_{m_i,m_j}$.
Measures of centrality		
Closeness centrality	Closeness centrality of node i (e.g., (Freeman, 1978)), $L_i^{-1} = \frac{n-1}{\sum_{j\in N, j\neq i} d_{ij}}$.	Weighted closeness centrality, $(L_i^{\mathrm{w}})^{-1} = \frac{n-1}{\sum_{j\in N, j\neq i} d_{ij}^{\mathrm{w}}}$. Directed closeness centrality, $(L_i^{\rightarrow})^{-1} = \frac{n-1}{\sum_{j\in N, j\neq i} d_{ij}^{\rightarrow}}$.
Betweenness centrality	Betweenness centrality of node i (e.g., (Freeman, 1978)), $b_i = \frac{1}{(n-1)(n-2)}\sum_{\substack{h,j\in N \\ h\neq j, h\neq i, j\neq i}}\frac{\rho_{hj}(i)}{\rho_{hj}}$, where ρ_{hj} is the number of shortest paths between h and j, and $\rho_{hj}(i)$ is the number of shortest paths between h and j that pass through i.	Betweenness centrality is computed equivalently on weighted and directed networks, if path lengths are computed on respective weighted or directed paths.
Participation coefficient	Participation coefficient of node i (Guimerà & Amaral, 2005), $y_i = 1 - \sum_{m\in M}\left(\frac{k_i(m)}{k_i}\right)^2$, where M is the set of modules (see modularity), and $k_i(m)$ is the number of links between i and all nodes in module m.	Weighted participation coefficient, $y_i^{\mathrm{w}} = 1 - \sum_{m\in M}\left(\frac{k_i^{\mathrm{w}}(m)}{k_i^{\mathrm{w}}}\right)^2$. Out-degree participation coefficient, $y_i^{\mathrm{out}} = 1 - \sum_{m\in M}\left(\frac{k_i^{\mathrm{out}}(m)}{k_i^{\mathrm{out}}}\right)^2$. In-degree participation coefficient, $y_i^{\mathrm{in}} = 1 - \sum_{m\in M}\left(\frac{k_i^{\mathrm{in}}(m)}{k_i^{\mathrm{in}}}\right)^2$.
Measures of resilience		
Average neighbor degree	Average degree of neighbors of node i (Pastor-Satorras & Vespignani, 2001), $k_{\mathrm{nn},i} = \frac{\sum_{j\in N} a_{ij} k_j}{k_i}$.	Average weighted neighbor degree (modified from (Barrat et al., 2004)), $k_{\mathrm{nn},i}^{\mathrm{w}} = \frac{\sum_{j\in N} w_{ij} k_j^{\mathrm{w}}}{k_i^{\mathrm{w}}}$. Average directed neighbor degree, $k_{\mathrm{nn},i}^{\rightarrow} = \frac{\sum_{j\in N}(a_{ij}+a_{ji})\left(k_j^{\mathrm{out}}+k_j^{\mathrm{in}}\right)}{2(k_i^{\mathrm{out}}+k_i^{\mathrm{in}})}$.

The connector hubs are commonly estimated using participation coefficient graph metric (Power et al., 2013), that extracts the connector hubs by measuring the extent to which a network node (or a parcel) connects to multiple modules (brain networks). Our group also proposed complementary methods to estimate connector hubs from resting state fMRI data, using sparse decomposition to explicitly assess spatial overlap between brain networks (see (K. Lee et al., 2016), more details later in this chapter). Connector hubs can also be further classified into three category sets: control-default, cross-control, and control-processing hubs regions (Figure 2.13). These hubs are placed in different positions within the brain's network structure, where they affect networks differently while integrating the information between them. The control-default connector hubs have strong connectivity with frontoparietal (FPN), default mode (DMN), and contextual association (CAN) networks. They are localized in the dorsal angular gyrus, the superior and inferior frontal gyrus, the retrosplenial cortex, the precuneus, and the ventromedial prefrontal cortex. The cross-control connector hubs are exhibiting strong connectivity within the cingulo-opercular network (CON), the dorsal attention network (DAN) and the FPN. They are localized in the inferior parietal lobule, the supramarginal gyrus, the middle and superior frontal gyrus, and the posterior precuneus. Finally, the control-processing connector hubs are exhibiting strong connectivity within sensory and motor processing systems (lateral visual (lVis), auditory (Aud), premotor (PMot), and the somatomotor networks hand somatomotor (hSM), face somatomotor (fSM), and leg somatomotor (lSM)) as well as CON and DAN. They are localized in the pre- and postcentral gyrus, the lateral occipital cortex, the dorsomedial prefrontal cortex, and the posterior insula (Gordon et al., 2018; Y. Zhang et al., 2016).

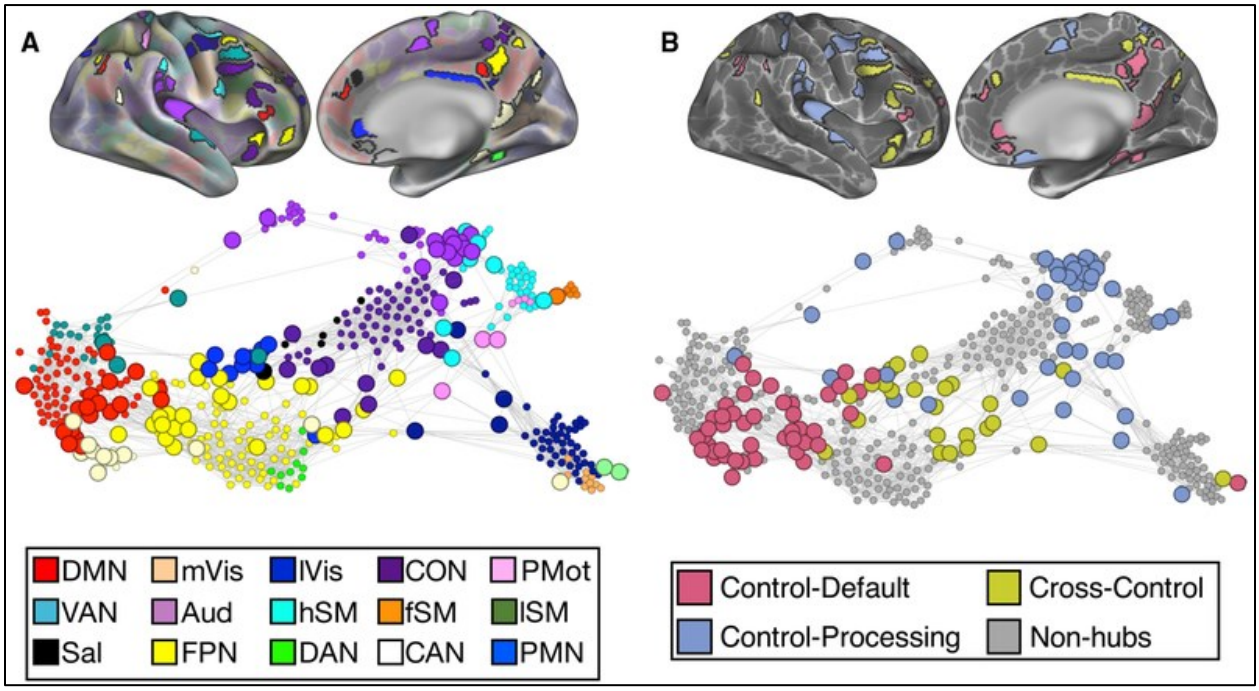

Figure 2.13. Hubs Cluster into Distinct Sets. A) Network identities of cortical parcels in a single subject (top) and a spring embedding plot (bottom), illustrating relationships between these parcels. Hubs are highlighted on the cortex and enlarged in the spring embedding plot (B) The same parcels and plot, with parcels colored based on the hub set. Figure adapted from (Gordon et al., 2018)

2.2.3 Model-based and model-free functional connectivity approaches

Functional connectivity methods in fMRI studies can broadly be defined using model-based and model-free groups. The model-based methods basically examine the existence of a linear relationship between particular regions called seed regions, from which fMRI BOLD signal is compared with the signal from all other brain regions. The model-free approaches do not require the definition of such a predefined seed region, usually consisting of multivariate data analysis strategies (Farahani et al., 2019; M. P. Van Den Heuvel et al., 2010).

2.2.3.1 Model-based methods

Model-based methods consist in estimating the cross-correlation between the BOLD signal time series of specific seed regions and all other brain voxels/regions, resulting in the estimation of a functional connectivity map exhibiting how all regions linearly covary with the BOLD signal from the seed region (Andrews-Hanna et al., 2007; Biswal et al., 1995; Cao & Worsley, 1999; Cordes et al., 2000; Fransson, 2005; Larson-Prior et al., 2009; M. Song et al., 2008).

Once functional connectivity maps are estimated, second-level statistical can be done within the general linear model (GLM) framework combined with statistical multiple comparisons methods (Farahani et al., 2019), i.e. statistical parametric mapping (SPM) investigations, allowing to asses of the effect of a specific condition or a specific population on connectivity patterns associated with a specific hypothesis, defined by the seed region. The GLM is a statistical method that model the time course of observed RS-fMRI data as a linear mixture of the predictors (regressors), making design matrix (matrix of regressors) (Figure 2.14f), based on the linearity, homoscedastic (constant variance) and normality assumption of predictors (Gelman & Hill, 2007; Nelder & Wedderburn, 1972). GLM approaches assess the contribution of every voxel independently (Huberty et al., 1997). Hence, in neuroimaging data in other to address the multiple comparisons problem when making statistical inferences over a volume of the brain, combined with GLM a multivariate normal density modeling, is employed to detect regional-specific brain activation patterns (Farahani et al., 2019; Jones et al., 1991; Rencher, 1995).

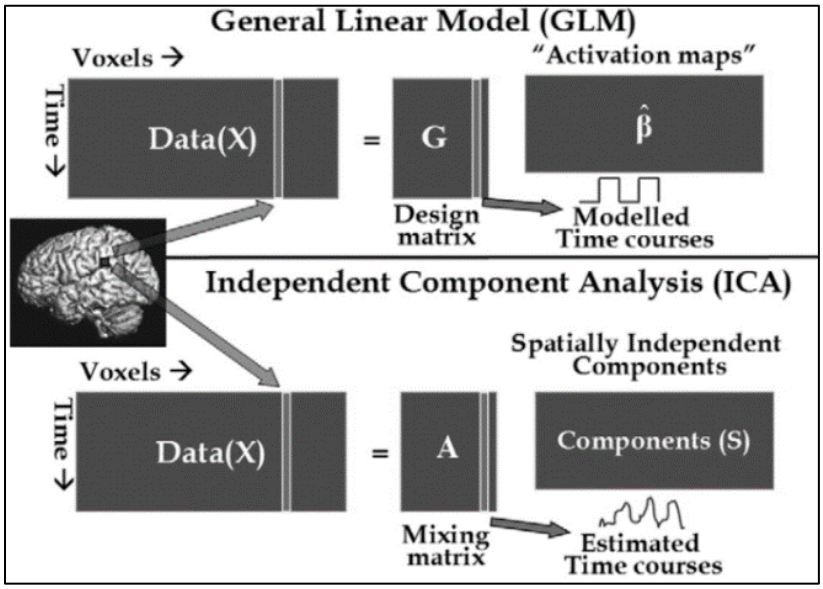

Figure 2.14. Comparison of GLM and spatial ICA for fMRI data: the GLM requires the specification of the temporal model in the design matrix, whereas ICA estimates the time courses from the data by maximizing independences between the component images, Adapted from (Calhoun et al., 2009)

2.2.3.2 Model-free multivariate approaches

While the seed-based approaches require prior information (predefined reference region), the complementary model-free methods, are driven by the intrinsic structure of the data and are able to detect linear and also non-linear neuronal interactions between regions, resulting in whole brain connectivity patterns that can reveal the resting state networks (M. P. Van Den Heuvel et al., 2010; Y. Zhong et al., 2009).

2.2.3.2.1 Signal decomposition-based methods

The most common multivariate decomposition-based techniques to investigate high dimensional spatio-temporal data are principal component analysis (PCA) (Friston et al., 1993) and independent component analysis(ICA) (Calhoun et al., 2001; De Luca et al., 2006; van de Ven et al., 2004). The objective of these methods is to decompose the spatiotemporal structure contained within the measured RS-fMRI signals, as a mixture of hidden spatial sources or maps, each associated with a specific time course. The main underlying assumption driving these decompositions is that spatial sources or maps should be decorrelated for PCA and statistically independent for ICA, which is a blind source separation problem. Additionally, resulting spatial components will also be decorrelated/independent from other signal sources of non-neuronal origins, such as brain motion, and physiological fluctuations associated with respiration and heartbeat (Y. Zhong et al., 2009). PCA and ICA are also statistical transformation techniques, that aim to transform original data into lower-dimensional space while preserving the main structure. PCA dealing with decorrelation benefits from second-order statistics (Gaussian approximation), while ICA dealing with statistical independence takes advantage of higher-order statistics (non-Gaussian). In the standard ICA model, mixtures are linear, and the source maps are assumed to be statistically mutually independent, while at least one of them should be non-Gaussian (Bordier et al., 2011).

In more detail, let us assume that we are applying PCA or ICA on fMRI signals represented by a Spatio-temporal matrix of measurements $X_{j,t}$, where index (j) accounts for J spatial elements (voxels, regions), and index (t) accounts for the T time points of the signal. The objective of PCA and ICA is to characterize the data within a sub-space of lower dimensionality (K<< J, T). First, PCA decomposes the data within such lower dimensionality sub-space using the singular value decomposition (SVD) method:

$$X_{jt} = \sum_{k=1}^{K} U_{jk} \Lambda_{kk} V_{tk} \tag{2.1}$$

where U and V are orthogonal matrices that span the spatial and temporal patterns and Λ is a diagonal matrix consisting of singular values. The columns of U and V are called eigenvectors of covariance matrices, respectively reflecting the inter-relationship between the voxels/regions ($\sum_t^T \mathrm{X}_{jt}\mathrm{X}_{kt}/T$) and between the voxels/regions across the time series of the signal ($\sum_j^J \mathrm{X}_{js}\mathrm{X}_{jt}/J$) (McKeown et al., 2003).

However, in order to consider the output of decomposition used in ICA and PCA as decent components in which their linear matrix correctly represents the matrix X, both number of sources, K, compares to J and T and the variance of noise exists in the model needs to be small. In such

cases, the major signal variances will be covered by spatial or temporal subspaces spanned by the first vectors of either U or V as identified by SVD(L. K. Hansen, 2000; McKeown et al., 1998).

ICA assumes that the data matrix X can be modeled as a linear mixture of K (k=3 for fMRI data) spatial component maps that are statistically independent together with the corresponding time course associated with each component:

$$X_{jt} = \sum_{k=1}^{K} A_{jk} S_{kt} + E_{jt} \tag{2.2}$$

Where the A and S are composed of K independent components and E is a spatial and temporally white noise. The ICA model can be employed in either spatial or temporal versions. For spatial ICA, the method assumes that each column of matrix A ($\lfloor A_{jk} \rfloor$) are statistically independent (usually preferred for fMRI data), whereas for temporal ICA, each row of A ($\lfloor S_{jk} \rfloor$) are assumed to be statistically independent. The second row of Figure 2.14, illustrates the application of ICA technique to estimate the time courses from the data by maximizing independence between the component images.

Despite mentioned advantages, interpreting the output of model-free multivariate analyses is more challenging when compared to seed-based functional connectivity studies. These decomposition methods are usually exhibiting complex spatial patterns that include interesting components of brain activity together with remaining noisy/artefactual components (effects of motion, non-neuronal physiology fluctuations of non-neuronal origin, scanner artifacts and other nuisance sources). However, having access to the analysis of neuroimaging data set with thousands of subjects provides the possibility to use statistical/machine learning approaches to guide the automatic detection of noisy/artefactual components (K. Lee et al., 2019; Perlbarg et al., 2007). One can also take advantage of several functional brain atlases (Glasser et al., 2016; J. L. Ji et al., 2019; Landau et al., 2011; Shirer et al., 2012; Thomas Yeo et al., 2011) to correctly assign the spatial component of ICA/PCA to the closest RS networks in which they belong to (Du et al., 2020; J. Lu et al., 2017; Pruim et al., 2015).

2.2.3.2.2 Clustering-based methods

Another family of model-free approaches consists in clustering-based methods, which aim at searching for similarity between BOLD signals time series of several voxels or brain regions, and to group them into homogeneous clusters (Cordes et al., 2002; Salvador et al., 2005; Thirion et al., 2006; M. van den Heuvel et al., 2008). The most popular clustering techniques to analyze resting state fMRI data are k-means clustering (and its fuzzy version), hierarchical clustering, self-organizing maps, and bootstrapping approaches (Bellec et al., 2009; Cordes et al., 2002; Farahani et al., 2019; K. Lee et al., 2016; Ngan & Hu, 1999; M. van den Heuvel et al., 2008). The k-means clustering method consists in assigning each voxel (or region) to a few predefined or random cluster centers and then updating the clusters memberships as well as cluster centers according to fulfillment of optimization criteria. In this context, k-means fuzzy clustering will not consider a binary value to define clustering membership but rather a probability (Lahijanian et al., 2016). In k-means algorithm, the initial centers of the clusters and the total number of clusters (k) need to be set a priori. As an alternative, hierarchical clustering methods consist of aggregating voxels/regions by their closest element, resulting in the estimation of a binary cluster tree, called dendrogram, offering a multi-level hierarchy. In hierarchical models, clusters at one specific level

are fused base on a similarity metric to build new clusters at the next levels. Data are therefore stratified into a hierarchical organization using the agglomerative or divisive models (Cordes et al., 2002; Rokach & Maimon, 2005). The important feature of hierarchical clustering is that the total number of cluster should not be defined a priori.

The self-organizing maps methods start from a few random noise time courses and then iteratively update them by reducing the distance of each time course with time course of the closest brain voxels/regions (as for k-Means clustering) (Ngan & Hu, 1999; Peltier et al., 2003).

2.2.3.2.3 Bootstrapping approach

The question of reliability of functional connectivity analyses is a very important topic (Noble et al., 2019). To handle this issue it might be useful to compute a specific functional connectivity data analysis method (e.g. ICA, clustering) not only once but several to assess test/retest reliability of the proposed methods (Damoiseaux et al., 2006; Smith & Dubes, 1980). In this context, Bellec et al. (Bellec et al., 2009) proposed to assess the stability of resting-state components in fMRI data by applying k-means clustering algorithm on several data sets that have been resampled using a bootstrap approach. In statistics, resampling a data set using bootstrap consists of sampling a data set of the same size "with replacement", resulting in several surrogate datasets following the same statistical distribution as the original one (Efron & Tibshirani, 1994). In his methods entitled multi-level bootstrap analysis of stable clusters (BASC) the k-means algorithm of RS- fMRI data set is resulting in a binary adjacency matrix $\Phi(y)$ where the $\Phi_{i,j}(y)$ equals 1 if the regions i and j belong to the same cluster in the partition and equals 0 otherwise. The main idea consists in repeating the same clustering several times on "bootstrap resampled" dataset, resulting in B = 200 binary adjacency matrices. Averaging those binary matrices results in the estimation of a probability matrix S, and called the stability matrix, assessing the stability/reliability of features estimated by the clustering process. For the case of individual-level analysis, the stability matrix, is produced by bootstrapping the dataset y, which is a time × space array of size T × R, where T is the number of time points and R is the number of regions (Figure 2.15). The standard bootstrap resampling strategy consists in generating in a non parametric manner new samples of same size, by drawing with replacement from the original datasets (Divenyi & Efron, 1979). Such an approach ensures that the resample datasets are following the same distribution as the original one, only when samples are independent. However, in the context of resting state fMRI, we have to handle statistical dependencies in space and time (Bullmore et al., 2000). In this context, the circular block bootstrap (CBB) approach has been proposed to generate bootstrap samples of resting state fMRI data (Bellec et al., 2009; Politis & Romano, 1992). Whereas the original spatial organization of the data is kept, data are divided into block along time, and bootstrap resampling with replacement is then performed among those blocks. The block should be sufficiently long so that the inherent autocorrelation of the fMRI data is embedded within each block so that every block could then be considered as independent sample (Bellec et al., 2009). In the BASC method, a second-level bootstrap analysis approach is then performed by applying standard bootstrap resampling (with replacement) to binarized stability matrices S estimated from all subjects, resulting in a functional connectivity stability matrix estimated at the population level.

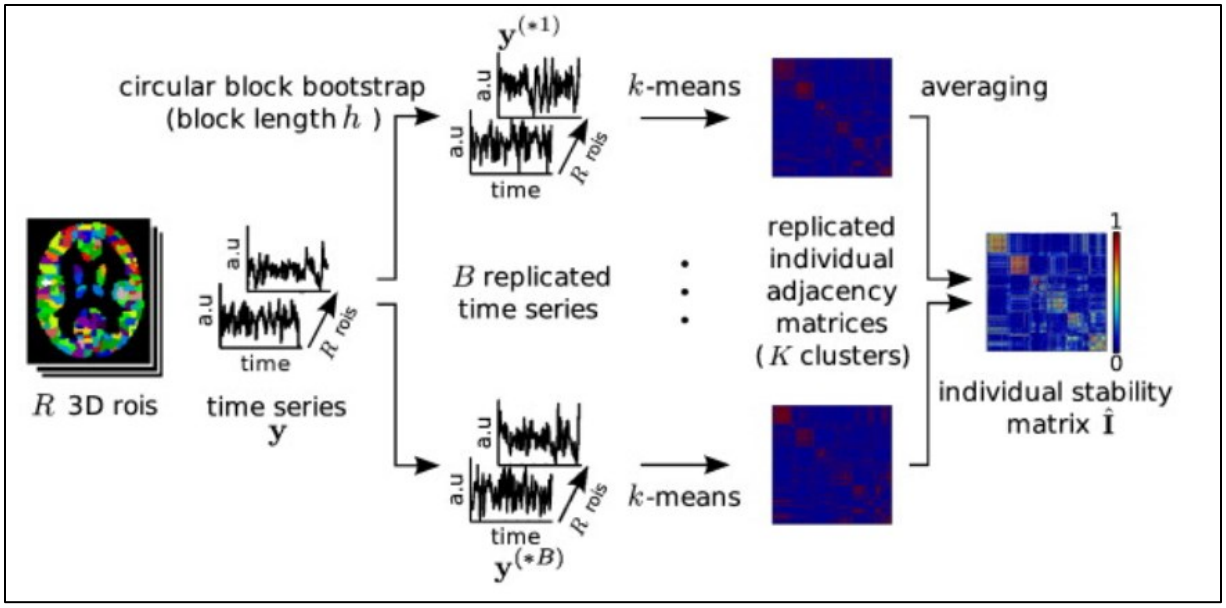

Figure 2.15. Stability matrix of k-means clustering using Bootstrap estimation of fMRI time series (Bellec et al., 2009)

2.2.3.2.1 A Mutual information-based analysis of brain functional networks

Another model-free approach to assess characteristics of brain networks is to quantify the flow of information within and between resting state networks, as a key methodology to assess the level of integration/segregation of information within a specified hierarchical network architecture. In this context, mutual information (MI) can be considered as an information-theoretic metric to assess the amount of shared information among BOLD regional activities (Grassberger et al., 1991; Kraskov et al., 2004). In statistics, mutual information (MI) quantifies the amount of information one random variable contains about another one. MI-based methods can be applied to both linear and non-linear dependency problems and have been shown to capture physiologically relevant features of the brain regional connectivity, more accurately than correlation-based similarity measures techniques (Garrido et al., 2012; W. Zhang et al., 2018).

Given a specific hierarchical network structure, MI measures can quantify and characterize interaction between and within brain networks, therefore allowing for carefully assess functional integration and segregation (Marrelec et al., 2008; Tononi et al., 1998; Zeki & Shipp, 1988). Segregation implies functional/anatomical specializations of specific brain regions characterized by local flow of information. On the other hand, the concept of integration principle acknowledges the merging of information flows across networks and systems distributed in the whole brain, using reciprocal and long-range interactions (Figure 2.16) (Mesulam, 1990; Varela et al., 2001). There is actually a hierarchical balance between these two main properties of brain activity, which deeply influence the brain topological design and structure at muti-scales (Haimovici et al., 2013; Marrelec et al., 2008).

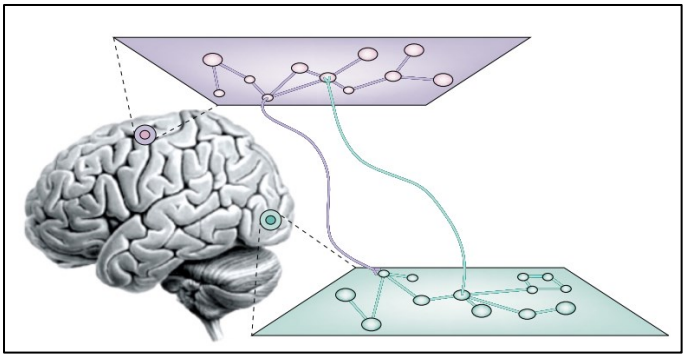

Figure 2.16. Schematic representation of brain short- and long-range transient of information implying the brain segregation and integration. Figure adapted from (Varela et al., 2001)

MI is actually a special case of a more general quantity called relative entropy or Kullback–Leibler divergence, which is a kind of measure of the "distance" between two probability mass functions $p(x)$, $q(x)$, as below (Cover & Thomas, 1991):

$$D(p \parallel q) = \sum_{x \in \mathcal{X}} p(x) \log \frac{p(x)}{q(x)} \tag{2.3}$$

$$= E_p \left[\log \frac{p(X)}{q(X)} \right] \tag{2.4}$$

Where $\mathcal{X}$ is the alphabet (i.e., the set of all possible outcomes) of X. The second line in the formula shows the entropy, which expresses the self-information of a random variable X and can also be interpreted as expected value of the random variable $\log \frac{1}{p(X)}$, where X is drawn according to probability mass function $p(x)$ and defined as

$$H(X) = E_p \left[\log \frac{1}{p(X)} \right] \tag{2.5}$$

The mutual information between two variables X with alphabet $\mathcal{X}$ and probability mass function $p(x)$ and Y with alphabet $\mathcal{Y}$ and probability mass function $p(y)$, then is the relative entropy between the joint probability mass function $p(x, y)$ and the product distribution $p(x)p(y)$, which would be the joint distribution in the case of statistical independence, defined as follows

$$I(X;Y) = \sum_{x \in \mathcal{X}} \sum_{y \in \mathcal{Y}} p(x,y) \log \frac{p(x,y)}{p(x)p(y)} \tag{2.6}$$

$$= D\big(p(x,y) \parallel p(x)p(y)\big) \tag{2.7}$$

$$= E_{p(x,y)} \left[\log \frac{p(X,Y)}{p(X)p(Y)} \right] \tag{2.8}$$

Rearranging formula, the mutual information can be defined as below (Gierlichs et al., 2008):

$$I(X;Y) = H(X) + H(Y) - H(X,Y) \tag{2.9}$$

Where the $H(X,Y)$ is the joint entropy of (X,Y).

Marrelec et al. (Marrelec et al., 2008) proposed a MI-based model-free approach to assess integration within a hierarchical structure spanning from the mesoscale level (regions) to the macro-scale level (networks and systems). In their model, the total integration (I_t) was introduced as a summation of mutual information between the systems or networks (I_b) and the grand sum of the mutual information within each system or network (I_w). To do so, MI, was estimated in bottom-up manner, from the mesoscale to the macroscale level. At the meso-scale level, we extracted from original fMRI data, $Y = (y_1, \dots, y_N)$, the mean signal time course associated with each region, N being the total number of regions, and each region was defined as belonging to one of K brain (non-overlapping) systems/networks of the macroscale level $S = \{S_1, \dots, S_K\}$.

The (between) integration, or mutual information between the K partitions, is defined as follows:

$$I_b = I\left(Y_{S_1}, \dots, Y_{S_K}\right) = \left[\sum_{k=1}^{K} H\left(p\left(Y_{S_k}\right)\right)\right] - H\left(p\left(Y_{S_1}, \dots, Y_{S_K}\right)\right) \tag{2.10}$$

While the within integration is defined as:

$$I_w = \sum_{k=1}^{K} I\left(Y_{S_k}\right) \tag{2.11}$$

Since the fMRI data are shown to follow a multivariate normal distribution with mean μ and covariance matrix $\boldsymbol{\Sigma} = \left(\Sigma_{n,n}\right)$, the entropy formulation can then be simplified as follows:

$$H\left(p\left(Y_{S_k}\right)\right) = \frac{1}{2}\ln\left[(2\pi e)^{N_k}\left|\boldsymbol{\Sigma}_{S_k,S_k}\right|\right] \tag{2.12}$$

where N_k is the number of regions comprising system or network S_k and $\boldsymbol{\Sigma}_{S_k,S_k} = \left(\Sigma_{l,m}\right)_{l,m\in S_k}$ is the covariance submatrix associated with Y_{S_k}.

Then the total integration is defined as:

$$I_t = I_b + I_w \tag{2.13}$$

Using such framework, hierarchical measures of integration (i.e., I_t, I_b, and I_w) can be calculated at different nested spatial scales, where elements (for example regions, or networks) at the finest level are combined to form larger elements. Additionally, a measure of functional clustering ratio (or functional segregation) can be defined (Boly et al., 2012) as:

$$\mathrm{FCR}\left(Y_{S_k}\right) = \frac{I_w\left(Y_{S_k}\right)}{I_b\left(Y_{S_k}\right)} \tag{2.14}$$

Here, $I_w\left(Y_{S_k}\right)$ and $I_b\left(Y_{S_k}\right)$ are calculated based on a sub-partition of S_k. FCR is a measure of clustering inside a given system because an increase in FCR indicates that subsystems become functionally more independent of each other. In Figure 2.17 (Boly et al., 2012), the hierarchical integration and segregation model is applied at two nested levels: at the whole-brain level (with respect to a partition of the brain into 6 networks), and in each and every brain network (with respect to a partition of each network into assemblies).

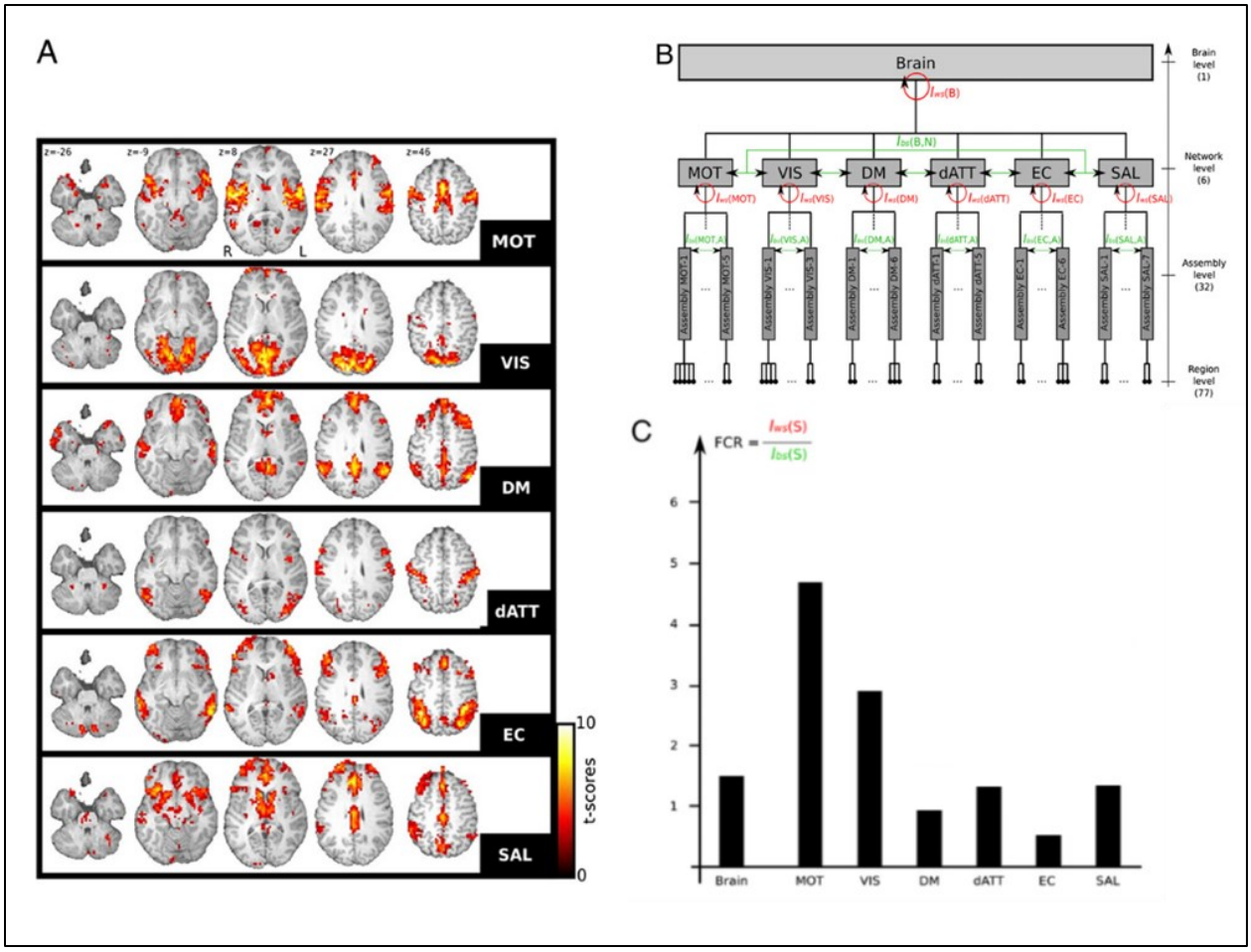

Figure 2.17. (A) The brain was decomposed into six networks. (B) Brain connectivity was considered at three nested levels: brain, networks, and assemblies of areas. (C) Functional clustering ratios both at the whole-brain level and in each and every brain network. Networks: dATT, dorsal attentional; DM, default mode; EC, executive control; MOT, sensorimotor; SAL, salience; VIS, visual. Figure is adapted from (Boly et al., 2012).

2.2.3.3 Estimation of hubs of brain network using free model approaches

In section 2.2.2.1 we introduced functional hubs regions and graph theorical techniques to measure them. Even though the estimation of connector hubs using graph theory-based approaches is relatively easy to apply; however, they are rapidly becoming computationally demanding when applied at the voxel-level resolution, while other approaches will consider different parcellations

of the brain. As an example, Bagarinao et al. (Bagarinao et al., 2020) proposed a method entitled functional connectivity overlap ratio (FCOR) to estimate connector hubs at the voxel level. To do so, a template of all RSN is identified using independent component analysis and used as the reference to identify the RSNs associated with seed-based functional connectivity maps of every voxel (using Pearson correlation). For each voxel, to assess how much overlap a specific seed-based functional connectivity is exhibiting with a specific template RSN, a functional connectivity overlap ratio (FCOR) could be estimated as the number of voxels in the overlap divided by the total number of voxels for this specific RSN. The FCOR estimation process is repeated for all voxels within the brain to generate the final FCOR map associated with the given RSN template (Bagarinao et al., 2020) (Figure 2.18).

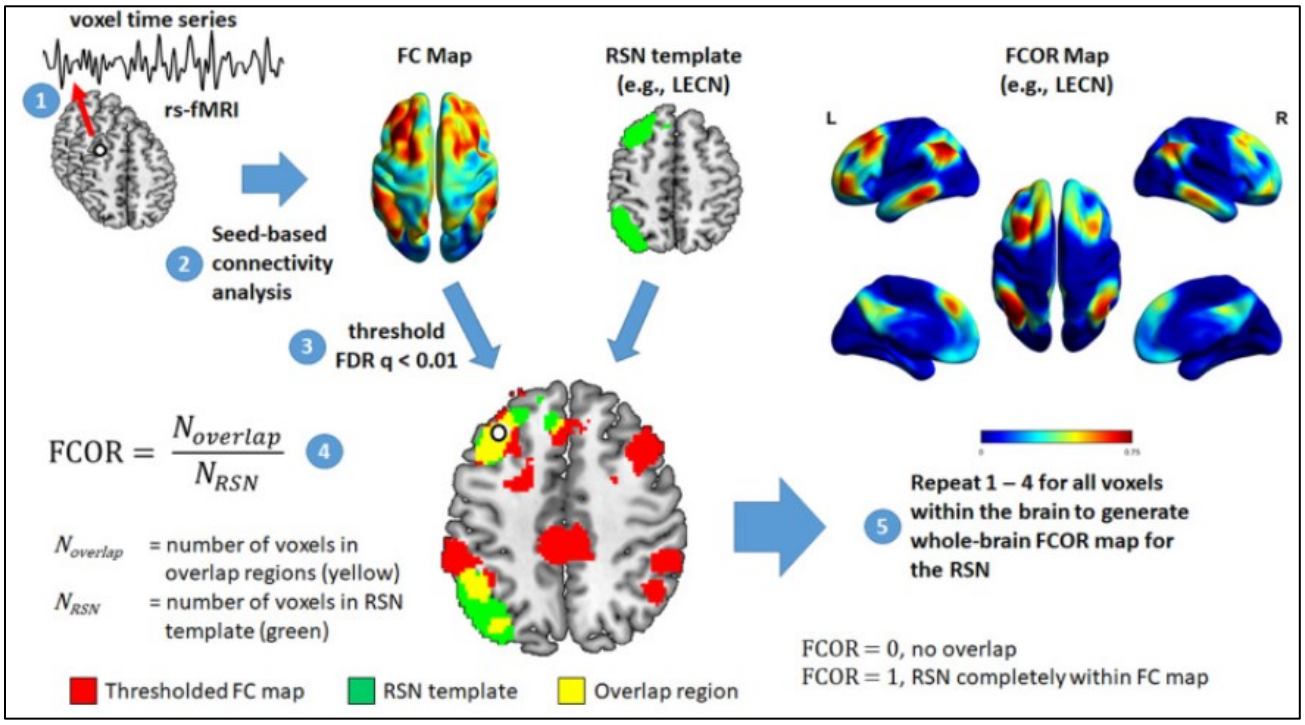

Figure 2.18. Outline of the approach to construct the FCOR map of a given RSN template. Figure adapted from (Bagarinao et al., 2020)

2.2.3.3.1 Sparsity-based analysis of brain functional network

Our group proposed and carefully validated another variant of model-free method, taking advantage of sparse GLM decomposition (K. Lee et al., 2011) together with that took advantage of both GLM and bootstrapping approaches suggested by Bellec et al. (Bellec et al., 2010). The method is entitled SPARK: Sparsity-based Analysis of Reliable k-hubness (K. Lee et al., 2016). SPARK is able to reliably detect the data-driven spatiotemporally pattern of resting-state fMRI with a focus on influential regions of the brain called connector hub regions.

As opposed to graph theory metrics, likely biased by the use of binary connectome matrix analysis, the main originality of SPARK is its ability to carefully handle spatial overlap between brain networks, an important characteristic to estimate of hubs of brain networks. SPARK core decomposition consists of a data-driven sparse variant of GLM, able to extract overlapping network structure in individual resting-state fMRI (Figure 2.19) (K. Lee et al., 2011). When applied to an fMRI data set $Y \in T \times V$ (with T the time-points and V the voxels in grey matter),

sparse GLM, using the concept of k-SVD decomposes fMRI data on a data driven RSN dictionary $\Omega \in$T×N composed of N time-course atoms. The method allows estimating a sparse coefficient matrix X ∈N×V, carefully assessing the sparse contribution of the time course of a few atoms among N, with the corresponding remaining noise matrix E ∈T×V as below:

$$y_i = \Omega x_i + e_i, subject\ to\ \forall i: \|x_i\|_0 \leq k_i, \tag{2.15}$$

where y_i is a time course measured in a voxel i and each column of Ω is an atom (time course) ω_j. An atom is therefore a network-characteristic temporal feature that is shared by a subset of voxels [4]. $\|x_i\|_0$ denotes the L0 norm of the vector xi, i.e., limiting the number of non-zero elements to maximum k_i. Each column of X (x_i) is a sparse code for the voxel i, where the number of non-zeros in x_i defines the sparsity level and the coefficients indicate the signal amplitudes of the atoms in each voxel, defining the concept of k-hubness estimation.

To estimate the global dictionary Ω and the sparse representation of each voxel in X the following optimization problem needs to be solved:

$$min_{\Omega x} \|\mathrm{Y} - \Omega X\|_F^2 , subject\ to\ \forall i \|x_i\|_0 \leq k_{opt_i} \tag{2.16}$$

where $\|.\|_F^2$ denotes the Frobenius norm, and k_{opt_i} denotes the optimal estimation of sparsity for the voxel i.

At the next step, a sparse dictionary learning algorithm called K-SVD (Aharon et al., 2006; Daubechies et al., 2009) is used to solve the problem and to estimate (X) decomposed in N temporal and spatial patterns of resting state networks. Where in this context the SVD stands for Singular Value Decomposition and K indicates a sparsity assumption (k) applied for the algorithm. The sparsity assumption means that the inter-network connection is sparse and at most a small number of RSNs (k < k_{opt_i}) can be identified for each voxel, suggesting the presence of a hub on which a few RSNs overlap, whereas a larger number of RSNs (N >> k) is considered to describe the whole brain activity. In the sparse GLM, k or $k_{opt_i}$is the same for all voxels and its values are determined using a method called minimum description length (MDL), that provides the best trade-off between goodness-of-fit and model complexity (Saito, 1994).

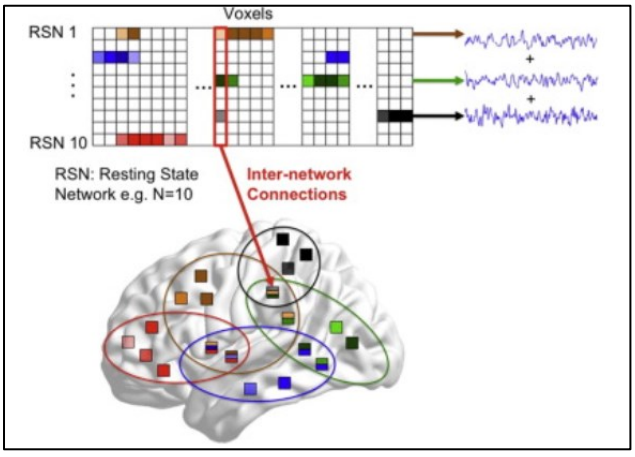

Figure 2.19. The sparse GLM model. The spars information is given by the sparse coefficient matrix (e.g., sparse design matrix), in which each column of the matrix represents a local code for each voxel. Each color in the figure

represents an exemplar RSN. The number of overlapping networks can be measured by counting the non-zeros in each column. Figure adapted from (K. Lee et al., 2016)

Inspired by the work of Bellec et al., our group then proposed a stable/reliable version of k-SVD by adding CBB resampling of fMRI dataset, generating B reproducible replicated datasets from Y (RS-fMRI) data, leading to SPARK methods ensuring stable and reliable detection of connector hubs. K-SVD is therefore applied sequentially on each B resampled date. Pooling results from each replica, i.e., N×B (N=50, B=100) spatial maps, a k-means clustering algorithm (K = 20) is applied to obtain a stable sparse matrix (XS), by averaging the corresponding sparse codes in each cluster. The resulting matrix XS was not spared anymore (because of local averaging), and background noise was removed using thresholding. The resulting atom maps (spatial topography of the networks) are obtained by taking and mapping each row in thresholded XS. Finally, using a sparse GLM model, the BOLD signal in each voxel is modelled as a voxel-specific linear combination of k atoms, selected among N atoms from this stable data-driven dictionary. The "hubness" of each voxel was estimated by counting the number k of nonzero spatiotemporally overlapped resting state network describing the signal time course of each specific voxel (Figure 2.20). In practice, hubness values are between 1 and 4–6. Our group has shown that SPARK is able to extract similar RSNs as other ICA and clustering approaches with hubness maps that are consistent with the literature (Figure 2.20).

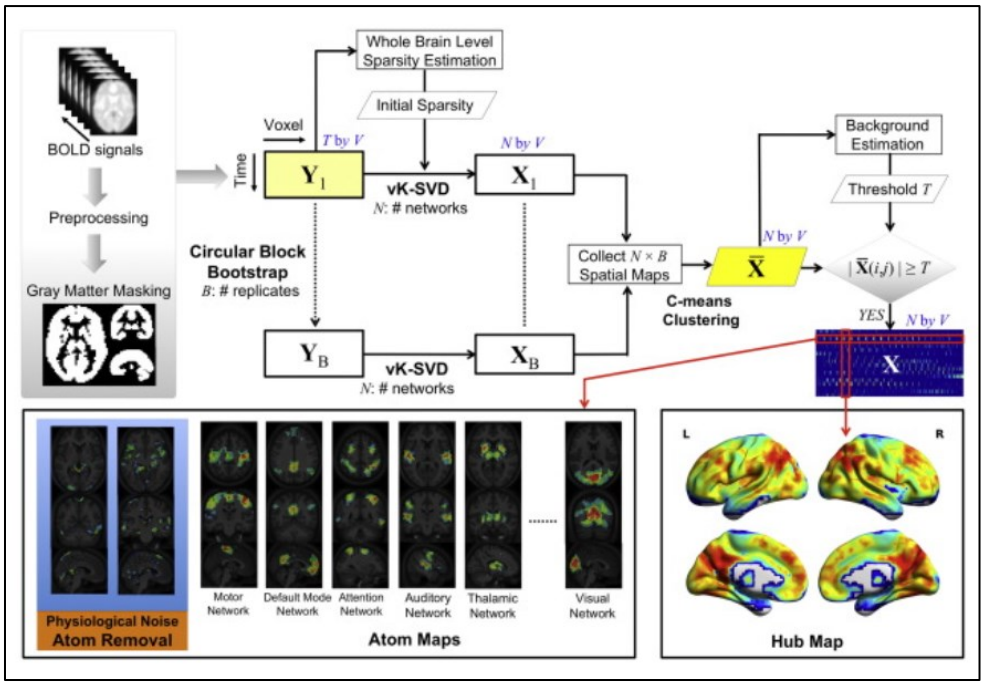

Figure 2.20. Summary description of SPARK framework. Figure adapted from (K. Lee et al., 2016)

2.3 Summary

In this chapter, we introduced the concept of brain functional organization spanning different spatial scales from molecular, voxel and regions, and network resolutions. At the micro-scale or molecular level, we summarized the main brain cell types and their contribution to signalling and generation of electrical potentials. In the following, we introduced the conventional human brain transcriptional atlas that provides opportunities for investigating the brain molecular process. Then we discussed the brain functional structures at the neuronal population scale and introduced the

major brain parcellation atlases. The anatomical and modular organization of the brain was discussed next, where we introduced its anatomical position and functions. We introduced the notion of brain functional connectivity described the most consistent resting-state brain networks reported in the literature. We reviewed graph theoretical approaches to characterize the brain network organization and topology, while describing the role of few functionally important brain regions, and notably hub regions. Finally, we reviewed several methodologies that have been proposed to study functional connectivity, including SPARK to measure brain functional hubness and MI-based hierarchical integration framework to measure brain functional integration. SPARK was used to estimate functional hubness in Manuscript 1 when assessing brain functional hubness. In manuscript 2, we considered four metrics from graph theory including eigenvector centrality and global efficiency, clustering coefficient and local efficiency, to estimate brain functional global and local centralities. In manuscript 3, we considered MI-based measures to quantify brain functional integration and segregation at network level.

Chapter 3: Manuscript 1 — Multiresolution Metabolic Profile of Functional Hubness in the Resting Human Brain

3.1 Context

Whereas in Chapter 1 we discussed the main brain metabolic substrates, including glucose and oxygen metabolisms and the main neuroimaging techniques to probe them (PET and MRI), we then described in Chapter 2 the brain functional network organization, emphasizing the importance of functional hubs, which are highly connected regions that play an important role in brain functional integration.

Few key studies addressing these important questions as well as linking brain metabolism and brain network structures have been described in our first state-of-the-art chapters I (Barabási, 2009; Baronchelli et al., 2013; Leontiev et al., 2013; Liang et al., 2013; Shokri-Kojori et al., 2019; D. Tomasi et al., 2013; Vaishnavi et al., 2010). Most of those studies were suggesting that highly functionally connected regions are associated with high metabolic and vascular costs and that these associations are network-dependent. In particular, Tomasi et al (D. Tomasi et al., 2013) proposed a power-law model to link functional hubness and glucose metabolism, based on biophysical arguments. They quantified cerebral metabolic rate of glucose (CMRGlc) from fluorodeoxyglucose (FDG) positron emission tomography (PET) data using an extension of Sokoloff's model (Sokoloff et al., 1977). To measure functional hubness, they quantified global and local degree of functional connectivity from blood oxygen level-dependent (BOLD) functional magnetic resonance imaging (fMRI) data using graph theory. Liang et al (Liang et al., 2013) considered a linear regression model to relate the functional hubness of brain regions with cerebral blood flow. Cerebral Blood Flow (CBF) was quantified using arterial spin labelling (ASL) data and a one-compartment model. Using graph theory metrics applied to resting state BOLD fMRI data, they quantified functional connectivity strength, efficiency and betweenness centrality. They showed that CBF was an adequate surrogate for cerebral metabolism by correlating their CBF results to CMRGlc and cerebral metabolic rate of oxygen ($CMRO_2$) map estimated using PET in a different cohort (Vaishnavi et al., 2010). Both these studies were carried out at the voxel-scale of the brain.

In this chapter, we are presenting the first original contribution of this PhD thesis, where we examined the metabolic and vascular properties of functional hubness using multimodal data combining FDG PET, and BOLD and calibrated fMRI data. We quantified glucose metabolism (CMRGlc) from FDG PET, oxygen metabolism ($CMRO_2$) as well as other physiological/hemodynamic components of interest, namely CBF, and oxygen extraction fraction (OEF), from calibrated fMRI data. We quantified functional hubness from BOLD fMRI data. We tested the hypothesis that there exists a concave down increasing power-law model that relates metabolic, vascular (CMRGlc, $CMRO_2$, CBF, and OEF) and functional hubness properties. The semi-quantitative SUVR model was used to estimate normalized voxel-maps of glucose metabolism (CMRGlc), the generalized calibration model (GCM) proposed by Gauthier et al. (Gauthier & Hoge, 2012) was used to estimate voxel-wise maps of oxygen metabolism ($CMRO_2$), CBF and OEF. The SPARK method (K. Lee et al., 2016), an original methodology to estimate functional hubness in a reliable manner at the voxel level, while carefully modeling spatial overlap between brain networks, was used to estimate voxel-wise maps of functional hubness. We examined our hypothesis across large-scale networks nested over two spatial resolutions from the

Multiresolution Intrinsic Segmentation Template (MIST) atlas using a multi-level Bayesian model (Gelman et al., 2020).

3.2 Abstract

Brain regions exhibit heterogeneous metabolic properties and varying functional connectivity levels within and between networks. Understanding the links between functional hubness ($\mathcal{H}$) and oxygen/glucose metabolism is of primary importance.

We investigated whether increase in $\mathcal{H}$ is associated with a non-linear increase in cerebral metabolic rate of glucose/oxygen (CMRGlc/$CMRO_2$), within large-scale resting-state networks (RSNs).

We recruited 19 healthy adults who underwent RS BOLD and gas-inhalation based calibrated fMRI, and Fluoro-Deoxy-Glucose (FDG) PET acquisitions. Whole-brain maps of $\mathcal{H}$ were estimated from BOLD data (K. Lee et al., 2016). CMRGlc maps were obtained from FDG-PET data. $CMRO_2$ maps were obtained from calibrated fMRI data (Gauthier & Hoge, 2012). A multiresolution atlas was used to define nested RSNs at two spatial resolutions (7 and 20 networks), and a Bayesian multilevel power-law model was fitted to infer increase trends.

Evidence ratios were estimated to assess quantitatively the hypothesis of a power-law model increase. At the whole-brain-scale, we found extreme (respectively very strong) evidence in favour of the hypothesis for CMRGlc (respectively $CMRO_2$). At the 7-networks-scale, we reported moderate-to-extreme evidence. At the 20-networks-scale, we found anecdotal-to-extreme evidence in favour of the hypothesis within 20/20 networks for CMRGlc and within 17/20 networks for $CMRO_2$. $CMRO_2$ and cerebral blood flow maps were exhibiting similar non-linear trends, whereas the oxygen extraction fraction map was not varying much as a function of $\mathcal{H}$.

In conclusion, we demonstrated that increase in functional hubness was associated with non-linear increase in glucose/oxygen metabolism, suggesting hubs efficiency regarding metabolism.

3.3 Significance Statement

We proposed novel perspectives of macroscale/mesoscale brain function-metabolism relationships by linking the hubness of brain regions to their glucose/oxygen metabolism across different spatial scales using multimodal neuroimaging data. We adopted a sparse time-series decomposition strategy to estimate hubness as a count number of overlapping networks a brain region relates to, thereby complementing traditional graph-theory-based approaches. We used a general calibrated model of quantitative MRI data to derive oxygen metabolism, thereby complementing traditional PET studies. We formulated a Bayesian workflow on high-dimensional voxel data, thereby complementing traditional region-based or frequentist approaches. We reported specific differences and similarities linking PET-glucose and MRI-oxygen metabolism to sparsity-based measures of hubness, suggesting hubs are overall efficient when dealing with both glucose/oxygen metabolism, while exhibiting regional variabilities.

3.4 Introduction

The human brain is a complex dynamical system exhibiting functional activity patterns at multiple spatiotemporal scales (Bassett & Sporns, 2017) with energy demands accounting for at least 20% of body energy consumption (Magistretti & Allaman, 2015). Linking the structure of brain functional activity and the associated metabolism of key molecules, as oxygen and glucose, is of primary importance since these are the main sources of energy sustaining neuronal activity. In

humans, these studies are preferentially done during resting-state (RS) conditions thanks to non-invasive neuroimaging techniques such as functional Magnetic Resonance Imaging (fMRI) or Positron Emission Tomography (PET). Together, these techniques allow to probe at a macroscale of typically 2-mm isotropic voxel resolution, or within brain parcels (around 10 mm radius), whole-brain network dynamics, through slow hemodynamic fluctuations measured using fMRI, as well as glucose and oxygen cerebral metabolism (Bassett & Sporns, 2017; Magistretti & Allaman, 2015). At such macroscales, coherent neuronal assemblies (brain regions) parsimoniously interconnect, forming large-scale networks that support several functions of the brain such as motion control, cognition, and perception (Bassett & Sporns, 2017; Magistretti & Allaman, 2015). Within those brain networks, functional hubs are defined as specific brain regions exhibiting dense connections to other regions. Whereas provincial hubs are ensuring dense connections within a specific resting state network, connector hubs are promoting global and hierarchical communications between distant functionally specialized resting state networks (Pessoa, 2014). Indices of functional hubness ($\mathcal{H}$) can be used to quantitively assess the relative importance of a brain region within such underlying hierarchical network architecture. These indices indicate connectivity levels of brain regions to the rest of the brain on a continuous or discrete scale (K. Lee et al., 2016, 2018; J. Xu et al., 2016). In addition, multiresolution brain parcellations could be useful to summarize the higher-order organization principles that link together brain regions across multiple spatial scales (Arslan et al., 2018; Messé, 2020; Urchs et al., 2019). The recent literature highlights that the interplay between glucose and oxygen cerebral metabolism, and their interrelations with $\mathcal{H}$ across different spatial scales remain poorly understood (Fulcher & Fornito, 2016; Hahn et al., 2020; Nugent et al., 2015; Shokri-Kojori et al., 2019; D. Tomasi et al., 2013; Vaishnavi et al., 2010; Voigt et al., 2022).

In this study, we investigated how the resting cerebral metabolic rate of glucose (CMRGlc) and the resting cerebral metabolic rate of oxygen ($CMRO_2$) of specific brain regions may relate to their functional hubness $\mathcal{H}$, and how these relationships differ across the known large-scale RS networks at multiple spatial scales. We used standardized uptake value ratios (SUVR) of 2-[fluorine-18]-fluoro-2-deoxy-D-glucose (18F-FDG) PET data to quantify CMRGlc maps. We used a generalized calibration model (GCM; (Gauthier & Hoge, 2012)) with gas-manipulation applied during dual Arterial Spin Labeling (ASL) / Blood Oxygen Level-Dependent (BOLD) data acquisition to quantify absolute baseline $CMRO_2$ maps. To quantify $\mathcal{H}$, we used SPARK, Sparsity-based Analysis of Reliable k-hubness, a method developed and validated by our team (K. Lee et al., 2016, 2019) and successfully applied in few clinical applications (K. Lee et al., 2018, 2022). Complementing traditional graph-theory-based approaches, SPARK method provides voxel maps of $\mathcal{H}$ from RS BOLD fMRI data through sparse linear decomposition, carefully modeling spatial overlap between brain networks, and advanced bootstrapping strategies to ensure reliability of $\mathcal{H}$ maps. In SPARK, $\mathcal{H}$ values are small discrete numbers (e.g., typically 1 to 10) indicating the number of networks a brain region or a specific voxel connects to. Our central hypothesis is that we expect a concave down increasing power-law model (i.e., $y = \mathrm{A}x^{\mathrm{B}}$, $0 < \mathrm{B} < 1$) between CMRGlc or $CMRO_2$ and $\mathcal{H}$ at the whole-brain level and across brain networks at multiple spatial resolutions. This hypothesis was based on results suggested by Tomasi et al. (D. Tomasi et al., 2013), who showed this type of power-law relationship using PET-CMRGlc and graph-theoretic-based indices of fMRI-$\mathcal{H}$. Here, we take a more comprehensive approach, using calibrated MRI to fill in this picture by investigating the relationship between $\mathcal{H}$ and $CMRO_2$, cerebral blood flow (CBF) and oxygen extraction fraction (OEF) resulting from $CMRO_2$ mappings to investigate the power-law scaling, in addition to CMRGlc. We used a multi-resolution group-level parcellation

template of RS BOLD fMRI networks, the MIST atlas (Urchs et al., 2019), covering the cortical, subcortical, and cerebellar gray matter to describe power-law scaling across two resolutions with 7 and 20 (fully nested) networks (MIST7 and MIST20 respectively). To quantitatively test our hypotheses, we developed a Bayesian workflow (Gelman et al., 2020) which provides principled ways to make flexible inferences from all available data while accounting for their structure and different sources of variability.

3.5 Results

In this study, we reported the results for 19 healthy subjects who each completed RS MRI and PET acquisitions. Our analyses were restricted to grey-matter voxels in the cortex, cerebellum, amygdala, caudate, hippocampus, nucleus accumbens, pallidum, putamen, and thalamus, and unless otherwise specified, these voxels will constitute the "whole brain" here.

3.5.1 Functional hubness

A voxel-based measure of functional hubness ($\mathcal{H}$) was estimated for each subject from their fMRI data, using SPARK method (K. Lee et al., 2016). This method provided voxel maps of discrete numbers indicating the number of brain networks explaining the BOLD signal within a specific voxel. The total number of networks estimated by SPARK was 20 for all participants. After removing components exhibiting remaining artefacts of physiological fluctuations of non-neuronal origins (around 12 to 15 components on average), SPARK was able to identify, from the data and at the single subject level, consistent RSN similar to the ones usually reported in the literature. Figure 3.1*A* shows the spatial distribution of most frequently identified $\mathcal{H}$ values across subjects. Voxels with $\mathcal{H} = 1$ were most frequent in cerebellum, superior frontal, and central regions, while those with $\mathcal{H} = 2$ were most frequent in occipital and cingulate isthmus regions, , and those with $\mathcal{H} = 3$ in cuneus, precuneus, and superior frontal regions. Voxels with the largest $\mathcal{H}$, $6 \geq \mathcal{H} \geq 4$, were prominent in the precuneus. When taken altogether, voxels with $\mathcal{H} \geq 2$ were highly probable in the cuneus, inferior parietal, and lingual regions (see also Figure 3.7). We further determined that although there was variability between subjects, all $\mathcal{H}$ between 1 and 6 were consistently found within all the networks of MIST after pulling the data of all subjects together, as shown in Figure 3.2 (see also Figure 3.8). We also noted that there was a peak distribution for the whole-brain at $\mathcal{H} = 2$ and for the networks of MIST at either $\mathcal{H} = 2$ (mainly for the default-mode, frontoparietal, and visual networks), whereas the peak of hubness distribution was found for $\mathcal{H} = 1$ for the other networks. In addition, all frequency distributions decayed non-linearly when considering only $\mathcal{H} \geq 2$ values.

3.5.2 CMRGlc, $CMRO_2$, CBF and OEF

PET data were used to estimate CMRGlc using pons-referenced SUVR, and quantitative MRI data were used to obtain $CMRO_2$, CBF, and OEF using the GCM (Gauthier & Hoge, 2012). Figure 3.1*B* shows average maps for CMRGlc, $CMRO_2$, CBF, and OEF. We found that whole-brain values were 1.8 ± 0.5 for CMRGlc (SUVR), 150 ± 40 μmol / (100 g) / min for $CMRO_2$, 51 ± 10 mL / (100 g) / min for CBF, and 0.38 ± 0.05 for OEF (mean ± SD calculated on the average volumes; see also Table 3.4 for regional estimates). We also determined that for all four maps, the highest regional cortical values were found in the pericalcarine, and the subcortical regional peaks were found in the putamen (see also Figure 3.9). Spatial correlation analyses between CMRGlc, $CMRO_2$, CBF, and OEF average maps, as shown in Table 3.1, further revealed significant positive correlations between all maps. In particular, the highest correlation was between $CMRO_2$ and CBF (0.935), and the lowest between CMRGlc and OEF (0.254).

3.5.3 Bayesian multilevel power-law model fits

To analyze relationships between $\mathcal{H}$ and CMRGlc, $CMRO_2$, CBF, or OEF, we formulated a Bayesian multilevel regression model for the power-law model given by $y = \mathrm{A}x^{\mathrm{B}}$ where x (represents $\mathcal{H}$; predictor variable) and y (represents CMRGlc, $CMRO_2$, CBF, or OEF; response variables) are observed, and A and B are estimated. We formulated an inference scheme based on Hamiltonian Monte Carlo methods, allowing us to incorporate our prior knowledge that our subjects belong to a homogeneous population and also that functional networks are interdependent and organized across multiple functionally meaningful spatial resolutions. In this way, we derived, *a posteriori*, *global* estimates for A and B corresponding to the whole brain of a hypothetical "mean" subject, as well as *entity* estimates indicating how different subjects (i.e., their whole brain) or different brain networks (i.e., the networks of MIST7 or MIST20) deviate from the whole brain of the mean subject. Note that in this context, "whole brain" and "subject" are actually synonyms. Also note that in the Bayesian literature, *global* estimates commonly refer to *population*-level effects, while *entity* estimates refer to *group*-level effects (in our case subjects and networks being the grouping variables). See also *Materials and Methods* and *Supplementary Information* for further details. In this study, only the scaling exponent B was a parameter of interest, and we analyzed the exponents obtained for the whole brain of the mean subject as well as the exponents for the different networks of the mean subject.

If a model is a good fit, then we should be able to use it to generate data very similar to the observed data (posterior predictive checks). Figure 3.3*A* shows summaries of posterior predictive distributions overlayed on the observed data within the whole brain for each response variable. We observed that the models could reasonably well fit the bulk of their corresponding data (e.g., mean or median) and the largest errors actually occurred at the tails (mainly for extreme quantiles; see also *Supplementary Information* and Table 3.7, Table 3.8, and Table 3.9 for model summary and detailed numerical diagnostics). Mispredictions (i.e., here negative *y-axis* values) were found for $CMRO_2$ only and they were negligible in number (only appearing in the q-quantiles with $q > 0.95$). We also noted that after $\mathcal{H} = 3$, there were decreasing and constant trends both from the observed and predicted data (see also Figure 3.10, Figure 3.11, Figure 3.12, and Figure 3.13) which were driven by the fact that $\mathcal{H} \geq 4$ are less commonly detected in most subjects and networks (as seen before, e.g., Figure 3.8).

3.5.4 Multilevel power-law scaling

Brain mappings of posterior median of scaling coefficients, i.e., B, within the networks of MIST7 and MIST20 are represented in Figure 3.3B, suggesting highest effect sizes for CMRGlc, comparable effect sizes for $CMRO_2$ and CBF, and smallest effect sizes for OEF. A median estimate is convenient being, by definition, the 50^{th}-percentile of a distribution. Hence, at the scale of MIST7, the hypothesis of a concave down increasing power-law model was the most likely within all networks and all maps (i.e., CMRGlc, $CMRO_2$, CBF, and OEF), whereas at the scale of MIST20, few networks were more likely to adhere to a decreasing power law model for $CMRO_2$, CBF, and especially OEF. Regions within posteromedial and perigenual anterior cingulate, and ventromedial prefrontal cortices were mainly the one exhibiting the largest B values for CMRGlc, $CMRO_2$, and CBF.

Figure 3.4 shows the results for our central hypothesis of a concave down increasing power-law model, i.e., $0 < \mathrm{B} < 1$ for each response variable. The hypothesis was tested by estimating evidence ratios (F; i.e., the posterior probability under the hypothesis against its alternative) and

the ratios were reported according to the following scale. No evidence when $F = 1$, anecdotal when $1 < F \leq 3$, moderate when $3 < F \leq 10$, strong when $10 < F \leq 30$, very strong when $30 < F \leq 100$, and extreme when $F > 100$. For $F < 1$, the same scale was applied to $\bar{F} = 1/F$ instead to evaluate the evidence of the alternative hypothesis, i.e., $(B < 0) \cup (B > 1)$. See also *Materials and Methods*.

Within the whole brain (tile 1 in Figure 3.4), we determined that the evidence for each response variable was in favor of our hypothesis of a concave down increasing power-law model. The evidence was evaluated as extreme for CMRGlc and CBF, very strong for $CMRO_2$, and anecdotal for OEF. When analyzing the posterior summaries with medians (M) and 89% highest density credible intervals ($89CI$), we further determined that the scaling exponents were overall very small (between 0 and 0.02) suggesting that on average maximum relative increases in CMRGlc, $CMRO_2$, CBF, or OEF (i.e., $\max(y)/\min(y) - 1$) within the whole brain during RS conditions as a function of $\mathcal{H}$ was small (e.g., about 3.6% when exponent = 0.02). Here, we found $M = 0.021$ and $89CI = [0.012, 0.029]$ for CMRGlc, $M = 0.012$ and $89CI = [0.003, 0.022]$ for $CMRO_2$, $M = 0.011$ and $89CI = [0.005, 0.018]$ for CBF, and quite smaller $M = 0.002$ and $89CI = [-0.005, 0.009]$ for OEF.

Within the networks of MIST7 (tiles 2–8 in Figure 3.4), evidence remained all in favor of the hypothesis of a concave down increasing power-law model for all response variables, but at different levels. For CMRGlc, evidence was extreme within all networks except the cerebellum (CER_1) where it was moderate. For $CMRO_2$, evidence was strong-to-extreme within all networks except for the somatomotor network (MOTnet_3) where it was moderate. For CBF, evidence was strong-to-extreme within all networks. For OEF, evidence was anecdotal within all networks except for the default mode network (DMnet_5) where it was moderate. When comparing posterior median estimates, the greatest exponents were found within default mode network (DMnet_5) for all response variables.

Within the networks of MIST20, results were exhibiting more variability. For CMRGlc, our results are confirming our hypothesis of a concave down increasing power-law model for all networks, whereas the alternative hypothesis was found for few networks when considering $CMRO_2$ and OEF maps. Figure 3.4 illustrates such detailed results for four networks (tiles 9–12; see also Figure 3.14 for full results). For example, for OEF, within the basal ganglia and thalamus (BG_THAL_1), evidence was extreme in favor of the hypothesis a concave down increasing power-law model. For $CMRO_2$ (respectively OEF), within the frontoparietal task control network (FPTCnet_7), evidence was strong (respectively extreme) in favor of the alternative hypothesis (here more specifically the hypothesis of a decreasing power-law model). For CMRGlc, within the motor cerebellum (MOCER_17), evidence was anecdotal in favor of the hypothesis. For each response variable, within the perigenual anterior cingulate and ventromedial prefrontal cortices (PGACcor_V#_5), the evidence was extreme in favor of the hypothesis for each response variable.

3.5.5 Power-law scaling differences

Figure 3.5 provides evidence of scaling differences between the networks of MIST7 for each response variable (see also Figure 3.15, Figure 3.16, Figure 3.17, and Figure 3.18 for MIST20). Analyzing the median of the posterior differences (i.e., the color of the circles; M) together with the 89% highest density credible intervals (i.e., the numbers on the upper diagonals; $89CI$) suggested the following. For CMRGlc, the extent of power-law scaling within the default mode network (DMnet_5) was the highest, while within the cerebellum (CER_1) it was the lowest.

Analyzing the maximum between probability of positive difference and probability of negative difference (i.e., the numbers on the diagonals or the size of the circles) for each pairwise difference further provided evidence of scaling differences. Specifically, for CMRGlc, the maximum between probability of positive difference and probability of negative difference ranged 0.54–1.00 (i.e., evidence ratios $F \geq 0.54/0.46 \approx 1.17$), indicating anecdotal-to-extreme evidence , and in particular, evidence was extreme in favor of a positive difference between DMnet_5 and CER_1 (coordinates [2, 1] or [1, 2] in the matrix; $M = 0.024$, $89CI = [0.014,0.033]$). Likewise, for $CMRO_2$, the maximum between probability of positive difference and probability of negative difference ranged 0.50–0.79 (i.e., $3.76 \gtrsim F \geq 1$), indicating no-to-moderate evidence, and in particular, evidence was moderate in favor of a negative difference between the somatomotor network (MOTnet_3) and DMnet_5 (coordinates [5, 2] or [2, 5] in the matrix; $M = -0.004$, $89CI = [-0.020,0.004]$). For CBF, those probabilities ranged 0.52–0.86 (i.e., $6.14 \gtrsim F \gtrsim 1.08$), indicating anecdotal-to-moderate evidence, and in particular, evidence was moderate in favor of a negative difference between MOTnet_3 and DMnet_5 (coordinates [5, 2] or [2, 5] in the matrix; $M = -0.005$, $89CI = [-0.015,0.002]$). For OEF, the probabilities ranged 0.50–0.78 (i.e., $3.55 \gtrsim F \geq 1$), indicating anecdotal-to-moderate evidence, and in particular, evidence was moderate in favor of a negative difference between the frontoparietal network and visual downstream (FPnet_VIS#_6) and DMnet_5 (coordinates [3, 2] or [2, 3] in the matrix; $M = -0.002$, $89CI = [-0.012,0.003]$).

Figure 3.6 (formatted as Figure 3.4) provides evidence of scaling differences between response variables within the whole brain, all the networks of MIST7, and four networks of MIST20 (see Figure 3.19 for complementary results). Within the whole brain, the evidence for the hypothesis of (a positive) scaling difference between $CMRO_2$ and CBF was anecdotal, indicating a similarity between $CMRO_2$ and CBF. The evidence of scaling differences was moderate between CMRGlc and $CMRO_2$, and strong between CMRGlc and CBF, whereas the evidence was strong-to-extreme for all differences involving OEF suggesting overall smaller scaling coefficients for OEF. When analyzing the networks of MIST7, we found overall similar patterns than those reported for the whole brain, with some variabilities. For instance, the evidence of positive scaling differences between CMRGlc and $CMRO_2$ was very strong within the frontoparietal and visual downstream networks (FPnet_VIS#_6), strong within default mode (DMnet_5) and mesolimbic (LIM_net2) networks, suggesting highest increase rates for CMRGlc, whereas it was mostly anecdotal or moderate within the other networks. However, it is worth mentioning that within the cerebellum (CER_1), we reported very different patterns when compared to other networks, since the evidence of all scaling differences were mostly anecdotal or moderate. Besides, within CER_1 only, the scaling exponent for CMRGlc was smaller than the one found for $CMRO_2$ or CBF. Results were more variable within the networks of MIST20. For example, we found very strong and extreme evidence for the scaling differences between $CMRO_2$ and CBF within BG_THAL_1 (positive difference) and FPTCnet_7 (negative difference), and mostly anecdotal evidence for the scaling differences within MOCER_17.

3.6 Discussion

In this study, we analyzed BOLD fMRI, gas-inhalation based ASL/BOLD, and FDG PET data for 19 healthy subjects during resting-state conditions. We derived voxel maps of functional hubness from BOLD fMRI data. We estimated quantitative baseline measures of $CMRO_2$, CBF and OEF from calibrated fMRI data, and computed relative maps CMRGlc from FDG PET data, using SUVR normalization. Hubness maps were derived using a multivariate time-series sparse

decomposition strategy, SPARK (K. Lee et al., 2016), rather than graph theory, therefore allowing to estimate specifically the number of RS networks (from 1 to 6) associated with each voxel. We are proposing a unique investigation involving not only several maps characterizing the metabolism and hemodynamic properties of the healthy brain (CMRGlc, $CMRO_2$, CBF and OEF), allowing a detailed comprehensive overview of these important mechanisms, together with a new method to estimate functional hubness as a discrete/sparse number of networks involved in each voxel. Finally using an advanced multilevel Bayesian model implemented using Hamiltonian Monte Carlo simulations, we were able to carefully assess our hypothesis of a concave down increasing power-law model linking metabolism/hemodynamic maps with functional hubness, at the whole brain level and across two nested spatial scales: (i) within a parcellation composed of 7 consistent RSN (MIST7) and (ii) within a parcellation composed of 20 consistent RSN (MIST20).

First of all, we determined that our results were overall consistent with those from previously published studies. At the whole-brain-level, our results using SPARK showed that more than 70% of voxels were associated with two or more RS networks. At the network-level, two classes of networks could qualitatively be defined based on the peak of their hubness frequency distribution. Namely, on one hand, the default mode, frontoparietal, and visual networks, within which most voxels (peak of frequency distribution) were associated with the activity of two networks, and on the other hand, the cerebellum, mesolimbic, somatomotor, ventral attention, salience, basal ganglia, and thalamus networks within which most voxels were linked to the activity of a single network. Besides, a broad distribution of hubness values (here, ranging from 1 to 6) could consistently be found within all considered functional brain divisions. At the same time, brain regions with the highest hubness were the fewest in number and further adhered to a short-tailed or heavy-tailed frequency distribution. These distributions of hubness measures within the normal brain have been reported before using various methods (Bagarinao et al., 2020; K. Lee et al., 2016; Najafi et al., 2016; Power et al., 2014; Yeo et al., 2014; Zucca et al., 2019) , while providing us the opportunity to reproduce our previously published SPARK results (K. Lee et al., 2016) on new data. It is worth mentioning that SPARK analysis applied on the present dataset, was not only able to extract from the data typical RSN maps reported in the literature (N = 20 networks identified by SPARK here, results not shown), but also provided reliable hubness voxel maps by counting how many of those networks were involved in each voxel (see between subject's probability maps represented in Figure 3.1A). The fact that many methodologies support such findings reinforce the hypothesis that these features of brain network organization are not merely artifacts of the methods used to estimate them. Together these results provide evidence that RS networks could be characterized by their hubness profiles, making hubness measures of fMRI data interesting correlates of brain network integrity. For most previous published studies assessing the correspondence between functional connectivity/hubness and glucose metabolism (M. Bernier et al., 2017; Nugent et al., 2015; Palombit et al., 2022; Shokri-Kojori et al., 2019; Thompson et al., 2016; D. Tomasi et al., 2013) or with cerebral blood flow (Leontiev et al., 2013; Tak et al., 2015), conventional functional connectivity metrics were considered, including amplitude of low frequency fluctuations (ALFF), regional homogeneity (ReHo), functional connectivity strength, or metric derived from graph theory (e.g. degree centrality, node strength). Most of those metrics are derived from Pearson correlation between the BOLD time series of different voxels/regions. In their basic format, graph theory metrics suffer from requiring the influence analysis of connectome density threshold or the specification of binary versus weighted graph models. Therefore overlap/intersection between brain networks is not carefully handled using primitive graph theoretical pipelines. Moreover, when standard Pearson correlation is considered as a measure of

similarity to define the edges, graph theory approaches are most of the times also biased by the size of the different networks (impacting the number of correlations between voxels). Participation coefficient (Power et al., 2013) has been proposed to address these issues and was considered in Palombit et al (Palombit et al., 2022). By counting a sparse/discrete number of networks involved in each voxel, SPARK has been designed to carefully model spatial overlaps between networks, while handling network size issues. Bagarinao et al (Bagarinao et al., 2020) recently proposed an original approach similar to SPARK, counting for every voxel-based seed functional connectivity, the amount with spatial overlap with a template of RSN. SPARK is a complete data-driven approach, and it is not relying on a template definition of RSN. It is worth mentioning that SPARK has been successfully applied to study reorganization of brain networks and hubness in epilepsy (K. Lee et al., 2018) and changes in hubness associated with arousal fluctuation (K. Lee et al., 2022) .

Combining FDG PET and calibrated fMRI, our results showing linear associations between (relative) PET CMRGlc map and (quantitative) MRI $CMRO_2$, CBF, and OEF maps corroborated earlier studies based on PET-ASL or PET-only data with different mapping methods (Cha et al., 2013; Hyder et al., 2013; Liang et al., 2013; Shokri-Kojori et al., 2019; Vaishnavi et al., 2010). In particular, our results suggested the existence of spatial covariations between CMRGlc, $CMRO_2$, CBF, and OEF voxel maps while the relative regional differences of OEF values across the brain were rather small. Our results also supported the potential role of CBF, as a proxy for oxygen metabolism, since the two maps were exhibiting very high spatial correlations, a direct consequence of the underlying multiplication factor linking the two quantity within the GCM model (Gauthier & Hoge, 2012). CMRGlc and CBF maps were also exhibiting moderate spatial correlations, results that are in agreement with previous studies suggesting that CMRGlc PET findings could be predicted from ReHo functional measures estimated from resting state fMRI (M. Bernier et al., 2017). It is important to note, that comparatively to other published studies, our cohort was composed of healthy young adults (mean ± SD age = 24.0 ± 4.3 y; 9 females). Although we only reported here global features of our dataset, it could be desirable to further characterize detailed features of CMRGlc mappings from SUVR, and $CMRO_2$, CBF, OEF mappings from the GCM, and their interrelations, given that such data are rarely acquired together on a population of healthy young adults. These further detailed investigations were falling outside the scope of our present study comparing hubness and metabolism. In general, our non-invasive multimodal dataset offers promising opportunities to guide future theoretical and experimental designs to study function-metabolism macroscale relationships in normal aging as well as in populations affected with disease conditions.

Our main goal in this study was to relate functional hubness to CMRGlc $CMRO_2$, CBF, and OEF within the known RS networks of healthy human brains. We chose to model the relationship thanks to a multilevel power-law model with parameters that can vary by networks across nested spatial scales, starting from the whole brain as the top-most parent network. Our central hypothesis was a concave down increasing power-law model following a previous study by (D. Tomasi et al., 2013) and further confirmed in Shokri-Kojori et al (Shokri-Kojori et al., 2019). The power-law model is interesting as it reflects a natural belief that as brain regions establish more functional connections, their local increase rate (in CMRGlc, $CMRO_2$, CBF, or OEF) get smaller when compared to linear increase, therefore indicating increased efficiency of hubs when dealing with glucose/oxygen metabolism and blood flow. Previous studies investigating such relationship between network properties and metabolism/hemodynamic features, mainly considered CMRGlc measured using

FDG PET (Palombit et al., 2022; Shokri-Kojori et al., 2019; Thompson et al., 2016; D. Tomasi et al., 2013) or with cerebral blood flow using ASL (Leontiev et al., 2013; Tak et al., 2015) with network properties, whereas we are proposing a complete picture involving CMRGlc, $CMRO_2$, CBF, and OEF to be compared with an advanced reliable method to measure hubness (SPARK). Recent studies have also benefitted from simultaneous PET/MRI recordings to study this important mechanism characterizing the healthy brain (Palombit et al., 2022; Thompson et al., 2016), whereas our study like several others studied baseline features from PET and MRI data recorded in different sessions. However since we used calibrated MRI to measure $CMRO_2$ and CBF (Gauthier & Hoge, 2012) and not PET (Vaishnavi et al., 2010), our baseline $CMRO_2$ measures were indeed (almost) simultaneously acquired with our fMRI functional hubness maps. Despite the fact that hubness values $\mathcal{H}$ were difficult to model as discrete values covering a limited range (typically from 1 to 6), our proposed multilevel Bayesian model was able to characterize accurately the intrinsic variability of our data at several levels, allowing us to make statistical inferences to assess the relevance of our hypothesis, while allowing to compare how power law increase rates B were impacted by a specific network structures (from MIST7 or MIST20 atlases) or by a specific modality of interest (CMRGlc, $CMRO_2$, CBF or OEF). Overall, our results suggested that a power-law model was plausible and there were indeed trends of increases at the level of the whole brain as well as at the levels of networks, suggesting that increased connectivity could be associated with efficient a metabolic, and blood circulation and supply cost. At the whole-brain-level, our results provided non-ambiguous evidence of power-law increases for CMRGlc, $CMRO_2$, and CBF. For OEF, we also found evidence in favor of the hypothesis of a power-law increase, but it was very small when compared to other explored modalities. Our results are therefore confirming previous findings for glucose metabolism (Shokri-Kojori et al., 2019; D. Tomasi et al., 2013), while showing for the first time that such power law model could also be applied to characterize oxygen metabolism and CBF. Shokri-Kojori et al (Shokri-Kojori et al., 2019) proposed the promising concepts of relative power and relative cost to further investigate relationship between glucose metabolism and the logarithm of local functional connectivity density. Applying such a quantification approach on our multimodal data could have been of great interest but was falling outside the scope of present study.

Further detailed analyses at the network level provided some refinements to the power-law relationships, and in particular our results revealed that power-law scaling operated differently within distinct functional brain divisions. For all measures including OEF, we found definite evidence of power-law increases within the default mode network, and most precisely within the perigenual anterior cingulate, ventromedial prefrontal, and middle temporal cortices (see results for MIST7 networks for DMnet_5, FPnet_VIS#_6, LIMnet_2 in Figure 3.4). When comparing network-level estimates of power-law scaling exponents to that of the whole brain, we determined that for both CMRGlc and CBF, network-level exponents for the default mode, frontoparietal and mesolimbic networks were greater than the whole-brain-level exponent. These results for CMRGlc and CBF are in agreement with the findings in previous studies that investigated the overlap between indices of functional connectivity strengths and quantitative PET CMRGlc or CBF (Liang et al., 2013; Shokri-Kojori et al., 2019; Tak et al., 2015; D. Tomasi et al., 2013). For $CMRO_2$, the network-level exponents within the default mode, mesolimbic, and visual networks were greater than the whole-brain-level exponent while for OEF, the network-level exponents within the default mode, ventral attention, salience, basal ganglia and thalamus networks were greater than the whole-brain-level exponent, even if power law increase coefficients were clearly smaller for OEF when compared to other modalities (see Figure 3.6). In general, such differences of power-law

scaling between networks could also be expected, owing to the fact that different RS networks possess characteristically different molecular and cellular makeup (Magistretti & Allaman, 2015). Overall our results for CMRGlc, $CMRO_2$ and CBF are suggesting that the largest power law increase rates B, were found within the so called intrinsic networks involved (default mode, fronto-parietal, mesolimbic networks) as opposed to extrinsic network dealing mainly with primary sensation (visual, auditory) and motor (Doucet et al., 2011; Mesmoudi et al., 2013). Our results are showing that more connector hubs are involved within those intrinsic networks (cf. probability of maps of $\mathcal{H}$ in Figure 3.1) and that those hubs are efficient in term of glucose and oxygen metabolism as well as blood flow supply. Specific properties of extrinsic versus intrinsic networks are commonly found within the network literature, suggesting larger SUVR glucose metabolism results within the intrinsic networks (Palombit et al., 2022), or specific involvement of aerobic glycolysis (Vaishnavi et al., 2010). Using simultaneous FDG-PET/fMRI data acquisitions and graph theory metrics of functional hubness (degree centrality, nodes strength, betweenness centrality and participation coefficient), Palombit et al (Palombit et al., 2022) reported rather a moderate linear relationship between strength of functional connectivity and glucose metabolism, whereas such linear correlation was found stronger for connector hubs when compared to provincial hubs. It is important to mention that their proposed measure of hubness from graph theory were obtained by significantly thresholding the distribution of degree centrality values within the connectome matrix. Therefore, their analysis suggesting moderate linear relationship is taking into consideration only the tail of the distribution of hubness measures, which could typically correspond to $\mathcal{H} \geq 3$ voxels in our study. It is also important to mention that since SPARK is estimating the amount of discrete spatial overlap between consistent resting state network, SPARK hubness values are mainly sensitive to connector hubness, suggesting long-distance connection between brain networks. When considering the complete distribution of hubness values ($\mathcal{H}$ ranging from 1 to 6) we found clear evidence of nonlinear a concave down increasing power-law model linking hubness and metabolism or blood flow. Restricting our analysis to the few voxels exhibiting the largest hubness values $\mathcal{H} \geq 3$, could have suggested a similar moderate linear relationship as the one reported by Palombit et al (Palombit et al., 2022).

Whereas our CMRGlc PET results could reliably be interpreted for all networks of MIST7 and MIST20 atlases, it is worth mentioning that our results for $CMRO_2$, CBF, and OEF within networks that included portions of the precentral and postcentral gyri could be questionable due to ASL signal loss in those regions. Indeed, our results within frontoparietal task control, dorsal somatomotor, and lateral ventral attention networks indicated that trends of decreases (rather than increases) were likely to occur for $CMRO_2$. These networks have in common the fact they include a significant portion of the slab masks used to exclude voxels due to low SNR of ASL data. They were also the only ones associated with evidence in favor of power-law decreases. Our analyses further revealed that within the networks that included the slab masks, $CMRO_2$ results critically depended on OEF results more than CBF. This is understandable based on two factors: (i) first, given the fact that OEF maps are more error prone than CBF maps, being derived from a more sensitive numerical strategy (Bulte et al., 2012; Gauthier & Hoge, 2012), (ii) second, because $CMRO_2$ was determined by a multiplicative model of CBF and OEF. Therefore, those results should be interpreted with caution and improvement of the ASL sequence might be considered to solve this issue in our future investigations.

In this study, we also explicitly compared the power-law scaling exponents of the different measures within different functional brain divisions. Overall, largest power law increases rates B

lc were the greatest for CMRG within most RS networks, while the increase rates slightly smaller and similar for $CMRO_2$ and CBF, and the smallest for OEF. Although all the comparisons were done objectively based on the analyses of posterior distributions, here we note that our comparisons including CMRGlc could benefit from further investigations. Indeed, any mismatch between CMRGlc and $CMRO_2$ could be due to network-level differences in aerobic glycolysis, which is the production of lactate in the presence of oxygen (Vaishnavi et al., 2010). However, we could only make limited inferences here since our comparisons are made between relative PET CMRGlc, estimated using SUVR normalization, and quantitative MRI $CMRO_2$ or CBF, even if comparisons were based on indices making abstraction of data units. As such, the observed differences might very well be explained by the specific physiological processes characterizing each modality. PET captures signal emanating intracellularly at the temporal scale of 30 minutes to an hour as phosphorylated FDG becomes trapped after being taken up by cells. On the other hand, ASL measures mostly signal from extracellular space elicited by water molecules that transit through the arterioles, capillaries, and into the brain tissue at the temporal scale of seconds to minutes (Thompson et al., 2016). Moreover, regarding the quantification of relative CMRGlc based on SUVR, it is important to underline that the computation of SUVR is time-dependent and it is non-trivially affected by different plasma clearance rates between subjects and study conditions, although it may improve the precision of PET (Thompson et al., 2016). All above factors may contribute to the observed power-law scaling differences between CMRGlc and $CMRO_2$ or CBF. Future studies could account for these factors and investigate whether mismatches in network-level scaling exponents between CMRGlc and $CMRO_2$ could be explained by correlates of lactate metabolism.

We are also acknowledging several limitations in our proposed study. We are mentioning here three examples. First, concerning the choice of a non-linear model to relate hubness with CMRGlc, $CMRO_2$, CBF, or OEF, power-law models, especially those with small scaling exponents are difficult to characterize when their domain is very restricted (here, between 1 and 6). Here, an exponential or a rational function such as the Michaelis-Menten model which both include a horizontal asymptote, could more likely equally well fit the data and potentially provide more biological insight by coding, for instance, biological saturation. Second, as most network-based study reported in the literature, our results critically depend on the choice of a brain parcellation atlas. Here we chose the MIST atlas as it enabled us to define fully nested networks across a broad range of resolutions while covering the cortex, the subcortical structures, and the cerebellum. Future studies could aim to investigate the influence of parcellations (Arslan et al., 2018; Messé, 2020) as well as the influence of including subcortical and cerebellum signals for which signal-to-noise ratios are usually lower than for the cortical ones. Third, our modular Bayesian modeling was designed to take advantage of the similarities between individuals and between brain networks to derive better estimates. For the sake of simplicity, critical covariates such as the age or sex of the subjects, or network neuronal densities were not included. Future studies involving larger samples could consider more complete models including such covariates of interest to better explain the observed relationships.

3.7 Materials and Methods

A summary of our analysis methods is provided here, with additional details provided in *Supplementary Information*.

3.7.1 Subjects and multimodal data acquisitions

Nineteen right-handed healthy young subjects (mean ± SD age = 24.0 ± 4.3 y; 9 females; see demographics in Table 3.3) were recruited from the student community of Concordia and McGill universities and underwent imaging acquisitions including anatomical MRI, RS BOLD fMRI, and gas-inhalation-based calibrated fMRI, all with a GE Discovery MR750 3.0T, and RS FDG-PET with a GE Discovery PET/CT 690. Regarding participant selection, exclusion criteria included any history of chronic mental or physical illness, MRI or PET contradictions, possible pregnancy, and respiratory problems. Ethics approval was given by le Comité Central d'Éthique de la Recherche. Written informed consent was provided by all subjects and both MRI and PET acquisitions were completed within the imaging suite of PERFORM Centre. Detailed acquisition procedures are provided in *Supplementary Information*.

3.7.2 Functional hubness quantification and analysis

Conventional preprocessing of RS BOLD fMRI data was done using NIAK (Bellec et al., 2011) with a target template space provided by the ICBM 2009a nonlinear symmetric template (Fonov et al., 2011) at a 4-mm isotropic voxel resolution (see details in *Supplementary Information*). A voxel-based measure of functional hubness, $\mathcal{H} \in \mathbb{N}$, was then estimated for each subject from their preprocessed fMRI data, using the SPARK method (K. Lee et al., 2016). The method is detailed in *Supplementary Information*, and in brief, it attempts to reliably explain the BOLD time series of each voxel as a linear combination of few latent network time series through sparse linear modeling and advanced bootstrapping strategies. In the end, reliable estimates of network time series are obtained along with a sparse mixing weight matrix from which a count-number of RS networks can be assigned to each voxel, i.e., the so-called hubness maps. For our analyses, only voxels with $1 \leq \mathcal{H} \leq 6$ were considered, given that voxels exhibiting $\mathcal{H} \geq 7$ values were anecdotal. For each discrete hubness value (or interval), a probability map $\mathcal{P}(\mathcal{H})$ was estimated by calculating for each voxel the relative frequency of occurrence of that $\mathcal{H}$ value (or interval) across subjects. Hubness frequency distributions, within specific networks were also estimated.

3.7.3 CMRGlc, $CMRO_2$, CBF and OEF quantification and analysis

FDG-PET data underwent conventional reconstructions using an iterative 3D ordered subset expectation maximization algorithm (Kinahan et al., 1998) and were used to derive CMRGlc maps using standardized uptake value ratios (SUVR) referenced by the pons (Byrnes et al., 2014). Dual BOLD-ASL data were preprocessed with FSL (Jenkinson et al., 2012). Preprocessed BOLD-ASL data and together with respiratory data were used to determine $CMRO_2$, CBF, and OEF maps with a GCM as in (Gauthier & Hoge, 2012). In brief, the method proposed in (Gauthier & Hoge, 2012) formulates a generalised BOLD signal model within a numerical modeling framework to first yield estimates of OEF and absolute CBF maps, and subsequently estimates of absolute $CMRO_2$ maps through a multiplicative model. ASL data were further analyzed to define a slab mask for each subject indicating the brain slices where temporal signal-to-noise-ratio drops were greater than 50%, resulting in discarding some slices located at the very top of the head, since they were exhibiting poor SNR ASL data to be included in our analyses. At the end, CMRGlc, $CMRO_2$, CBF, and OEF maps, together with the slab masks were all resampled to the target MRI template space used for hubness quantification at a 4-mm isometric voxel resolution. See *Supplementary Information* for additional details.

3.7.4 Brain masking and parcellation

All analyses were performed in the ICBM 2009a symmetric template space at a 4-mm isometric voxel resolution. The brain voxels were labeled according to both the Mindboggle (Manera et al.,

2020) and the MIST atlases (Urchs et al., 2019). The Mindboggle atlas was used to discard voxels that are not grey-matter voxels in the cortex, cerebellum, amygdala, caudate, hippocampus, nucleus accumbens, pallidum, putamen, or thalamus. The MIST atlas was used to define fully nested brain networks at two levels of spatial resolutions involving respectively 7 (MIST7) and 20 (MIST20) networks. For $CMRO_2$, CBF and OEF maps only, the intersection between slab masks were used to exclude additional grey-matter voxels. In the end, only labeled voxels with valid $\mathcal{H}$ values (i.e., ranging between 1 and 6), and valid CMRGlc, $CMRO_2$, CBF, and OEF values (i.e., positive) were kept for further analyses. See *Supplementary Information* for additional details.

3.7.5 Surface mapping and brain visualization

For visualization purposes the ICBM 2009c symmetric template (Fonov et al., 2011) was used. We used the Human Connectome Project pipelines (Marcus et al., 2011) to reconstruct a surface for the template. Volume-to-surface mappings as well as brain volume and surface visualizations were all performed using the Connectome Workbench software (Marcus et al., 2011).

3.7.6 Bayesian multilevel power-law analysis

Let $y_{i,j,k,l} > 0$ be an observation of a response variable (i.e., CMRGlc, $CMRO_2$, CBF, or OEF) at the i-th voxel of the j-th subject, within the k-th network of MIST20, within the l-th network of MIST7, and let $x_{i,j,k,l} \in \mathbb{N}^*$ be the corresponding observation of the main predictor variable (i.e., $\mathcal{H}$). Here, $i \in [\![1, N_j]\!]$, $j \in [\![1,19]\!]$, $k \in [\![1,20]\!]$, $l \in [\![1,7]\!]$, N_j is the number of voxels for the j-th subject (see Table 3.5 for an overview of sample sizes). Let us also note that since MIST20 networks are fully nested within MIST7 networks, there exists a surjective function f_{20}^{7} that maps a network of MIST20 to MIST7 so that in fact $l = f_{20}^{7}(k)$. We assumed the model given by $y_{i,j,k,l} \sim \mathrm{Skew}\mathcal{N}\left(\mu_{j,k,l} = \mathrm{A}_{j,k,l} x_{i,j,k,l}^{\mathrm{B}_{j,k,l}}, \sigma_j, \alpha_j\right)$ where $\mathrm{Skew}\mathcal{N}$ is the skew-normal density (a generalization of the normal density) with mean μ, standard deviation σ, and shape α. The skew-normal density was chosen to reflect our assumption that the conditional responses are most likely skewed. While the parameters A and B were specified to vary by subjects and by networks, parameters σ and α varied by subjects only. Denoting by $\mathcal{N}(.,.)$ the normal density parametrized with mean (first argument) and standard deviation, we specified $\mathrm{B}_{j,k,l} \sim \mathcal{N}\left(\overline{\mathrm{B}} + \mathrm{B}_j^{\mathrm{sub}} + \mathrm{B}_k^{\mathrm{MIST20}} + \mathrm{B}_l^{\mathrm{MIST7}}, \sigma_{j,k,l}^{\mathrm{B}}\right)$. Doing so provided us with $\overline{\mathrm{B}}$ as an estimate for the whole brain of the "mean" subject ($\overline{\mathcal{WB}}$), $\mathrm{B}_j^{\mathrm{sub}}$ as an estimate for the whole brain of the j-th subject coding deviation of the j-th subject from $\overline{\mathcal{WB}}$, $\mathrm{B}_k^{\mathrm{MIST20}}$ as an estimate for the k-th network within MIST20 of the "mean" subject coding deviation from the l-th network within MIST7, and $\mathrm{B}_l^{\mathrm{MIST7}}$ as an estimate for the l-th network within MIST7 of the "mean" subject coding deviation from $\overline{\mathcal{WB}}$. In this study, only the multilevel scaling exponents $\overline{\mathrm{B}}$, $\left(\mathrm{B}_k^{\mathrm{MIST20}}\right)_k$, and $\left(\mathrm{B}_l^{\mathrm{MIST7}}\right)_l$ were considered of interest. See *Supplementary Information* for full modeling details. The model was implemented in Stan and inferences were made using the No-U-Turn sampler variant Hamiltonian Monte Carlo (Carpenter et al., 2017). Model fits and analyses were done primarily with *brms* ((Bürkner, 2017) (see Table 3.6 for sampling specification). Model diagnostic was done graphically by analyzing plots of simulated datasets from the posterior predictive distributions overlayed on the observed datasets as well as numerically (see *Supplementary Information* for details).

Posterior distributions were summarized by their median (M), and their 89% highest density credible interval ($89CI$). Assessing the extent of power-law scaling for each response variable (i.e., CMRGlc, $CMRO_2$, CBF, or OEF) within the whole brain or a network n of MIST7 or MIST20,

was done by characterizing the posterior distribution of $\overline{\mathrm{B}}$, $\overline{\mathrm{B}} + \mathrm{B}_{n}^{\mathrm{MIST7}}$ or $\overline{\mathrm{B}} + \mathrm{B}_{f_{20}^{7}(n)}^{\mathrm{MIST7}} + \mathrm{B}_{n}^{\mathrm{MIST20}}$ respectively. In addition, if d denotes one of such posterior distributions, assessing the existence of a concave down increasing power-law model, i.e., $0 < \mathrm{B} < 1$, was done by estimating an evidence ratio (F) as the ratio of the posterior probability of $0 < d < 1$ to the posterior probability of $(d < 0) \cup (d > 1)$ (i.e., the alternative hypothesis). Such ratios were further reported according to the following scale (see also (Jeffreys, 1998)). No evidence when $F = 1$, anecdotal when $1 < F \leq 3$, moderate when $3 < F \leq 10$, strong when $10 < F \leq 30$, very strong when $30 < F \leq 100$, and extreme when $F > 100$. For $F < 1$, the same scale is applied to $\bar{F} = 1/F$ instead to characterize the evidence of rather choosing the alternative hypothesis, i.e., $(d < 0) \cup (d > 1)$. When calculating F, the entire posterior distribution rather than a percentage of it was used. Assessing the pairwise differences of power-law scaling between two distinct networks n_1 and n_2 of MIST7 or MIST20 for each response, was then done by characterizing the posterior distribution of $\mathrm{B}_{n_1}^{\mathrm{MIST7}} - \mathrm{B}_{n_2}^{\mathrm{MIST7}}$ or $\mathrm{B}_{f_{20}^{7}(n_1)}^{\mathrm{MIST7}} - \mathrm{B}_{f_{20}^{7}(n_2)}^{\mathrm{MIST7}} + \mathrm{B}_{n_1}^{\mathrm{MIST20}} - \mathrm{B}_{n_2}^{\mathrm{MIST20}}$. Likewise, assessing the pairwise differences of power-law scaling between two distinct response variables r_1 and r_2 (e.g. CMRGlc versus $\mathrm{CMRO_2}$) within the whole brain or within a network n of MIST7 or MIST20, was done by characterizing the posterior distribution of $\overline{\mathrm{B}_{\mathrm{r}_1}} - \overline{\mathrm{B}_{\mathrm{r}_2}}$ or $\mathrm{B}_{n,r_1}^{\mathrm{MIST7}} - \mathrm{B}_{n,r_2}^{\mathrm{MIST7}}$ or $\mathrm{B}_{f_{20}^{7}(n),r_1}^{\mathrm{MIST7}} - \mathrm{B}_{f_{20}^{7}(n),r_2}^{\mathrm{MIST7}} + \mathrm{B}_{n,r_1}^{\mathrm{MIST20}} - \mathrm{B}_{n,r_2}^{\mathrm{MIST20}}$.

3.8 Figures and Tables

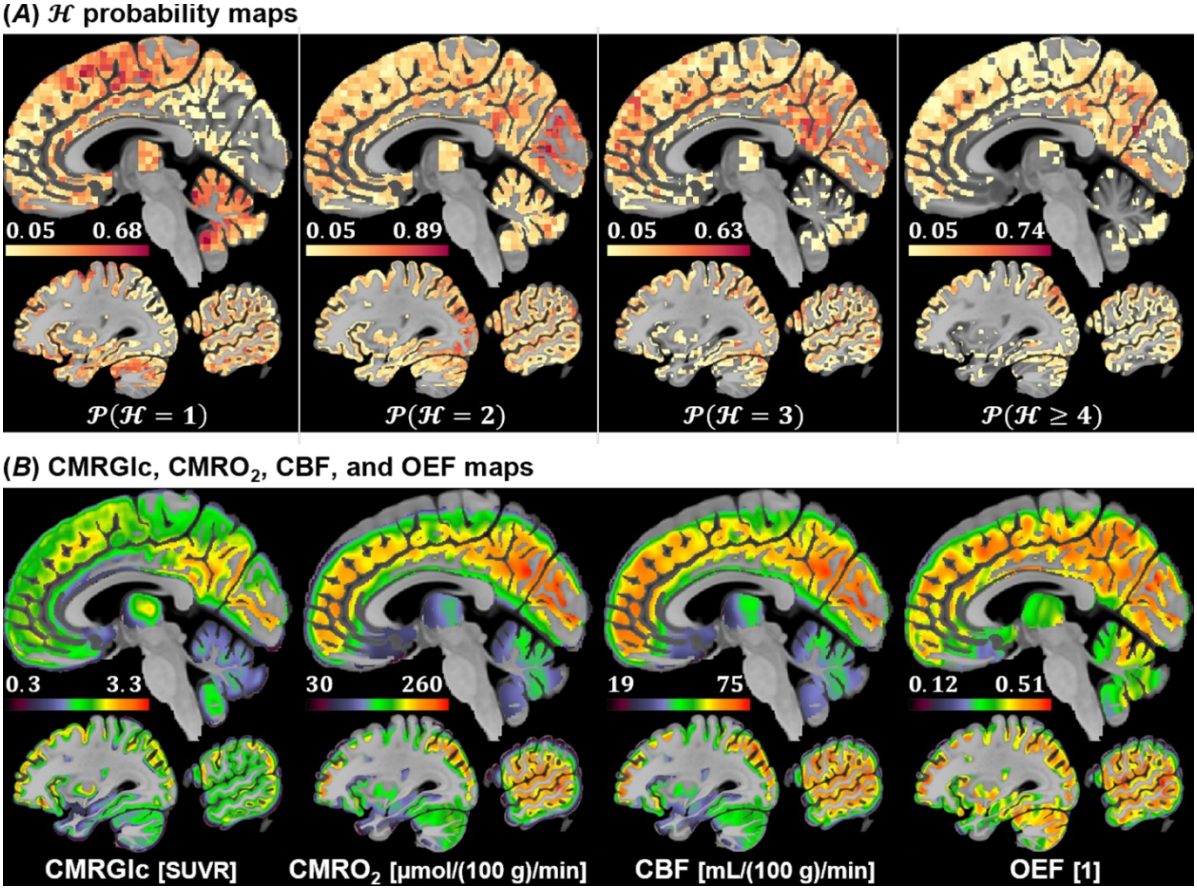

Figure 3.1 (A) Functional hubness ($\mathcal{H}$) probability ($\mathcal{P}$) maps for $\mathcal{H} = 1$, $\mathcal{H} = 2$, $\mathcal{H} = 3$, and $\mathcal{H} \geq 4$. For each map $\mathcal{P}(\mathcal{H})$, a voxel codes the relative frequency (0–1) of $\mathcal{H}$ across subjects, and the color-bars indicate the smallest non-

null and largest relative frequencies. (B) Average maps taken across subjects for CMRGlc in SUVR, $CMRO_2$ in units of µmol / (100 g) / min, CBF in units of mL / (100 g) / min, and OEF. (A) and (B) The same set of three parasagittal slices in the left hemisphere (at -3.8, -31.1, and -58.4 mm) is shown every time. See also Figure 3.7 and Figure 3.9 for additional slices.

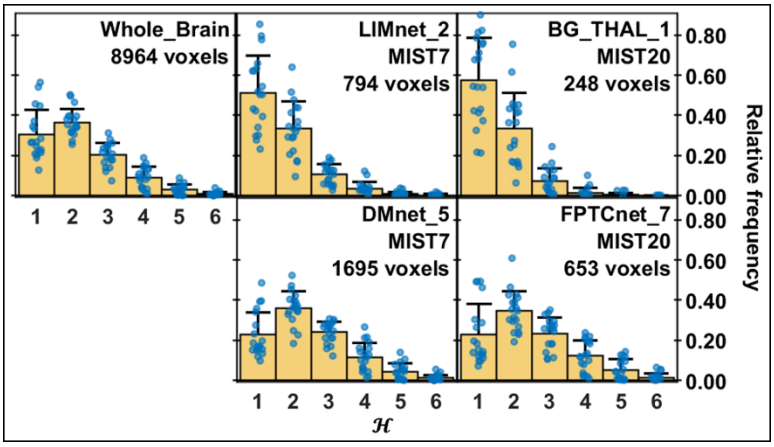

Figure 3.2 Functional hubness ($\mathcal{H}$) frequency distributions within the whole brain and within two selected networks of MIST7 and of MIST20. The selected networks from MIST7 and MIST20 are those exhibiting the lowest (top row) and highest (bottom row) average proportion of voxels with $\mathcal{H} = 6$. The frequencies (i.e., y-axes) range between 0 and 1. The indicated number of voxels on each tile are the means taken across subjects. The blue circles are the frequencies for each subject and only non-null frequencies are shown (e.g., though very small, there are a few voxels with $\mathcal{H} = 6$ within BG_THAL_1). The yellow bars and their whiskers are the mean and standard deviation respectively of frequencies taken across subjects. See also Figure 3.8 LIMnet_2: mesolimbic network; DMnet_5: default mode network; BG_THAL_1: basal ganglia and thalamus; FPTCnet_7: frontoparietal task control network.

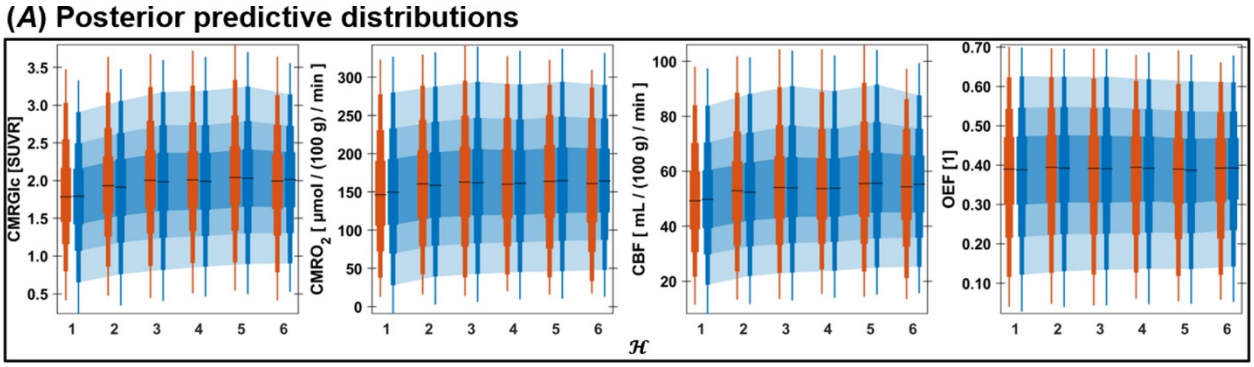

Figure 3.3 (A) Graphical posterior predictive checks. Red colors are the original observations (in the entire dataset), and blue ones are the predictions. To summarize the distribution of the data for every $\mathcal{H}$, we overlaid for each distribution four vertical lines with different thicknesses, to represent equal-tailed credible intervals at 50%, 80%,

95%, and 99%, from thickest to thinnest respectively. Blue shaded areas correspond to the credible intervals at 50%, 80% and 95%. Horizontal black lines are the median estimates. See also Figure 3.10, Figure 3.11, Figure 3.12, and Figure 3.13 for further detailed results . (B) Brain mappings of the estimated posterior median of scaling exponents within MIST7 and MIST20 for CMRGlc, $CMRO_2$, CBF, and OEF. The same set of two parasagittal slices in the left hemisphere (at -18.5, and -10.8 mm) is shown every time and highlights the cerebellum, amygdala, caudate, hippocampus, nucleus accumbens, pallidum, putamen, and thalamus. The color-bar is global for all figures.

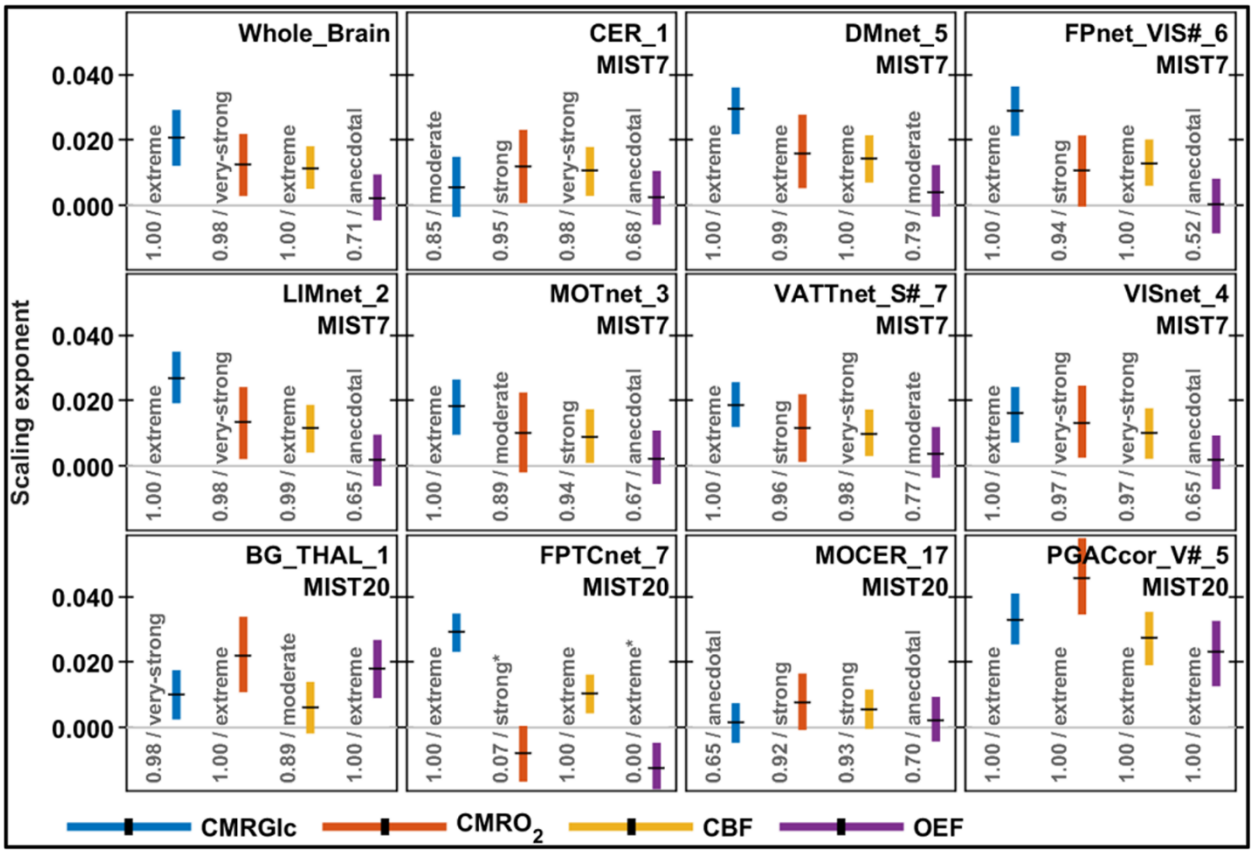

Figure 3.4 Posterior summaries of scaling exponents within the whole brain, all the networks of MIST7 and four networks of MIST20. The colored vertical lines delimit the 89% highest density credible intervals of, and the black horizontal lines are the median of the estimated posteriors. The number on the left side of each vertical line indicates probability that the scaling exponent is between 0 and 1 (i.e., the probability of a concave down increasing power-law) and the corresponding text indicates an interpreted evidence ratio. A star symbol at the end of a text (i.e., when probabilities are less than 0.5) indicates that the interpreted evidence ratio applies to the alternative hypothesis (i.e., non-concave down increasing power-law). Note that the probability values reported here as 0.00 or 1.00 are not true zeros or ones. See also Figure 3.14. MIST labels are detailed in the text as well as in Table 3.2.

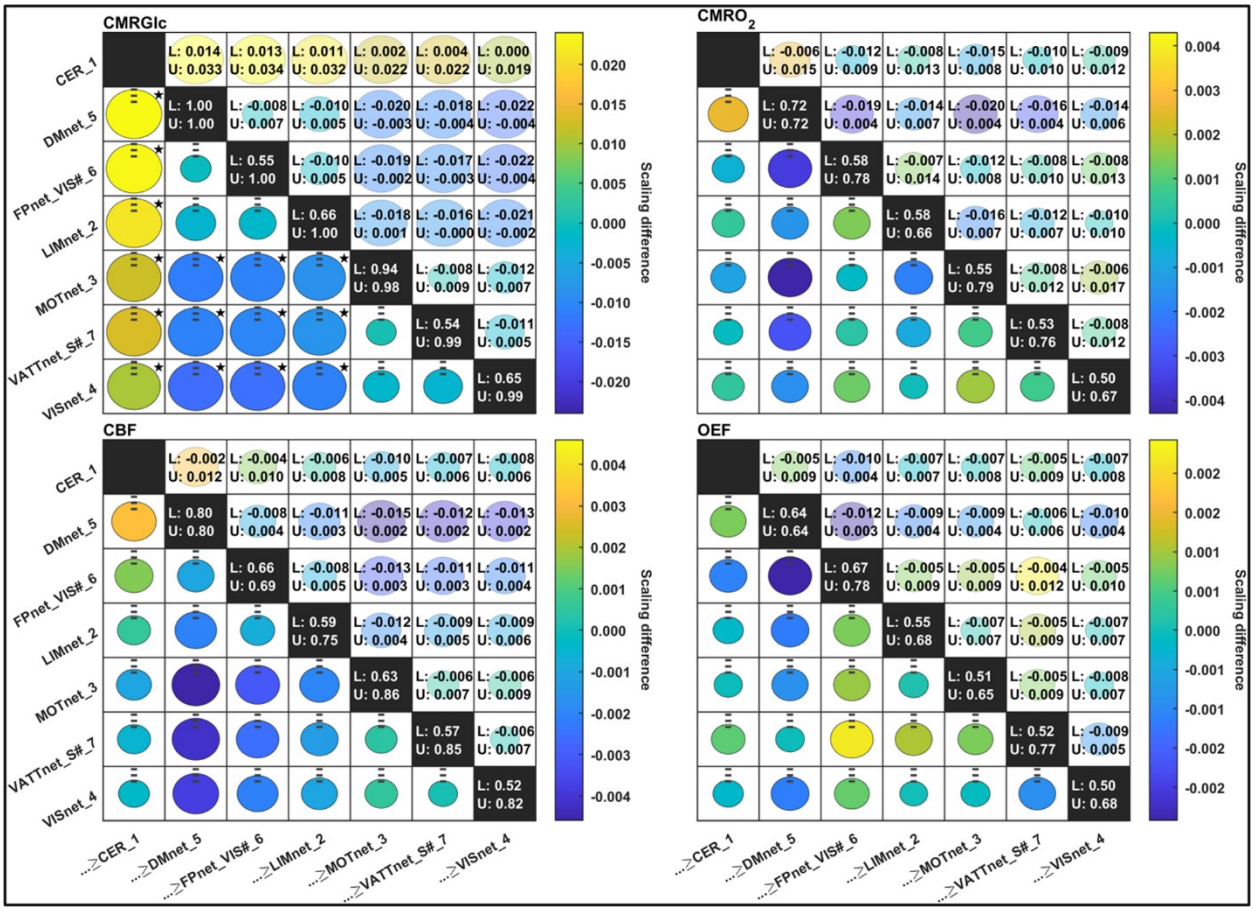

Figure 3.5 Posterior summaries of scaling differences between the networks of MIST7 for CMRGlc, $CMRO_2$, CBF, and OEF. The comparisons ROW ≥ COLUMN indicate that the difference was calculated between the posterior of ROW and COLUMN. Here we report comparisons only for the lower triangular. The color-bars are median estimates of posterior differences. The numbers on the upper diagonals give the lower (L) and upper (U) bounds of the 89% highest density credible intervals of the posterior differences. The size of each circle represents probability of direction (i.e., maximum between probability of positive difference and probability of negative difference), the horizontal tick marks on the top of each circle delimit probabilities of 0.5, 0.75, and 1, and a star symbol on the top-right of a circle indicate if the probability is greater than or equal to 0.89. The numbers on the diagonals summarize the lowest (L) and highest (U) probability of directions found on each row. Note that the probability values reported here as 1.00 are not true ones. See also Figure 3.15, Figure 3.16, Figure 3.17, and Figure 3.18. MIST labels are detailed in Table 3.2.

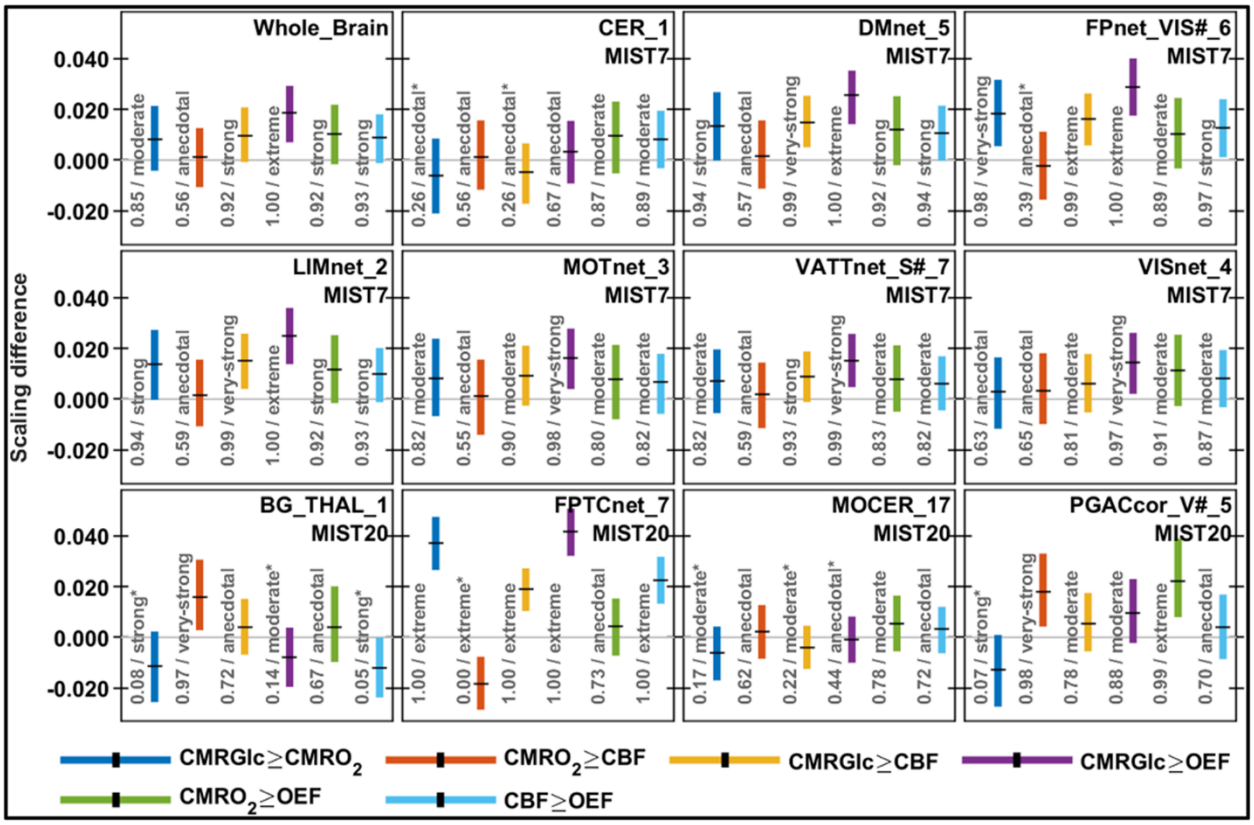

Figure 3.6 Posterior summaries of scaling differences between responses within the whole brain, all the networks of MIST7 and four networks of MIST20. The colored vertical lines delimit the 89% highest density credible intervals of, and the black horizontal lines are the median of the estimated posteriors. The number on the left side of each vertical line indicates probability of positive difference and the corresponding text indicates an interpreted evidence ratio. A star symbol at the end of a text (i.e., when probabilities are less than 0.5) indicates that the interpreted evidence ratio applies to the hypothesis of negative difference instead of positive. Note that the probability values reported here as 0.00 or 1.00 are not true zeros or ones. See also Figure 3.19. The labels of MIST20 are detailed in Table 3.2.

*Table 3.1 Spatial Pearson's linear correlation (ρ) analyses between the average maps shown in Figure 3.1.B. The * symbol indicates two-tailed p-values smaller than 0.05. P-values for Pearson's correlation was computed using a Student's t distribution for a transformation of the correlation (MATLAB's corr function).*

Variables		ρ
$CMRO_2$	**CBF**	0.935*
$CMRO_2$	**OEF**	0.831*
CBF	**OEF**	0.702*
CMRGlc	**CBF**	0.570*
CMRGlc	**$CMRO_2$**	0.429*
CMRGlc	**OEF**	0.254*

3.9 Supporting Information

3.9.1 Materials and Methods

3.9.1.1 Multimodal data acquisitions

Participants were asked to avoid sugary, alcoholic, or caffeinated drinks for at least two hours, and to not have eaten any food for at least 4 hours before data acquisitions. All data acquisitions took place in the imaging suite of PERFORM Centre (Concordia University). Data acquisitions included an anatomical MRI, followed by a 10-minute eyes-opened resting-state (RS) blood oxygen level-dependent (BOLD) fMRI, followed by an 18-minute gas-inhalation-based calibrated fMRI, and followed by a 45-minute eyes-closed static RS 2-[fluorine-18]-fluoro-2-deoxy-D-glucose (18F-FDG) PET. There was a 60-minute gap between the calibrated fMRI and PET acquisitions (post-radiotracer-injection period) during which participants stayed in a RS condition in a calm environment.

3.9.1.1.1 Anatomical MRI

High-resolution structural images were acquired using a 3D sagittal T1-weighted (T1w) MPRAGE sequence with the following parameters: TE = 3.18 ms; TR = 4,500 ms; TI = 8,160 ms; flip angle = 12°; 256 × 256 acquisition matrix, 192 slices; 1 mm isotropic voxel.

3.9.1.1.2 BOLD fMRI

RS BOLD fMRI data were acquired with the following sequence parameters: length = 10 min; field of view (FOV) = (2,400 mm) × (240 mm); TR = 2,300 ms; TE = 30 ms; 3.5 mm isotropic voxel.

3.9.1.1.3 Gas-inhalation-based calibrated fMRI

Calibrated fMRI data were acquired using a dual-echo pseudo-continuous arterial spin labeling (pCASL) sequence with the following parameters: TR = 4,150 ms; TE1 = 8.4 ms; TE2 = 30 ms; alpha = 90°; 4 mm × 4 mm in-plane resolution and 16 slices of 7 mm (1 mm slice gap) on a 64 × 64 matrix; post-labeling delay = 1,650 ms; flip angle of labeling pulse = 25°; tagging duration = 1.6 s. In addition, four $\mathcal{M}_0$ images were acquired with the same parameters except TR = 10,000 ms; TE = 8.4 ms.

Gas challenges were applied to make iso-metabolism changes in blood flow and BOLD signal, and to estimate $\mathcal{M}$ the calibration parameter corresponding to the maximum possible increase in BOLD signal from baseline (Hoge, 2012). A low concentration of CO_2 (5%), i.e., a hypercapnic challenge, was applied to stimulate iso-metabolism vasodilation and CBF increase to achieve a controlled, partial washout of venous deoxyhemoglobin (dHb) and the maximal BOLD response $\mathcal{M}$. A high concentration of O_2 (80%), i.e., a hyperoxic challenge, was applied to model the dHb concentration by taking the arterial O_2 content before and after hyperoxic manipulation from end-tidal respiratory data.

A computer-controlled gas system was used to control mixing concentration of the gases and their delivery to the MRI room. The respiratory and breathing data of each subject were monitored and sampled using a physiological monitoring system MP160 BIOPAC unit (BIOPAC Systems Inc., Goleta, California, USA). Throughout the experiment, the BIOPAC AcqKnowledge software was used on the console of the scanner to constantly monitor participants' partial pressure of CO_2 (PCO_2), partial pressure of O_2 (PO_2), as well as heart and respiration rates. An oximeter was also connected to the output of the system to control the flow rate and the oxygen content of the outgoing gases. At the beginning of the experiment, subjects were fitted with a non-rebreathing

face mask (Hudson RCI, #1059, Temecula, California, USA) connected to the gas controller machine with the $CO_2$100C and $O_2$100C modules of BIOPAC through soft circuits. These modules were used to sample the output of participants' O_2 and CO_2 respiratory content and were also calibrated in advance to the partial pressure of water (47 mmHg). Subjects were asked to breathe through their nose to ensure only expired gas was sampled in BIOPAC modules, using an indwelling nasal cannula (15 mm, Airlife^{TM} Nasal Oxygen Cannula #001321, Cardinal Health, McGraw Park, Illinois, USA).

The first 4 minutes of acquisitions with medical air inhalation was considered as RS data. The acquisition continued with three functional runs, each including different gas manipulations. During each gas manipulation run, a single two-minute block of gas was preceded by a block of three minutes of medical air. The three gas manipulations used were: 80% O_2 (hyperoxia), 21% O_2 + 5% CO_2 + 74% N_2 (hypercapnia), and 50% O_2 + 5% CO_2 + 45% N_2 (simultaneous hyperoxia/hypercapnia). End-tidal O_2 and CO_2 values were then selected manually from measured continuous PO_2 and PCO_2 respiratory traces with 200 Hz sampling rate. The first middle 10 breaths of the four-minute baseline period and the last 10 breaths of each two-minute gas-inhalation block was averaged as baseline and gas manipulation end-tidal values, respectively.

3.9.1.1.4 18F-FDG PET

Prior to PET acquisition, a catheter was placed in the vein of the subjects' arms by a PET technician, to inject 4 MBq/kg of the 18F-FDG radiotracer. Afterwards, subjects remained in a RS condition in a calm environment. The PET/CT imaging started approximately 1-hour post-injection using a hybrid PET/CT system (axial FOV = 157 mm). The CT portion of the imaging was performed right before the PET portion. Subjects were instructed to remain still during the acquisition, and a padded head holder was used to ensure no motion during the 60 minutes scan.

3.9.1.2 Multimodal data preprocessing

3.9.1.2.1 Anatomical MRI

The anatomical T1w images were preprocessed using CIVET version 2.1.0 (Ad-Dab'bagh et al., 2006) and included: T1 non-uniformity correction, transformation to stereotaxic space (target = ICBM 2009a symmetric template), brain mask extraction, segmentation, and tissue classification in stereotaxic space.

3.9.1.2.2 BOLD fMRI

The preprocessing of RS fMRI data was done using NIAK version niak-boss-0.13.0 (Bellec et al., 2011) and included: slice timing correction, motion correction with rigid-body motion estimation and co-registration to T1w-space, high-pass temporal filtering with a cut-off of 0.01 Hz, regression of confounds of no interest (including the average white matter signal, the average ventricles signals, motion parameters, PCA-based estimation of the global signal and scrubbing of time frames with excessive motion (Power et al., 2014)), spatial smoothing (FWHM = 8 mm). The fMRI volumes were resampled to the ICBM 2009a symmetric template (Fonov et al., 2011) at a 4-mm isotropic voxel resolution with trilinear interpolations by combining a linear transformation from fMRI to T1w spaces and a non-linear transformation from T1w to ICBM template space. A mask was applied to restrict further analyses to grey-matter voxels.

3.9.1.2.3 Gas-inhalation-based calibrated fMRI

The calibrated fMRI data were preprocessed with FSL version 5 (Jenkinson et al., 2012), including motion-correction, spatial smoothing (gaussian kernel FWHM = 8 mm) and high-pass filtering

with cut-off frequency 0.01Hz. Analyses were restricted to intra-cerebral voxels after applying a brain mask extracted from averaged BOLD signals using FSL. A spatial mask was applied to remove large veins by identifying voxel exhibiting relative BOLD increases greater than 10% in the unsmoothed data corresponding to CO_2 inhalation. The large arteries exhibiting decreases in pre-T1-correction absolute CBF that were greater than 50 mL / (100 g) / min during O_2 inhalation were also masked out from the analyses. An additional slab mask for each subject was defined by analyzing the temporal SNR of ASL signals and for each subject, the last slices towards to the top of the brain with SNR drops greater than 50% were therefore discarded from further analyses.

3.9.1.2.4 FDG-PET

PET images were reconstructed using an iterative 3D ordered subset expectation maximization algorithm (Kinahan et al., 1998) involving corrections for scatter, random, dead time, attenuation, and normalization. A (scanner specific) 3D point spread function (GEMS name = Sharp-IR) based on experimental measurements of point sources acquired in different positions within the 3D-PET FOV, was modeled and coded in a system matrix and projection space to improve the reconstruction scheme. The reconstructions were done on a 192 × 192 × 47 grid from 30 minutes of static images and on a 256 × 256 × 47 grid from six 5-minute frames, with a voxel size of 1.6 mm × 1.6 mm × 3.25 mm, and with 3D trans axial filter = ramp, FOV = 20 cm, centered at x = 5 cm and y = 5 cm, matrix size = 256 × 256. Reconstructed PET images together with T1w images were smoothed with a 3D Gaussian kernel where FWHM = 2 mm isotropic using minc-toolkit (Toolkit, 2019) (*mincblur* command) before being co-registered based on a multi-resolution strategy with 6 transformation parameters, maximizing mutual information as a similarity measure (*minctracc* command). In the end, the PET images were realigned to the ICBM 2009a symmetric template space at a 4-mm isotropic voxel resolution following the same procedure described for RS fMRI (i.e., combining linear and non-linear transforms).

3.9.1.3 Multimodal data postprocessing

3.9.1.3.1 Estimation of functional hubness

Whole-brain voxel maps of functional hubness ($\mathcal{H}$) were estimated from RS BOLD fMRI data using SPARK method, as detailed in (K. Lee et al., 2016). The SPARK method attempts to reliably explain the BOLD time series of each voxel as a linear combination of few latent network time series through sparse linear modeling and advanced bootstrapping strategies. Here, a circular block bootstrap was used to generate $B = 100$ replicates of the original RS fMRI data with a random block size ranging between 10 and 30 timeframes. This resampling strategy was done to preserve temporal structures in the fMRI data. Then, a sparse dictionary learning algorithm, based on a variant of K-SVD, was applied on each replica to obtain sparse representations of the data with N spatiotemporal patterns of RS networks. N was estimated from the data using the methodology proposed in Lee et al (K. Lee et al., 2018) , and resulting in a total of N temporal atoms, or N RS networks. Doing so, SPARK allows modeling explicitly sparse spatial overlap between RS networks, while bootstrap resampling allows reliability and reproducibility of the results. Pooling results from each replica, the resulting $N \times B$ spatial maps were clustered using k-means clustering to obtain a stable set of N spatial maps X. Assuming a gaussian density on the distributions of the elements of X, a threshold was estimated (significance level = 5%) and applied on X providing N background-noise-free spatial maps $\tilde{X}$, resulting in a reliable sparse coding matrix. A manual screening of the N maps in $\tilde{X}$ further ensured that maps contaminated by physiological artefacts would not be included in further analyses. In the end, functional hubness

voxel maps were obtained by counting the number of non-zeros elements in $\tilde{X}$, resulting in a discrete number ranging from 0 to N.

Given that hubness maps were obtained at the subject level, we restricted our analyses to the voxels where $1 \leq \mathcal{H} \leq 6$ as this range was consistently found both in the whole brain of at least 80% of all subjects, and in all the networks of MIST20 parcellation after pulling the data of all subjects together.

3.9.1.3.2 $CMRO_2$, CBF, and OEF quantification

$CMRO_2$, CBF, and OEF maps were estimated from gas-inhalation-based calibrated fMRI data as follows. The perfusion and BOLD signals were isolated respectively from the series of first and second echoes acquired in the ASL data, using linear surround subtraction and addition methods respectively (Aguirre et al., 2002). Absolute CBF maps in units of mL / (100 g) / min were determined from the perfusion signals using the procedure described in (J. Wang et al., 2003). The fractional changes in BOLD and CBF signals were computed for each gas manipulation by fitting a linear model to the respective signals with normalized regressors obtained from end-tidal respiratory data. Regarding the regressors, they were convolved with a single-gamma hemodynamic response function with parameters described in (Glover, 1999), and they were then corrected by a time delay estimated from average signal across the grey matter to account for the delay between the respiratory and neuronal signal. From the CBF maps, absolute $CMRO_2$ maps in units of µmol / (100 g) / min were estimated as $CMRO_2 = CaO_2 \times CBF \times OEF$ where CaO_2 is the total arterial O_2 content determined as the sum of O_2 bound to hemoglobin and O_2 dissolved in plasma. CaO_2 was determined from PO_2 from the averaged end tidal O_2 taken from the respiratory data (Chiarelli, Bulte, Piechnik, et al., 2007). OEF was estimated using the GCM described in (Gauthier & Hoge, 2012). In the end, $CMRO_2$, CBF, and OEF maps, as well as the slab masks obtained during preprocessing, were all resampled to the ICBM 2009a symmetric template space at a 4-mm isometric voxel resolution. The resampling was done with cubic B-spline interpolations using ANTs (Avants et al., 2011) by combining a transformation from subjects' native to subjects' T1w spaces with a transformation from subjects' T1w space to the T1w space of the ICBM template. Once in the analysis template space, for each $CMRO_2$, CBF, and OEF map, voxels still exhibiting negative or null values were flagged to be discarded from further analyses. A global slab mask calculated as the intersection between all slab masks was used to further flag voxels to be discarded from all analyses.

3.9.1.3.3 CMRGlc quantification

CMRGlc maps were estimated from PET data using standardized uptake value ratios (SUVR) referenced by the pons (Byrnes et al., 2014). First, SUVR maps were estimated as $\mathrm{SUVR} = C_t/(\mathrm{ID}/w_t \times D)$ where C_t is the decay-corrected activity concentration in the tissue (in MBq/cc which can be converted to MBq/kg by dividing by tissue density 1 g/cc), ID is the injected dose (in MBq), and w_t is the subject's weight (in kg). $D = 2^{-\Delta_t/T_{1/2}}$ is a decay factor with Δ_t being the time elapsed between injection and scanning (approximately 1 hour), and $T_{1/2}$ is the half lifetime of the 18F-FDG radiotracer (6582 s). Then, SUVR maps, i.e., CMRGlc maps were determined by normalizing SUVR maps with mean uptakes in the pons. The pons was readily delineated in T1w space during anatomical preprocessing.

3.9.1.4 Brain masking and parcellation

The common analysis space for all brain volumes of interest, i.e., $\mathcal{H}$, CMRGlc, $CMRO_2$, CBF, and OEF, was provided by the ICBM 2009a symmetric template (Fonov et al., 2011) at a 4-mm

isovoxel resolution. All grey-matter voxels of the analysis space were labeled according to both the Mindboggle (Manera et al., 2020) and the MIST (Urchs et al., 2019) atlases. The Mindboggle atlas was originally defined in the ICBM 2009c symmetric template space at a 1-mm isometric voxel resolution. It was resliced to the analysis space with nearest interpolations using FreeSurfer (Fischl, 2012; *mri_convert* command). A modal dilation of zero voxels was performed using FSL (*fslmaths* command) to ensure that all grey-matter voxels would be labeled. Any subcortical voxel with a label different from the amygdala, caudate, hippocampus, nucleus accumbens, pallidum, putamen, and thalamus, was flagged to be discarded from further analyses. The MIST atlas was originally defined in the ICBM 2009b symmetric template space at a 3-mm isometric voxel resolution. The volume corresponding to the finest resolution of the atlas (MIST_ATOM) was resliced to the analysis space and dilated in the same way as Mindboggle. From there, two other resolutions of the atlas involving respectively 7 (MIST7) and 20 (MIST20) networks were derived by using the provided parcellation file (MIST_PARCEL_ORDER_ROI.csv). This procedure ensured the full nesting of networks across resolutions. In the end, only labeled voxels with valid $\mathcal{H}$, CMRGlc, $CMRO_2$, CBF, and OEF were retained for further analyses.

3.9.1.5 Bayesian multilevel power-law analysis

Our goal was to formulate a multilevel regression model for the power-law model given by $y = Ax^B$ where x (representing $\mathcal{H}$) and y (representing CMRGlc, $CMRO_2$, CBF, or OEF) are observed, and A and B are estimated. Considering that observations (i.e., voxel values) can be consistently grouped by subjects and into networks, we specified a fully crossed design where all subjects had the same set of networks together with a fully nested design where networks were further aggregated according to a hierarchical tree (i.e., the MIST atlas) with the whole brain as the top-most parent network. We did so in a way to obtain global estimates for A and B corresponding to the whole brain (i.e., the union of all child networks) of a hypothetical "mean" subject, denoted $\overline{\mathcal{WB}}$ (noting that in this context, "whole brain" and "subject" represent the same entity and are synonyms), as well as estimates indicating how the different subjects (i.e., their whole brain) or the different child networks deviate from $\overline{\mathcal{WB}}$.

3.9.1.5.1 Data

Before fitting the model, the main predictor variable was non-linearly transformed with $x \mapsto x^\delta$ where $\delta = \ln(1 + 0.05)/\ln\left(\max_i(x_i)/\min_i(x_i)\right)$. Such transformation was done so to bring on a unit scale the increase rate parameter, i.e., B, and it is exactly equivalent to directly scaling B. The assumption behind the value of δ was that on average, maximum relative increases in resting CMRGlc, $CMRO_2$, CBF, or OEF, i.e., $\left(\max_i(x_i)/\min_i(x_i)\right)^B - 1$, are most likely ranging between 0 and 10% (so centered at 5%). This assumption was based on the analysis of our datasets and a review of previously published studies with similar data (see *Discussion*). Given that $\min_i(x_i) = 1$ and $\max_i(x_i) = 6$ in the present study, $\delta \approx 0.027$.

In addition, all response variables were brought to a unit scale as well through the linear mapping $y \mapsto \left(y - \min_i(y_i)\right)/\mu_y + 1$ where $\mu_y = 2$ SUVR for CMRGlc, $\mu_y = 170$ µmol / (100 g) / min for $CMRO_2$, $\mu_y = 55$ mL / (100 g) / min for CBF, and $\mu_y = 0.4$ for OEF. The values μ_y roughly represented whole brain mean values, and they were chosen based on both the analysis of our datasets and a review of previously published studies with similar data (see *Discussion*). Such

mapping was done so to bring on a unit scale the baseline value with respect to the lowest $\mathcal{H}$ value, i.e., A. In this case, A should on average be approximately equal to 2. Besides, the smallest observation of the response variables will be exactly equal to 1, and most observations should fall into the interval [1,3]. Adding an offset of 1 conveniently excluded null values.

3.9.1.5.2 Model specification

Let $y_{i,j,k,l} > 0$ be an observation of a response variable (i.e., CMRGlc, $CMRO_2$, CBF, or OEF) at the i-th voxel of the j-th subject, within the k-th network of MIST20, within the l-th network of MIST7, and let $x_{i,j,k,l} \in \mathbb{N}^*$ be the corresponding observation of the main predictor variable (i.e., $\mathcal{H}$). Here, $i \in [\![1, N_j]\!]$, $j \in [\![1,19]\!]$, $k \in [\![1,20]\!]$, $l \in [\![1,7]\!]$, N_j is the number of voxels for the j-th subject (see also Table 3.5 for an overview of sample sizes), and we note that since the networks of MIST20 are fully nested within the networks of MIST7, there exists a surjective function f_{20}^{7} that maps a network of MIST20 to MIST7 so that in fact $l = f_{20}^{7}(k)$.

We assumed the skew-normal model (being a generalization of the normal model able to handle skewness) given by

$$p\left(y_{i,j,k,l} \middle| \xi_{i,j,k,l}, \omega_j, \alpha_j\right) = \frac{1}{\omega_j\sqrt{2\pi}} \exp\left(-\frac{1}{2}\left(\frac{y_{i,j,k,l} - \xi_{i,j,k,l}}{\omega_j}\right)^2\right)\left(1 + \operatorname{erf}\left(\alpha_j\left(\frac{y_{i,j,k,l} - \xi_{i,j,k,l}}{\omega_j\sqrt{2}}\right)\right)\right)$$

$$\xi_{i,j,k,l} = \mu_{i,j,k,l} - \delta_j\omega_j;\ \mu_{i,j,k,l} = \mathrm{A}_{j,k,l}\, x_{i,j,k,l}^{\mathrm{B}_{j,k,l}}$$

$$\delta_j = \sqrt{2/\pi}\,\alpha_j \Big/ \sqrt{1 + \alpha_j^2}\ ;\ \omega_j = \sigma_j \Big/ \sqrt{1 - \delta_j^2}$$

$$\mathrm{A}_{j,k,l} = 2 + \gamma\left(\overline{\mathrm{A}} + \mathrm{A}_j^{\mathrm{sub}} + \mathrm{A}_k^{\mathrm{MIST20}} + \mathrm{A}_l^{\mathrm{MIST7}}\right)$$

$$\mathrm{B}_{j,k,l} = 1 + \overline{\mathrm{B}} + \mathrm{B}_j^{\mathrm{sub}} + \mathrm{B}_k^{\mathrm{MIST20}} + \mathrm{B}_l^{\mathrm{MIST7}}$$

$$\sigma_j = \bar{\sigma} + \sigma_j^{\mathrm{sub}}$$

$$\alpha_j = \bar{\alpha} + \alpha_j^{\mathrm{sub}}$$

ξ is the location, ω is the scale, α is the shape (or skewness), μ is the mean, and σ is the standard deviation of the skew-normal density. $\overline{\mathrm{A}}$ and $\overline{\mathrm{B}}$ are estimates for the whole brain of the "mean" subject, i.e., $\overline{\mathcal{WB}}$. $\mathrm{A}_j^{\mathrm{sub}}$ and $\mathrm{B}_j^{\mathrm{sub}}$ are estimates for the whole brain of the j-th subject and they code the deviations of the j-th subject from $\overline{\mathcal{WB}}$. $\mathrm{A}_k^{\mathrm{MIST20}}$ and $\mathrm{B}_k^{\mathrm{MIST20}}$ are estimates for the k-th network within MIST20 of the "mean" subject and they code the deviations from the l-th network within MIST7, while $\mathrm{A}_l^{\mathrm{MIST7}}$ and $\mathrm{B}_l^{\mathrm{MIST7}}$ are estimates for the l-th network within MIST7 of the "mean" subject and they code the deviations from $\overline{\mathcal{WB}}$. $\bar{\alpha}$ and $\bar{\sigma}$ are estimates for $\overline{\mathcal{WB}}$, while α_j^{sub} and σ_j^{sub} are estimates for the whole brain of the of the j-th subject and they code the deviations of the j-th subject from $\overline{\mathcal{WB}}$.

The skew-normal density which is a generalization of the normal density to handle data with skewness was chosen to reflect our assumption that the conditional responses are most likely

skewed. For instance, values in the subcortical structures or in the cerebellum are more likely to substantially contribute to the tails of the data distributions rather than to their bulks which are mainly ruled by cortical values. Therefore, the location ξ and the scale ω were parametrized with the shape α, the mean μ, and the standard deviation σ to allow the incorporation of prior knowledge more easily. Subject and network deviations with respect to the whole brain of a "mean" subject were modeled to reflect our assumption that subjects most likely belong to a homogeneous population although each subject is unique, and there exists a homogeneous structure shared between brain networks across multiple spatial scales although each network and each spatial scale are unique too. For the sake of simplicity, we assumed independence between the different levels of any grouping factor, as well as between the group-level parameters associated with the different levels of the same grouping factor.

We specified the priors

$$\overline{\mathrm{A}} \sim N(0,1); \mathrm{A}_{\cdot}^{\mathrm{g}} \sim^{i.i.d} \mathcal{N}\left(0, \tau_{\mathrm{A}}^{\mathrm{g}}\right); \tau_{\mathrm{A}}^{\mathrm{g}} \sim \mathcal{N}^{+}(0,0.5)$$

$$\overline{\mathrm{B}} \sim \mathcal{N}(0,1); \mathrm{B}_{\cdot}^{\mathrm{g}} \sim^{i.i.d} \mathcal{N}\left(0, \tau_{\mathrm{B}}^{\mathrm{g}}\right); \tau_{\mathrm{B}}^{\mathrm{g}} \sim \mathcal{N}^{+}(0,0.5)$$

$$\bar{\sigma} \sim \mathcal{N}^{+}(\gamma, \gamma); \sigma_{\cdot}^{\mathrm{sub}} \sim^{i.i.d} \mathcal{N}\left(0, \tau_{\sigma}^{\mathrm{sub}}\right); \tau_{\sigma}^{\mathrm{sub}} \sim \mathcal{N}^{+}(0, \gamma)$$

$$\bar{\alpha} \sim \mathcal{N}(0,2); \alpha_{\cdot}^{\mathrm{sub}} \sim^{i.i.d} \mathcal{N}\left(0, \tau_{\alpha}^{\mathrm{sub}}\right); \tau_{\alpha}^{\mathrm{sub}} \sim \mathcal{N}^{+}(0,0.5)$$

where erf is the error function, $g \in \{\mathrm{sub}, \mathrm{MIST20}, \mathrm{MIST7}\}$, $\mathcal{N}$ is the normal distribution parametrized with mean (first argument) and standard deviation, $\mathcal{N}^{+}$ is the half-normal distribution parametrized with mean (first argument) and standard deviation, and $\gamma = 0.25$. For OEF only, we supplied $\overline{\mathrm{B}} \sim \mathcal{N}(-1,1)$ rather than $\overline{\mathrm{B}} \sim \mathcal{N}(0,1)$. The hyperparameters τ capture variability between group means.

When specifying priors, we assumed that on a unit scale, dispersion about mean response values are, on average, unlikely to be larger than 0.5, so much so that A and σ could be scaled by $\gamma = 0.5/2 = 0.25$ (the division factor 2 accounts for *two* standard deviations where 95% of the observations would lie within, if normally distributed). For OEF, the specification of $\overline{\mathrm{B}} \sim \mathcal{N}(-1,1)$ reflected our assumption that the increase rate is most likely close to zero (recall the offset of 1 when specifying B above). Overall, we deemed that our priors were all reasonably weakly informative. Although we acknowledge that the priors on τ are particularly wide. Nonetheless, our priors provided sufficient regularization so that the sampler would not encounter difficult geometries all the while exploring parameter space with decent efficiency. In addition, given the very large sample size, the priors were most likely to be dominated by the data.

3.9.1.5.3 Model fit

The model was implemented in Stan and included within-chain parallelization via threading. Model fit was run on the computer clusters of Compute Canada. Model fit and analyses were done primarily with *brms* version 2.15.0 ((Bürkner, 2017); see sampling specification in Table 3.6) and with *rstan* version 2.28.1.

3.9.1.5.4 Model diagnostic and performance

A combination of graphical and numerical checks was employed to confirm that the samples obtained during the parameter estimation step adequately described the posteriors and that the observed data were plausible under the model (see (Gelman et al., 2020), for workflow details).

For the sake of conciseness, we only reported here one visual check including plots of simulated datasets from the posterior predictive distributions overlayed on the observed datasets, and numerical checks including $\hat{R}$ statistic which is based on comparing the variation between the Markov chains to the variation within the chains (values close to 1 and less than 1.01 being desirable), effective sample sizes for the central tendency and the tail quantiles (values at least equal to 100 times the number of chains being desirable). We also indicated whether any warning occurred during the parameter estimation steps regarding the number of divergent transitions (no divergence is desirable), the number of prematurely terminated evaluations due to excessively long execution time (zero is desirable), and the Bayesian fraction of missing information (higher than 0.2 being desirable).

3.9.2 Figures and Tables

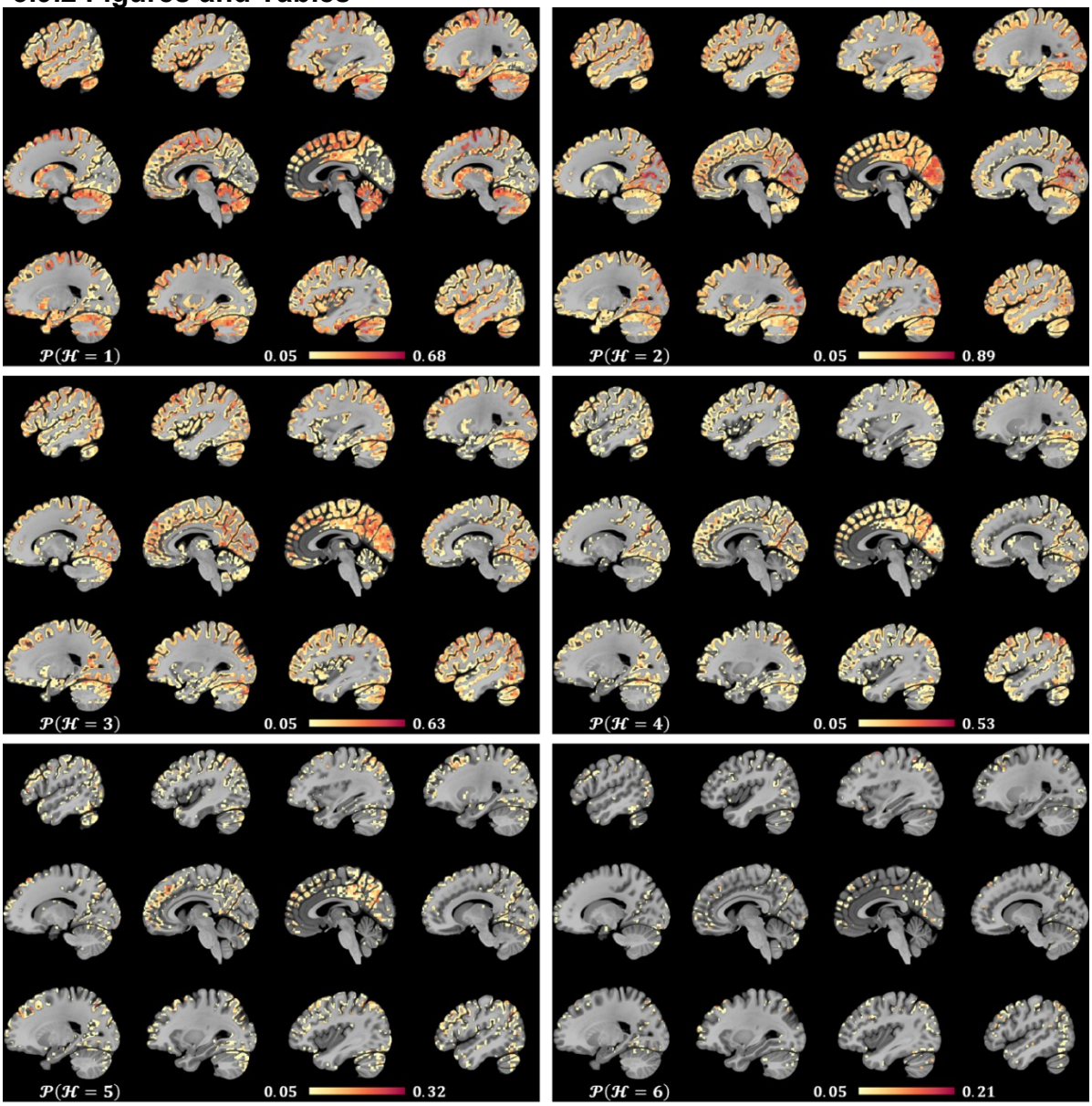

Figure 3.7 Functional hubness ($\mathcal{H}$) probability maps for each $\mathcal{H}$ in $[\![1,6]\!]$. For each map $\mathcal{P}(\mathcal{H})$, a voxel codes the relative frequency of $\mathcal{H}$ (between 0 and 1) across subjects, and the color-bars indicate the smallest non-null and

largest relative frequencies. In each panel, the top-left parasagittal slice is at -51.4 mm, and the montage (left to right, then top to bottom) was constructed with a step of -9.1 mm.

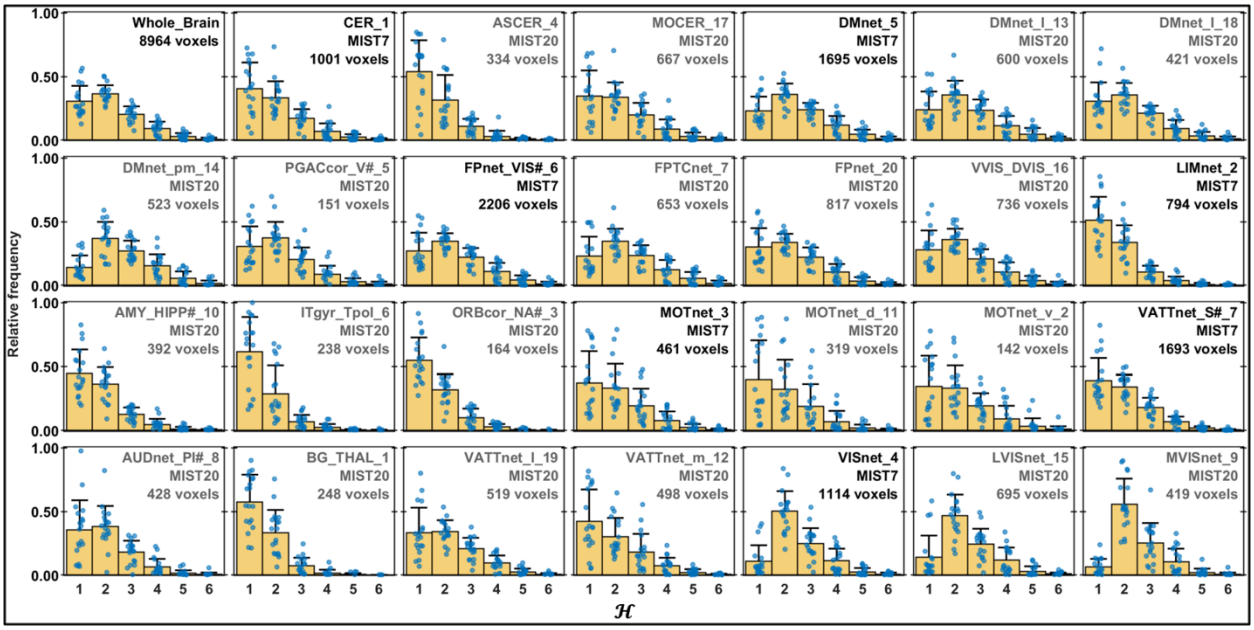

Figure 3.8 Functional hubness (ℋ) frequency distributions within the whole brain, as well as within the networks of MIST7 and MIST20. The ordering from left to right, then top to bottom, is such that the networks of MIST7 (in bold font) are directly followed by their children (network) in MIST20. The frequencies (i.e., y-axes) range between 0 and 1. The indicated number of voxels on each tile are the means taken across subjects. The blue circles are the frequencies for each subject and only non-null frequencies are shown. The yellow bars and their whiskers are the mean and standard deviation respectively of frequencies taken across subjects. The labels of MIST7 and MIST20 networks are detailed in Table 3.2.

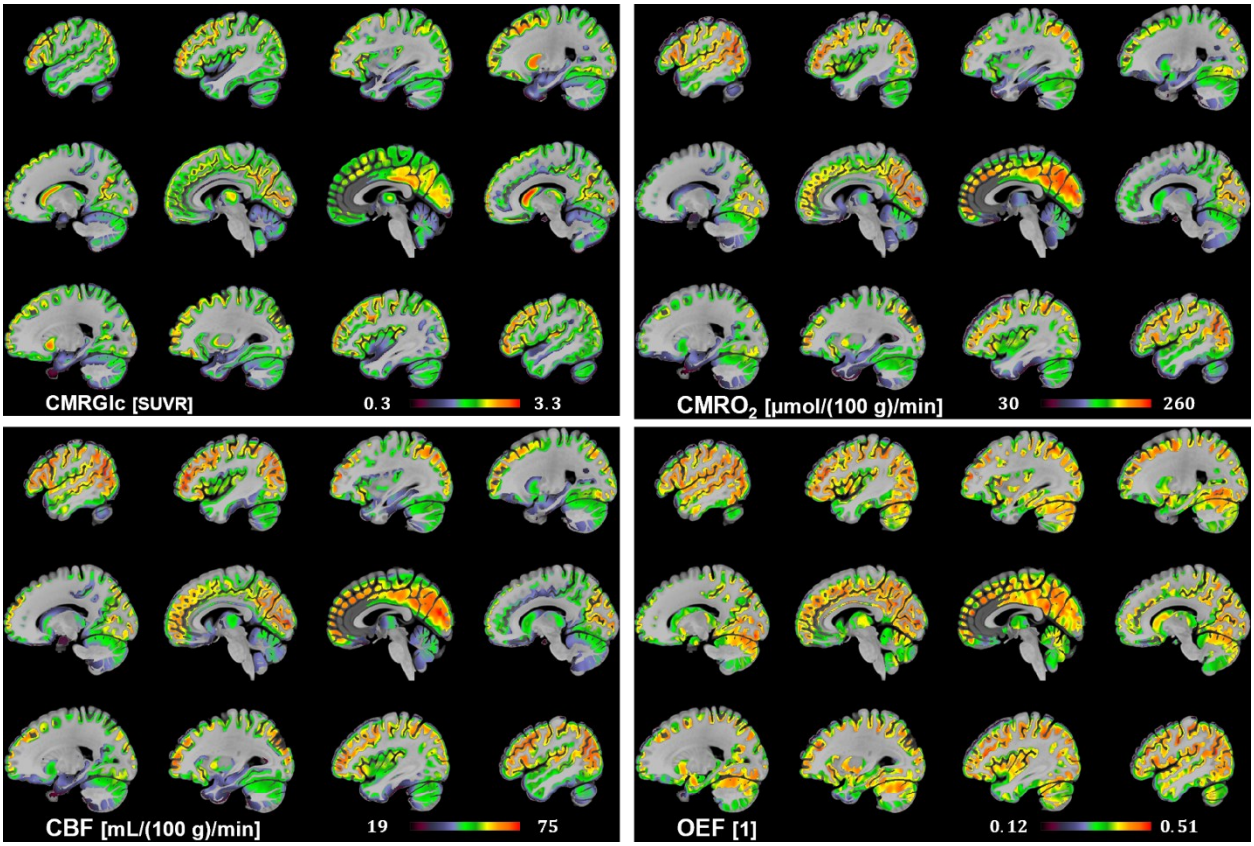

Figure 3.9 Average maps taken across subjects for CMRGlc in units of SUVR, $CMRO_2$ in units of µmol / (100 g) / min, CBF in units of mL / (100 g) / min, and OEF. In each panel, the top-left parasagittal slice is at -51.4 mm, and the montage (left to right, then top to bottom) was constructed with a step of -9.1 mm.

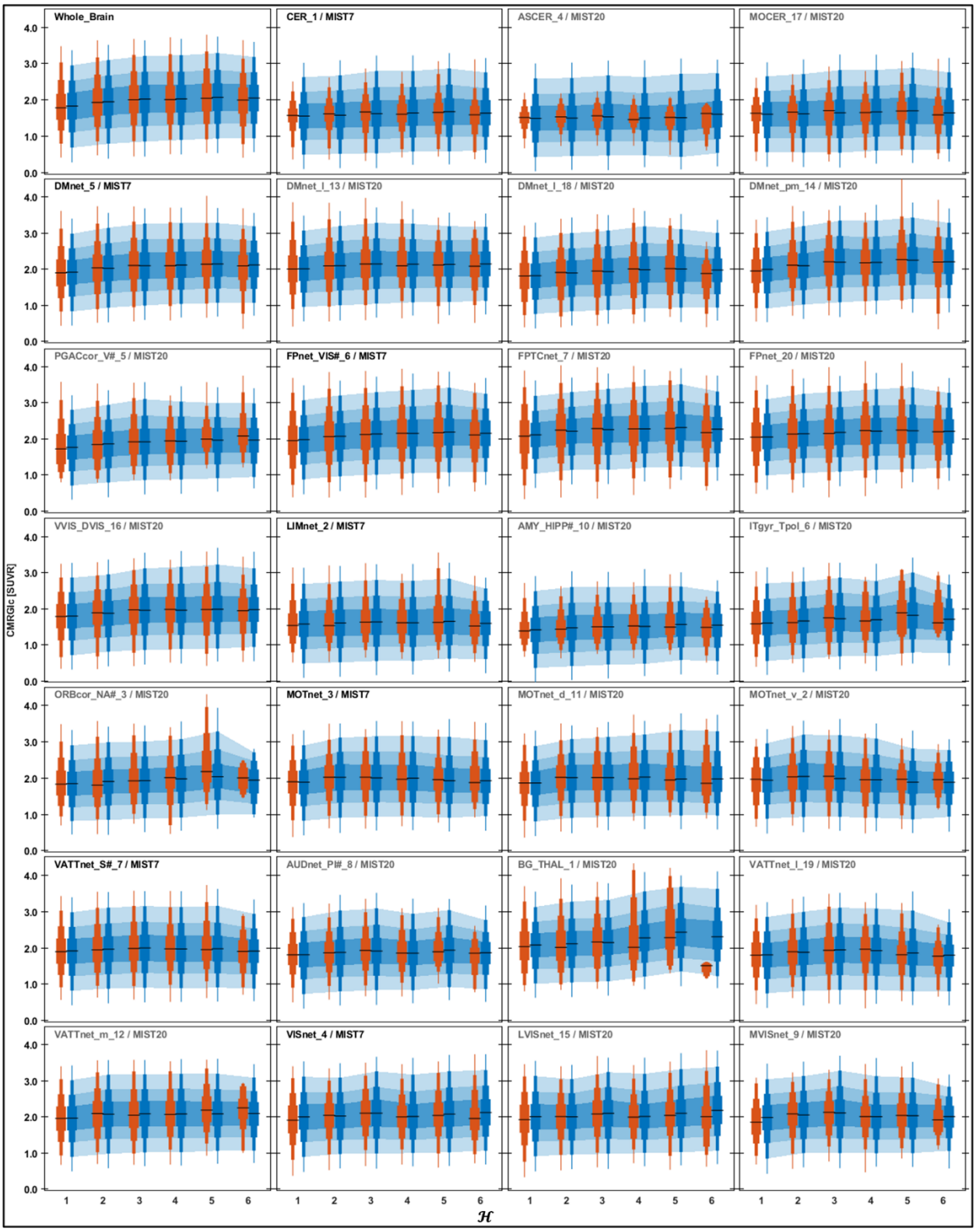

Figure 3.10 Graphical posterior predictive checks for Bayesian multilevel power-law analysis for CMRGlc. Vertical lines are sets of four overlayed lines with different thicknesses, and they delimit equal-tailed credible intervals at 50%, 80%, 95%, and 99%, from thickest to thinnest in that order. Red colors are the original observations, and blue ones are predictions. Blue shaded areas correspond to the credible intervals at 50%, 80% and 95%. Horizontal black lines

are the median estimates. The ordering of the tiles from left to right, then top to bottom, is such that the networks of MIST7 are directly followed by their (network) children in MIST20. The labels of MIST7 and MIST20 are detailed in Table 3.2. These figures suggest well behaved fits and illustrate how partial pooling operated.

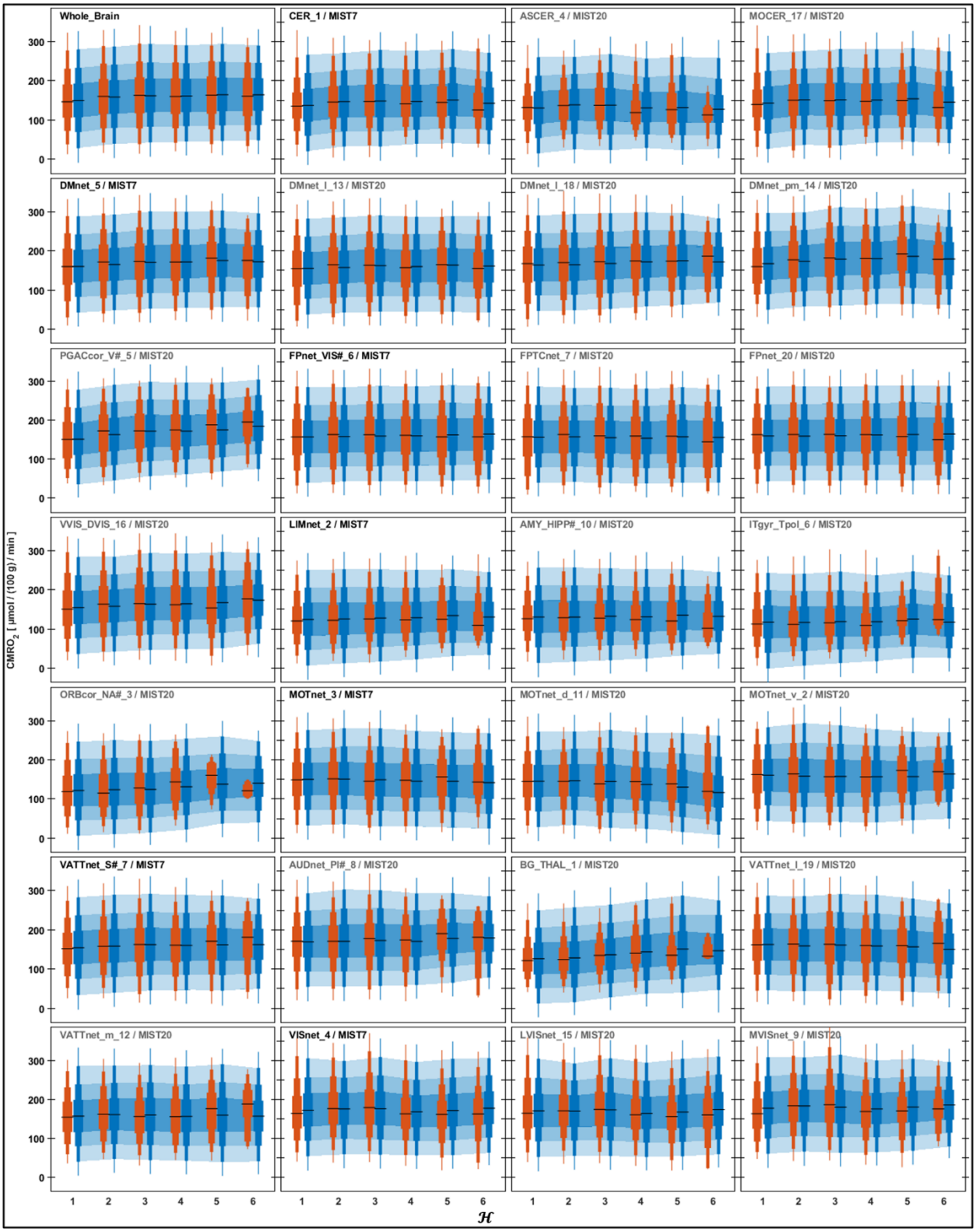

Figure 3.11 Graphical posterior predictive checks for Bayesian multilevel power-law analysis for $CMRO_2$. Vertical lines are sets of four overlayed lines with different thicknesses, and they delimit equal-tailed credible intervals at 50%, 80%, 95%, and 99%, from thickest to thinnest in that order. Red colors are the original observations, and blue ones are predictions. Blue shaded areas correspond to the credible intervals at 50%, 80% and 95%. Horizontal black lines

are the median estimates. The ordering of the tiles from left to right, then top to bottom, is such that the networks of MIST7 are directly followed by their (network) children in MIST20. The labels of MIST7 and MIST20 are detailed in Table 3.2. These figures suggest well behaved fits and illustrate how partial pooling operated.

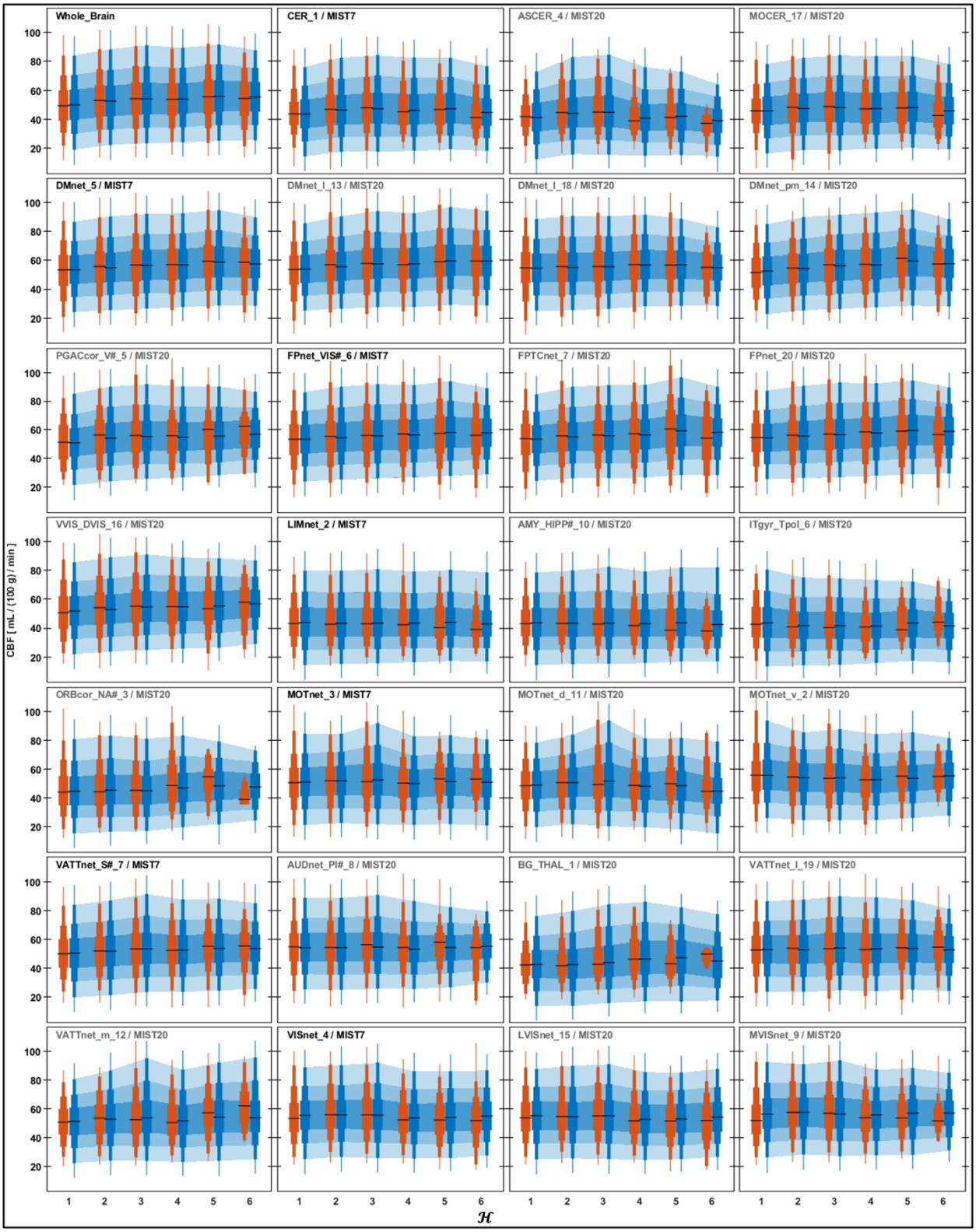

Figure 3.12 Graphical posterior predictive checks for Bayesian multilevel power-law analysis for CBF. Vertical lines are sets of four overlayed lines with different thicknesses, and they delimit equal-tailed credible intervals at 50%, 80%, 95%, and 99%, from thickest to thinnest in that order. Red colors are the original observations, and blue ones are predictions. Blue shaded areas correspond to the credible intervals at 50%, 80% and 95%. Horizontal black lines

are the median estimates. The ordering of the tiles from left to right, then top to bottom, is such that the networks of MIST7 are directly followed by their (network) children in MIST20. The labels of MIST7 and MIST20 are detailed in Table 3.2. These figures suggest well behaved fits and illustrate how partial pooling operated.

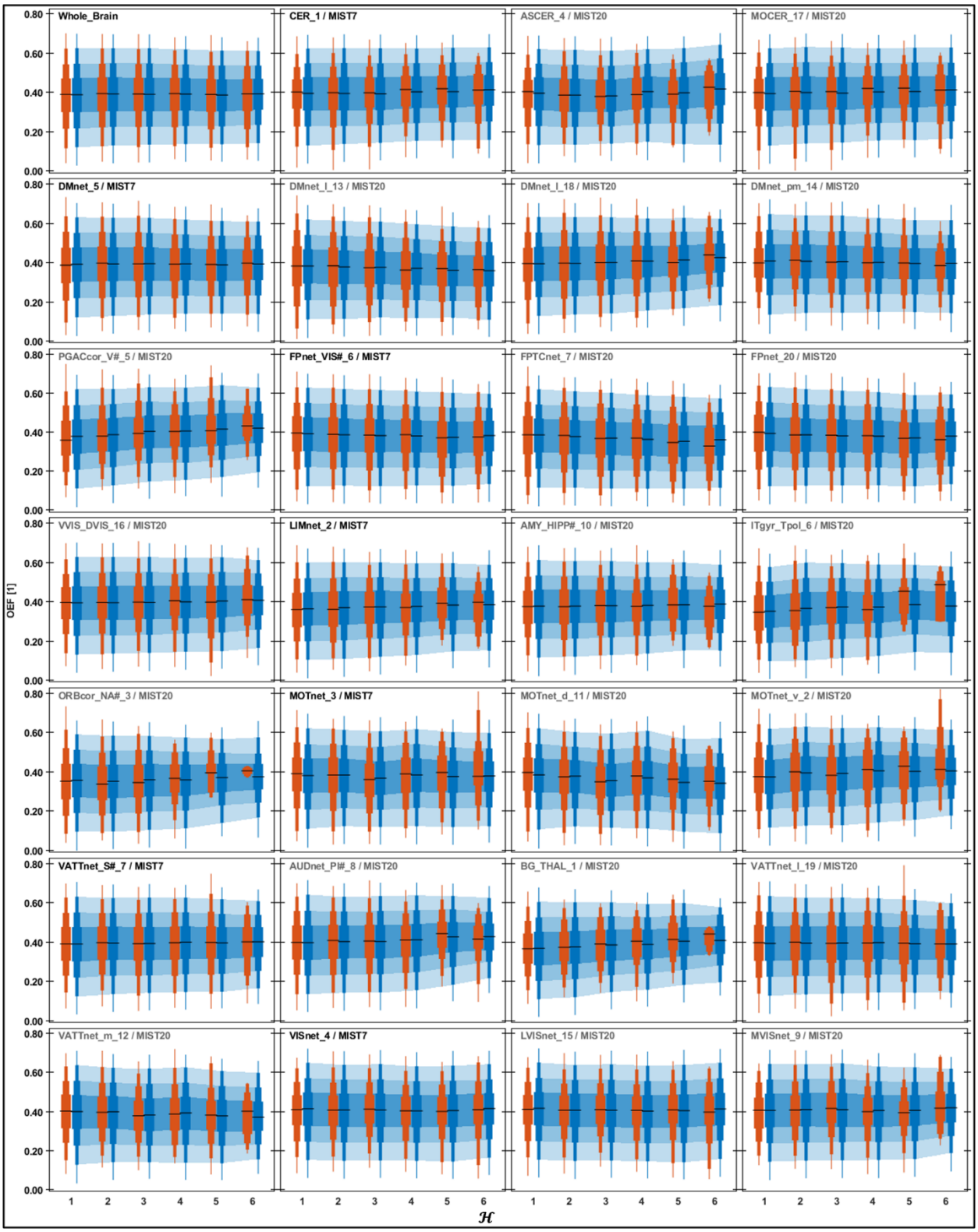

Figure 3.13 Graphical posterior predictive checks for Bayesian multilevel power-law analysis for OEF. Vertical lines are sets of four overlayed lines with different thicknesses, and they delimit equal-tailed credible intervals at 50%, 80%, 95%, and 99%, from thickest to thinnest in that order. Red colors are the original observations, and blue ones are predictions. Blue shaded areas correspond to the credible intervals at 50%, 80% and 95%. Horizontal black lines

are the median estimates. The ordering of the tiles from left to right, then top to bottom, is such that the networks of MIST7 are directly followed by their (network) children in MIST20. The labels of MIST7 and MIST20 are detailed in Table 3.2. These figures suggest well behaved fits and illustrate how partial pooling operated.

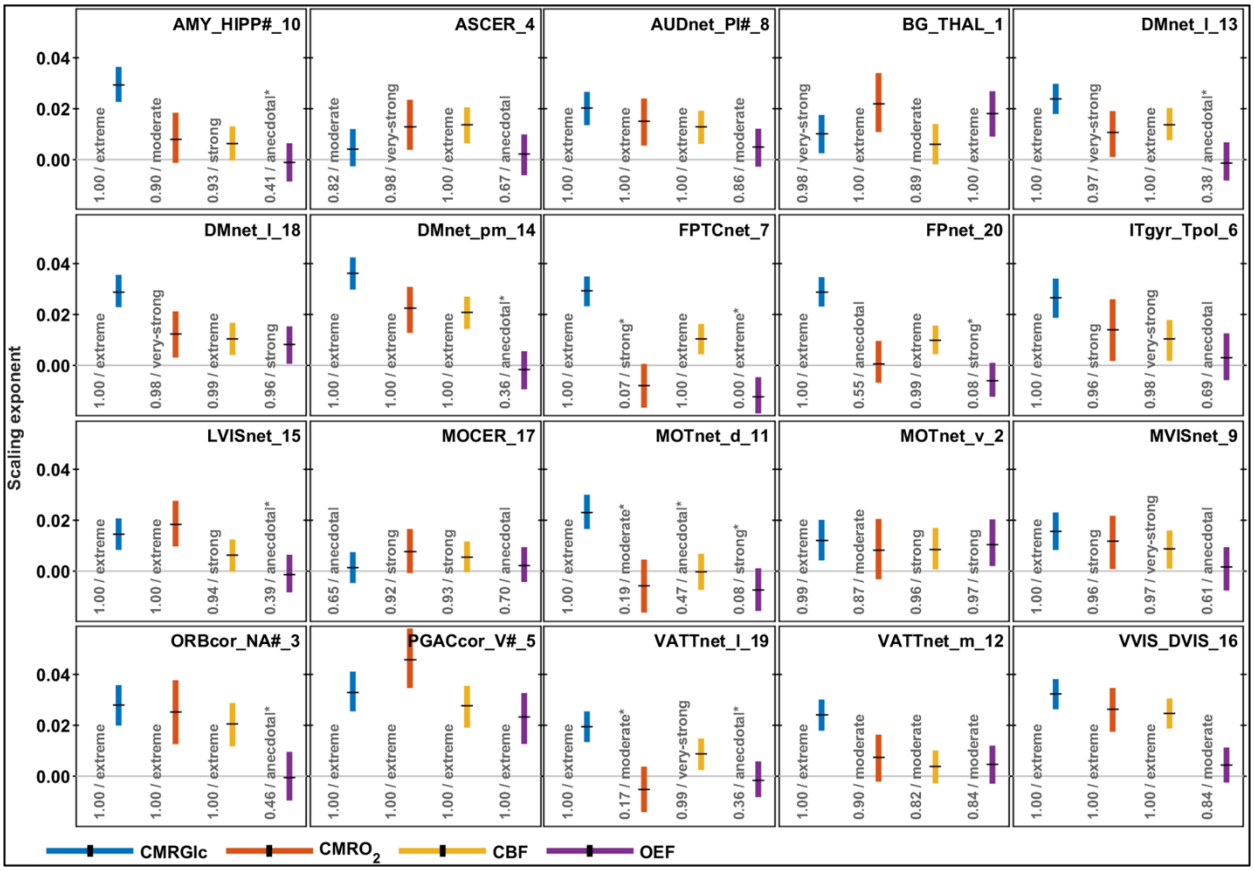

Figure 3.14 Posterior summaries of scaling exponents within the networks of MIST20 for CMRGlc, $CMRO_2$, CBF, and OEF. The colored vertical lines delimit the 89% highest density credible intervals of, and the black horizontal lines are the median of the estimated posteriors. The number on the left side of each vertical line indicates probability that the scaling exponent is between 0 and 1 (i.e., the probability of a concave down increasing power-law) and the corresponding text indicates an interpreted evidence ratio. A star symbol at the end of a text (i.e., when probabilities are less than 0.5) indicates that the interpreted evidence ratio applies to the alternative hypothesis (i.e., non-concave down increasing power-law model). Note that the probability values reported here as 0.00 or 1.00 are not true zeros or ones. The labels of MIST20 are detailed in Table 3.2.

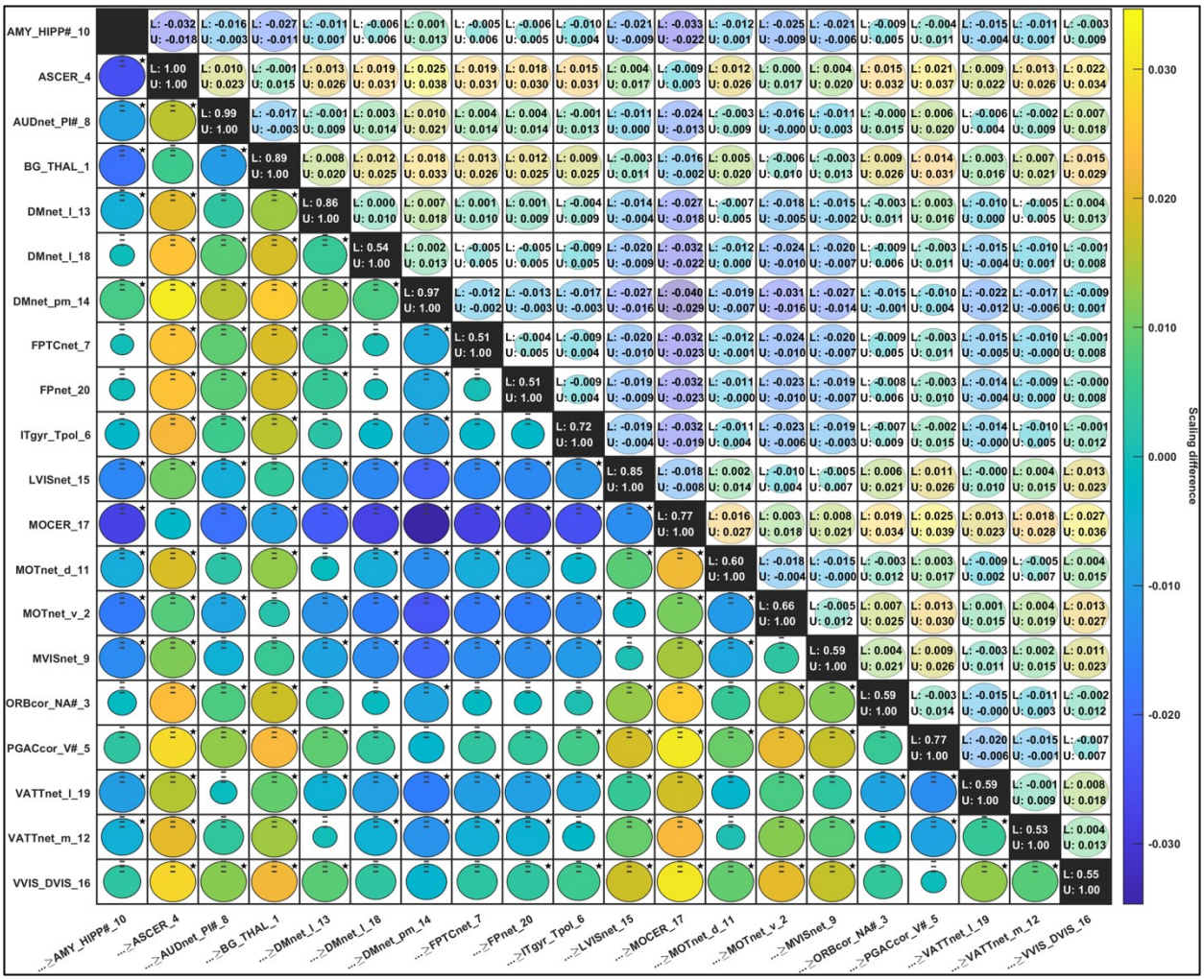

Figure 3.15 Posterior summaries of scaling differences between the networks of MIST20 for CMRGlc. The comparisons ROW ≥ COLUMN indicate that the difference was calculated between the posterior of ROW and COLUMN. Here we report comparisons only for the lower triangular. The color-bars are median estimates of posterior differences. The numbers on the upper diagonals give the lower (L) and upper (U) bounds of the 89% highest density credible intervals of the posterior differences. The size of each circle represents probability of direction (i.e., maximum between probability of positive difference and probability of negative difference), the horizontal tick marks on the top of each circle delimit probabilities of 0.5, 0.75, and 1, and a star symbol on the top-right of a circle indicate if the probability is greater than or equal to 0.89. The numbers on the diagonals summarize the lowest (L) and highest (U) probability of directions found on each row. Note that the probability values reported here as 1.00 are not true ones. The labels of MIST20 are detailed in Table 3.2. This figure provides evidence of the existence of scaling differences between networks.

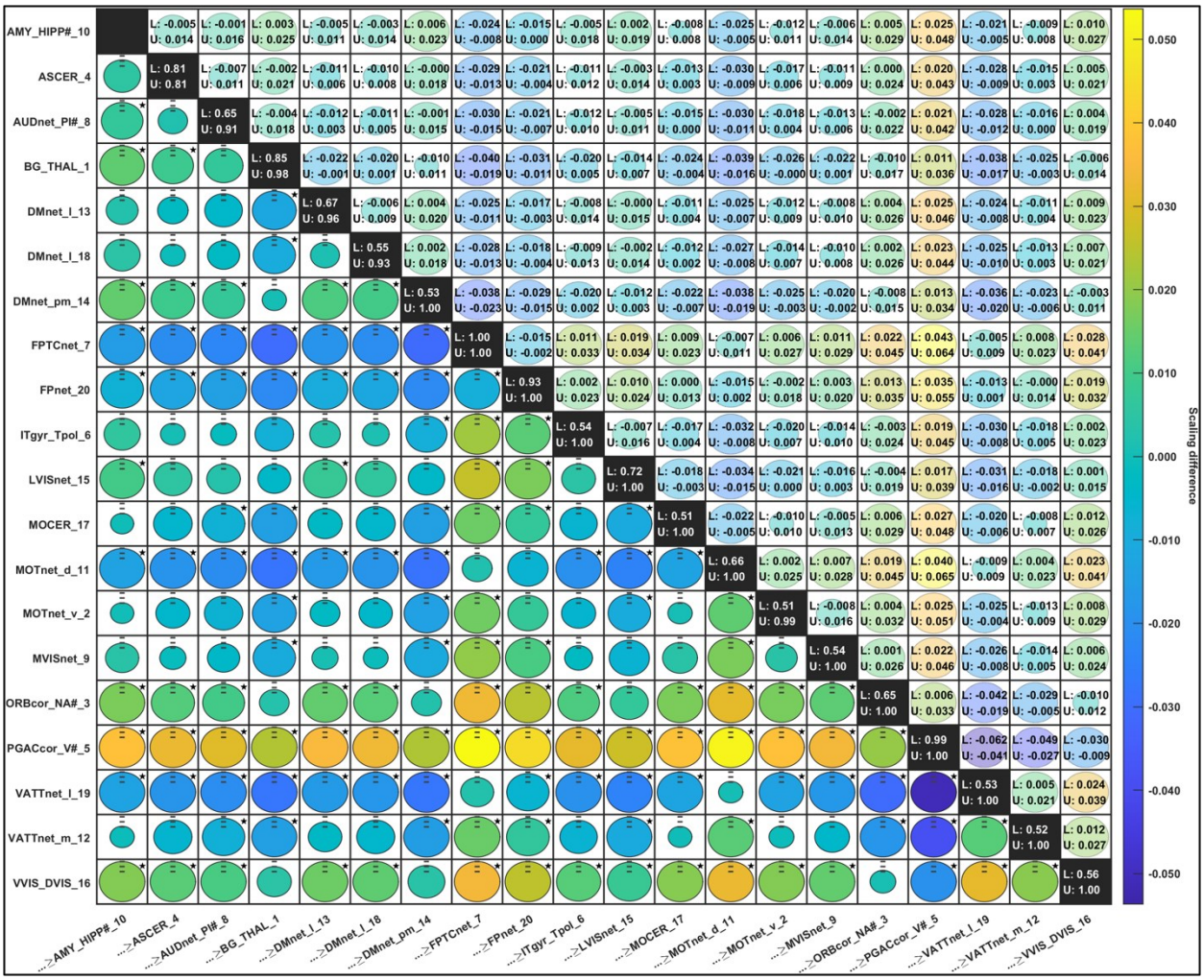

Figure 3.16 Posterior summaries of scaling differences between the networks of MIST20 for $CMRO_2$. The comparisons $ROW \geq COLUMN$ indicate that the difference was calculated between the posterior of ROW and $COLUMN$. Here we report comparisons only for the lower triangular. The color-bars are median estimates of posterior differences. The numbers on the upper diagonals give the lower (L) and upper (U) bounds of the 89% highest density credible intervals of the posterior differences. The size of each circle represents probability of direction (i.e., maximum between probability of positive difference and probability of negative difference), the horizontal tick marks on the top of each circle delimit probabilities of 0.5, 0.75, and 1, and a star symbol on the top-right of a circle indicate if the probability is greater than or equal to 0.89. The numbers on the diagonals summarize the lowest (L) and highest (U) probability of directions found on each row. Note that the probability values reported here as 1.00 are not true ones. The labels of MIST20 are detailed in Table 3.2. This figure provides evidence of the existence of scaling differences between networks.

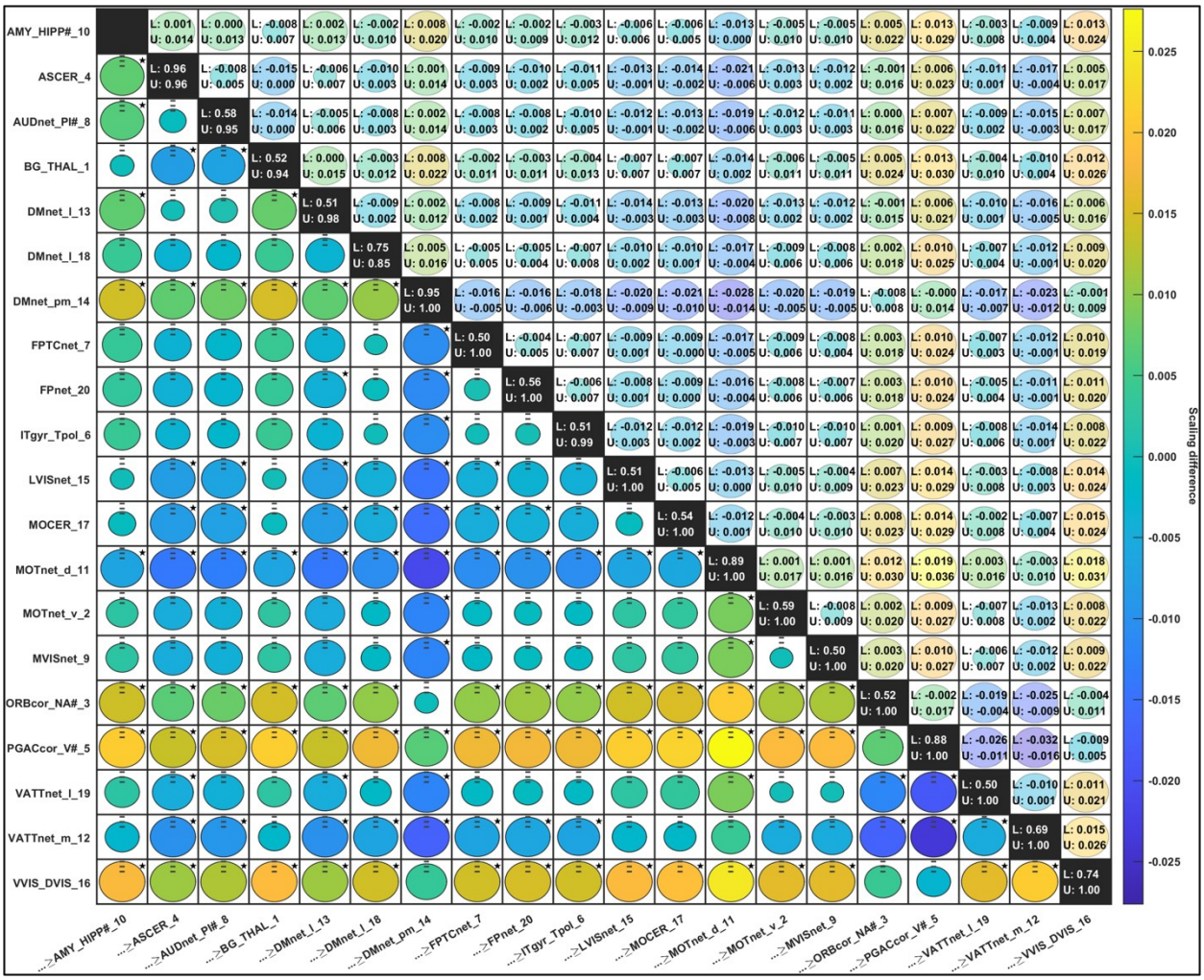

Figure 3.17 Posterior summaries of scaling differences between the networks of MIST20 for CBF. The comparisons $ROW \geq COLUMN$ *indicate that the difference was calculated between the posterior of* ROW *and* $COLUMN$*. Here we report comparisons only for the lower triangular. The color-bars are median estimates of posterior differences. The numbers on the upper diagonals give the lower (L) and upper (U) bounds of the 89% highest density credible intervals of the posterior differences. The size of each circle represents probability of direction (i.e., maximum between probability of positive difference and probability of negative difference), the horizontal tick marks on the top of each circle delimit probabilities of 0.5, 0.75, and 1, and a star symbol on the top-right of a circle indicate if the probability is greater than or equal to 0.89. The numbers on the diagonals summarize the lowest (L) and highest (U) probability of directions found on each row. Note that the probability values reported here as 1.00 are not true ones. The labels of MIST20 are detailed in Table 3.2. This figure provides evidence of the existence of scaling differences between networks.*

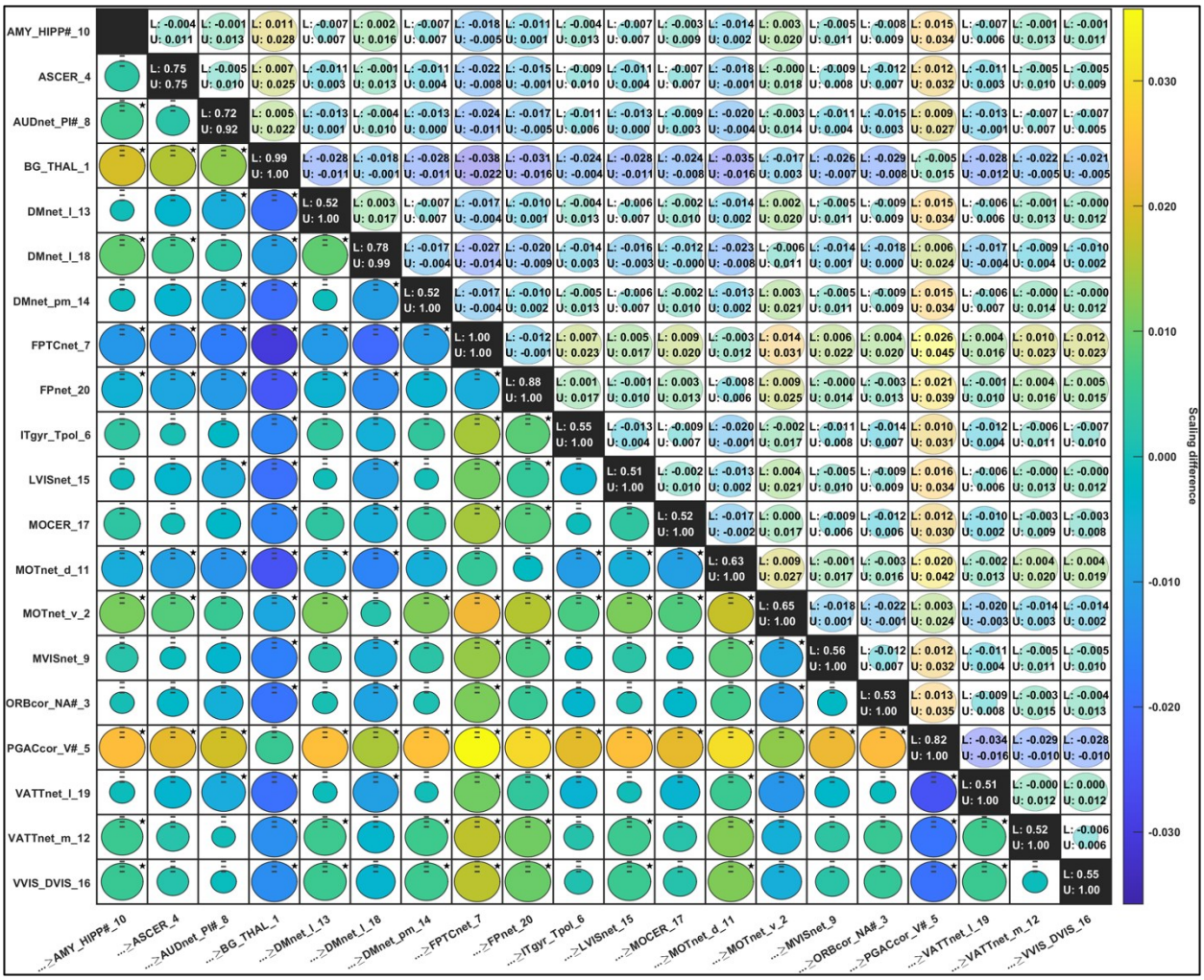

Figure 3.18 Posterior summaries of scaling differences between the networks of MIST20 for OEF. The comparisons $ROW \geq COLUMN$ *indicate that the difference was calculated between the posterior of* ROW *and* $COLUMN$*. Here we report comparisons only for the lower triangular. The color-bars are median estimates of posterior differences. The numbers on the upper diagonals indicate the lower (L) and upper (U) bounds of the 89% highest density credible intervals of the posterior differences. The size of each circle represents probability of direction (i.e., maximum between probability of positive difference and probability of negative difference), the horizontal tick marks on the top of each circle delimit probabilities of 0.5, 0.75, and 1, and a star symbol on the top-right of a circle indicate if the probability is greater than or equal to 0.89. The numbers on the diagonals summarize the lowest (L) and highest (U) probability of directions found on each row. Note that the probability values reported here as 1.00 are not true ones. The labels of MIST20 are detailed in Table 3.2. This figure provides evidence of the existence of scaling differences between networks.*

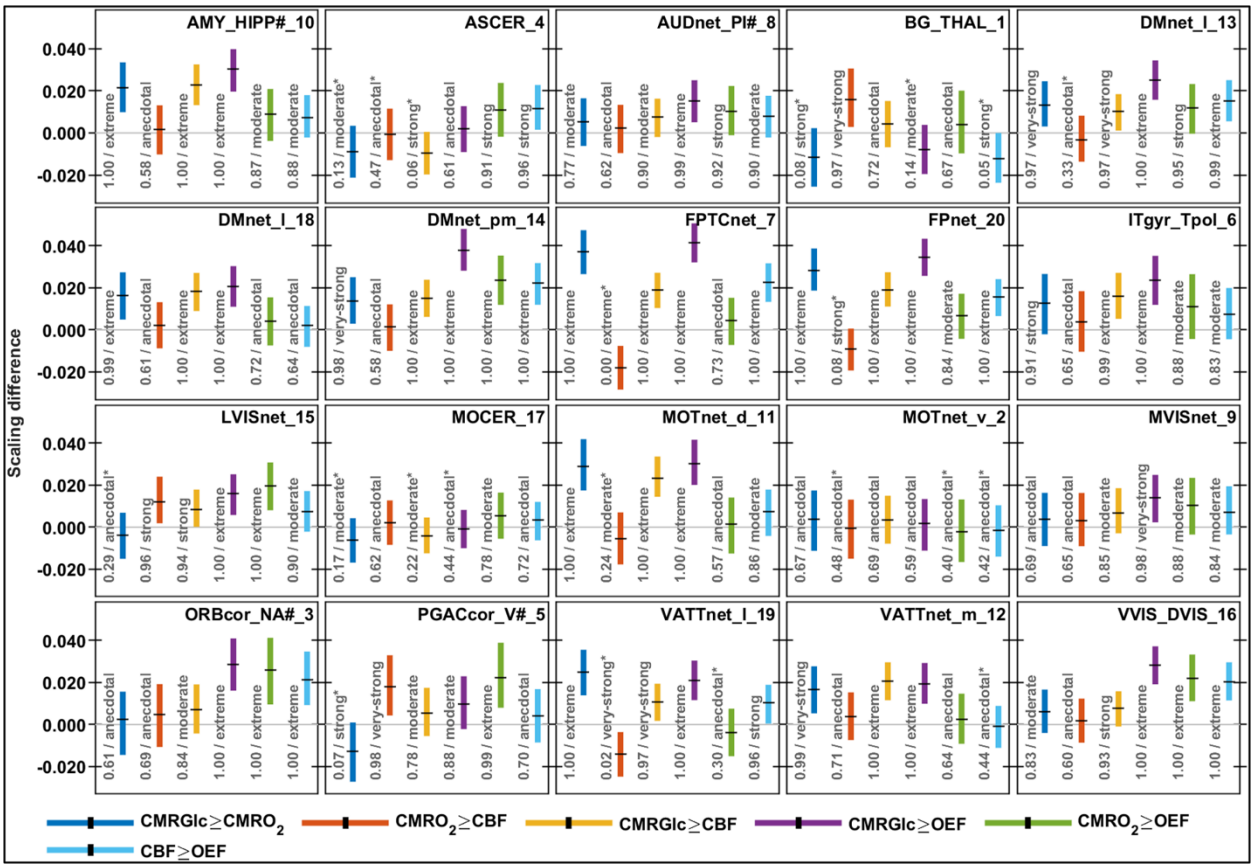

Figure 3.19 Posterior summaries of scaling differences between CMRGlc, $CMRO_2$, CBF, and OEF within the networks of MIST20. The colored vertical lines delimit the 89% highest density credible intervals of, and the black horizontal lines are the median of the estimated posteriors. The number on the left side of each vertical line indicates probability of positive difference and the corresponding text indicates an interpreted evidence ratio. A star symbol at the end of a text (i.e., when probabilities are less than 0.5) indicates that the interpreted evidence ratio applies to the hypothesis of negative difference instead of positive. Note that the probability values reported here as 0.00 or 1.00 are not true zeros or ones. The labels of MIST20 are detailed in Table 3.2. This figure provides evidence of the existence of scaling differences between CMRGlc, $CMRO_2$, CBF, and OEF.

Table 3.2 Labels of the MIST atlas for two resolutions (7 and 20 networks).

Scale	Label	Name
MIST7	CER_1	CEREBELLUM
	DMnet_5	DEFAULT_MODE_NETWORK
	FPnet_VIS#_6	FRONTO_PARIETAL_NETWORK_and_VISUAL_DOWNSTREAM
	LIMnet_2	MESOLIMBIC_NETWORK
	MOTnet_3	SOMATOMOTOR_NETWORK
	VATTnet_S#_7	VENTRAL_ATTENTION_NETWORK_and_SALIENCE_NETWORK_and_BASAL_GANGLIA_and_THALAMUS
	VISnet_4	VISUAL_NETWORK
MIST20	AMY_HIPP#_10	AMYGDALA_and_HIPPOCAMPUS_and_Peri_Insular_Sulcus
	ASCER_4	ASSOCIATIVE_CEREBELLUM
	AUDnet_P#_8	AUDITORY_NETWORK_and_POSTERIOR_INSULA
	BG_THAL_1	BASAL_GANGLIA_and_THALAMUS
	DMnet_l_13	DEFAULT_MODE_NETWORK_lateral
	DMnet_l_18	DEFAULT_MODE_NETWORK_lateral
	DMnet_pm_14	DEFAULT_MODE_NETWORK_posteromedial
	FPTCnet_7	FRONTO_PARIETAL_TASK_CONTROL_NETWORK
	FPnet_20	FRONTO_PARIETAL_NETWORK
	ITgyr_Tpol_6	INFERIOR_TEMPORAL_GYRUS_and_TEMPORAL_POLE
	LVISnet_15	LATERAL_VISUAL_NETWORK
	MOCER_17	MOTOR_CEREBELLUM
	MOTnet_d_11	SOMATOMOTOR_NETWORK_dorsal
	MOTnet_v_2	SOMATOMOTOR_NETWORK_ventral
	MVISnet_9	MEDIAL_VISUAL_NETWORK
	ORBcor_NA#_3	ORBITOFRONTAL_CORTEX_and_NUCLEUS_ACCUMBENS
	PGACcor_V#_5	PERIGENUAL_ANTERIOR_CINGULATE_CORTEX_and_VENTROMEDIAL_PREFRONTAL_CORTEX
	VATTnet_l_19	VENTRAL_ATTENTION_NETWORK_lateral
	VATTnet_m_12	VENTRAL_ATTENTION_NETWORK_medial
	VVIS_DVIS_16	VENTRAL_VISUAL_STREAM_and_DORSAL_VISUAL_STREAM

Table 3.3 Demographics data.

Height [cm]	Weight [lb]	Gender	Age
166	157	Female	19
171	153	Male	19
176	148	Male	19
181	193	Male	19
159	119	Female	20
178	210	Male	20
170	117	Female	21
157	134	Female	22
176	144	Male	22
162	131	Female	23
167	261	Female	23
180	189	Male	23
188	228	Male	23
165	113	Female	24
180	148	Male	24
173	128	Male	25
176	150	Male	25
159	115	Female	32
170	128	Female	33

Table 3.4 Regional values (mean ± SD) for CMRGlc [SUVR], $CMRO_2$ [µmol / (100 g) / min], CBF [mL / (100 g) / min], and OEF [1]. Values were calculated directly on the average maps. The labels are those of the Mindboggle atlas.

Label	CMRGlc	$CMRO_2$	CBF	OEF
Accumbens-Area	1.7 ± 0.2	120 ± 20	43 ± 5	0.35 ± 0.02
Amygdala	1.2 ± 0.2	120 ± 20	38 ± 5	0.38 ± 0.04
Caudal-Anterior-Cingulate	1.4 ± 0.4	160 ± 20	50 ± 6	0.40 ± 0.03
Caudal-Middle-Frontal	2.2 ± 0.4	150 ± 40	54 ± 9	0.37 ± 0.07
Caudate	1.8 ± 0.7	100 ± 30	38 ± 9	0.35 ± 0.04
Cerebellum-Gray-Matter	1.5 ± 0.3	140 ± 30	44 ± 6	0.37 ± 0.04
Cuneus	2.0 ± 0.4	190 ± 40	61 ± 8	0.40 ± 0.04
Entorhinal	1.2 ± 0.3	80 ± 10	32 ± 4	0.33 ± 0.04
Fusiform	1.7 ± 0.3	130 ± 30	44 ± 7	0.38 ± 0.04
Hippocampus	1.3 ± 0.2	110 ± 10	38 ± 4	0.36 ± 0.03
Inferior-Parietal	2.0 ± 0.4	170 ± 50	58 ± 10	0.39 ± 0.07
Inferior-Temporal	1.6 ± 0.4	120 ± 30	45 ± 8	0.35 ± 0.05
Insula	1.6 ± 0.4	160 ± 20	50 ± 6	0.40 ± 0.03
Isthmus-Cingulate	2.1 ± 0.5	160 ± 40	50 ± 11	0.40 ± 0.04
Lateral-Occipital	1.9 ± 0.5	160 ± 40	55 ± 8	0.39 ± 0.05
Lateral-Orbitofrontal	1.9 ± 0.4	120 ± 30	45 ± 8	0.35 ± 0.04
Lingual	2.0 ± 0.3	170 ± 20	53 ± 5	0.41 ± 0.03
Medial-Orbitofrontal	1.8 ± 0.4	130 ± 40	47 ± 11	0.35 ± 0.05
Middle-Temporal	1.8 ± 0.4	160 ± 50	54 ± 10	0.39 ± 0.06
Pallidum	1.1 ± 0.1	90 ± 20	33 ± 4	0.35 ± 0.03
Paracentral	1.8 ± 0.3	140 ± 30	46 ± 8	0.38 ± 0.03
Parahippocampal	1.4 ± 0.2	120 ± 20	41 ± 4	0.39 ± 0.02
Pars-Opercularis	2.1 ± 0.3	180 ± 30	58 ± 7	0.40 ± 0.04
Pars-Orbitalis	1.9 ± 0.5	160 ± 40	55 ± 8	0.39 ± 0.04
Pars-Triangularis	2.2 ± 0.4	160 ± 50	57 ± 10	0.39 ± 0.06
Pericalcarine	2.4 ± 0.3	200 ± 20	62 ± 5	0.43 ± 0.03
Postcentral	1.8 ± 0.4	150 ± 40	52 ± 9	0.38 ± 0.07
Posterior-Cingulate	2.0 ± 0.5	170 ± 40	54 ± 10	0.41 ± 0.03
Precentral	2.0 ± 0.4	160 ± 40	54 ± 9	0.39 ± 0.06
Precuneus	2.1 ± 0.4	180 ± 40	55 ± 9	0.40 ± 0.04
Putamen	2.1 ± 0.6	140 ± 20	45 ± 5	0.39 ± 0.03
Rostral-Anterior-Cingulate	1.4 ± 0.4	140 ± 30	48 ± 8	0.37 ± 0.04
Rostral-Middle-Frontal	2.2 ± 0.5	160 ± 50	56 ± 11	0.37 ± 0.08
Superior-Frontal	2.0 ± 0.4	160 ± 40	54 ± 8	0.38 ± 0.06
Superior-Parietal	1.9 ± 0.4	150 ± 40	52 ± 8	0.38 ± 0.06
Superior-Temporal	1.5 ± 0.4	150 ± 50	50 ± 10	0.37 ± 0.06
Supramarginal	1.9 ± 0.3	160 ± 50	53 ± 10	0.38 ± 0.07
Thalamus	1.8 ± 0.4	120 ± 10	42 ± 4	0.36 ± 0.03
Transverse-Temporal	2.3 ± 0.3	180 ± 10	58 ± 3	0.40 ± 0.03

Table 3.5 Number of observations (i.e., voxels) in total and for different grouping variables. The ranges minimum–maximum indicate the minimum and maximum number of observations within a group element.

Group	CMRGlc	$CMRO_2$	CBF	OEF
sub	6480–10701	6110–10021	6110–10021	6103–10021
MIST7	8754–41907	7712–39726	7715–39736	7707–39673
MIST20	2702–15515	2683–15272	2682–15276	2683–15246
global	170322	159654	159698	159534

Table 3.6 Sampling specification for Bayesian multilevel power-law analysis with brms.

Argument	Value	Description
init	*manual*	Initial values for parameters were randomly generated by drawing from the prior predictive distributions.
chains	*4*	Four Markov chains were used.
iter	*2000*	Number of iterations for each chain (including warmup).
warmup	*1000*	Number of warmup (or burnin) iterations per chain.
algorithm	*NUTS*	Use the No-U-Turn sampler variant of Hamiltonian Monte Carlo (Hoffman and Gelman 2011, Betancourt 2017) for inference.
seed	*random*	Seed for random number generation.
adapt_delta	*0.99*	Target average proposal acceptance probability during the adaptation period of Stan.
max_treedepth	*15*	Cap on the depth of the trees to evaluate during each iteration.
backend	*rstan*	Package to use as the backend for fitting the Stan model.

Table 3.7 Convergence diagnostics for Bayesian multilevel power-law analysis. "Resp." stands for response variable, "Par." stands for parameter, and ESS stands for effective sample size. Here, all convergence diagnostics were reasonable. There was no warning for all fits, all $\hat{R}$ values were equal to 1.00, and all ESSs were greater than 879.

Resp.	Par.	$\widehat{R}$	Bulk ESS	Tail ESS	Resp.	Par.	$\widehat{R}$	Bulk ESS	Tail ESS
CMRGlc	$\overline{\mathrm{A}}$	1.00	2534	2762	**$CMRO_2$**	$\overline{\mathrm{A}}$	1.00	1608	3056
	$\overline{\mathrm{B}}$	1.00	2653	2864		$\overline{\mathrm{B}}$	1.00	2149	2573
	$\bar{\sigma}$	1.00	1052	1708		$\bar{\sigma}$	1.00	981	1663
	$\bar{\alpha}$	1.00	1175	1756		$\bar{\alpha}$	1.00	1539	2115
	$\tau_{\sigma}^{\mathrm{sub}}$	1.00	1660	2361		$\tau_{\sigma}^{\mathrm{sub}}$	1.00	1381	2151
	$\tau_{\alpha}^{\mathrm{sub}}$	1.00	1579	2249		$\tau_{\alpha}^{\mathrm{sub}}$	1.00	2290	2641
	$\tau_{\mathrm{A}}^{\mathrm{MIST7}}$	1.00	1506	1689		$\tau_{\mathrm{A}}^{\mathrm{MIST7}}$	1.00	1996	1765
	$\tau_{\mathrm{A}}^{\mathrm{MIST20}}$	1.00	1795	2536		$\tau_{\mathrm{A}}^{\mathrm{MIST20}}$	1.00	1998	2379
	$\tau_{\mathrm{A}}^{\mathrm{sub}}$	1.00	1523	2227		$\tau_{\mathrm{A}}^{\mathrm{sub}}$	1.00	1518	2498
	$\tau_{\mathrm{B}}^{\mathrm{MIST7}}$	1.00	2288	2194		$\tau_{\mathrm{B}}^{\mathrm{MIST7}}$	1.00	1393	2265
	$\tau_{\mathrm{B}}^{\mathrm{MIST20}}$	1.00	1442	2279		$\tau_{\mathrm{B}}^{\mathrm{MIST20}}$	1.00	2003	2647
	$\tau_{\mathrm{B}}^{\mathrm{sub}}$	1.00	1663	2291		$\tau_{\mathrm{B}}^{\mathrm{sub}}$	1.00	2012	2116
CBF	$\overline{\mathrm{A}}$	1.00	1487	1910	**OEF**	$\overline{\mathrm{A}}$	1.00	1086	1775
	$\overline{\mathrm{B}}$	1.00	1976	2574		$\overline{\mathrm{B}}$	1.00	1996	2452
	$\bar{\sigma}$	1.00	998	1730		$\bar{\sigma}$	1.00	879	1334
	$\bar{\alpha}$	1.00	1473	2185		$\bar{\alpha}$	1.00	975	1658
	$\tau_{\sigma}^{\mathrm{sub}}$	1.00	1444	2237		$\tau_{\sigma}^{\mathrm{sub}}$	1.00	1390	2604
	$\tau_{\alpha}^{\mathrm{sub}}$	1.00	1953	2573		$\tau_{\alpha}^{\mathrm{sub}}$	1.00	1741	2249
	$\tau_{\mathrm{A}}^{\mathrm{MIST7}}$	1.00	1759	2050		$\tau_{\mathrm{A}}^{\mathrm{MIST7}}$	1.00	1318	975
	$\tau_{\mathrm{A}}^{\mathrm{MIST20}}$	1.00	1573	2317		$\tau_{\mathrm{A}}^{\mathrm{MIST20}}$	1.00	1290	2038
	$\tau_{\mathrm{A}}^{\mathrm{sub}}$	1.00	2052	2551		$\tau_{\mathrm{A}}^{\mathrm{sub}}$	1.00	1525	1859
	$\tau_{\mathrm{B}}^{\mathrm{MIST7}}$	1.00	1353	2441		$\tau_{\mathrm{B}}^{\mathrm{MIST7}}$	1.00	1290	1667
	$\tau_{\mathrm{B}}^{\mathrm{MIST20}}$	1.00	1799	2422		$\tau_{\mathrm{B}}^{\mathrm{MIST20}}$	1.00	2173	2504
	$\tau_{\mathrm{B}}^{\mathrm{sub}}$	1.00	1585	2019		$\tau_{\mathrm{B}}^{\mathrm{sub}}$	1.00	1755	2470

Table 3.8 Model summary for Bayesian multilevel power-law analysis. "Resp." stands for response variable, "Par." stands for parameter, M indicates median values, and 89CI indicates 89% highest density credible intervals.

Resp.	Par.	M	$89CI$	Resp.	Par.	M	$89CI$
CMRGlc	$\bar{A}$	-0.4297	[-0.7437, -0.1919]	**$CMRO_2$**	$\bar{A}$	-0.3902	[-0.6910, -0.0652]
	$\bar{B}$	-0.2362	[-0.5554, 0.0730]		$\bar{B}$	-0.5444	[-0.8942, -0.1963]
	$\bar{\sigma}$	0.2486	[0.2343, 0.2624]		$\bar{\sigma}$	0.3397	[0.3237, 0.3564]
	$\bar{\alpha}$	-1.2768	[-1.5137, -1.0113]		$\bar{\alpha}$	0.3481	[-0.0328, 0.7299]
	τ_{σ}^{sub}	0.0371	[0.0279, 0.0480]		τ_{σ}^{sub}	0.0427	[0.0316, 0.0555]
	τ_{α}^{sub}	0.6338	[0.4450, 0.8375]		τ_{α}^{sub}	1.024	[0.7865, 1.2462]
	τ_{A}^{MIST7}	0.3094	[0.0854, 0.5663]		τ_{A}^{MIST7}	0.3528	[0.1747, 0.6014]
	τ_{A}^{MIST20}	0.3177	[0.2190, 0.4316]		τ_{A}^{MIST20}	0.261	[0.1773, 0.3604]
	τ_{A}^{sub}	0.3816	[0.2849, 0.4872]		τ_{A}^{sub}	0.5304	[0.3961, 0.6762]
	τ_{B}^{MIST7}	0.365	[0.1883, 0.6078]		τ_{B}^{MIST7}	0.1664	[0.0000, 0.3771]
	τ_{B}^{MIST20}	0.2036	[0.1183, 0.3090]		τ_{B}^{MIST20}	0.4802	[0.3416, 0.6337]
	τ_{B}^{sub}	0.4906	[0.3693, 0.6324]		τ_{B}^{sub}	0.7076	[0.5360, 0.8973]
CBF	$\bar{A}$	-0.2877	[-0.5994, 0.0404]	**OEF**	$\bar{A}$	-0.1617	[-0.3493, 0.0219]
	$\bar{B}$	-0.5858	[-0.8130, -0.3340]		$\bar{B}$	-0.9198	[-1.1674, -0.6514]
	$\bar{\sigma}$	0.2452	[0.2314, 0.2598]		$\bar{\sigma}$	0.2991	[0.2825, 0.3150]
	$\bar{\alpha}$	-1.2485	[-1.4496, -1.0276]		$\bar{\alpha}$	-1.1124	[-1.4063, -0.8177]
	τ_{σ}^{sub}	0.0372	[0.0278, 0.0480]		τ_{σ}^{sub}	0.0413	[0.0310, 0.0541]
	τ_{α}^{sub}	0.579	[0.4281, 0.7388]		τ_{α}^{sub}	0.8085	[0.6114, 1.0117]
	τ_{A}^{MIST7}	0.3203	[0.1415, 0.5432]		τ_{A}^{MIST7}	0.1264	[0.0183, 0.2309]
	τ_{A}^{MIST20}	0.2296	[0.1550, 0.3092]		τ_{A}^{MIST20}	0.1092	[0.0735, 0.1546]
	τ_{A}^{sub}	0.5926	[0.4528, 0.7631]		τ_{A}^{sub}	0.4219	[0.3206, 0.5452]
	τ_{B}^{MIST7}	0.1302	[0.0002, 0.2841]		τ_{B}^{MIST7}	0.1077	[0.0002, 0.2581]
	τ_{B}^{MIST20}	0.267	[0.1791, 0.3696]		τ_{B}^{MIST20}	0.3256	[0.2262, 0.4477]
	τ_{B}^{sub}	0.4856	[0.3531, 0.6198]		τ_{B}^{sub}	0.5587	[0.4193, 0.7233]

Table 3.9 Observed (Obs.) and predicted (Pred.) statistics for the different response variables (Resp.). The predictions were obtained from 100 draws and all statistics were applied on the normalized datasets. Overall, predictions were reasonable. Means and standard deviations were all in agreement. Medians were in agreement for $CMRO_2$ and CBF, and they were slightly overestimated for CMRGlc and underestimated for OEF. The quantiles suggested that reasonable errors occurred at the distribution tails.

Resp.	Statistic	Obs.	Pred. (mean ± 2×SD)	Resp.	Statistic	Obs.	Pred. (mean ± 2×SD)
CMRGlc	mean	1.933	1.932 ± 0.002	**$CMRO_2$**	mean	1.933	1.933 ± 0.002
	standard deviation	0.292	0.293 ± 0.002		standard deviation	0.377	0.377 ± 0.002
	median	1.918	1.932 ± 0.002		median	1.922	1.925 ± 0.003
	1% quantile	1.264	1.233 ± 0.008		1% quantile	1.138	1.089 ± 0.007
	5% quantile	1.478	1.453 ± 0.005		5% quantile	1.332	1.329 ± 0.004
	25% quantile	1.737	1.742 ± 0.002		25% quantile	1.664	1.676 ± 0.003
	75% quantile	2.116	2.121 ± 0.002		75% quantile	2.190	2.181 ± 0.003
	95% quantile	2.434	2.413 ± 0.003		95% quantile	2.571	2.564 ± 0.005
	99% quantile	2.680	2.644 ± 0.007		99% quantile	2.842	2.849 ± 0.009
CBF	mean	1.960	1.960 ± 0.002	**OEF**	mean	1.967	1.967 ± 0.002
	standard deviation	0.302	0.303 ± 0.001		standard deviation	0.317	0.316 ± 0.002
	median	1.948	1.950 ± 0.002		median	1.981	1.976 ± 0.002
	1% quantile	1.313	1.277 ± 0.007		1% quantile	1.182	1.189 ± 0.008
	5% quantile	1.495	1.481 ± 0.004		5% quantile	1.418	1.434 ± 0.004
	25% quantile	1.750	1.759 ± 0.002		25% quantile	1.760	1.759 ± 0.003
	75% quantile	2.150	2.148 ± 0.002		75% quantile	2.185	2.185 ± 0.003
	95% quantile	2.480	2.478 ± 0.004		95% quantile	2.463	2.470 ± 0.004
	99% quantile	2.745	2.746 ± 0.009		99% quantile	2.661	2.665 ± 0.007

Chapter 4: Manuscript 2 — Investigating the transcriptional profile of the blood flow and metabolic costs of functional global and local network connectivity

4.1 Context

In Chapter 2, we described the structural and functional organization of the brain across different spatial scales (Dumoulin et al., 2018; Mišić & Sporns, 2016; Rah et al., 2015). Molecular processes involved in synaptic and non-synaptic connections at the cellular scale of the brain are actually shaping macroscale connections and network organizations. Neuroimaging methods can be used to indirectly probe brain activity at its macroscale level whereas neuroimaging-genetics is a nascent neuroimaging discipline which helps uncover some of the molecular mechanisms underpinning neuroimaging data. Genetic neuroimaging approaches could also provide greater insights into the cellular processes that are associated with brain metabolic, vascular, and hemodynamic responses.

Due to the substantial resolution gap between transcriptional genetic data and neuroimaging data, analyzing genetic neuroimaging data requires a dedicated approach involving either dimension reduction of such high-dimensional data or employing multivariate statistical methods that can handle interdependent high-dimensional datasets. The primary approach for integrating neuroimaging and transcriptional data uses Pearson or Spearman correlations, or Euclidean distances as an index of similarity to find the overall correspondence between the entire cerebral distribution of neuroimaging data and averaged gene expression data. Using such an approach, the genes exhibiting the most similar patterns with neuroimaging data are kept for further analysis (Diez & Sepulcre, 2021; Ortiz-Terán et al., 2017). Even though these methods are simple to use, they may discard inherent regional associations between transcriptional and neuroimaging data. To address this problem, co-expression approaches have been proposed, which seek to detect the genes that are jointly expressed within the same regions. The most popular gene co-expression approach is the weighted gene co-expression network analysis (B. Zhang & Horvath, 2005). This method operates by estimating a gene × gene correlation matrix that contains a pairwise correlation between gene expression levels. Graph modularity detection algorithms or principal component analysis are then applied to such a correlation matrix to find the genes exhibiting the largest inter-connection profiles. However, though these methods can find clusters of highly correlated genes, the so-called “eigen”-genes, they just capture the characteristics of gene expression data, with no importance on how such information is related to the neuroimaging data. Hence, additional genetic neuroimaging-genetics analyses, using PCA for instance, have been considered to rank the genes according to their relationship with neuroimaging data. But, because this is usually performed as a separate step, it does not consider the regional variability in the neuroimaging data while initially deriving eigen genes. Two other multivariate techniques have been proposed to address these limitations: canonical correlation analysis (CCA (Hotelling, 1936)) and partial least squares (PLS (Wold et al., 1984)). Both methods attempt to find two linear projections, one for each set of observations in a paired dataset, such that the projected data points are exhibiting either maximal correlation in the case of CCA or maximal covariance in the case of PLS. In general, when the input data matrices are featuring low within-correlation and high between-correlation, both CCA and PLS provide comparable results, with equivalent sensitivity and false-positive rate (McIntosh, 2022). However, when there is a high within-correlation among each block of the data, as is the case, especially for the gene expression data matrix, the reliability of CCA becomes questionable

(McIntosh, 2022) and PLS should be preferred. In this second study, we, therefore, decided to consider PLS framework to assess the relationship between transcriptional and neuroimaging data (metabolic/hemodynamic mapping and functional connectivity properties).

As introduced in Chapter 2, the graph theoretical analysis of brain functional networks provides informative metrics to measure different features of brain functional network topologies, including global and local centralities, that reflect aspects of functional integration and segregation. In the present chapter, we present the second original contribution of this PhD thesis, where we examined the molecular and cellular processes associated with spatial patterns of metabolic and vascular properties, and functional global and local network connectivity. We considered the dataset acquired for our first project for this second analysis. Our hypothesis was that vascular, metabolic and functional connectivity patterns share spatial architectures that are shaped by underlying molecular and cellular processes that can be accessed using transcriptional data atlases. The Allen human brain atlas was used to estimate gene expression data. The vascular and metabolic neuroimaging data consisted of CMRGlc, $CMRO_2$, and CBF maps estimated as in the first manuscript. We also added Cerebrovascular reactivity (CVR) map measuring the ability of cerebral vessels to dilate or constrict in response to vasodilator and vasoconstrictor challenges, in this case, inhalation of CO_2. These four maps will be referred to as physio-metabolic data in the present manuscript. Regarding functional connectivity neuroimaging data, we considered graph theory to estimate four maps, two dedicated to measure network integration using global centrality indices, eigenvector centrality and global efficiency, and two dedicated to measure network segregation using local centrality indices, clustering coefficient and local efficiency. To propose an analysis at the regional, mesoscale level, while reducing dimensionality, all data were first constrained by a functional parcellation of the cortex, the Schaefer atlas (Schaefer et al., 2018) (see 2.1.2). Finally, we considered PLS methodology to relate transcriptomic and neuroimaging data, while gene ontology enrichment and cell-types deconvolution analyses were used to determine the molecular and cellular processes underlying the PLS-derived relations.

4.2 Abstract

Resting-state functional brain connectivity is metabolically costly and can be disrupted in diseases. While imaging can be used to assess both, imaging markers can only be sampled in mixed tissue due to their low spatial resolution and typically suffer from physiological ambiguity. Understanding the molecular basis of neuroimaging signals of connectivity and metabolism would enable a better understanding of the meaning of neuroimaging signals in health and disease. Transcription-neuroimaging association studies can be used to probe some of these molecular mechanisms. Here, we used an open-access transcriptomic dataset of the Allen Human Brain Atlas combined with a neuroimaging dataset from 19 healthy young adults including magnetic resonance imaging (MRI) measures of calibrated functional MRI (fMRI) and resting state connectivity, and a fluorodeoxyglucose positron emission tomography (FDG-PET) acquisition. The neuroimaging data were used to estimate markers of brain functional connectivity including both global and local network centralities, as well as biomarkers of brain metabolism including the cerebral metabolic rates of oxygen and glucose, cerebral blood flow, and cerebrovascular reactivity. Using partial least squares regression, we determined that 85% of the shared covariance between transcriptional data and neuroimaging-based network centrality and physio-metabolic data could be explained by two latent components. In addition, distinct sets of neuroimaging biomarkers contributed to the transcriptional patterns of each latent component, mostly distinguishing between different combinations of global centrality and physio-metabolic data on the one hand, and local centrality

and physio-metabolic data on the other hand. Using gene ontology enrichment analysis, we found that the highest enriched gene ontologies were associated with several signaling and metabolic processes, indicating a high metabolic cost and reliance on oxidative metabolism for global network centrality. Using a cell-types deconvolution analysis, we further found that neurons were the most enriched wherever global centrality together with physio-metabolic data contributed significantly to defining transcriptional patterns, whereas oligodendrocytes were the most enriched wherever local centrality together with cerebrovascular reactivity were the main contributors. These findings highlight that distinct molecular processes shape the metabolic costs associated with functional global and local connectivity observed at the scale of neuroimaging data.

4.3 Introduction

The human brain is a highly interconnected complex system with a high energy cost, accounting for nearly 20% of human basal metabolism. Because it lacks a reservoir to store fuel, the brain is dependent on a consistent and responsive vascular supply to bring required substrates and remove waste. The brain typically uses glucose and oxygen, though it can also use fatty acids (FAs) and ketone bodies in both glia and neurons in some circumstances (Bruce et al., 2017; Romano et al., 2017). In the cerebral cortex, a large fraction of this metabolic cost is used to sustain the resting membrane potential in neurons and glia and postsynaptic receptors activity (Attwell & Laughlin, 2001; Sengupta et al., 2010).

The brain is an avid user of oxygen since it requires oxidative phosphorylation to generate the full complement of adenosine tri-phosphate (ATP) from glucose to meet its high energy needs (Tiwari et al., 2013). The main pathway for glucose usage is therefore glycolysis, followed by the citric acid cycle and oxidative phosphorylation in the mitochondrial electron transport chain to generate ATP. Despite the preponderance of oxidative phosphorylation across most brain regions, some studies have suggested an important role for aerobic glycolysis within some part of the brain such as the default mode networks (Hyder et al., 2006; Vaishnavi et al., 2010). In contrast, the pentose phosphate pathway (PPP) has been shown to be used in the thalamus, which is enriched in oligodendrocytes, and may contribute in the motor cortex, which is enriched in neurons and has an intermediate levels of oligodendrocytes and astrocytes (Kleinridders et al., 2018). Energy pathway dominance is thought to be cell-type dependent, with neurons mainly relying on oxidation of glucose and pyruvate, while glycolysis and lactate production may play a larger role in astrocytes (Magistretti & Allaman, 2015). In addition, astrocytes can store glycogen to be used to export lactate to neurons to complement energy from other sources (Hyder et al., 2006; Iadecola, 2017; Lyons et al., 2016; Magistretti & Allaman, 2015).

Neurovascular organization and therefore neurovascular coupling (NVC), the amplitude of the vascular response that accompanies neuronal activity, also differ across brain regions (Bloch et al., 2015; Kaplan et al., 2020; Phillips et al., 2014; H. Zhang et al., 2022). Neurovascular coupling is associated with a local increase cerebral blood flow (CBF) occurring following neuronal demand (X. Ji et al., 2021), though CBF amplitude does not completely match the regional activation and is spatially heterogeneous (Chaigneau et al., 2003; Harrison et al., 2002; Iadecola, 2002; Iadecola et al., 1997; O'Herron et al., 2016). The amplitude of NVC also depends on cell type with studies using magnetic resonance spectroscopy (MRS) for example showing higher CBF increase and lower oxygen consumption following inhibitory neurons activity compared to excitatory neurons (Vazquez et al., 2018). In addition, heterogeneity in transit time and density of capillaries across brain layers (Huber et al., 2019; Uludağ & Blinder, 2018), differential expression of metabolic

transporter across brain regions and cell type dependent metabolic signature may also influence regional metabolism and NVC (Szablewski, 2021). Therefore, the metabolic and NVC pathways that support brain function vary regionally depending on the cell type composition, vascular properties and type of function that characterizes different regions. These regional differences are reflected in the heterogeneity of gene expression across the brain (L. P. Bernier et al., 2021; Kaplan et al., 2020; Vanlandewijck et al., 2018), but our understanding of how these are linked is limited. There are currently some important gaps in our understanding of how gene expression across the brain differs and reflects the physiological properties of different regions.

Functional magnetic resonance imaging (fMRI) using the Blood-oxygen-level dependent (BOLD) signal can capture the spontaneous slow fluctuation of the baseline hemodynamic state of the brain called the resting state. The BOLD signal is proportional to the oxy- and deoxyhemoglobin ratio arising from the NVC response. Therefore, the BOLD signal is intrinsically ambiguous, reflecting a mixture of oxidative metabolism, and the blood flow and blood volume response. All of which can differ between regions, stimuli and individuals (Ances et al., 2008; Leontiev et al., 2013). However, calibrated fMRI can be used to disentangle several of these components, most importantly the cerebral metabolic rate of O_2 ($CMRO_2$), CBF and cerebrovascular reactivity (CVR) (J. J. Chen et al., 2008; J. J. Chen & Gauthier, 2021; Davis et al., 1998; Gauthier & Fan, 2019; Gauthier & Hoge, 2013). CVR is the hemodynamic response amplitude to a vasodilatory challenge, in this case hypercapnia. CO_2 is a potent vasodilator and the ability of blood vessels to dilate in response to it is an indication of vascular reserve (J. J. Chen & Gauthier, 2021; Liu et al., 2019; Mächler et al., 2016). Furthermore, as the vasodilatory response to CO_2 is mediated by nitric oxide (NO), which is also thought to be an important mediator of NVC (Hosford & Gourine, 2019; Iadecola, 2017; Magistretti & Allaman, 2015), CVR is an important physiological component of the BOLD response. By isolating these components, calibrated fMRI thereby provides many of the elements needed to investigate how regional gene expression from genetic atlases (Arnatkevičiūtė et al., 2019; M. J. Hawrylycz et al., 2012) reflects differences in energy pathway usage and NVC, especially when complemented by glucose metabolism maps from positron emission tomography (PET).

In addition, the network organization of the brain and the role different regions play within these networks may also be an important contributor to energy pathway profile. The BOLD signal can also be used to investigate these properties since temporal correlations between the signals in different regions is thought to be an indication of functional connectivity (Biswal et al., 1995; Boellaard et al., 2004; Cordes et al., 2001; Toro et al., 2008) and there is a large body of work using BOLD and graph theory to infer the role of regions within network architecture and hierarchy (Kitzbichler et al., 2009; Power et al., 2011; M. P. van den Heuvel & Sporns, 2013). The mathematical representation of brain networks in graph theory consists of nodes (which are neural elements, brain regions) and edges (which are connected neural units), whose connection matrix summarizes the organization of the coupling between these network units (Fornito et al., 2016; Muldoon et al., 2016; M. E. J. Newman & Barkema, n.d.). Using this type of representation allows the identification of central and important ROIs with strong influence on communication, integration, segregation, and global functioning of brain networks (M. P. Van Den Heuvel et al., 2010; Latora & Marchiori, 2001).

The spatial scale of human neuroimaging (0.5-2mm), as well as the physiological ambiguity of most imaging techniques (Tardif et al., 2015) makes linking imaging results to underlying molecular pathways challenging. However, transcriptional data is becoming more widely

available, allowing us to probe some of these underlying pathways. The Allen human brain atlas (AHBA) provides gene expression levels for around 20,000 genes at approximately 500 locations, mapped to the same anatomical space as human neuroimaging data. This enables the investigation of the link between neuroimaging markers of vascular and metabolic properties and the underlying transcriptomics to better understand the mechanisms at play. (M. J. Hawrylycz et al., 2012)

The primary goal of this project is to identify the distinctive gene expression profiles that characterize the spatial heterogeneity in vascular and metabolic properties at rest, and their link to brain regions with global and local centrality attributes. To do so, we used a partial least squares (PLS) multivariate statistical technique (Krishnan et al., 2011) to analyze the association between quantitative neuroimaging data and brain gene expression patterns in the Allen human atlas. Neuroimaging data includes PET measures of cerebral metabolic rate of glucose (CMRGlc) and calibrated fMRI measures of $CMRO_2$, CBF and CVR, all important determinants of the BOLD signal and brain physiology. The centrality measures were estimated from the resting state fMRI signal using graph theory metrics (M. P. Van Den Heuvel & Sporns, 2011). Gene enrichment and pathway analysis were used to investigate the biological and molecular processes associated with PLS components.

4.4 Materials and Methods

4.4.1 Subjects and multimodal data acquisitions

Nineteen right-handed healthy young subjects (mean ± SD age = 24.0 ± 4.3 y; 9 females) were recruited from the student community of local universities and underwent imaging acquisitions including anatomical MRI, RS BOLD fMRI, and gas-inhalation-based calibrated fMRI, all with a 3.0T GE Discovery MR750, and a RS FDG-PET with a GE Discovery PET/CT 690. Exclusion criteria included any history of chronic mental or physical illness, MRI or PET contraindications, possible pregnancy, and chronic respiratory disease. Ethics approval was obtained from the Comité Central d'Éthique de la Recherche. Written informed consent was provided by all subjects and both MRI and PET acquisitions were completed at the imaging suite of the PERFORM Centre. The participants were asked to avoid sugary, alcoholic, or caffeinated drinks for at least two hours prior to imaging, and to not have eaten any food for at least 4 hours before the acquisitions. Data acquisitions started by an anatomical MRI, followed by a 10-minute eyes-opened resting-state (RS) blood oxygen level-dependent (BOLD) fMRI, followed by an 18-minute gas-inhalation-based calibrated fMRI, and a 45-minute eyes-closed static RS 2-[fluorine-18]-fluoro-2-deoxy-D-glucose (18F-FDG) PET. There was a 60-minute gap between the calibrated fMRI and PET acquisitions (post-radiotracer-injection period) during which participants stayed in a RS condition in a calm environment.

Anatomical MRI data was acquired using a 3D sagittal T1-weighted (T1w) MPRAGE sequence with the following parameters: TE = 3.18 ms; TR = 4,500 ms; TI = 8,160 ms; flip angle = 12°; 256 × 256 acquisition matrix, 192 slices; 1 mm isovoxel. RS BOLD fMRI data were acquired with the following sequence parameters: length = 10 min; field of view (FOV) = (2,400 mm) × (240 mm); TR = 2,300 ms; TE = 30 ms; slice thickness = 3.5 mm.

4.4.2 Gas-inhalation-based calibrated fMRI

Calibrated fMRI data were acquired using a dual-echo pseudo-continuous arterial spin labeling (pCASL) sequence with the following parameters: TR = 4,150 ms; TE1 = 8.4 ms; TE2 = 30 ms; alpha = 90°; 4 mm × 4 mm in-plane resolution and 16 slices of 7 mm (1 mm slice gap) on a 64 × 64 matrix; post-labeling delay = 950 ms; flip angle of labeling pulse = 25°; tagging duration = 1.6

s. In addition, four M0 images were acquired with the same parameters except TR = 10,000 ms; TE = 8.4 ms.

Gas challenges were applied to evoke iso-metabolic changes in blood flow and BOLD signal, to estimate the calibration parameter M, corresponding to the maximum possible increase in BOLD signal from baseline (Hoge, 2012). A computer-controlled gas system was used to control gas concentration mixing and delivery to the subject in the MRI room. The respiratory and breathing data of each subject were sampled to constantly monitor participants' partial pressures of CO_2 (PCO_2), O_2 (PO_2), as well as their heart and respiration rates. Subjects were asked to breathe through their nose to ensure only expired gas was sampled in an indwelling nasal cannula. The first 4 minutes of acquisitions with medical air inhalation were considered as RS data. The acquisition continued with three functional runs, each including a different gas manipulation. During each gas manipulation run, a single two-minute block of gas was preceded and followed by a block of three minutes of medical air. The three gas manipulations used were: 80% O_2 (hyperoxia), 21% O_2 + 5% CO_2 + 74% N2 (hypercapnia), and 50% O_2 + 5% CO_2 + 45% N_2 (simultaneous hyperoxia/hypercapnia). End-tidal O_2 and CO_2 values were then selected manually from continuous partial O_2 and CO_2 respiratory traces acquired at 200 Hz. The first middle 10 breaths of the four-minute baseline period and the last 10 breaths of each two-minute gas-inhalation block was averaged as baseline and gas manipulation end-tidal values, respectively.

4.4.3 Anatomical MRI data preprocessing

For each subject, the T1w image was corrected for intensity non-uniformity with N4BiasFieldCorrection (Tustison et al., 2010) , distributed with ANTs 2.3.3 (Avants et al., 2008) RRID:SCR_004757, and used as T1w-reference throughout the workflow. The T1w-reference was then skull-stripped with a *Nipype* implementation of the antsBrainExtraction.sh workflow (from ANTs), using OASIS30ANTs as target template. Brain tissue segmentation of cerebrospinal fluid (CSF), white-matter (WM) and gray-matter (GM) was performed on the brain-extracted T1w using fast (FSL 6.0.5.1:57b01774, RRID:SCR_002823,(Y. Zhang et al., 2001)). Volume-based spatial normalization to standard space (MNI152NLin6Asym) was performed through nonlinear registration with antsRegistration (ANTs 2.3.3), using brain-extracted versions of both the T1w reference and the T1w template. The following template was selected for spatial normalization: *FSL's MNI ICBM 152 non-linear 6th Generation Asymmetric Average Brain Stereotaxic Registration Model* (Evans et al., 2012),RRID:SCR_002823; TemplateFlow ID: MNI152NLin6Asym).

4.4.4 Resting-state BOLD fMRI data preprocessing

For each subject, the following preprocessing was performed. First, a reference volume and its skull-stripped version were generated using *fMRIPrep* 21.0.1 ((Esteban, Markiewicz, et al., 2018); RRID:SCR_016216). Head-motion parameters were extracted using mcflirt (FSL 6.0.5.1:57b01774 (Jenkinson et al., 2002)). BOLD runs were slice-time corrected to 1.12s using 3dTshift from AFNI ((Cox & Hyde, 1997), RRID:SCR_005927). The BOLD time-series were resampled onto their original native space by applying the transforms to correct for head-motion. These resampled BOLD time-series will be referred to as *preprocessed BOLD*. The BOLD reference was then co-registered with 6 degrees of freedom to the T1w reference using mri_coreg (FreeSurfer) followed by flirt (FSL 6.0.5.1:57b01774 (Jenkinson et al., 2002)) with the boundary-based registration (Greve & Fischl, 2009) cost-function. Several confounding time-series were calculated based on the *preprocessed BOLD*: framewise displacement (FD) via absolute sum of relative motions (Power et al., 2014), relative root mean square displacement between affines,

(Jenkinson et al., 2002), DVARS and three region-wise global signals using *Nipype*. The three global signals are extracted within the CSF, the WM, and the whole-brain masks. Head-motion estimates were also placed within the confounds file. The confound time series derived from head motion estimates and global signals were expanded with the inclusion of temporal derivatives and quadratic terms (Satterthwaite et al., 2013). Frames that exceeded a threshold of 0.5 mm FD or 1.5 standardized DVARS were annotated as motion outliers. The BOLD time-series were resampled into standard space, correspondingly generating the *spatially-normalized, preprocessed BOLD runs*. Resampling was performed with *a single interpolation step* by composing all the pertinent transformations (i.e., head-motion transform matrices, susceptibility distortion correction when available, and co-registrations to anatomical and output spaces). Gridded (volumetric) resampling were performed using antsApplyTransforms (ANTs), configured with Lanczos interpolation to minimize the smoothing effects of other kernels (Lanczos et al., 1964). Non-gridded (surface) resampling was performed using mri_vol2surf (FreeSurfer).

4.4.5 ASL data preprocessing

The first ASL run with medical air inhalation was considered as RS data and it was used to estimate resting cerebral blood flow (CBF) maps, while the other three included specific gas challenges used for cerebrovascular reactivity and calibrated fMRI. For each subject and runs, the middle volume of the ASL timeseries was selected as the reference volume and the brain extracted using *Nipype*'s custom brain extraction workflow. Head-motion parameters were estimated using *FSL*'s mcflirt (Jenkinson et al., 2002). Next, ASLPrep 0.2.8 was used to write head-motion parameters to the ASL run's confound file. ASLPrep co-registered the ASL reference to the T1w reference using *FSL*'s flirt (Jenkinson & Smith, 2001), which implemented the boundary-based registration cost-function (Greve & Fischl, 2009). Co-registration used 6 degrees of freedom. The quality of co-registration and normalization to template was quantified using the Dice and Jaccard indices, the cross-correlation with the reference image, and the overlap between the ASL and reference images (e.g., image coverage). FD and DVARS are calculated using *Nipype* (Power et al., 2014) for each ASL run. ASLPrep summarizes in-scanner motion as the mean framewise displacement and relative root-mean square displacement. *ASLPrep* was configured to calculate CBF with Bayesian Inference for Arterial Spin Labeling (BASIL) (Woolrich et al., 2009), as implemented in *FSL* 6.0.3. All resampling in *ASLPrep* use a single interpolation step that concatenates all transformations. Gridded (volumetric) resampling was performed using antsApplyTransforms, configured with *Lanczos* interpolation (Lanczos et al., 1964).

A spatial mask was applied on preprocessed calibrated fMRI to remove large veins by identifying voxel with relative BOLD increases greater than 10% in the unsmoothed hypercapnia data. The large arteries exhibiting decreases in pre-T1-correction absolute CBF that were greater than 50 mL / (100 g) / min during O_2 inhalation were also masked out. A slab mask for each subject was defined by analyzing the temporal SNR of ASL signals and for each subject, and the uppermost with SNR drops greater than 50% were discarded from further analyses.

4.4.6 PET data preprocessing

PET images were reconstructed using an iterative 3D ordered subset expectation maximization (Kinahan et al., 1998) algorithm with all the corrections (scatter, random, dead time, attenuation, and normalization). A 3D point spread function (GEMS name = Sharp-IR) based on experimental measurements of point sources acquired in different positions within the 3D-PET FOV, was modeled and coded in a system matrix and projection space for the reconstruction scheme. The reconstructions were done on a 192 × 192 × 47 grid from 30 minutes of static images and on a 256

× 256 × 47 grid from six 5-minute frames, with a voxel size of 1.6 mm × 1.6 mm × 3.25 mm, and with 3D trans axial filter = ramp, FOV = 20 cm, centered at x = 5 cm and y = 5 cm, matrix size = 256 × 256. Reconstructed PET images together with T1w images were smoothed with a 3D gaussian kernel where FWHM = 2 mm isotropic using minc-toolkit ((Vincent et al., 2016); *mincblur* command) before being co-registered based on a multi-resolution strategy with 6 transformation parameters and the mutual information as a similarity measure (*minctracc* command). In the end, the PET images were brought to the *MNI152NLin6Asym* standard space using the same non-linear resampling strategy as for the BOLD images.

4.4.7 CMRGlc, $CMRO_2$, CBF, and CVR quantification and analysis

CMRGlc maps were estimated from FDG-PET data using standardized uptake value (SUV) ratios referenced to the pons (Minoshima et al., 1995). First, SUV maps were estimated as $\mathrm{SUV} = C_t/(\mathrm{ID}/w_t \times D)$ where C_t is the decay-corrected activity concentration in the tissue (in MBq/cc which can be converted to MBq/kg by dividing by tissue density 1 g/cc), ID is the injected dose (in MBq), and w_t is the subject's weight (in kg). $D = 2^{-\Delta_t/T_{1/2}}$ is a decay factor with Δ_t being the time elapsed between injection and scanning (approximately 1 hour), and $T_{1/2}$ is the half lifetime of the 18F-FDG radiotracer (6582 s). Then, SUV ratios (i.e., CMRGlc maps) were determined by normalizing SUV maps with mean uptakes in pons.

$CMRO_2$, and CBF, maps were estimated from gas-inhalation-based calibrated fMRI data. The perfusion and BOLD signals were isolated respectively from the series of first and second echoes in the ASL data using linear surround subtraction and addition methods (Aguirre et al., 2002). Absolute CBF maps in units of mL / (100 g) / min were determined from the perfusion signals using the procedure described in (J. Wang et al., 2003). The fractional changes in BOLD and CBF were computed for each gas manipulation by fitting a linear model to the respective signals with normalized regressors obtained from end-tidal respiratory data. Regressors were convolved with a single-gamma hemodynamic response function with parameters described in (Glover, 1999), and corrected by a time delay estimated from the average GM signal to account for the delay between the respiratory and neuronal signals. From the CBF maps, $CMRO_2$ maps were estimated as $CMRO_2 = CaO_2 \times CBF \times OEF$, where CaO_2 is the total arterial O_2 content estimated as the sum of O_2 bound to hemoglobin, and O_2 dissolved in plasma. CaO_2 was determined from PaO_2 from the averaged end tidal O_2 taken from the respiratory data (Piechnik et al., 2008). OEF was calculated using the GCM described in (Gauthier & Hoge, 2013) using in-house MATLAB scripts. $CMRO_2$, CBF, and OEF maps as well as the slab masks obtained during preprocessing were all resampled to the ICBM 2009a symmetric template space at a 4-mm isovoxel resolution. The resampling was done with cubic B-spline interpolations using ANTs (Avants et al., 2011) by composing a transform from subjects' native to subjects' T1w spaces with a transform from subjects' T1w space to the T1w space of the template. Once in the analysis template space, for each $CMRO_2$, CBF and OEF map, voxels with negative or null values were flagged to be discarded from all analyses. A global slab mask calculated as the intersection between all slab masks.

CVR maps were calculated as a ratio of the difference between the baseline BOLD signal and the BOLD signal during the hypercapnic challenge, divided by the change in expired PCO_2. ASL data were further analyzed to define a slab mask for each subject indicating the brain slices where temporal signal-to-noise-ratio drops were greater than 50%. In the end, CMRGlc, $CMRO_2$, CBF, and CVR maps, together with the slab masks were all resampled to the *MNI152NLin6Asym* standard spaces.

4.4.8 Brain masking and parcellation

All analyses were performed in the *MNI152NLin6Asym* standard in each method's native resolution. The Schaefer atlas with 200 regions was used to define cortical brain parcels. For $CMRO_2$, CBF and CVR maps only, slab masks were used to exclude voxels prior to applying the mean operator.

4.4.9 Functional connectivity analysis

The graph theory representation of brain networks provides a matrix of centrality metrics. We estimated Pearson correlation coefficients between pairs of regional timeseries from post-processed BOLD fMRI data for each subject. The post-processing strategy was applied using Nilearn version 0.9.0 and included a one-step linear regression of the following standardized confounds: full head motion estimates (i.e., translation/rotation + derivatives + quadratic terms + power2d derivatives; so, 24 parameters), full white matter and cerebrospinal fluid signals (i.e., averages + derivatives + quadratic terms + power2d derivatives; so, 8 parameters), global signal, discrete cosines transformation basis regressors to handle low-frequency signal drifts (i.e., for high-pass filtering), and full scrubbing regressors (with framewise displacement threshold of 0.2 mm, standardized DVARS of 3, and removal of segments shorter than 5 frames after accounting for time frames with excessive motion). During signal regression, regional BOLD signals were extracted by specifying a spatial filter with a 7 mm Gaussian kernel and a low pass filter with a cutoff of 0.09 Hz. A group-level Pearson correlation functional connectome was obtained by first applying the Fisher z-transformation to each correlation connectome, then taking the mean of the connectomes across subjects in the z-domain and applying the inverse Fisher z-transformation to the mean connectome. Network centralities were estimated from the thresholded group-level functional connectome, where ~22.5% of the strongest weights in absolute value were retained. To establish the matrix of network centralities, we considered four continuous graph metrics. On the one hand, two global centrality indices (reflecting network information integration): eigenvector centrality and global efficiency. On the other hand, two local centrality indices (reflecting network information segregation): clustering coefficient and local efficiency. Eigenvector centrality is a self-referential measure of centrality. Nodes have high eigenvector centrality if they connect to other nodes that have high eigenvector centrality (Golbeck, 2013). Global efficiency is the average inverse shortest path length in the network and is inversely related to the characteristic path length (Latora & Marchiori, 2001; Rubinov & Sporns, 2010; Strang et al., 2018). Local efficiency is the global efficiency computed on the neighborhood of the node and is related to the clustering coefficient (Rubinov & Sporns, 2010). The clustering coefficient is the fraction of triangles around a node and is equivalent to the fraction of the node's neighbors that are neighbors of each other (Latora & Marchiori, 2001; Rubinov & Sporns, 2010; Strang et al., 2018). These metrics were estimated using the Brain Connectivity Toolbox version 2019-03-03. The matrix of network centralities was constructed by the column-wise concatenation of vectorized centrality metrics for multivariate statistical analysis.

4.4.10 Microarray data and pre-processing

We used the regional microarray expression data of Allen Human Brain Atlas (AHBA, http://human.brain-map.org/) which consists of microarray expression of 20,737 genes, measured by 58,692 probes from 3702 spatially distinct tissue samples obtained from six healthy post-mortem brain (1 female, ages 24.0–57.0, 42.50 ± 13.38). Since only two of the six brains included samples from the right hemisphere and because of the inconsistent gene expression levels between cortical and subcortical regions, all the analyses were conducted on the cortical left hemisphere

grey matter nodes according to the Schaefer functional atlas. The micro array data were processed using the AHBA processing toolbox (https://github.com/BMHLab/AHBAprocessing). The summary of the pre-processing procedures applied to the data is outlined below and details can be found in (Arnatkevičiūtė et al., 2019). The microarray probes were first reannotated using data provided by (Arnatkevičiūtė et al., 2019) and probes not matched to a valid Entrez ID were discarded. The tissue samples annotated to the brainstem and cerebellum were removed from further analysis. The probes were filtered based on their expression intensity relative to background noise (Quackenbush, 2002), such that probes with intensity less than the background in >=50.00% of samples across donors were discarded. When multiple probes indexed the expression of the same gene, we selected the probe with the most consistent pattern of regional variation across donors (i.e., differential stability; (Richiardi et al., 2015)). The samples assigned to the hemisphere (left/right) and structural designations (cortex/subcortex) were provided in the ontology from the AHBA. The MNI coordinates of tissue samples were updated to those generated via non-linear registration using the ANTs (https://github.com/chrisfilo/alleninf). Samples were assigned to brain regions by minimizing the Euclidean distance between the MNI coordinates of each sample and the nearest surface vertex. Samples where the Euclidean distance to the nearest vertex was more than 2 standard deviations above the mean distance for all samples belonging to that donor were excluded (Arnatkevičiūtė et al., 2019). All tissue samples not assigned to a brain region in the atlas and those that were assigned to subcortical regions or the right hemisphere were discarded. Inter-subject variation was addressed by normalizing tissue sample expression values across genes using a robust sigmoid function (Fulcher et al., 2013) and rescaling the expression values to the unit interval. Expression values were then normalized across tissue samples using an identical procedure. Samples assigned to the same brain region were averaged separately for each donor and then across donors, yielding a regional expression matrix. Gene expression values were normalized across tissue samples using the same procedure. Scaled regional expression profiles were averaged across donors, resulting in a single matrix X with r rows corresponding to brain regions and g columns corresponding to 45,821 probes corresponding to the total of 15,634 genes.

4.4.11 PLS analysis

To identify the spatial transcriptional profiles across the whole genome associated with regional variation of metabolic and centrality biomarkers derived from neuroimaging data, partial least squares (PLS) regressions was used to rank the genes according to the degree of spatial alignment of their expression with the neuroimaging biomarkers, following (J. Y. Hansen et al., 2021). PLS is commonly used to find orthogonal singular vectors that explain the maximum covariance between a highly collinear input matrix, as in the brain transcriptome, and output matrix, like neuroimaging biomarkers. The method works by decomposing the centered and normalized cross-correlation matrices of input data and extracting left and right singular vectors (latent variable), as well as a diagonal matrix of ranked singular values that are proportional to covariances between the saliences. The strength of such correlation between input measures and effect size in this analysis was estimated using the ratio of the squared singular value to the sum of all squared singular values. The major latent variables used in subsequent analyses were chosen by employing a spatial autocorrelation-preserving permutation model called spin test. The null model for the spin test was constructed such that it disrupts the relationship between two topographic maps while maintaining their spatial autocorrelation (Markello & Misic, 2021). Using the spin test generated coordinates, the rows (brain regions) of neuroimaging data matrix were permuted 10,000 times. Then a null distribution of latent variables was obtained by applying the PLS analysis on the original gene expression matrix and the new permuted neuroimaging data matrix. The first singular

vectors related to latent variables with lowest p-values (< 0.05) were kept for further analysis. Left latent variables represent the extent to which each genes characterizes the correlation with the output matrix (neuroimage data) and are called gene weights, while the right saliences signify the degree to which each neuroimage biomarker contributes to the correlation with the gene matrix and are called the neuroimaging biomarker weights. By projecting the original data matrices on the left and right (significant) singular vectors, the relation between original gene expression level and biomarkers activity within each brain ROI were estimated and expressed as gene scores and brain scores respectively. The brain regions with positive scores show the amount of covariance between the gene with positive weights and neuroimaging biomarker with positive weights and vice versa for negative regions.

For the gene ranking analysis, we estimated the loading of each gene by measuring the Pearson's correlation between their original expression level and their gene scores. The square of these loadings represents the percentage of the variance shared between the original data and the PLS-derived score. The reliability of gene and neuroimaging data loadings was measured using bootstrapping. To do so the rows (brain regions) of the gene expression matrix (neuroimaging data) were randomly selected with replacement 10,000 times, and the PLS analysis was performed using the new bootstrapped gene expression matrix and the original neuroimaging data matrix. We note that the bootstrap ratios are highly correlated with gene (neuroimaging data) loadings. The robustness and the prediction strength of the PLS model were assessed by examining the correlation between gene scores and neuroimaging data scores using cross-validation. The PLS model was applied on a randomly selected training set of 75% of brain regions. The Pearson correlation between gene and neuroimaging data scores were estimated using left and right singular vector PLS results of the training set. For the remaining 25% randomly selected test set, the correlation between the gene and neuroimaging scores were measured using the training set PLS-derived singular vectors. This process was repeated 10,000 times and the significance of the results was assessed against the null model constructed by the spatial autocorrelation-preserving permutation of the neuroimaging data matrix for the same number of repetitions.

4.4.12 Gene enrichment analysis

In our analysis we scored the genes using the PLS-derived loadings, which reflect the correspondence between their spatial expression level and the parcel-wise variation of our independently measured neuroimaging data. To reduce the interpretation burden of inferencing on a long list of individual genes, we performed functional enrichment analysis, including cellular component (CC), molecular function (MF), biological process (BP), and Kyoto Encyclopedia of Genes and Genomes (KEGG) pathway analysis, on strongly contributing positive and negative genes with 50% most positive and negative loadings separately. We employed the open-access platform Metascape (https://metascape.org) for the enrichment analysis that integrates membership search, gene annotation, interactome analysis, and functional enrichment premised on over 40 separate knowledge bases via an integrated interface (Zhou et al., 2019) . Metascape utilizes the hypergeometric test and Benjamini-Hochberg false discovery rates (FDR) and multiple comparisons correction algorithm to identify significant terms. To address the issue of term redundancies pairwise similarities between any two enriched terms are computed based on a Kappa-test score (Cohen, 1960). The similarity matrix is then hierarchically clustered, and a 0.3 similarity threshold is applied to trim the resultant tree into separate clusters. Metascape chooses the most significant (lowest p-value) term within each cluster (Supplementary Data 4) to represent the cluster. We run Metascape with Min Overlap=3, P-value Cutoff=0.05, Min Enrichment=1.5

and further refines the results with FDR Cutoff 0.05 and represented the gene ontology (GO) and KEGG term with highest enrichment level.

In addition to gene enrichment analysis, a cell type analysis of the genes was performed using cell-specific aggregate gene sets across five human adult postmortem single-cell and single-nucleus RNA sequencing studies (Habib et al., 2017; Lake et al., 2018; M. Li et al., 2018; McKenzie et al., 2018; Y. Zhang et al., 2016). To do so, the ratio of genes in each of the seven cell types: astrocytes, microglia, oligodendrocyte precursors, oligodendrocytes, endothelial cells, excitatory neurons, and inhibitory neurons was calculated. The statistical significance of this analysis was assessed against a null distribution of ratios constructed by repeating the process 10,000 times on a set of random genes.

4.5 Results

4.5.1 Human resting-state neuroimaging-derived physio-metabolic and network centrality data

Figure 4.1 shows the average brain maps derived from resting-state neuroimaging data as well as their spatial intercorrelations. For the sake of concise discussion, we qualitatively distinguished between three types of maps as follows: (i) physio-metabolic maps including CMRGlc, $CMRO_2$, CBF, and CVR, (ii) network global centrality maps reflecting network integration and including global efficiency (GE) and eigenvector centrality (EC), and (iii) network local centrality maps reflecting network segregation and including local efficiency (LE) and clustering coefficient (CC).

When focusing on the physio-metabolic maps, we determined that overall, with only two exceptions, all spatial intercorrelations were significant, low and positive (magnitudes of about 0.4). The two exceptions were the very high correlation ($R = 0.98$) between $CMRO_2$ and CBF, and a lack of correlation ($R = 0.05$) between CMRGlc and CVR. In addition, we observed that all physio-metabolic maps showed maximum regional values within or in the vicinity of the precuneus. We also observed higher physio-metabolic values within regions of the default-mode and attentional networks, and the cuneus.

We observed significant high positive correlations (R of about 0.9) between the two global centralities (i.e., GE and EC), as well as between the two local centralities (i.e., LE and CC). Correlations between global and local centralities were non-significant (R of about -0.1 with GE, and R of about 0.02 with EC). High values of global centralities could be observed within the precuneus and regions of the default-mode network, whereas values of local centralities were highest within medial regions of the visual cortex and within paracentral regions.

All physio-metabolic maps, except for CVR, were significantly positively spatially correlated with network global centrality (R of about 0.4 with GE, and about 0.3 with EC). All physio-metabolic maps were not significantly correlated with network local centrality except for CMRGlc and CC which showed an $R = -0.22$.

4.5.2 Partial least squares analysis relating gene expression and neuroimaging data

Figure 4.2 summarizes the results of PLS analyses relating gene expression (AHBA) data to physio-metabolic and network centrality neuroimaging data. We determined (Figure 4.2.a.) that two latent variables were significant and together they accounted for about 85% of the shared covariance between neuroimaging and gene expression data. We further uncovered (Figure 4.2.b.) that distinct sets of neuroimaging biomarkers contributed to the gene score patterns of each latent

variable. We found that all physio-metabolic maps except CVR, together with both local centrality maps (but not the global centrality maps) equally contributed (i.e., their loadings were of comparable magnitudes) significantly to the pattern of gene scores of the first latent variable. Concerning the second latent variable, CMRGlc, CBF, and GE showed significant negative loadings, while LE and CC were both significantly positive. Interestingly, although the third latent variable (accounting for about 7.5% of the shared covariance) was not significant, it was the first one with EC and CVR as significant components, in addition to a significant contribution of the other global network variable GE.

Figure 4.2c also shows the spatial pattern of gene and neuroimaging scores for the three latent variables. We observed that the first latent variable captured all global features of both the resting physio-metabolic and network centrality maps. In this latent variable, regions of the occipital lobe showed both highly positive gene scores and neuroimaging scores. For the second latent variable, positively scored regions (from both gene and neuroimaging score patterns) were mostly present in visual, somatosensory and auditory regions (i.e., within sensory networks), whereas negatively scored regions were mostly in parietal, temporal, and frontal regions (i.e., within higher order cognitive networks). For the third latent variable, we observed a concordance of negative loadings for gene scores and global centrality measures in somato-motor regions, whereas positively scored regions throughout the rest of the brain mainly reflected regions with high CVR values (see also supplementary Figure 4.7).

To confirm the patterns identified in the combined physio-metabolic and network centrality analyses, complementary analyses were performed on physio-metabolic and network properties in isolation. Supplementary Figure 4.8 details the results of a PLS analysis relating the physio-metabolic data in isolation to gene expression data, while Supplementary Figure 4.9 relates network centrality data to gene expression data. There we show how two distinct latent variables are used to discriminate between CMRGlc, $CMRO_2$, CBF on one side and CVR on the other, while global centralities and local centralities are also represented in distinct latent variables. These two additional analyses and the similar spatial patterns observed therefore confirm our findings detailed in Figure 4.2.

4.5.3 Gene enrichment analyses

Gene enrichment analyses were performed to determine the gene ontology (GO) of biological, cellular, molecular processes and pathways associated with genes with the highest positive and negative loadings (absolute-magnitude-top-50% genes). Figures 3, 4 and 5 detail the gene enrichment biological and pathways results for latent variables 1, 2 and 3 respectively.

For the first latent variable (Figure 4.3), significantly enriched GO biological processes (Figure 4.3.a.) included localization, metabolic and signaling. Localization processes included transmembrane transport of potassium, calcium and carboxylic acid, while significant metabolic processes included histone H3-K9 demethylation, macromolecule deacylation and phosphatidylinositol metabolism. Enrichment of genes associated with intracellular receptor signaling was also identified. Enriched pathways (Figure 4.3.b.) included phosphatidylinositol signaling, ABC transporters, as well as several important signaling pathways that together contribute in various cellular functions such as cell proliferation, differentiation and vascular regulation (Harper & Lograsso, 2001; Sassone-Corsi, 2012), including calcium, cGMP-PKG (cyclic guanosine monophosphate dependent protein kinase G) ,cAMP (cyclic adenosine monophosphate) and MAPK (mitogen-activated protein kinase) pathways.

For the second latent variable (Figure 4.4), we focused on the results for the negative genes, reflecting both resting physio-metabolic and global network centrality data (CMRGlc, CBF, and GE). Results for the positive component are consistent with results from the centrality-only analyses detailed in Supplementary Figure 4.18 and Supplementary Figure 4.19. We found that enriched biological processes (Figure 4.4.a.) included phosphatase regulation and the electron transport chain (metabolic GO), detoxification of inorganic compound and L-glutamate import (localization GO), regulation of AMPA (α-amino-3-hydroxy-5-methyl-4-isoxazolepropionic acid) receptor activity, calcium channel regulation, regulation of excitatory postsynaptic potential, and the gamma-aminobutyric acid (GABA) signaling pathway (signaling GO). Enriched pathways (Figure 4.4.b) included synaptic pathways (glutamatergic, GABAergic, dopaminergic, and serotonergic), signaling pathways (cAMP, neurotrophin, PPAR and endocannabinoid), as well as gap junction and long-term potentiation pathways.

For the third latent variable (Figure 4.5), we summarize the results for the negative reflecting the contribution of both global network centralities. Results for the contribution of CVR, reflected in the positive components are consistent with the results of the latent variable 2 in the physio-metabolic only analysis detailed in Supplementary Figure 4.16. We found that the most enriched biological processes (Figure 4.5.a.) belonging to the metabolic GO included oxidative phosphorylation, electron transport chain, as well as fatty acid beta-oxidation and carboxyl group binding. We also found cellular homeostasis, transcription related and major histocompatibility complex (MHC) protein complex GO processes. Finally, enriched pathways (Figure 4.5.b) included multiple metabolic pathways such as propanoate (carbohydrate metabolism), valine, leucine, and isoleucine degradation, amino acids metabolism, oxidative phosphorylation, pentose phosphate and glycolysis/gluconeogenesis (glucose metabolism).

Figure 4.6 summarizes the results of cell-type enrichment analysis in the gene sets previously analyzed for the first three latent variables. We determined (Figure 4.6.a.) that the positive genes of the first latent variable (associated with CMRGlc, $CMRO_2$, CBF, LE, and CC) were preferentially expressed in excitatory and inhibitory neurons, astrocytes, and oligodendrocyte precursors (ordered from highest to lowest ratio). We also found (Figure 4.6.b.) that the negative genes of the second latent variable (associated with CMRGlc, CBF, and GE) were significantly expressed in all cell types, with the order of preferential expression going from excitatory and inhibitory neurons, endothelial cells, microglia, astrocytes, oligodendrocytes to oligodendrocyte precursors. Finally, we found (Figure 4.6.c.) that the negative genes of the third latent variable (associated with GE and EC) were preferentially expressed in oligodendrocytes, astrocytes, endothelial cells, microglia, excitatory and inhibitory interneurons (i.e., all cell types but oligodendrocyte precursors). It is interesting to highlight the dichotomy between the gene sets associated with CMRGlc, $CMRO_2$ and CBF, which were primarily preferentially expressed in neurons, while cell-type patterns were more complex for centralities. For example, while global centralities were preferentially expressed in cells involved in supporting neurons in the negative component of the third latent variable (i.e. Figure 4.6.c.), the negative component of the second latent variable, also associated with GE, was preferentially expressed in neurons. This is also consistent with the connectivity alone analysis showing that the global centrality metrics were more associated with a neuronal pattern of gene expression. Finally, local centralities were associated with oligodendrocytes in the positive component of latent variable 2. This is also consistent with the centrality alone cell-type analysis (Supplementary Figure 20). (Figure XXX). Finally, we note that our observations remained mostly unchanged when performing cell-type

enrichment with different gene thresholds between 25%, 50%, or 100% of genes making up a gene set (see supplementary Figure 4.13).

For completeness, full machine-readable tables are provided in appendices for all previous gene enrichment analyses. We also provide the results of gene and cell-type enrichments corresponding to the PLS analysis relating the physio-metabolic data (alone) to gene expression data (supplementary Figure 4.14, Figure 4.15, Figure 4.16, and Figure 4.17) as well as to the PLS analysis relating the network centrality data (alone) to gene expression data (supplementary Figure 4.18, Figure 4.19, and Figure 4.20), which are consistent with the combined approach detailed here.

4.6 Discussion

In this paper, we employed multivariate statistical PLS technique and rich microarray data from the AHBA, to investigate the gene expression profiles underlying spatial patterns in cortical physio-metabolic measures and both local and global centrality metrics. Exploration of the spatial relationships between these measurements demonstrated relationships between all calibrated fMRI variables, as well as between all baseline variables (CBF, $CMRO_2$ and CMRGlc). However, CVR was not related to CMRGlc, reflecting the fact that CVR represents a measure of vascular reserve unrelated to baseline glucose consumption. Network centrality metrics (GE and EC) were correlated with baseline vascular and metabolic properties, while local centrality metrics were not related to any physio-metabolic variables. PLS analysis of the relationship between regional transcriptional information and neuroimaging metrics yielded two significant latent variables. The first reflected global relationships with a positive component associated with resting physio-metabolic features and local centrality measures. This latent variable was predominantly associated with important signalling components of cellular function. The second latent variable had a negative component reflecting resting physio-metabolic properties and global centrality, as measured by global efficiency. This latent variable was associated with synaptic and neurotransmitter pathways, as well as the electron transport chain. Spatial patterns are consistent with a differential relationship between gene expression and neuroimaging markers in primary sensory and motor regions versus in higher function areas. Finally, we explored the significant metrics associated with the negative component of the third latent variable and show that this component, which reflects the contribution of both global centrality metrics is associated with genes involved in the oxidative metabolism of glucose, demonstrating the high metabolic cost of integration in highly connected regions. Cell type analysis demonstrated a pattern whereby components associated with resting physio-metabolic data were associated with more neuronal expression, whereas centrality measures had a more mixed pattern, with some latent variables reflecting neuronal and some glial contributions.

4.6.1 Spatial relationships between physio-metabolic and network features

Our parcel-wise correlation analysis between physio-metabolic data showed that all calibrated fMRI metrics were spatially correlated, likely due to the fact that CVR and CBF are part of the model used to determine $CMRO_2$ (Gauthier & Hoge, 2013). CMRGlc showed the highest spatial correlation with CBF and least spatial correlation with CVR. The relationship between CMRGlc and CBF reflects the fact that CBF is also a baseline variable and is highly regulated to meet the energy needs of neurons (M. Li et al., 2018), while CVR is a dynamic variable that depends on vascular reserve and vasodilation rather than the baseline state of the brain (J. J. Chen & Gauthier, 2021).

Correlation analysis of the centrality measures confirmed the dichotomy of brain parcels based on global and local centrality features. Collectively, these patterns delineate a ventromedial–dorsolateral axis, separating brain regions into segregated networks with short path connections linking pairs of more peripheral nodes as well as long range intra module connections that support functional integration (de Reus & van den Heuvel, 2013; M. P. van den Heuvel & Sporns, 2013). Our results are consistent with the resting state functional connectivity literature showing that regions identified as the most central nodes using global efficiency and eigenvector centrality measures have strong spatial correspondence mainly with longer-range and functional connector hubs regions (M. P. Van Den Heuvel et al., 2009; Zuo et al., 2012). Hub regions are distributed throughout the brain, are involved in integrating diverse specialized functional modules and play a critical role in information processing and communications (Fulcher & Fornito, 2016). Brain hub regions also have been shown to have low clustering coefficient, as well as high centrality levels ("Centrality and Hubs," 2016; M. P. Van Den Heuvel et al., 2010).

The spatial correlation between centrality metrics and physio-metabolic information showed that higher regional physio-metabolic values overlapped with hubs regions characterized by high global centrality metrices. Among physio-metabolic data, CVR had the least spatial correlation with both global and local centrality metrics, reflecting its dependence on dynamic features of the vasculature rather than baseline properties. The fact that CVR was poorly correlated with all centrality metrics also indicates that these metrics are likely to be robust to biases related to blood volume and vascular reserve, at least in this young and healthy population. The other baseline physio-metabolic data had a higher positive correlation with global efficiency, which particularly accounts for network integration, and a slightly lower correlation with eigenvector centrality, which reflects network connectomics. These spatial relationships support the higher metabolic demand of hubs, consistent with other combined functional connectivity and metabolism studies (Liang et al., 2013; Palombit et al., 2022; D. Tomasi et al., 2013).

4.6.2 Link between gene expression and neuroimaging

PLS analysis using all neuroimaging data demonstrated two significant latent variables. The positive components of the first identified genes associated with resting physio-metabolic values and local centrality metrics. This is interesting given the higher spatial correlation of these physiological metrics with global centrality indicators. These genes may however reflect the common vascular and metabolic features of locally connected areas. In contrast, the negative component of the second latent variable reflects the genes associated with the physiological properties of global centrality, with a strong influence of CMRGlc and global efficiency, and a lesser influence of CBF. This component likely reflects the unique costs associated with high global centrality, especially in terms of processes with high metabolic costs. While not significant overall, some components of the third latent variables were thought worthy of note as they highlight these relationships in novel ways. This component reflects the differential gene expression information between the centrality metrics and physio-metabolic data. This is reflected by the sign of the loading elements, with significant contribution of negatively loaded global centrality metrics and positively loaded CVR data. These results imply that despite high spatial correlation between global centrality and physio-metabolic data, two distinctive set of gene control aspects of what is measured using centrality measures and physio-metabolic features. It also indicates that these aspects may be related more to dynamic signal features given the opposing relationship with CVR.

The results of the overall analysis are consistent with the results of the PLS analyses for physio-metabolic and centralities measures separately, presented in supplementary materials. Features such as the separation between global and local centrality components, as well as baseline variables versus CVR over separate latent variables are borne out by these separate analyses.

We used pathway and gene enrichment analysis to understand the biological functions that underlie the transcriptional components extracted by our PLS analysis. These results using the positive component of the first PLS latent variable, showed higher enrichment of genes attributed to cation and ion transmembrane transport, amino acid transport and several signalling pathways for the combined physio-metabolic and local centrality metrics data. This is likely linked to the crucial role of active transport in maintaining brain function and its high metabolic cost, as well as the central role of several signalling pathways in the existence of local networks. For example, calcium, cAMP and MAPK are all involved in many functions, including housekeeping (Brini et al., 2014; Iroegbu et al., 2021; L. Yang, 2018) and mitochondrial function (Cheng et al., 2010), two crucial aspects of brain function. Furthermore, these functions are linked to underlying aspects of metabolism, oxidative especially, and therefore also resting CBF. The genes that are enriched in this component show important overlap with the positive component of the first latent variable of the physio-metabolic alone PLS analysis, which is mostly related to the resting data (CBF, CMRGlc, $CMRO_2$). This component was also enriched in similar signalling pathways, as well as synaptic pathways such as long-term potentiation, GABAergic and dopaminergic synapses, similarly to the negatively loaded genes of the second PLS component of the combined analysis. These results are also concordant with results from Rachel et al. (Goyal et al., 2014) using a similar set of physio-metabolic data (CMRGlc, $CMRO_2$, CBF and OEF) showing higher enrichment genes related to synapse and signalling activities in regions with high baseline metabolism and CBF.

The negatively loaded genes from the second PLS component that were significantly related to both global centrality metrics and baseline physio-metabolic data were found to be involved in detoxification, signaling and synaptic function. We also found significant enrichment of different metabolic processes, including the electron transport chain and fatty acid metabolism. The enrichment of electron transport chain related genes is in line with the high metabolism of more centrally connected regions (Vértes et al., 2016), and the efficiency of oxidative metabolism. The enrichment of these genes also makes sense since this component is significantly related to CBF and CMRGlc, which also partly depend on oxidative phosphorylation of glucose metabolites and neurovascular coupling. The fatty acid metabolism genes on the other hand are likely related to phagocytosis, which has been shown to be involved in synaptic plasticity and homeostasis, as well as detoxification and potentially ketone body metabolism (Achanta & Rae, 2017; Galloway et al., 2019; Garcia Corrales et al., 2021). The presence of this alternate metabolic pathway could reflect the fact that participants were asked to fast for at least 4 hours, but some had not yet broken their overnight fast at the time of data acquisition. Finally, several synaptic and neurotransmitter pathways are represented in this PLS component, highlighting the high degree of neuronal activity and its tight regulation required for effective global centrality (Howarth et al., 2012; Ivannikov et al., 2010).

The negative component of the third PLS latent variable was predominantly related to the global centrality metrics. This latent variable was similar to the negative component of the second latent variable in the PLS analysis on the centrality metrics alone, with meaningful overlap in the genes enriched. Focusing on the combined physio-metabolic and centrality PLS analysis component, we identified enriched genes related to several metabolic pathways including the TCA cycle, the

pentose phosphate pathway, amino acid metabolism and the electron transport chain. This component highlights most strongly the metabolic cost of centrally connected regions (Fornito et al., 2019).

Synaptic activity requires coordinated gene expression which directs the synthesis of neurotransmitters, receptors and ion channels in the pre- and post-synaptic cell (Polleux et al., 2007; Ressler et al., 2002). In agreement with our findings, work by Richiardi et al. comparing brain imaging and gene expression data showed significant correlations between functional connectivity and the genes coding for ion channels and other synaptic functions such as neurotransmitters (Richiardi et al., 2015). However functional connectivity patterns are not distributed evenly. Instead, some regions contain highly connected neural elements and act as network hubs. have identified with higher cytoarchitectonic similarity and correlation with transcriptional data (Arnatkeviciute, Fulcher, Bellgrove, et al., 2021; G. Z. Wang et al., 2015). Other studies also identified higher expression of genes related to specific metabolic pathways in hubs, including purine metabolism, ATP biosynthesis and oxidative metabolism, in agreement with our own findings showing the costliness of long-range and densely connected brain networks and an important role of oxidative metabolism (Arnatkeviciute, Fulcher, Oldham, et al., 2021; Vértes et al., 2016).

Previous work using anatomical data and the Allen mouse gene expression data found distinctive gene expression signatures in neurons and oligodendrocytes. This cell type analysis suggested that regions expressing the neuron-enriched pattern have more incoming and outgoing connections with other regions, while the oligodendrocyte pattern was present in less connected regions (French et al., 2011; Voigt et al., 2022). Our cell type analysis is in partial agreement with this observation. In our combined analysis, PLS components related to resting physio-metabolic data were associated with an enrichment of neuronal-related genes. The relationship with centrality was however more complex with some latent variables associated with neuronal and some with glial, and especially oligodendrocyte, gene expression. For example, the positive component of latent variable 1 and the negative component of latent variable 2 were both associated with a more neuronal pattern, though one reflects local (latent variable 1) and the other global centrality (latent variable 2). The dominance of neuronal expression was higher for the negative component of latent variable 2, in accordance with the data from French et al., though the negative component of latent variable 3, reflecting both global centrality metrics was associated with a pattern consistent with oligodendrocyte gene enrichment. However, this may simply reflect the presence of different spatial patterns associated with global centrality with one reflecting a glial and another a neuronal component, which also corresponds to the metabolic cost of hub connectivity. This would be consistent with the centrality alone PLS analysis, which identified a local centrality component associated with oligodendrocyte expression and a global centrality component reflective of neuronal contributions (Supplementary Figure 4.20). Finally, the finding that CVR is more related to an oligodendrocyte pattern (positive component of latent variable 3, Supplementary figure 13c) is novel and somewhat surprising given that endothelial and neuronal signaling are thought to be most important in determining the amplitude of CVR (Fathi et al., 2011; Horvath et al., 1994). More studies are needed to understand this result.

4.6.3 Limitation

There are several limitations and considerations related to the present work that warrant further investigation. First, our results were obtained using only the AHBA atlas. However, the BrainSpan open-database (Miller et al., 2014) could also be used for cross-validation, sensitivity testing and

robustness analysis. Second, the AHBA atlas is based on six post-mortem human brains, aged between 24 and 57 years (mean age = 43 years), and sampled at approximately 500 locations in each hemisphere. In contrast, our neuroimaging data was acquired on 19 healthy young adults between 19 and 33 years (mean age = 23 years) and was sampled across 200 cortical parcels of a functional atlas covering the entire cortex. Hence, there were mismatches between gene expression and neuroimaging data related to the spatial resolution, sample size, and age range of the subjects. This is important when considering for instance that increasing risk of neurovascular dysfunction has been found to be associated with normal aging due in part to compromised cerebral energy metabolism, or structural/functional cerebral network integrity (Akiyama et al., 1997; Buckner et al., 2004; Morrison & Hof, 1997; Salat et al., 2004). Therefore, future studies should seek to use better matching and additional data for a more comprehensive analysis. Third, we only focused on the left hemisphere of the cerebral cortex when relating gene expression and neuroimaging data. We did so because only two brains out of six in the AHBA atlas included samples from the right hemisphere, and because of significant differences in the transcriptional signatures of the cortex, subcortex and cerebellum (Patania et al., 2019). Future studies could aim at providing a more complete picture of the association between gene expression and neuroimaging data by investigating the whole brain (both hemispheres, neo-cortex, cerebellum, and subcortical areas).

4.6.4 Conclusion

In conclusion, we found significant contribution of resting physio-metabolic feature in neuronal pre and post synaptic activity as well as signaling pathways. The global and local centrality metrics spatially segregated into two clusters of regions driven by two distinctive transcriptional profile. One densely connected with long-range linkage and another sparser with shorter connections. Our results support a reliance on oxidative phosphorylation to support the higher cost of synaptic functions in highly connected regions involved in integrating signals from long-range connections. Our cell-type analyses demonstrated the enrichment of neuronal transcriptional signatures related to resting physio-metabolic features and to some extent long-range connections. In contrast, locally-connected regions and, as a novel finding CVR, were found to be associated with a more oligodendrocyte enriched pattern. Overall, our analysis highlighted the link between central connectivity and high physio-metabolic cost, met predominantly through oxidative metabolism of glucose.

4.7 Figures

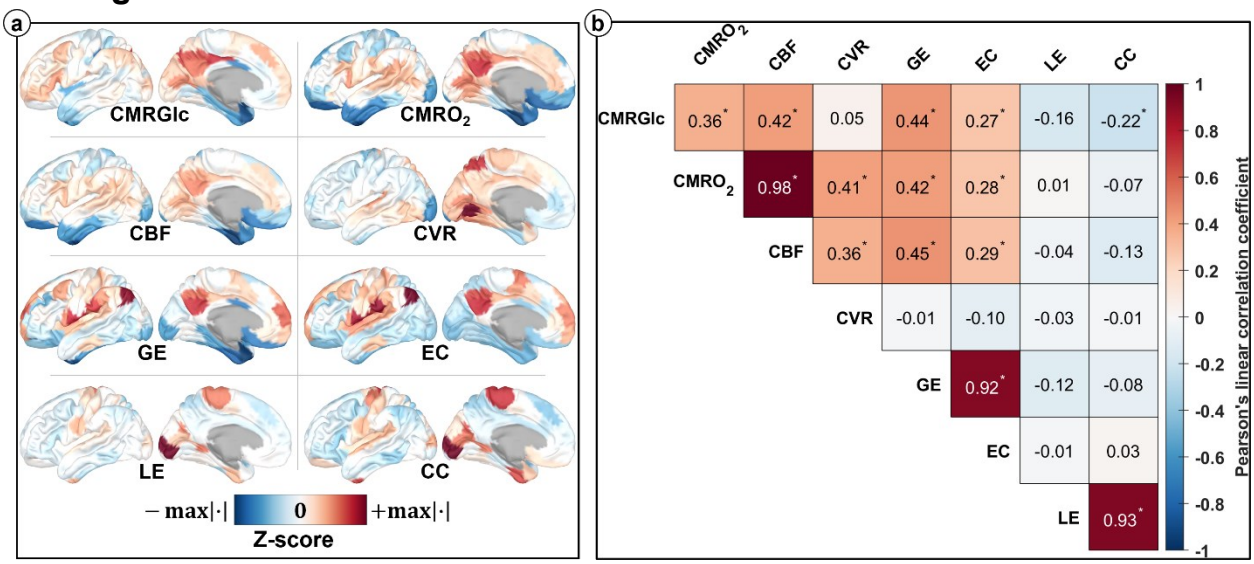

*Figure 4.1. Resting-state neuroimaging data derivatives. a. Average physio-metabolic (CMRGlc, $CMRO_2$, CBF, and CVR) and network centrality (GE, EC, LE, CC) brain maps estimated from 20 subjects. Data are shown for the left cerebral cortex only and projected on a semi-inflated (25%) mid-surface of the ICBM 2009c asymmetric brain template. Regional values were defined using the Schaefer 2018 7 networks atlas with 100 parcels in the left hemisphere. b. Pearson's linear correlation coefficients between neuroimaging brain maps. The * symbol indicates two-tailed* p*-values smaller than 0.05. CMRGlc: cerebral metabolic rate of glucose; $CMRO_2$: cerebral metabolic rate of dioxygen; CBF: cerebral blood flow; CVR: cerebrovascular reactivity; GE: global efficiency; EC: eigenvector centrality; LE: local efficiency; CC: clustering coefficient.*

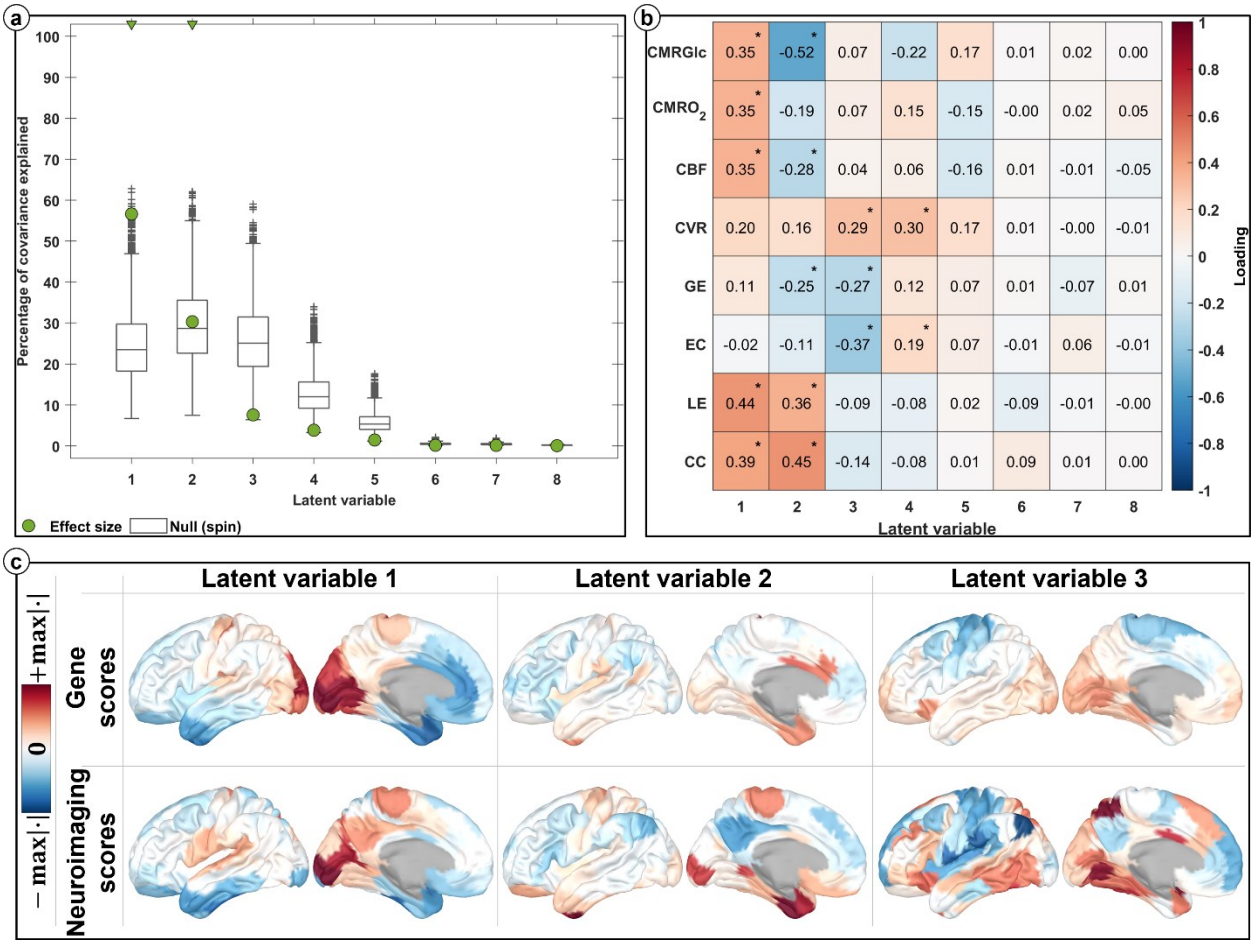

*Figure 4.2. Relating gene expression to resting-state neuroimaging data. PLS analysis was used to identify spatially covarying patterns of gene expression and neuroimaging biomarkers. a. Latent variables effect sizes (i.e., percentage of covariance explained between gene expression and neuroimaging data). A triangle on the top indicates right-tailed p-values smaller than 0.05 as obtained from spatial autocorrelation-preserving permutation testing. The box charts are the permuted effect sizes and represent median (line inside a box), 0.25 and 0.75 quantiles (bottom and top edges of a box, the distance between which is called interquartile range), outliers (defined as values away from the bottom or top of the box more than 150% the interquartile range), and nonoutlier minimum and maximum (bottom and top whiskers of a box). Note that significance is assessed on eigenvalue distributions and not effect size distributions. b. Neuroimaging loadings with respect to the pattern of gene scores for a particular latent variable are calculated as the Pearson's linear correlation coefficient between neuroimaging brain maps (indicated on the rows) and the PLS-derived pattern of gene scores for that latent variable. Latent variables are indicated on the columns by a number and ordered according to their accounted percentage of data covariance explained from highest to lowest. A * symbol indicates bootstrap-estimated 95% confidence intervals not including zero (i.e., reliable loadings). c. Latent variables gene and neuroimaging score distributions for the first three latent variables.*

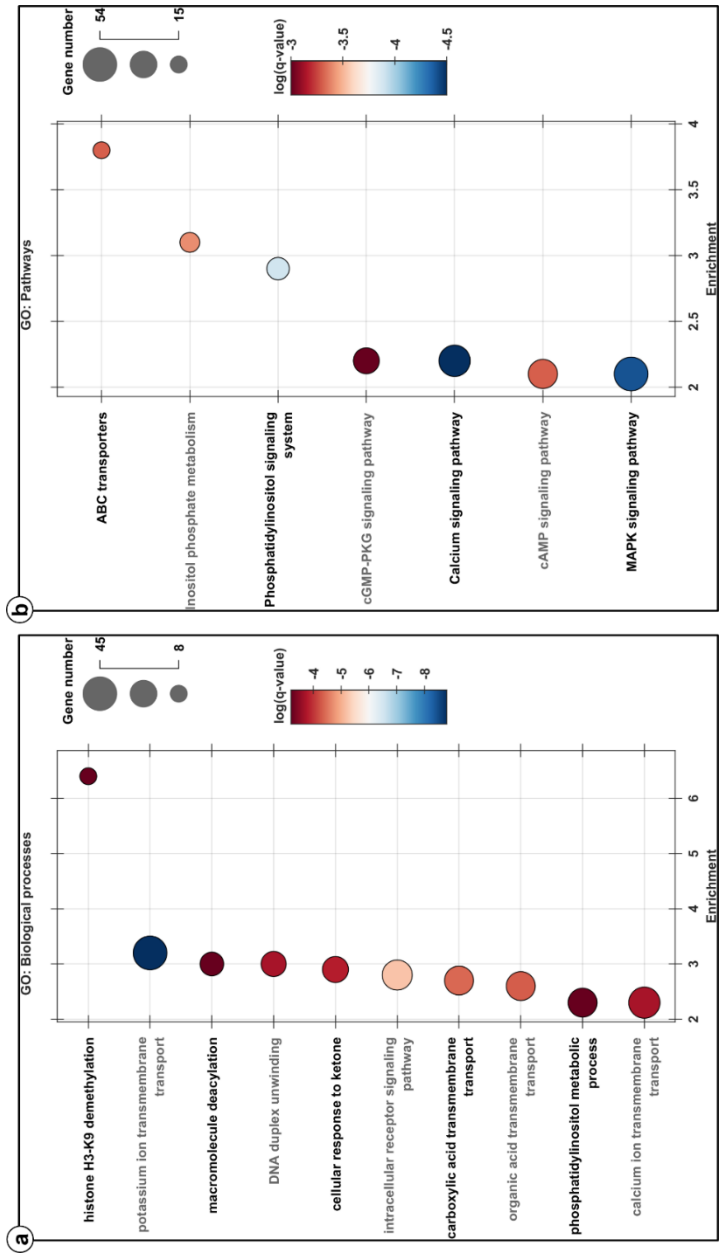

Figure 4.3. Enrichment analysis of the genes of latent variable 1 with highest (50%) positive loadings. A subset of significantly (i.e., positive false discovery rate smaller than 0.05) enriched gene ontologies (GOs) is shown. a. GO biological processes. b. GO pathways.

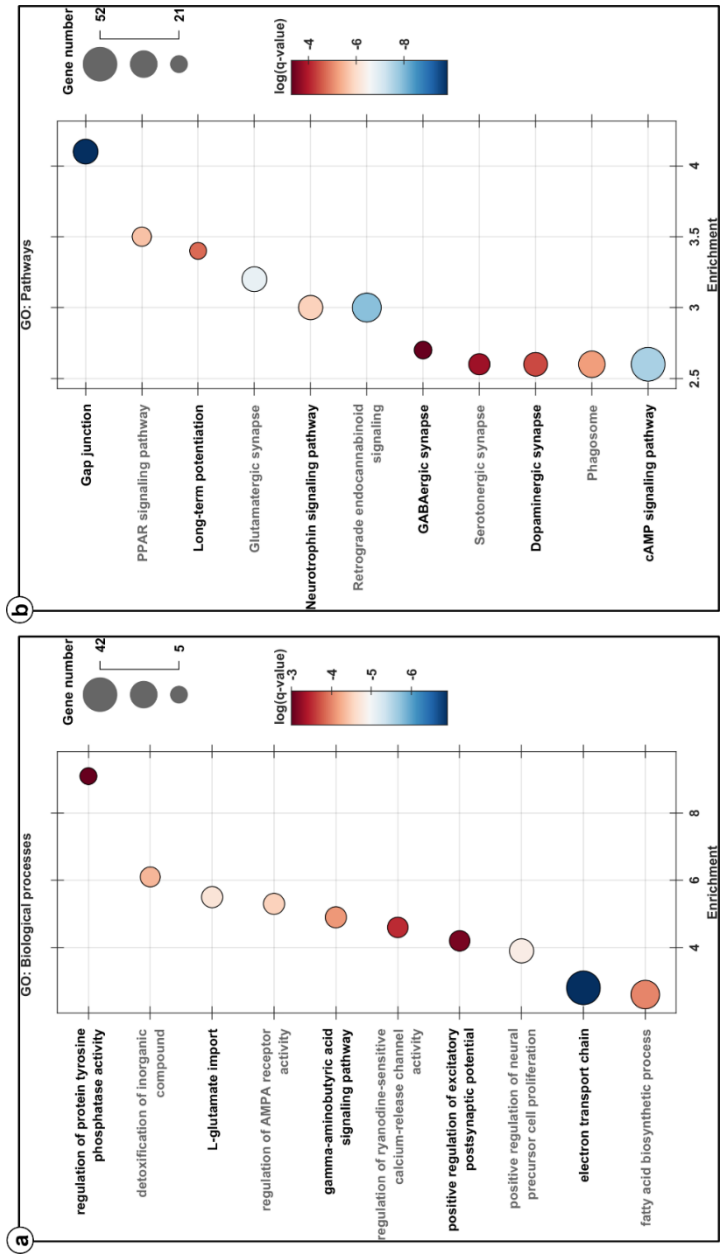

Figure 4.4. Enrichment analysis of the genes of latent variable 2 with highest (50%) negative loadings. A subset of significantly (i.e., positive false discovery rate smaller than 0.05) enriched gene ontologies (GOs) is shown. a. GO biological processes. b. GO pathways.

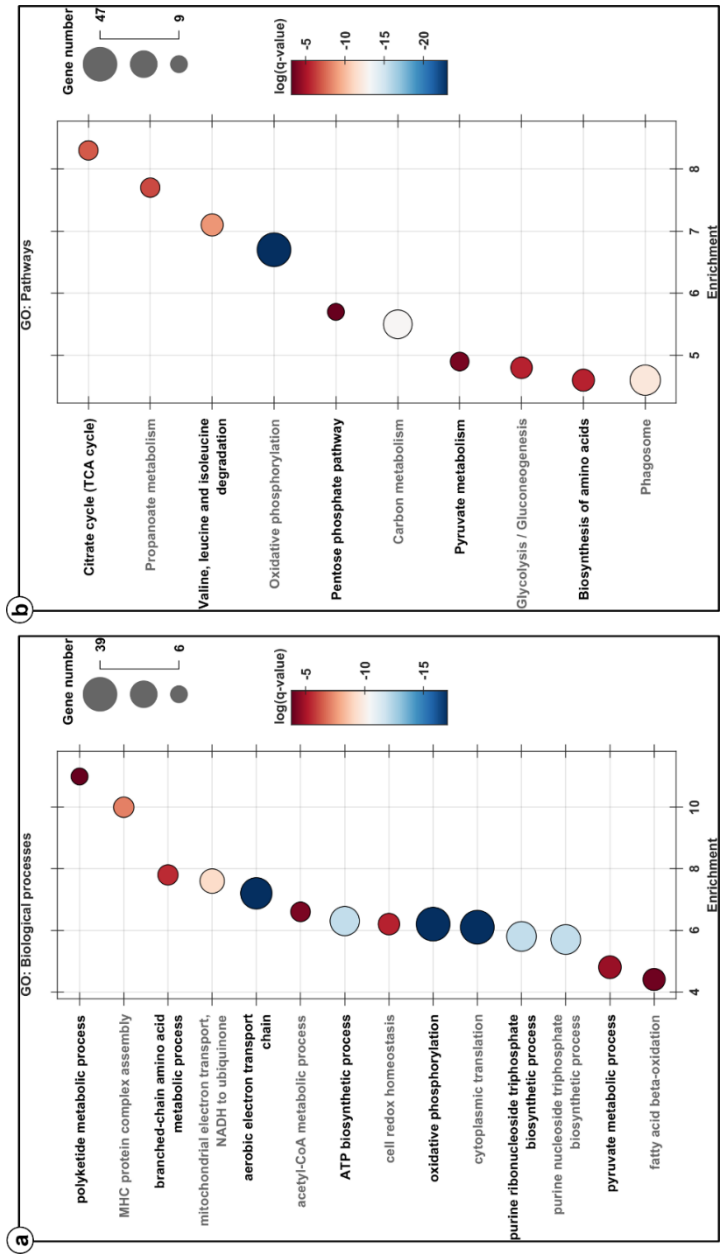

Figure 4.5. Enrichment analysis of the genes of latent variable 3 with highest (50%) negative loadings. A subset of significantly (i.e., positive false discovery rate smaller than 0.05) enriched gene ontologies (GOs) is shown. a. GO biological processes. b. GO pathways.

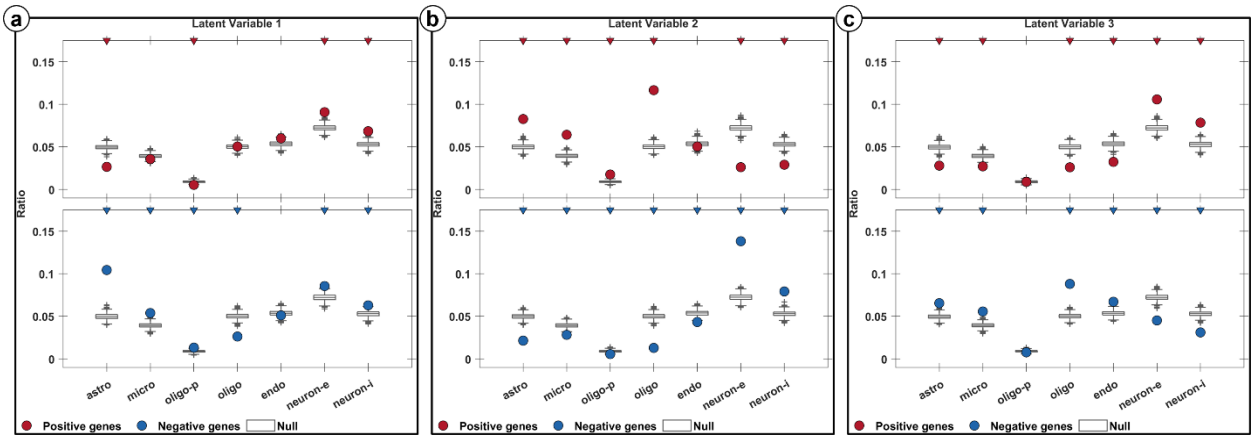

Figure 4.6. Cell-types deconvolution. The ratio of genes preferentially expressed in seven cell types is shown for the genes of latent variable 1 (a.), latent variable 2 (b.), and latent variable 3 (c.), using their highest (50%) positive (red) or negative (blue) loadings. A triangle on the top indicates positive false discovery rates smaller than 0.05 (i.e., significant ratios) as obtained from bootstrap resampling. The box charts are the null ratios and represent median (line inside a box), 0.25 and 0.75 quantiles (bottom and top edges of a box, the distance between which is called interquartile range), outliers (defined as values away from the bottom or top of the box more than 150% the interquartile range), and nonoutlier minimum and maximum (bottom and top whiskers of a box). Astro: astrocyte; micro: microglia; oligo-p: oligodendrocyte precursor; oligo: oligodendrocyte; endo: endothelial cells; neuron-e: excitatory neurons; neuron-i: inhibitory neurons.

4.8 Supporting Information

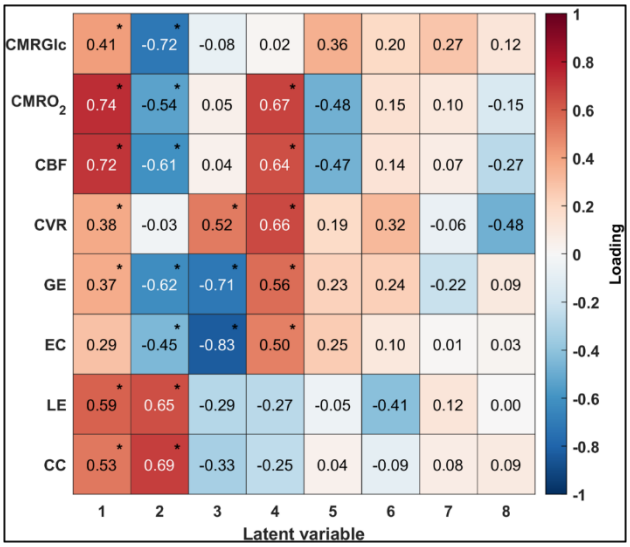

*Figure 4.7. Neuroimaging loadings with respect to neuroimaging scores. Neuroimaging loadings with respect to the neuroimaging scores of a particular latent variable are calculated as the Pearson's linear correlation coefficient between neuroimaging brain maps (indicated on the rows) and the PLS-derived pattern of neuroimaging scores for that latent variable. Latent variables are indicated on the columns by a number and ordered according to their accounted percentage of data covariance explained from highest to lowest. A * symbol indicates bootstrap-estimated 95% confidence intervals not including zero (i.e., reliable loadings). A high loading in absolute magnitude indicates that a particular neuroimaging biomarker highly contributes to the PLS-derived pattern of neuroimaging scores. We can observe how the first latent variable possessed (global) features of almost all neuroimaging biomarkers (except EC) whereas the other latent variables distinguished between different sets of neuroimaging biomarkers (e.g., the second latent variable distinguished between physio-metabolic and global centralities on one side, and local centralities on the other side).*

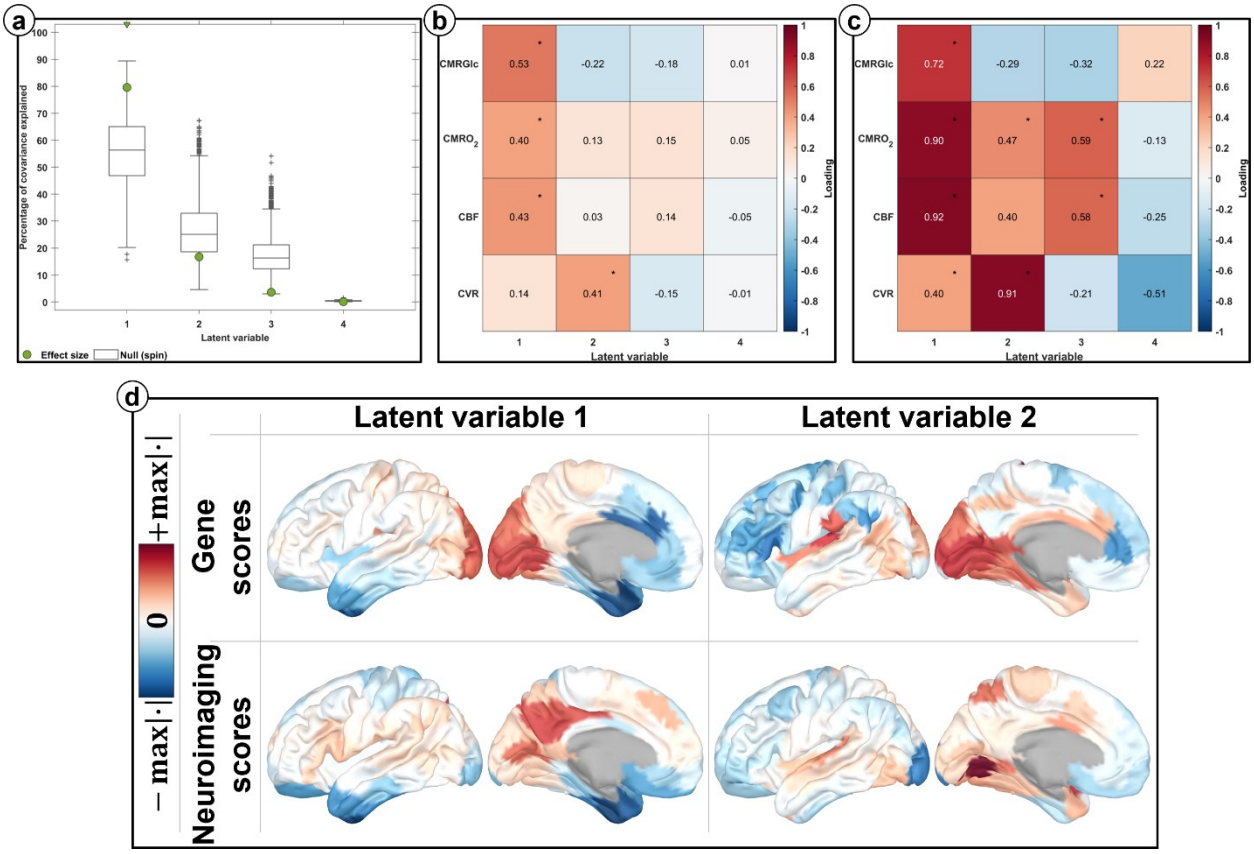

Figure 4.8. PLS analysis relating gene expression data to neuroimaging-derived physio-metabolic data. a. Latent variables effect sizes (i.e., percentage of covariance explained between gene expression and neuroimaging data). A triangle on the top indicates right-tailed p*-values smaller than 0.05 as obtained from spatial autocorrelation-preserving permutation testing. The box charts are the permuted effect sizes and represent median (line inside a box), 0.25 and 0.75 quantiles (bottom and top edges of a box, the distance between which is called interquartile range), outliers (defined as values away from the bottom or top of the box more than 150% the interquartile range), and nonoutlier minimum and maximum (bottom and top whiskers of a box). Note that significance is assessed on eigenvalue distributions and not effect size distributions. b. Neuroimaging loadings with respect to the pattern of gene scores for a particular latent variable are calculated as the Pearson's linear correlation coefficient between neuroimaging brain maps (indicated on the rows) and the PLS-derived pattern of gene scores for that latent variable. Latent variables are indicated on the columns by a number and ordered according to their accounted percentage of data covariance explained from highest to lowest. A * symbol indicates bootstrap-estimated 95% confidence intervals not including zero (i.e., reliable loadings). A high loading in absolute magnitude indicates that a particular neuroimaging biomarker highly contributes to the PLS-derived pattern of gene scores. c. Same as b. but loadings are with respect to patterns of neuroimaging scores. d. Latent variables gene and neuroimaging score distributions for the first two latent variables.*

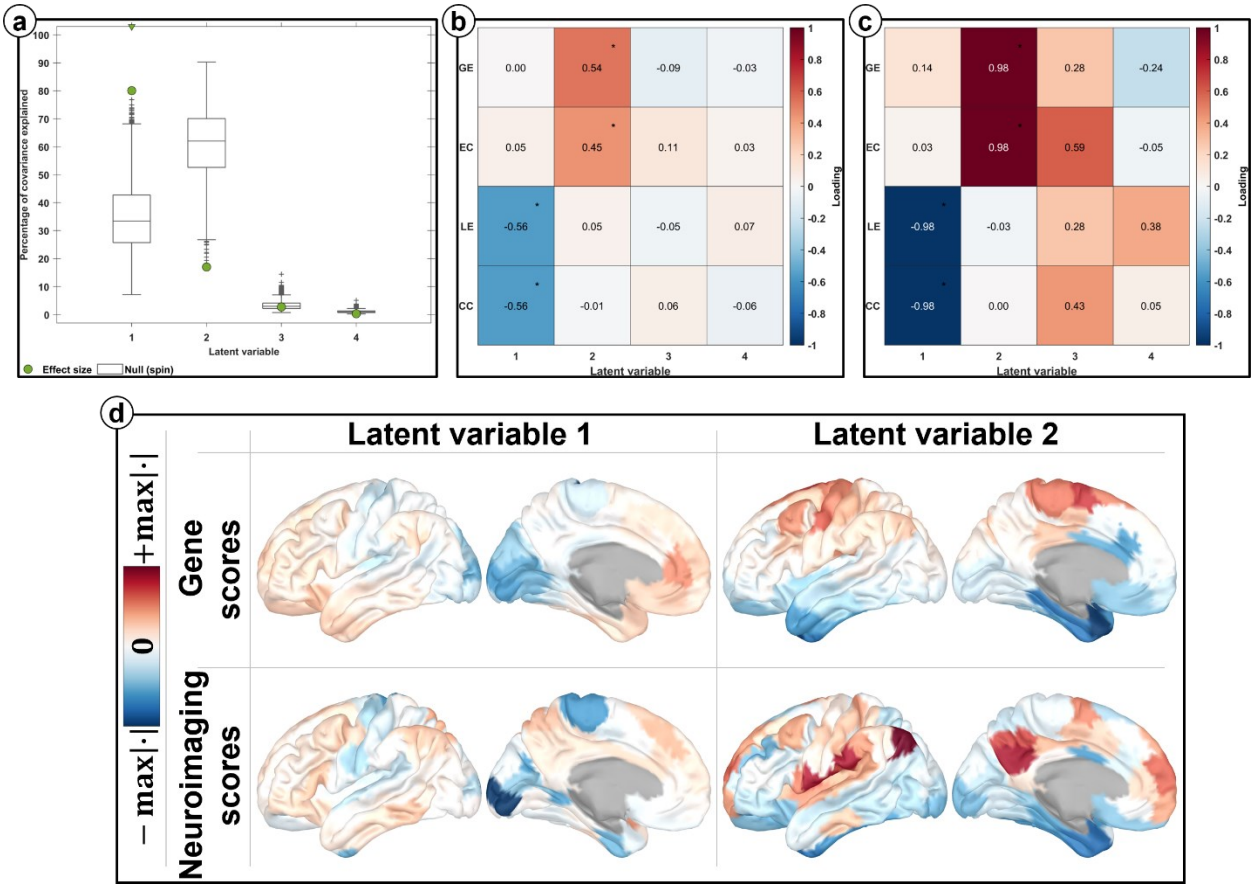

*Figure 4.9. PLS analysis relating gene expression data to neuroimaging-derived network centrality data. a. Latent variables effect sizes. A triangle on the top indicates right-tailed p-values smaller than 0.05 as obtained from spatial autocorrelation-preserving permutation testing. The box charts are the permuted effect sizes and represent median (line inside a box), 0.25 and 0.75 quantiles (bottom and top edges of a box), outliers (values outside the 150% the interquartile range), and nonoutlier minimum and maximum (bottom and top whiskers of a box). Significance is assessed on eigenvalue distributions. b. Neuroimaging loadings with respect to the pattern of gene scores for a particular latent variable are calculated as the Pearson's linear correlation coefficient between neuroimaging brain maps (indicated on the rows) and the PLS-derived pattern of gene scores for that latent variable. Latent variables are indicated on the columns by a number and ordered according to their accounted percentage of data covariance explained from highest to lowest. A * symbol indicates bootstrap-estimated 95% confidence intervals not including zero (i.e., reliable loadings). c. Same as b. but loadings are with respect to patterns of neuroimaging scores. d. Latent variables gene and neuroimaging score distributions for the first two latent variables.*

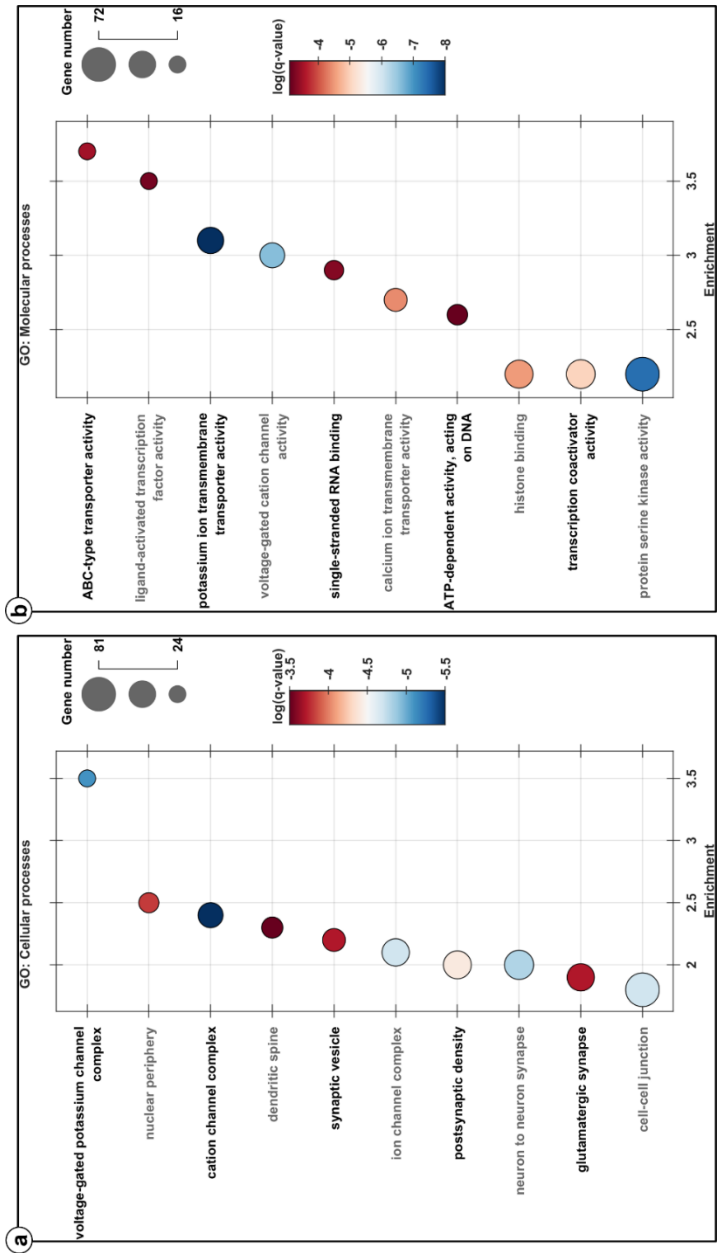

Figure 4.10. Enrichment analysis of the genes of latent variable 1 with highest (50%) positive loadings. A subset of significantly (i.e., positive false discovery rate smaller than 0.05) enriched gene ontologies (GOs) is shown. a. GO cellular processes. b. GO molecular processes.

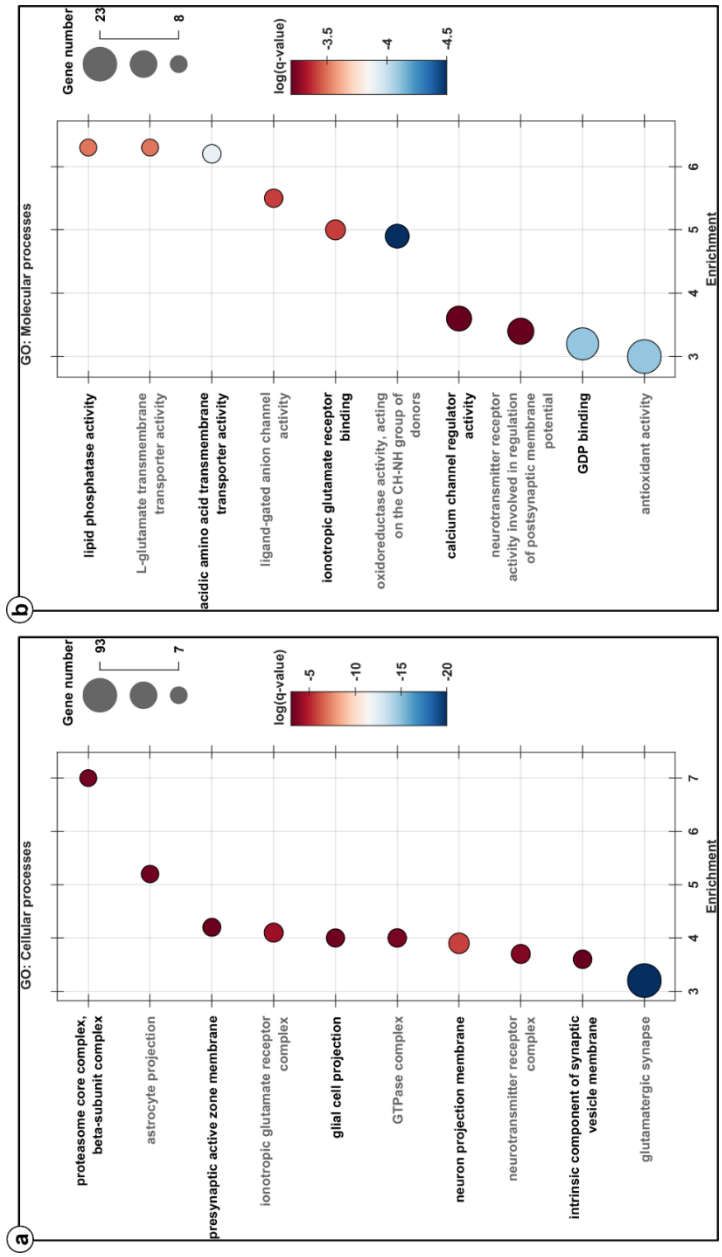

Figure 4.11. Enrichment analysis of the genes of latent variable 2 with highest (50%) negative loadings. A subset of significantly (i.e., positive false discovery rate smaller than 0.05) enriched gene ontologies (GOs) is shown. a. GO cellular processes. b. GO molecular processes.

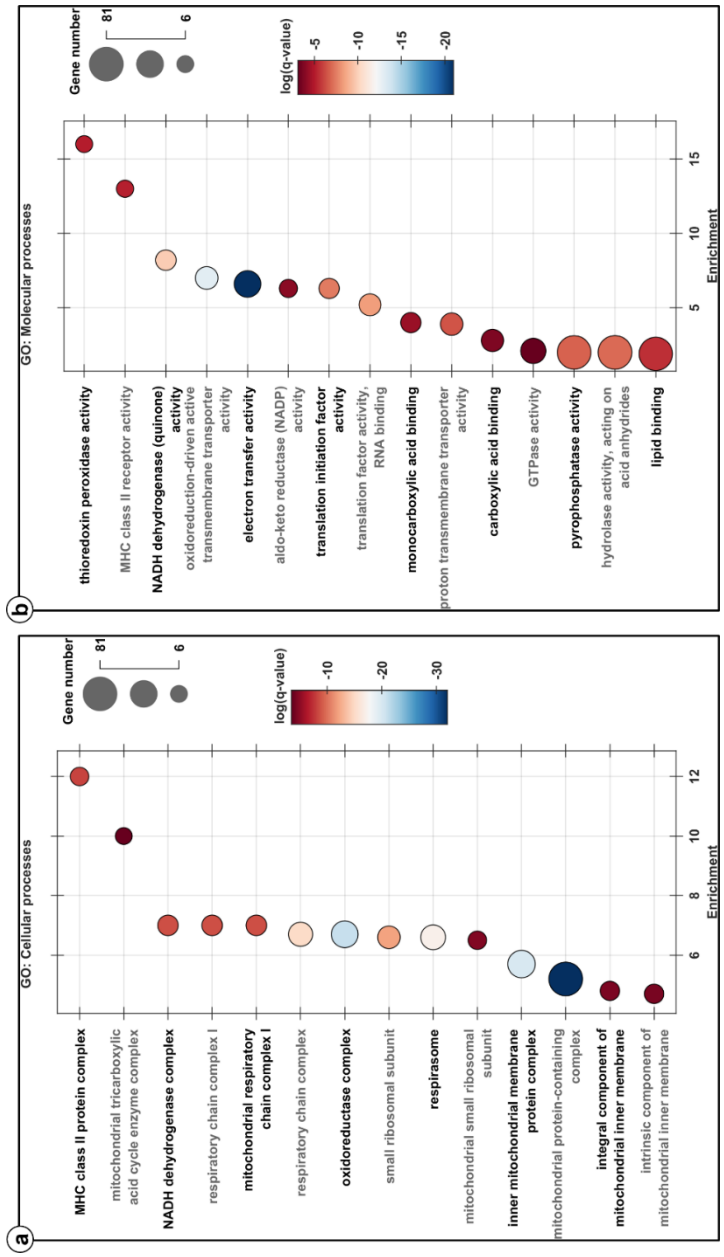

Figure 4.12. Enrichment analysis of the genes of latent variable 3 with highest (50%) negative loadings. A subset of significantly (i.e., positive false discovery rate smaller than 0.05) enriched gene ontologies (GOs) is shown. a. GO cellular processes. b. GO molecular processes.

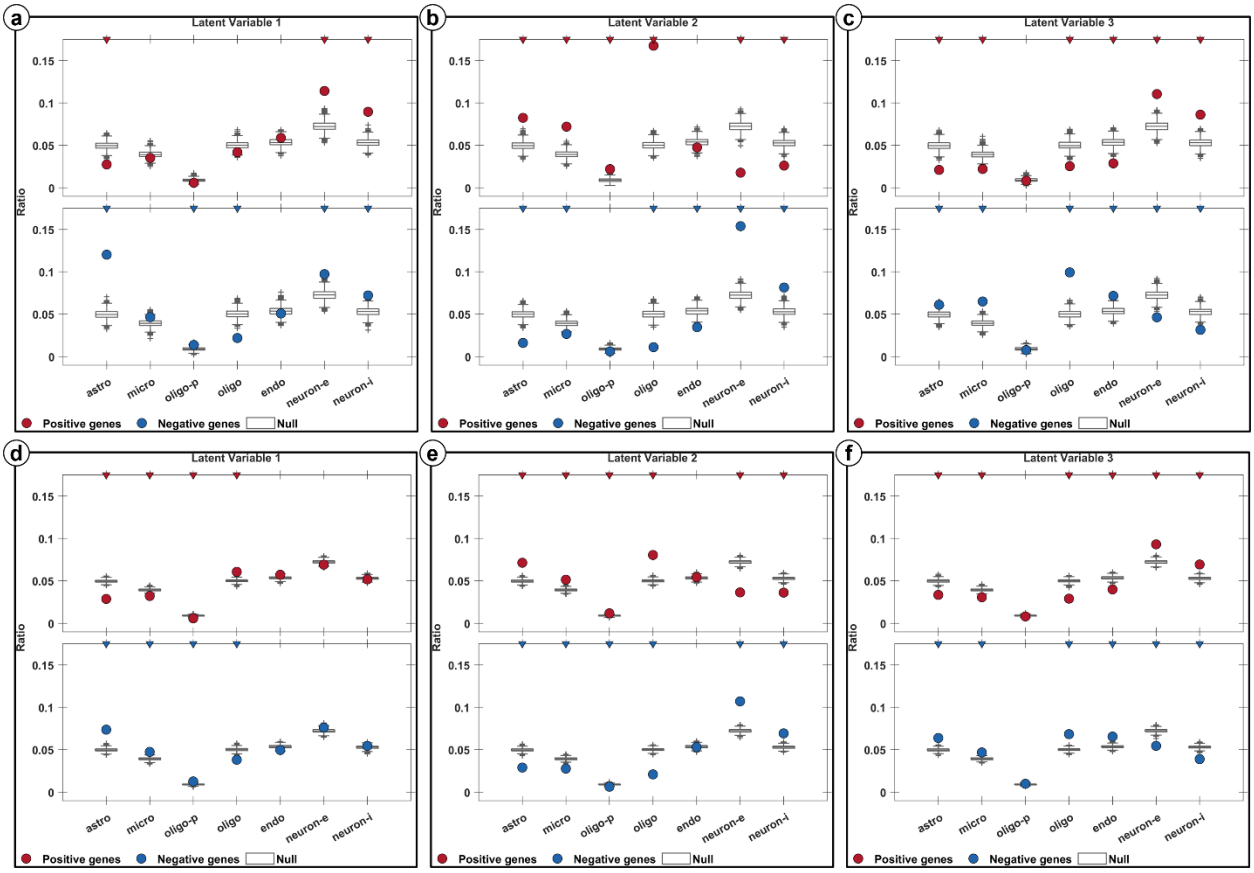

Figure 4.13. Influences of gene thresholds on cell-types deconvolution. The legends of the figures are the same as for Figure 4.6 which was for a threshold of 50%. Here a., b., and c. are for a threshold of 25% while d., e., and f. are for a threshold of 100%.

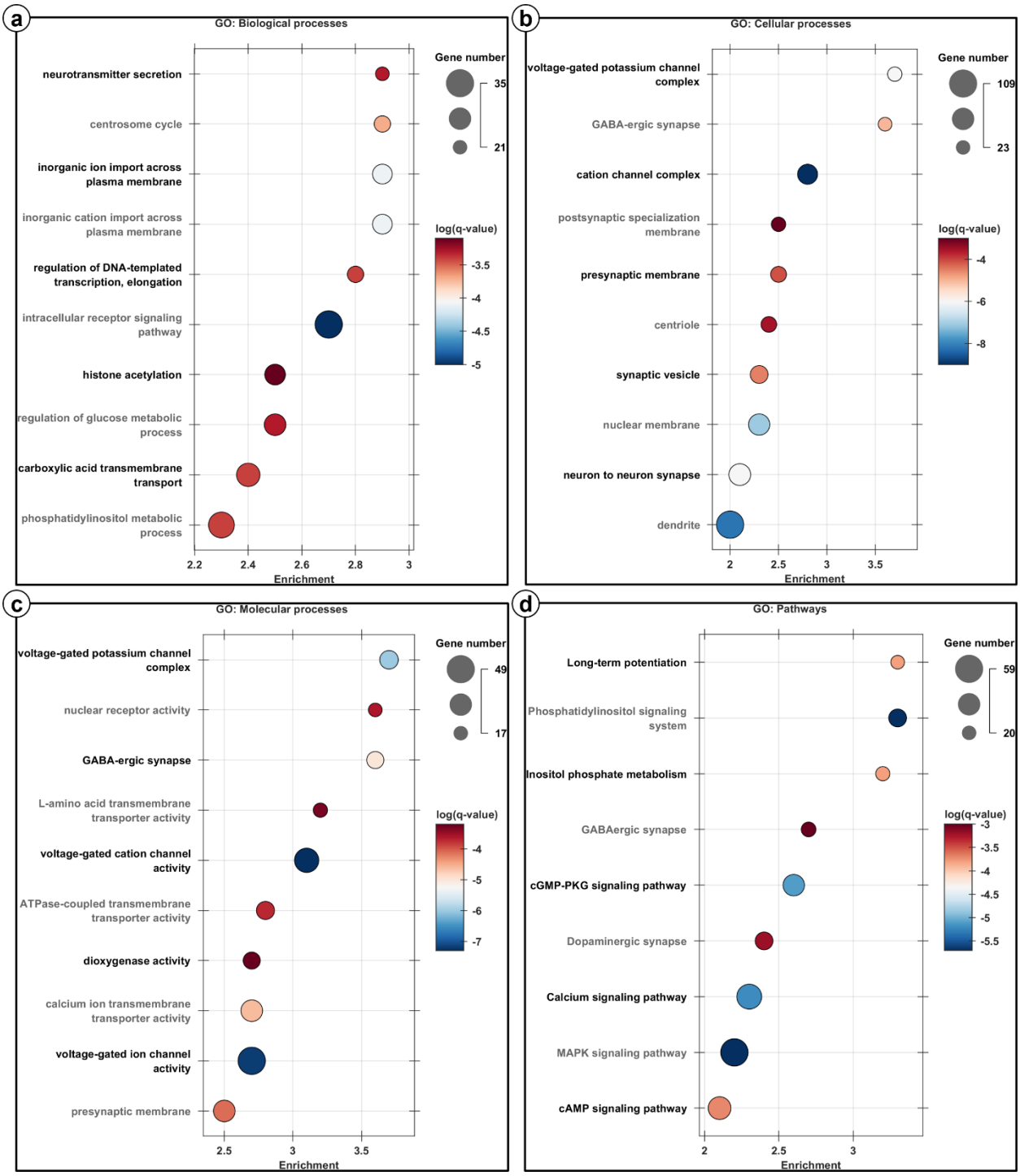

Figure 4.14. Enrichment analysis of the genes of latent variable 1 with highest (50%) positive loadings corresponding to the PLS analysis relating the physio-metabolic data (alone) to gene expression data. A subset of significantly (i.e., positive false discovery rate smaller than 0.05) enriched gene ontologies (GOs) is shown. a. GO biological processes. b. GO cellular processes. c. GO molecular processes. d. GO pathways.

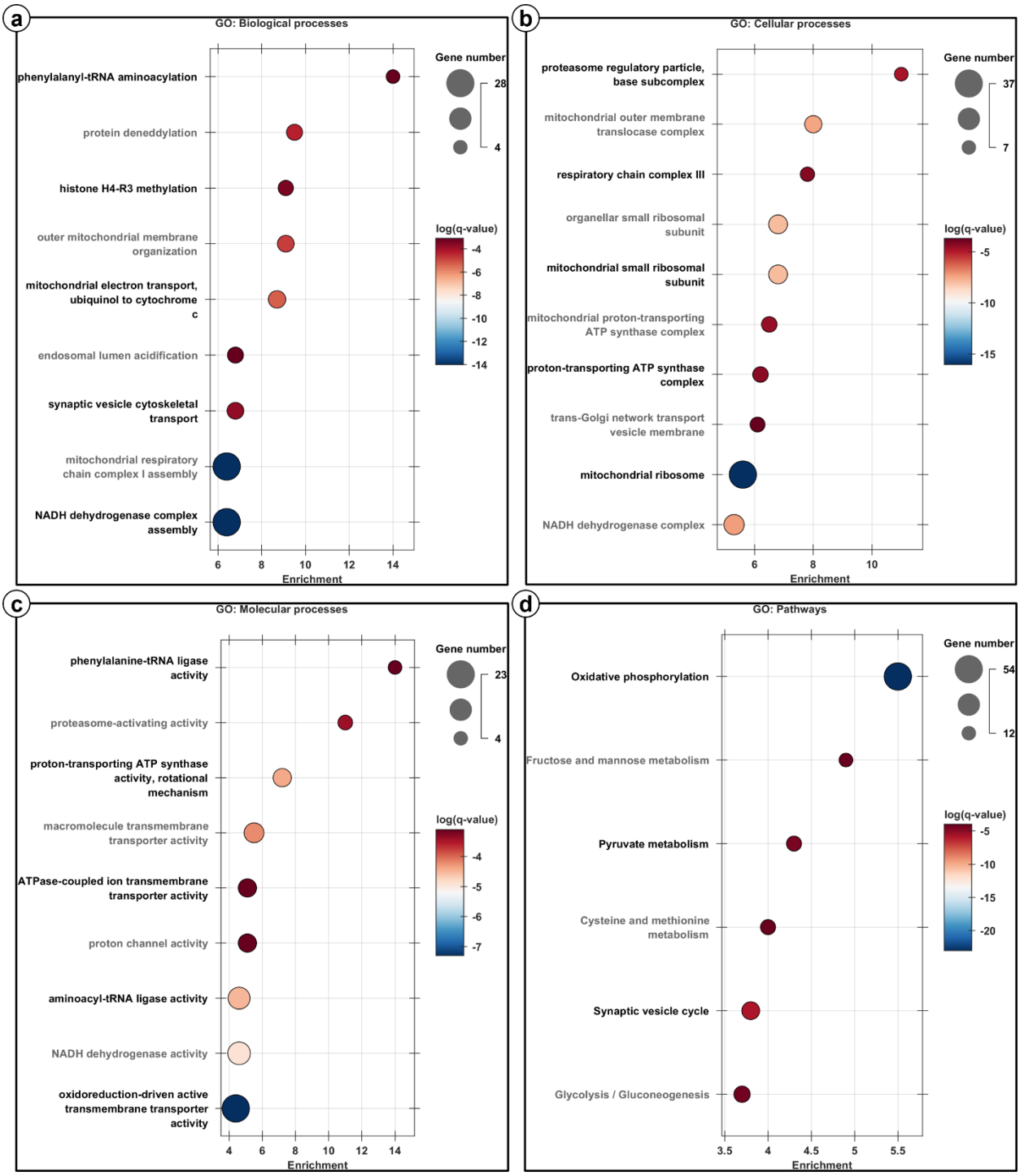

Figure 4.15. Enrichment analysis of the genes of latent variable 2 with highest (50%) negative loadings corresponding to the PLS analysis relating the physio-metabolic data (alone) to gene expression data. A subset of significantly (i.e., positive false discovery rate smaller than 0.05) enriched gene ontologies (GOs) is shown. a. GO biological processes. b. GO cellular processes. c. GO molecular processes. d. GO pathways.

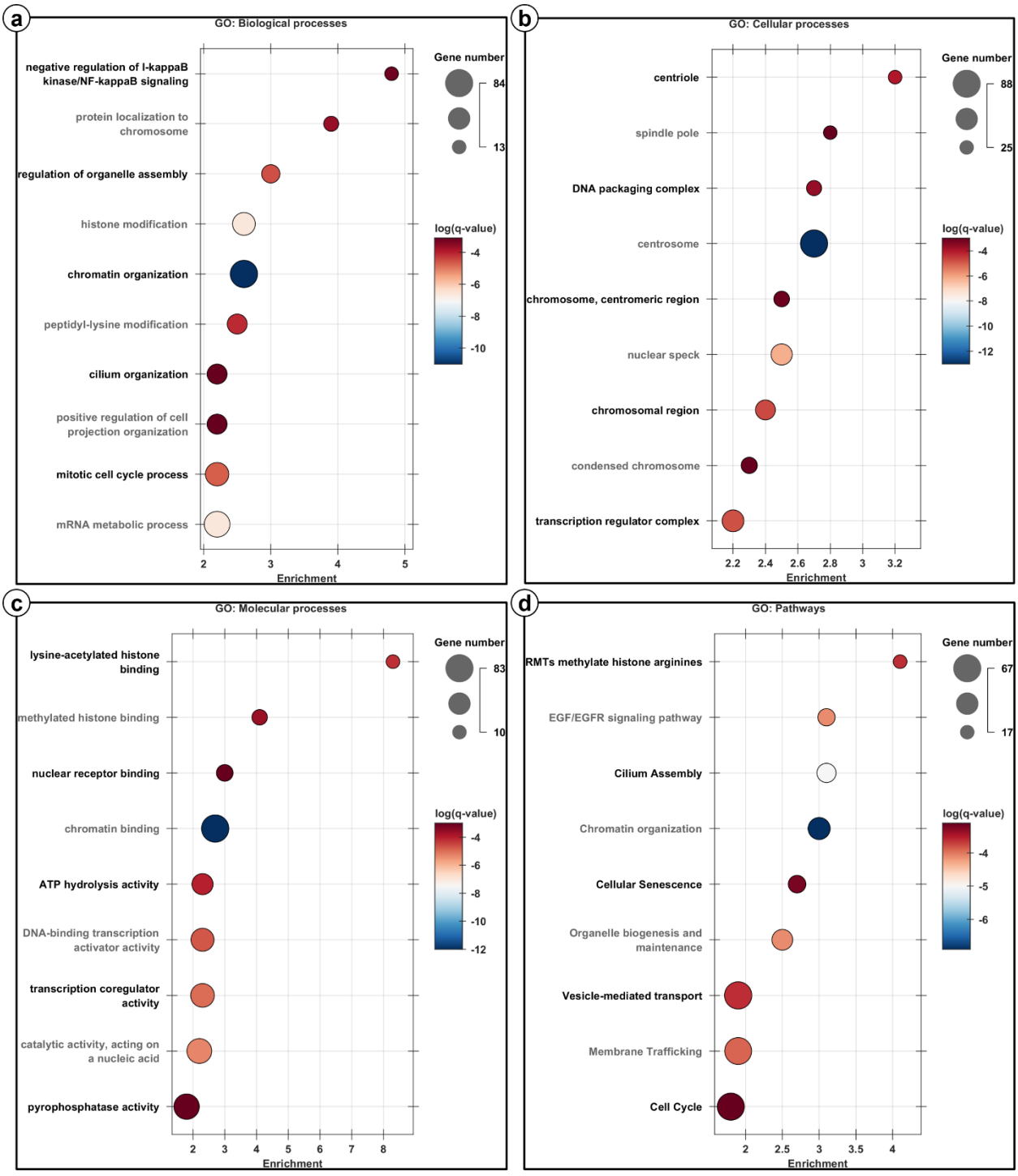

Figure 4.16. Enrichment analysis of the genes of latent variable 2 with highest (50%) positive loadings corresponding to the PLS analysis relating the physio-metabolic data (alone) to gene expression data. A subset of significantly (i.e., positive false discovery rate smaller than 0.05) enriched gene ontologies (GOs) is shown. a. GO biological processes. b. GO cellular processes. c. GO molecular processes. d. GO pathways.

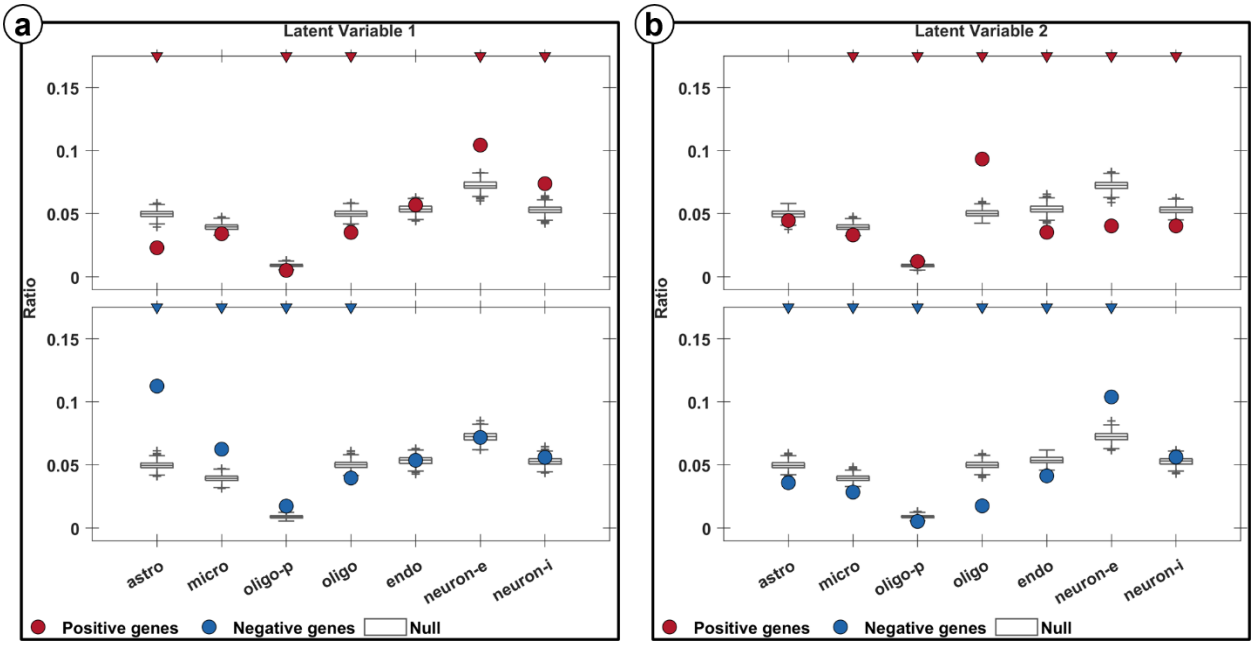

Figure 4.17. Cell-types deconvolution corresponding to the PLS analysis relating the physio-metabolic data (alone) to gene expression data. The ratio of genes preferentially expressed in seven cell types is shown for the genes of latent variable 1 (a.) and latent variable 2 (b.), using their highest (50%) positive (red) or negative (blue) loadings. A triangle on the top indicates positive false discovery rates smaller than 0.05 (i.e., significant ratios) as obtained from bootstrap resampling. The box charts are the null ratios and represent median (line inside a box), 0.25 and 0.75 quantiles (bottom and top edges of a box), outliers (values outside the 150% the interquartile range), and nonoutlier minimum and maximum (bottom and top whiskers of a box). Astro: astrocyte; micro: microglia; oligo-p: oligodendrocyte precursor; oligo: oligodendrocyte; endo: endothelial cells; neuron-e: excitatory neurons; neuron-i: inhibitory neurons.

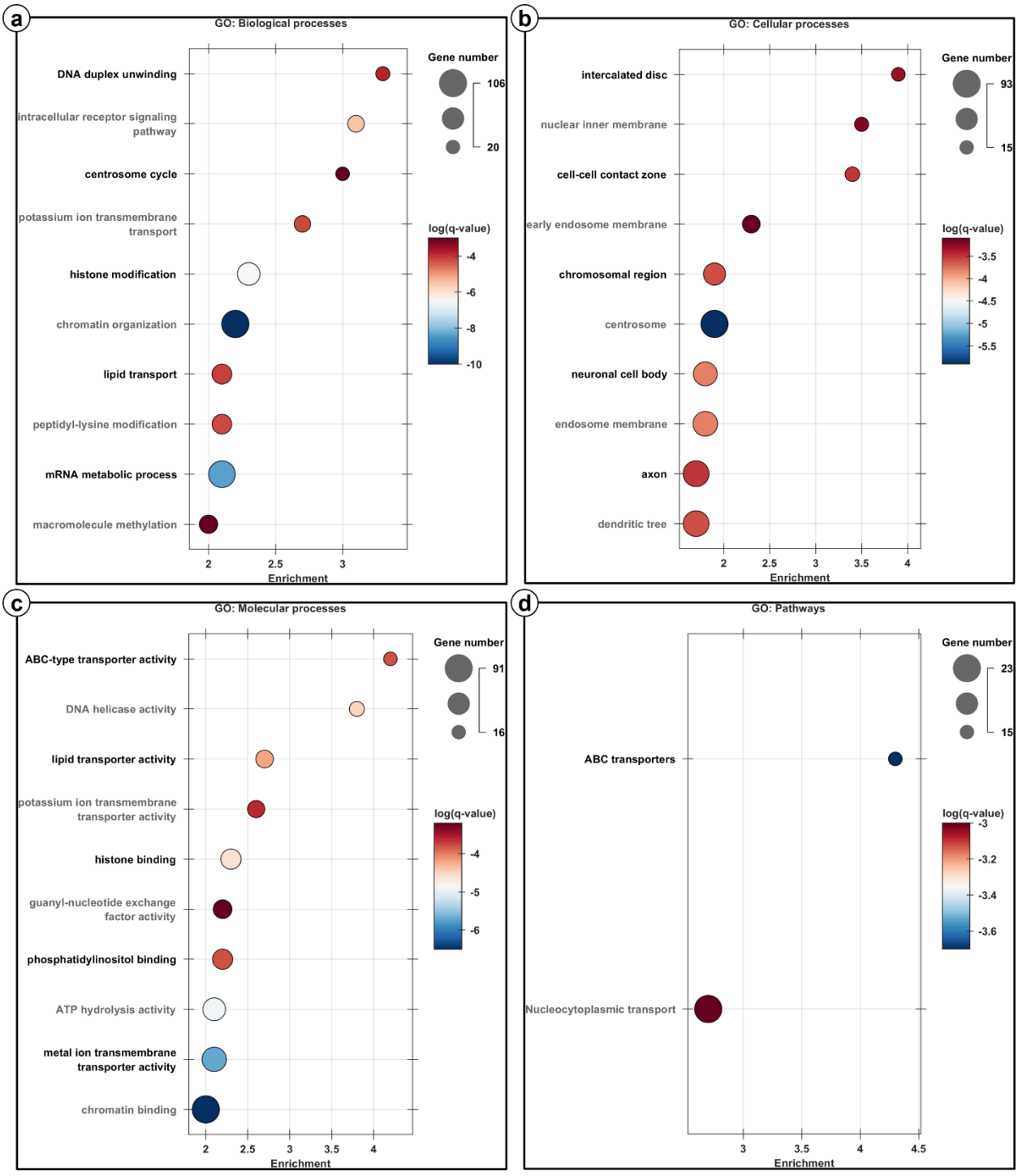

Figure 4.18. Enrichment analysis of the genes of latent variable 1 with highest (50%) negative loadings corresponding to the PLS analysis relating the network centrality data (alone) to gene expression data. A subset of significantly (i.e., positive false discovery rate smaller than 0.05) enriched gene ontologies (GOs) is shown. a. GO biological processes. b. GO cellular processes. c. GO molecular processes. d. GO pathways.

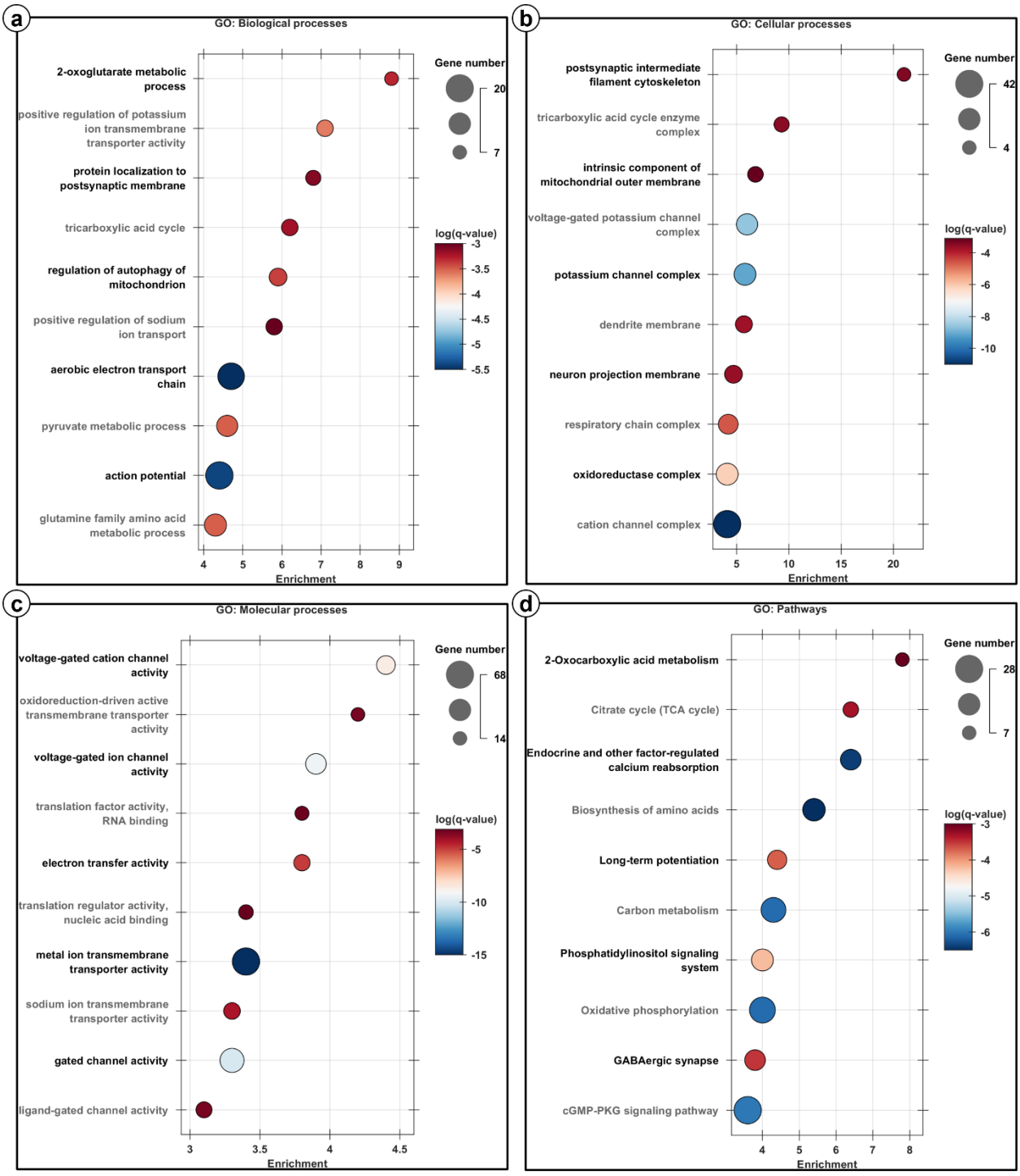

Figure 4.19. Enrichment analysis of the genes of latent variable 2 with highest (50%) positive loadings corresponding to the PLS analysis relating the network centrality data (alone) to gene expression data. A subset of significantly (i.e., positive false discovery rate smaller than 0.05) enriched gene ontologies (GOs) is shown. a. GO biological processes. b. GO cellular processes. c. GO molecular processes. d. GO pathways.

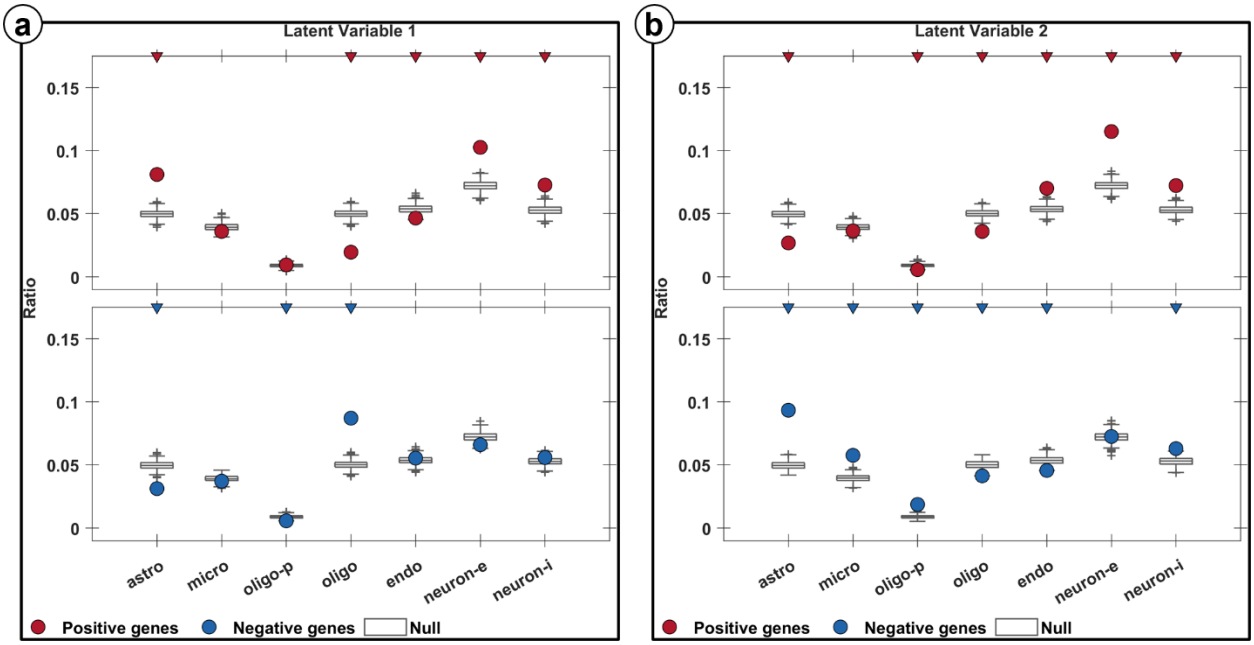

Figure 4.20. Cell-types deconvolution corresponding to the PLS analysis relating the network centrality data (alone) to gene expression data. The ratio of genes preferentially expressed in seven cell types is shown for the genes of latent variable 1 (a.) and latent variable 2 (b.), using their highest (50%) positive (red) or negative (blue) loadings. A triangle on the top indicates positive false discovery rates smaller than 0.05 (i.e., significant ratios) as obtained from bootstrap resampling. The box charts are the null ratios and represent median (line inside a box), 0.25 and 0.75 quantiles (bottom and top edges of a box), outliers (values outside the 150% the interquartile range), and nonoutlier minimum and maximum (bottom and top whiskers of a box). Astro: astrocyte; micro: microglia; oligo-p: oligodendrocyte precursor; oligo: oligodendrocyte; endo: endothelial cells; neuron-e: excitatory neurons; neuron-i: inhibitory neurons.

Chapter 5: Manuscript 3 — Investigating the metabolic and blood flow costs of functional integration and segregation in resting-state networks

5.1 Context

In Chapter 2, we discussed how the brain is organized as a network of specialized segregated components at different spatial resolutions ranging from cells to circuits to systems (Bassett & Sporns, 2017). We highlighted the fact that segregated components of the brain spread and integrate information to form networks that support important functions such as motion, cognition, and perception. In the two first manuscripts of this thesis, we used different approaches to characterize functional connectivity patterns either at the voxel-scale using a time-series decomposition strategy (SPARK methodology (K. Lee et al., 2016)) or at the region scale using graph theory, applied on Schaefer brain parcellation (Schaefer et al., 2018), to further investigate how metabolic and vascular properties are shaping these functional connectivity patterns. In these two studies, our proposed functional connectivity metrics could also be interpreted within the perspective of functional information integration and segregation within brain networks. For instance, voxels exhibiting high functional hubness values using SPARK are most likely integrating a large quantity of information, since their time course is characterized by a linear combination of the activity of several networks (typically 3 to 5 networks) (see Manuscript 1 presented in Chapter 3). Additionally, brain regions exhibiting high global or local centralities, as quantified using graph theory in our Manuscript 2 (Chapter 4) are commonly interpreted as representing either highly integrated or segregated brain regions. However, these interpretations are implicit and remain speculative because they capture sequences of statistical associations which may not correspond to the notion of information flow within and between networks. In Chapter 2, we introduced an information theoretical model that can provide a better characterization of the notions of information exchange within and between brain networks, as well as dedicated measures of functional integration and segregation, that are defined at the network macroscale level (Boly et al., 2012; Marrelec et al., 2008) .

In the present chapter, we present the third original contribution of this PhD thesis, where we examined the metabolic and vascular properties associated with the global measures of functional integration and segregation within and between large-scale resting-state fMRI networks. These networks reside at the system scale of the brain, which is an intermediate scale between the regional level (mesoscale) and the whole brain. Our hypothesis was that the functional integration and functional segregation of large-scale resting-state fMRI networks are associated with specific glucose or oxygen metabolic costs, as well as blood supply costs. The same data acquired for manuscript 1 were considered for this third complementary analysis of our data. The metabolic and vascular data consisted of CMRGlc, $CMRO_2$, and CBF maps estimated as in previous manuscripts. We considered the information-theoretic framework proposed by Marrelec et al (Marrelec et al., 2008), to quantify functional integration and segregation measures of resting-state networks. For this last analysis, we considered an atlas of cortical brain networks defined at two spatial scales, typically the Yeo-7 and the Yeo-17 cortical atlases (Thomas Yeo et al., 2011). Robust linear regressions as well as principal component analysis were considered to investigate the linear relationships between metabolic, vascular, and functional connectivity data.

5.2 Abstract

A growing number of studies are supporting the hypothesis that the intrinsic functional organization of brain networks is tightly coupled to metabolic demands. Additionally, the organization of brain activity has been shown to balance between two competing tendencies: (i) functional integration, referring to the tendency of various brain networks to behave as one and (ii) functional segregation, referring to the tendency of various brain networks to behave independently. In this study, we assessed whether functional integration and segregation between and within intrinsic brain networks could covary with measures of glucose and oxygen metabolism and cerebral blood flow, indicating a cost for these functional processes. To do so, we acquired resting-state neuroimaging data from 19 healthy young adults including functional magnetic resonance imaging (fMRI) and fluorodeoxyglucose (FDG) positron emission tomography (PET) scans to estimate functional connectivity, cerebral metabolic rates of glucose and oxygen ($CMRGlc/CMRO_2$), and cerebral blood flow (CBF). Using information theory measures to assess flow of information within and between brain networks, we characterized the levels of integration/segregation within hierarchical intrinsic network architecture to assess how those measure covary with measures of glucose and oxygen metabolic costs, or blood supply cost of these networks. We consistently found strong linear associations between integration, segregation, metabolism and CBF, further confirming with the hypothesis that functional interactions of intrinsic brain networks are metabolically costly. We also found that the intrinsic networks of the brain could be segmented, with respect to their functional connectivity and physio-metabolic linear relationships, into the extrinsic networks composed of primary sensory and motor family that includes visual, somatic, and auditory areas on the one hand, and the intrinsic networks involving parietal, temporal, and frontal regions on the other hand. Our study suggests distinct physio-metabolic needs for performing fast real-time multimodal integration of sensory and motor information on the one hand, and for performing broad multi-temporal integration on the other hand.

5.3 Introduction

The structural and functional architecture of the brain consists in a set of networks of specialized segregated components, that can be defined in a hierarchical manner at different resolutions spanning from cells microstructure to circuits and systems macrostructure (Bassett & Sporns, 2017). At each resolution, segregated components cluster are characterized by short-distance connections, whereas few components are ensuring connections at a long range scale, ensuring efficient communication pathways within and between clusters or modules (Bassett & Sporns, 2017). Such a multiscale wiring diagram is known to be cost-efficient to minimize the total number of connections while maximizing information transfer (Bullmore & Sporns, 2009). Such an overall network organization results in a flexible dynamic system characterized by the co-called small-world topology (Barabási, 2009; Baronchelli et al., 2013), which supports efficient integration and spread of the information between brain regions, within and between systems. The functional segregation of brain components is only meaningful in the context of their functional integration. The brain's specialized segregated components spread and integrate information to form networks that support movement, cognition, and perception (Mišić & Sporns, 2016; Pessoa, 2014; Sporns, 2014) . As such, the concepts of functional segregation and integration of brain networks are not exclusive, but rather complementary (Sporns, 2014). The concepts of brain functional segregation and integration have been investigated in many areas of functional neuroimaging (see (Sporns & Kötter, 2004) for a detailed review).

Moreover, several studies are supporting the hypothesis that such a brain network organization is tightly coupled to metabolic demands (Bassett & Bullmore, 2017; M. Lin et al., 2013; Meunier et al., 2010; Palombit et al., 2022; Samu et al., 2014; Shokri-Kojori et al., 2019; D. Tomasi et al., 2013). More specifically, three studies considered graph theory metric applied on blood oxygen level-dependent (BOLD) fMRI data combined with glucose consumption measured using fluorodeoxyglucose (FDG) positron emission tomography (PET) imaging or cerebral blood flow (CBF) measured using MRI (Liang et al., 2013; Palombit et al., 2022; D. Tomasi et al., 2013). Overall, these studies suggested brain regions involved in long-range functional connections between networks, ensuring integration between networks, are more metabolically demanding than other regions, and this relationship is network-dependent (Liang et al., 2013; Palombit et al., 2022; D. Tomasi et al., 2013). Such network/metabolism relationship was found to follow a nonlinear concave down power law (Shokri-Kojori et al., 2019; D. Tomasi et al., 2013), an important results we further confirmed for glucose/oxygen metabolism and CBF while showing interesting network specificities (Razavipour et al., in preparation, Manuscript 1 — Multiresolution Metabolic Profile of Functional Hubness in the Resting Human Brain). These previous published studies were considering two common features: (i) the use of temporal cross-correlations to reconstruct functional networks from resting-state (RS) Blood Oxygen Level-Dependent (BOLD) fMRI data, and (ii) the use of the well-established graph theory to characterize one or several aspects of global and local brain connectivity (mostly at the voxel or regional levels), focusing essentially on measures of centrality, functional integration, or segregation. In the studies proposed by Tomasi and colleagues (D. Tomasi et al., 2013) and later Palombit and colleagues (Palombit et al., 2022), one objective was to characterize the glucose metabolic cost of functional connectivity where cerebral metabolic rate of glucose (CMRGlc) was quantified thanks to FDG-PET data (although Palombit and colleagues used a simultaneously acquired FDG-PET and fMRI dataset rather than a separately dataset as Tomasi and colleagues); while in the study proposed by Liang and colleagues (Liang et al., 2013) one objective was to characterize the blood flow cost of functional connectivity where CBF was quantified thanks to arterial spin labeling (ASL) data. Although, the study of Liang and colleagues (Liang et al., 2013) provided evidences that CBF can be considered as a surrogate for cerebral metabolism by correlating their CBF data to the CMRGlc and $CMRO_2$ data of a previously acquired PET dataset in a different cohort (Vaishnavi et al., 2010). However, some important questions remained unanswered, including the role of oxidative metabolism, and the hierarchical spatial organization of brain networks.

In this study, we propose to investigate the relationship between glucose (CMRGlc) and oxidative ($CMRO_2$) metabolism, CBF and measures of functional integration in resting state networks. To do so, we considered BOLD fMRI to derive functional connectivity measures, we used standardized uptake value ratios (SUVR) of FDG- PET data to quantify CMRGlc maps. We used a generalized calibration model (GCM; (Gauthier & Hoge, 2012)) with gas-manipulation applied during dual ASL / BOLD data acquisition to quantify absolute baseline $CMRO_2$ and CBF maps. Our functional connectivity measures were based on an information theory model that quantifies integration versus segregation of the flow of information within and between brain networks in a hierarchical manner (Boly et al., 2012; Cross et al., 2021; Marrelec et al., 2008) . The hierarchy explicitly accounts for the fact that the brain can be divided into functionally meaningful networks (here the Yeo-7 networks (Thomas Yeo et al., 2011)), whereas each network can then be further decomposed into several functionally meaningful sub-networks in a hierarchical nested manner (here the Yeo-17 networks (Thomas Yeo et al., 2011)). Four interrelated information theory metrics that originally proposed in Marrelec et al. (Marrelec et al., 2008) have been considered in

this study: (i) the total-integration metric of a specific Yeo-7 network was used to quantify the sum of information exchanged between its corresponding sub-networks in Yeo-17, as a measure of between networks integration, (ii) the within-integration metric estimating the sum of information exchanged within each sub-network of each Yeo-7 network, (iii) the functional clustering ratio (FCR) for a specific network in Yeo-7, was used assesses the proportion of interactions within each sub-network (in Yeo-17) relative to integration between them, as a measure of network segregation (Boly et al., 2012). Interestingly, these functional measures are obtained directly at the system-level of the brain which is an intermediate scale between brain regions and whole brain results (Marrelec et al., 2008), while allowing capturing nonlinear functional interactions. In addition, these information theory measures of network integration /segregation can be applied to increasingly fine-grain sub-networks, they also are interrelated and complementary to standard graph theoretical indices of functional connectivity (Toussaint et al., 2014).

5.4 Materials and Methods

5.4.1 Subjects and multimodal data acquisitions

Nineteen right-handed healthy young subjects (mean ± SD age = 24.0 ± 4.3 y; 9 females) were recruited from the student community of local universities and underwent imaging acquisitions including anatomical MRI, RS BOLD fMRI, and gas-inhalation-based calibrated fMRI, all acquired using a 3.0T GE Discovery MR750 MRI. RS FDG-PET have been acquired using a GE Discovery PET/CT 69. Exclusion criteria included any history of chronic mental or physical illness, MRI or PET contraindications, possible pregnancy, and chronic respiratory disease. Ethics approval was obtained from the Comité Central d'Éthique de la Recherche. Written informed consent was provided by all subjects and both MRI and PET acquisitions were completed within the imaging suite of Concordia PERFORM Centre. The participants were asked to avoid sugary, alcoholic, or caffeinated drinks for at least two hours prior to imaging, and to not have eaten any food for at least 4 hours before the acquisitions. Data acquisitions started by an anatomical MRI, followed by a 10-minute eyes-opened resting-state (RS) blood oxygen level-dependent (BOLD) fMRI, followed by an 18-minute gas-inhalation-based calibrated fMRI, and followed by a 45-minute eyes-closed static RS 2-[fluorine-18]-fluoro-2-deoxy-D-glucose (18F-FDG) PET. There was a 60-minute gap between the calibrated fMRI and PET acquisitions (post-radiotracer-injection period) during which participants stayed in a RS condition in a calm environment.

Anatomical MRI data was acquired using a 3D sagittal T1-weighted (T1w) MPRAGE sequence with the following parameters: TE = 3.18 ms; TR = 4,500 ms; TI = 8,160 ms; flip angle = 12°; 256 × 256 acquisition matrix, 192 slices; 1 mm isovoxel. RS BOLD fMRI data were acquired with the following sequence parameters: length = 10 min; field of view (FOV) = (2,400 mm) × (240 mm); TR = 2,300 ms; TE = 30 ms; isotropic voxel size = 3.5 mm.

5.4.2 Gas-inhalation-based calibrated fMRI

Calibrated fMRI data were acquired using a dual-echo pseudo-continuous arterial spin labeling (pCASL) sequence with the following parameters: TR = 4,150 ms; TE1 = 8.4 ms; TE2 = 30 ms; alpha = 90°; 4 mm × 4 mm in-plane resolution and 16 slices of 7 mm (1 mm slice gap) on a 64 × 64 matrix; post-labeling delay = 950 ms; flip angle of labeling pulse = 25°; tagging duration = 1.6 s. In addition, four M0 images were acquired with the same parameters except TR = 10,000 ms; TE = 8.4 ms.

Gas challenges were applied to evoke iso-metabolic changes in blood flow and BOLD signal, to estimate M the calibration parameter, corresponding to the maximum possible increase in BOLD

signal from baseline (Hoge, 2012). A computer-controlled gas system was used to control mixing concentration of the gases and their delivery to the MRI room. The respiratory and breathing data of each subject were sampled to constantly monitor participants' partial pressure of CO_2 (PCO_2), partial pressure of O_2 (PO_2), as well as their heart and respiration rates. Subjects were asked to breathe through their nose to ensure only expired gas in an indwelling nasal cannula was sampled. The first 4 minutes of acquisitions with medical air inhalation were considered as RS data. The acquisition continued with three functional runs, each including a different gas manipulation. During each gas manipulation run, a single two-minute block of gas was preceded and followed by a block of three minutes of medical air. The three gas manipulations used were: 80% O_2 (hyperoxia), 21% O_2 + 5% CO_2 + 74% N2 (hypercapnia), and 50% O_2 + 5% CO_2 + 45% N_2 (simultaneous hyperoxia/hypercapnia). End-tidal O_2 and CO_2 values were then selected manually from continuous partial O_2 and CO_2 respiratory traces with acquired at 200 Hz. The first middle 10 breaths of the four-minute baseline period and the last 10 breaths of each two-minute gas-inhalation block was averaged as baseline and gas manipulation end-tidal values, respectively.

5.4.3 Anatomical MRI data preprocessing

For each subject, the T1w image was corrected for intensity non-uniformity with N4BiasFieldCorrection (Tustison et al., 2010) , distributed with ANTs 2.3.3 (Avants et al., 2008) RRID:SCR_004757, and used as T1w-reference throughout the workflow. The T1w-reference was then skull-stripped with a *Nipype* implementation of the antsBrainExtraction.sh workflow (from ANTs), using OASIS30ANTs as target template. Brain tissue segmentation of cerebrospinal fluid (CSF), white-matter (WM) and gray-matter (GM) was performed on the brain-extracted T1w using fast (FSL 6.0.5.1:57b01774, RRID:SCR_002823, (Y. Zhang et al., 2001)). Volume-based spatial normalization to standard space (MNI152NLin6Asym) was performed through nonlinear registration with antsRegistration (ANTs 2.3.3), using brain-extracted versions of both the T1w reference and the T1w template. The following template was selected for spatial normalization: *FSL's MNI ICBM 152 non-linear 6th Generation Asymmetric Average Brain Stereotaxic Registration Model* (Evans et al., 2012), RRID:SCR_002823; TemplateFlow ID: MNI152NLin6Asym).

5.4.4 Resting-state BOLD fMRI data processing

For each subject, the following preprocessing was performed using *fMRIPrep* 21.0.1 (Esteban, Blair, et al., 2018; Esteban, Markiewicz, et al., 2018), which is based on *Nipype* 1.6.1 (Esteban, Markiewicz, et al., 2018); RRID:SCR_002502). First, a reference volume and its skull-stripped version were generated. Head-motion parameters with respect to the BOLD reference (transformation matrices, and six corresponding rotation and translation parameters) were estimated before any spatiotemporal filtering using mcflirt (FSL 6.0.5.1:57b01774, (Jenkinson et al., 2002)). The BOLD time-series were resampled onto their original, native space by applying the transforms to correct head motion. These resampled BOLD time series will be referred to as *preprocessed BOLD*. The BOLD reference was then co-registered with 6 degrees of freedom to the T1w reference using mri_coreg (FreeSurfer) followed by flirt (FSL 6.0.5.1:57b01774,(Jenkinson et al., 2002)) with the boundary-based registration (Greve & Fischl, 2009) cost-function. Several confounding time-series were calculated based on the *preprocessed BOLD*: framewise displacement (FD), root-mean-square of voxelwise differentiated signal (DVARS) and three region-wise global signals. FD was computed using two formulations following Power (absolute sum of relative motions, (Power et al., 2014)) and Jenkinson (relative root mean square displacement between affines, (Jenkinson et al., 2002)). FD and DVARS are

calculated for each functional run, both using their implementations in *Nipype* (following the definitions by (Power et al., 2014)). The three global signals are extracted within the CSF, the WM, and the whole-brain masks. The head-motion estimates calculated in the correction step were also placed within the corresponding confounds file. The confound time series derived from head motion estimates and global signals were expanded with the inclusion of temporal derivatives and quadratic terms for each (Satterthwaite et al., 2013). Frames that exceeded a threshold of 0.5 mm FD or 1.5 standardised DVARS were annotated as motion outliers. The BOLD time-series were resampled into the *MNI152NLin6Asym* standard space, correspondingly generating a *spatially normalized, preprocessed BOLD run*. Automatic removal of motion artifacts using independent component analysis (ICA-AROMA, (Pruim et al., 2015)) was performed on the *preprocessed BOLD on MNI space* time-series after removal of non-steady state volumes and spatial smoothing with an isotropic, Gaussian kernel of 6mm FWHM (full-width half-maximum). Corresponding "non-aggressively" denoised runs were produced after such smoothing. Additionally, the "aggressive" noise-regressors were collected and placed in the corresponding confounds file. Resampling was performed with *a single interpolation step* by composing all the pertinent transformations (i.e., head-motion transform matrices, susceptibility distortion correction when available, and co-registrations to anatomical and output spaces). Gridded (volumetric) resampling were performed using antsApplyTransforms (ANTs), configured with Lanczos interpolation to minimize the smoothing effects of other kernels (Lanczos et al., 1964) . Non-gridded (surface) resamplings were performed using mri_vol2surf (FreeSurfer).

The post-processing strategy was applied on the ICA-AROMA runs using Nilearn version 0.9.0 and included a one-step linear regression of the following standardized confounds: basic white matter and cerebrospinal fluid signals (i.e., the averages in each mask; so, 2 parameters), global signal, discrete cosines transformation basis regressors to handle low-frequency signal drifts (i.e., for high-pass filtering). During signal regression, regional BOLD signals were extracted by further specifying a spatial filter with a Gaussian kernel of 7 mm, and a low pass filter with a cutoff of 0.09 Hz.

5.4.5 ASL data preprocessing

The first ASL run with medical air inhalation was considered as RS data and it was used to estimate resting cerebral blood flow (CBF) maps, while the other three included specific gas challenges used for cerebrovascular reactivity and calibrated fMRI. For each subject and runs, the middle volume of the ASL timeseries was selected as the reference volume and the brain extracted using *Nipype*'s custom brain extraction workflow. Head-motion parameters were estimated using *FSL*'s mcflirt (Jenkinson et al., 2002). Next, ASLPrep 0.2.8 was used to write head-motion parameters to the ASL run's confound file. ASLPrep co-registered the ASL reference to the T1w reference using *FSL*'s flirt (Jenkinson & Smith, 2001), which implemented the boundary-based registration cost-function (Greve & Fischl, 2009). Co-registration used 6 degrees of freedom. The quality of co-registration and normalization to template was quantified using the Dice and Jaccard indices, the cross-correlation with the reference image, and the overlap between the ASL and reference images (e.g., image coverage). FD and DVARS are calculated using *Nipype* (Power et al., 2014) for each ASL run. ASLPrep summarizes in-scanner motion as the mean framewise displacement and relative root-mean square displacement. *ASLPrep* was configured to calculate CBF with Bayesian Inference for Arterial Spin Labeling (BASIL) (Woolrich et al., 2009), as implemented in *FSL* 6.0.3. All resampling in *ASLPrep* use a single interpolation step that concatenates all

transformations. Gridded (volumetric) resampling was performed using antsApplyTransforms, configured with *Lanczos* interpolation (Lanczos et al., 1964).

A spatial mask was applied on preprocessed calibrated fMRI to remove large veins by identifying voxel with relative BOLD increases greater than 10% in the unsmoothed hypercapnia data. The large arteries exhibiting decreases in pre-T1-correction absolute CBF that were greater than 50 mL / (100 g) / min during O_2 inhalation were also masked out. A slab mask for each subject was defined by analyzing the temporal SNR of ASL signals and for each subject, and the uppermost with SNR drops greater than 50% were discarded from further analyses.

5.4.6 PET data preprocessing

PET images were reconstructed using an iterative 3D ordered subset expectation maximization (Kinahan et al., 1998) algorithm including all the usual corrections (scatter, random, dead time, attenuation, and normalization). A 3D point spread function (GEMS name = Sharp-IR) based on experimental measurements of point sources acquired in different positions within the 3D-PET FOV, was modeled and coded in a system matrix and projection space for the reconstruction scheme. The reconstructions were done on a 192 × 192 × 47 grid from 30 minutes of static images and on a 256 × 256 × 47 grid from six 5-minute frames, with a voxel size of 1.6 mm × 1.6 mm × 3.25 mm, and with 3D trans axial filter = ramp, FOV = 20 cm, centered at x = 5 cm and y = 5 cm, matrix size = 256 × 256. Reconstructed PET images together with T1w images were smoothed with a 3D gaussian kernel where FWHM = 2 mm isotropic using minc-toolkit ((Vincent et al., 2016); *mincblur* command). PET data were finally co-registered with T1w images using a multi-resolution strategy estimating 6 transformation parameters (rigid transformation) by maximizing the mutual information as a similarity measure (*minctracc* command). At the end, the PET images were brought to the *MNI152NLin6Asym* standard space using the same non-linear resampling strategy previously applied on BOLD images.

5.4.7 CMRGlc, $CMRO_2$, and CBF quantification and analysis

CMRGlc maps were estimated from FDG-PET data using standardized uptake value ratios (SUVR) referenced to the pons (Minoshima et al., 1995). First, SUV maps were estimated as $\mathrm{SUV} = C_t/(\mathrm{ID}/w_t \times D)$ where C_t is the decay-corrected activity concentration in the tissue (in MBq/cc which can be converted to MBq/kg by dividing by tissue density 1 g/cc), ID is the injected dose (in MBq), and w_t is the subject's weight (in kg). $D = 2^{-\Delta_t/T_{1/2}}$ is a decay factor with Δ_t being the time elapsed between injection and scanning (approximately 1 hour), and $T_{1/2}$ is the half lifetime of the 18F-FDG radiotracer (6582 s). Then, SUV ratios, i.e., our estimates of CMRGlc maps, were finally determined by normalizing SUV maps with mean uptakes in pons.

$CMRO_2$, and CBF, maps were estimated from gas-inhalation-based calibrated fMRI data. The perfusion and BOLD signals were isolated respectively from the series of first and second echoes in the ASL data using linear surround subtraction and addition methods (Aguirre et al., 2002). Absolute CBF maps in units of mL / (100 g) / min were determined from the perfusion signals using the procedure described in (J. Wang et al., 2003). The fractional changes in BOLD and CBF were computed for each gas manipulation by fitting a linear model to the respective signals with normalized regressors obtained from end-tidal respiratory data. Regressors were convolved with a single-gamma hemodynamic response function with parameters described in (Glover, 1999), and corrected by a time delay estimated from the average grey matter (GM) signal to account for the delay between the respiratory and neuronal signals. From the CBF maps, $CMRO_2$ maps were estimated as $CMRO_2 = CaO_2 \times CBF \times OEF$ where CaO_2 is the total arterial O_2 content determined

as the sum of O_2 bound to hemoglobin, and O_2 dissolved in plasma. CaO_2 was determined from PO_2 from the averaged end tidal O_2 taken from the respiratory data (Piechnik et al., 2008). OEF was finally estimated using the GCM described in (Gauthier & Hoge, 2013) using in-house MATLAB scripts. $CMRO_2$, CBF, and OEF maps as well as the slab masks obtained during preprocessing, were all resampled to the ICBM 2009a symmetric template space at a 4-mm isometric voxel resolution. The resampling was done with cubic B-spline interpolations using ANTs (Avants et al., 2011) by combining a transform from subjects' native to subjects' T1w spaces with a transform from subjects' T1w space to the T1w space of the template. Once in the analysis template space, for each $CMRO_2$, CBF, and OEF map, voxels with negative or null values were flagged to be discarded from all analyses, as these were the results of noisy measurements in some voxels. A global slab mask calculated as the intersection between all slab masks of all participants.

5.4.8 Brain masking and parcellations

All analyses were performed in the *MNI152NLin6Asym* standard template space, considering the native resolution of every modality. To infer measurements at the brain networks level, we first considered the Schaefer atlas as a parcellation of the cortical regions in 200 parcels (Schaefer et al., 2018). All regions from the limbic networks, i.e., involving the temporal pole, some inferior-temporal regions, and some orbitofrontal regions, for a total of 14 parcels, were excluded from further analyses since they were exhibiting low signal-to-noise ratio. For $CMRO_2$ and CBF maps only, slab masks were also used to exclude voxels from the uppermost slices exhibiting low SNR in ASL data.

A functional network parcellations of the cerebral cortex into 7 and 17 networks introduced by Yeo et al. (Thomas Yeo et al., 2011), excluding limbic networks, were considered in this analysis. Each region of the Schaefer atlas was then natively assigned to a network in Yeo-17 (excluding the two limbic networks), based on their name. Then, each network of Yeo-17 was uniquely assigned to a network in Yeo-7 qualitatively as reported in Table 5.1.

Table 5.1. Assignment of Yeo-17 networks to Yeo-7 networks.

Yeo-17 networks	**Yeo-7 networks**
control A; control B; control C	control
default A; default B; default C; temporal parietal	default
dorsal attention A; dorsal attention B	dorsal attention
somatomotor A; somatomotor B	somatomotor
central visual; peripheral visual	visual
ventral attention A; ventral attention B	ventral attention

5.4.9 Estimation of functional network integration and segregation

To characterize levels of brain network integration or segregation, where networks are defined in a hierarchical nested manner from Yeo atlases (Thomas Yeo et al., 2011), we considered measures of hierarchical integration and functional clustering ratio (FCR) as introduced and described in (Boly et al., 2012; Marrelec et al., 2008).

First, we defined standardized mean BOLD fMRI time courses in each of the R regions defined by an atlas: $y = (y_1, \dots, y_R)$. Second, we combined the different R regions into $\widetilde{K}$ non-overlapping networks $\{\widetilde{N}_1, \dots, \widetilde{N}_{\widetilde{K}}\}$, and computed the following hierarchical measures of integration:

$I[y_1, \ldots, y_R] = I_b + I_s$, where $I_b = I\left[y_{\widetilde{N}_1}, \ldots, y_{\widetilde{N}_{\widetilde{K}}}\right]$ is referred to as between(-network)-integration, $I_w = \sum_{k=1}^{\widetilde{K}} I\left((y_r)_{r\in\widetilde{N}_k}\right)$ is referred to as within(-network)-integration, and their sum is referred to as total-integration. Assuming that y follows a multivariate normal distribution with mean μ and covariance matrix Σ, integration is defined as: $I[(y_r)_{r\in N}] = \left[\sum_{r\in N} H\left(p(y_r)\right)\right] - H(p(y_r)_{r\in N})$ where N is any set of regions and where $H(\cdot)$ denotes the entropy measure computed as $H\left(p(y)\right) = \ln\left|\Sigma_{N,N}\right|/2$. Third, we combined the different $\widetilde{K}$ networks into another set of K non-overlapping networks $\{N_1, \ldots, N_K\}$ (thereby providing a nested tree of networks), and computed FCR for each network $N_k \in \{N_1, \ldots, N_K\}$ as $\mathrm{FCR}(N_k) = I_w(N_k)/I_b(N_k)$ where $I_b(N_k) = I\left[(y_{\widetilde{N}})_{\widetilde{N}\in N_k}\right]$ and $I_w(N_k) = \sum_{\widetilde{N}\in N_k} I((y_r)_{r\in\widetilde{N}})$.

In our case, $R = 186$ regions of the Schaefer-200 atlas were used since the limbic networks were excluded. Hierarchical integration measures and FCR were estimated for each network of Yeo-7. For calculating FCR, the sub-networks of each Yeo-7 network were obtained from Yeo-17 as in Table 5.1.

Covariance matrices (sized $R \times R$) for each subject were numerically inferred from the data using a Gibbs sampler of the hierarchical Bayesian model detailed in (Marrelec et al., 2008) with 1000 samples (after discarding 1000 other samples at the beginning to allow for burn-in effect) and using the identity matrix for initial conditions. The hierarchical Bayesian model also provided a group-level covariance matrix. At the end, probable values of hierarchical integration measures and FCR were calculated using the previous equations from the posterior distribution of the different covariance matrices. The hierarchical Bayesian model ensured that the covariance matrices were positive definite.

5.4.10 Linear regression and principal component analyses

To assess the correspondence between hierarchical integration or FCR measures assessing network properties, to physio-metabolic data (CMRGlc, CMRO2 and CBF) across the Yeo-7 networks, we considered a robust linear regression model (MATLAB default robust linear regression model *robustfit*). While standard linear regression models are very sensitive to outliers or unusual values (e.g., a single atypical value may have a large effect on the their parameter estimations), robust regression models can better handle these issues (Yu & Yao, 2014). For each network, network-level values of CMRGlc, $CMRO_2$ and CBF were calculated by taking the grand sum of regional values. The sum operator was used to represent "total demands" (of glucose, oxygen, or blood flow) for a given network. This parallels the various functional measures that capture "overall interactions" rather than average ones. An *F*-test was used to assess whether the linear regression model would fit significantly better than a degenerate model consisting of only a constant term. A *t*-test was used to assess the null hypothesis that the slope was zero against the alternative hypothesis that it was different from zero. Prior to regression analyses, all variables were Z-scored across networks for each subject independently.

Principal component analysis (PCA) was used to better understand the different types of relationships between hierarchical integration, FCR and physio-metabolic data across networks. MATLAB's default principal component analysis routine (*pca*) was considered for such analysis.

For both regression and principal component analyses, model parameter estimations were done based on all 19 subjects, while a prediction was done for the "average" subject. The hierarchical integration or FCR data for the "average" subject was obtained from the group-level covariance

matrix provided by the hierarchical Bayesian model described earlier. The physio-metabolic data for the "average" subject was obtained from the arithmetic mean of CMRGlc, $CMRO_2$, and CBF subject maps.

5.5 Results

5.5.1 Hierarchical functional integration measures and functional clustering ratio

Figure 5.1 shows the group-level mean values of total-integration, within-integration, and FCR for each Yeo-7 network. Total-integration was the largest within the somatomotor network, followed in decreasing order by the default mode, visual, control, ventral attention and dorsal attention networks. Within-integration was strongly positively correlated with total integration (Spearman-correlation = 0.94; two-tailed *p*-value = 0.02) thus providing a similar ordering of networks. The only difference in network ordering was between the default mode and visual networks, where we found a slightly higher within network integration for the visual network. Between network integration (which is the difference between total-integration and within-integration) was the largest within the default mode network, then followed in decreasing order by the control, visual, ventral attention, somatomotor and dorsal attention networks. FCR, as a measure of network segregation estimated as the ratio between within-integration and between-integration, was the lowest within the default mode network, suggesting more integration between corresponding subnetworks, followed in ascending order by the control, ventral attention, dorsal attention, visual and somatomotor networks, suggesting more segregation between corresponding somatomotor subnetworks. It is interesting to note that FCR was found to be perfectly anti-correlated with both within-integration and total-integration, only when considering the so-called *higher-order function* or intrinsic networks (i.e., control, default, and attention networks).

5.5.2 Metabolic costs of functional network integration and clustering

Figure 5.2.A. presents the results of robust linear regression for the glucose metabolic cost of total-integration. We found that higher total-integration was strongly associated with higher CMRGlc (slope ± SE = 0.92 ± 0.04; see also Table 5.2). Interestingly, we also observed that the line of best fit was able to subdivide the different networks into three groups: (i) default and control networks exhibiting higher than expected glucose consumption from the linear fit, (ii) somatomotor and visual networks exhibiting lower than expected glucose consumption from the linear fit, and (iii) attention networks showing close agreement with the linear prediction. We highlighted these results in Figure 5.2 by mapping the signed distance of the group point to the line of best fit. Such brain mapping showed how parieto-temporo-frontal regions on the one hand (red-colored), and visuo-somato-auditory regions on the other hand (blue-colored) were at the two extremes of the linear relationship linking total-integration to CMRGlc measures. The mapping also shows how the attention networks (white-colored) could anatomically outline regions that border the two previously described sets, consistent with these regions being at the overlap between the red and blue sets in terms of physiological properties. We also found overall similar results when investigating the oxygen metabolic costs of total-integration (see Figure 5.2.B; slope ± SE = 0.87 ± 0.05; see also Table 5.2), as well as the blood supply costs of total-integration (see Figure 5.2.C; slope ± SE = 0.89 ± 0.05; see also Table 5.2).

Figure 5.3 illustrates the relationship between CMRGlc and other measures of integration, within-integration, between-integration and the inverse of FCR. In Figure 5.3.A, our results are showing that the slope for the glucose metabolic cost of within-integration was smaller than the one found

for total-integration, but resulting overall in similar network subdivisions (slope ± SE = 0.61 ± 0.08; see also Table 5.2). In fact, upon closer inspections, we noted two regimes of linear relationships where the control, default mode, and ventral attention networks defined the first regime associated with the highest slope, and the somatomotor, visual, and dorsal attention networks defined the second regime associated with the smallest slope. This last observation was further confirmed when investigating glucose metabolic cost of between-integration in Figure 5.3.B and of the reciprocal of FCR in Figure 5.3.C (see also summary in Table 5.2). There, although we found that higher between-integration and lower FCR were both strongly associated with higher CMRGlc (slope ± SE = 0.93 ± 0.04 and slope ± SE = 0.93 ± 0.06, respectively), different combinations of network emerged in relation to the best line of fit across all networks: *primary sensory and motor* networks (i.e., the somatomotor and visual networks) on the one hand, the dorsal attention network and other *higher-order function* networks (default mode, control) on the other hand.

Because some of the networks were indeed exhibiting large deviations from the linear fit, we also investigated the presence of different patterns of the relationship between network integration and physio-metabolic measures using PCA. Our PCA analysis presented in Figure 5.4 revealed that the score mappings found for the second component for total-integration and within-integration, or for the first component for between-integration and the reciprocal of FCR were qualitatively similar, mainly distinguishing between parieto-temporo-frontal regions on the one hand, and visuo-somato-auditory regions on the other hand. It is interesting to note that these patterns are overall quite similar to the ones we reported in Figure 5.2.A when investigating the glucose metabolic cost of total-integration, or in Figure 5.3.A when investigating the glucose metabolic cost of within-integration.

Similar analyses were also performed for $CMRO_2$ and CBF. The patterns observed for CMRGlc were similar to those observed for $CMRO_2$ (see Table 5.2, Figure 5.5 and Figure 5.6) and CBF (see Table 5.2, Figure 5.7 and Figure 5.8), with slopes in agreement within standard error ranges.

5.6 Discussion

This original study assesses the relationship between functional integration and functional clustering ratio as a measure f segregation, within and between resting-state fMRI networks with glucose (CMRGlc) and oxygen ($CMRO_2$) metabolism, and CBF. We consistently found strong linear associations between measures of integration and segregation, and measures of metabolism and blood flow. This indicates that information processing within and across brain networks is indeed metabolically costly. We also found that some networks showed similar fingerprints and could be clustered into families of networks exhibiting similar relationships between integration and physio-metabolic properties. This included a primary sensory and motor family that includes visual, somatic, primary motor and auditory areas on the one hand, and a higher order family that was composed of parietal, temporal, and frontal regions on the other hand. This suggests distinct metabolic needs when performing fast real-time multimodal integration of primary sensory information on the one hand, and when for performing broad multitemporal integration on the other hand (Fuster & Bressler, 2012; Mesmoudi et al., 2013), corresponding respectively to the concepts of extrinsic and intrinsic networks proposed by Doucet et al (Doucet et al., 2011; Mesmoudi et al., 2013)

In agreement with previous studies (Boly et al., 2012; Cross et al., 2021), we found that among the *higher-order function* networks (i.e., control, default mode, and attention networks) within-

integration and FCR were anti-correlated. In addition, total-integration was actually high because of a balance between higher within-integration and higher between-integration. The default network showed a distinctive pattern, exhibiting the largest total-integration, within-integration, between integration (meaning that its sub-networks exchange significant amount information), and resulting in the lowest FCR value. FCR being an index of segregation and integration balance between subnetworks (Boly et al., 2012), our results are indeed suggesting a large amount of information integration between the subnetworks of the default mode network. On the other hand, we found that among the *primary sensory and motor* networks (i.e., somatomotor and visual networks) between-integration was very low, so much so that they exhibited both high within-integration and high FCR, while total-integration was almost equal to within-integration. Our results are therefore suggesting more segregation between the subnetworks of these so-called *primary sensory and motor* networks. Overall, both *primary sensory motor* networks were as highly integrated as the default network (total integration), but their clustering levels defined the two extremes of variations for all networks. This was largely expected since increased clustering of brain activity or segregation (a hallmark of functional specialization) goes hand in hand with lower ability to integrate information (Boly et al., 2012). Furthermore, information integration is expected to decrease for heterogeneous compared with more homogeneously interconnected systems because integrated information is predicted to be maximal for systems that are both highly connected and not decomposable in individual subsystems (Boly et al., 2012). In a similar manner, using similar methodology defined on Yeo-7 and Yeo-17 networks, we found that brain networks were exhibiting more segregation during sleep and also after whole night sleep deprivation, whereas increase in integration after a recovery nap was associated with improved cognitive performance (Cross et al., 2021).

Among the *higher-order function* networks, we consistently observed that the most functionally integrated and therefore least functionally segregated networks, one prime example of which is the default mode network, were exhibiting the highest glucose metabolism, oxygen metabolism and CBF. This important finding is in agreement with previous studies (Liang et al., 2013; Palombit et al., 2022; Shokri-Kojori et al., 2019; D. Tomasi et al., 2013) using different methods and datasets, while the originality of our study was to proposed a comprehensive investigation of oxygen and glucose metabolism, CBF and network properties in the young healthy brain. These partly reflects the presence of functional hub regions in these networks, which consist of energy-demanding long-range connections that mediate functional integration among segregated brain areas. Indeed, in our previous study on the same data set (Razavipour et al in prep, Chapter 3), we showed that connector hubs were indeed largely distributed within these *higher-order function* networks and were associated with the largest increase rate, when modeling the metabolism/hubness function using a concave down power law model. These hub regions are also known to have an intricate vascular network and proximal mesh of glial cells to provide glucose, oxygen and other metabolites to maintain their crucial function (Attwell & Laughlin, 2001; Iadecola, 2017; Magistretti & Allaman, 2015).

When considering both the *primary sensory and motor* and *higher-order function* networks, we observed that they could be distinguished in their linear relationship linking integration and physio-metabolic properties. In particular, the default mode and control networks exhibited higher glucose and oxygen metabolism, and higher blood flow in relation to total-integration or within-integration than the one predicted by the linear relationship across all networks. In contrast, the somatomotor and visual networks required were associated with lower metabolism and CBF, when compared to

the ones linearly predicted. Finally, the attention networks were in good agreement with the prediction from all networks. As a result of such network partitions, we found that parieto-temporo-frontal regions on the one hand, and visuo-somato-auditory regions on the other hand, defined the two extremes' patterns of those linear relationships. Indeed, comparisons of these linear relationships between physio-metabolic properties and integration can be used to capture the relative cost of functional connectivity for different networks (Shokri-Kojori et al., 2019). Our results suggest that such measure of *relative cost*, can identify the unique physiological features of *primary sensory and motor* and *higher-order function* networks.

Interestingly, the linear mappings allowed us to identify spatial patterns between either between-integration or FCR and physio-metabolic that were indeed similar to the one obtained after PCA decomposition, suggesting that some patterns were indeed orthogonal to the one defined by the linear mapping. The orthogonal space captures the extent of concurrent physio-metabolic and functional connectivity activities, resulting in a so-called measure of *relative power* (Shokri-Kojori et al., 2019). These important spatial properties are illustrated in Figure 5.4, Figure 5.6, and Figure 5.8 using PCA. The reason that distance mappings (from linear regressions) and score mappings (from PCA) were actually (qualitatively) similar is because, with singular-value-decomposition-based PCA, error squares are minimized perpendicular to a straight line (by definition). In addition, unless data variables are weakly correlated, a line of best fit as given by a linear regression is almost collinear to the first component of PCA. This means that distance mappings (from linear regressions) captured the same qualitative information as the projection of data points to the second component of PCA, i.e., score mappings along the second component (see Figure 5.9 for illustrations). Similarly, distance mappings from a line orthogonal to the line of best fit (from linear regressions) capture the same qualitative information as the score mappings along the first principal component.

Altogether, our results are agreement with previous studies investigating the relationships between functional connectivity and physio-metabolic data (Liang et al., 2013; Palombit et al., 2022; Shokri-Kojori et al., 2019; D. Tomasi et al., 2013). In addition, the distinctive spatial patterns we identified are showing differential relationship between connectivity and physio-metabolic. These spatial patterns are actually very similar to those identified by Mesmoudi and colleagues and Cioli and colleagues (Cioli et al., 2014; Mesmoudi et al., 2013) using combined resting-state fMRI, diffusion MRI, behavioral and cognitive, and human gene expression data. These authors suggested that brain networks are organized in a "dual intertwined rings architecture". The first ring forms a continuous ensemble and includes visual, somatic, and auditory cortices, with interspersed bimodal cortices (auditory-visual, visualsomatic and auditory-somatic) (Mesmoudi et al., 2015). The second ring integrates distant parietal, temporal and frontal regions through a network of association fiber tracts which closes the ring anatomically and ensures a functional continuity within the ring (Mesmoudi et al., 2015) and relates association cortices specialized in attention, language and working memory, to the networks involved in motivation and biological regulation and rhythms (Mesmoudi et al., 2015). A similar decomposition intro extrinsic versus intrinsic network was proposed by Doucet et al (Doucet et al., 2011). Cioli et al (Cioli et al., 2014) also showed that each ring possesses distinct gene expression patterns that show different metabolic properties. In this way, our results are consistent with distinct metabolic needs for performing fast real-time multimodal integration of sensorimotor information on the one hand, and for performing broad multi-temporal integration on the other hand (Fuster & Bressler, 2012; Mesmoudi et al., 2013). Similarly, our results exhibiting a higher integration and glucose metabolic

profile for the networks of the parieto-temporo-frontal ring when compared to the networks of the visuo-somato-auditory ring are in agreement with earlier studies combining graph theorical indices of fMRI connectomes and FDG-PET data (Hyder et al., 2015; Leontiev et al., 2013; Palombit et al., 2022; Shokri-Kojori et al., 2019; D. Tomasi et al., 2013) and our proposed analysis linking hubness and metabolism (Razavipour et al in prep, Chap 3). Results reported in this study also reflect recent findings showing significant overlap between the topological network structures of $CMRO_2$ and BOLD fluctuations. For instance, a recent study using calibrated fMRI and the low-frequency fluctuations in $CMRO_2$, showed that $CMRO_2$ connectivity can also exhibit spatial patterns consistent with the following canonical resting-state networks: frontoparietal and default (association networks), and auditory and occipital-visual (perceptual networks) (Hubbard et al., 2021). Altogether, our results together with the existant literature offer strong evidence for a physio-metabolic cost of functional network interaction.

Although consistent within standard error ranges, we found that the strengths of linear associations between functional connectivity and physio-metabolic data were generally highest for CMRGlc, followed by CBF and $CMRO_2$. This may be due to higher inter-subject variability for $CMRO_2$ and CBF when compared to for CMRGlc. In general, calibrated-fMRI-based approaches to estimate $CMRO_2$ and CBF are associated with higher inter-subject variability (more so for $CMRO_2$ than CBF) when compared to PET-based approaches (Fan et al., 2020; Ibaraki et al., 2004). For instance, it has been shown how inter-subject variability could be induced by the choice of a fixed post-labeling delay parameter across subjects (Mezue et al., 2014), or other physiological factors such as variability in vascular reactivity or hematocrit across subjects (D'Esposito et al., 2003; Gustard et al., 2003; Handwerker et al., 2007). However, assessing whether these systematic slight differences in linear association strengths between functional connectivity and glucose or oxygen metabolism is of biological significance is a question that would deserve further investigations. For instance, network-level differences in aerobic glycolysis would results in some degree of mismatch between the ways functional connectivity couples to glucose and oxygen metabolism (Magistretti & Allaman, 2015; Vaishnavi et al., 2010). Future studies using complementary techniques could help determine the presence of these effects.

5.6.1 Limitation

This study suffers from some limitations. Inter-subject variability in physio-metabolic data has already been mentioned, as well as the limitations inherent to having a single post labelling delay in ASL sequence. In addition, inter-subject variability may lead to the overestimation of deviation from the linear trend. The hierarchical Bayesian model that we employed to estimate covariance matrices explicitly accounted for the fact that subjects belong to a homogeneous population that possesses its own (group-level) covariance matrix (Marrelec et al., 2008). Afterwards, the posterior distributions of the subject-level and group-level covariance matrices were used to derive, respectively, subject-level and group-level hierarchical integration measures or FCR (Boly et al., 2012; Marrelec et al., 2008). Since such computations consist mainly of logarithm and matrix-determinant operations, any original signed (i.e., positive and negative) deviations of subject-level covariances from the group-level covariance may not be preserved, and the derived deviations in turn may appear substantial when graphed on a linear scale (Marrelec et al., 2008).

Overall, the choice of an appropriate statistical model is an important component for handling data variability. For instance, some models can cohesively account for various sources of variability (such as a mixed-effect models) and could have provided us with a clearer idea of where the observed differences in linear association strengths may be coming from. Moreover, regarding

linear modeling, we do not claim that variations in functional integration or functional clustering arise only from metabolic properties. However, our results are consistent with a dependence between functional connectivity and metabolic properties. Future studies should aim at investigating more biologically grounded models of the relationships between functional connectivity and physio-metabolic data.

Finally, our results and interpretations critically depended on the choice of region-based and network-based parcellations. Indeed, the calculation of hierarchical integration measures as well as functional clustering ratio requires to first define regions of interest and then identifying for each region the network it belongs to (across different nested scales as necessary). Here we used two linked group-level functional atlases, namely Yeo-atlases (Thomas Yeo et al., 2011) and Schaefer-atlases (Schaefer et al., 2018) to constrain both our physio-metabolic and functional resting-state data. However, we must note that many other different state-of-the-art atlases and procedures to define regions and networks are commonly used across neuroimaging studies (Arslan et al., 2018). Indeed, most brain parcellations are designed to capture different facets of brain function and anatomy. Hence, it is of interest to understand what complementary information and new insights different atlases (e.g., multimodal versus functional versus structural, or cortical vs whole-brain, or group-level versus subject-level) may provide when investigating metabolism-function relationships.

5.6.2 Conclusion

In summary, our results are demonstrating strong linear associations between functional integration and segregation, glucose and oxygen metabolism, and blood flow, consistent with the hypothesis that functional interactions of intrinsic brain networks are metabolically costly. Our results also demonstrated that the intrinsic networks of the brain could be segmented, with respect to their functional connectivity and physio-metabolic linear relationships, into a primary sensory and motor family that includes visual, somatic, and auditory areas on the one hand, and a large association family that comprises parietal, temporal, and frontal regions on the other hand. This is consistent with the literature and suggests distinct physio-metabolic needs for performing fast real-time multimodal integration of sensory and motor information on the one hand, and for performing broad multi-temporal integration on the other hand. All our analyses were carried out at the system-scale of the brain which is an intermediate scale between regions and the whole brain. We postulate that the fact that many different datasets and methodologies from voxel-based to region-based (and to network-based with our study) converge to such results, suggests that the biological principles underlying function-metabolism coupling may be scale free.

5.7 Figures and Tables

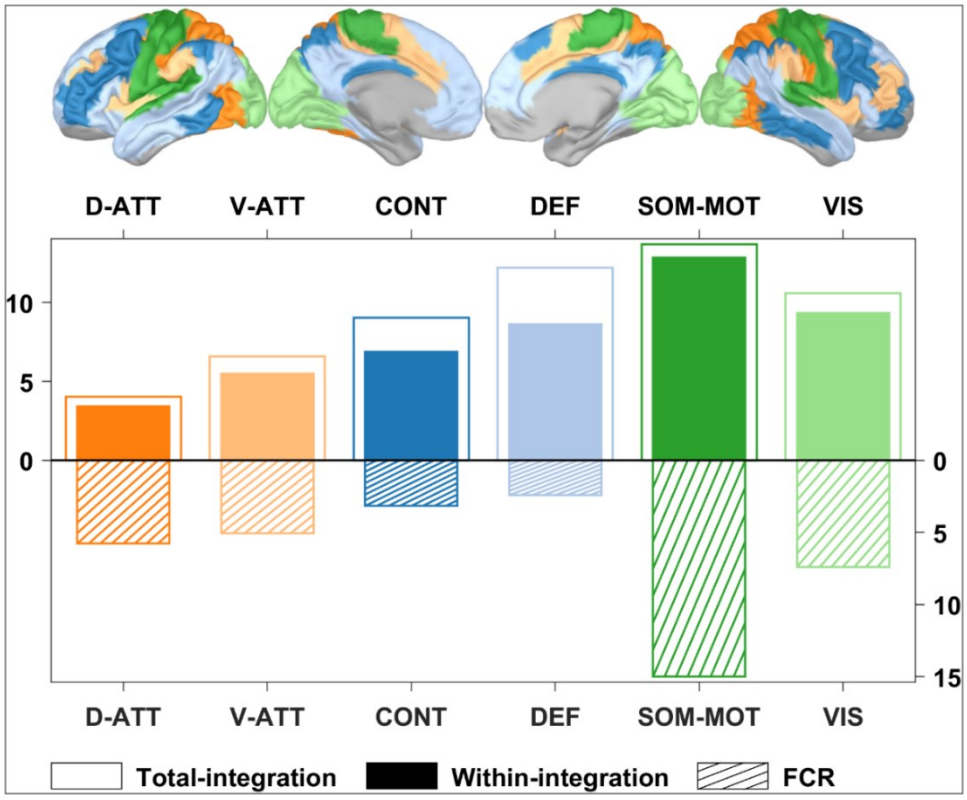

Figure 5.1. Group-level (posterior) mean values of hierarchical integration and functional clustering ratio (FCR) for the networks of Yeo-7. Each network of Yeo-7 is uniquely identified by a color and can be visualized on the brain maps. Three vertical bar graphs are overlaid, and their height represents: (i) total-integration (the non-filled bars associated with the left y-axis), (ii) within-integration (the fully-filled bars inside the non-filled ones, associated with the left y-axis), and (iii) FCR (the semi-filled bars associated with the right y-axis). Between-integration can be estimated as the difference between total-integration and within-integration (i.e., the height of the white boxes stacked on top of the filled boxes). D-ATT: dorsal attention; V-ATT: ventral attention; CONT: control; DEF: default; SOM-MOT: somatomotor; VIS: visual

Table 5.2. Robust linear fit summary of the metabolic costs of total-integration, within-integration, between-integration, and the reciprocal of FCR for the Yeo-7 networks. The numbers represent slope and standard error. The letter (a) indicates whether the linear regression model fits significantly better than a degenerate model consisting of only a constant term at a 5% significance level with respect to an F-test. The letter (b) indicates if the p-value of two-tailed hypothesis t-test that "the slope is zero" against the alternative that "the slope is different from zero" was less than 5%.

	Total-integration	**Within-integration**	**Between-integration**	**$(FCR)^{-1}$**
CMRGlc	$0.92 \pm 0.04^{(ab)}$	$0.61 \pm 0.08^{(ab)}$	$0.93 \pm 0.04^{(ab)}$	$0.93 \pm 0.06^{(ab)}$
$CMRO_2$	$0.87 \pm 0.05^{(ab)}$	$0.55 \pm 0.09^{(ab)}$	$0.92 \pm 0.04^{(ab)}$	$0.82 \pm 0.06^{(ab)}$
CBF	$0.89 \pm 0.05^{(ab)}$	$0.56 \pm 0.08^{(ab)}$	$0.95 \pm 0.03^{(ab)}$	$0.86 \pm 0.06^{(ab)}$

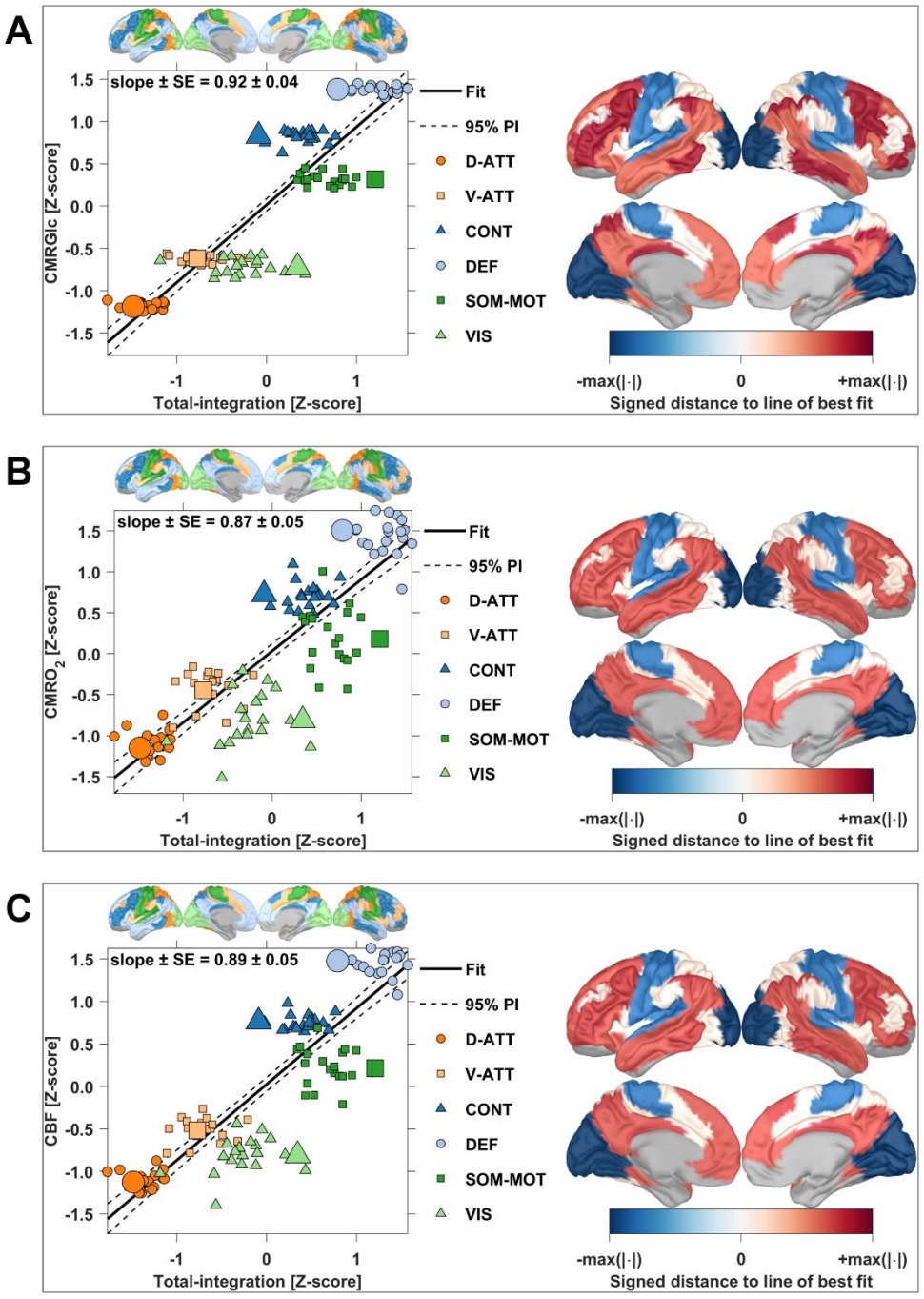

Figure 5.2.Metabolic costs of total-integration for the Yeo-7 networks. A: glucose metabolic costs; B: oxygen metabolic costs; C: blood supply costs. Each network of Yeo-7 is uniquely identified by a color and can be visualized on the corresponding brain maps displayed on the top side of each graph. The smallest-sized points in each graph represent individual subjects while the largest-sized points represent the group. Note that group-level total-integrations are generally different from the arithmetic mean of total-integrations across subjects because they were estimated for a hierarchical statistical model involving non-linear operators, and so the largest-sized points of a certain color are not always located at the center of the cloud of points with that same color. The dashed lines in each graph represent the 95% predicted intervals (PI). The slope and standard error (SE) of the line of best fit that are indicated in each graph are also presented in Table 5.2. The signed distance of a point to the line of best fit displayed on the right side of each graph is for the group (i.e., the largest-sized points). D-ATT: dorsal attention; V-ATT: ventral attention; CONT: control; DEF: default; SOM-MOT: somatomotor; VIS: visual

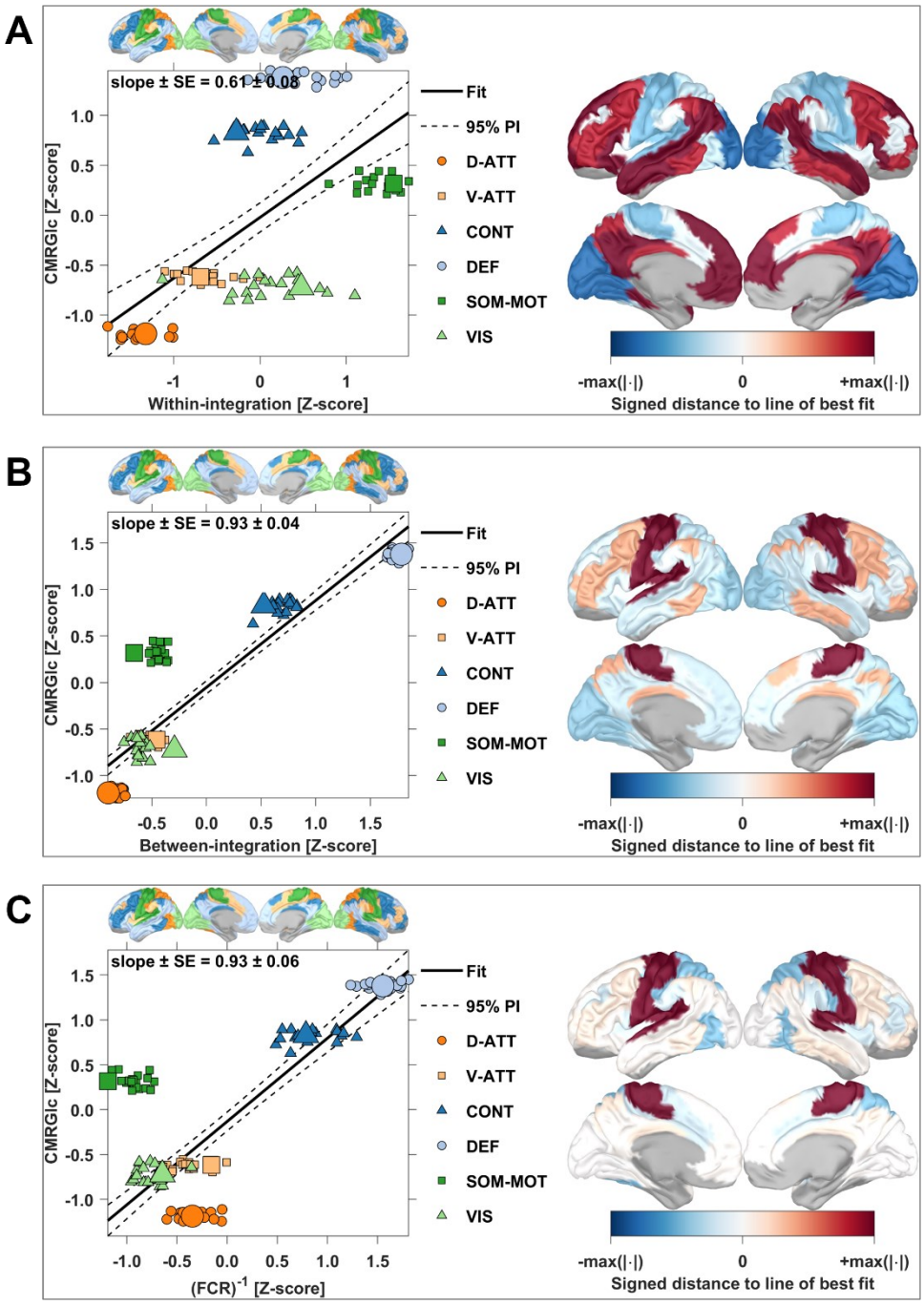

Figure 5.3. Glucose metabolic costs of within-integration (A), between-integration (B), and the reciprocal of FCR (C) for the Yeo-7 networks. Details in this figure are presented as for in Figure 5.2. D-ATT: dorsal attention; V-ATT: ventral attention; CONT: control; DEF: default; SOM-MOT: somatomotor; VIS: visual

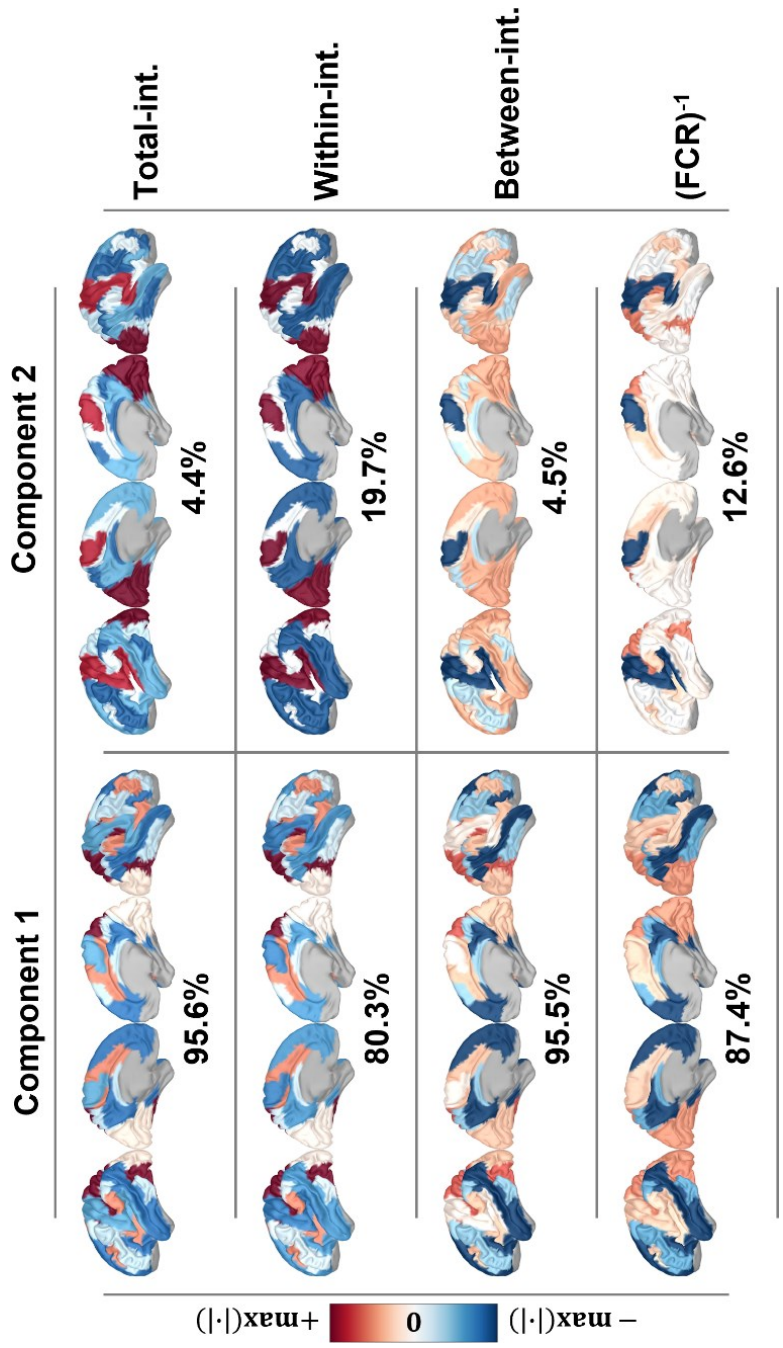

Figure 5.4. PCA-score mappings for CMRGlc datasets (i.e., CMRGlc and either total-integration or within-integration or between integration or the reciprocal of FCR) for the Yeo-7 networks. Maps are based on group prediction scores. Here we can observe that the score patterns of component 2 for total-integration and within-integration are qualitatively similar to the score patterns of component 1 for between-integration and the reciprocal of FCR.

5.8 Supporting Information

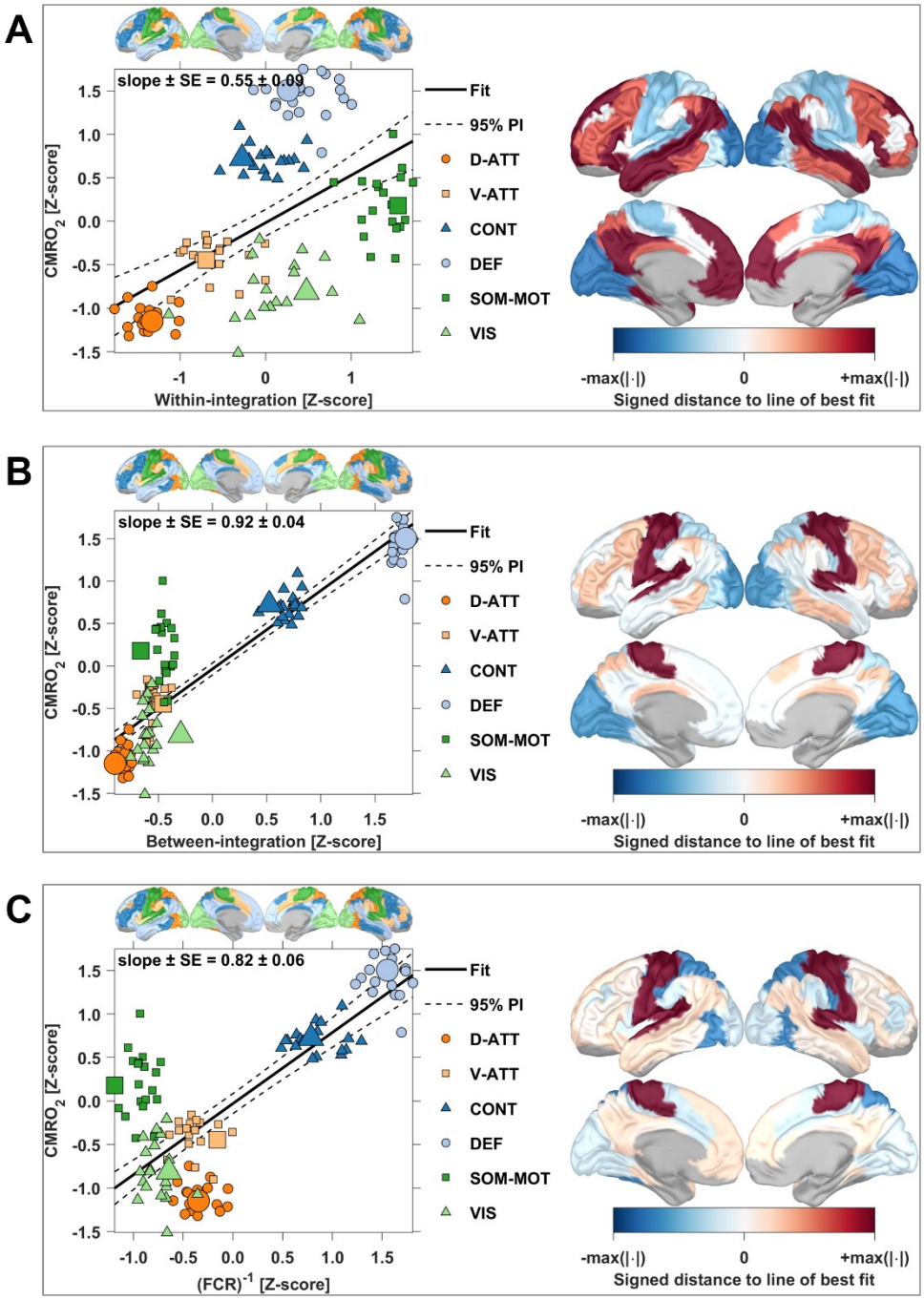

Figure 5.5. Oxygen metabolic costs of within-integration (A), between-integration (B), and the reciprocal of FCR (C) for the Yeo-7 networks. Details in this figure are presented as for in Figure 5.2. D-ATT: dorsal attention; V-ATT: ventral attention; CONT: control; DEF: default; SOM-MOT: somatomotor; VIS: visual

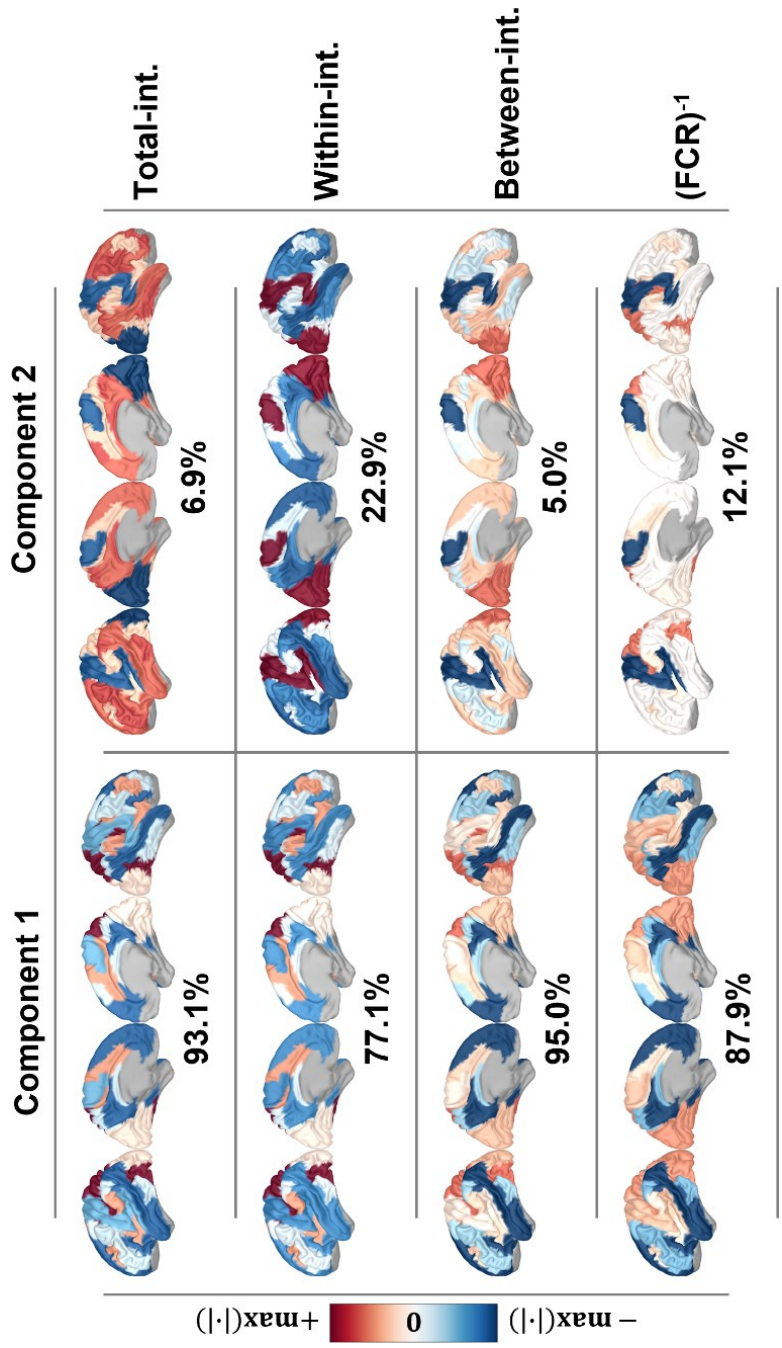

Figure 5.6. PCA-score mappings for $CMRO_2$ datasets. Maps are based on group prediction scores.

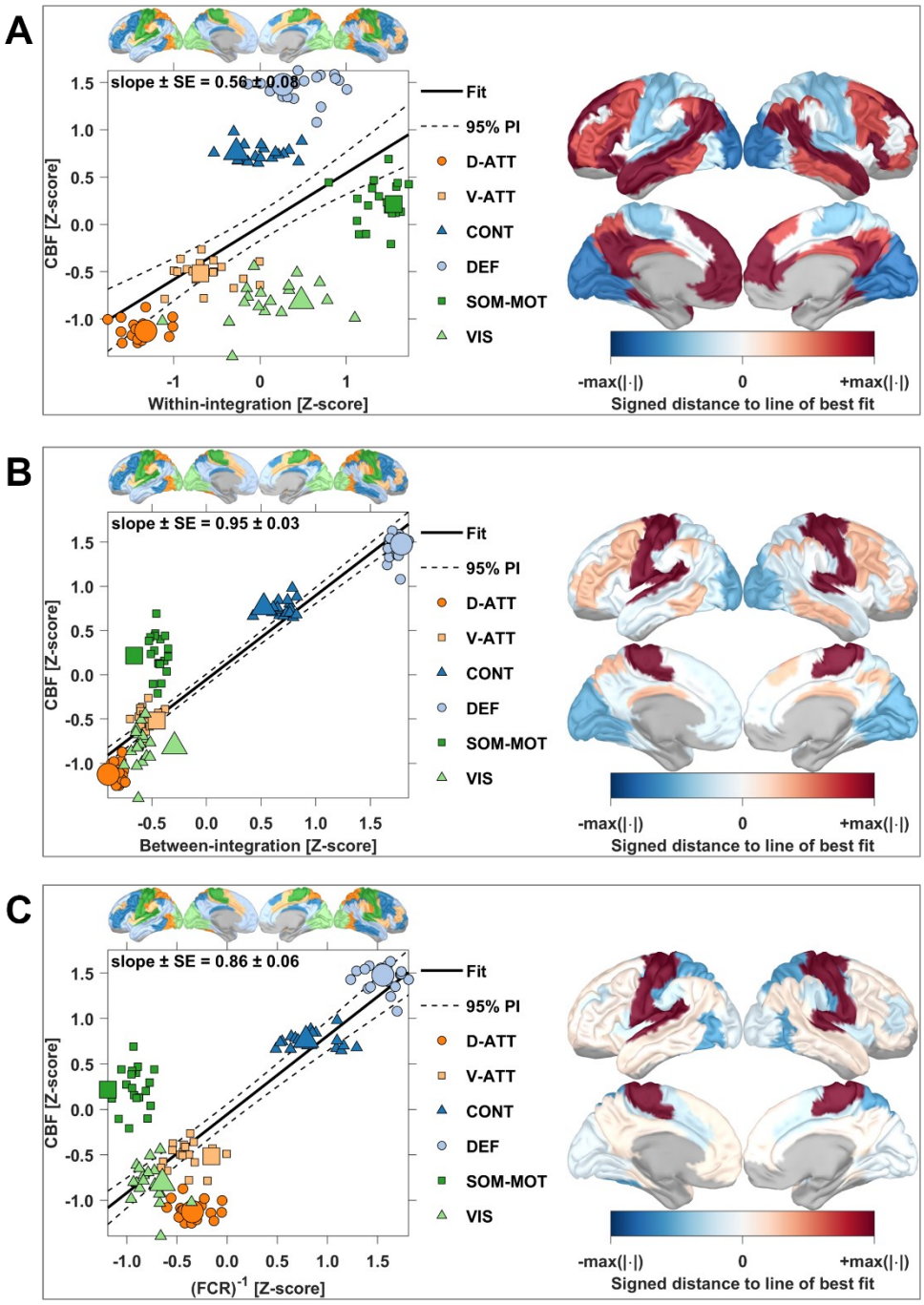

Figure 5.7. Blood supply costs of within-integration (A), between-integration (B), and the reciprocal of FCR (C) for the yeo-7 networks of Yeo-7. Details in this figure are presented as for in Figure 5.2. D-ATT: dorsal attention; V-ATT: ventral attention; CONT: control; DEF: default; SOM-MOT: somatomotor; VIS: visual

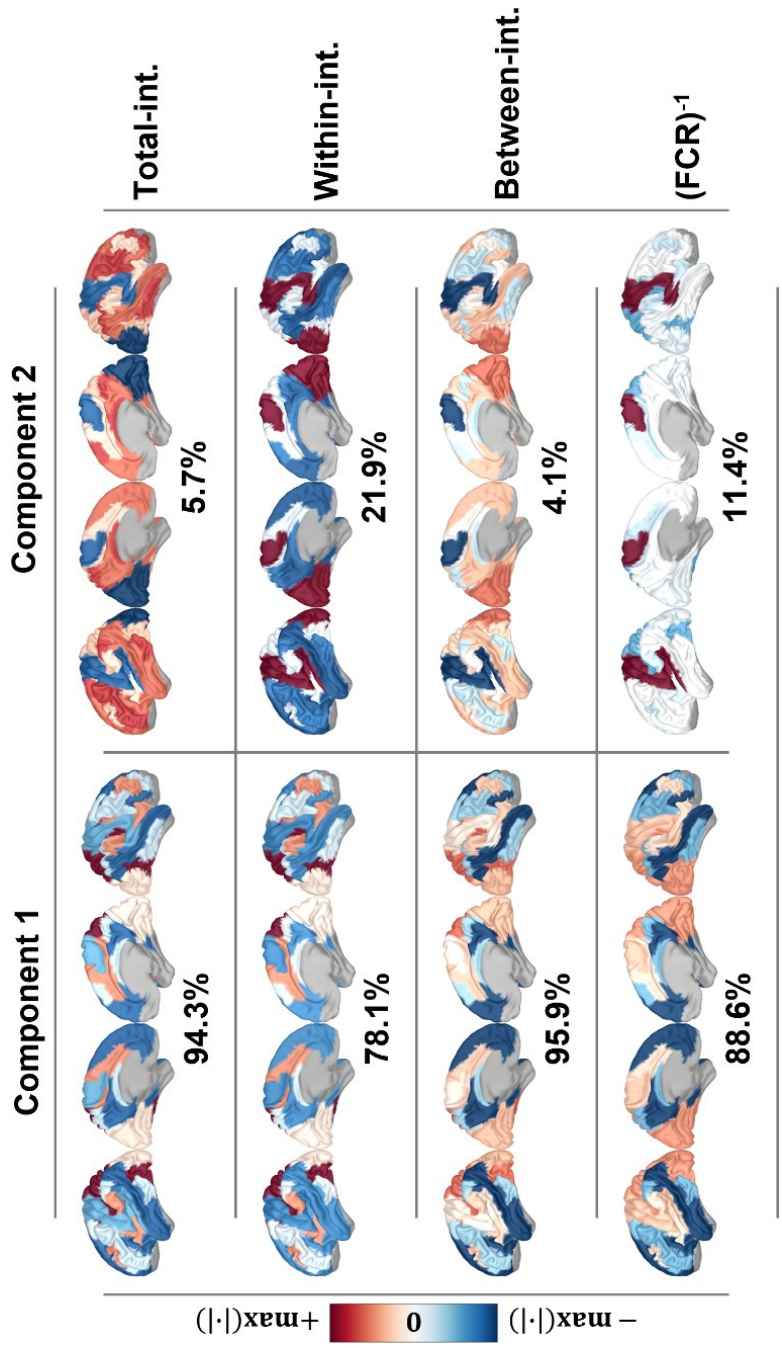

Figure 5.8. PCA-score mappings for CBF datasets. Maps are based on group prediction scores.

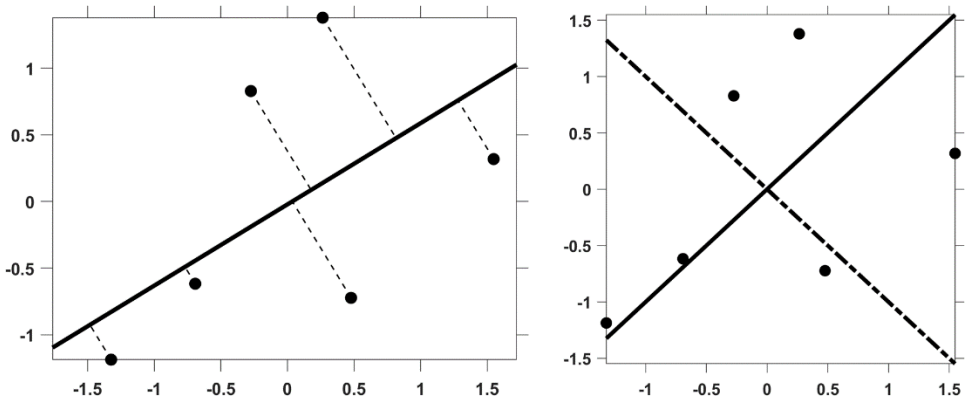

Figure 5.9 Link between signed distance mapping of a point to a regression line and score mapping of a point along a principal component. The graph on the left shows the results of a linear regression. The line of best fit is the solid line and the distance of each point to the line of best fit is represented in dotted lines. The distance is considered positive when the point lies above the line of best fit, and negative otherwise. The graph on the right shows the results of a PCA. The direction of the first component is indicated by the solid line while the direction of the second component is indicated by the dash-dotted line. We understand here that the signed distance mapping with respect to the line of best fit can capture the same qualitative information as the score mapping along the second principal component. Indeed, in the PCA plane, scores along the second principal component are y-coordinates. Similarly, the signed distance mapping with respect to a line perpendicular to the line of best fit that passes though the center of the point cloud can capture the same qualitative information as the score mapping along the first principal component.

Chapter 6: General Discussion

6.1 Summary of main contributions and limitations

The main objective of this thesis was to investigate the vascular and metabolic properties underlying hemodynamic-based resting-state functional connectivity from the healthy human brain. We quantified glucose metabolism (CMRGlc) from FDG PET, oxygen metabolism ($CMRO_2$) as well as other physiological components of cerebral metabolism (CBF, OEF, and CVR) from calibrated fMRI, and functional connectivity from resting state fMRI data. We also used the AHBA, a multimodal atlas of the human brain integrating anatomic and genomic information, to investigate the transcriptional signature of the spatial association between vascular, metabolic, and functional connectivity properties. The following sections detail the main contributions and limitations of each study included in this thesis.

6.1.1 Manuscript 1 — Multiresolution Metabolic Profile of Functional Hubness in the Resting Human Brain

In the first study, we investigated the vascular and metabolic properties of functional hubness. We tested the hypothesis that there exists a concave down increasing power-law model that relates vascular, metabolic (CMRGlc, $CMRO_2$, CBF, and OEF) and functional hubness properties. The semi-quantitative SUVR model (see 1.2.2, (Keyes, 1995)) was used to estimate normalized voxel-maps of glucose metabolism (CMRGlc). The GCM (see 1.11, (Gauthier & Hoge, 2013)) was used to estimate quantitative voxel wise maps of baseline oxygen metabolism ($CMRO_2$), CBF and OEF. SPARK pipeline (see 2.2.3.3.1, (K. Lee et al., 2016)) was used to estimate voxel wise maps of functional hubness. We examined our hypothesis across large-scale networks nested over two spatial resolutions from the MIST atlas (see 2.1.2, (Urchs et al., 2019)) using a multi-level Bayesian model (Gelman et al., 2020). In summary, we generally found strong statistical evidence that an increase in functional hubness is associated with a non-linear (i.e., power-law) increase in CMRGlc, $CMRO_2$, and CBF where increase rates are both network-dependent and resolution-dependent. We also found different increase rates for CMRGlc and $CMRO_2$ suggesting different underlying mechanisms dealing on how different classes of functional hubs are handling glucose versus oxygen consumption. Whereas $CMRO_2$ and CBF results were quite similar, we also found weaker evidence or even no evidence of changes in OEF as a function of hubness.

This study includes several novel contributions. It is the most comprehensive investigation of the vascular and metabolic properties of functional hubs, since it includes both oxygen and glucose metabolism, as well as CBF and the balance between $CMRO_2$ and CBF. Furthermore, our model allows us to probe these relationships across two spatial scales, allowing us to understand whether these properties are dependent on the network scales probed. Investigating both CMRGlc and $CMRO_2$ data not only can provide a comprehensive coverage of the principal substrates of brain metabolism, but can also indirectly reflect the potential contributions of glucose in the oxidative and non-oxidative metabolic pathways (Magistretti & Allaman, 2015). When adding CBF and OEF data, we are also able to reconcile our knowledge of neurovascular coupling in hemodynamic functional connectivity (Magistretti & Allaman, 2015). By employing the GCM on gas-inhalation-based calibrated fMRI data to estimate voxel-maps of $CMRO_2$ and OEF (Gauthier & Hoge, 2013), we are able to offer an alternative to the traditional PET-based studies. Although PET measures of these parameters are accurate, they suffer from the requirement of an injection of exogenous agent with potential exposure to radiation and the need of arterial/venous lines, the need of an on-site cyclotron due to the short half-life of 15O, as well as the relatively long duration of the procedure,

which includes preparation, multiple injections, agent clearance. The cost of these neuroimaging approaches is also relatively high due to the need for special equipment (e.g., cyclotron) or a special agent (F. Xu et al., 2009). In this study we demonstrated that calibrated fMRI combined with GCM proposed by Gauthier et al (Gauthier & Hoge, 2012) offers a promising alternative when studying oxygen metabolism, together with other components monitoring neurovascular coupling processes (CBF, OEF, CVR). Our comparison of MR-based measure of oxygen metabolism with PET glucose metabolism are in agreement with previous PET literature (Hyder et al., 2015), while allowing absolute quantification of baseline metabolism, whereas absolute quantification using PET is a more complex procedure. In addition, we considered our proposed and validated SPARK pipeline (K. Lee et al., 2016) to estimate voxel wise maps of functional hubness. SPARK is offering an interesting alternative to conventional graph-theory-based analyses that have been reported in previous studies (Palombit et al., 2022; D. Tomasi et al., 2013). In their basic format, graph theory metrics suffer from requiring the influence analysis of connectome density threshold or the specification of binary versus weighted graph models. Moreover graph theory metrics, and especially degree centrality considered in Tomasi et al. (D. Tomasi et al., 2013) are also metric known to be biased by the underlying size of the network, whether estimated at the voxel level or on a specific parcellation of the brain. SPARK uses sparse multivariate linear modeling and advanced bootstrapping strategies to build reliable voxel-maps of functional hubness, where the functional hubness of a voxel captures a small and discrete number of "networks" (typically between 1 and 6) the voxel is linearly associated with. The spatial overlap between networks is specifically modelled using sparse GLM, whereas the total number of networks (typically around 20) is estimated from the data. We previously carefully demonstrated that SPARK was able to estimate typical RSN similar to the ones usually reported in the literature, while exhibiting excellent test/ retest reliability (K. Lee et al., 2016). SPARK allows estimating hubness for each voxel, as a discrete number of connected networks (sparse discrete number), as opposed to a large number of connected voxels or regions when using graph theory. It is worth mentioning that SPARK has been successfully applied to study reorganization of brain networks and hubness in epilepsy (K. Lee et al., 2018) (Lee et al NIMG Clin 2018), but also as a function of the level of arousal (K. Lee et al., 2022) and sleep (MSc Thesis of Y. Wang (Y. Wang, 2022)). In our first study, not only we reproduced main results of SPARK reported in Lee et al (NIMG 2016) on another population of healthy controls data, but we also demonstrated very interesting patterns on how vascular and metabolic properties of the healthy brain are varying as a function of functional hubness in a nonlinear manner. However, modeling an effect when considering discrete hubness values ranging only from 1 to 6 is quite challenging from a statistical point of view. We proposed an advance multilevel Bayesian model to carefully model all the sources of variability in our high-dimensional data. By formulating a Bayesian workflow on high-dimensional voxel data, we offer an alternative to traditional frequentist-based approaches which suffer from multiple testing issue, or *p*-value hacking, or the non-specificity of the null hypothesis significant testing on false positive rate (G. Chen et al., 2019). Finally, the Bayesian workflow we used in this work (Gelman et al., 2020) formulates a flexible inference scheme that incorporates our prior knowledge that our subjects belong to a homogeneous population and also that functional networks are interdependent and organized across multiple functionally meaningful spatial resolutions (Urchs et al., 2019). In this way, it not only handles various sources of variability in our data, but it also increases the biological interpretability by indicating areas where metabolism-function relationships may be homogeneous or heterogeneous. Such an approach allowed us to promote very interesting and unique findings on how glucose and oxygen metabolism are supplying

functional hubs in a nonlinear manner, showing inverse power law rates of increase that are modality specific and network specific.

However, our study also suffers from some limitations. First, our acquisition protocol did not allow us to quantitatively estimate PET-CMRGlc (contrasting with quantitative MRI-$CMRO_2$) as we did not have arterial cannulation that is required for modeling absolute CMRGlc estimations or a long enough scanning durations (Heurling et al., 2017). The ability to estimate absolute quantitative CMRGlc maps together with quantitative $CMRO_2$ maps would have been very useful to derive the oxygen-glucose index (OGI; see 1.6.4) which reflects the extent to which glucose is consumed via oxidative pathways, as previously proposed considering PET data only (Hyder et al., 2015; Vaishnavi et al., 2010). Characterizing the spatial distribution of OGI would have been of great interest to further determine the role of aerobic glycolysis in hub regions.

Second, our calibrated fMRI methodology is based on dual fMRI/ASL acquisition. It is worth mentioning that our ASL sequence included a single post labelling delay (PLD), which is shorter than that recommended in the white paper (Alsop et al., 2015). This PLD was optimized by our group in young participants and represents a balance between SNR during rest and during hypercapnia. The choice of such a parameter may be more problematic in older subjects who are known to exhibit longer arterial transit times (Hu et al., 2020; Kochonowicz et al., 2009). In agreement with these findings, we noted during our analyses that the SNR of ASL data was indeed lower for the two oldest subjects in our cohort (aged 32 and 33). However, it also worth mentioning that our overall cohort was mainly composed of healthy "relatively" young adults (mean ± SD age = 24.0 ± 4.3; 9 females). In addition, two of our 19 subjects fainted during FDG injection prior to their respective PET scans. Consequently, we observed that their corresponding CBF data were noticeably lower when compared to the median of CBF ranges measured across the group. However, considering our limited sample size, we decided to include data from these subjects in our analyses. Therefore, inclusion of these lower SNR ASL data could have impacted our results and future studies should aim to consider a larger sample size and to use a multi-PLD ASL implementation.

Third, it is important to mention that SPARK was developed to be reliable at the individual level, it does not include any mathematical constraint for potential group-level analyses. As such, functional hubness maps across subjects can have different ranges and spatial distributions. This implies that the same hubness value between two subjects may not have the same biological significance. This is particularly important for the largest hubness values, which, because they are the fewest in number, they are also the least likely to be found within the same functional brain division across subjects. Although, our Bayesian model took the latter factor into account, it remains unclear how such variability which is expressed voxel-wise on a small range of discrete values affect our analyses. Despite these inherent limitations, test/retest reliability of SPARK was demonstrated in Lee et al (K. Lee et al., 2016), and the group level probability distribution found for hubness $\mathcal{H} = 1, 2, 3$ and ≥ 4 are showing some degree of reproducibility at the group level even if no constraints were considered (see Fig. 3.1.A). However it is worth mentioning that some initiatives have been proposed to promote the development of k-SVD sparse modeling and dictionary learning at the group level (Y. B. Lee et al., 2016). It worth mentioning that a new implementation of SPARK featuring group level dictionary learning will be considered in our group in future investigations.

Fourth, our modular Bayesian modeling was designed to take advantage of the similarities between individuals and between brain networks to derive better estimates. For the sake of simplicity, critical covariates such as the age or sex of our participants were not included. In addition, power-law models, especially those with small scaling exponents cannot be properly characterized when their domain is very restricted (here, our functional hubness values are only ranging between 1 and 6). Preliminary results indicated that an exponential or a rational function such as the Michaelis-Menten model which includes both a horizontal asymptote could fit the data equally well and potentially provide more biological insights by coding, for instance, biological saturations. Future studies should explore these effects to gain additional insight into these relationships and their underlying mechanisms, while considering a larger population to model the effect of other covariates (age, biological sex).

Finally, as for most functional connectivity studies reported in the literature, our results critically depended on the choice of a specific brain parcellation. Here, we chose the MIST atlas (Urchs et al., 2019) because it enabled us to define, in a consistent way across subjects, fully nested networks across a broad range of resolutions, while covering the cortex, the subcortical regions, and the cerebellum. However, it is unclear what the effect of choosing a specific parcellation scheme would have on our data analysis (Arslan et al., 2018; Messé, 2020). This is indeed a fundamental problem faced by many neuroscientific studies. For example, Arslan and colleagues (Arslan et al., 2018) performed an extensive evaluation of different state-of-the-art parcellations generated at the subject and group levels, investigating parcellation accuracy from four different aspects: (i) reproducibility across different acquisitions and groups, (ii) fidelity to the underlying connectivity data, (iii) agreement with fMRI task activation, myelin maps, and cytoarchitectural areas, and (iv) network analysis. In the end, the authors suggested that there is no optimal method able to simultaneously address all the challenges faced in this endeavor. Similarly, Messé (Messé, 2020) performed an extensive evaluation of the influence of a set of state-of-the-art group-wise atlases (including various spatial resolutions) on the connectivity-based structure-function relationship in the human brain. The author observed significant effect of the choice of brain parcellations. In our study, there could be an impact from the inclusion subcortical and cerebellum signals for which signal-to-noise ratios are usually lower than cortical ones. In addition, SPARK provides for each subject data-driven spatial maps of the different "networks" each voxel is associated with. It is unclear how the analysis carried out from such data-driven "networks", or the predefined networks of an atlas may differ or coincide. Future studies should investigate the effects of choosing a specific atlas when investigating the relationship between functional hubness and brain metabolism.

6.1.2 Manuscript 2 — Investigating the transcriptional profile of the blood flow and metabolic cost of functional global and local network connectivity

In the second study, we investigated the cellular and molecular processes associated with spatial patterns of f patterns (M. J. Hawrylycz et al., 2012). Our hypothesis was that vascular, metabolic and functional connectivity patterns share spatial architectures that are shaped by underlying cellular and molecular processes that can be accessed by studying transcriptional data atlases. In this study, we used the Allen Human Brain Atlas (AHBA) to estimate gene expression data. Our vascular and metabolic neuroimaging data consisted of CMRGlc, $CMRO_2$, and CBF maps estimated as in the first study. We also added Cerebrovascular reactivity (CVR) map measuring the ability of cerebral vessels to dilate or constrict in response to vasodilator and vasoconstrictor challenges, in this case, inhalation of CO2. These four maps (CMRGlc, $CMRO_2$, CBF and CVR)

have been referred to as physio-metabolic data in this manuscript. The functional connectivity neuroimaging data consisted of four maps estimated using graph theory, including two measures of global centrality, reflecting integration within networks (eigenvector centrality and global efficiency) and two measures of local centrality, reflecting segregation within networks): (clustering coefficient and local efficiency, see 2.2.2.). We conducted this second analysis at the mesoscale level using Schaefer. Brain parcellation atlas composed of 200 Regions (Schaefer et al., 2018). Using partial least squares (PLS) decomposition of high-dimensionality data (Krishnan et al., 2011), we found two distinct transcriptional patterns characterizing different combinations of global centrality and physio-metabolic data versus local centrality and physio-metabolic data. Using gene ontology (GO) enrichment analysis, we found that the most enriched GOs associated with these two patterns included several signaling and metabolic processes, indicating a high metabolic cost and reliance on oxidative metabolism for global network centrality. Using cell-types deconvolution analysis, we also found that neurons were the most enriched when global centrality together with physio-metabolic data contributed significantly to defining transcriptional patterns. On the other hand, oligodendrocytes were the most enriched when local centrality together with cerebrovascular reactivity were the main contributors.

This original contribution has several novel aspects. We conducted a regional transcription-neuroimaging association study with the most comprehensive set to date of (i) biomarkers of brain metabolic and vascular properties including CMRGlc, $CMRO_2$, CBF, and CVR, as well as (ii) biomarkers of hemodynamic functional connectivity patterns including metrics assessing global and local network centralities. We then applied state-of-the-art procedures (Arnatkevičiūtė et al., 2019) to analyze our gene expression data, including filtering gene expression level, brain samples assignment, data normalization and gene filtering (Arnatkevičiūtė et al., 2019). Finally, a PLS correlation model was considered to describe the relationship between vascular and metabolic properties, and functional global and local network connectivity patterns and transcriptional data. When compared to other multivariate techniques that scale to very large datasets, such as weighted gene co-expression network analysis (B. Zhang & Horvath, 2005), principal component analysis (Bair et al., 2006), or canonical correlation analysis (Hotelling, 1936), PLS methods have been shown to not only optimally and reliably capture the information shared between two data tables, while remaining stable to inter-correlation among data variables (Maitra & Yan, 2008). Our analysis also took advantage of recent strategies to ensure reliability and robustness of our results by using bootstrap and spatial autocorrelation-preserving permutation models (Markello & Misic, 2021). We also sought to obtain a comprehensive understanding of the enriched genes using the functional gene enrichment method (Zhou et al., 2019), to analyze the four following GOs: biological processes, cellular processes, molecular processes, and pathways. Finally, we performed a cell-types deconvolution analysis to determine whether relevant genes are preferentially expressed in specific cell types thereby increasing results interpretability. We found that the most enriched gene ontologies were associated with several signaling and metabolic processes, indicating a high metabolic cost and reliance on oxidative metabolism for global network centrality. We further found that neurons were the most enriched wherever global centrality together with physio-metabolic data contributed significantly to defining transcriptional patterns, whereas oligodendrocytes were the most enriched wherever local centrality together with cerebrovascular reactivity were the main contributors.

Our proposed study nevertheless suffers from some limitations. First**,** we found that our results depended on the choice of brain parcellation. Although, for the sake of conciseness, we did not

report those results, we briefly investigated the effect of using an anatomical atlas (e.g., the Lausanne atlas (Cammoun et al., 2012)) rather than a functional one (e.g., the Schaefer atlas, (Schaefer et al., 2018)). We also investigated the effect of several of atlas resolutions: 57 versus 111 regions for the Lausanne atlas, and 50 versus 100 regions for the Schaefer atlas (results not shown). We determined that the extraction of latent variables and the estimation of gene scores were clearly impacted by such choices. However, we decided to report results obtained using the Schaefer atlas composed of 200 regions to remain consistent with our other studies that were constrained by functional atlases. Future studies should investigate the effects of brain parcellations by taking the use-case of multimodal datasets with markedly different resolutions and SNR (Arslan et al., 2018; Messé, 2020).

Second**,** the estimation of measures of global and local network centrality relies on thresholded and sometimes binarized weighted functional connectomes. In our study, we investigated the effects of connectome density thresholds ranging 20% to 32.5% and found that overall, our main results remained unchanged. We then also investigated the effects of binarizing functional connectomes and found meaningful differences between extracted latent variables as well as gene scores, therefore suggesting that connectivity weights should be kept when estimating graph theory metrics. In addition, we also investigated the effects of deriving group-level graph metrics directly from a group-level functional connectome versus indirectly from the graph metrics obtained at the subject-level. We observed meaningful differences here as well when extracting latent variables or when scoring genes. These detailed explorations indicate that the choice of a graph-theoretical pipeline for identifying connectivity patterns is important (Farahani et al., 2019) and therefore care must be taken when interpreting the results.

Third**,** different approaches for gene enrichment and pathway analysis have been proposed. The two predominant enrichment methods are: (i) over-representation analysis (ORA), which iteratively tests one GO or pathway term at a time against a list of interesting genes for enrichment (Boyle et al., 2004); and (ii) functional class scoring (FCS), which is similar to ORA methods, but considers the distribution of the GO/pathway terms in the entire list of genes (Subramanian et al., 2005). The effect of employing different approaches for gene enrichment analysis has been largely discussed in the literature (Abatangelo et al., 2009; Fabris et al., 2020; Mathur et al., 2018; Tarca et al., 2013). In our study, we employed multiple frameworks of gene and pathway analysis and observed meaningful differences between results. Although we reported here the results for a single reliable framework (Zhou et al., 2019), more thorough comparisons would be warranted.

Fourth, during the preprocessing of gene data, (Arnatkevičiūtė et al., 2019) suggested to apply threshold of 0.1 to the differential stability of gene sets to preferentially retain genes whose expression is consistent across brains, therefore improving overall stability of the results. Increasing gene selection threshold would also improve specificity by filtering out genes that are known to be related to disease or drug targets GO terms (M. Hawrylycz et al., 2015). However, our preliminary analysis showed that employing such a strict threshold not only significantly affected the FDR of resulting GO and pathway terms, but also removed many biologically relevant genes from our analysis. It is possible that this is due to a parcellation-dependent effect of threshold. Future studies are needed to further understand the impact of filtering out genes in high-resolution versus low-resolution or unimodal versus multimodal neuroimaging data.

Finally, we only focused on the left hemisphere of the cerebral cortex when relating gene expression and neuroimaging data. We did so because only two brains out of six in the AHBA

atlas included samples from the right hemisphere, and because of significant differences in the transcriptional signatures of the cortex, subcortex and cerebellum (Patania et al., 2019). By adding between hemispheres projections that are mainly involved long-distance connection, we would expect to see more oxidative metabolic pathway in our results (Vértes et al., 2016). However, future studies could aim at providing a more complete picture of the association between gene expression and neuroimaging data by investigating the whole brain (both hemispheres, neo-cortex, cerebellum, and subcortical areas).

6.1.3 Manuscript 3 — Investigating the metabolic and blood flow costs of functional integration and segregation in resting-state networks

In this third study, we investigated whether patterns of functional integration and functional segregation estimated at the level large-scale resting-state fMRI networks were associated with higher CBF, glucose or oxygen metabolism. The CMRGlc, $CMRO_2$, and CBF data considered for this project were the same as the one considered in our previous projects. In this study we are proposing an analysis at the macroscale network level. To do so, we considered an information theoretic model (see 2.2.3.2.1) to quantify hierarchical measures of resting-state network integration and segregation proposed by Marrelec et al (Marrelec et al., 2008) and further applied in several important studies assessing brain networks integration/segregation patterns in different conditions such as sleep, sleep deprivation or anesthesia (Boly et al., 2012; Marrelec et al., 2008) . Using a robust linear regression model, we consistently found strong linear associations between vascular, metabolic and between integration, segregation data consistent with the hypothesis that functional interactions of intrinsic brain networks are metabolically costly. Importantly, when further analysing the slope of the linear relationship between functional connectivity integration and segregation and physiological properties of brain baseline activity, our results are suggesting resting-state networks of the brain could be further classified into a primary sensory and motor network that include visual, somatic, and auditory areas, versus large association networks involving parietal, temporal, and frontal regions.

In this study, we provided a novel perspective of metabolism-function coupling at the system-scale level of the brain (i.e., the macroscale level) by linking the functional integration and segregation of brain networks to their glucose and oxygen metabolism and blood flow spatial patterns. By employing Shannon information theory to derive functional connectivity measures over a nested hierarchical description of brain networks, the original method proposed by (Marrelec et al., 2008) allows measuring flow of information between and within brain networks, resulting in a complementary approach when compared to SPARK estimating functional hubness at the voxel level and conventional graph-theory-based analyses usually providing results at the regional level of a specific brain parcellation. For instance, the metric f of functional connectivity investigated in this study are directly obtained at the systems level of the brain, which is an intermediate scale between regions (mesoscale) and the whole brain level (Marrelec et al., 2008). Importantly, using measures derived from information theory, the proposed methodology allows capturing nonlinear functional interactions. These functional connectivity metrics can be intuitively interpreted as shared informational content between brain regions within networks and across networks. They are also explicitly embedded as prior assumption that the brain activity can be divided into networks and that each network can in turn be made up of several sub-networks, within a hierarchical architecture. Finally, by combining measures of CMRGlc, $CMRO_2$, and CBF, our analysis is providing a comprehensive coverage of the main markers of brain metabolic and vascular properties in response to neural activity (Magistretti & Allaman, 2015). This suggests

distinct physio-metabolic needs for performing fast real-time multimodal integration of sensory and motor information on the one hand, and for performing broad multi-temporal integration on the other hand. However, we would like to discuss some limitations and future directions for this study. First, the link between connectivity measures, CBF and metabolism was found to be dependent on the choice on the parcellation and underlying hierarchical network structure. We identified this dependency in preliminary analyses using two functional brain parcellations (Schaefer-100 and Schaefer-200) as well as different procedures to assign regions to networks (where networks were defined from Yeo atlases (Thomas Yeo et al., 2011)). This effect was identified in previous studies and would deserve careful investigations in future studies (Arslan et al., 2018; Boly et al., 2012; Messé, 2020).

Second, the MI model proposed by Marrelec et al. (2008) assumes stationarity and Gaussianity of BOLD fMRI data. Although this assumption is commonly used (Liégeois et al., 2017; Marrelec et al., 2008), we note that it is a limited model given the dynamic nature of brain activity (Liégeois et al., 2017). Future studies could adopt an autoregressive model allowing to account for some temporal coherence in the data (Liégeois et al., 2017).

Finally, although we employed a hierarchical Bayesian model to estimate functional connectivity measures (Marrelec et al., 2008), we did not cohesively account for inter-subject variability effects when linking vascular, metabolic and functional connectivity. Therefore, we are limited in our ability to pinpoint where the source of differences in vascular and metabolic profiles of functional connectivity. We are planning to propose to Bayesian multi-level models or mixed effect models as an immediate step to remedy such a limitation in our future studies.

It is worth mentioning that during the MSc thesis of Wang in our laboratory (Y. Wang, 2022), we reconciled the concept of measuring segregation/integration between brain networks using two complementary approaches: (i) using the Functional Clustering Ratio based on MI methodology considered in our present study, (ii) proposing a Hierarchical Segregation Index (HSI), reflects the network segregation at the voxel level derived from SPARK methodology. When applying these two approaches on sleep EEG/fMRI data published in Cross et al (Cross et al., 2021), Y. Wang found a moderate correlation between the HSI and FCR in somatomotor (R2=0.34), dorsal attention (R2= 0.42) and default (R2=0.35) networks during sleep with recovery of cognitive performance following a nap after whole night sleep deprivation (Lee, Wang et al in preparation). In our future investigations, we are planning to extend the present analysis on the relationship between network integration/segregation and patterns of brain blood flow and metabolism to such a complementary metric.

6.2 Future directions

One well-known but nonetheless major bias in our neuroimaging studies originates from the use of non-simultaneously acquired datasets to study the brain, while not accounting for the natural temporal changes associated with different physiological, arousal or behavioral states. Recent technology is now allowing acquiring simultaneous PET-MRI or PET-MRI-EEG data, which would help alleviate this limitation (Aiello et al., 2015; Del Guerra et al., 2018; Ding et al., 2014; Palombit et al., 2022; Shah et al., 2017). For instance, Palombit and colleagues considered simultaneously acquiring PET-fMRI data (Palombit et al., 2022). Using these data, they were able to further confirm previous findings on the relationship between functional hubness and glucose metabolism reported by Tomasi et al (D. Tomasi et al., 2013) and -non-simultaneously acquired data. Collectively, they suggested that brain regions involved in long-range functional connections

are also exhibiting higher glucose metabolism than other regions and that such dependence is network dependent. It would be of great importance to further confirm published findings on the relationship between brain network properties and brain metabolism using simultaneous recordings. Other studies using this type of simultaneous acquisition are necessary to confirm or provide a deeper understanding of the existing metabolism-function literature. MR-compatible PET systems are very costly, difficult to install and only available in a few imaging centres for the moment. On that account, as the first step towards using simultaneously acquired datasets, we could envision collaborations between laboratories where datasets and analysis pipelines could be shared. This is a potential extension of the work done in this thesis, where we could apply our proposed methodologies to simultaneously acquired datasets from other groups and assess statistically to which degree results may remain concordant or differ, or potentially derive confounds that can correct for biases introduced by non-simultaneous acquisitions.

Another well-known bias in our neuroimaging studies originates from using static measures to characterize brain activity (e.g., metabolic activity, vascular activity, or functional activity). However, brain activity is notoriously dynamic and spans multiple spatiotemporal scales. Along these lines, two current trends in metabolism-function coupling studies have been considered: (i) to apply to metabolic data such as CMRGlc or $CMRO_2$ the same connectomic methodologies proposed to analyze BOLD fMRI data (Hubbard et al., 2021; D. G. Tomasi et al., 2017; Voigt et al., 2022); as well as (ii) to start by characterizing dynamic measures of functional connectivity using BOLD fMRI, before assessing the corresponding metabolic and vascular components (Thompson, 2018). Together, these studies suggest that metabolic activity and functional activity share similar network topologies. However, other studies are needed to assess whether dynamic models are able to provide further concordance beyond static models while having to handle underlying mechanisms which are likely to fluctuate at different temporal scales (e.g., glucose versus oxygen metabolism.)

Including simultaneous PET-MRI acquisitions and dynamic functional connectivity analyses of fMRI data to study the metabolic and vascular costs of brain functional integration and segregation is suggested as possible promising perspectives of the work proposed in this thesis. In what follows, we present two other lines of research that can benefit more directly from the neuroimaging data acquisitions and analysis pipelines used in this thesis.

6.2.1 Including a measure of aerobic glycolysis

Aerobic glycolysis (AG) represents the non-oxidative metabolism of glucose that is converted to pyruvate and lactate and produce ATP, despite presence of abundant oxygen (Rogatzki et al., 2015). Glycolysis occurs in the cytoplasm of the cell and the first step of its reaction is:

$$\begin{aligned} &\mathrm{Glucose} + 2\mathrm{NAD}^+ + 2\mathrm{ADP} + 2\mathrm{P_i} \\ &\rightarrow 2\mathrm{Pyruvate} + 2\mathrm{NADH} + 2\mathrm{ATP} + 2\mathrm{H}^+ + 2\mathrm{H_2O} \end{aligned} \tag{6.1}$$

where the resultant pyruvates are staying in the cytoplasm and being converted to lactate by the enzyme lactate dehydrogenase (Chaudhry & Varacallo, 2022).

$$2\mathrm{Pyruvate} + 2\mathrm{NADH} \rightarrow 2\mathrm{Lactate} + 2\mathrm{NAD}^+ \tag{6.2}$$

AG is mainly determined by the molar ratio of oxygen to glucose consumption and is most commonly quantified using the oxygen-glucose index (OGI) (Blazey et al., 2018). As mentioned

in section 1.2 and 1.6.4, in the case of full oxidation of a molecule of glucose, OGI should be 6, while a lower value would indicate that AG is present.

Since PET data acquired for this thesis were only providing semi-quantitative measurements of glucose metabolisms, we were not able to estimate OGI. Moreover, even when quantitative measurements of oxygen and glucose metabolisms are available, the estimation of OGI requires computing a ratio at the voxel level, which may be problematic and sensitive to some numerical instabilities in brain areas with low metabolism (Goyal et al., 2017; Vaishnavi et al., 2010). To overcome this latter issue, Vaishnavi and colleagues (Vaishnavi et al., 2010) suggested an alternative measure, called the glycolytic index (GI), which is estimated from the scaled residuals of a linear regressing CMRGlc as a function of $CMRO_2$ between CMRGlc and $CMRO_2$ Figure 6.1. In this case, positive versus negative GI values away from the predicted regression line would correspond to brain regions exhibiting more and less AG. GI has been shown to exhibit a high spatial anti-correlation with quantitative OGI (Vaishnavi et al., 2010). The cortical regions exhibiting the highest GI value have been found to be within prefrontal cortex, lateral parietal cortex, posterior cingulate/precuneus, lateral temporal gyrus, gyrus rectus, and caudate nuclei. These brain regions are also characterized by elevated functional connectivity profiles and include long-range hub regions. In contrast, the lowest GI was found in the inferior temporal gyrus and throughout the cerebellum. Although quantifying glycolysis using GI provides reasonable results, it does not yield interpretable quantitative values. As an alternative option, Goyal and colleagues (Goyal et al., 2017) suggested defining AG by subtracting the oxidative fraction from CMRGlc as $AG = CMRGlc - CMRO_2/6$. This new alternative measure has been shown to be in agreement with both GI and OGI.

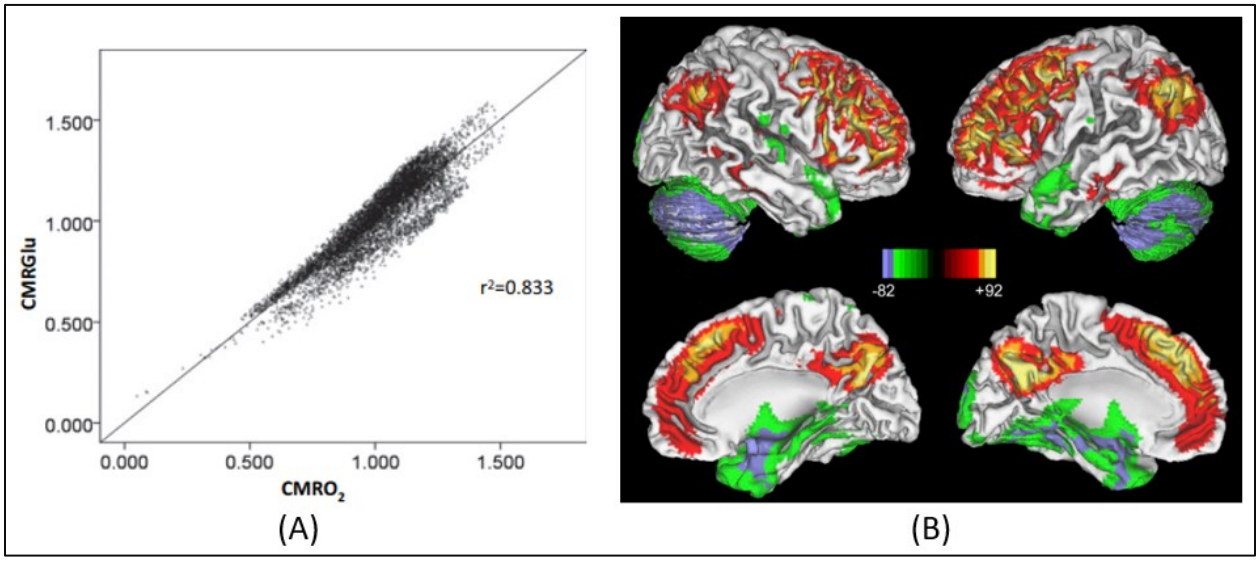

Figure 6.1. Aerobic glycolysis using glycolytic index (GI). (A) Voxel wise linear regression of CMRGlc on $CMRO_2$. GI is defined as the residuals of the linear regression scaled by 1000. (B) Distribution of aerobic glycolysis in resting human brain using GI (number of subjects = 33, groupwise t-test, $|Z|>4.4$, $P < 0.0001$). Figure adapted from (Vaishnavi et al., 2010)

As an extension of the work presented in this thesis, it would have been of great interest to include measures of GI and AG measure, which can significantly increase the way we could interpret the relationship between metabolic and vascular properties of functional connectivity patterns by disentangling between glucose, oxygen and lactate contributions (Magistretti & Allaman, 2015).

This can be considered by investigating the GI and specifying the regions in the brain where the GI is lower than 6, which can be interpreted as utilization of lactate and glycolysis pathway.

While quantifying GI using semi-quantitative CMRGlc and quantitative $CMRO_2$ is plausible; however, considering the scaling difference between the CMRGlc and $CMRO_2$ data, quantifying $AG = CMRGlc - CMRO_2/6$ required defining an appropriate region of interest with respect to which $CMRO_2$ data could be normalized. Hence, in order to be able to include an accurate measure of GI and AG into our analyses, we need to either revisited the CMRGlc data acquisition protocol (to provide quantitative maps) or attempt to build an appropriate model of $CMRO_2$ normalizations, to be used alongside semi-quantitative CMRGlc. Such an approach will be considered in our future investigations but was falling outside the scope of this thesis.

6.2.2 Characterizing metabolic and vascular profiles of functional hubs in focal epilepsy

Brain neurological disorders compromise not only the quality of life of a large population, but also impose a physical, social, and economic burden on individuals and the health and social systems (Gaskin et al., 2017; Gooch et al., 2017; Raggi & Leonardi, 2015). Epilepsy, primarily characterized by recurrent epileptic seizures affects close to 1% of the global population, making it one of the most prevalent neurological condition (De Boer et al., 2008; Tellez‐Zenteno et al., 2004). Focal epilepsy is a sub-type of epilepsy in which seizures affect a small part of the brain and can further be classified by the anatomical location of epileptic seizure: temporal, frontal, parietal and occipital lobe epilepsies. Temporal lobe epilepsy (TLE) is the most common form of focal epilepsy and is associated with recurrent seizures involving paroxysmic bioelectrical neuronal discharges in mesial or lateral/neocortical temporal lobes (Wiebe, 2000).

Several neuroimaging studies have suggested abnormalities and reorganization of brain functional networks in distributed brain regions associated with epilepsy (Maccotta et al., 2013; J. Song et al., 2015; van Diessen et al., 2013; J. Wang et al., 2014). In particular, in TLE, we have reported decreased functional connectivity between the pathological mesial temporal region with contralateral mesial temporal region, as well as regions from the default mode network and mesolimbic regions, i.e. particularly within brain areas containing connector hub regions (Pittau et al., 2012). A review by Stam has shown that in TLE, hub regions tend to become non-hubs, with acute network disruptions where long-range connection hub regions are normally located (van Diessen et al., 2013) . Other resting-state fMRI studies have reported similar disruptions in hub regions (Ridley et al., 2015; Vaughan et al., 2016). Using SPARK, our group proposed some methodology to quantify the disruption and emergence of connector hubs in TLE patients and found specific reorganization of asymmetrical connector hubs, disruption of hubs' distant connections, and the emergence of local connections (K. Lee et al., 2018). A commonly accepted hypothesis is that an epileptic network that is getting regularized, i.e. only locally connected and isolated from the rest of the brain, would correspond to good prediction of postsurgical outcome after resection of the epileptic focus (Y. Wang et al., 2022). On the other hand, resecting an epileptic focus associated with a widespread network, involving the emergence of several long-distance connections, would be more likely to bad postsurgical outcomes. Our preliminary results applying functional connectivity analysis on resting-state MEG data are confirming these hypotheses (Aydin et al., 2020)

FDG-PET is also frequently used to identify brain regions exhibiting abnormal glucose metabolism in epilepsy patients (Chugani et al., 1990, 1993; Chugani & Conti, 1996). Epilepsy

patients with very frequent or continuous seizures have disrupted metabolic profiles, usually resulting in glucose hypermetabolism within epileptic foci (Alkonyi et al., 2011; Bansal et al., 2016; Ding et al., 2014). Furthermore, epileptic seizures not only disrupt glucose metabolism but also regional cerebral blood flow, oxygen extraction fraction and oxygen consumption. Epilepsy patients show an imbalance between blood flow, glucose utilization, and oxygen consumption within most regions affected by epileptic seizures (Bruehl et al., 1998; Franck et al., 1989).

As a direct extension of the developments proposed in this thesis, our next objective will be a neuroimaging-based study of the link between metabolism and function in epileptic patients, when compared to healthy subjects. We expect to find a degree of deviation in the relationship between the vascular-metabolic and brain functional connectivity features. Hence, we hypothesize that epilepsy is associated not only with differences in the vascular and metabolic costs of functional hubness but also with differences in the vascular and metabolic costs of large-scale network integration and segregation. To assess these effects, an imaging framework such as the one developed in this thesis could be of great interest. Since our analyses cohesively bridge various "macroscales" that ultimately link to large-scale brain networks, we expect to provide a more comprehensive understanding of disease network phenotypes. Ultimately, this may translate into better-targeted treatments, from drugs to surgeries. We further suggest that estimating a glycolytic index to quantify which brain regions exhibit excess aerobic glycolysis in the healthy brain and in epilepsy, would be more likely to result in developing new promising biomarkers to predict epilepsy postsurgical outcomes. Epileptic hubs are hypothesized to be more metabolically demanding than healthy hubs, so they are expected to express greater anaerobic glycolysis as a means to synthesize ATP more rapidly.

6.3 Conclusion

This PhD thesis focused on the relationships between resting-state brain vascular and metabolic patterns and functional hemodynamic connectivity patterns in healthy humans. We proposed an innovative multimodal neuroimaging acquisition protocol based on PET and MRI to non-invasively capture different facets of brain metabolic and vascular activities. Our vascular and metabolic maps included: glucose metabolism (CMRGlc), oxygen metabolism ($CMRO_2$), blood flow (CBF), the fraction of oxygen extracted (OEF), and vessels' ability to dilate or constrict following a dilatory stimulus (CVR). We also quantified different facets of brain functional connectivity at different spatial scales spanning from voxels to regions to large-scale networks, providing brain maps of functional hubness, functional global and local network centralities and functional network's capacity to integrate and segregate information. A multimodal atlas of the human brain integrating anatomic and genomic information, the AHBA, was additionally used to non-invasively bridge between molecular content and neuroimaging findings.

In our first project, we showed that a non-linear monotonic increasing model can be used to describe how CMRGlc, $CMRO_2$ and CBF vary with respect to functional hubness at the voxel level, whereas we found almost no dependence of OEF with functional hubness. We also provided evidence that there is a significant dependence between these relationships and the nature or size of the functional brain parcellation used, our findings are network-dependent and spatial resolution/scale-dependent). Hence, our results suggest that higher hubness implies higher vascular and metabolic costs, especially within *higher-order function* networks. In our second project, we showed that vascular, metabolic and functional global and local network centrality patterns share spatial architectures that are shaped by distinctive molecular processes. In particular,

the spatial architectures consisted of different combinations of functional global network centralities and vascular and metabolic data on one hand, and functional local network centralities and vascular and metabolic data on the other hand. In addition, we showed that the most enriched gene ontologies associated with the different spatial architectures were distinct and included several signalling and metabolic processes, suggesting a high metabolic cost and reliance on oxidative metabolism for functional global network centralities. Meanwhile, neurons were the most enriched for spatial architectures including functional global network centralities, whereas oligodendrocytes were the most enriched for spatial architectures including functional local network centralities. In our third project, we demonstrated that higher integration or lower segregation levels are associated with higher vascular and metabolic costs. We also demonstrated that the resting-state networks of the brain can be classified according to their relationship with vascular and metabolic properties into a primary sensory and motor cluster that includes visual, somatic, and auditory areas, and a large association cluster that comprises parietal, temporal, and frontal regions. Our results are therefore suggesting distinct vascular and metabolic needs for performing fast real-time multimodal integration of sensory and motor information on the one hand, and for performing higher-order multi-temporal integration on the other hand.

Bibliography

Aanerud, J., Borghammer, P., Mallar Chakravarty, M., Vang, K., Rodell, A. B., Jónsdottir, K. Y., Møller, A., Ashkanian, M., Vafaee, M. S., Iversen, P., Johannsen, P., & Gjedde, A. (2012). Brain energy metabolism and blood flow differences in healthy aging. *Journal of Cerebral Blood Flow and Metabolism*, *32*(7), 1177–1187. https://doi.org/10.1038/jcbfm.2012.18

Abatangelo, L., Maglietta, R., Distaso, A., D'Addabbo, A., Creanza, T. M., Mukherjee, S., & Ancona, N. (2009). Comparative study of gene set enrichment methods. *BMC Bioinformatics*, *10*(1), 1–12.

Achanta, L. B., & Rae, C. D. (2017). β-Hydroxybutyrate in the Brain: One Molecule, Multiple Mechanisms. *Neurochemical Research*, *42*(1), 35–49. https://doi.org/10.1007/S11064-016-2099-2

Achard, S., Salvador, R., Whitcher, B., Suckling, J., & Bullmore, E. (2006). A resilient, low-frequency, small-world human brain functional network with highly connected association cortical hubs. *Journal of Neuroscience*, *26*(1), 63–72. https://doi.org/10.1523/JNEUROSCI.3874-05.2006

Ad-Dab'bagh, Y., Lyttelton, O., Muehlboeck, J. S., Lepage, C., Einarson, D., Mok, K., Ivanov, O., Vincent, R. D., Lerch, J., & Fombonne, E. (2006). The CIVET image-processing environment: a fully automated comprehensive pipeline for anatomical neuroimaging research. *Proceedings of the 12th Annual Meeting of the Organization for Human Brain Mapping*, *2266*.

Adachi, Y., Osada, T., Sporns, O., Watanabe, T., Matsui, T., Miyamoto, K., & Miyashita, Y. (2012). Functional Connectivity between Anatomically Unconnected Areas Is Shaped by Collective Network-Level Effects in the Macaque Cortex. *Cerebral Cortex*, *22*(7), 1586–1592. https://doi.org/10.1093/cercor/bhr234

Adair, J. C., & Meador, K. J. (2003). *Parietal lobe*.

Aguirre, G. K., Detre, J. A., Zarahn, E., & Alsop, D. C. (2002). Experimental design and the relative sensitivity of BOLD and perfusion fMRI. *NeuroImage*, *15*(3), 488–500. https://doi.org/10.1006/nimg.2001.0990

Aharon, M., Elad, M., & Bruckstein, A. (2006). K-SVD: An Algorithm for Designing Overcomplete Dictionaries for Sparse Representation. *IEEE Transactions on Signal Processing*, *54*(11), 4311–4322. https://doi.org/10.1109/TSP.2006.881199

Ahmad, M., Wolberg, A., & Kahwaji, C. I. (2022). Biochemistry, Electron Transport Chain. *StatPearls*.

Aiello, M., Salvatore, E., Cachia, A., Pappatà, S., Cavaliere, C., Prinster, A., Nicolai, E., Salvatore, M., Baron, J. C., & Quarantelli, M. (2015). Relationship between simultaneously acquired resting-state regional cerebral glucose metabolism and functional MRI: A PET/MR hybrid scanner study. *NeuroImage*, *113*, 111–121. https://doi.org/10.1016/j.neuroimage.2015.03.017

Akiyama, H., Meyer, J. S., Mortel, K. F., Yasuo Terayama, Thornby, J. I., & Konno, S. (1997).

Normal human aging: Factors contributing to cerebral atrophy. *Journal of the Neurological Sciences*, *152*(1), 39–49. https://doi.org/10.1016/S0022-510X(97)00141-X

Albert, N. B., Robertson, E. M., & Miall, R. C. (2009). The resting human brain and motor learning. *Current Biology*, *19*(12), 1023–1027.

Alberts, B., Johnson, A., Lewis, J., Raff, M., Roberts, K., & Walter, P. (2002). *How Cells Obtain Energy from Food*.

Alkonyi, B., Chugani, H. T., & Juhász, C. (2011). Transient focal cortical increase of interictal glucose metabolism in Sturge-Weber syndrome: Implications for epileptogenesis. *Epilepsia*, *52*(7), 1265–1272.

Alsop, D. C., Detre, J. A., Golay, X., Günther, M., Hendrikse, J., Hernandez-Garcia, L., Lu, H., Macintosh, B. J., Parkes, L. M., Smits, M., Van Osch, M. J. P., Wang, D. J. J., Wong, E. C., & Zaharchuk, G. (2015). Recommended Implementation of Arterial Spin Labeled Perfusion MRI for Clinical Applications: A consensus of the ISMRM Perfusion Study Group and the European Consortium for ASL in Dementia. *Magnetic Resonance in Medicine*, *73*(1), 102. https://doi.org/10.1002/MRM.25197

Ances, B. M., Leontiev, O., Perthen, J. E., Liang, C., Lansing, A. E., & Buxton, R. B. (2008). Regional differences in the coupling of cerebral blood flow and oxygen metabolism changes in response to activation: implications for BOLD-fMRI. *Neuroimage*, *39*(4), 1510–1521.

Andrews-Hanna, J. R., Snyder, A. Z., Vincent, J. L., Lustig, C., Head, D., Raichle, M. E., & Buckner, R. L. (2007). Disruption of Large-Scale Brain Systems in Advanced Aging. *Neuron*, *56*(5), 924–935. https://doi.org/10.1016/j.neuron.2007.10.038

Anna Chruścik, Kate Kauter, Louisa Windus, E. W. (2013). *Fundamentals of Anatomy and Physiology*. by OpenStax is licensed under Creative Commons Attribution License v4.0.

Arango-Lievano, M., Boussadia, B., De Terdonck, L. D. T., Gault, C., Fontanaud, P., Lafont, C., Mollard, P., Marchi, N., & Jeanneteau, F. (2018). Topographic Reorganization of Cerebrovascular Mural Cells under Seizure Conditions. *Cell Reports*, *23*(4), 1045–1059. https://doi.org/10.1016/j.celrep.2018.03.110

Arnatkeviciute, A., Fulcher, B. D., Bellgrove, M. A., & Fornito, A. (2021). Where the genome meets the connectome: understanding how genes shape human brain connectivity. *Neuroimage*, *244*, 118570.

Arnatkevičiūtė, A., Fulcher, B. D., & Fornito, A. (2019). A practical guide to linking brain-wide gene expression and neuroimaging data. *NeuroImage*, *189*(July 2018), 353–367. https://doi.org/10.1016/j.neuroimage.2019.01.011

Arnatkeviciute, A., Fulcher, B. D., Oldham, S., Tiego, J., Paquola, C., Gerring, Z., Aquino, K., Hawi, Z., Johnson, B., Ball, G., Klein, M., Deco, G., Franke, B., Bellgrove, M. A., & Fornito, A. (2021). Genetic influences on hub connectivity of the human connectome. *Nature Communications*, *12*(1). https://doi.org/10.1038/S41467-021-24306-2

Arslan, S., Ktena, S. I., Makropoulos, A., Robinson, E. C., Rueckert, D., & Parisot, S. (2018). Human brain mapping: A systematic comparison of parcellation methods for the human cerebral cortex. *NeuroImage*, *170*, 5–30.

https://doi.org/10.1016/J.NEUROIMAGE.2017.04.014

Assaf, Y., Alexander, D. C., Jones, D. K., Bizzi, A., Behrens, T. E., & Clark, C. A. (2013). The CONNECT project: combining macro-and micro-structure. *Neuroimage*, *80*, 273–282. https://doi.org/10/f46mwn

Attwell, D., Buchan, A. M., Charpak, S., Lauritzen, M., MacVicar, B. A., & Newman, E. A. (2010). Glial and neuronal control of brain blood flow. *Nature*, *468*(7321), 232–243.

Attwell, D., & Iadecola, C. (2002). The neural basis of functional brain imaging signals. *Trends in Neurosciences*, *25*(12), 621–625.

Attwell, D., & Laughlin, S. B. (2001). An energy budget for signaling in the grey matter of the brain. *Journal of Cerebral Blood Flow and Metabolism*, *21*(10), 1133–1145. https://doi.org/10.1097/00004647-200110000-00001

Aubert-Broche, B., Grova, C., Pike, G. B., & Collins, D. L. (2009). Clustering of atlas-defined cortical regions based on relaxation times and proton density. *NeuroImage*, *47*(2), 523–532. https://doi.org/10.1016/J.NEUROIMAGE.2009.04.079

Avants, B. B., Epstein, C. L., Grossman, M., & Gee, J. C. (2008). Symmetric diffeomorphic image registration with cross-correlation: evaluating automated labeling of elderly and neurodegenerative brain. *Medical Image Analysis*, *12*(1), 26–41. https://doi.org/10.1016/J.MEDIA.2007.06.004

Avants, B. B., Tustison, N. J., Song, G., Cook, P. A., Klein, A., & Gee, J. C. (2011). A reproducible evaluation of ANTs similarity metric performance in brain image registration. *NeuroImage*, *54*(3), 2033–2044. https://doi.org/10.1016/J.NEUROIMAGE.2010.09.025

Aydin, Ü., Pellegrino, G., Ali, O. B. K., Abdallah, C., Dubeau, F., Lina, J.-M., Kobayashi, E., & Grova, C. (2020). Magnetoencephalography resting state connectivity patterns as indicatives of surgical outcome in epilepsy patients. *Journal of Neural Engineering*, *17*(3), 035007. https://doi.org/10.1088/1741-2552/ab8113

Badhwar, A. P., Tam, A., Dansereau, C., Orban, P., Hoffstaedter, F., & Bellec, P. (2017). Resting-state network dysfunction in Alzheimer's disease: A systematic review and meta-analysis. *Alzheimer's & Dementia : Diagnosis, Assessment & Disease Monitoring*, *8*, 73. https://doi.org/10.1016/J.DADM.2017.03.007

Bagarinao, E., Watanabe, H., Maesawa, S., Mori, D., Hara, K., Kawabata, K., Ohdake, R., Masuda, M., Ogura, A., Kato, T., Koyama, S., Katsuno, M., Wakabayashi, T., Kuzuya, M., Hoshiyama, M., Isoda, H., Naganawa, S., Ozaki, N., & Sobue, G. (2020). Identifying the brain's connector hubs at the voxel level using functional connectivity overlap ratio. *NeuroImage*, *222*(117241), 117241. https://doi.org/10.1016/j.neuroimage.2020.117241

Bair, E., Hastie, T., Paul, D., & Tibshirani, R. (2006). Prediction by Supervised Principal Components. *Journal of the American Statistical Association*, *101*(473), 119–137. https://doi.org/10.1198/016214505000000628

Bak, L. K., Walls, A. B., Schousboe, A., Ring, A., Sonnewald, U., & Waagepetersen, H. S. (2009). Neuronal glucose but not lactate utilization is positively correlated with NMDA-induced neurotransmission and fluctuations in cytosolic Ca2+ levels. *Journal of Neurochemistry*, *109*,

87–93.

Ball, T., Rahm, B., Eickhoff, S. B., Schulze-Bonhage, A., Speck, O., & Mutschler, I. (2007). Response Properties of Human Amygdala Subregions: Evidence Based on Functional MRI Combined with Probabilistic Anatomical Maps. *PLoS ONE*, *2*(3), e307. https://doi.org/10.1371/journal.pone.0000307

Banks, W. A. (2009). Characteristics of compounds that cross the blood-brain barrier. *BMC Neurology*, *9*(SUPPL. 1), 1–5. https://doi.org/10.1186/1471-2377-9-S1-S3/FIGURES/1

Bansal, L., Miller, I., Hyslop, A., Bhatia, S., Duchowny, M., & Jayakar, P. (2016). PET hypermetabolism in medically resistant childhood epilepsy: incidence, associations, and surgical outcome. *Epilepsia*, *57*(3), 436–444.

Baraba, A. L. (1999). si, R. Albert, H. Joeng. *Physica A*, *272*, 173.

Barabási, A.-L. (2009). Scale-Free Networks: A Decade and Beyond. *Science*, *325*(5939), 412–413. https://doi.org/10.1126/science.1173299

Barber, T. W., Brockway, J. A., & Higgins, L. S. (1970). The density of tissues in and about the head. *Acta Neurologica Scandinavica*, *46*(1), 85–92.

Barhoum, S., Rodgers, Z. B., Langham, M., Magland, J. F., Li, C., & Wehrli, F. W. (2015). Comparison of MRI methods for measuring whole-brain venous oxygen saturation. *Magnetic Resonance in Medicine*, *73*(6), 2122–2128.

Baronchelli, A., Ferrer-i-Cancho, R., Pastor-Satorras, R., Chater, N., & Christiansen, M. H. (2013). Networks in cognitive science. *Trends in Cognitive Sciences*, *17*(7), 348–360.

Barrat, A., Barthélemy, M., Pastor-Satorras, R., & Vespignani, A. (2004). The architecture of complex weighted networks. *Proceedings of the National Academy of Sciences*, *101*(11), 3747–3752. https://doi.org/10.1073/PNAS.0400087101

Basser, P. J., & Roth, B. J. (2000). New Currents in Electrical Stimulation of Excitable Tissues. *Annual Review of Biomedical Engineering*, *2*(1), 377–397. https://doi.org/10.1146/annurev.bioeng.2.1.377

Bassett, D. S., & Bullmore, E. (2006). Small-world brain networks. *Neuroscientist*, *12*(6), 512–523. https://doi.org/10.1177/1073858406293182

Bassett, D. S., & Bullmore, E. T. (2017). Small-World Brain Networks Revisited. *The Neuroscientist*, *23*(5), 499–516. https://doi.org/10.1177/1073858416667720

Bassett, D. S., & Siebenhühner, F. (2013). Multiscale Network Organization in the Human Brain. *Multiscale Analysis and Nonlinear Dynamics: From Genes to the Brain*, 179–204. https://doi.org/10.1002/9783527671632.CH07

Bassett, D. S., & Sporns, O. (2017). Network neuroscience. *Nature Neuroscience*, *20*(3), 353–364. https://doi.org/10.1038/nn.4502

Béard, E., & Braissant, O. (2010). Synthesis and transport of creatine in the CNS: Importance for cerebral functions. *Journal of Neurochemistry*, *115*(2), 297–313. https://doi.org/10.1111/j.1471-4159.2010.06935.x

Beggs, J. M., & Plenz, D. (2003). Neuronal Avalanches in Neocortical Circuits. *The Journal of Neuroscience*, *23*(35), 11167–11177. https://doi.org/10.1523/JNEUROSCI.23-35-11167.2003

Bélanger, M., Allaman, I., & Magistretti, P. J. (2011). Brain Energy Metabolism: Focus on Astrocyte-Neuron Metabolic Cooperation. *Cell Metabolism*, *14*(6), 724–738. https://doi.org/10.1016/J.CMET.2011.08.016

Bélanger, M., & Magistretti, P. J. (2022). The role of astroglia in neuroprotection. *Https://Doi.Org/10.31887/DCNS.2009.11.3/Mbelanger*, *11*(3), 281–296. https://doi.org/10.31887/DCNS.2009.11.3/MBELANGER

Bell, R. D., Winkler, E. A., Singh, I., Sagare, A. P., Deane, R., Wu, Z., Holtzman, D. M., Betsholtz, C., Armulik, A., Sallstrom, J., Berk, B. C., & Zlokovic, B. V. (2012). Apolipoprotein E controls cerebrovascular integrity via cyclophilin A. *Nature*, *485*(7399), 512–516. https://doi.org/10.1038/NATURE11087

Bellec, P., Carbonnell, F., Perlbarg, V., Lepage, C., Lyttelton, O., Fonov, V., Janke, A., Tohka, J., & Evans, A. (2011). A neuroimaging analyses kit for Matlab and octave. *Human Brain Mapping HBM 2011 17th Annual Meeting of the Organization on Human Brain Mapping, Quebec City, Canada, June 26-30, 2011*, 1–5.

Bellec, P., Rosa-Neto, P., Benali, H., & Evans, A. C. (2009). Multi-level bootstrap analysis of stable clusters (BASC) in resting-state fMRI. *Neuroimage*, *47*, S123. https://doi.org/10.1016/j.neuroimage.2010.02.082

Bellec, P., Rosa-Neto, P., Lyttelton, O. C., Benali, H., & Evans, A. C. (2010). Multi-level bootstrap analysis of stable clusters in resting-state fMRI. *NeuroImage*, *51*(3), 1126–1139. https://doi.org/10.1016/j.neuroimage.2010.02.082

Bentivoglio, M. (1998). Life and discoveries of Santiago Ramón y Cajal. *Nobelprize. Org*, *20*.

Benveniste, H., Dienel, G., Jacob, Z., Lee, H., Makaryus, R., Gjedde, A., Hyder, F., & Rothman, D. L. (2018). Trajectories of brain lactate and re-visited oxygen-glucose index calculations do not support elevated non-oxidative metabolism of glucose across childhood. *Frontiers in Neuroscience*, *12*, 631.

Berg, J. M., Tymoczko, J. L., & Stryer, L. (2002a). Glycolysis is an energy-conversion pathway in many organisms. *Biochemistry. 5th Ed. New York: WH Freeman*, 433–434.

Berg, J. M., Tymoczko, J. L., & Stryer, L. (2002b). Metabolism is composed of many coupled, interconnecting reactions. *Biochemistry. 5th Ed. New York: WH Freeman*.

Berg, J. M., Tymoczko, J. L., & Stryer, L. (2002c). Proteins are degraded to amino acids. *Biochemistry; WH Freeman: New York, NY, USA*.

Bergers, G., & Song, S. (2005). The role of pericytes in blood-vessel formation and maintenance. *Neuro-Oncology*, *7*(4), 452. https://doi.org/10.1215/S1152851705000232

Bergles, D. E., Jabs, R., & Steinhäuser, C. (2010). Neuron-glia synapses in the brain. *Brain Research Reviews*, *63*(1–2), 130. https://doi.org/10.1016/J.BRAINRESREV.2009.12.003

Bernier, L. P., Brunner, C., Cottarelli, A., & Balbi, M. (2021). Location Matters: Navigating Regional Heterogeneity of the Neurovascular Unit. *Frontiers in Cellular Neuroscience*, *15*, 696540. https://doi.org/10.3389/FNCEL.2021.696540

Bernier, M., Croteau, E., Castellano, C.-A., Cunnane, S. C., & Whittingstall, K. (2017). Spatial distribution of resting-state BOLD regional homogeneity as a predictor of brain glucose uptake: a study in healthy aging. *Neuroimage*, *150*, 14–22.

Berti, V., Mosconi, L., & Pupi, A. (2014). Brain: normal variations and benign findings in fluorodeoxyglucose-PET/computed tomography imaging. *PET Clinics*, *9*(2), 129–140.

Berto, S., Treacher, A. H., Caglayan, E., Luo, D., Haney, J. R., Gandal, M. J., Geschwind, D. H., Montillo, A. A., & Konopka, G. (2022). Association between resting-state functional brain connectivity and gene expression is altered in autism spectrum disorder. *Nature Communications 2022 13:1*, *13*(1), 1–11. https://doi.org/10.1038/s41467-022-31053-5

Bertolero, M. A., Yeo, B. T. T., & D'Esposito, M. (2017). The diverse club. *Nature Communications*, *8*(1), 1277. https://doi.org/10.1038/s41467-017-01189-w

Bettinardi, V., Pagani, E., Gilardi, M., Alenius, S., Thielemans, K., Teras, M., & Fazio, F. (2002). Implementation and evaluation of a 3D one-step late reconstruction algorithm for 3D positron emission tomography brain studies using median root prior. *European Journal of Nuclear Medicine*, *29*(1), 7–18. https://doi.org/10.1007/s002590100651

Betts, J. G., Young, K. A., Wise, J. A., Johnson, E., Poe, B., Kruse, D. H., Korol, O., Johnson, J. E., Womble, M., & DeSaix, P. (2013). *Anatomy and physiology*.

Biswal, B., Zerrin Yetkin, F., Haughton, V. M., & Hyde, J. S. (1995). Functional connectivity in the motor cortex of resting human brain using echo-planar mri. *Magnetic Resonance in Medicine*, *34*(4), 537–541. https://doi.org/10.1002/mrm.1910340409

Blaustein, M. P., Kao, J. P. Y., & Matteson, D. R. (2011). *Cellular Physiology and Neurophysiology*. Elsevier Health Sciences.

Blazey, T., Snyder, A. Z., Goyal, M. S., Vlassenko, A. G., & Raichle, M. E. (2018). A systematic meta-analysis of oxygen-toglucose and oxygen-to-carbohydrate ratios in the resting human brain. *PLoS ONE*, *13*(9), 1–14. https://doi.org/10.1371/journal.pone.0204242

Bloch, S., Obari, D., & Girouard, H. (2015). Angiotensin and neurovascular coupling: beyond hypertension. *Microcirculation*, *22*(3), 159–167.

Blondel, V. D., Guillaume, J.-L., Lambiotte, R., & Lefebvre, E. (2008). Fast unfolding of communities in large networks. *Journal of Statistical Mechanics: Theory and Experiment*, *2008*(10), P10008. https://doi.org/10.1088/1742-5468/2008/10/P10008

Boellaard, R. (2009). Standards for PET image acquisition and quantitative data analysis. *Journal of Nuclear Medicine*, *50*(SUPPL. 1), 11–20. https://doi.org/10.2967/jnumed.108.057182

Boellaard, R., Krak, N. C., Hoekstra, O. S., & Lammertsma, A. A. (2004). Effects of noise, image resolution, and ROI definition on the accuracy of standard uptake values: A simulation study. *Journal of Nuclear Medicine*, *45*(9), 1519–1527.

Bohland, J. W., Bokil, H., Allen, C. B., & Mitra, P. P. (2009). The Brain Atlas Concordance Problem: Quantitative Comparison of Anatomical Parcellations. *PLoS ONE*, *4*(9), e7200. https://doi.org/10.1371/journal.pone.0007200

Bolar, D. S., Rosen, B. R., Sorensen, A. G., & Adalsteinsson, E. (2011). QUantitative Imaging of eXtraction of oxygen and TIssue consumption (QUIXOTIC) using venular-targeted velocity-selective spin labeling. *Magnetic Resonance in Medicine*, *66*(6), 1550–1562.

Boly, M., Perlbarg, V., Marrelec, G., Schabus, M., Laureys, S., Doyon, J., Pélégrini-Issac, M., Maquet, P., & Benali, H. (2012). Hierarchical clustering of brain activity during human nonrapid eye movement sleep. *Proceedings of the National Academy of Sciences of the United States of America*, *109*(15), 5856–5861. https://doi.org/10.1073/pnas.1111133109

Bonacich, P. (2007). Some unique properties of eigenvector centrality. *Social Networks*, *29*(4), 555–564. https://doi.org/10.1016/J.SOCNET.2007.04.002

Bordier, C., Dojat, M., & Micheaux, P. L. de. (2011). Temporal and Spatial Independent Component Analysis for fMRI Data Sets Embedded in the AnalyzeFMRI R Package. *Journal of Statistical Software*, *44*(9), 1–24. https://doi.org/10.18637/jss.v044.i09

Borowsky, I. W., & Collins, R. C. (1989). Metabolic anatomy of brain: A comparison of regional capillary density, glucose metabolism, and enzyme activities. *Journal of Comparative Neurology*, *288*(3), 401–413. https://doi.org/10.1002/cne.902880304

Bota, M., Sporns, O., & Swanson, L. W. (2015). Architecture of the cerebral cortical association connectome underlying cognition. *Proceedings of the National Academy of Sciences*, *112*(16), E2093-101. https://doi.org/10.1073/pnas.1504394112

Bouzier-Sore, A.-K., Voisin, P., Canioni, P., Magistretti, P. J., & Pellerin, L. (2003). Lactate is a preferential oxidative energy substrate over glucose for neurons in culture. *Journal of Cerebral Blood Flow & Metabolism*, *23*(11), 1298–1306.

Boyle, E. I., Weng, S., Gollub, J., Jin, H., Botstein, D., Cherry, J. M., & Sherlock, G. (2004). GO:: TermFinder—open source software for accessing Gene Ontology information and finding significantly enriched Gene Ontology terms associated with a list of genes. *Bioinformatics*, *20*(18), 3710–3715.

Braissant, O. (2012). Creatine and guanidinoacetate transport at blood-brain and blood-cerebrospinal fluid barriers. *Journal of Inherited Metabolic Disease*, *35*(4), 655–664.

Brini, M., Calì, T., Ottolini, D., & Carafoli, E. (2014). Neuronal calcium signaling: function and dysfunction. *Cellular and Molecular Life Sciences : CMLS*, *71*(15), 2787–2814. https://doi.org/10.1007/S00018-013-1550-7

Brodmann, K., & Garey, L. J. (2006). Brodmann's localisation in the cerebral cortex: The principles of comparative localisation in the cerebral cortex based on cytoarchitectonics. *Brodmann's Localisation in the Cerebral Cortex: The Principles of Comparative Localisation in the Cerebral Cortex Based on Cytoarchitectonics*, 1–298. https://doi.org/10.1007/B138298

Brody, T. (1999). REGULATION OF ENERGY METABOLISM. *Nutritional Biochemistry*, 157–271. https://doi.org/10.1016/B978-012134836-6/50007-X

Brookes, M. J., Woolrich, M., Luckhoo, H., Price, D., Hale, J. R., Stephenson, M. C., Barnes, G. R., Smith, S. M., & Morris, P. G. (2011). Investigating the electrophysiological basis of resting state networks using magnetoencephalography. *Proceedings of the National Academy of Sciences of the United States of America*, *108*(40), 16783–16788. https://doi.org/10.1073/PNAS.1112685108

Brooks, G. A. (2009). Cell–cell and intracellular lactate shuttles. *The Journal of Physiology*, *587*(Pt 23), 5591. https://doi.org/10.1113/JPHYSIOL.2009.178350

Brown, A. M. (2004). Brain glycogen re-awakened. *Journal of Neurochemistry*, *89*(3), 537–552.

Bruce, K. D., Zsombok, A., & Eckel, R. H. (2017). Lipid processing in the brain: A key regulator of systemic metabolism. *Frontiers in Endocrinology*, *8*(APR), 1–11. https://doi.org/10.3389/fendo.2017.00060

Bruehl, C., Hagemann, G., & Witte, O. W. (1998). Uncoupling of blood flow and metabolism in focal epilepsy. *Epilepsia*, *39*(12), 1235–1242.

Buckner, R. L., Head, D., Parker, J., Fotenos, A. F., Marcus, D., Morris, J. C., & Snyder, A. Z. (2004). A unified approach for morphometric and functional data analysis in young, old, and demented adults using automated atlas-based head size normalization: Reliability and validation against manual measurement of total intracranial volume. *NeuroImage*, *23*(2), 724–738. https://doi.org/10.1016/j.neuroimage.2004.06.018

Buckner, R. L., Sepulcre, J., Talukdar, T., Krienen, F. M., Liu, H., Hedden, T., Andrews-Hanna, J. R., Sperling, R. A., & Johnson, K. A. (2009). Cortical Hubs Revealed by Intrinsic Functional Connectivity: Mapping, Assessment of Stability, and Relation to Alzheimer's Disease. *Journal of Neuroscience*, *29*(6), 1860–1873. https://doi.org/10.1523/JNEUROSCI.5062-08.2009

Bullmore, E., Horwitz, B., Honey, G., Brammer, M., Williams, S., & Sharma, T. (2000). How Good Is Good Enough in Path Analysis of fMRI Data? *NeuroImage*, *11*(4), 289–301. https://doi.org/10.1006/NIMG.2000.0544

Bullmore, E., & Sporns, O. (2009). Complex brain networks: Graph theoretical analysis of structural and functional systems. *Nature Reviews Neuroscience*, *10*(3), 186–198. https://doi.org/10.1038/nrn2575

Bullmore, E., & Sporns, O. (2012). The economy of brain network organization. *Nature Reviews Neuroscience*, *13*(5), 336–349. https://doi.org/10.1038/nrn3214

Bulte, D. P., Drescher, K., & Jezzard, P. (2009). Comparison of hypercapnia-based calibration techniques for measurement of cerebral oxygen metabolism with MRI. *Magnetic Resonance in Medicine: An Official Journal of the International Society for Magnetic Resonance in Medicine*, *61*(2), 391–398.

Bulte, D. P., Kelly, M., Germuska, M., Xie, J., Chappell, M. A., Okell, T. W., Bright, M. G., & Jezzard, P. (2012). Quantitative measurement of cerebral physiology using respiratory-calibrated MRI. *NeuroImage*, *60*(1), 582–591. https://doi.org/10.1016/j.neuroimage.2011.12.017

Bürkner, P.-C. (2017). brms : An R Package for Bayesian Multilevel Models Using Stan. *Journal*

of Statistical Software, *80*(1). https://doi.org/10.18637/jss.v080.i01

Buxton, R. (2010). Interpreting oxygenation-based neuroimaging signals: the importance and the challenge of understanding brain oxygen metabolism. *Frontiers in Neuroenergetics*, 8.

Byrne, A. B., McWhirter, R. D., Sekine, Y., Strittmatter, S. M., Miller, D. M., & Hammarlund, M. (2016). Inhibiting poly(ADP-ribosylation) improves axon regeneration. *ELife*, *5*(OCTOBER2016). https://doi.org/10.7554/ELIFE.12734

Byrne, J. H. (2016). *Introduction to neurons and neuronal networks.*

Byrnes, K. R., Wilson, C. M., Brabazon, F., Von Leden, R., Jurgens, J. S., Oakes, T. R., & Selwyn, R. G. (2014). FDG-PET imaging in mild traumatic brain injury: a critical review. *Frontiers in Neuroenergetics*, *5*, 13.

Calhoun, V. D., Adali, T., Pearlson, G. D., & Pekar, J. J. (2001). A method for making group inferences from functional MRI data using independent component analysis. *Human Brain Mapping*, *14*(3), 140–151. https://doi.org/10.1002/hbm.1048

Calhoun, V. D., Liu, J., & Adalı, T. (2009). A review of group ICA for fMRI data and ICA for joint inference of imaging, genetic, and ERP data. *NeuroImage*, *45*(1), S163–S172. https://doi.org/10.1016/j.neuroimage.2008.10.057

Cammoun, L., Gigandet, X., Meskaldji, D., Thiran, J. P., Sporns, O., Do, K. Q., Maeder, P., Meuli, R., & Hagmann, P. (2012). Mapping the human connectome at multiple scales with diffusion spectrum MRI. *Journal of Neuroscience Methods*, *203*(2), 386–397. https://doi.org/10.1016/j.jneumeth.2011.09.031

Cao, J., & Worsley, K. (1999). The geometry of correlation fields with an application to functional connectivity of the brain. *The Annals of Applied Probability*, *9*(4), 1021–1057. https://doi.org/10.1214/aoap/1029962864

Carpenter, B., Gelman, A., Hoffman, M. D., Lee, D., Goodrich, B., Betancourt, M., Brubaker, M. A., Guo, J., Li, P., & Riddell, A. (2017). Stan: A probabilistic programming language. *Journal of Statistical Software*, *76*(1). https://doi.org/10.18637/jss.v076.i01

Cataldi, M., Avoli, M., & de Villers-Sidani, E. (2013). Resting state networks in temporal lobe epilepsy. *Epilepsia*, *54*(12), 2048–2059.

Catani, M., & Thiebaut de Schotten, M. (2012). Atlas of Human Brain Connections (all tracts). In *Atlas of Human Brain Connections* (pp. 75–238). Oxford University Press. https://doi.org/10.1093/med/9780199541164.003.0073

Cauli, B., & Hamel, E. (2010). Revisiting the role of neurons in neurovascular coupling. *Frontiers in Neuroenergetics*, *0*, 9. https://doi.org/10.3389/FNENE.2010.00009

Centeno, M., & Carmichael, D. W. (2014). Network Connectivity in Epilepsy: Resting State fMRI and EEG–fMRI Contributions. *Frontiers in Neurology*, *5*. https://doi.org/10.3389/FNEUR.2014.00093

Centrality and Hubs. (2016). *Fundamentals of Brain Network Analysis*, 137–161. https://doi.org/10.1016/B978-0-12-407908-3.00005-4

Cha, Y. H. K., Jog, M. A., Kim, Y. C., Chakrapani, S., Kraman, S. M., & Wang, D. J. J. (2013). Regional correlation between resting state FDG PET and pCASL perfusion MRI. *Journal of Cerebral Blood Flow and Metabolism*, *33*(12), 1909–1914. https://doi.org/10.1038/jcbfm.2013.147

Chaigneau, E., Oheim, M., Audinat, E., & Charpak, S. (2003). Two-photon imaging of capillary blood flow in olfactory bulb glomeruli. *Proceedings of the National Academy of Sciences*, *100*(22), 13081–13086.

Chaudhry, R., & Varacallo, M. (2022). Biochemistry, Glycolysis. *StatPearls*.

Chen, G., Xiao, Y., Taylor, P. A., Rajendra, J. K., Riggins, T., Geng, F., Redcay, E., & Cox, R. W. (2019). Handling Multiplicity in Neuroimaging Through Bayesian Lenses with Multilevel Modeling. *Neuroinformatics*, *17*(4), 515–545. https://doi.org/10.1007/s12021-018-9409-6

Chen, J. J., & Gauthier, C. J. (2021). The Role of Cerebrovascular-Reactivity Mapping in Functional MRI: Calibrated fMRI and Resting-State fMRI. *Frontiers in Physiology*, *12*. https://doi.org/10.3389/FPHYS.2021.657362

Chen, J. J., & Pike, G. B. (2009). BOLD-specific cerebral blood volume and blood flow changes during neuronal activation in humans. *NMR in Biomedicine*, *22*(10), 1054–1062. https://doi.org/10.1002/NBM.1411

Chen, J. J., Wieckowska, M., Meyer, E., & Pike, G. B. (2008). Cerebral blood flow measurement using fMRI and PET: A cross-validation study. *International Journal of Biomedical Imaging*, *2008*(1). https://doi.org/10.1155/2008/516359

Cheng, A., Hou, Y., & Mattson, M. P. (2010). Mitochondria and neuroplasticity. *ASN Neuro*, *2*(5), 243–256. https://doi.org/10.1042/AN20100019

Chiarelli, P. A., Bulte, D. P., Piechnik, S., & Jezzard, P. (2007). Sources of systematic bias in hypercapnia-calibrated functional MRI estimation of oxygen metabolism. *Neuroimage*, *34*(1), 35–43.

Chiarelli, P. A., Bulte, D. P., Wise, R., Gallichan, D., & Jezzard, P. (2007). A calibration method for quantitative BOLD fMRI based on hyperoxia. *Neuroimage*, *37*(3), 808–820.

Chini, C. C. S., Zeidler, J. D., Kashyap, S., Warner, G., & Chini, E. N. (2021). Evolving concepts in NAD+ metabolism. *Cell Metabolism*, *33*(6), 1076–1087.

Cho, J., Lee, J., An, H., Goyal, M. S., Su, Y., & Wang, Y. (2021). Cerebral oxygen extraction fraction (OEF): Comparison of challenge-free gradient echo QSM+ qBOLD (QQ) with 15O PET in healthy adults. *Journal of Cerebral Blood Flow & Metabolism*, *41*(7), 1658–1668.

Choi, I., Lee, S., Merkle, H., & Shen, J. (2004). Single-shot two-echo technique for simultaneous measurement of GABA and creatine in the human brain in vivo. *Magnetic Resonance in Medicine: An Official Journal of the International Society for Magnetic Resonance in Medicine*, *51*(6), 1115–1121.

Chugani, H. T., & Conti, J. R. (1996). Etiologic classification of infantile spasms in 140 cases: role of positron emission tomography. *Journal of Child Neurology*, *11*(1), 44–48.

Chugani, H. T., Shewmon, D. A., Shields, W. D., Sankar, R., Comair, Y., Vinters, H. V, & Peacock, W. J. (1993). Surgery for intractable infantile spasms: neuroimaging perspectives. *Epilepsia*, *34*(4), 764–771.

Chugani, H. T., Shields, W. D., Shewmon, D. A., Olson, D. M., Phelps, M. E., & Peacock, W. J. (1990). Infantile spasms: I. PET identifies focal cortical dysgenesis in cryptogenic cases for surgical treatment. *Annals of Neurology: Official Journal of the American Neurological Association and the Child Neurology Society*, *27*(4), 406–413.

Cioli, C., Abdi, H., Beaton, D., Burnod, Y., & Mesmoudi, S. (2014). Differences in human cortical gene expression match the temporal properties of large-scale functional networks. *PLoS ONE*, *9*(12), 1–28. https://doi.org/10.1371/journal.pone.0115913

Cipolla, M. J. (2009). *Control of Cerebral Blood Flow*.

Cohen, J. (1960). A coefficient of agreement for nominal scales. *Educational and Psychological Measurement*, *20*(1), 37–46.

Colantuoni, C., Lipska, B. K., Ye, T., Hyde, T. M., Tao, R., Leek, J. T., Colantuoni, E. A., Elkahloun, A. G., Herman, M. M., Weinberger, D. R., & Kleinman, J. E. (2011). Temporal dynamics and genetic control of transcription in the human prefrontal cortex. *Nature*, *478*(7370), 519–523. https://doi.org/10.1038/nature10524

Cole, M. W., Ito, T., Bassett, D. S., & Schultz, D. H. (2016). Activity flow over resting-state networks shapes cognitive task activations. *Nature Neuroscience*, *19*(12), 1718–1726. https://doi.org/10.1038/nn.4406

Coles, J. P., Fryer, T. D., Bradley, P. G., Nortje, J., Smielewski, P., Rice, K., Clark, J. C., Pickard, J. D., & Menon, D. K. (2006). Intersubject variability and reproducibility of 15O PET studies. *Journal of Cerebral Blood Flow and Metabolism*, *26*(1), 48–57. https://doi.org/10.1038/sj.jcbfm.9600179

Cooper, G. M. (2000). *Metabolic Energy*.

Cordes, D., Haughton, V., Carew, J. D., Arfanakis, K., & Maravilla, K. (2002). Hierarchical clustering to measure connectivity in fMRI resting-state data. *Magnetic Resonance Imaging*, *20*(4), 305–317. https://doi.org/10.1016/S0730-725X(02)00503-9

Cordes, D., Haughton, V. M., Arfanakis, K., Carew, J. D., Turski, P. A., Moritz, C. H., Quigley, M. A., & Meyerand, M. E. (2001). Frequencies contributing to functional connectivity in the cerebral cortex in "resting-state" data. *AJNR Am. J. Neuroradiol.*, *22*(7), 1326–1333.

Cordes, D., Haughton, V. M., Arfanakis, K., Wendt, G. J., Turski, P. A., Moritz, C. H., Quigley, M. A., & Meyerand, M. E. (2000). Mapping functionally related regions of brain with functional connectivity MR imaging. *American Journal of Neuroradiology*, *21*(9), 1636–1644.

Coulson, R. J., Cipolla, M. J., Vitullo, L., & Chesler, N. C. (2004). Mechanical Properties of Rat Middle Cerebral Arteries With and Without Myogenic Tone. *Journal of Biomechanical Engineering*, *126*(1), 76–81. https://doi.org/10.1115/1.1645525

Cover, T. M., & Thomas, J. A. (1991). Entropy, relative entropy and mutual information. *Elem.*

Inf. Theory, *2*(1), 12–13. https://doi.org/10/cgkq6f

Coverdale, N. S., Gati, J. S., Opalevych, O., Perrotta, A., & Shoemaker, J. K. (2014). Cerebral blood flow velocity underestimates cerebral blood flow during modest hypercapnia and hypocapnia. *Journal of Applied Physiology*, *117*(10), 1090–1096.

Cox, R. W., & Hyde, J. S. (1997). Software tools for analysis and visualization of fMRI data. *NMR in Biomedicine: An International Journal Devoted to the Development and Application of Magnetic Resonance In Vivo*, *10*(4-5), 171–178.

Craddock, R. C., Jbabdi, S., Yan, C.-G., Vogelstein, J. T., Castellanos, F. X., Di Martino, A., Kelly, C., Heberlein, K., Colcombe, S., & Milham, M. P. (2013). Imaging human connectomes at the macroscale. *Nature Methods*, *10*(6), 524–539. https://doi.org/10.1038/nmeth.2482

Cross, N. E., Pomares, F. B., Nguyen, A., Perrault, A. A., Jegou, A., Uji, M., Lee, K., Razavipour, F., Ka'b Ali, O. Bin, Aydin, U., Benali, H., Grova, C., & Dang-Vu, T. T. (2021). An altered balance of integrated and segregated brain activity is a marker of cognitive deficits following sleep deprivation. *PLOS Biology*, *19*(11), e3001232. https://doi.org/10.1371/JOURNAL.PBIO.3001232

Crossley, N. A., Mechelli, A., Scott, J., Carletti, F., Fox, P. T., McGuire, P., & Bullmore, E. T. (2014). The hubs of the human connectome are generally implicated in the anatomy of brain disorders. *Brain*, *137*(8), 2382–2395. https://doi.org/10/gb9rjh

D'Esposito, M., Deouell, L. Y., & Gazzaley, A. (2003). Alterations in the BOLD fMRI signal with ageing and disease: a challenge for neuroimaging. *Nature Reviews Neuroscience*, *4*(11), 863–872.

Damoiseaux, J. S., Rombouts, S. A. R. B., Barkhof, F., Scheltens, P., Stam, C. J., Smith, S. M., & Beckmann, C. F. (2006). Consistent resting-state networks across healthy subjects. *Proceedings of the National Academy of Sciences*, *103*(37), 13848–13853. https://doi.org/10.1073/pnas.0601417103

Daneman, R., & Prat, A. (2015). The Blood–Brain Barrier. *Cold Spring Harbor Perspectives in Biology*, *7*(1). https://doi.org/10.1101/CSHPERSPECT.A020412

Darmanis, S., Sloan, S. A., Zhang, Y., Enge, M., Caneda, C., Shuer, L. M., Gephart, M. G. H., Barres, B. A., & Quake, S. R. (2015). A survey of human brain transcriptome diversity at the single cell level. *Proceedings of the National Academy of Sciences of the United States of America*, *112*(23), 7285–7290. https://doi.org/10.1073/PNAS.1507125112/SUPPL_FILE/PNAS.1507125112.SAPP.PDF

Dash, R. K., Korman, B., & Bassingthwaighte, J. B. (2016). Simple accurate mathematical models of blood HbO2 and HbCO2 dissociation curves at varied physiological conditions: evaluation and comparison with other models. *European Journal of Applied Physiology*, *116*(1), 97–113.

Daubechies, I., Roussos, E., Takerkart, S., Benharrosh, M., Golden, C., D'Ardenne, K., Richter, W., Cohen, J. D., & Haxby, J. (2009). Independent component analysis for brain fMRI does not select for independence. *Proceedings of the National Academy of Sciences of the United States of America*, *106*(26), 10415–10422.

https://doi.org/10.1073/PNAS.0903525106/SUPPL_FILE/0903525106SI.PDF

Davidoff, R. A. (1977). From Neuron to Brain. *Neurology*, *27*(7), 699–699. https://doi.org/10.1212/WNL.27.7.699

Davis, T. L., Kwong, K. K., Weisskoff, R. M., & Rosen, B. R. (1998). Calibrated functional MRI: mapping the dynamics of oxidative metabolism. *Proceedings of the National Academy of Sciences*, *95*(4), 1834–1839.

De Boer, H. M., Mula, M., & Sander, J. W. (2008). The global burden and stigma of epilepsy. *Epilepsy & Behavior*, *12*(4), 540–546.

De Luca, M., Beckmann, C. F., De Stefano, N., Matthews, P. M., & Smith, S. M. (2006). fMRI resting state networks define distinct modes of long-distance interactions in the human brain. *NeuroImage*, *29*(4), 1359–1367. https://doi.org/10.1016/j.neuroimage.2005.08.035

de Reus, M. A., & van den Heuvel, M. P. (2013). The parcellation-based connectome: Limitations and extensions. *NeuroImage*, *80*, 397–404. https://doi.org/10.1016/J.NEUROIMAGE.2013.03.053

de Robertis, E., Rodriguez de Lores Arnaiz, G., & Pellegrino de Iraldi, A. (1962). Isolation of synaptic vesicles from nerve endings of the rat brain. *Nature*, *194*(4830), 794–795. https://doi.org/10/btv9j4

Deco, G., Jirsa, V., McIntosh, A. R., Sporns, O., & Kötter, R. (2009). Key role of coupling, delay, and noise in resting brain fluctuations. *Proceedings of the National Academy of Sciences*, *106*(25), 10302–10307. https://doi.org/10.1073/pnas.0901831106

Deco, G., McIntosh, A. R., Shen, K., Matthew Hutchison, R., Menon, R. S., Everling, S., Hagmann, P., & Jirsa, V. K. (2014). Identification of Optimal Structural Connectivity Using Functional Connectivity and Neural Modeling. *The Journal of Neuroscience*, *34*(23), 7910. https://doi.org/10.1523/JNEUROSCI.4423-13.2014

Del Guerra, A., Ahmad, S., Avram, M., Belcari, N., Berneking, A., Biagi, L., Bisogni, M. G., Brandl, F., Cabello, J., Camarlinghi, N., Cerello, P., Choi, C. H., Coli, S., Colpo, S., Fleury, J., Gagliardi, V., Giraudo, G., Heekeren, K., Kawohl, W., … Ziegler, S. (2018). TRIMAGE: A dedicated trimodality (PET/MR/EEG) imaging tool for schizophrenia. *European Psychiatry*, *50*, 7–20. https://doi.org/10.1016/j.eurpsy.2017.11.007

Detre, J. A., Leigh, J. S., Williams, D. S., & Koretsky, A. P. (1992). Perfusion imaging. *Magnetic Resonance in Medicine*, *23*(1), 37–45.

Deutch, A. Y., Giuffrida, A., & Roberts, J. L. (2014). Nonclassic signaling in the brain. In *From Molecules to Networks* (pp. 239–255). Elsevier.

Devor, A., Sakadžić, S., Saisan, P. A., Yaseen, M. A., Roussakis, E., Srinivasan, V. J., Vinogradov, S. A., Rosen, B. R., Buxton, R. B., & Dale, A. M. (2011). "Overshoot" of O2 is required to maintain baseline tissue oxygenation at locations distal to blood vessels. *Journal of Neuroscience*, *31*(38), 13676–13681.

Díaz Parra, A. (2018). *A network science approach of the macroscopic organization of the brain: analysis of structural and functional brain networks in health and disease* [Universitat

Politècnica de València]. https://doi.org/10.4995/Thesis/10251/106966

Dienel, G. A. (2012). Brain lactate metabolism: the discoveries and the controversies. *Journal of Cerebral Blood Flow & Metabolism*, *32*(7), 1107–1138.

Diez, I., & Sepulcre, J. (2021). Unveiling the neuroimaging-genetic intersections in the human brain. *Current Opinion in Neurology*, *34*(4), 480–487. https://doi.org/10.1097/WCO.0000000000000952

Ding, Y.-S., Chen, B.-B., Glielmi, C., Friedman, K., & Devinsky, O. (2014). A pilot study in epilepsy patients using simultaneous PET/MR. *American Journal of Nuclear Medicine and Molecular Imaging*, *4*(5), 459.

Dipasquale, O., Sethi, A., Lagan, M. M., Baglio, F., Baselli, G., Kundu, P., Harrison, N. A., & Cercignani, M. (2017). Comparing resting state fMRI de-noising approaches using multi- and single-echo acquisitions. *PLoS ONE*, *12*(3). https://doi.org/10.1371/JOURNAL.PONE.0173289

Divenyi, P. L., & Efron, R. (1979). Spectral versus temporal features in dichotic listening. *Brain and Language*, *7*(3), 375–386. https://doi.org/10.1016/0093-934X(79)90030-0

Donahue, C. J., Sotiropoulos, S. N., Jbabdi, S., Hernandez-Fernandez, M., Behrens, T. E., Dyrby, T. B., Coalson, T., Kennedy, H., Knoblauch, K., Van Essen, D. C., & Glasser, M. F. (2016). Using Diffusion Tractography to Predict Cortical Connection Strength and Distance: A Quantitative Comparison with Tracers in the Monkey. *The Journal of Neuroscience*, *36*(25), 6758–6770. https://doi.org/10.1523/JNEUROSCI.0493-16.2016

Doot, R. K., Christian, P. E., Mankoff, D. A., & Kinahan, P. E. (2007). Reproducibility of quantifying tracer uptake with PET/CT for evaluation of response to therapy. *2007 IEEE Nuclear Science Symposium Conference Record*, *4*, 2833–2837.

Doucet, G., Naveau, M., Petit, L., Delcroix, N., Zago, L., Crivello, F., Jobard, G., Tzourio-Mazoyer, N., Mazoyer, B., Mellet, E., & Joliot, M. (2011). Brain activity at rest: a multiscale hierarchical functional organization. *Journal of Neurophysiology*, *105*(6), 2753–2763. https://doi.org/10.1152/jn.00895.2010

Downes, J. H., Hammond, M. W., Xydas, D., Spencer, M. C., Becerra, V. M., Warwick, K., Whalley, B. J., & Nasuto, S. J. (2012). Emergence of a Small-World Functional Network in Cultured Neurons. *PLOS Computational Biology*, *8*(5), e1002522. https://doi.org/10.1371/JOURNAL.PCBI.1002522

Du, Y., Fu, Z., Sui, J., Gao, S., Xing, Y., Lin, D., Salman, M., Abrol, A., Rahaman, M. A., Chen, J., Hong, L. E., Kochunov, P., Osuch, E. A., & Calhoun, V. D. (2020). NeuroMark: An automated and adaptive ICA based pipeline to identify reproducible fMRI markers of brain disorders. *NeuroImage: Clinical*, *28*, 102375. https://doi.org/10.1016/j.nicl.2020.102375

Dubey, T., Sahu, G., Kumari, S., Yadav, B., & Sahu, A. (2018). Role of herbal drugs on neurotransmitters for treating various CNS disorders: A review. *Undefined*.

Dumoulin, S. O., Fracasso, A., van der Zwaag, W., Siero, J. C. W., & Petridou, N. (2018). Ultra-high field MRI: Advancing systems neuroscience towards mesoscopic human brain function. *NeuroImage*, *168*, 345–357. https://doi.org/10.1016/j.neuroimage.2017.01.028

Dunn, J., & Grider, M. H. (2022). Physiology, Adenosine Triphosphate. *StatPearls*.

Eaton, S. (2002). Control of mitochondrial β-oxidation flux. *Progress in Lipid Research*, *41*(3), 197–239. https://doi.org/10.1016/S0163-7827(01)00024-8

Ebert, D., Haller, R. G., & Walton, M. E. (2003). Energy contribution of octanoate to intact rat brain metabolism measured by 13C nuclear magnetic resonance spectroscopy. *The Journal of Neuroscience : The Official Journal of the Society for Neuroscience*, *23*(13), 5928–5935. https://doi.org/10.1523/JNEUROSCI.23-13-05928.2003

Eddleston, M., & Mucke, L. (1993). Molecular profile of reactive astrocytes—Implications for their role in neurologic disease. *Neuroscience*, *54*(1), 15–36. https://doi.org/10.1016/0306-4522(93)90380-X

Efron, B., & Tibshirani, R. J. (1994). *An Introduction to the bootstrap (Chapman & Hall/CRC monographs on statistics & applied probability): Chapman and Hall/CRC*.

Eickhoff, S. B., Yeo, B. T. T., & Genon, S. (2018). Imaging-based parcellations of the human brain. *Nature Reviews Neuroscience*, *19*(11), 672–686. https://doi.org/10.1038/s41583-018-0071-7

El Bacha, T., Luz, M., & Da Poian, A. (2010). Dynamic adaptation of nutrient utilization in humans. *Nat Educ*, *3*(8).

Emre Erdi, Y. (2007). The use of PET for radiotherapy. *Current Medical Imaging*, *3*(1), 3–16.

Englund, E. K., Fernández-Seara, M. A., Rodríguez-Soto, A. E., Lee, H., Rodgers, Z. B., Vidorreta, M., Detre, J. A., & Wehrli, F. W. (2020). Calibrated fMRI for dynamic mapping of CMRO2 responses using MR-based measurements of whole-brain venous oxygen saturation. *Journal of Cerebral Blood Flow and Metabolism*, *40*(7), 1501–1516. https://doi.org/10.1177/0271678X19867276

Esteban, O., Blair, R., Markiewicz, C. J., Berleant, S. L., Moodie, C., Ma, F., Isik, A. I., Erramuzpe, A., Kent, M., & James, D. (2018). fmriprep. *Software*.

Esteban, O., Markiewicz, C. J., Blair, R. W., Moodie, C. A., Isik, A. I., Erramuzpe, A., Kent, J. D., Goncalves, M., DuPre, E., Snyder, M., Oya, H., Ghosh, S. S., Wright, J., Durnez, J., Poldrack, R. A., & Gorgolewski, K. J. (2018). fMRIPrep: a robust preprocessing pipeline for functional MRI. *Nature Methods 2018 16:1*, *16*(1), 111–116. https://doi.org/10.1038/s41592-018-0235-4

Evans, A. C., Janke, A. L., Collins, D. L., & Baillet, S. (2012). Brain templates and atlases. *NeuroImage*, *62*(2), 911–922. https://doi.org/10.1016/J.NEUROIMAGE.2012.01.024

Fabris, F., Palmer, D., de Magalhães, J. P., & Freitas, A. A. (2020). Comparing enrichment analysis and machine learning for identifying gene properties that discriminate between gene classes. *Briefings in Bioinformatics*, *21*(3), 803–814.

Fagiolo, G. (2007). Clustering in complex directed networks. *Physical Review E - Statistical, Nonlinear, and Soft Matter Physics*, *76*(2), 1–8. https://doi.org/10.1103/PhysRevE.76.026107

Fan, A. P., An, H., Moradi, F., Rosenberg, J., Ishii, Y., Nariai, T., Okazawa, H., & Zaharchuk, G.

(2020). Quantification of brain oxygen extraction and metabolism with [15O]-gas PET: a technical review in the era of PET/MRI. *Neuroimage*, *220*, 117136.

Fantini, S., Sassaroli, A., Tgavalekos, K. T., & Kornbluth, J. (2016). Cerebral blood flow and autoregulation: current measurement techniques and prospects for noninvasive optical methods. *Neurophotonics*, *3*(3), 31411.

Farahani, F. V., Karwowski, W., & Lighthall, N. R. (2019). Application of graph theory for identifying connectivity patterns in human brain networks: A systematic review. *Frontiers in Neuroscience*, *13*(JUN), 1–27. https://doi.org/10.3389/fnins.2019.00585

Fathi, A. R., Yang, C., Bakhtian, K. D., Qi, M., Lonser, R. R., & Pluta, R. M. (2011). Carbon dioxide influence on nitric oxide production in endothelial cells and astrocytes: cellular mechanisms. *Brain Research*, *1386*, 50–57. https://doi.org/10.1016/J.BRAINRES.2011.02.066

Feihl, F., & Perret, C. (1994). Permissive hypercapnia. How permissive should we be? *American Journal of Respiratory and Critical Care Medicine*, *150*(6), 1722–1737.

Fernández-Klett, F., Offenhauser, N., Dirnagl, U., Priller, J., & Lindauer, U. (2010). Pericytes in capillaries are contractile in vivo, but arterioles mediate functional hyperemia in the mouse brain. *Proceedings of the National Academy of Sciences of the United States of America*, *107*(51), 22290–22295. https://doi.org/10.1073/PNAS.1011321108/SUPPL_FILE/SM10.MOV

Filler, A. (2009). The history, development and impact of computed imaging in neurological diagnosis and neurosurgery: CT, MRI, and DTI. *Nature Precedings*, 1.

Filosa, J. A., & Iddings, J. A. (2013). Astrocyte regulation of cerebral vascular tone. *American Journal of Physiology-Heart and Circulatory Physiology*, *305*(5), H609–H619.

Fonov, V., Evans, A. C., Botteron, K., Almli, C. R., McKinstry, R. C., & Collins, D. L. (2011). Unbiased average age-appropriate atlases for pediatric studies. *NeuroImage*, *54*(1), 313–327. https://doi.org/10.1016/j.neuroimage.2010.07.033

Fornito, A., Arnatkevičiūtė, A., & Fulcher, B. D. (2019). Bridging the gap between connectome and transcriptome. *Trends in Cognitive Sciences*, *23*(1), 34–50.

Fornito, A., Zalesky, A., & Breakspear, M. (2013). Graph analysis of the human connectome: promise, progress, and pitfalls. *Neuroimage*, *80*, 426–444. https://doi.org/10/f46mv9

Fornito, A., Zalesky, A., & Bullmore, E. (2016). *Fundamentals of brain network analysis*. Academic Press.

Fox, M. D., & Raichle, M. E. (2007). Spontaneous fluctuations in brain activity observed with functional magnetic resonance imaging. In *Nature Reviews Neuroscience* (Vol. 8, Issue 9, pp. 700–711). https://doi.org/10.1038/nrn2201

Fox, P. T., & Raichle, M. E. (1986). Focal physiological uncoupling of cerebral blood flow and oxidative metabolism during somatosensory stimulation in human subjects. *Proceedings of the National Academy of Sciences of the United States of America*, *83*(4), 1140. https://doi.org/10.1073/PNAS.83.4.1140

Frahm, J., Krüger, G., Merboldt, K. D., & Kleinschmidt, A. (1996). Dynamic uncoupling and recoupling of perfusion and oxidative metabolism during focal brain activation in man. *Magnetic Resonance in Medicine*, *35*(2), 143–148. https://doi.org/10.1002/MRM.1910350202

Franck, G., Salmon, E., Sadzot, B., & Maquet, P. (1989). Epilepsy: The use of oxygen-15-labeled gases. *Seminars in Neurology*, *9*(04), 307–316.

Fransson, P. (2005). Spontaneous low-frequency BOLD signal fluctuations: an fMRI investigation of the resting-state default mode of brain function hypothesis. *Hum. Brain Mapp.*, *26*(1), 15–29. https://doi.org/10/b46cgn

Freeman, L. C. (1978). /79) 215-239 @Elsevier Sequoia S.A., Lausanne-Printed in the Netherlands. *Social Networks*, *1*.

French, L., Tan, P. P. C., & Pavlidis, P. (2011). Large-scale analysis of gene expression and connectivity in the rodent brain: Insights through data integration. *Frontiers in Neuroinformatics*, *5*, 12. https://doi.org/10.3389/FNINF.2011.00012/ABSTRACT/

Friston, K. J., Frith, C. D., Liddle, P. F., & Frackowiak, R. S. J. (1993). Functional Connectivity: The Principal-Component Analysis of Large (PET) Data Sets. *Journal of Cerebral Blood Flow & Metabolism*, *13*(1), 5–14. https://doi.org/10.1038/jcbfm.1993.4

Fulcher, B. D., & Fornito, A. (2016). A transcriptional signature of hub connectivity in the mouse connectome. *Proceedings of the National Academy of Sciences of the United States of America*, *113*(5), 1435–1440. https://doi.org/10.1073/PNAS.1513302113/SUPPL_FILE/PNAS.201513302SI.PDF

Fulcher, B. D., Little, M. A., & Jones, N. S. (2013). Highly comparative time-series analysis: the empirical structure of time series and their methods. *Journal of the Royal Society Interface*, *10*(83), 20130048.

Fuster, J. M., & Bressler, S. L. (2012). Cognit activation: a mechanism enabling temporal integration in working memory. *Trends in Cognitive Sciences*, *16*(4), 207–218. https://doi.org/10.1016/J.TICS.2012.03.005

Galloway, D. A., Phillips, A. E. M., Owen, D. R. J., & Moore, C. S. (2019). Phagocytosis in the Brain: Homeostasis and Disease. *Frontiers in Immunology*, *10*(MAR). https://doi.org/10.3389/FIMMU.2019.00790

Garcia-Lopez, P., Garcia-Marin, V., & Freire, M. (2010). The histological slides and drawings of Cajal. *Frontiers in Neuroanatomy*, *4*(MARCH), 1–16. https://doi.org/10.3389/neuro.05.009.2010

Garcia Corrales, A. V., Haidar, M., Bogie, J. F. J., & Hendriks, J. J. A. (2021). Fatty Acid Synthesis in Glial Cells of the CNS. *International Journal of Molecular Sciences*, *22*(15). https://doi.org/10.3390/IJMS22158159

Garcia, D. C. G., & Longden, T. A. (2020). Ion channels in capillary endothelium. *Current Topics in Membranes*, *85*, 261–300. https://doi.org/10.1016/BS.CTM.2020.01.005

Garey, L. (1999). *Localisation in the cerebral cortex*. London: Imperial College Press.

Garrido, L., Vaziri-Pashkam, M., Nakayama, K., & Wilmer, J. (2012). The case against normalization in fMRI pattern analysis. *Journal of Vision*, *12*(9), 516. https://doi.org/10/gqpfwj

Garrity, A. G., Pearlson, G. D., McKiernan, K., Lloyd, D., Kiehl, K. A., & Calhoun, V. D. (2007). Aberrant "default mode" functional connectivity in schizophrenia. *American Journal of Psychiatry*, *164*(3), 450–457.

Gaskin, J., Gomes, J., Darshan, S., & Krewski, D. (2017). Burden of neurological conditions in Canada. *Neurotoxicology*, *61*, 2–10.

Gauthier, C. J., & Fan, A. P. (2019). BOLD signal physiology: Models and applications. *NeuroImage*, *187*(March), 116–127. https://doi.org/10.1016/j.neuroimage.2018.03.018

Gauthier, C. J., & Hoge, R. D. (2012). Magnetic resonance imaging of resting OEF and CMRO2 using a generalized calibration model for hypercapnia and hyperoxia. *NeuroImage*, *60*(2), 1212–1225. https://doi.org/10.1016/j.neuroimage.2011.12.056

Gauthier, C. J., & Hoge, R. D. (2013). A generalized procedure for calibrated MRI incorporating hyperoxia and hypercapnia. *Human Brain Mapping*, *34*(5), 1053–1069.

Gauthier, C. J., Madjar, C., Tancredi, F. B., Stefanovic, B., & Hoge, R. D. (2011). Elimination of visually evoked BOLD responses during carbogen inhalation: implications for calibrated MRI. *Neuroimage*, *54*(2), 1001–1011.

Gelman, A., & Hill, J. (2007). *Data analysis using regression and hierarchical/multilevel models*.

Gelman, A., Vehtari, A., Simpson, D., Margossian, C. C., Carpenter, B., Yao, Y., Kennedy, L., Gabry, J., Bürkner, P.-C., & Modrák, M. (2020). *Bayesian Workflow*.

Germuska, M., & Wise, R. G. (2019). Calibrated fMRI for mapping absolute CMRO2: Practicalities and prospects. *Neuroimage*, *187*, 145–153.

Geyer, S., Weiss, M., Reimann, K., Lohmann, G., & Turner, R. (2011). Microstructural parcellation of the human cerebral cortex - from Bbrodmann's post-mortem map to in vivo mapping with high-field magnetic resonance imaging. *Frontiers in Human Neuroscience*, *5*(FEBRUARY), 1–7. https://doi.org/10.3389/fnhum.2011.00019

Ghersi-Egea, J. F., Strazielle, N., Catala, M., Silva-Vargas, V., Doetsch, F., & Engelhardt, B. (2018). Molecular anatomy and functions of the choroidal blood-cerebrospinal fluid barrier in health and disease. *Acta Neuropathologica 2018 135:3*, *135*(3), 337–361. https://doi.org/10.1007/S00401-018-1807-1

Gierlichs, B., Batina, L., Tuyls, P., & Preneel, B. (2008). Mutual information analysis: A generic side-channel distinguisher. *Lecture Notes in Computer Science (Including Subseries Lecture Notes in Artificial Intelligence and Lecture Notes in Bioinformatics)*, *5154 LNCS*, 426–442. https://doi.org/10.1007/978-3-540-85053-3_27/COVER

Gjedde, A. (2007). 4.4 Coupling of Brain Function to Metabolism: Evaluation of Energy Requirements. *Handbook of Neurochemistry and Molecular Neurobiology: Brain Energetics. Integration of Molecular and Cellular Processes*.

Gjedde, A., Johannsen, P., Cold, G. E., & Østergaard, L. (2005). Cerebral metabolic response to low blood flow: possible role of cytochrome oxidase inhibition. *Journal of Cerebral Blood Flow & Metabolism*, *25*(9), 1183–1196.

Gladden, L. B. (2004). Lactate metabolism during exercise. *MEDICINE AND SPORT SCIENCE*, *46*, 152–196.

Glasser, M. F., Coalson, T. S., Robinson, E. C., Hacker, C. D., Harwell, J., Yacoub, E., Ugurbil, K., Andersson, J., Beckmann, C. F., Jenkinson, M., Smith, S. M., & Van Essen, D. C. (2016). A multi-modal parcellation of human cerebral cortex. *Nature*, *536*(7615), 171–178. https://doi.org/10.1038/nature18933

Glover, G. H. (1999). Deconvolution of Impulse Response in Event-Related BOLD fMRI1. *NeuroImage*, *9*(4), 416–429. https://doi.org/10.1006/NIMG.1998.0419

Glover, G. H. (2011). Overview of Functional Magnetic Resonance Imaging. *Neurosurgery Clinics of North America*, *22*(2), 133. https://doi.org/10.1016/J.NEC.2010.11.001

Golbeck, J. (2013). Network Structure and Measures. *Analyzing the Social Web*, 25–44. https://doi.org/10.1016/B978-0-12-405531-5.00003-1

Goldman, B. (2010). *New imaging method developed at Stanford reveals stunning details of brain connections*. Stanford Medicine News Center.

Gooch, C. L., Pracht, E., & Borenstein, A. R. (2017). The burden of neurological disease in the United States: A summary report and call to action. *Annals of Neurology*, *81*(4), 479–484.

Goodwin, J. A., Vidyasagar, R., Balanos, G. M., Bulte, D., & Parkes, L. M. (2009). Quantitative fMRI using hyperoxia calibration: reproducibility during a cognitive Stroop task. *NeuroImage*, *47*(2), 573–580.

Gordji-Nejad, A., Möllenhoff, K., Oros-Peusquens, A. M., Pillai, D. R., & Shah, N. J. (2014). Characterizing cerebral oxygen metabolism employing oxygen-17 MRI/MRS at high fields. *Magnetic Resonance Materials in Physics, Biology and Medicine*, *27*(1), 81–93.

Gordon, E. M., Laumann, T. O., Adeyemo, B., Huckins, J. F., Kelley, W. M., & Petersen, S. E. (2016). Generation and Evaluation of a Cortical Area Parcellation from Resting-State Correlations. *Cerebral Cortex (New York, NY)*, *26*(1), 288. https://doi.org/10.1093/CERCOR/BHU239

Gordon, E. M., Lynch, C. J., Gratton, C., Laumann, T. O., Gilmore, A. W., Greene, D. J., Ortega, M., Nguyen, A. L., Schlaggar, B. L., Petersen, S. E., Dosenbach, N. U. F., & Nelson, S. M. (2018). Three Distinct Sets of Connector Hubs Integrate Human Brain Function. *Cell Reports*, *24*(7), 1687-1695.e4. https://doi.org/10.1016/j.celrep.2018.07.050

Goyal, M. S., Hawrylycz, M., Miller, J. A., Snyder, A. Z., & Raichle, M. E. (2014). Aerobic glycolysis in the human brain is associated with development and neotenous gene expression. *Cell Metabolism*, *19*(1), 49–57. https://doi.org/10.1016/j.cmet.2013.11.020

Goyal, M. S., Vlassenko, A. G., Blazey, T. M., Su, Y., Couture, L. E., Durbin, T. J., Bateman, R. J., Benzinger, T. L.-S., Morris, J. C., & Raichle, M. E. (2017). Loss of brain aerobic glycolysis in normal human aging. *Cell Metabolism*, *26*(2), 353–360.

Gratton, C., Nomura, E. M., Pérez, F., & D'Esposito, M. (2012). Focal brain lesions to critical locations cause widespread disruption of the modular organization of the brain. *J. Cogn. Neurosci.*, *24*(6), 1275–1285. https://doi.org/10/gqpfwb

Greicius, M. D., & Menon, V. (2004). Default-mode activity during a passive sensory task: uncoupled from deactivation but impacting activation. *Journal of Cognitive Neuroscience*, *16*(9), 1484–1492.

Greicius, M. D., Supekar, K., Menon, V., & Dougherty, R. F. (2009). Resting-state functional connectivity reflects structural connectivity in the default mode network. *Cereb. Cortex*, *19*(1), 72–78. https://doi.org/10/b3cvhw

Greve, D. N., & Fischl, B. (2009). Accurate and robust brain image alignment using boundary-based registration. *NeuroImage*, *48*(1), 63–72. https://doi.org/10.1016/J.NEUROIMAGE.2009.06.060

Griffeth, V. E. M., & Buxton, R. B. (2011). A theoretical framework for estimating cerebral oxygen metabolism changes using the calibrated-BOLD method: modeling the effects of blood volume distribution, hematocrit, oxygen extraction fraction, and tissue signal properties on the BOLD signal. *Neuroimage*, *58*(1), 198–212.

Grubb Jr, R. L., Raichle, M. E., Eichling, J. O., & Ter-Pogossian, M. M. (1974). The effects of changes in PaCO2 cerebral blood volume, blood flow, and vascular mean transit time. *Stroke*, *5*(5), 630–639.

Guimerà, R., & Amaral, L. A. N. (2005). Cartography of complex networks: modules and universal roles. *Journal of Statistical Mechanics: Theory and Experiment*, *2005*(02), P02001. https://doi.org/10.1088/1742-5468/2005/02/P02001

Guimerà, R., Mossa, S., Turtschi, A., & Amaral, L. A. N. (2005). The worldwide air transportation network: Anomalous centrality, community structure, and cities' global roles. *Proc. Natl. Acad. Sci. U. S. A.*, *102*(22), 7794–7799. https://doi.org/10/ff823k

Gustard, S., Williams, E. J., Hall, L. D., Pickard, J. D., & Carpenter, T. A. (2003). Influence of baseline hematocrit on between-subject BOLD signal change using gradient echo and asymmetric spin echo EPI. *Magnetic Resonance Imaging*, *21*(6), 599–607.

Haacke, E. M., Duhaime, A. C., Gean, A. D., Riedy, G., Wintermark, M., Mukherjee, P., Brody, D. L., DeGraba, T., Duncan, T. D., & Elovic, E. (2010). Common data elements in radiologic imaging of traumatic brain injury. *Journal of Magnetic Resonance Imaging*, *32*(3), 516–543.

Habib, N., Basu, A., Avraham-Davidi, I., Burks, T., Choudhury, S. R., Aguet, F., Gelfand, E., Ardlie, K., Weitz, D. A., Rozenblatt-Rosen, O., Zhang, F., & Regev, A. (2017). *DroNc-Seq: Deciphering cell types in human archived brain tissues by massively-parallel single nucleus RNA-seq*.

Hahn, A., Breakspear, M., Rischka, L., Wadsak, W., Godbersen, G. M., Pichler, V., Michenthaler, P., Vanicek, T., Hacker, M., & Kasper, S. (2020). Reconfiguration of functional brain networks and metabolic cost converge during task performance. *Elife*, *9*, e52443.

Haimovici, A., Tagliazucchi, E., Balenzuela, P., & Chialvo, D. R. (2013). Brain Organization into Resting State Networks Emerges at Criticality on a Model of the Human Connectome.

Physical Review Letters, *110*(17), 178101. https://doi.org/10.1103/PhysRevLett.110.178101

Haken, H. (1983). *Synopsis and Introduction* (pp. 3–25). https://doi.org/10.1007/978-3-642-69421-9_2

Hall, C. N., Klein-Flügge, M. C., Howarth, C., & Attwell, D. (2012). Oxidative Phosphorylation, Not Glycolysis, Powers Presynaptic and Postsynaptic Mechanisms Underlying Brain Information Processing. *Journal of Neuroscience*, *32*(26), 8940–8951. https://doi.org/10.1523/JNEUROSCI.0026-12.2012

Hanani, M. (2005). Satellite glial cells in sensory ganglia: from form to function. *Brain Research Reviews*, *48*(3), 457–476. https://doi.org/10.1016/J.BRAINRESREV.2004.09.001

Handwerker, D. A., Gazzaley, A., Inglis, B. A., & D'Esposito, M. (2007). Reducing vascular variability of fMRI data across aging populations using a breathholding task. *Human Brain Mapping*, *28*(9), 846–859.

Hans Liljenström. (2012). Mesoscopic brain dynamics. *Scholarpedia*, *7*(9), 4601. https://doi.org/10.4249/scholarpedia.4601

Hansen, J. Y., Markello, R. D., Vogel, J. W., Seidlitz, J., Bzdok, D., & Misic, B. (2021). Mapping gene transcription and neurocognition across human neocortex. *Nat. Hum. Behav.*, *5*(9), 1240–1250. https://doi.org/10/gm7dgg

Hansen, L. K. (2000). *Advances in Independent Component Analysis, Perspectives in Neural Computing*.

Harper, S. J., & Lograsso, P. (2001). Signalling for survival and death in neurones: the role of stress-activated kinases, JNK and p38. *Cellular Signalling*, *13*(5), 299–310. https://doi.org/10.1016/S0898-6568(01)00148-6

Harrison, R. V., Harel, N., Panesar, J., & Mount, R. J. (2002). Blood Capillary Distribution Correlates with Hemodynamic-based Functional Imaging in Cerebral Cortex. *Cerebral Cortex*, *12*(3), 225–233. https://doi.org/10.1093/CERCOR/12.3.225

Hartmann, D. A., Underly, R. G., Grant, R. I., Watson, A. N., Lindner, V., & Shih, A. Y. (2015). Pericyte structure and distribution in the cerebral cortex revealed by high-resolution imaging of transgenic mice. *Https://Doi.Org/10.1117/1.NPh.2.4.041402*, *2*(4), 041402. https://doi.org/10.1117/1.NPH.2.4.041402

Hawrylycz, M. J., Lein, E. S., Guillozet-Bongaarts, A. L., Shen, E. H., Ng, L., Miller, J. A., van de Lagemaat, L. N., Smith, K. A., Ebbert, A., Riley, Z. L., Abajian, C., Beckmann, C. F., Bernard, A., Bertagnolli, D., Boe, A. F., Cartagena, P. M., Chakravarty, M. M., Chapin, M., Chong, J., … Jones, A. R. (2012). An anatomically comprehensive atlas of the adult human brain transcriptome. *Nature*, *489*(7416), 391–399. https://doi.org/10.1038/nature11405

Hawrylycz, M., Miller, J. A., Menon, V., Feng, D., Dolbeare, T., Guillozet-Bongaarts, A. L., Jegga, A. G., Aronow, B. J., Lee, C.-K., & Bernard, A. (2015). Canonical genetic signatures of the adult human brain. *Nature Neuroscience*, *18*(12), 1832–1844.

He, L., Vanlandewijck, M., Raschperger, E., Andaloussi Mäe, M., Jung, B., Lebouvier, T., Ando, K., Hofmann, J., Keller, A., & Betsholtz, C. (2016). Analysis of the brain mural cell

transcriptome. *Scientific Reports*, *6*(1), 1–13.

Heller, C., & Sadava, D. (2009). *Life: the science of biology*. Sinauer Associates.

Henriksen, O. M., Gjedde, A., Vang, K., Law, I., Aanerud, J., & Rostrup, E. (2021). Regional and interindividual relationships between cerebral perfusion and oxygen metabolism. *Journal of Applied Physiology*, *130*(6), 1836–1847.

Henriksen, O. M., Kruuse, C., Olesen, J., Jensen, L. T., Larsson, H. B. W., Birk, S., Hansen, J. M., Wienecke, T., & Rostrup, E. (2013). Sources of variability of resting cerebral blood flow in healthy subjects: a study using 133Xe SPECT measurements. *Journal of Cerebral Blood Flow & Metabolism*, *33*(5), 787–792.

Henriksen, O. M., Vestergaard, M. B., Lindberg, U., Aachmann-Andersen, N. J., Lisbjerg, K., Christensen, S. J., Rasmussen, P., Olsen, N. V, Forman, J. L., & Larsson, H. B. W. (2018). Interindividual and regional relationship between cerebral blood flow and glucose metabolism in the resting brain. *Journal of Applied Physiology*, *125*(4), 1080–1089.

Heurling, K., Leuzy, A., Jonasson, M., Frick, A., Zimmer, E. R., Nordberg, A., & Lubberink, M. (2017). Quantitative positron emission tomography in brain research. *Brain Research*, *1670*, 220–234. https://doi.org/10.1016/j.brainres.2017.06.022

Heuvel, M. P. Van Den, Pol, H. E. H., van den Heuvel, M. P., & Hulshoff Pol, H. E. (2010). Exploring the brain network: A review on resting-state fMRI functional connectivity. *European Neuropsychopharmacology*, *20*(8), 519–534. https://doi.org/10.1016/j.euroneuro.2010.03.008

Hill, R. A., Tong, L., Yuan, P., Murikinati, S., Gupta, S., & Grutzendler, J. (2015). Regional Blood Flow in the Normal and Ischemic Brain Is Controlled by Arteriolar Smooth Muscle Cell Contractility and Not by Capillary Pericytes. *Neuron*, *87*(1), 95–110. https://doi.org/10.1016/j.neuron.2015.06.001

Hillman, C. H., Themanson, J. R., Pontifex, M. B., George, D. C., Thompson, K. M., Valentim, T. A., & Wnek, K. J. (2007). Neuroelectric indices of error correction and the regulation of cognitive control. *PSYCHOPHYSIOLOGY*, *44*, S64–S65.

Hillman, E. M. C. (2014). Coupling Mechanism and Significance of the BOLD Signal: A Status Report. *Annual Review of Neuroscience*, *37*, 161. https://doi.org/10.1146/ANNUREV-NEURO-071013-014111

Hipp, J. F., Hawellek, D. J., Corbetta, M., Siegel, M., & Engel, A. K. (2012). *Large-scale cortical correlation structure of spontaneous oscillatory activity*. *15*(6). https://doi.org/10.1038/nn.3101

Hodgkin, A. L., & Huxley, A. F. (1952). A quantitative description of membrane current and its application to conduction and excitation in nerve. *The Journal of Physiology*, *117*(4), 500. https://doi.org/10.1113/JPHYSIOL.1952.SP004764

Hoge, R. D. (2012). Calibrated fMRI. *NeuroImage*, *62*(2), 930–937. https://doi.org/10.1016/j.neuroimage.2012.02.022

Hoge, R. D., Atkinson, J., Gill, B., Crelier, G. R., Marrett, S., & Pike, G. B. (1999a). Investigation

of BOLD signal dependence on cerebral blood flow and oxygen consumption: the deoxyhemoglobin dilution model. *Magnetic Resonance in Medicine: An Official Journal of the International Society for Magnetic Resonance in Medicine*, *42*(5), 849–863.

Hoge, R. D., Atkinson, J., Gill, B., Crelier, G. R., Marrett, S., & Pike, G. B. (1999b). Linear coupling between cerebral blood flow and oxygen consumption in activated human cortex. *Proceedings of the National Academy of Sciences*, *96*(16), 9403–9408.

Hoiland, R. L., Fisher, J. A., & Ainslie, P. N. (2011). Regulation of the cerebral circulation by arterial carbon dioxide. *Comprehensive Physiology*, *9*(3), 1101–1154.

Hoiland, R. L., Fisher, J. A., & Ainslie, P. N. (2019). Regulation of the cerebral circulation by arterial carbon dioxide. *Comprehensive Physiology*, *9*(3), 1101–1154. https://doi.org/10.1002/cphy.c180021

Honda, Y., Watanabe, S., Hashizume, I., Satomura, Y., Hata, N., Sakakibara, Y., & Severinghaus, J. W. (1979). Hypoxic chemosensitivity in asthmatic patients two decades after carotid body resection. *Journal of Applied Physiology*, *46*(4), 632–638.

Horvath, I., Sandor, N. T., Ruttner, Z., & McLaughlin, A. C. (1994). Role of nitric oxide in regulating cerebrocortical oxygen consumption and blood flow during hypercapnia. *Journal of Cerebral Blood Flow and Metabolism : Official Journal of the International Society of Cerebral Blood Flow and Metabolism*, *14*(3), 503–509. https://doi.org/10.1038/JCBFM.1994.62

Hosford, P. S., & Gourine, A. V. (2019). What is the key mediator of the neurovascular coupling response? *Neuroscience & Biobehavioral Reviews*, *96*(November 2018), 174–181. https://doi.org/10.1016/j.neubiorev.2018.11.011

Hotelling, H. (1936). CCA: an r package to extend canonical correlation analysis. *Biometrika*, *28*, 321–377.

Hou, X., Liu, P., Li, Y., Jiang, D., Jill, B., Lin, Z., Sur, S., Baker, Z., Mao, D., & Ravi, H. (2020). The association between BOLD-based cerebrovascular reactivity (CVR) and end-tidal CO2 in healthy subjects. *Neuroimage*, *207*, 116365.

Howarth, C., Gleeson, P., & Attwell, D. (2012). Updated energy budgets for neural computation in the neocortex and cerebellum. *Journal of Cerebral Blood Flow and Metabolism*, *32*(7), 1222–1232. https://doi.org/10.1038/jcbfm.2012.35

Hu, Y., Lv, F., Li, Q., & Liu, R. (2020). Effect of post-labeling delay on regional cerebral blood flow in arterial spin-labeling MR imaging. *Medicine*, *99*(27), e20463. https://doi.org/10.1097/MD.0000000000020463

Hubbard, N. A., Turner, M. P., Sitek, K. R., West, K. L., Kaczmarzyk, J. R., Himes, L., Thomas, B. P., Lu, H., & Rypma, B. (2021). Resting cerebral oxygen metabolism exhibits archetypal network features. *Human Brain Mapping*, *42*(7), 1952–1968. https://doi.org/10.1002/hbm.25352

Hubel, D. H., & Wiesel, T. N. (2005). *Brain and visual perception: The story of a 25-year collaboration*. Oxford University Press.

Huber, L., Uludağ, K., & Möller, H. E. (2019). Non-BOLD contrast for laminar fMRI in humans: CBF, CBV, and CMRO2. *Neuroimage*, *197*, 742–760.

Huberty, C. J., DiStefano, C., & Kamphaus, R. W. (1997). Behavioral clustering of school children. *Multivariate Behav. Res.*, *32*(2), 105–134. https://doi.org/10/bms3v8

Hutchison, R. M., Womelsdorf, T., Gati, J. S., Everling, S., & Menon, R. S. (2013). Resting-state networks show dynamic functional connectivity in awake humans and anesthetized macaques. *Hum. Brain Mapp.*, *34*(9), 2154–2177. https://doi.org/10/gf5nfm

Hyder, F., Fulbright, R. K., Shulman, R. G., & Rothman, D. L. (2013). Glutamatergic function in the resting awake human brain is supported by uniformly high oxidative energy. *Journal of Cerebral Blood Flow & Metabolism*, *33*(3), 339–347.

Hyder, F., Herman, P., Bailey, C. J., Møller, A., Globinsky, R., Fulbright, R. K., Rothman, D. L., & Gjedde, A. (2015). Uniform distributions of glucose oxidation and oxygen extraction in gray matter of normal human brain: No evidence of regional differences of aerobic glycolysis. *Journal of Cerebral Blood Flow and Metabolism*, *36*(5), 903–916. https://doi.org/10.1177/0271678X15625349

Hyder, F., Patel, A. B., Gjedde, A., Rothman, D. L., Behar, K. L., & Shulman, R. G. (2006). Neuronal-glial glucose oxidation and glutamatergic-GABAergic function. *Journal of Cerebral Blood Flow and Metabolism*, *26*(7), 865–877. https://doi.org/10.1038/sj.jcbfm.9600263

Hyder, F., Shulman, R. G., & Rothman, D. L. (1998). A model for the regulation of cerebral oxygen delivery. *Journal of Applied Physiology*, *85*(2), 554–564. https://doi.org/10.1152/JAPPL.1998.85.2.554/ASSET/IMAGES/LARGE/JAPP05825004X.JPEG

Iadecola, C. (2002). CC COMMENTARYIntrinsic Signals and Functional Brain Mapping: Caution, Blood Vessels at Work. *Cerebral Cortex*, *12*(3), 223–224. https://doi.org/10.1093/CERCOR/12.3.223

Iadecola, C. (2017). The Neurovascular Unit Coming of Age: A Journey through Neurovascular Coupling in Health and Disease. *Neuron*, *96*(1), 17–42. https://doi.org/10.1016/J.NEURON.2017.07.030

Iadecola, C., Yang, G., Ebner, T. J., & Chen, G. (1997). Local and propagated vascular responses evoked by focal synaptic activity in cerebellar cortex. *Journal of Neurophysiology*, *78*(2), 651–659. https://doi.org/10.1152/JN.1997.78.2.651/ASSET/IMAGES/LARGE/JNP.AU01F7B.JPEG

Ibaraki, M., Matsubara, K., & Kinoshita, T. (2019). *Evaluation of non-invasive, semi-quantitative 15O PET for patients with cerebrovascular steno-occlusive disease*. Soc Nuclear Med.

Ibaraki, M., Shimosegawa, E., Miura, S., Takahashi, K., Ito, H., Kanno, I., & Hatazawa, J. (2004). PET measurements of CBF, OEF, and CMRO2 without arterial sampling in hyperacute ischemic stroke: method and error analysis. *Annals of Nuclear Medicine*, *18*(1), 35–44.

Ido, Y., Chang, K., Woolsey, T. A., & Williamson, J. R. (2001). NADH: sensor of blood flow need in brain, muscle, and other tissues. *The FASEB Journal*, *15*(8), 1419–1421.

https://doi.org/10.1096/FJ.00-0652FJE

Ioannou, M. S., Jackson, J., Sheu, S. H., Chang, C. L., Weigel, A. V., Liu, H., Pasolli, H. A., Xu, C. S., Pang, S., Matthies, D., Hess, H. F., Lippincott-Schwartz, J., & Liu, Z. (2019). Neuron-Astrocyte Metabolic Coupling Protects against Activity-Induced Fatty Acid Toxicity. *Cell*, *177*(6), 1522-1535.e14. https://doi.org/10.1016/J.CELL.2019.04.001

Iroegbu, J. D., Ijomone, O. K., Femi-Akinlosotu, O. M., & Ijomone, O. M. (2021). ERK/MAPK signalling in the developing brain: Perturbations and consequences. *Neuroscience and Biobehavioral Reviews*, *131*, 792–805. https://doi.org/10.1016/J.NEUBIOREV.2021.10.009

Ishii, K., Hosaka, K., Mori, T., & Mori, E. (2004). Comparison of FDG-PET and IMP-SPECT in patients with dementia with Lewy bodies. *Annals of Nuclear Medicine*, *18*(5), 447–451. https://doi.org/10.1007/BF02984489

Ito, H., Ibaraki, M., Kanno, I., Fukuda, H., & Miura, S. (2005). Changes in cerebral blood flow and cerebral oxygen metabolism during neural activation measured by positron emission tomography: comparison with blood oxygenation level-dependent contrast measured by functional magnetic resonance imaging. *Journal of Cerebral Blood Flow & Metabolism*, *25*(3), 371–377.

Ito, H., Kubo, H., Takahashi, K., Nishijima, K. I., Ukon, N., Nemoto, A., Sugawara, S., Yamakuni, R., Ibaraki, M., & Ishii, S. (2021). Integrated PET/MRI scanner with oxygen-15 labeled gases for quantification of cerebral blood flow, cerebral blood volume, cerebral oxygen extraction fraction and cerebral metabolic rate of oxygen. *Annals of Nuclear Medicine*, *35*(4), 421–428. https://doi.org/10.1007/s12149-021-01578-8

Ivannikov, M. V, Sugimori, M., & Llinás, R. R. (2010). Calcium clearance and its energy requirements in cerebellar neurons. *Cell Calcium*, *47*(6), 507–513.

Jain, V., Langham, M. C., & Wehrli, F. W. (2010). MRI estimation of global brain oxygen consumption rate. *Journal of Cerebral Blood Flow & Metabolism*, *30*(9), 1598–1607.

Javed, K., Reddy, V., & Lui, F. (2022). Neuroanatomy, Cerebral Cortex. *StatPearls*.

Jeffreys, H. (1998). *The theory of probability*. OUP Oxford.

Jenkinson, M., Bannister, P., Brady, M., & Smith, S. (2002). Improved optimization for the robust and accurate linear registration and motion correction of brain images. *NeuroImage*, *17*(2), 825–841. https://doi.org/10.1016/S1053-8119(02)91132-8

Jenkinson, M., Beckmann, C. F., Behrens, T. E. J., Woolrich, M. W., & Smith, S. M. (2012). Fsl. *Neuroimage*, *62*(2), 782–790.

Jenkinson, M., & Smith, S. (2001). A global optimisation method for robust affine registration of brain images. *Medical Image Analysis*, *5*(2), 143–156. https://doi.org/10.1016/S1361-8415(01)00036-6

Jensen, N. J., Wodschow, H. Z., Nilsson, M., & Rungby, J. (2020). Effects of Ketone Bodies on Brain Metabolism and Function in Neurodegenerative Diseases. *International Journal of Molecular Sciences*, *21*(22), 8767. https://doi.org/10.3390/ijms21228767

Jessen, S. B., Mathiesen, C., Lind, B. L., & Lauritzen, M. (2017). Interneuron deficit associates attenuated network synchronization to mismatch of energy supply and demand in aging mouse brains. *Cereb. Cortex*, *27*(1), 646–659. https://doi.org/10/f9vn3x

Ji, J. L., Spronk, M., Kulkarni, K., Repovš, G., Anticevic, A., & Cole, M. W. (2019). Mapping the human brain's cortical-subcortical functional network organization. *Neuroimage*, *185*, 35–57. https://doi.org/10/ggd8dm

Ji, X., Ferreira, T., Friedman, B., Liu, R., Liechty, H., Bas, E., Chandrashekar, J., & Kleinfeld, D. (2021). Brain microvasculature has a common topology with local differences in geometry that match metabolic load. *Neuron*, *109*(7), 1168–1187.

Jiang, D., & Lu, H. (2022). Cerebral oxygen extraction fraction MRI: Techniques and applications. *Magnetic Resonance in Medicine*.

Jones, A. K. P., Brown, W. D., Friston, K. J., Qi, L. Y., & Frackowiak, R. S. J. (1991). Cortical and subcortical localization of response to pain in man using positron emission tomography. *Proceedings of the Royal Society of London. Series B: Biological Sciences*, *244*(1309), 39–44. https://doi.org/10.1098/RSPB.1991.0048

Kandel, E. R., Schwartz, J. H., & Jessell, T. M. (1995). Essentials of neural science and behavior. Appleton and Lange. *Norwalk Connecticut*.

Kang, H. J., Kawasawa, Y. I., Cheng, F., Zhu, Y., Xu, X., Li, M., Sousa, A. M. M., Pletikos, M., Meyer, K. A., Sedmak, G., Guennel, T., Shin, Y., Johnson, M. B., Krsnik, Z., Mayer, S., Fertuzinhos, S., Umlauf, S., Lisgo, S. N., Vortmeyer, A., … Sestan, N. (2011). Spatio-temporal transcriptome of the human brain. *Nature*, *478*(7370), 483–489. https://doi.org/10/bdwbwd

Kaplan, L., Chow, B. W., & Gu, C. (2020). Neuronal regulation of the blood–brain barrier and neurovascular coupling. *Nature Reviews Neuroscience*, *21*(8), 416–432.

Kasischke, K. A. (2009). Activity-Dependent Metabolism in Glia and Neurons. *Encyclopedia of Neuroscience*, 53–60. https://doi.org/10.1016/B978-008045046-9.01711-3

Katz-Brull, R., Alsop, D. C., Marquis, R. P., & Lenkinski, R. E. (2006). Limits on activation-induced temperature and metabolic changes in the human primary visual cortex. *Magnetic Resonance in Medicine*, *56*(2), 348–355. https://doi.org/10.1002/MRM.20972

Kay, K., Jamison, K. W., Zhang, R., & Ugurbil, K. (2019). TDM: a temporal decomposition method for removing venous effects from task-based fMRI. *BioRxiv*, 868455.

Keil, J. M., Qalieh, A., & Kwan, K. Y. (2018). Brain transcriptome databases: a user's guide. *Journal of Neuroscience*, *38*(10), 2399–2412.

Kennedy, M. B. (2016). Synaptic Signaling in Learning and Memory. *Cold Spring Harbor Perspectives in Biology*, *8*(2), 1–16. https://doi.org/10.1101/CSHPERSPECT.A016824

Keyes, J. W. (1995). SUV: Standard uptake or silly useless value? *Journal of Nuclear Medicine*, *36*(10), 1836–1839.

Khambhati, A. N., Bassett, D. S., Oommen, B. S., Chen, S. H., Lucas, T. H., Davis, K. A., & Litt,

B. (2017). Recurring functional interactions predict network architecture of interictal and ictal states in neocortical epilepsy. *ENeuro*, *4*(1). https://doi.org/10/gjghbj

KhanAcademy. (2017). *Khan Academy*.

Kierdorf, K., Masuda, T., Jordão, M. J. C., & Prinz, M. (2019). Macrophages at CNS interfaces: ontogeny and function in health and disease. *Nature Reviews Neuroscience 2019 20:9*, *20*(9), 547–562. https://doi.org/10.1038/s41583-019-0201-x

Kiliç, T., & Akakin, A. (2008). Anatomy of Cerebral Veins and Sinuses. *Frontiers of Neurology and Neuroscience*, *23*, 4–15. https://doi.org/10.1159/000111256

Kim, B., Kim, H., Kim, S., & Hwang, Y. ran. (2021). A brief review of non-invasive brain imaging technologies and the near-infrared optical bioimaging. *Applied Microscopy*, *51*(1). https://doi.org/10.1186/S42649-021-00058-7

Kinahan, P. E., & Fletcher, J. W. (2010). Positron Emission Tomography-Computed Tomography Standardized Uptake Values in Clinical Practice and Assessing Response to Therapy. *Seminars in Ultrasound, CT and MRI*, *31*(6), 496–505. https://doi.org/10.1053/j.sult.2010.10.001

Kinahan, P. E., Townsend, D. W., Beyer, T., & Sashin, D. (1998). Attenuation correction for a combined 3D PET/CT scanner. *Medical Physics*, *25*(10), 2046–2063. https://doi.org/10.1118/1.598392

Kisler, K., Nelson, A. R., Rege, S. V., Ramanathan, A., Wang, Y., Ahuja, A., Lazic, D., Tsai, P. S., Zhao, Z., Zhou, Y., Boas, D. A., Sakadžić, S., & Zlokovic, B. V. (2017). Pericyte degeneration leads to neurovascular uncoupling and limits oxygen supply to brain. *Nature Neuroscience 2017 20:3*, *20*(3), 406–416. https://doi.org/10.1038/nn.4489

Kitzbichler, M. G., Smith, M. L., Christensen, S. R., & Bullmore, E. (2009). Broadband criticality of human brain network synchronization. *PLoS Comput. Biol.*, *5*(3), e1000314. https://doi.org/10/dpm29z

Kleinfeld, D., Blinder, P., Drew, P. J., Driscoll, J. D., Muller, A., Tsai, P. S., & Shih, A. Y. (2011). A guide to delineate the logic of neurovascular signaling in the brain. *Frontiers in Neuroenergetics*, *3*, 1.

Kleinridders, A., Ferris, H. A., Reyzer, M. L., Rath, M., Soto, M., Manier, M. L., Spraggins, J., Yang, Z., Stanton, R. C., Caprioli, R. M., & Kahn, C. R. (2018). Regional differences in brain glucose metabolism determined by imaging mass spectrometry. *Molecular Metabolism*, *12*(April), 113–121. https://doi.org/10.1016/j.molmet.2018.03.013

Knowles, J. R. (1980). Enzyme-catalyzed phosphoryl transfer reactions. *Annual Review of Biochemistry*, *49*(1), 877–919.

Kobari, M., Fukuuchi, Y., Tomita, M., Tanahashi, N., & Takeda, H. (1994). Role of nitric oxide in regulation of cerebral microvascular tone and autoregulation of cerebral blood flow in cats. *Brain Research*, *667*(2), 255–262. https://doi.org/10.1016/0006-8993(94)91503-2

Kochonowicz, J., Mariak, Z., Rutkowski, R., Turek, G., Łysoń, T., & Krejza, J. (2009). Age and sex dependency of blood flow velocity in the internal carotid artery. *Neurologia i*

Neurochirurgia Polska, *43*(1), 3–8.

Koller, A., & Toth, P. (2012). Contribution of Flow-Dependent Vasomotor Mechanisms to the Autoregulation of Cerebral Blood Flow. *Journal of Vascular Research*, *49*(5), 375–389. https://doi.org/10.1159/000338747

Krieger, S. N., Streicher, M. N., Trampel, R., & Turner, R. (2012). Cerebral blood volume changes during brain activation. *Journal of Cerebral Blood Flow & Metabolism*, *32*(8), 1618. https://doi.org/10.1038/JCBFM.2012.63

Krishnamurthy, V., Sprick, J. D., Krishnamurthy, L. C., Barter, J. D., Turabi, A., Hajjar, I. M., & Nocera, J. R. (2021). The utility of cerebrovascular reactivity MRI in brain rehabilitation: a mechanistic perspective. *Frontiers in Physiology*, *12*, 642850.

Krishnan, A., Williams, L. J., McIntosh, A. R., & Abdi, H. (2011). Partial Least Squares (PLS) methods for neuroimaging: A tutorial and review. *NeuroImage*, *56*(2), 455–475. https://doi.org/10.1016/j.neuroimage.2010.07.034

Kudo, K., Liu, T., Murakami, T., Goodwin, J., Uwano, I., Yamashita, F., Higuchi, S., Wang, Y., Ogasawara, K., Ogawa, A., & Sasaki, M. (2016). Oxygen extraction fraction measurement using quantitative susceptibility mapping: Comparison with positron emission tomography. *Journal of Cerebral Blood Flow and Metabolism*, *36*(8), 1424–1433. https://doi.org/10.1177/0271678X15606713

Kudomi, N., Hirano, Y., Koshino, K., Hayashi, T., Watabe, H., Fukushima, K., Moriwaki, H., Teramoto, N., Iihara, K., & Iida, H. (2013). Rapid quantitative CBF and CMRO 2 measurements from a single PET scan with sequential administration of dual 15O-labeled tracers. *Journal of Cerebral Blood Flow & Metabolism*, *33*(3), 440–448.

Kugler, E. C., Greenwood, J., & MacDonald, R. B. (2021). The "Neuro-Glial-Vascular" Unit: The Role of Glia in Neurovascular Unit Formation and Dysfunction. *Frontiers in Cell and Developmental Biology*, *9*. https://doi.org/10.3389/FCELL.2021.732820

Lahijanian, B., Zarandi, M. H. F., & Farahani, F. V. (2016). *Proposing a model for operating room scheduling based on fuzzy surgical duration*.

Lake, B. B., Chen, S., Sos, B. C., Fan, J., Kaeser, G. E., Yung, Y. C., Duong, T. E., Gao, D., Chun, J., Kharchenko, P. V., & Zhang, K. (2018). Integrative single-cell analysis of transcriptional and epigenetic states in the human adult brain. *Nature Biotechnology*, *36*(1), 70–80. https://doi.org/10.1038/nbt.4038

Lanczos, C., Lanczos, & C. (1964). A Precision Approximation of the Gamma Function. *SJNA*, *1*(1), 86–96. https://doi.org/10.1137/0701008

Landau, S. M., Harvey, D., Madison, C. M., Koeppe, R. A., Reiman, E. M., Foster, N. L., Weiner, M. W., & Jagust, W. J. (2011). Associations between cognitive, functional, and FDG-PET measures of decline in AD and MCI. *Neurobiology of Aging*, *32*(7), 1207–1218. https://doi.org/10.1016/j.neurobiolaging.2009.07.002

Lapenna, A., De Palma, M., & Lewis, C. E. (2018). Perivascular macrophages in health and disease. *Nature Reviews Immunology 2018 18:11*, *18*(11), 689–702. https://doi.org/10.1038/s41577-018-0056-9

Larner, A. J. (2018). *A dictionary of neurological signs*. Springer International Publishing.

Larson-Prior, L. J., Zempel, J. M., Nolan, T. S., Prior, F. W., Snyder, A. Z., & Raichle, M. E. (2009). Cortical network functional connectivity in the descent to sleep. *Proc. Natl. Acad. Sci. U. S. A.*, *106*(11), 4489–4494. https://doi.org/10/bznxcr

Latora, V., & Marchiori, M. (2001). Efficient Behavior of Small-World Networks. *Physical Review Letters*, *87*(19), 198701. https://doi.org/10.1103/PhysRevLett.87.198701

Laufs, H., Krakow, K., Sterzer, P., Eger, E., Beyerle, A., Salek-Haddadi, A., & Kleinschmidt, A. (2003). Electroencephalographic signatures of attentional and cognitive default modes in spontaneous brain activity fluctuations at rest. *Proc. Natl. Acad. Sci. U. S. A.*, *100*(19), 11053–11058. https://doi.org/10/cwjxjb

Lawrence, R. M., Bridgeford, E. W., Myers, P. E., Arvapalli, G. C., Ramachandran, S. C., Pisner, D. A., Frank, P. F., Lemmer, A. D., Nikolaidis, A., & Vogelstein, J. T. (2021). Standardizing human brain parcellations. *Scientific Data 2021 8:1*, *8*(1), 1–9. https://doi.org/10.1038/s41597-021-00849-3

Lee, K., Han, P. K., & Ye, J. C. (2011). Sparse dictionary learning for resting-state fMRI analysis. *Https://Doi.Org/10.1117/12.894241*, *8138*, 500–506. https://doi.org/10.1117/12.894241

Lee, K., Horien, C., O'Connor, D., Garand-Sheridan, B., Tokoglu, F., Scheinost, D., Lake, E. M. R., & Constable, R. T. (2022). Arousal impacts distributed hubs modulating the integration of brain functional connectivity. *NeuroImage*, *258*, 119364. https://doi.org/10.1016/j.neuroimage.2022.119364

Lee, K., Khoo, H. M., Fourcade, C., Gotman, J., & Grova, C. (2019). Automatic classification and removal of structured physiological noise for resting state functional connectivity MRI analysis. *Magnetic Resonance Imaging*, *58*, 97–107. https://doi.org/10.1016/j.mri.2019.01.019

Lee, K., Khoo, H. M., Lina, J. M., Dubeau, F., Gotman, J., & Grova, C. (2018). Disruption, emergence and lateralization of brain network hubs in mesial temporal lobe epilepsy. *NeuroImage: Clinical*, *20*(December 2017), 71–84. https://doi.org/10.1016/j.nicl.2018.06.029

Lee, K., Lina, J. M., Gotman, J., & Grova, C. (2016). SPARK: Sparsity-based analysis of reliable k-hubness and overlapping network structure in brain functional connectivity. *NeuroImage*, *134*, 434–449. https://doi.org/10.1016/j.neuroimage.2016.03.049

Lee, Y. B., Lee, J., Tak, S., Lee, K., Na, D. L., Seo, S. W., Jeong, Y., & Ye, J. C. (2016). Sparse SPM: Group Sparse-dictionary learning in SPM framework for resting-state functional connectivity MRI analysis. *NeuroImage*, *125*, 1032–1045. https://doi.org/10.1016/J.NEUROIMAGE.2015.10.081

Leicht, E. A., & Newman, M. E. J. (2008). Community structure in directed networks. *Physical Review Letters*, *100*(11), 118703. https://doi.org/10.1103/PHYSREVLETT.100.118703/FIGURES/3/MEDIUM

Leithner, C., & Royl, G. (2014). The oxygen paradox of neurovascular coupling. *Journal of Cerebral Blood Flow & Metabolism*, *34*(1), 19. https://doi.org/10.1038/JCBFM.2013.181

Lennox, W. G., & Gibbs, E. L. (1932). The blood flow in the brain and the leg of man, and the changes induced by alteration of blood gases. *The Journal of Clinical Investigation*, *11*(6), 1155–1177.

Leontiev, O., Buracas, G. T., Liang, C., Ances, B. M., Perthen, J. E., Shmuel, A., & Buxton, R. B. (2013). Coupling of cerebral blood flow and oxygen metabolism is conserved for chromatic and luminance stimuli in human visual cortex. *Neuroimage*, *68*, 221–228.

Leontiev, O., & Buxton, R. B. (2007). Reproducibility of BOLD, perfusion, and CMRO2 measurements with calibrated-BOLD fMRI. *Neuroimage*, *35*(1), 175–184.

Li, B., Esipova, T. V., Sencan, I., Kılıç, K., Fu, B., Desjardins, M., Moeini, M., Kura, S., Yaseen, M. A., Lesage, F., Østergaard, L., Devor, A., Boas, D. A., Vinogradov, S. A., & Sakadži Ć, S. (2019). More homogeneous capillary flow and oxygenation in deeper cortical layers correlate with increased oxygen extraction. *ELife*, *8*. https://doi.org/10.7554/ELIFE.42299

Li, B., Ohtomo, R., Thunemann, M., Adams, S. R., Yang, J., Fu, B., Yaseen, M. A., Ran, C., Polimeni, J. R., & Boas, D. A. (2020). Two-photon microscopic imaging of capillary red blood cell flux in mouse brain reveals vulnerability of cerebral white matter to hypoperfusion. *Journal of Cerebral Blood Flow & Metabolism*, *40*(3), 501–512.

Li, M., Santpere, G., Kawasawa, Y. I., Evgrafov, O. V., Gulden, F. O., Pochareddy, S., Sunkin, S. M., Li, Z., Shin, Y., Zhu, Y., Sousa, A. M. M., Werling, D. M., Kitchen, R. R., Kang, H. J., Pletikos, M., Choi, J., Muchnik, S., Xu, X., Wang, D., … Sestan, N. (2018). Integrative functional genomic analysis of human brain development and neuropsychiatric risks. *Science*, *362*(6420). https://doi.org/10.1126/SCIENCE.AAT7615/SUPPL_FILE/AAT7615_LI_TABLES_S1_TO_S16.XLSX

Li, S., Hu, N., Zhang, W., Tao, B., Dai, J., Gong, Y., Tan, Y., Cai, D., & Lui, S. (2019). Dysconnectivity of multiple brain networks in schizophrenia: A meta-analysis of resting-state functional connectivity. *Frontiers in Psychiatry*, *10*(JULY). https://doi.org/10.3389/FPSYT.2019.00482/FULL

Li, W., Xu, X., Liu, P., Strouse, J. J., Casella, J. F., Lu, H., van Zijl, P. C. M., & Qin, Q. (2020). Quantification of whole-brain oxygenation extraction fraction and cerebral metabolic rate of oxygen consumption in adults with sickle cell anemia using individual T2-based oxygenation calibrations. *Magnetic Resonance in Medicine*, *83*(3), 1066–1080.

Liang, X., Zou, Q., He, Y., & Yang, Y. (2013). Coupling of functional connectivity and regional cerebral blood flow reveals a physiological basis for network hubs of the human brain. *Proceedings of the National Academy of Sciences of the United States of America*, *110*(5), 1929–1934. https://doi.org/10.1073/pnas.1214900110

Liao, X., Vasilakos, A. V., & He, Y. (2017). Small-world human brain networks: Perspectives and challenges. *Neuroscience & Biobehavioral Reviews*, *77*, 286–300. https://doi.org/10.1016/J.NEUBIOREV.2017.03.018

Liégeois, R., Laumann, T. O., Snyder, A. Z., Zhou, J., & Yeo, B. T. T. (2017). Interpreting temporal fluctuations in resting-state functional connectivity MRI. In *NeuroImage* (Vol. 163, Issue September, pp. 437–455). https://doi.org/10.1016/j.neuroimage.2017.09.012

Lin, A.-L., Gao, J.-H., & Fox, P. T. (2012). Neurovascular and neurometabolic uncoupling in the visual cortex. In *Visual Cortex-Current Status and Perspectives*. IntechOpen.

Lin, A., Peiris, N. J., Dhaliwal, H., Hakim, M., Li, W., Ganesh, S., Ramaswamy, Y., Patel, S., & Misra, A. (2021). Mural Cells: Potential Therapeutic Targets to Bridge Cardiovascular Disease and Neurodegeneration. *Cells 2021, Vol. 10, Page 593*, *10*(3), 593. https://doi.org/10.3390/CELLS10030593

Lin, M., Chen, Q., & Yan, S. (2013). Network In Network. *2nd International Conference on Learning Representations, ICLR 2014 - Conference Track Proceedings*. https://doi.org/10.48550/arxiv.1312.4400

Linkenkaer-Hansen, K., Nikouline, V. V, Palva, J. M., & Ilmoniemi, R. J. (2001). Long-range temporal correlations and scaling behavior in human brain oscillations. *J. Neurosci.*, *21*(4), 1370–1377. https://doi.org/10/gdvh4g

Liu, P., De Vis, J. B., & Lu, H. (2019). Cerebrovascular reactivity (CVR) MRI with CO2 challenge: A technical review. *NeuroImage*, *187*(3), 104–115. https://doi.org/10.1016/j.neuroimage.2018.03.047

Lu, H., & Ge, Y. (2008). Quantitative evaluation of oxygenation in venous vessels using T2-relaxation-under-spin-tagging MRI. *Magnetic Resonance in Medicine: An Official Journal of the International Society for Magnetic Resonance in Medicine*, *60*(2), 357–363.

Lu, J., Zhang, H., Hameed, N. U. F., Zhang, J., Yuan, S., Qiu, T., Shen, D., & Wu, J. (2017). An automated method for identifying an independent component analysis-based language-related resting-state network in brain tumor subjects for surgical planning. *Scientific Reports*, *7*(1), 13769. https://doi.org/10.1038/s41598-017-14248-5

Lurito, J. T., Kareken, D. A., Lowe, M. J., Chen, S. H. A., & Mathews, V. P. (2000). Comparison of rhyming and word generation with FMRI. *Hum. Brain Mapp.*, *10*(3), 99–106. https://doi.org/10/d5886r

Lyons, D. G., Parpaleix, A., Roche, M., & Charpak, S. (2016). Mapping oxygen concentration in the awake mouse brain. *ELife*, *5*(FEBRUARY2016), 1–16. https://doi.org/10.7554/eLife.12024

Ma, Y. (2020). *Quantification of cerebral oxygen metabolism using MRI*. McGill University (Canada).

Ma, Y., Mazerolle, E. L., Cho, J., Sun, H., Wang, Y., & Pike, G. B. (2020). Quantification of brain oxygen extraction fraction using QSM and a hyperoxic challenge. *Magnetic Resonance in Medicine*, *84*(6), 3271–3285.

Maaniitty, T., Knuuti, J., & Saraste, A. (2020). 15O-Water PET MPI: Current Status and Future Perspectives. *Seminars in Nuclear Medicine*, *50*(3), 238–247. https://doi.org/10.1053/J.SEMNUCLMED.2020.02.011

Maccotta, L., He, B. J., Snyder, A. Z., Eisenman, L. N., Benzinger, T. L., Ances, B. M., Corbetta, M., & Hogan, R. E. (2013). Impaired and facilitated functional networks in temporal lobe epilepsy. *NeuroImage: Clinical*, *2*, 862–872.

Mächler, P., Wyss, M. T., Elsayed, M., Stobart, J., Gutierrez, R., Von Faber-Castell, A., Kaelin, V., Zuend, M., San Martín, A., Romero-Gómez, I., Baeza-Lehnert, F., Lengacher, S., Schneider, B. L., Aebischer, P., Magistretti, P. J., Barros, L. F., & Weber, B. (2016). In Vivo Evidence for a Lactate Gradient from Astrocytes to Neurons. *Cell Metabolism*, *23*(1), 94–102. https://doi.org/10.1016/J.CMET.2015.10.010

Madsen, P. L., Hasselbalch, S. G., Hagemann, L. P., Olsen, K. S., Bülow, J., Holm, S., Wildschiødtz, G., Paulson, O. B., & Lassen, N. A. (1995). Persistent resetting of the cerebral oxygen/glucose uptake ratio by brain activation: Evidence obtained with the Kety-Schmidt technique. *Journal of Cerebral Blood Flow and Metabolism*, *15*(3), 485–491. https://doi.org/10.1038/jcbfm.1995.60

Magistretti, P. J. (2016). Imaging brain aerobic glycolysis as a marker of synaptic plasticity. *Proceedings of the National Academy of Sciences*, *113*(26), 7015–7016.

Magistretti, P. J., & Allaman, I. (2015). A Cellular Perspective on Brain Energy Metabolism and Functional Imaging. *Neuron*, *86*(4), 883–901. https://doi.org/10.1016/j.neuron.2015.03.035

Maitra, S., & Yan, J. (2008). Principle Component Analysis and Partial Least Squares : *Applying Multivariate Statistical Models*, *79*, 79–90.

Mandeville, J. B., & Marota, J. J. A. (1999). Vascular filters of functional MRI: spatial localization using BOLD and CBV contrast. *Magnetic Resonance in Medicine: An Official Journal of the International Society for Magnetic Resonance in Medicine*, *42*(3), 591–598.

Manera, A. L., Dadar, M., Fonov, V., & Collins, D. L. (2020). CerebrA, registration and manual label correction of Mindboggle-101 atlas for MNI-ICBM152 template. *Scientific Data*, *7*(1), 1–9.

Manning, H. L., & Schwartzstein, R. M. (1995). Pathophysiology of dyspnea. *New England Journal of Medicine*, *333*(23), 1547–1553.

Marcus, D. S., Harwell, J., Olsen, T., Hodge, M., Glasser, M. F., Prior, F., Jenkinson, M., Laumann, T., Curtiss, S. W., & Van Essen, D. C. (2011). Informatics and data mining tools and strategies for the human connectome project. *Frontiers in Neuroinformatics*, *5*(June), 1–12. https://doi.org/10.3389/fninf.2011.00004

Markello, R. D., & Misic, B. (2021). Comparing spatial null models for brain maps. In *NeuroImage* (Vol. 236). https://doi.org/10.1016/j.neuroimage.2021.118052

Marrelec, G., Bellec, P., Krainik, A., Duffau, H., Pélégrini-Issac, M., Lehéricy, S., Benali, H., & Doyon, J. (2008). Regions, systems, and the brain: Hierarchical measures of functional integration in fMRI. *Medical Image Analysis*, *12*(4), 484–496. https://doi.org/10.1016/j.media.2008.02.002

Mathiesen, C., Thomsen, K., & Lauritzen, M. (2014). Integrated measurements of electrical activity, Oxygen tension, Blood flow, And Ca2+-Signaling in rodents in vivo. *Neuromethods*, *90*(November), 243–264. https://doi.org/10.1007/978-1-4939-1059-5_11

Mathur, R., Rotroff, D., Ma, J., Shojaie, A., & Motsinger-Reif, A. (2018). Gene set analysis methods: a systematic comparison. *BioData Mining*, *11*(1), 1–19.

Matta, B. F., Menon, D. K., & Smith, M. (2011). *Core topics in neuroanaesthesia and neurointensive care*. Cambridge University Press.

Matthews, W. B. (1976). From Neuron to Brain. *Bmj*, *2*(6045), 1202–1202. https://doi.org/10.1136/bmj.2.6045.1202-a

Mazzarello, P. (1999). A unifying concept: the history of cell theory. *Nature Cell Biology*, *1*(1), E13–E15.

McIntosh, A. R. (2022). *Comparison of Canonical Correlation and Partial Least Squares analyses of simulated and empirical data*.

McKenzie, A. T., Wang, M., Hauberg, M. E., Fullard, J. F., Kozlenkov, A., Keenan, A., Hurd, Y. L., Dracheva, S., Casaccia, P., Roussos, P., & Zhang, B. (2018). Brain Cell Type Specific Gene Expression and Co-expression Network Architectures. *Scientific Reports 2018 8:1*, *8*(1), 1–19. https://doi.org/10.1038/s41598-018-27293-5

McKeown, M. J., Hansen, L. K., & Sejnowsk, T. J. (2003). Independent component analysis of functional MRI: What is signal and what is noise? *Current Opinion in Neurobiology*, *13*(5), 620–629. https://doi.org/10.1016/j.conb.2003.09.012

McKeown, M. J., Jung, T. P., Makeig, S., Brown, G., Kindermann, S. S., Lee, T. W., & Sejnowski, T. J. (1998). Spatially independent activity patterns in functional MRI data during the Stroop color-naming task. *Proceedings of the National Academy of Sciences of the United States of America*, *95*(3), 803–810. https://doi.org/10.1073/PNAS.95.3.803

Meier, J., Tewarie, P., Hillebrand, A., Douw, L., Van Dijk, B. W., Stufflebeam, S. M., & Van Mieghem, P. (2016). A Mapping Between Structural and Functional Brain Networks. *Brain Connectivity*, *6*(4), 298. https://doi.org/10.1089/BRAIN.2015.0408

Mergenthaler, P., Lindauer, U., Dienel, G. A., & Meisel, A. (2013). Sugar for the brain: the role of glucose in physiological and pathological brain function. *Trends in Neurosciences*, *36*(10), 587–597. https://doi.org/10.1016/j.tins.2013.07.001

Merola, A., Germuska, M. A., Murphy, K., & Wise, R. G. (2018). Assessing the repeatability of absolute CMRO2, OEF and haemodynamic measurements from calibrated fMRI. *Neuroimage*, *173*, 113–126.

Mesmoudi, S., Perlbarg, V., Rudrauf, D., Messe, A., Pinsard, B., Hasboun, D., Cioli, C., Marrelec, G., Toro, R., Benali, H., & Burnod, Y. (2013). Resting State Networks' Corticotopy: The Dual Intertwined Rings Architecture. *PLoS ONE*, *8*(7). https://doi.org/10.1371/journal.pone.0067444

Mesmoudi, S., Rodic, M., Cioli, C., Cointet, J. P., Yarkoni, T., & Burnod, Y. (2015). LinkRbrain: Multi-scale data integrator of the brain. *Journal of Neuroscience Methods*, *241*, 44–52. https://doi.org/10.1016/j.jneumeth.2014.12.008

Messé, A. (2020). Parcellation influence on the connectivity-based structure–function relationship in the human brain. *Human Brain Mapping*, *41*(5), 1167–1180. https://doi.org/10.1002/hbm.24866

Messé, A., Rudrauf, D., Benali, H., & Marrelec, G. (2014). Relating Structure and Function in the

Human Brain: Relative Contributions of Anatomy, Stationary Dynamics, and Non-stationarities. *PLoS Computational Biology*, *10*(3). https://doi.org/10.1371/journal.pcbi.1003530

Mesulam, M. M. (1990). Large-scale neurocognitive networks and distributed processing for attention, language, and memory. *Ann. Neurol.*, *28*(5), 597–613. https://doi.org/10/fnq75m

Meunier, D., Lambiotte, R., & Bullmore, E. T. (2010). Modular and Hierarchically Modular Organization of Brain Networks. *Frontiers in Neuroscience*, *4*(DEC), 200. https://doi.org/10.3389/fnins.2010.00200

Meyer, E., Tyler, J. L., Thompson, C. J., Redies, C., Diksic, M., & Hakim, A. M. (1987). Estimation of cerebral oxygen utilization rate by single-bolus 15O2 inhalation and dynamic positron emission tomography. *Journal of Cerebral Blood Flow and Metabolism*, *7*(4), 403–414. https://doi.org/10.1038/jcbfm.1987.83

Mezue, M., Segerdahl, A. R., Okell, T. W., Chappell, M. A., Kelly, M. E., & Tracey, I. (2014). Optimization and reliability of multiple postlabeling delay pseudo-continuous arterial spin labeling during rest and stimulus-induced functional task activation. *Journal of Cerebral Blood Flow & Metabolism*, *34*(12), 1919. https://doi.org/10.1038/JCBFM.2014.163

Milgram, S. (1967). The small world problem. *Psychology Today*, *2*(1), 60–67.

Miller, J. A., Ding, S.-L., Sunkin, S. M., Smith, K. A., Ng, L., Szafer, A., Ebbert, A., Riley, Z. L., Royall, J. J., Aiona, K., Arnold, J. M., Bennet, C., Bertagnolli, D., Brouner, K., Butler, S., Caldejon, S., Carey, A., Cuhaciyan, C., Dalley, R. A., … Lein, E. S. (2014). Transcriptional landscape of the prenatal human brain. *Nature*, *508*(7495), 199–206. https://doi.org/10/f5wwbm

Minoshima, S., Frey, K. A., Foster, N. L., & Kuhl, D. E. (1995). Preserved pontine glucose metabolism in Alzheimer disease: a reference region for functional brain image (PET) analysis. *Journal of Computer Assisted Tomography*, *19*(4), 541–547.

Mintun, M. A., Vlassenko, A. G., Rundle, M. M., & Raichle, M. E. (2004). Increased lactate/pyruvate ratio augments blood flow in physiologically activated human brain. *Proceedings of the National Academy of Sciences of the United States of America*, *101*(2), 659–664. https://doi.org/10.1073/pnas.0307457100

Mišić, B., & Sporns, O. (2016). From regions to connections and networks: new bridges between brain and behavior. *Current Opinion in Neurobiology*, *40*, 1–7. https://doi.org/10.1016/j.conb.2016.05.003

Moore, K. L., Dalley, A. F., & Agur, A. M. (2019). *Clinically oriented anatomy* (8th ed.). Wolters Kluwer Health.

Morgenthaler, F. D., Kraftsik, R., Catsicas, S., Magistretti, P. J., & Chatton, J.-Y. (2006). Glucose and lactate are equally effective in energizing activity-dependent synaptic vesicle turnover in purified cortical neurons. *Neuroscience*, *141*(1), 157–165.

Morrison, J. H., & Hof, P. R. (1997). Life and death of neurons in the aging brain. *Science (New York, N.Y.)*, *278*(5337), 412–419. https://doi.org/10.1126/SCIENCE.278.5337.412

Mount, C. A., & Das, J. M. (2021). Cerebral perfusion pressure. In *StatPearls [Internet]*. StatPearls Publishing.

Muldoon, S. F., Bridgeford, E. W., & Bassett, D. S. (2016). Small-World Propensity and Weighted Brain Networks. *Scientific Reports 2016 6:1*, *6*(1), 1–13. https://doi.org/10.1038/srep22057

Munakomi, S., & Das, J. M. (2022). Intracranial Pressure Monitoring. *StatPearls*.

Murakami, T., Tsurusaki, M., Hyodo, T., & Imai, Y. (2014). Clinical utility of imaging for evaluation of hepatocellular carcinoma. *Journal of Hepatocellular Carcinoma*, *1*, 101.

Muzik, O., Mangner, T. J., Leonard, W. R., Kumar, A., Janisse, J., & Granneman, J. G. (2013). 15O PET Measurement of Blood Flow and Oxygen Consumption in Cold-Activated Human Brown Fat. *Journal of Nuclear Medicine*, *54*(4), 523–531. https://doi.org/10.2967/JNUMED.112.111336

Nabavi, D. G., Cenic, A., Henderson, S., Gelb, A. W., & Lee, T.-Y. (2001). Perfusion mapping using computed tomography allows accurate prediction of cerebral infarction in experimental brain ischemia. *Stroke*, *32*(1), 175–183.

Najafi, M., McMenamin, B. W., Simon, J. Z., & Pessoa, L. (2016). Overlapping communities reveal rich structure in large-scale brain networks during rest and task conditions. *NeuroImage*, *135*, 92–106. https://doi.org/10.1016/j.neuroimage.2016.04.054

Nehlig, A. (2004). Brain uptake and metabolism of ketone bodies in animal models. *Prostaglandins Leukotrienes and Essential Fatty Acids*, *70*(3), 265–275. https://doi.org/10.1016/j.plefa.2003.07.006

Nelder, J. A., & Wedderburn, R. W. M. (1972). Generalized Linear Models. *Journal of the Royal Statistical Society: Series A (General)*, *135*(3), 370–384. https://doi.org/10.2307/2344614

Nelson, A. R., Sweeney, M. D., Sagare, A. P., & Zlokovic, B. V. (2016). Neurovascular dysfunction and neurodegeneration in dementia and Alzheimer's disease. *Biochimica et Biophysica Acta (BBA) - Molecular Basis of Disease*, *1862*(5), 887–900. https://doi.org/10.1016/J.BBADIS.2015.12.016

Nelson, D. L., Lehninger, A. L., & Cox, M. M. (2008). *Lehninger principles of biochemistry*. Macmillan.

Newman, M. (2010). *Networks: An Introduction*. Oxford University Press. https://doi.org/10.1093/acprof:oso/9780199206650.001.0001

Newman, M. E. J. (2004). Analysis of weighted networks. *Physical Review E - Statistical Physics, Plasmas, Fluids, and Related Interdisciplinary Topics*, *70*(5), 9. https://doi.org/10.1103/PhysRevE.70.056131

Newman, M. E. J. (2006). Modularity and community structure in networks. *Proceedings of the National Academy of Sciences*, *103*(23), 8577–8582. https://doi.org/10.1073/pnas.0601602103

Newman, M. E. J., & Barkema, G. T. (n.d.). Oxford University Press; New York: 2010. *Networks: An Introduction.[Google Scholar]*.

Ngan, S.-C., & Hu, X. (1999). Analysis of functional magnetic resonance imaging data using self-organizing mapping with spatial connectivity. *Magnetic Resonance in Medicine*, *41*(5), 939–946. https://doi.org/10.1002/(SICI)1522-2594(199905)41:5<939::AID-MRM13>3.0.CO;2-Q

Nguyen, N., Hogan, E., El-Sadda, W., Oliver, D., & Osman, M. (2006). *Comparison of SUV of the pons and cerebellum in F-18 FDG PET/CT: Pons is a better internal reference point*. Soc Nuclear Med.

Nicholls, J. G., Martin, A. R., Wallace, B. G., & Fuchs, P. A. (2001). Principles of signaling and organization. *From Neuron to Brain*, *1*, 3–22.

Niven, J. E., & Laughlin, S. B. (2008). Energy limitation as a selective pressure on the evolution of sensory systems. *J. Exp. Biol.*, *211*(Pt 11), 1792–1804. https://doi.org/10.1242/jeb.017574

Noble, S., Scheinost, D., & Constable, R. T. (2019). A decade of test-retest reliability of functional connectivity: A systematic review and meta-analysis. *NeuroImage*, *203*, 116157. https://doi.org/10.1016/J.NEUROIMAGE.2019.116157

Nugent, A. C., Martinez, A., D'Alfonso, A., Zarate, C. A., & Theodore, W. H. (2015). The relationship between glucose metabolism, resting-state fMRI BOLD signal, and GABA A -binding potential: A preliminary study in healthy subjects and those with temporal lobe epilepsy. *Journal of Cerebral Blood Flow and Metabolism*, *35*, 583–591. https://doi.org/10.1038/jcbfm.2014.228

Nunez, P. L., & Williamson, S. J. (1996). Neocortical dynamics and human EEG rhythms. *Phys. Today*, *49*(4), 57. https://doi.org/10/b9j4qm

O'Herron, P., Chhatbar, P. Y., Levy, M., Shen, Z., Schramm, A. E., Lu, Z., & Kara, P. (2016). Neural correlates of single-vessel haemodynamic responses in vivo. *Nature*, *534*(7607), 378–382.

Ogawa, A., Kameyama, M., Muraishi, K., Yoshimoto, T., Ito, M., & Sakurai, Y. (1992). Cerebral blood flow and metabolism following superficial temporal artery to superior cerebellar artery bypass for vertebrobasilar occlusive disease. *Journal of Neurosurgery*, *76*(6), 955–960.

Oh, S. W., Harris, J. A., Ng, L., Winslow, B., Cain, N., Mihalas, S., Wang, Q., Lau, C., Kuan, L., Henry, A. M., Mortrud, M. T., Ouellette, B., Nguyen, T. N., Sorensen, S. A., Slaughterbeck, C. R., Wakeman, W., Li, Y., Feng, D., Ho, A., … Zeng, H. (2014). A mesoscale connectome of the mouse brain. *Nature*, *508*(7495), 207–214. https://doi.org/10.1038/nature13186

Ohta, S., Meyer, E., Thompson, C. J., & Gjedde, A. (1992). Oxygen consumption of the living human brain measured after a single inhalation of positron emitting oxygen. *Journal of Cerebral Blood Flow & Metabolism*, *12*(2), 179–192.

Ortiz-Prado, E., Natah, S., Srinivasan, S., & Dunn, J. F. (2010). A method for measuring brain partial pressure of oxygen in unanesthetized unrestrained subjects: the effect of acute and chronic hypoxia on brain tissue PO2. *Journal of Neuroscience Methods*, *193*(2), 217. https://doi.org/10.1016/J.JNEUMETH.2010.08.019

Ortiz-Terán, L., Diez, I., Ortiz, T., Perez, D. L., Aragón, J. I., Costumero, V., Pascual-Leone, A., El Fakhri, G., & Sepulcre, J. (2017). Brain circuit-gene expression relationships and

neuroplasticity of multisensory cortices in blind children. *Proc. Natl. Acad. Sci. U. S. A.*, *114*(26), 6830–6835. https://doi.org/10/gmwd3g

Ortiz, A., Gherasim, C., Manana, M., Renedo, C. J., Eguiluz, L. I., & Belmans, R. J. M. (2005). Total harmonic distortion decomposition depending on distortion origin. *IEEE Trans. Power Deliv.*, *20*(4), 2651–2656. https://doi.org/10/bqm5kc

Palombit, A., Silvestri, E., Volpi, T., Aiello, M., Cecchin, D., Bertoldo, A., & Corbetta, M. (2022). Variability of regional glucose metabolism and the topology of functional networks in the human brain. *NeuroImage*, *257*(January), 119280. https://doi.org/10.1016/j.neuroimage.2022.119280

Panov, A., Orynbayeva, Z., Vavilin, V., & Lyakhovich, V. (2014). Fatty Acids in Energy Metabolism of the Central Nervous System. *BioMed Research International*, *2014*. https://doi.org/10.1155/2014/472459

Pantano, P., Baron, J.-C., Lebrun-Grandie, P., Duquesnoy, N., Bousser, M.-G., & Comar, D. (1984). Regional Cerebral Blood Flow and Oxygen Consumption in Human Aging. *Stroke*, *15*.

Pastor-Satorras, R., & Vespignani, A. (2001). Epidemic dynamics and endemic states in complex networks. *Physical Review E*, *63*(6), 066117. https://doi.org/10.1103/PhysRevE.63.066117

Patania, A., Selvaggi, P., Veronese, M., Dipasquale, O., Expert, P., & Petri, G. (2019). Topological gene expression networks recapitulate brain anatomy and function. *Network Neuroscience*, *3*(3), 744. https://doi.org/10.1162/NETN_A_00094

Patestas, M. A., & Gartner, L. P. (2016). *A Textbook of Neuroanatomy* (2nd ed.). John Wiley {\&} Sons.

Pearigen, P., Gwinn, R., & Simon, R. P. (1996). The effects in vivo of hypoxia on brain injury. *Brain Research*, *725*(2), 184–191.

Peltier, S. J., Polk, T. A., & Noll, D. C. (2003). Detecting low-frequency functional connectivity in fMRI using a self-organizing map (SOM) algorithm. *Human Brain Mapping*, *20*(4), 220–226. https://doi.org/10.1002/hbm.10144

Pereda, A. E. (2014). Electrical synapses and their functional interactions with chemical synapses. *Nature Reviews Neuroscience 2014 15:4*, *15*(4), 250–263. https://doi.org/10.1038/nrn3708

Perlbarg, V., Bellec, P., Anton, J. L., Pélégrini-Issac, M., Doyon, J., & Benali, H. (2007). CORSICA: correction of structured noise in fMRI by automatic identification of ICA components. *Magnetic Resonance Imaging*, *25*(1), 35–46. https://doi.org/10.1016/J.MRI.2006.09.042

Pessoa, L. (2014). Understanding brain networks and brain organization. *Physics of Life Reviews*, *11*(3), 400. https://doi.org/10.1016/J.PLREV.2014.03.005

Petersen, E. T., Zimine, I., Ho, Y. C. L., & Golay, X. (2006). Non-invasive measurement of perfusion: a critical review of arterial spin labelling techniques. *The British Journal of Radiology*, *79*(944), 688–701.

Petzold, G. C., & Murthy, V. N. (2011). Role of astrocytes in neurovascular coupling. *Neuron*, *71*(5), 782–797.

Philip, M., Snow, R. J., Gatta, P. A. D., Bellofiore, N., & Ellery, S. J. (2020). Creatine metabolism in the uterus: potential implications for reproductive biology. *Amino Acids*, *52*(9), 1275–1283. https://doi.org/10.1007/s00726-020-02896-3

Phillips, A. A., Warburton, D. E. R., Ainslie, P. N., & Krassioukov, A. V. (2014). Regional neurovascular coupling and cognitive performance in those with low blood pressure secondary to high-level spinal cord injury: improved by alpha-1 agonist midodrine hydrochloride. *Journal of Cerebral Blood Flow & Metabolism*, *34*(5), 794–801.

Piechnik, S. K., Chiarelli, P. A., & Jezzard, P. (2008). Modelling vascular reactivity to investigate the basis of the relationship between cerebral blood volume and flow under CO2 manipulation. *NeuroImage*, *39*(1), 107–118. https://doi.org/10.1016/J.NEUROIMAGE.2007.08.022

Pierre, K., & Pellerin, L. (2005). Monocarboxylate transporters in the central nervous system: distribution, regulation and function. *Journal of Neurochemistry*, *94*(1), 1–14.

Pittau, F., Grova, C., Moeller, F., Dubeau, F., & Gotman, J. (2012). Patterns of altered functional connectivity in mesial temporal lobe epilepsy. *Epilepsia*, *53*(6), 1013–1023. https://doi.org/10.1111/j.1528-1167.2012.03464.x

Politis, D. N., & Romano, J. P. (1992). A General Resampling Scheme for Triangular Arrays of α-Mixing Random Variables with Application to the Problem of Spectral Density Estimation. *The Annals of Statistics*, *20*(4). https://doi.org/10.1214/aos/1176348899

Polleux, F., Ince-Dunn, G., & Ghosh, A. (2007). Transcriptional regulation of vertebrate axon guidance and synapse formation. *Nature Reviews. Neuroscience*, *8*(5), 331–340. https://doi.org/10.1038/NRN2118

Pons, P., & Latapy, M. (2005). Computing communities in large networks using random walks. *Lecture Notes in Computer Science (Including Subseries Lecture Notes in Artificial Intelligence and Lecture Notes in Bioinformatics)*, *3733 LNCS*, 284–293. https://doi.org/10.1007/11569596_31/COVER

Poublanc, J., Crawley, A. P., Sobczyk, O., Montandon, G., Sam, K., Mandell, D. M., Dufort, P., Venkatraghavan, L., Duffin, J., & Mikulis, D. J. (2015). Measuring cerebrovascular reactivity: the dynamic response to a step hypercapnic stimulus. *Journal of Cerebral Blood Flow & Metabolism*, *35*(11), 1746–1756.

Poulsen, P. H., Smith, D. F., Østergaard, L., Danielsen, E. H., Gee, A., Hansen, S. B., Astrup, J., & Gjedde, A. (1997). In vivo estimation of cerebral blood flow, oxygen consumption and glucose metabolism in the pig by [15O] water injection,[15O] oxygen inhalation and dual injections of [18F] fluorodeoxyglucose. *Journal of Neuroscience Methods*, *77*(2), 199–209.

Power, J. D., Cohen, A. L., Nelson, S. M., Wig, G. S., Barnes, K. A., Church, J. A., Vogel, A. C., Laumann, T. O., Miezin, F. M., Schlaggar, B. L., & Petersen, S. E. (2011). Functional network organization of the human brain. *Neuron*, *72*(4), 665–678. https://doi.org/10/fgp7r9

Power, J. D., Mitra, A., Laumann, T. O., Snyder, A. Z., Schlaggar, B. L., & Petersen, S. E. (2014).

Methods to detect, characterize, and remove motion artifact in resting state fMRI. *NeuroImage*, *84*, 320–341. https://doi.org/10.1016/J.NEUROIMAGE.2013.08.048

Power, J. D., Schlaggar, B. L., Lessov-Schlaggar, C. N., & Petersen, S. E. (2013). Evidence for hubs in human functional brain networks. *Neuron*, *79*(4), 798–813. https://doi.org/10.1016/J.NEURON.2013.07.035

Pruim, R. H. R., Mennes, M., Buitelaar, J. K., & Beckmann, C. F. (2015). Evaluation of ICA-AROMA and alternative strategies for motion artifact removal in resting state fMRI. *Neuroimage*, *112*, 278–287. https://doi.org/10/f68wz3

Purves, D., Augustine, G. J., Fitzpatrick, D., Katz, L. C., LaMantia, A.-S., McNamara, J. O., & Williams, S. M. (2001). *Neuroscience*. 1–2.

Purves, M. J. (1972). Cerebral blood flow and arterial pressure. *Physiology of the Cerebral Circulation. Cambridge: Cambridge University Press*, *156*.

Qin, Q., Grgac, K., & Van Zijl, P. C. M. (2011). Determination of whole-brain oxygen extraction fractions by fast measurement of blood T2 in the jugular vein. *Magnetic Resonance in Medicine*, *65*(2), 471–479.

Quackenbush, J. (2002). Microarray data normalization and transformation. *Nature Genetics*, *32 Suppl*(4S), 496–501. https://doi.org/10.1038/NG1032

Raggi, A., & Leonardi, M. (2015). Burden and cost of neurological diseases: a E uropean N orth–S outh comparison. *Acta Neurologica Scandinavica*, *132*(1), 16–22.

Rah, J. C., Feng, L., Druckmann, S., Lee, H., & Kim, J. (2015). From a meso- to micro-scale connectome: Array tomography and mGRASP. *Frontiers in Neuroanatomy*, *9*(June), 78. https://doi.org/10.3389/FNANA.2015.00078/BIBTEX

Raichle, M. E., MacLeod, A. M., Snyder, A. Z., Powers, W. J., Gusnard, D. A., & Shulman, G. L. (2001). A default mode of brain function. *Proceedings of the National Academy of Sciences*, *98*(2), 676–682.

Rajan, A. M., Ma, R. C., Kocha, K. M., Zhang, D. J., & Huang, P. (2020). Dual function of perivascular fibroblasts in vascular stabilization in zebrafish. *PLOS Genetics*, *16*(10), e1008800. https://doi.org/10.1371/JOURNAL.PGEN.1008800

Reece, J. B., Urry, L. A., Cain, M. L., S. A. Wasserman, P. V. M., & Jackson, R. B. (2011). Cellular Respiration and Fermentation. *In Campbell Biology*, 162–184.

Reece, J. B., Urry, L. A., Cain, M. L., Wasserman, S. A., Minorsky, P. V, & Jackson, R. B. (2014). *Campbell biology* (Vol. 9). Pearson Boston.

Regina Bailey. (n.d.). *What Does the Brain's Cerebral Cortex Do?*

Rencher, A. C. (1995). Multivariate analysis of variance. *Methods of Multivariate Analysis. New York, NY: Wiley*, 174–257.

Ressler, K. J., Paschall, G., Zhou, X. L., & Davis, M. (2002). Regulation of Synaptic Plasticity Genes during Consolidation of Fear Conditioning. *The Journal of Neuroscience*, *22*(18), 7892. https://doi.org/10.1523/JNEUROSCI.22-18-07892.2002

Restom, K., Perthen, J. E., & Liu, T. T. (2008). Calibrated fMRI in the medial temporal lobe during a memory-encoding task. *Neuroimage*, *40*(4), 1495–1502.

Richiardi, J., Altmann, A., Milazzo, A. C., Chang, C., Chakravarty, M. M., Banaschewski, T., Barker, G. J., Bokde, A. L. W., Bromberg, U., Büchel, C., Conrod, P., Fauth-Bühler, M., Flor, H., Frouin, V., Gallinat, J., Garavan, H., Gowland, P., Heinz, A., Lemaître, H., … Greicius, M. D. (2015). Correlated gene expression supports synchronous activity in brain networks. *Science*, *348*(6240), 1241–1244. https://doi.org/10.1126/SCIENCE.1255905/SUPPL_FILE/RICHIARDI_DATA_FILE_S3.TXT

Ridley, B. G. Y., Rousseau, C., Wirsich, J., Le Troter, A., Soulier, E., Confort-Gouny, S., Bartolomei, F., Ranjeva, J.-P., Achard, S., & Guye, M. (2015). Nodal approach reveals differential impact of lateralized focal epilepsies on hub reorganization. *Neuroimage*, *118*, 39–48.

Riske, L., Thomas, R. K., Baker, G. B., & Dursun, S. M. (2017). Lactate in the brain: an update on its relevance to brain energy, neurons, glia and panic disorder. *Therapeutic Advances in Psychopharmacology*, *7*(2), 85. https://doi.org/10.1177/2045125316675579

Robert Bear, D. R. (2016). *Overview of Cellular Respiration*. OpenStax CNX.

Robinson, P. A. (2012). Interrelating anatomical, effective, and functional brain connectivity using propagators and neural field theory. *Physical Review. E, Statistical, Nonlinear, and Soft Matter Physics*, *85*(1 Pt 1). https://doi.org/10.1103/PHYSREVE.85.011912

Robinson, P. A., Sarkar, S., Pandejee, G. M., & Henderson, J. A. (2014). Determination of effective brain connectivity from functional connectivity with application to resting state connectivities. *Physical Review. E, Statistical, Nonlinear, and Soft Matter Physics*, *90*(1). https://doi.org/10.1103/PHYSREVE.90.012707

Rodgers, Z. B., Detre, J. A., & Wehrli, F. W. (n.d.). *MRI-based methods for quantification of the cerebral metabolic rate of oxygen*. https://doi.org/10.1177/0271678X16643090

Rogatzki, M. J., Ferguson, B. S., Goodwin, M. L., & Gladden, L. B. (2015). Lactate is always the end product of glycolysis. *Frontiers in Neuroscience*, *9*(FEB). https://doi.org/10.3389/FNINS.2015.00022

Rokach, L., & Maimon, O. (2005). *Clustering methods. In Data mining and knowledge discovery handbook*. Springer.

Rolfe, D. F., & Brown, G. C. (1997). Cellular energy utilization and molecular origin of standard metabolic rate in mammals. *Physiological Reviews*, *77*(3), 731–758.

Romano, A., Koczwara, J. B., Gallelli, C. A., Vergara, D., Micioni Di Bonaventura, M. V., Gaetani, S., & Giudetti, A. M. (2017). Fats for thoughts: An update on brain fatty acid metabolism. *International Journal of Biochemistry and Cell Biology*, *84*, 40–45. https://doi.org/10.1016/j.biocel.2016.12.015

Rombouts, S. A. R. B., Barkhof, F., Goekoop, R., Stam, C. J., & Scheltens, P. (2005). Altered resting state networks in mild cognitive impairment and mild Alzheimer's disease: An fMRI study. *Human Brain Mapping*, *26*(4), 231–239. https://doi.org/10.1002/hbm.20160

Ross, J. M., Kim, C., Allen, D., Crouch, E. E., Narsinh, K., Cooke, D. L., Abla, A. A., Nowakowski, T. J., & Winkler, E. A. (2020). The Expanding Cell Diversity of the Brain Vasculature. *Frontiers in Physiology*, *11*, 1574. https://doi.org/10.3389/FPHYS.2020.600767/XML/NLM

Rouquet, G., Moore, D. E., Spain, M., Allwood, D. M., Battilocchio, C., Blakemore, D. C., Fish, P. V, Jenkinson, S., Jessiman, A. S., & Ley, S. V. (2015). Design, synthesis, and evaluation of tetrasubstituted pyridines as potent 5-HT2C receptor agonists. *ACS Medicinal Chemistry Letters*, *6*(3), 329–333.

Roy, C. S., & Sherrington, C. S. (1890). On the regulation of the blood-supply of the brain. *The Journal of Physiology*, *11*(1–2), 85.

Rubinov, M., & Sporns, O. (2010). Complex network measures of brain connectivity: Uses and interpretations. *NeuroImage*, *52*(3), 1059–1069. https://doi.org/10.1016/j.neuroimage.2009.10.003

Rye, C., Avissar, Y., Choi, J. H., DeSaix, J., & Jurukovski, V. (2013). *Biology.* OpenStax College, Rice University, Houston, Texas, 2013.

Saito, N. (1994). Simultaneous noise suppression and signal compression using a library of orthonormal bases and the minimum description length criterion. In *Wavelet Analysis and Its Applications* (Vol. 4, pp. 299–324). Elsevier.

Salat, D. H., Buckner, R. L., Snyder, A. Z., Greve, D. N., Desikan, R. S. R., Busa, E., Morris, J. C., Dale, A. M., & Fischl, B. (2004). Thinning of the cerebral cortex in aging. *Cerebral Cortex (New York, N.Y. : 1991)*, *14*(7), 721–730. https://doi.org/10.1093/CERCOR/BHH032

Salazar, A. L. (2017). *Improving Adolescent's Working Memory Through a Long-Term MBSR Curriculum*.

Salvador, R., Suckling, J., Schwarzbauer, C., & Bullmore, E. (2005). Undirected graphs of frequency-dependent functional connectivity in whole brain networks. *Philosophical Transactions of the Royal Society B: Biological Sciences*, *360*(1457), 937–946. https://doi.org/10.1098/rstb.2005.1645

Samu, D., Seth, A. K., & Nowotny, T. (2014). Influence of Wiring Cost on the Large-Scale Architecture of Human Cortical Connectivity. *PLoS Computational Biology*, *10*(4), e1003557. https://doi.org/10.1371/journal.pcbi.1003557

Saramäki, J., Kivelä, M., Onnela, J. P., Kaski, K., & Kertész, J. (2007). Generalizations of the clustering coefficient to weighted complex networks. *Physical Review E - Statistical, Nonlinear, and Soft Matter Physics*, *75*(2), 027105. https://doi.org/10.1103/PHYSREVE.75.027105/FIGURES/3/MEDIUM

Sassone-Corsi, P. (2012). The Cyclic AMP Pathway. *Cold Spring Harbor Perspectives in Biology*, *4*(12). https://doi.org/10.1101/CSHPERSPECT.A011148

Satterthwaite, T. D., Elliott, M. A., Gerraty, R. T., Ruparel, K., Loughead, J., Calkins, M. E., Eickhoff, S. B., Hakonarson, H., Gur, R. C., Gur, R. E., & Wolf, D. H. (2013). An improved framework for confound regression and filtering for control of motion artifact in the preprocessing of resting-state functional connectivity data. *NeuroImage*, *64*(1), 240–256.

https://doi.org/10.1016/J.NEUROIMAGE.2012.08.052

Saunders, A., Macosko, E. Z., Wysoker, A., Goldman, M., Krienen, F. M., de Rivera, H., Bien, E., Baum, M., Bortolin, L., Wang, S., Goeva, A., Nemesh, J., Kamitaki, N., Brumbaugh, S., Kulp, D., & McCarroll, S. A. (2018). Molecular Diversity and Specializations among the Cells of the Adult Mouse Brain. *Cell*, *174*(4), 1015-1030.e16. https://doi.org/10.1016/J.CELL.2018.07.028

Schaefer, A., Kong, R., Gordon, E. M., Laumann, T. O., Zuo, X.-N., Holmes, A. J., Eickhoff, S. B., & Yeo, B. T. T. (2018). Local-global parcellation of the human cerebral cortex from intrinsic functional connectivity MRI. *Cerebral Cortex*, *28*(9), 3095–3114.

Schaeffer, S., & Iadecola, C. (2021). Revisiting the neurovascular unit. *Nature Neuroscience*, *24*(9), 1198–1209. https://doi.org/10.1038/s41593-021-00904-7

Schönfeld, P., & Reiser, G. (2013). Why does brain metabolism not favor burning of fatty acids to provide energy-Reflections on disadvantages of the use of free fatty acids as fuel for brain. *Journal of Cerebral Blood Flow and Metabolism*, *33*(10), 1493–1499. https://doi.org/10.1038/jcbfm.2013.128

Schroeter, M. S., Charlesworth, P., Kitzbichler, M. G., Paulsen, O., & Bullmore, E. T. (2015). Emergence of rich-club topology and coordinated dynamics in development of hippocampal functional networks in vitro. *J. Neurosci.*, *35*(14), 5459–5470. https://doi.org/10/f68w4d

Seitzman, B. A., Snyder, A. Z., Leuthardt, E. C., & Shimony, J. S. (2019). The State of Resting State Networks. *Topics in Magnetic Resonance Imaging : TMRI*, *28*(4), 189. https://doi.org/10.1097/RMR.0000000000000214

Sengupta, B., Stemmler, M., Laughlin, S. B., & Niven, J. E. (2010). Action potential energy efficiency varies among neuron types in vertebrates and invertebrates. *PLoS Computational Biology*, *6*(7), 35. https://doi.org/10.1371/journal.pcbi.1000840

Severinghaus, J. W. (1979). Simple, accurate equations for human blood O2 dissociation computations. *Journal of Applied Physiology*, *46*(3), 599–602.

Shah, N. J., Arrubla, J., Rajkumar, R., Farrher, E., Mauler, J., Kops, E. R., Tellmann, L., Scheins, J., Boers, F., Dammers, J., Sripad, P., Lerche, C., Langen, K. J., Herzog, H., & Neuner, I. (2017). Multimodal Fingerprints of Resting State Networks as assessed by Simultaneous Trimodal MR-PET-EEG Imaging. *Scientific Reports*, *7*(1), 1–13. https://doi.org/10.1038/s41598-017-05484-w

Shehzad, Z., Kelly, A. M. C., Reiss, P. T., Gee, D. G., Gotimer, K., Uddin, L. Q., Lee, S. H., Margulies, D. S., Roy, A. K., Biswal, B. B., Petkova, E., Castellanos, F. X., & Milham, M. P. (2009). The Resting Brain: Unconstrained yet Reliable. *Cerebral Cortex*, *19*(10), 2209–2229. https://doi.org/10.1093/CERCOR/BHN256

Shen, Y., Zhang, C., Cui, S., Wang, R., Cai, H., Zhao, W., Zhu, J., & Yu, Y. (2022). Transcriptional substrates underlying functional connectivity profiles of subregions within the human sensorimotor cortex. *Human Brain Mapping*.

Shih, C.-T., Sporns, O., Yuan, S.-L., Su, T.-S., Lin, Y.-J., Chuang, C.-C., Wang, T.-Y., Lo, C.-C., Greenspan, R. J., & Chiang, A.-S. (2015). Connectomics-Based Analysis of Information

Flow in the Drosophila Brain. *Current Biology*, *25*(10), 1249–1258. https://doi.org/10.1016/j.cub.2015.03.021

Shiraishi, T., Sakaki, S., & Uehara, Y. (1986). Architecture of the media of the arterial vessels in the dog brain: A scanning electron-microscopic study. *Cell and Tissue Research*, *243*(2), 329–335.

Shirer, W. R., Ryali, S., Rykhlevskaia, E., Menon, V., & Greicius, M. D. (2012). Decoding subject-driven cognitive states with whole-brain connectivity patterns. *Cereb. Cortex*, *22*(1), 158–165. https://doi.org/10/b6cp7m

Shmuel, A., & Leopold, D. A. (2008). Neuronal correlates of spontaneous fluctuations in fMRI signals in monkey visual cortex: Implications for functional connectivity at rest. *Hum. Brain Mapp.*, *29*(7), 751–761. https://doi.org/10/csk373

Shoghi, K. I., & Gropler, R. J. (2015). PET measurements of organ metabolism: the devil is in the details. *Diabetes*, *64*(7), 2332–2334.

Shokri-Kojori, E., Tomasi, D., Alipanahi, B., Wiers, C. E., Wang, G.-J., & Volkow, N. D. (2019). Correspondence between cerebral glucose metabolism and BOLD reveals relative power and cost in human brain. *Nature Communications*, *10*(1), 690. https://doi.org/10.1038/s41467-019-08546-x

Simon, E. J., Dickey, J. L., Hogan, K. A., & Reece, J. B. (2016). *essential biology*. Pearson.

Skattebo, Ø., Calbet, J. A. L., Rud, B., Capelli, C., & Hallén, J. (2020). Contribution of oxygen extraction fraction to maximal oxygen uptake in healthy young men. *Acta Physiologica (Oxford, England)*, *230*(2), 13486. https://doi.org/10.1111/APHA.13486

Smielewski, P., Coles, J. P., Fryer, T. D., Minhas, P. S., Menon, D. K., & Pickard, J. D. (2002). Integrated image analysis solutions for PET datasets in damaged brain. *Journal of Clinical Monitoring and Computing*, *17*(7), 427–440.

Smith, S. P., & Dubes, R. (1980). Stability of a hierarchical clustering. *Pattern Recognition*, *12*(3), 177–187. https://doi.org/10.1016/0031-3203(80)90042-4

Smyth, L. C. D., Rustenhoven, J., Scotter, E. L., Schweder, P., Faull, R. L. M., Park, T. I. H., & Dragunow, M. (2018). Markers for human brain pericytes and smooth muscle cells. *Journal of Chemical Neuroanatomy*, *92*, 48–60. https://doi.org/10.1016/J.JCHEMNEU.2018.06.001

Sokoloff, L. (1977). Tomographic measurement of local cerebral glucose utilization: theory, procedure, and normal values in the conscious and anesthetized albino rat. *J Neurochem*, *28*, 897–916.

Sokoloff, L., Reivich, M., Kennedy, C., Rosiers, M. H. D., Patlak, C. S., Pettigrew, K. D., Sakurada, O., & Shinohara, M. (1977). The [14C]deoxyglucose method for the measurement of local cerebral glucose utilization: theory, procedure, and normal values in the conscious and anesthetized albino rat. *Journal of Neurochemistry*, *28*(5), 897–916. https://doi.org/10.1111/J.1471-4159.1977.TB10649.X

Song, J., Nair, V. A., Gaggl, W., & Prabhakaran, V. (2015). Disrupted brain functional organization in epilepsy revealed by graph theory analysis. *Brain Connectivity*, *5*(5), 276–

283.

Song, M., Zhou, Y., Li, J., Liu, Y., Tian, L., Yu, C., & Jiang, T. (2008). Brain spontaneous functional connectivity and intelligence. *Neuroimage*, *41*(3), 1168–1176. https://doi.org/10/bbcvz7

Sorg, C., Riedl, V., Mühlau, M., Calhoun, V. D., Eichele, T., Läer, L., Drzezga, A., Förstl, H., Kurz, A., & Zimmer, C. (2007). Selective changes of resting-state networks in individuals at risk for Alzheimer's disease. *Proceedings of the National Academy of Sciences*, *104*(47), 18760–18765.

Sporns, O. (2014). Contributions and challenges for network models in cognitive neuroscience. *Nature Neuroscience*, *17*(5), 652–660. https://doi.org/10.1038/nn.3690

Sporns, O., & Betzel, R. F. (2016). Modular Brain Networks. *Annual Review of Psychology*, *67*, 613. https://doi.org/10.1146/ANNUREV-PSYCH-122414-033634

Sporns, O., & Kötter, R. (2004). Motifs in brain networks. *PLoS Biol.*, *2*(11), e369. https://doi.org/10/cztgfv

Sporns, O., Tononi, G., & Kötter, R. (2005). The human connectome: A structural description of the human brain. *PLoS Computational Biology*, *1*(4), 0245–0251. https://doi.org/10.1371/journal.pcbi.0010042

Squire, L., Berg, D., Bloom, F. E., Du Lac, S., Ghosh, A., & Spitzer, N. C. (2012). *Fundamental neuroscience*. Academic press.

Stam, C. J. (2004). Functional connectivity patterns of human magnetoencephalographic recordings: a `small-world'network? *Neuroscience Letters*, *355*(1–2), 25–28. https://doi.org/10/fkbkdr

Stephan, K. E., Kamper, L., Bozkurt, A., Burns, G. A., Young, M. P., & Kötter, R. (2001). Advanced database methodology for the Collation of Connectivity data on the Macaque brain (CoCoMac). *Philos. Trans. R. Soc. Lond. B Biol. Sci.*, *356*(1412), 1159–1186. https://doi.org/10/c755ps

Strang, A., Haynes, O., Cahill, N. D., & Narayan, D. A. (2018). Generalized relationships between characteristic path length, efficiency, clustering coefficients, and density. *Social Network Analysis and Mining 2018 8:1*, *8*(1), 1–6. https://doi.org/10.1007/S13278-018-0492-3

Suárez, L. E., Markello, R. D., Betzel, R. F., & Misic, B. (2020). Linking Structure and Function in Macroscale Brain Networks. In *Trends in Cognitive Sciences* (Vol. 24, Issue 4, pp. 302–315). The Authors. https://doi.org/10.1016/j.tics.2020.01.008

Subramanian, A., Tamayo, P., Mootha, V. K., Mukherjee, S., Ebert, B. L., Gillette, M. A., Paulovich, A., Pomeroy, S. L., Golub, T. R., Lander, E. S., & Mesirov, J. P. (2005). Gene set enrichment analysis: A knowledge-based approach for interpreting genome-wide expression profiles. *Proceedings of the National Academy of Sciences of the United States of America*, *102*(43), 15545–15550. https://doi.org/10.1073/pnas.0506580102

Sweeney, M. D., Montagne, A., Sagare, A. P., Nation, D. A., Schneider, L. S., Chui, H. C., Harrington, M. G., Pa, J., Law, M., Wang, D. J. J., Jacobs, R. E., Doubal, F. N., Ramirez, J.,

Black, S. E., Nedergaard, M., Benveniste, H., Dichgans, M., Iadecola, C., Love, S., … Zlokovic, B. V. (2019). Vascular dysfunction—The disregarded partner of Alzheimer's disease. *Alzheimer's and Dementia*, *15*(1), 158–167. https://doi.org/10.1016/j.jalz.2018.07.222

Szablewski, L. (2021). Brain Glucose Transporters: Role in Pathogenesis and Potential Targets for the Treatment of Alzheimer's Disease. *International Journal of Molecular Sciences*, *22*(15). https://doi.org/10.3390/IJMS22158142

Szarka, A., Bánhegyi, G., & Sümegi, B. (2014). Mitochondria, oxidative stress and aging. *Orvosi Hetilap*, *155*(12), 447–452.

Tak, S., Polimeni, J. R., Wang, D. J. J., Yan, L., & Chen, J. J. (2015). Associations of Resting-State fMRI Functional Connectivity with Flow-BOLD Coupling and Regional Vasculature. *Https://Home.Liebertpub.Com/Brain*, *5*(3), 137–146. https://doi.org/10.1089/BRAIN.2014.0299

Talairach, J. (1988). *Co-planar stereotaxic atlas of the human brain-3-dimensional proportional system. An approach to cerebral imaging*.

Tarca, A. L., Bhatti, G., & Romero, R. (2013). A comparison of gene set analysis methods in terms of sensitivity, prioritization and specificity. *PloS One*, *8*(11), e79217.

Tardif, C. L., Bock, N. A., Villringer, A., & Bazin, P.-L. (2015). MR Morphometry of Myeloarchitecture for In-vivo Cortical Mapping. *Proc. Intl. Soc. Mag. Reson. Med*, *23*, 964.

Tellez-Zenteno, J. F., Pondal-Sordo, M., Matijevic, S., & Wiebe, S. (2004). National and regional prevalence of self-reported epilepsy in Canada. *Epilepsia*, *45*(12), 1623–1629.

Thirion, B., Dodel, S., & Poline, J.-B. (2006). Detection of signal synchronizations in resting-state fMRI datasets. *Neuroimage*, *29*(1), 321–327. https://doi.org/10/d6frzh

Thomas, C., Ye, F. Q., Irfanoglu, M. O., Modi, P., Saleem, K. S., Leopold, D. A., & Pierpaoli, C. (2014). Anatomical accuracy of brain connections derived from diffusion MRI tractography is inherently limited. *Proceedings of the National Academy of Sciences*, *111*(46), 16574–16579. https://doi.org/10.1073/pnas.1405672111

Thomas Yeo, B. T., Krienen, F. M., Sepulcre, J., Sabuncu, M. R., Lashkari, D., Hollinshead, M., Roffman, J. L., Smoller, J. W., Zöllei, L., Polimeni, J. R., Fischl, B., Liu, H., & Buckner, R. L. (2011). The organization of the human cerebral cortex estimated by intrinsic functional connectivity. *Journal of Neurophysiology*, *106*(3), 1125–1165. https://doi.org/10.1152/jn.00338.2011

Thompson, G. J. (2018). Neural and metabolic basis of dynamic resting state fMRI. *NeuroImage*, *180*(September 2017), 448–462. https://doi.org/10.1016/j.neuroimage.2017.09.010

Thompson, G. J., Riedl, V., Grimmer, T., Drzezga, A., Herman, P., & Hyder, F. (2016). The Whole-Brain "global" Signal from Resting State fMRI as a Potential Biomarker of Quantitative State Changes in Glucose Metabolism. *Brain Connectivity*, *6*(6), 435–447. https://doi.org/10.1089/brain.2015.0394

Thorell, S. E., Parry-Jones, A. R., Punter, M., Hurford, R., & Thachil, J. (2015). Cerebral venous

thrombosis-a primer for the haematologist. *Blood Reviews*, *29*(1), 45–50. https://doi.org/10.1016/J.BLRE.2014.09.006

Thrane, V. R., Thrane, A. S., Plog, B. A., Thiyagarajan, M., Iliff, J. J., Deane, R., Nagelhus, E. A., & Nedergaard, M. (2013). Paravascular microcirculation facilitates rapid lipid transport and astrocyte signaling in the brain. *Scientific Reports*, *3*. https://doi.org/10.1038/SREP02582

Thulborn, K. R., du Boulay, G. H., Duchen, L. W., & Radda, G. (1982). A 31P nuclear magnetic resonance in vivo study of cerebral ischaemia in the gerbil. *Journal of Cerebral Blood Flow & Metabolism*, *2*(3), 299–306.

Tiwari, V., Ambadipudi, S., & Patel, A. B. (2013). Glutamatergic and GABAergic TCA cycle and neurotransmitter cycling fluxes in different regions of mouse brain. *Journal of Cerebral Blood Flow & Metabolism*, *33*(10), 1523–1531.

Tomasi, D. G., Shokri-Kojori, E., Wiers, C. E., Kim, S. W., Demiral, Ş. B., Cabrera, E. A., Lindgren, E., Miller, G., Wang, G. J., & Volkow, N. D. (2017). Dynamic brain glucose metabolism identifies anti-correlated cortical-cerebellar networks at rest. *Journal of Cerebral Blood Flow and Metabolism*, *37*(12), 3659–3670. https://doi.org/10.1177/0271678X17708692/ASSET/IMAGES/LARGE/10.1177_0271678X17708692-FIG2.JPEG

Tomasi, D., & Volkow, N. D. (2010). Functional connectivity density mapping. *Proceedings of the National Academy of Sciences of the United States of America*, *107*(21), 9885–9890. https://doi.org/10.1073/pnas.1001414107

Tomasi, D., Wang, G. J., & Volkow, N. D. (2013). Energetic cost of brain functional connectivity. *Proceedings of the National Academy of Sciences of the United States of America*, *110*(33), 13642–13647. https://doi.org/10.1073/pnas.1303346110

Tong, S., Alessio, A. M., & Kinahan, P. E. (2010). Image reconstruction for PET/CT scanners: past achievements and future challenges. *Imaging in Medicine*, *2*(5), 529. https://doi.org/10.2217/IIM.10.49

Tononi, G., Edelman, G. M., & Sporns, O. (1998). Complexity and coherency: integrating information in the brain. *Trends Cogn. Sci.*, *2*(12), 474–484. https://doi.org/10/b464n3

Toolkit, M. (2019). *McConnell Brain Imaging Centre*.

Toosy, A. T., Ciccarelli, O., Parker, G. J. M., Wheeler-Kingshott, C. A. M., Miller, D. H., & Thompson, A. J. (2004). Characterizing function-structure relationships in the human visual system with functional MRI and diffusion tensor imaging. *Neuroimage*, *21*(4), 1452–1463. https://doi.org/10/bwj8wq

Toro, R., Fox, P. T., & Paus, T. (2008). Functional Coactivation Map of the Human Brain. *Cerebral Cortex*, *18*(11), 2553–2559. https://doi.org/10.1093/cercor/bhn014

Toussaint, P. J., Maiz, S., Coynel, D., Doyon, J., Messé, A., de Souza, L. C., Sarazin, M., Perlbarg, V., Habert, M. O., & Benali, H. (2014). Characteristics of the default mode functional connectivity in normal ageing and Alzheimer's disease using resting state fMRI with a combined approach of entropy-based and graph theoretical measurements. *NeuroImage*, *101*, 778–786. https://doi.org/10.1016/j.neuroimage.2014.08.003

Traag, V. A., Waltman, L., & van Eck, N. J. (2019). From Louvain to Leiden: guaranteeing well-connected communities. *Sci. Rep.*, *9*(1), 5233. https://doi.org/10/gfxg2v

Tracey, T. J., Steyn, F. J., Wolvetang, E. J., & Ngo, S. T. (2018). Neuronal Lipid Metabolism: Multiple Pathways Driving Functional Outcomes in Health and Disease. *Frontiers in Molecular Neuroscience*, *11*. https://doi.org/10.3389/FNMOL.2018.00010

Turner, R., Le Bihan, D., Maier, J., Vavrek, R., Hedges, L. K., & Pekar, J. (1990). Echo-planar imaging of intravoxel incoherent motion. *Radiology*, *177*(2), 407–414. https://doi.org/10.1148/radiology.177.2.2217777

Tustison, N. J., Avants, B. B., Cook, P. A., Zheng, Y., Egan, A., Yushkevich, P. A., & Gee, J. C. (2010). N4ITK: improved N3 bias correction. *IEEE Transactions on Medical Imaging*, *29*(6), 1310–1320. https://doi.org/10.1109/TMI.2010.2046908

Tzourio-Mazoyer, N., Landeau, B., Papathanassiou, D., Crivello, F., Etard, O., Delcroix, N., Mazoyer, B., & Joliot, M. (2002). Automated anatomical labeling of activations in SPM using a macroscopic anatomical parcellation of the MNI MRI single-subject brain. *NeuroImage*, *15*(1), 273–289. https://doi.org/10.1006/nimg.2001.0978

Uemura, M. T., Maki, T., Ihara, M., Lee, V. M. Y., & Trojanowski, J. Q. (2020). Brain Microvascular Pericytes in Vascular Cognitive Impairment and Dementia. *Frontiers in Aging Neuroscience*, *12*, 80. https://doi.org/10.3389/FNAGI.2020.00080/BIBTEX

Uludağ, K., & Blinder, P. (2018). Linking brain vascular physiology to hemodynamic response in ultra-high field MRI. *NeuroImage*, *168*(December 2016), 279–295. https://doi.org/10.1016/j.neuroimage.2017.02.063

Urchs, S., Armoza, J., Moreau, C., Benhajali, Y., St-Aubin, J., Orban, P., & Bellec, P. (2019). MIST: A multi-resolution parcellation of functional brain networks. *MNI Open Res.*, *1*, 3. https://doi.org/10.12688/mniopenres.12767.2

Vaishnavi, S. N., Vlassenko, A. G., Rundle, M. M., Snyder, A. Z., Mintun, M. A., & Raichle, M. E. (2010). Regional aerobic glycolysis in the human brain. *Proceedings of the National Academy of Sciences of the United States of America*, *107*(41), 17757–17762. https://doi.org/10.1073/pnas.1010459107

van de Ven, V. G., Formisano, E., Prvulovic, D., Roeder, C. H., & Linden, D. E. J. (2004). Functional connectivity as revealed by spatial independent component analysis of fMRI measurements during rest. *Human Brain Mapping*, *22*(3), 165–178. https://doi.org/10.1002/hbm.20022

van den Heuvel, M., Mandl, R., & Pol, H. H. (2008). Normalized Cut Group Clustering of Resting-State fMRI Data. *PLOS ONE*, *3*(4), e2001. https://doi.org/10.1371/JOURNAL.PONE.0002001

Van Den Heuvel, M. P., Mandl, R. C. W., Stam, C. J., Kahn, R. S., & Hulshoff Pol, H. E. (2010). Aberrant frontal and temporal complex network structure in schizophrenia: A graph theoretical analysis. *Journal of Neuroscience*, *30*(47), 15915–15926. https://doi.org/10.1523/JNEUROSCI.2874-10.2010

van den Heuvel, M. P., & Sporns, O. (2013). Network hubs in the human brain. In *Trends in*

Cognitive Sciences (Vol. 17, Issue 12, pp. 683–696). https://doi.org/10.1016/j.tics.2013.09.012

Van Den Heuvel, M. P., & Sporns, O. (2011). Rich-club organization of the human connectome. *Journal of Neuroscience*, *31*(44), 15775–15786.

van den Heuvel, M. P., Stam, C. J., Boersma, M., & Hulshoff Pol, H. E. (2008). Small-world and scale-free organization of voxel-based resting-state functional connectivity in the human brain. *NeuroImage*, *43*(3), 528–539. https://doi.org/10.1016/j.neuroimage.2008.08.010

Van Den Heuvel, M. P., Stam, C. J., Kahn, R. S., & Hulshoff Pol, H. E. (2009). Efficiency of functional brain networks and intellectual performance. *Journal of Neuroscience*, *29*(23), 7619–7624. https://doi.org/10.1523/JNEUROSCI.1443-09.2009

van Diessen, E., Diederen, S. J. H., Braun, K. P. J., Jansen, F. E., & Stam, C. J. (2013). Functional and structural brain networks in epilepsy: what have we learned? *Epilepsia*, *54*(11), 1855–1865.

Vanlandewijck, M., He, L., Mäe, M. A., Andrae, J., Ando, K., Del Gaudio, F., Nahar, K., Lebouvier, T., Laviña, B., Gouveia, L., Sun, Y., Raschperger, E., Räsänen, M., Zarb, Y., Mochizuki, N., Keller, A., Lendahl, U., & Betsholtz, C. (2018). A molecular atlas of cell types and zonation in the brain vasculature. *Nature*, *554*(7693), 475–480. https://doi.org/10.1038/nature25739

Varela, F., Lachaux, J.-P., Rodriguez, E., & Martinerie, J. (2001). The brainweb: Phase synchronization and large-scale integration. *Nature Reviews Neuroscience*, *2*(4), 229–239. https://doi.org/10.1038/35067550

Vaughan, D. N., Rayner, G., Tailby, C., & Jackson, G. D. (2016). MRI-negative temporal lobe epilepsy: a network disorder of neocortical connectivity. *Neurology*, *87*(18), 1934–1942.

Vavilala, M. S., Lee, L. A., & Lam, A. M. (2002). Cerebral blood flow and vascular physiology. *Anesthesiology Clinics of North America*, *20*(2), 247–264.

Vazquez, A. L., Fukuda, M., & Kim, S. G. (2018). Inhibitory Neuron Activity Contributions to Hemodynamic Responses and Metabolic Load Examined Using an Inhibitory Optogenetic Mouse Model. *Cerebral Cortex*, *28*(11), 4105–4119. https://doi.org/10.1093/CERCOR/BHY225

Venkat, P., Chopp, M., & Chen, J. (2016). New insights into coupling and uncoupling of cerebral blood flow and metabolism in the brain. *Croatian Medical Journal*, *57*(3), 223–228. https://doi.org/10.3325/cmj.2016.57.223

Ventura-Antunes, L., Dasgupta, O. M., & Herculano-Houzel, S. (2022). Resting Rates of Blood Flow and Glucose Use per Neuron Are Proportional to Number of Endothelial Cells Available per Neuron Across Sites in the Rat Brain. *Frontiers in Integrative Neuroscience*, *0*, 30. https://doi.org/10.3389/FNINT.2022.821850

Verbree, J., Bronzwaer, A.-S. G. T., Ghariq, E., Versluis, M. J., Daemen, M. J. A. P., van Buchem, M. A., Dahan, A., Van Lieshout, J. J., & van Osch, M. J. P. (2014). Assessment of middle cerebral artery diameter during hypocapnia and hypercapnia in humans using ultra-high-field MRI. *Journal of Applied Physiology*, *117*(10), 1084–1089.

Verger, A., Doyen, M., Campion, J. Y., & Guedj, E. (2021). The pons as reference region for intensity normalization in semi-quantitative analysis of brain 18FDG PET: application to metabolic changes related to ageing in conventional and digital control databases. *EJNMMI Research*, *11*(1). https://doi.org/10.1186/s13550-021-00771-0

Verkhratsky, A., & Nedergaard, M. (2018). Physiology of Astroglia. *Physiological Reviews*, *98*(1), 239. https://doi.org/10.1152/PHYSREV.00042.2016

Vértes, P. E., Rittman, T., Whitaker, K. J., Romero-Garcia, R., Váša, F., Kitzbichler, M. G., Wagstyl, K., Fonagy, P., Dolan, R. J., Jones, P. B., Goodyer, I. M., & Bullmore, E. T. (2016). Gene transcription profiles associated with inter-modular hubs and connection distance in human functional magnetic resonance imaging networks. *Philosophical Transactions of the Royal Society B: Biological Sciences*, *371*(1705), 20150362. https://doi.org/10.1098/rstb.2015.0362

Vincent, R. D., Neelin, P., Khalili-Mahani, N., Janke, A. L., Fonov, V. S., Robbins, S. M., Baghdadi, L., Lerch, J., Sled, J. G., Adalat, R., Macdonald, D., Zijdenbos, A. P., Collins, D. L., & Evans, A. C. (2016). MINC 2.0: A flexible format for multi-modal images. *Frontiers in Neuroinformatics*, *10*(AUG), 35. https://doi.org/10.3389/FNINF.2016.00035/BIBTEX

Voigt, K., Liang, E. X., Misic, B., Ward, P. G. D., Egan, G. F., & Jamadar, S. D. (2022). Metabolic and functional connectivity provide unique and complementary insights into cognition-connectome relationships. *Cerebral Cortex*. https://doi.org/10.1093/cercor/bhac150

Vovenko, E. (1999). Distribution of oxygen tension on the surface of arterioles, capillaries and venules of brain cortex and in tissue in normoxia: an experimental study on rats. *Pflügers Archiv*, *437*(4), 617–623.

Wagner, P. D. (2008). Systemic oxygen transport and utilization. *Journal of Breath Research*, *2*(2). https://doi.org/10.1088/1752-7155/2/2/024001

Wang, G. Z., Belgard, T. G., Mao, D., Chen, L., Berto, S., Preuss, T. M., Lu, H., Geschwind, D. H., & Konopka, G. (2015). Correspondence between Resting-State Activity and Brain Gene Expression. *Neuron*, *88*(4), 659–666. https://doi.org/10.1016/J.NEURON.2015.10.022

Wang, J., Licht, D. J., Jahng, G., Liu, C., Rubin, J. T., Haselgrove, J., Zimmerman, R. A., & Detre, J. A. (2003). Pediatric perfusion imaging using pulsed arterial spin labeling. *Journal of Magnetic Resonance Imaging: An Official Journal of the International Society for Magnetic Resonance in Medicine*, *18*(4), 404–413.

Wang, J., Qiu, S., Xu, Y., Liu, Z., Wen, X., Hu, X., Zhang, R., Li, M., Wang, W., & Huang, R. (2014). Graph theoretical analysis reveals disrupted topological properties of whole brain functional networks in temporal lobe epilepsy. *Clinical Neurophysiology*, *125*(9), 1744–1756.

Wang, Y. (2022). *Reorganization of functional hubs in sleep and in epilepsy*. Concordia University.

Wang, Y., Royer, J., Park, B., Vos de Wael, R., Larivière, S., Tavakol, S., Rodriguez-Cruces, R., Paquola, C., Hong, S.-J., & Margulies, D. S. (2022). Long-range functional connections mirror and link microarchitectural and cognitive hierarchies in the human brain. *Cerebral*

Cortex.

Wardlaw, J. M., Benveniste, H., Nedergaard, M., Zlokovic, B. V, Mestre, H., Lee, H., Doubal, F. N., Brown, R., Ramirez, J., & MacIntosh, B. J. (2020). Perivascular spaces in the brain: anatomy, physiology and pathology. *Nature Reviews Neurology*, *16*(3), 137–153.

Watts, D. J., & Strogatz, S. H. (1998). Collective dynamics of 'small-world' networks. *Nature*, *393*(6684), 440–442. https://doi.org/10.1038/30918

Weissenbacher, A., Kasess, C., Gerstl, F., Lanzenberger, R., Moser, E., & Windischberger, C. (2009). Correlations and anticorrelations in resting-state functional connectivity MRI: A quantitative comparison of preprocessing strategies. *NeuroImage*, *47*(4), 1408–1416. https://doi.org/10.1016/j.neuroimage.2009.05.005

Wernicke, C. (1970). The aphasic symptom-complex: a psychological study on an anatomical basis. *Archives of Neurology*, *22*(3), 280–282. https://doi.org/10/dqdrmp

Wesolowski, R., Blockley, N. P., Driver, I. D., Francis, S. T., & Gowland, P. A. (2019). Coupling between cerebral blood flow and cerebral blood volume: Contributions of different vascular compartments. *Nmr in Biomedicine*, *32*(3). https://doi.org/10.1002/NBM.4061

White, E. L. (1989). General Organization of the Cerebral Cortex. *Cortical Circuits*, 5–18. https://doi.org/10.1007/978-1-4684-8721-3_1

Whitfield-Gabrieli, S. (2009). Thermenos HW Milanovic S, Tsuang MT, Faraone SV McCarley RW et al. Hyperactivity and hyperconnectivity of the default network in schizophrenia and in first-degree relatives of persons with schizophrenia. *Proc Natl Acad Sci USA*, *106*(4), 1279–1284.

Wiebe, S. (2000). Epidemiology of temporal lobe epilepsy. *Canadian Journal of Neurological Sciences*, *27*(S1), S6–S10.

Winkler, E. A., Bell, R. D., & Zlokovic, B. V. (2011). Central nervous system pericytes in health and disease. *Nature Neuroscience 2011 14:11*, *14*(11), 1398–1405. https://doi.org/10.1038/nn.2946

Wise, R. G., Harris, A. D., Stone, A. J., & Murphy, K. (2013). Measurement of OEF and absolute CMRO2: MRI-based methods using interleaved and combined hypercapnia and hyperoxia. *NeuroImage*, *83*, 135–147. https://doi.org/10.1016/j.neuroimage.2013.06.008

Wold, S., Ruhe, A., Wold, H., & Dunn WJ, I. (1984). The collinearity problem in linear regression. The partial least squares (PLS) approach to generalized inverses. *SIAM Journal on Scientific and Statistical Computing*, *5*(3), 735–743.

Woolrich, M. W., Jbabdi, S., Patenaude, B., Chappell, M., Makni, S., Behrens, T., Beckmann, C., Jenkinson, M., & Smith, S. M. (2009). Bayesian analysis of neuroimaging data in FSL. *NeuroImage*, *45*(1), S173–S186. https://doi.org/10.1016/J.NEUROIMAGE.2008.10.055

Wu, T., Giudice, J. S., Alshareef, A., & Panzer, M. B. (2022). Modeling mesoscale anatomical structures in macroscale brain finite element models. In *Multiscale Biomechanical Modeling of the Brain* (pp. 103–118). Elsevier. https://doi.org/10.1016/B978-0-12-818144-7.00008-6

Xu, F., Ge, Y., & Lu, H. (2009). Noninvasive quantification of whole-brain cerebral metabolic rate of oxygen (CMRO2) by MRI. *Magnetic Resonance in Medicine*, *62*(1), 141–148. https://doi.org/10.1002/mrm.21994

Xu, J., Potenza, M. N., Calhoun, V. D., Zhang, R., Yip, S. W., Wall, J. T., Pearlson, G. D., Worhunsky, P. D., Garrison, K. A., & Moran, J. M. (2016). Large-scale functional network overlap is a general property of brain functional organization: Reconciling inconsistent fMRI findings from general-linear-model-based analyses. *Neuroscience & Biobehavioral Reviews*, *71*, 83–100.

y Cajal, S. R. (1995). *Histology of the Nervous System of Man and Vertebrates: General principles, spinal cord, spinal ganglia, medulia & pons* (Vol. 1). Oxford University Press.

Yablonskiy, D. A., Ackerman, J. J. H., & Raichle, M. E. (2000). Coupling between changes in human brain temperature and oxidative metabolism during prolonged visual stimulation. *Proceedings of the National Academy of Sciences*, *97*(13), 7603–7608. https://doi.org/10.1073/PNAS.97.13.7603

Yang, L. (2018). Neuronal cAMP/PKA Signaling and Energy Homeostasis. *Advances in Experimental Medicine and Biology*, *1090*, 31–48. https://doi.org/10.1007/978-981-13-1286-1_3

Yang, T., Guo, R., & Zhang, F. (2019). Brain perivascular macrophages: Recent advances and implications in health and diseases. *CNS Neuroscience & Therapeutics*, *25*(12), 1318–1328. https://doi.org/10.1111/CNS.13263

Yang, Z., Zuo, X.-N., McMahon, K. L., Craddock, R. C., Kelly, C., de Zubicaray, G. I., Hickie, I., Bandettini, P. A., Castellanos, F. X., & Milham, M. P. (2016). Genetic and environmental contributions to functional connectivity architecture of the human brain. *Cerebral Cortex*, *26*(5), 2341–2352.

Yellen, G. (2018). Fueling thought: Management of glycolysis and oxidative phosphorylation in neuronal metabolism. *Journal of Cell Biology*, *217*(7), 2235–2246.

Yeo, B. T. T., Krienen, F. M., Chee, M. W. L., & Buckner, R. L. (2014). Estimates of segregation and overlap of functional connectivity networks in the human cerebral cortex. *NeuroImage*, *88*, 212–227. https://doi.org/10.1016/j.neuroimage.2013.10.046

Young, K., Wise, J., DeSaix, P., Kruse, D., Poe, B., Johnson, E., Johnson, J., Korol, O., Betts, J., & Womble, M. (2016). *OpenStax Anatomy and Physiology*.

Yu, C., & Yao, W. (2014). Robust Linear Regression: A Review and Comparison. *Communications in Statistics: Simulation and Computation*, *46*(8), 6261–6282. https://doi.org/10.48550/arxiv.1404.6274

Zeisel, A., M͡oz-Manchado, A. B., Codeluppi, S., Lönnerberg, P., Manno, G. La, Juréus, A., Marques, S., Munguba, H., He, L., Betsholtz, C., Rolny, C., Castelo-Branco, G., Hjerling-Leffler, J., & Linnarsson, S. (2015). Cell types in the mouse cortex and hippocampus revealed by single-cell RNA-seq. *Science*, *347*(6226), 1138–1142. https://doi.org/10.1126/SCIENCE.AAA1934/SUPPL_FILE/ZEISEL-SM.PDF

Zeki, S., & Shipp, S. (1988). The functional logic of cortical connections. *Nature*, *335*(6188), 311–

317. https://doi.org/10/cng8z8

Zenker, D., Begley, D., Bratzke, H., Rübsamen-Waigmann, H., & von Briesen, H. (2003). Human blood-derived macrophages enhance barrier function of cultured primary bovine and human brain capillary endothelial cells. *The Journal of Physiology*, *551*(3), 1023–1032.

Zhang, B., & Horvath, S. (2005). A general framework for weighted gene co-expression network analysis. *Statistical Applications in Genetics and Molecular Biology*, *4*(1). https://doi.org/10.2202/1544-6115.1128/MACHINEREADABLECITATION/RIS

Zhang, H., Roman, R. J., & Fan, F. (2022). Hippocampus is more susceptible to hypoxic injury: has the Rosetta Stone of regional variation in neurovascular coupling been deciphered? *GeroScience*, *44*(1), 127–130. https://doi.org/10.1007/s11357-021-00449-4

Zhang, J. (2019). *Secrets of the Brain: An Introduction to the Brain Anatomical Structure and Biological Function*. 1–34. https://doi.org/https://doi.org/10.48550/arXiv.1906.03314

Zhang, J., & Liu, Q. (2015). Cholesterol metabolism and homeostasis in the brain. *Protein & Cell*, *6*(4), 254–264.

Zhang, K., Herzog, H., Mauler, J., Filss, C., Okell, T. W., Kops, E. R., Tellmann, L., Fischer, T., Brocke, B., & Sturm, W. (2014). Comparison of cerebral blood flow acquired by simultaneous [15O] water positron emission tomography and arterial spin labeling magnetic resonance imaging. *Journal of Cerebral Blood Flow & Metabolism*, *34*(8), 1373–1380.

Zhang, W., Muravina, V., Azencott, R., Chu, Z. D., & Paldino, M. J. (2018). Mutual information better quantifies brain network architecture in children with epilepsy. *Computational and Mathematical Methods in Medicine*, *2018*. https://doi.org/10.1155/2018/6142898

Zhang, Y., Brady, M., & Smith, S. (2001). Segmentation of brain MR images through a hidden Markov random field model and the expectation-maximization algorithm. *IEEE Transactions on Medical Imaging*, *20*(1), 45–57. https://doi.org/10.1109/42.906424

Zhang, Y., Sloan, S. A., Clarke, L. E., Caneda, C., Plaza, C. A., Blumenthal, P. D., Vogel, H., Steinberg, G. K., Edwards, M. S. B., Li, G., Duncan, J. A., Cheshier, S. H., Shuer, L. M., Chang, E. F., Grant, G. A., Gephart, M. G. H., & Barres, B. A. (2016). Purification and Characterization of Progenitor and Mature Human Astrocytes Reveals Transcriptional and Functional Differences with Mouse. *Neuron*, *89*(1), 37–53. https://doi.org/10.1016/J.NEURON.2015.11.013

Zhao, F., Jin, T., Wang, P., Hu, X., & Kim, S. (2007). Sources of phase changes in BOLD and CBV-weighted fMRI. *Magnetic Resonance in Medicine: An Official Journal of the International Society for Magnetic Resonance in Medicine*, *57*(3), 520–527.

Zhao, Z., Nelson, A. R., Betsholtz, C., & Zlokovic, B. V. (2015). Establishment and dysfunction of the blood-brain barrier. *Cell*, *163*(5), 1064–1078.

Zhong, C., Deng, Y., Hu, W., Qiao, J., Zhang, L., & Zhang, J. (2015). A review of electrolyte materials and compositions for electrochemical supercapacitors. *Chemical Society Reviews*, *44*(21), 7484–7539. https://doi.org/10.1039/C5CS00303B

Zhong, Y., Wang, H., Lu, G., Zhang, Z., Jiao, Q., & Liu, Y. (2009). Detecting functional

connectivity in fMRI using PCA and regression analysis. *Brain Topogr.*, *22*(2), 134–144. https://doi.org/10/fk3t6p

Zhou, Y., Zhou, B., Pache, L., Chang, M., Khodabakhshi, A. H., Tanaseichuk, O., Benner, C., & Chanda, S. K. (2019). Metascape provides a biologist-oriented resource for the analysis of systems-level datasets. *Nature Communications*, *10*(1). https://doi.org/10.1038/S41467-019-09234-6

Zhu, X.-H., & Chen, W. (2017). In vivo 17O MRS imaging–Quantitative assessment of regional oxygen consumption and perfusion rates in living brain. *Analytical Biochemistry*, *529*, 171–178.

Zhuge, Y., Zhang, J., Qian, F., Wen, Z., Niu, C., Xu, K., Ji, H., Rong, X., Chu, M., & Jia, C. (2020). Role of smooth muscle cells in cardiovascular disease. *International Journal of Biological Sciences*, *16*(14), 2741–2751. https://doi.org/10.7150/IJBS.49871

Zilles, K. (2018). Brodmann: a pioneer of human brain mapping—his impact on concepts of cortical organization. *Brain*, *141*(11), 3262. https://doi.org/10.1093/BRAIN/AWY273

Zlokovic, B. V. (2011). Neurovascular pathways to neurodegeneration in Alzheimer's disease and other disorders. *Nature Reviews Neuroscience 2011 12:12*, *12*(12), 723–738. https://doi.org/10.1038/nrn3114

Zlokovic, B. V. (2008). The blood-brain barrier in health and chronic neurodegenerative disorders. *Neuron*, *57*(2), 178–201.

Zucca, R., Arsiwalla, X. D., Le, H., Rubinov, M., Gurguí, A., & Verschure, P. (2019). The Degree Distribution of Human Brain Functional Connectivity is Generalized Pareto: A Multi-Scale Analysis. *BioRxiv*. https://doi.org/10.1101/840066

Zuo, X.-N., Ehmke, R., Mennes, M., Imperati, D., Castellanos, F. X., Sporns, O., & Milham, M. P. (2012). Network centrality in the human functional connectome. *Cerebral Cortex*, *22*(8), 1862–1875.